63 /2/ 2025

JOURNAL OF THEORETICAL AND APPLIED MECHANICS

WARSAW 2025, QUARTERLY, VOLUME 63, ISSN 1429-2955 eISSN 2543-6309

POLISH SOCIETY OF THEORETICAL AND APPLIED MECHANICS

POLISH SOCIETY OF THEORETICAL AND APPLIED MECHANICS

JOURNAL OF THEORETICAL AND APPLIED MECHANICS

Vol. 63 • No. 2

Quarterly

WARSAW 2025

JOURNAL OF THEORETICAL AND APPLIED MECHANICS
(until 1997 Mechanika Teoretyczna i Stosowana, ISSN 0079-3701)

Beginning with Vol. 45, No. 1, 2007, *Journal of Theoretical and Applied Mechanics* (JTAM) has been selected for coverage in Thomson Reuters products and custom information services. Now it is indexed and abstracted in the following:

- **Science Citation Index Expanded** (also known as SciSearch®)
- **Journal Citation Reports/Science Edition**

Editorial Office

Al. Armii Ludowej 16, room 650; 00-637 Warsaw, Poland
e-mail: jtam@ptmts.org.pl
www.jtam.pl

JOURNAL OF THEORETICAL
AND APPLIED MECHANICS
63, 2, pp. 217–226, Warsaw 2025
https://doi.org/10.15632/jtam-pl/194877

NUMERICAL STUDY ABOUT TENSION PROPERTIES OF NOVEL HIERARCHICAL REENTRANT HONEYCOMB STRUCTURE

Dongquan WU[1*], Zhenyi XU[1], Zhuo YUAN[1], Yupeng LI[1], Zixiang LIU[1], Zhiqiang ZHANG[2]

[1] *Sino-European Institute of Aviation Engineering, Civil Aviation University of China, Tianjin, China*
[2] *Institute of Aviation Engineering, Civil Aviation University of China, Tianjin, China*
*corresponding author, *dqwu@cauc.edu.cn*

This study designed and analyzed three novel hierarchical reentrant honeycomb structures, composed of nested subunits with varying Poisson's ratio characteristics, to evaluate their tensile performance through simulations and experiments. The results show that all three structures exhibit the negative Poisson's ratio under tensile loading in both axial directions, with the subunits' Poisson's ratios influencing the overall Poisson's ratio of the structure. The CH structure demonstrates higher stiffness under Y-axis loading, while the SRH structure exhibits higher stiffness under X-axis loading. In terms of deformation, the CH structure shows greater flexibility compared to the other two. The SRH structure consistently maintains an intermediate tensile strength among the three.

Keywords: reentrant structure; hierarchical; Poisson's ratio; tension performance.

Nomenclature of abbreviation

RH – novel hierarchical reentrant honeycomb structures with reentran honeycomb subunit,
SRH – novel hierarchical reentrant honeycomb structures with semi-reentrant honeycomb subunit,
CH – novel hierarchical reentrant honeycomb structures with classic hexagonal honeycomb subunit.

1. Introduction

The rapid development of aerospace (Heo *et al.*, 2013; Gong *et al.*, 2022; Solak *et al.*, 2023) and military industries has driven a significant demand for lightweight materials with superior mechanical properties (Wang, 2019). Among these, various honeycomb structures, which have shown great potential, have been extensively studied and applied. These structures can be designed to exhibit excellent performance in stiffness, strength, impact resistance, and energy absorption. It is well known that the key to achieving such outstanding mechanical behavior lies in the design of the structural topology. Based on this, researchers have developed honeycomb structures with various geometries, including hexagonal, Kagome (Liu *et al.*, 2021), circular (Ahmed & Xue, 2019), and triangular shapes.

Unlike traditional hexagonal honeycomb structures, reentrant honeycomb structures are characterized by inward-curved cell designs on both sides, providing excellent shear resistance and energy absorption properties. Additionally, reentrant honeycomb structures exhibit the unique property of the negative Poisson's ratio. This means that under axial tensile loading, the cross-section of the reentrant honeycomb structure expands, while under axial compression, the cross-section contracts. This characteristic endows reentrant honeycomb structures with significantly better macroscopic mechanical properties compared to traditional lattice structures (Photiou *et al.*, 2016) or foam materials (Köhnen *et al.*, 2018), such as superior dent resistance during elastic deformation (Patel *et al.*, 2018), higher shear modulus (Ju & Summers, 2011),

enhanced dynamic dent resistance during plastic yield (Hu *et al.*, 2019), and greater energy absorption capacity (Xiao *et al.*, 2019a; Jin *et al.*, 2016). Previous studies have explored these properties in depth: Boldrin *et al.* (2016) discussed the dynamic behavior of negative Poisson's ratio honeycombs and found that specific gradient topologies are highly sensitive to dynamic performance. Xiao *et al.* (2019b), through experimental analysis, examined the compressive behavior of reentrant honeycombs and identified V and I deformation modes. Liu *et al.* (2016) investigated the energy absorption of reentrant honeycombs, claiming that due to early densification, reentrant honeycombs absorb more energy than traditional honeycombs under the same compressive strain. Lee *et al.* (2019) elaborated on the crushing performance of reentrant honeycomb structures, including crushing stress and energy absorption.

However, all the design concepts mentioned above are limited to single-layer honeycomb structures, which have low in-plane stiffness and fail to meet the increasingly stringent requirements of engineering applications, thus limiting their potential use. Research by Chen *et al.* (2018) has shown that complex hierarchical structures are key to achieving high specific stiffness, specific strength, and energy absorption efficiency. This design is inspired by various natural organisms, such as bones (Liu *et al.*, 2022), shells, and bamboo (Reznikov *et al.*, 2018), which exhibit hierarchical structures at multiple scales, with each scale corresponding to the next. These biological materials achieve exceptional mechanical properties through their complex layered structures. The introduction of hierarchical structures can enhance the strength, toughness, and durability of materials. The interaction between layers allows the material to better distribute and absorb stress under external forces, thereby improving the overall mechanical performance of the structure.

While previous studies have extensively explored hierarchical and reentrant honeycomb structures, a significant research gap remains in understanding the tensile performance of novel hierarchical reentrant honeycomb structures. This study developed three new types of hierarchical reentrant honeycomb structures by incorporating honeycomb subunits with different Poisson's ratios and replacing the traditional cell walls with a double-layer nested configuration. Experimental and simulation methods were employed to investigate the tensile performance of these structures in two directions, with numerical comparisons made for elastic modulus, Poisson's ratio, fracture strain, and tensile strength. The deformation characteristics were also analyzed and summarized. The results indicate that these newly designed honeycomb structures effectively utilize hierarchical configurations to enhance the dynamic tensile behavior of honeycomb structures. This study offers insights and references for designing multifunctional lightweight structures with tailored Poisson's ratios.

2. Structure design and method

In this study, reentrant honeycomb structures with a negative Poisson's ratio, semi-reentrant honeycomb structures with the zero Poisson's ratio, and classical hexagonal honeycomb structures with the positive Poisson's ratio were employed as subunits. Unlike traditional hierarchical honeycomb structures, a novel double-layer nested configuration was introduced to replace the conventional cell walls of reentrant honeycomb structures. The detailed structural design is shown in Fig. 1. In order to facilitate the comparison and analysis of the subsequent simulation results, the dimensions of the three novel hierarchical reentrant honeycomb structures designed in this study are controlled at $c = 142\,\text{mm}$ long and $b = 87\,\text{mm}$ wide, and the cell wall thickness of all three cellular metamaterials $t = 0.6\,\text{mm}$ and a thickness of this substructure is $5\,\text{mm}$. Meanwhile, the detailed geometrical definition for the dimensions of the substructure is carried out in this study. The reentrant honeycomb subunit with negative Poisson's ratio (Shukla & Behera, 2022), the reentrant honeycomb substructure designed in this study has a wall length $h = 4\,\text{mm}$, $l = 1.8\,\text{mm}$, a turning angle $\beta = 33.69°$; and for the semi-reentrant honeycomb subunit with zero Poisson's ratio (Xiao *et al.*, 2019b; Ingrole *et al.*, 2017) designed in this study

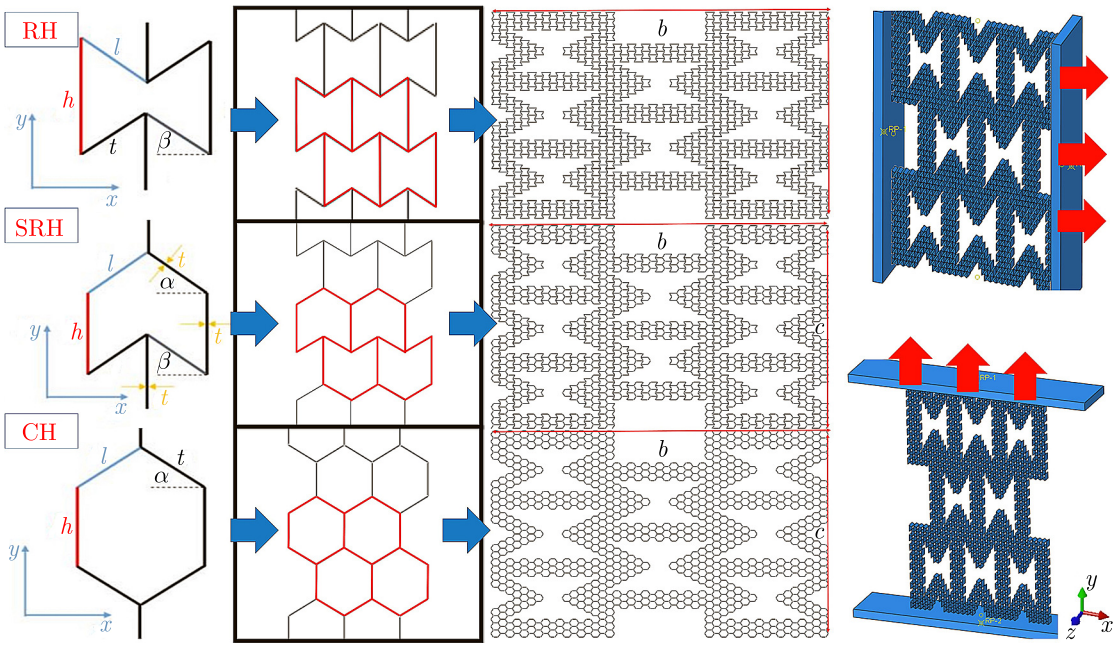

Fig. 1. Three novel hierarchical reentrant honeycomb structures and simulation.

has a wall length $h = 3\,\text{mm}$, $l = 1.8\,\text{mm}$, a turning angle $\alpha = \beta = 33.69°$. For the classical hexagonal honeycomb subunit which is positive Poisson's ratio (Xu *et al.*, 2024), the honeycomb wall length $h = 2\,\text{mm}$, $l = 1.8\,\text{mm}$, a turning angle $\alpha = 33.69°$.

This paper evaluates the tensile performance of three novel hierarchical reentrant honeycomb structures using the finite element analysis and tensile simulations conducted with Abaqus 2023. Additionally, tensile experiments were performed on 3D-printed samples produced with fused deposition modeling (FDM) technology to comprehensively assess the tensile properties of these structures. The tensile performance was examined in two directions.

In the finite element simulations, rigid plates were attached to both sides of the honeycomb structures. Axial displacement boundary conditions corresponding to the tensile direction were applied on one side, while fixed support boundary conditions were set on the opposite side. The simulation used a "dynamic/explicit" analysis step, with a friction coefficient of 0.3 applied tangentially, and a "hard contact", general contact setting applied in the normal direction. The honeycomb structures were meshed using S4R (four-node shell) elements with a mesh size of 2, while the plates were meshed using C3D8R (eight-node linear hexahedral) elements with a mesh size of 4. In total, the honeycomb structures consisted of approximately 90.000 mesh elements.

For the experimental analysis, the study included the hierarchical reentrant honeycomb structure designed by scholar Lian, referred to as RH1, to compare mechanical properties. To maintain scientific validity, the overall configuration and wall thickness were kept constant, with minor adjustments to the structure's dimensions to match the frame length of the structures designed in this study. All samples were fabricated using fused deposition modeling (FDM) 3D printing technology under consistent parameters: a printing temperature of 210 °C, a bed temperature of 40 °C, and a layer orientation angle of 0°. To analyze deformation behavior during tensile testing, a digital image correlation (DIC) system was used to capture precise deformation morphologies at specific tensile strains, with images recorded every 4 seconds. Tensile tests were conducted using a universal testing machine at a constant rate of 2 mm/min, as shown in Fig. 2.

The material used in this simulation analysis is polylactic acid (PLA), a biodegradable polymer prepared from renewable resources. The specific material property parameters used in the simulation are shown in Table 1.

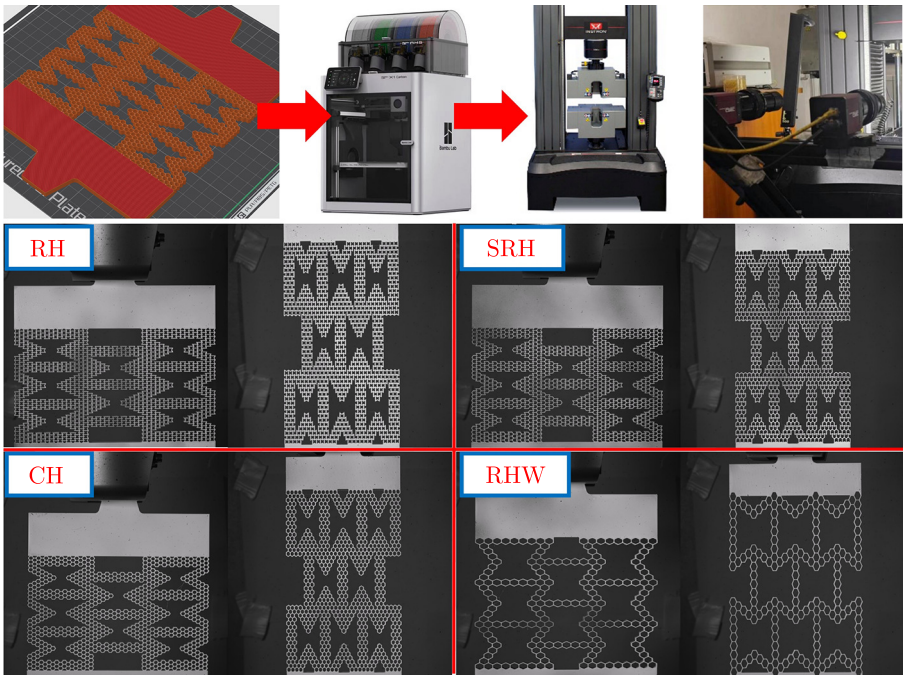

Fig. 2. Experiments on 3D printed solids under FDM

Table 1. Mechanical properties of PLA.

Materials	Elastic modulus [MPa]	Yield strength [MPa]	Fracture strain	Poison's ratio	Mass density ρ_A [kg/m^3]
PLA	2500	39.14	0.18	0.3	1378

3. Simulation of bi-directional tensile simulation

3.1. Simulation of stretching along the X-axis

As shown in Fig. 3, deformation characteristics were captured at tensile strains of 0.05, 0.10, 0.15, and 0.20. A comprehensive analysis revealed significant differences in the fracture strain of the three structures: RH fractured below 0.05, SRH between 0.05 and 0.10, and CH between 0.10 and 0.15. Notably, the fracture locations were similar across all three structures, occurring at the junctions of the hierarchical substructures, specifically in the central honeycomb subunits. This is due to the central honeycomb structure being more prone to deformation, as it is subjected to the combined effects of surrounding structures and vertical layers. As tensile strain increases, fractures extend from the center toward the outer regions of the structure. Additionally, at a tensile strain of 0.2, deformation occurs primarily in the middle layer, with the upper and lower hierarchical honeycomb layers remaining largely undeformed. This suggests that the novel hierarchical reentrant honeycomb structure has a unique ability to protect the outer layers during axial tensile loading as shown in Fig. 3.

Stress values are determined by dividing reaction forces (F) from the rigid grip section by the cross-sectional area of the grip section (S). Therefore, stress is represented as σ_1 or $\sigma_2 = F/S$. Strains ($\varepsilon = U/d$) are derived from the ratio of top grip displacements (U) to the structure's length (d). Poisson's ratio is defined as $\nu = -\varepsilon_v/\varepsilon$, where ε_v is the strain perpendicular to the axial load direction and ε is the axial strain value, the stress-strain curve plotted against Poisson's ratio-strain curve obtained is shown in Fig. 4.

The tensile stress-strain curve in Fig. 4a depicts the progression from initial tensile loading to the first fracture in the structure. The curve reveals that all three structures undergo an

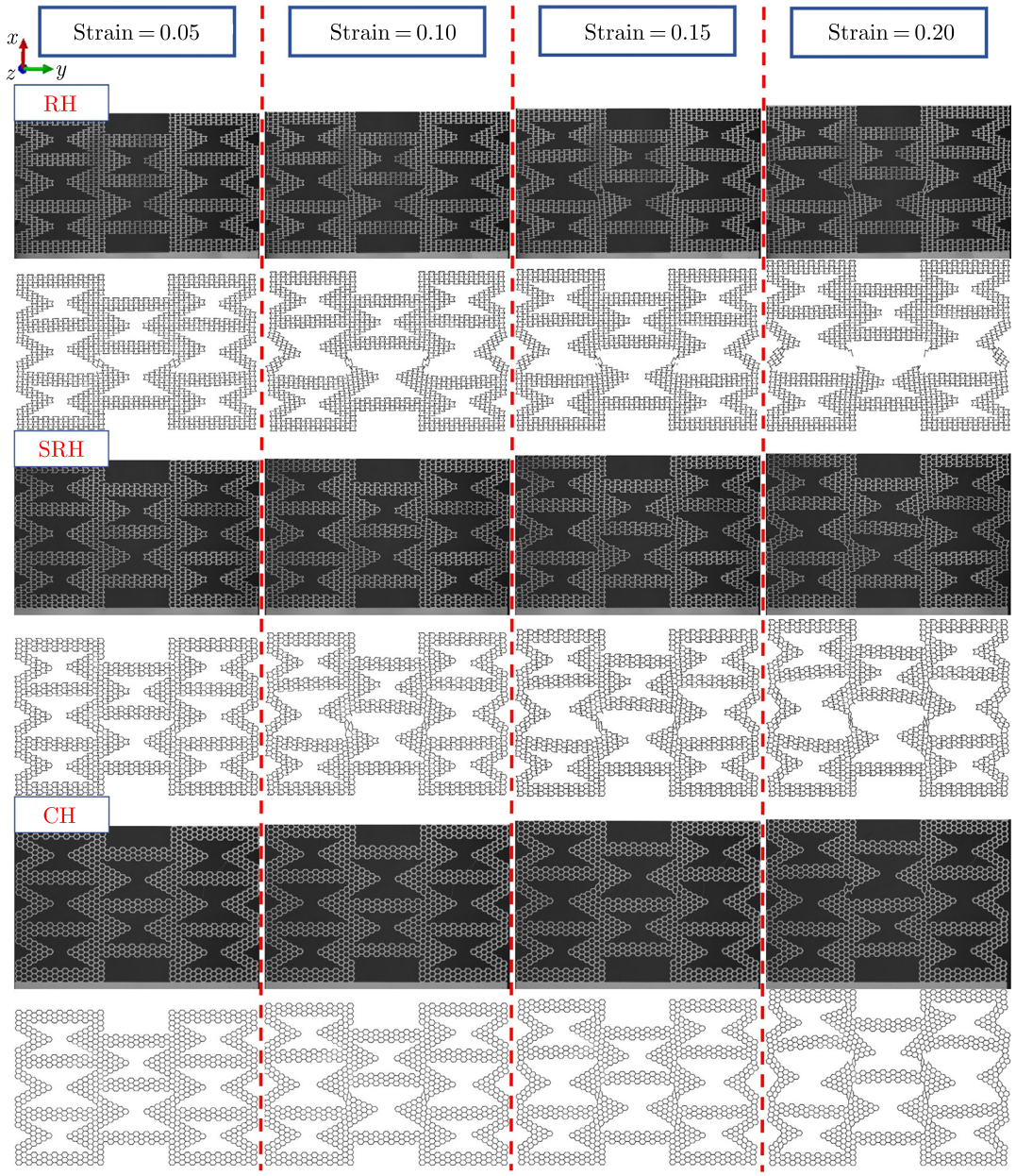

Fig. 3. Characteristics of tensile deformation along X-axis.

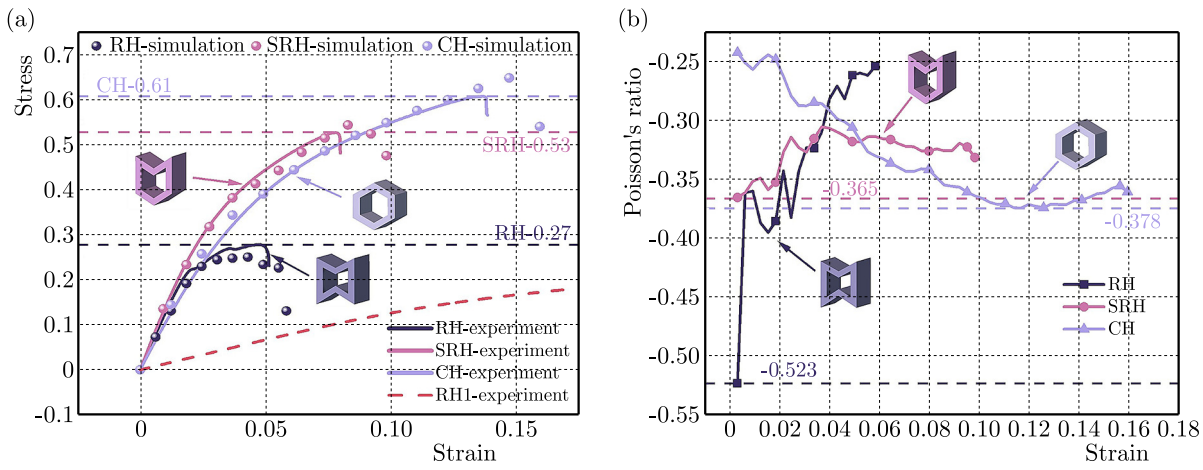

Fig. 4. Tensile stress-strain curves and Poisson's ratio-strain curves along the X-axis.

initial elastic phase, a buckling phase, and a final fracture during the tensile test. By applying Hooke's Law to the initial elastic phase, the elastic moduli of the three different structures can be calculated. The figure also shows the tensile strength of each structure at the fracture strain, with specific data provided in Table 2. The study results indicate that, in terms of the elastic modulus, SRH > RH > CH, suggesting that the SRH structure has greater stiffness and stability compared to the other two. This is because the semi-reentrant honeycomb subunits in the SRH structure combine the mechanical properties of the other two subunits, resulting in stronger interactions during tensile loading.

Table 2. Physical parameters related to stretching along the X-axis.

Type	Elastic modulus [MPa]	Rupture strain	Tensile strength [MPa]	Minimum Poisson's ratio
RH	12.68	0.05	0.27	−0.523
SRH	13.93	0.08	0.53	−0.365
CH	10.41	0.14	0.61	−0.378

However, in terms of tensile strength, the order is CH > SRH > RH. Despite having a lower elastic modulus, the CH structure's deformation characteristics allow it to undergo greater deformation during tensile loading. This increased deformation helps the CH structure disperse stress concentrations more effectively and absorb more energy before fracturing, resulting in superior tensile strength. On the other hand, the SRH and RH structures tend to transfer energy through fracture rather than significant deformation. As a result, they fracture under lower stress, leading to a relatively lower tensile strength. The SRH structure, which combines characteristics of both subunits, has a tensile strength between the other two. The RH structure, due to its earlier fracture strain, fractures earlier in the tensile process, exhibiting the lowest tensile strength among the three.

Additionally, when examining the RH1 structure individually, it is evident from the images that the novel hierarchical reentrant honeycomb structure designed in this study has a significantly higher elastic modulus compared to the RH1 structure. This suggests that the structure developed in this research offers greater stability.

As shown in Fig. 4b, all three structures exhibit negative Poisson's ratio characteristics during tensile loading up to the first fracture. However, Poisson's ratio trends differ: the RH and SRH structures show an overall increase, while the CH structure shows a decrease. The study also found that the RH structure has the smallest minimum Poisson's ratio among the three, with SRH and CH having relatively similar values. This phenomenon can be attributed to the inherent negative Poisson's ratio of the reentrant honeycomb subunits, which directly influences the overall Poisson's ratio of the RH structure. This observation further supports the conclusion that Poisson's ratio of the subunits directly impacts Poisson's ratio of the entire structure. Additionally, the tensile study under out-of-plane compression along the X-axis confirmed the alignment between the simulation results and the physical experiments.

3.2. Simulation of stretching along the Y-axis

During tensile loading along the Y-axis, deformation images were captured at four strain nodes: 0.05, 0.1, 0.15, and 0.2, as shown in Fig. 5. The results indicate that at a tensile strain of 0.15, the RH and SRH structures exhibited significant fractures, while the CH structure fractured at a tensile strain of 0.2. The fracture points for SRH and RH were located at the junctions of the hierarchical structures, with RH's fracture occurring on the walls of the middle hierarchical structure. These findings suggest that the CH structure has superior flexibility during tensile loading, consistent with the results from the X-axis tensile tests. Further analysis revealed that the reentrant and semi-reentrant honeycomb subunits did not undergo significant deformation;

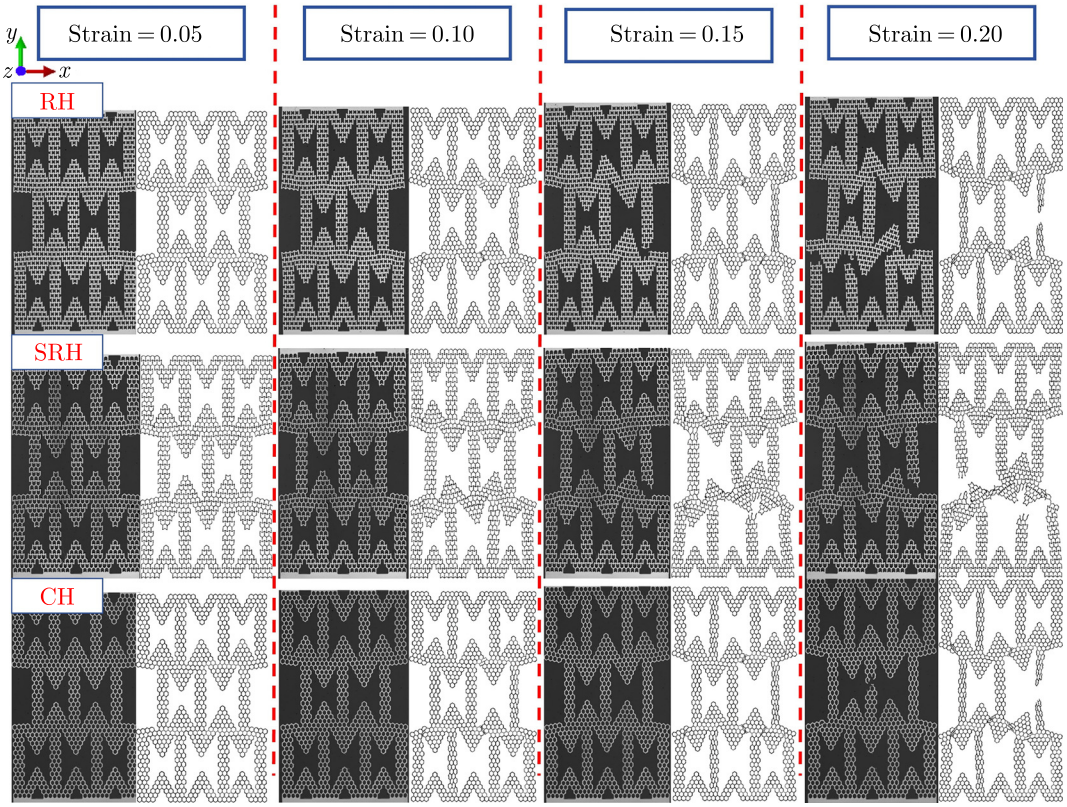

Fig. 5. Characteristics of tensile deformation along Y-axis.

instead, the energy of the structure was released through fracturing. In contrast, the classical hexagonal honeycomb subunits experienced greater deformation during tensile loading, which helped to distribute stress more evenly and delayed fracture, resulting in a later fracture point. Notably, the RH and SRH structures exhibited an outside-in fracture pattern, while the CH structure showed an inside-out fracture pattern.

Figure 6 shows the stress-strain and Poisson's ratio-strain curves for tensile loading along the Y-axis, with detailed mechanical properties presented in Table 3. Compared to the tensile data under X-axis loading (Table 2), the results reveal that the elastic moduli of all three structures are significantly higher under Y-axis loading. This is because, during Y-axis tensile loading, the axial tensile direction is parallel to the sidewalls of the hierarchical reentrant honeycomb

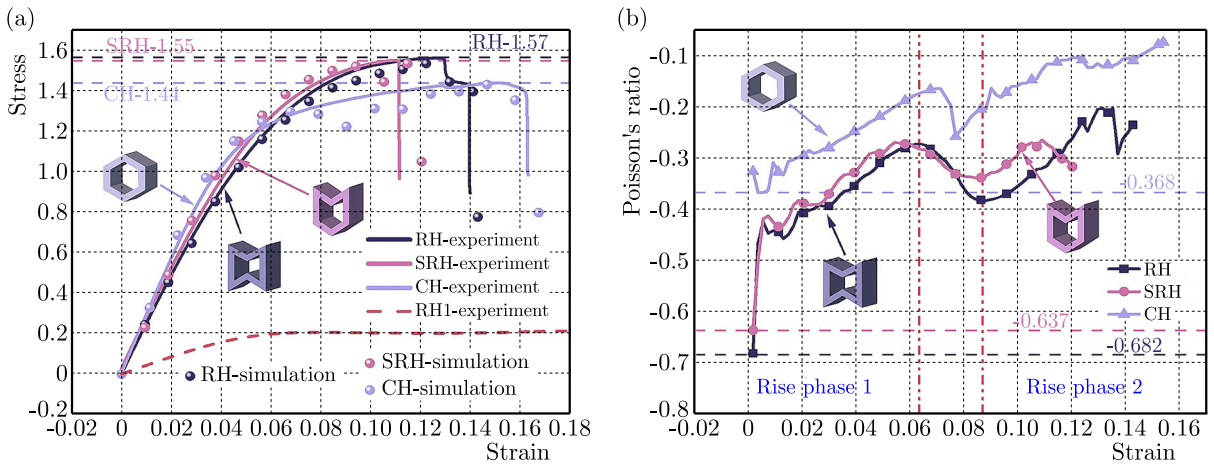

Fig. 6. Tensile stress-strain curves and Poisson's ratio-strain curves along the Y-axis.

Table 3. Physical parameters related to stretching along the X-axis.

Type	Elastic modulus [MPa]	Rupture strain	Tensile strength [MPa]	Minimum Poisson's ratio
RH	25.09	0.14	1.57	−0.682
SRH	25.54	0.11	1.55	−0.637
CH	28.91	0.16	1.44	−0.368

substructure, which provides greater stiffness and stability. However, the change in loading direction also alters the stiffness characterization. Under Y-axis tensile loading, the stiffness ranking is CH > SRH > RH. For fracture strain, the order is CH > RH > SRH, likely due to the unique flexibility of the classical hexagonal honeycomb structure. In terms of tensile strength, the order is RH > SRH > CH, with the values for SRH and RH being relatively close. The analysis of the curves suggests that the lower tensile strength of the CH structure is due to its extended yielding phase. Furthermore, the comparison of the simulation and experimental curves in Fig. 6a confirmed the alignment between the experimental results and simulations. Additionally, when comparing the RH1 structure based on experimental data, it was observed that the novel hierarchical reentrant honeycomb structures designed in this study generally exhibit higher stiffness and stability.

The analysis of Poisson's ratio characterization in different structures, as shown in Fig. 6b, reveals that Poisson's ratio-strain curves under Y-axis tensile loading not only exhibit a fully negative Poisson's ratio, but all three structures also display two distinct increasing phases, specifically in the strain intervals of 0–0.06 and 0.086–0.15. To further quantify the negative Poisson's ratio characteristics, the minimum Poisson's ratio is ranked as RH < SRH < CH, indicating that the RH structure has the most optimal negative Poisson's ratio under Y-axis tensile loading. This conclusion is consistent with the findings from tensile loading along the X-axis, further confirming that Poisson's ratio of the subunits significantly influences the overall Poisson's ratio of the structure. Additionally, the results suggest that the change in axial tensile direction has a relatively small impact on Poisson's ratio characteristics.

4. Conclusion

This study designed three novel hierarchical reentrant honeycomb structures by nesting various subunits to replace the cell walls of traditional reentrant honeycomb structures. The mechanical behavior of these structures under axial tensile loading in two directions was evaluated using the finite element analysis and tensile testing of 3D-printed samples.

In terms of elastic modulus, under X-axis tensile loading, the SRH structure exhibited the highest stiffness, followed by the RH and CH structures. However, under Y-axis tensile loading, the CH structure demonstrated superior stiffness, indicating its robustness and stability in this direction. Compared to RH1 designed by Lian, the structures in this study exhibited higher stiffness and stability, even with similar dimensions. Regarding tensile strength, under X-axis loading, the CH structure displayed the highest tensile strength, attributed to its ability to undergo greater deformation, which aids in the stress distribution. Conversely, under Y-axis loading, the RH structure exhibited the highest tensile strength, followed by the SRH and CH structures. The study of deformation morphology revealed significant differences in fracture patterns across different loading directions. The RH and SRH structures tended to fracture earlier, exhibiting an outside-in fracture mode in both loading directions, whereas the CH structure fractured later, showing an inside-out fracture mode, indicating its greater flexibility. In terms of Poisson's ratio, all three structures exhibited the consistent negative Poisson's ratio under tensile loading, with the RH structure showing the most pronounced effect. This consistency in both loading directions indicates that Poisson's ratio of the subunits significantly influences

the overall Poisson's ratio of the hierarchical structure. This study offers valuable insights for designing multifunctional lightweight materials with tailored mechanical properties.

Acknowledgments

The authors would like to acknowledge the support from the Fundamental Research Funds for the Central Universities (grant no. 3122024041) and the Graduate Research Innovation Program of Civil Aviation University of China (grant no. 2023YJSKC12002).

References

1. Ahmed, N. & Xue, P. (2019). Governing the in-plane axial crushing of honeycomb with regular hexagonal symmetric division cells using cross-hinge inserts. *International Journal of Mechanical Sciences*, *161–162*, Article 105062. https://doi.org/10.1016/j.ijmecsci.2019.105062
2. Boldrin, L., Hummel, S., Scarpa, F., Di Maio, D., Lira, C., Ruzzene, M., Remillat, C.D.L., Lim, T.C., Rajasekaran, R., & Patsias, S. (2016). Dynamic behaviour of auxetic gradient composite hexagonal honeycombs. *Composite Structures*, *149*, 114–124. https://doi.org/10.1016/j.compstruct.2016.03.044
3. Chen, Y., Li, T., Jia, Z., Scarpa, F., Yao, C.W., & Wang, L. (2018). 3D printed hierarchical honeycombs with shape integrity under large compressive deformations. *Materials & Design*, *137*, 226–234. https://doi.org/10.1016/j.matdes.2017.10.028
4. Gong, X., Ren, C., Sun, J., Zhang, P., Du, L., & Xie, F. (2022). 3D Zero Poisson's Ratio honeycomb structure for morphing wing applications. *Biomimetics*, *7*(4), 198. https://doi.org/10.3390/biomimetics7040198
5. Heo, H., Ju, J., & Kim, D.M. (2013). Compliant cellular structures: Application to a passive morphing airfoil. *Composite Structures*, *106*, 560–569. https://doi.org/10.1016/j.compstruct.2013.07.013
6. Hu, L.L., Zhou, M.Z., & Deng, H. (2019). Dynamic indentation of auxetic and non-auxetic honeycombs under large deformation. *Composite Structures*, *207*, 323–330. https://doi.org/10.1016/j.compstruct.2018.09.066
7. Ingrole, A., Hao, A., & Liang, R. (2017). Design and modeling of auxetic and hybrid honeycomb structures for in-plane property enhancement. *Materials & Design*, *117*, 72–83. https://doi.org/10.1016/j.matdes.2016.12.067
8. Jin, X., Wang, Z., Ning, J., Xiao, G., Liu, E., & Shu, X. (2016). Dynamic response of sandwich structures with graded auxetic honeycomb cores under blast loading. *Composites Part B: Engineering*, *106*, 206–217. https://doi.org/10.1016/j.compositesb.2016.09.037
9. Ju, J. & Summers, J.D. (2011). Compliant hexagonal periodic lattice structures having both high shear strength and high shear strain. *Materials & Design*, *32*(2), 512–524. https://doi.org/10.1016/j.matdes.2010.08.029
10. Köhnen, P., Haase, C., Bültmann, J., Ziegler, S., Schleifenbaum, J.H., & Bleck, W. (2018). Mechanical properties and deformation behavior of additively manufactured lattice structures of stainless steel. *Materials & Design*, *145*, 205–217. https://doi.org/10.1016/j.matdes.2018.02.062
11. Lee, W., Jeong, Y., Yoo, J., Huh, H., Park, S.J., Park, S.H., & Yoon, J. (2019). Effect of auxetic structures on crash behavior of cylindrical tube. *Composite Structures*, *208*, 836–846. https://doi.org/10.1016/j.compstruct.2018.10.068
12. Liu, H., Zhang, E.T., Wang, G., & Ng, B.F. (2022). In-plane crushing behavior and energy absorption of a novel graded honeycomb from hierarchical architecture. *International Journal of Mechanical Sciences*, *221*, Article 107202. https://doi.org/10.1016/j.ijmecsci.2022.107202
13. Liu, J., Chen, W., Hao, H., & Wang, Z. (2021). In-plane crushing behaviors of hexagonal honeycombs with different Poisson's ratio induced by topological diversity. *Thin-Walled Structures*, *159*, Article 107223. https://doi.org/10.1016/j.tws.2020.107223
14. Liu, W., Wang, N., Luo, T., & Lin, Z. (2016). In-plane dynamic crushing of re-entrant auxetic cellular structure. *Materials & Design*, *100*, 84–91. https://doi.org/10.1016/j.matdes.2016.03.086

15. Patel, P., Bhingole, P.P., & Makwana, D. (2018). Manufacturing, characterization and applications of lightweight metallic foams for structural applications: Review. *Materials Today: Proceedings*, *5*(9), 20391–20402. https://doi.org/10.1016/j.matpr.2018.06.414

16. Photiou, D., Prastiti, N., Sarris, E., & Constantinides, G. (2016). On the conical indentation response of elastic auxetic materials: Effects of Poisson's ratio, contact friction and cone angle. *International Journal of Solids and Structures*, *81*, 33–42. https://doi.org/10.1016/j.ijsolstr.2015.10.020

17. Reznikov, N., Bilton, M., Lari, L., Stevens, M.M., & Kröger, R. (2018). Fractal-like hierarchical organization of bone begins at the nanoscale. *Science*, *360*(6388), Article eaao2189. https://doi.org/10.1126/science.aao2189

18. Shukla, S. & Behera, B.K. (2022). Auxetic fibrous structures and their composites: A review. *Composite Structures*, *290*, Article 115530. https://doi.org/10.1016/j.compstruct.2022.115530

19. Solak, A., Aşçıoğlu Temiztaş, B., & Bolat, B. (2023). Numerical investigation of the mechanical behavior of the vertical stabilizer leading edge with wavy honeycomb sandwich structure under bird strike. *Journal of Sandwich Structures & Materials*, *25*(3), 387–400. https://doi.org/10.1177/10996362221146124

20. Wang, Z. (2019). Recent advances in novel metallic honeycomb structure. *Composites Part B: Engineering*, *166*, 731–741. https://doi.org/10.1016/j.compositesb.2019.02.011

21. Xiao, D., Chen, X., Li, Y., Wu, W., & Fang, D. (2019a). The structure response of sandwich beams with metallic auxetic honeycomb cores under localized impulsive loading-experiments and finite element analysis. *Materials & Design*, *176*, Article 107840. https://doi.org/10.1016/j.matdes.2019.107840

22. Xiao, D., Dong, Z., Li, Y., Wu, W., & Fang, D. (2019b). Compression behavior of the graded metallic auxetic reentrant honeycomb: Experiment and finite element analysis. *Materials Science and Engineering: A*, *758*, 163–171. https://doi.org/10.1016/j.msea.2019.04.116

23. Xu, P., Lan, X., Zeng, C., Zhang, X., Zhao, H., Leng, J., & Liu Y. (2024). Compression behavior of 4D printed metamaterials with various Poisson's ratios. *International Journal of Mechanical Sciences*, *264*, Article 108819. https://doi.org/10.1016/j.ijmecsci.2023.108819

Manuscript received February 21, 2024; accepted for publication October 18, 2024; published online March 14, 2025.

JOURNAL OF THEORETICAL
AND APPLIED MECHANICS
63, 2, pp. 227–237, Warsaw 2025
https://doi.org/10.15632/jtam-pl/199582

EFFECTS OF ADVANCED SEISMIC ANALYSIS WITH ARMA MODELS: ASSESSING DAMAGE IMPACT AND HYSTERESIS IN EARTHQUAKE TIME SERIES

Abderrazek MENASRI[1*], Ahmed SEDDIKI[1], Tahar BRAHIMI[2], Abdelmadjid BOUBAYA[3]

[1] *Civil Engineering Department, Technology Faculty, M'sila University, Algeria*
[2] *Laghouat Normal School (ENSL), Algeria*
[3] *Research Laboratory in Civil Engineering, Biskra University, Algeria*
[*]corresponding author, *abderrazek.menasri@univ-msila.dz*

Actual records of strong motion acceleration cannot meet engineering requirements. The simulated seismic waves become an equivalent source of seismic wave input. The time-varying autoregressive moving average (ARMA) process is a straightforward and effective method for simulating seismic ground motions. This model can accurately replicate the non-stationary amplitude and frequency characteristics of seismic ground accelerations, making it useful for assessing damage indicators, which are then compared to spectra derived from real seismic records. It is demonstrated that the chosen ARMA(2,1) model and the applied algorithm effectively capture the characteristics of real seismic records, even with the varying frequency content.

Keywords: seismic waves; non-stationary; damage predictors; ARMA model.

1. Introduction

Acceleration data presented as time series are a subject of considerable interest and significance in various applications. These time series exhibit significant irregularities in both amplitude and frequency characteristics, which are subject to change over time. Essentially, all acceleration data can be viewed as time series with nonstationary characteristics, and each acceleration time series is essentially a single realization of a nonstationary stochastic process (Sakellariou & Fassois, 2006; Zheng & Mita, 2007). To model these time series effectively, two main approaches are employed: in the frequency and in the time domains. The time-varying nature of the frequency content is taken into account by utilizing an evolutionary density function, a valuable tool for characterizing the frequency content in these data (Carden & Brownjohn, 2008). The connection between theoretical concepts and practical applications has led to the development of a practical technique for modeling acceleration using ARMA models (Ay & Wang, 2014; Luo & Yu, 2017). These models offer the flexibility needed to accurately represent real acceleration time series data (Bodeux & Golinval, 2001).

Analysis of linear and nonlinear response spectra reveals that the ARMA(2,1) process, when applied to simulated acceleration time series, effectively captures the key characteristics of acceleration records (Johnson *et al.*, 2004; El-Choum, 2014). This approach also characterizes dependency patterns in displacement plasticity and hysteretic energy (Nair *et al.*, 2006; Zhang, 2007). By analyzing response spectra from ARMA models, dynamic structural responses are assessed with precision, an approach also used in nonlinear analysis of concrete dams (Ouzandja *et al.*, 2023). In our study, the ARMA(2,1) model, analyzed in detail by Box *et al.* (2015), was found most suitable for computing hysteretic energy.

2. Earthquake process model modelling

2.1. Acceleration time series process models (ARMA)

ARMA (p, q) process model can be represented as follows:

$$z_t - \varphi_1 z_{t-1} - ... - \varphi_p z_{t-p} = a_t - \theta_1 a_{t-1} - ... - \theta_q a_{t-q}, \tag{2.1}$$

where φ_i and φ_j are constant coefficients; (p, q) is the order of the model.

The model contains $p + q + 1$ unknown parameters, which are usually estimated from data based on maximum likelihood and the model order is based on the Akaike information criteria.

2.2. Autocorrelation functions

To determine the appropriate order (p, q) for the ARMA model, representing an acceleration time series, it is essential to examine the theoretical autocorrelation function, $R(k)$. The theoretical autocovariance function, $C(k)$, can be derived by multiplying Eq. (2.1) by z_t and taking expectations (Brahimi, 1989):

$$C(k) = \varphi_1 C(k-1) + ... + \varphi_p C(k-p) + C_{za}(k) - \theta_1 C_{za}(k-1) - ... - \theta_q C_{za}(k-q), \tag{2.2}$$

where

$$C_{za}(k) = E[z_{t-k} \cdot a_t]. \tag{2.3}$$

The autocorrelation function $R(k)$ is obtained by dividing Eq. (2.2) by $C(0)$ and a similar form is obtained:

$$R(k) = \varphi_1 R(k-1) + ... + \varphi_p R(k-p) + RC_{za}(k) - \theta_1 R_{za}(k-1) - ... - \theta_q R_{za}(k-q). \tag{2.4}$$

The fact that the values of z_{t-k} are correlated only to white noise values up to time $t-k$ implies that:

$$C_{za}(k) = 0 \qquad \text{for} \quad k > 0. \tag{2.5}$$

Thus, for processes using AR, the function takes the form of an exponential decay or series of waves as the lag k increases. Alternatively, for MA, when the lag k reaches a specific order g, the function becomes equal to zero. Finally, when the ARMA process is used, when the first $g - p$ lag is overcome, the function takes the form of a combination of exponential decay waves.

2.3. The function of partial autocorrelation

The partial autocorrelation function describes the time dependence of the series, when combined with the use of AR, it becomes possible to accurately identify the order and type of the model being estimated. For stationary autoregressive (AR) processes, the autocorrelation function continues indefinitely.

Therefore, characterizing the autoregressive process involves counting the non-zero autocorrelation terms. The theoretical partial autocorrelation function $P(k)$ is calculated using the Yule–Walker equations. For a stationary and invertible ARMA process, the partial autocorrelation function $P(k)$ decays with a damped exponential or sine wave pattern, influenced by moving average parameters after the first $p - q$ lags (Brahimi, 1989).

2.4. AIC criteria

One major challenge in this study was estimating both the number and values of model parameters to minimize the discrepancy between the simulated model and the actual time series. The model order was determined using the Akaike information criterion (AIC), while the parameters were estimated through a nonlinear least squares approach. AIC focuses on maximum information criteria, considering entropy and Kullback–Liebler information for independent observations. For stationary time series, the optimal model minimizes this criterion:

$$\mathrm{AIC}(p,q) = N\ln(\sigma_a^2) + 2(p+q), \tag{2.6}$$

where N is the sample size, and σ_a^2 is the maximum likelihood estimate of the residual variance.

In this analysis, the ARMA(1,1), ARMA(1,2), ARMA(2,1), and ARMA(2,2) models were used for each seismic event. The final model selection for each earthquake was made based on a comparative AIC evaluation across the proposed models.

2.5. Modulating function

Another challenge in the simulation was estimating the variance or the envelope function. Variance regulates the non-stationarity of the process and considers statistical parameters, including structural responses or extreme acceleration values. The variance for the acceleration time series data, z_t, considered as random variables, is expressed as

$$\sigma_a^2 = E(z_t - \mu_t). \tag{2.7}$$

The common assumption $E(z_t) = 0$ is used in acceleration time series simulations, employing equally weighted two-second windows with 0.02-second intervals, estimating variance as

$$f_Z^2(t) = \frac{1}{100}\sum_{T-50}^{t+50} z_T^2. \tag{2.8}$$

Here, $f(t)$ approximates the modulating function, although it lacks criteria to differentiate between stationary and non-stationary data. Practically, a variance function with few parameters is ideal (Brahimi, 1989). This study uses a moving window with 0.5-second intervals to determine the variance across three acceleration time series, with MATLAB performing all necessary calculations.

2.6. Parametric envelope function

To simplify practical applications, a variance function with limited parameters is desirable. A smoothed function with limited parameters is used here (Brahimi, 1989):

$$s(t) = \alpha\exp\left(-\frac{t-\beta}{\gamma}\right)^2, \tag{2.9}$$

where α, β, γ are constants found by fitting the function to the estimated variance using the least squares method. This function is effective in fitting modulating functions with narrow peaks.

3. Procedure for modeling

To model ground motion acceleration as the ARMA process, the data is first transformed for stationarity by isolating the period of significant shaking. The ARMA modeling follows this procedure (Menasri *et al.*, 2012):

- calculate the experimental modulating function and normalize the data;
- assume an analytical form for $s(t)$ and estimate its parameters;

– calculate autocorrelation functions;
– choose model order (p, q) based on autocorrelation;
– estimate model coefficients using maximum likelihood, applying the Kalman filter for time-varying coefficients;
– select the model with the lowest AIC.

The three recorded accelerograms framed below were selected for our case.

Table 1. Characteristics of real earthquakes (Menasri, 2012).

Event	Affroun EW	Affroun NS	Affroun V
Magnitude	6.8	6.8	6.8
Duration [s]	80	80	80
Acceleration max × g	0.1644	0.09	0.03
Number of points	16001	16001	16001

4. Application of ARMA models

4.1. Models adopted

For this study, the ARMA model with a parametric envelope function was chosen to simplify parameter estimation for design purposes. Modeling begins with a modulating function to stabilize the series, which is then fitted to a smoothed parametric envelope function (e.g., Eq. (2.9)) effective for narrow peaks (Brahimi, 1989). Parameters are estimated from the stabilized series.

4.2. Acceleration time series

Three acceleration time series, including Affroun with 16000 data points (0.005 second digitization increment), were consistently used. The main difference between the series was the number of data points required for estimation, with the plots shown in Fig. 1.

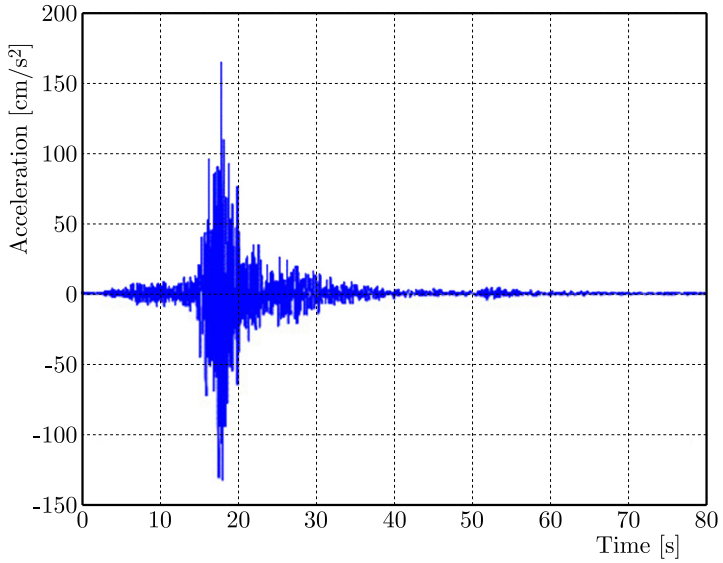

Fig. 1. Time series of acceleration measurements at the Affroun station in the East-West direction.

As the first step in model identification, the modulating function $f(t)$ was computed for each measured acceleration record using Eq. (2.2).

Figure 2 shows the appearance and envelope functions for Affroun EW, NS, and V earthquakes. It is evident that non-stationarity is significant across events.

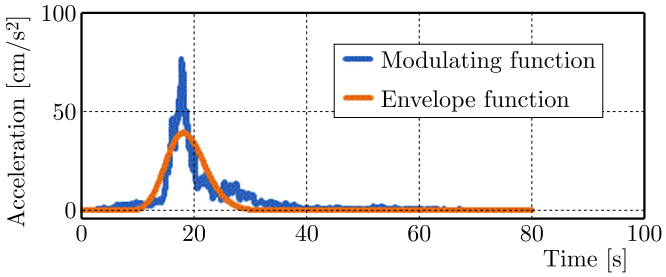

Fig. 2. Modulating and envelope functions extracted from the Affroun East-West acceleration data.

The single-peak envelope function in Eq. (2.9) is fitted to each measured modulating function using the least squares method, with results shown for four acceleration series in Fig. 2.

The original acceleration record and the obtained modulating function allow the estimation of the stabilized acceleration series, as shown for the El Affroun EW event in Fig. 3. The resulting series has an approximate variance of one and a mean near zero, with the frequency content incorporated into ARMA model parameters.

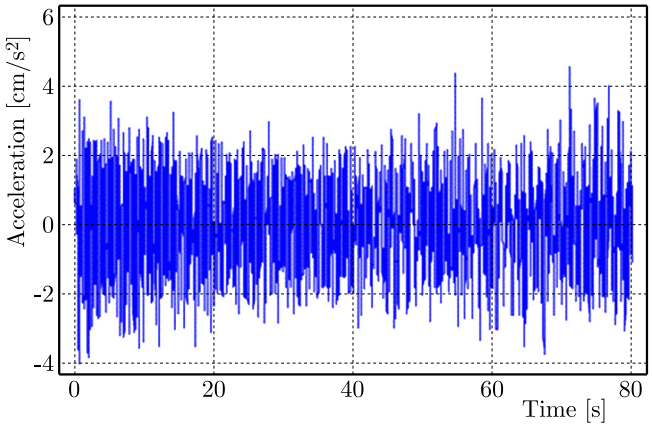

Fig. 3. Stabilized acceleration time series for the Affroun East-West component.

5. Results

Estimated autocorrelations for the three stabilized time series from measured records are shown in Fig. 4. The rapid decay of autocorrelations indicates that no roots of the characteristic equation are near the unit circle boundary, confirming stationarity.

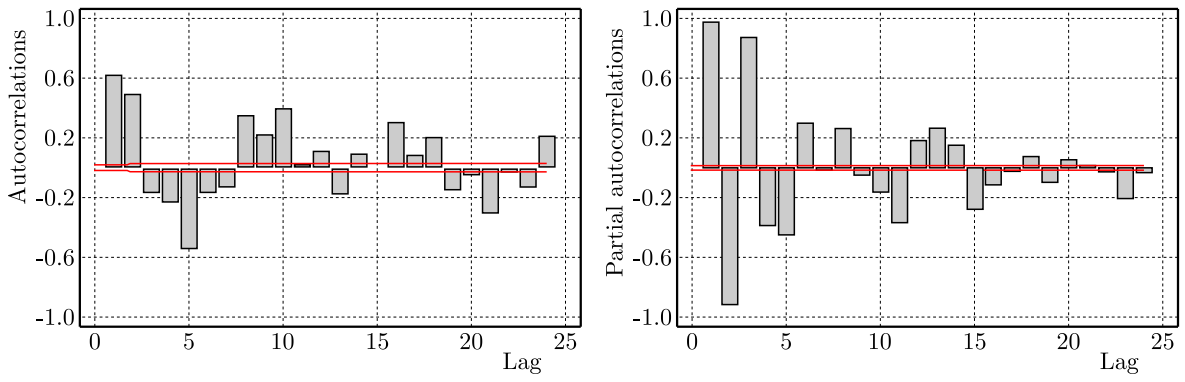

Fig. 4. Estimated and partial autocorrelation functions for the Affroun East-West acceleration data.

Partial autocorrelation functions are estimated for each record by fitting successive autoregressive processes of the order k in MATLAB, with results for Affroun EW in Fig. 4.

The partial autocorrelation function for the Affroun series indicates that after the lag $q = 2$ or $q = 3$, correlations decline, suggesting an ARMA model order with $p - q = 2$ or 3. Models based on AR and partial AR functions were tested for three events, using maximum likelihood estimates approximated by the least squares method. The model order selection was guided by the AIC criteria, and ARMA simulations with one or two MA terms were found optimal. Table 2 presents AIC values for ARMA models, showing ARMA(2,1) as the best fit for Affroun series.

Table 2. Application of AIC criteria to different ARMA models (Menasri, 2012).

Model	AIC (Affroun EW)	AIC (Affroun NS)	AIC (Affroun V)
ARMA(1,1)	−4.21635	−4.21958	−3.64068
ARMA(1,2)	−5.11995	−5.29379	−4.78432
ARMA(2,1)	−5.84522*	−5.73424*	−5.09023
ARMA(2,2)	−5.71991	−5.61231	−5.26325*

*Optimal set by AIC criterion. [Source: Menasri (2012)].

Table 3 lists the AR parameters φ_1, φ_2, the moving average θ_1, θ_2, while Table 4 provides envelope function parameters α, β, γ, with 95 % confidence limits. Stability and invisibility conditions are verified by the coefficients.

Table 3. Parameters of the selected models (Menasri, 2012).

Parameters	Affroun EW	Affroun NS	Affroun V
AR (1)	1.82986	1.85144	1.80244
AR (2)	−0.879019	−0.900216	−0.888599
MA (1)	−0.7313	−0.634745	−0.754022
σ_a	0.0543099	0.0571895	0.0785381

Table 4. Parameters of the envelope function.

Event	Parameters envelope function		
	α	β	γ
Affroun EW	3.475e-8	10.78	0.59
Affroun NS	8.48e-8	9.958	0.5285
Affroun V	9.61e-9	10.91	0.6055

6. Acceleration time series

Simulated ARMA process systems, using a time-based approach, yield good results with a limited number of parameters. The method involved generating stationary time series via the ARMA model, then applying the envelope function. The ARMA model was treated as a linear combination of Gaussian random variables (a_t) and existing values (z_t), enabling recursive simulation of the time series. A simulation of the acceleration time series shown in Fig. 5.

The comparison of the main characteristics of real and simulated earthquakes is shown in Table 5.

The results show that the ARMA(2,1) process, combined with the envelope function parameters, better represents the Affroun EW, NS, and V events.

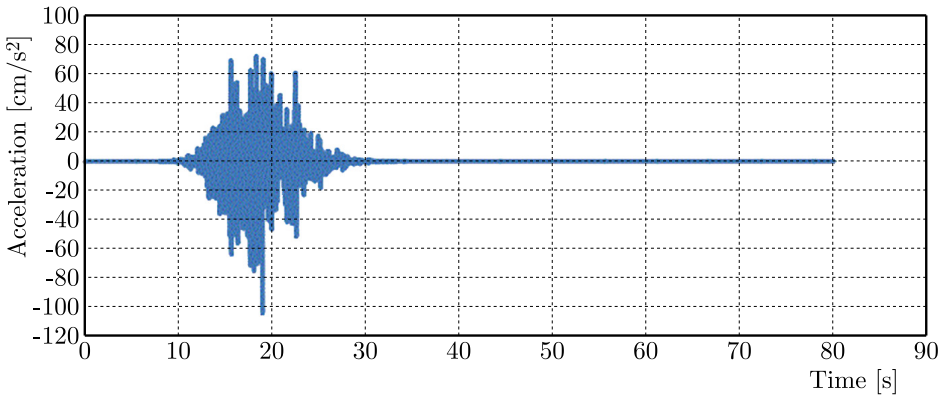

Fig. 5. Simulated acceleration time series for the Affroun East-West component.

Table 5. Characteristics of real and simulated earthquakes.

Earthquake		Affroun EW	Affroun NS	Affroun V
Real	Maximum acceleration × g	0.1644	0.09	0.03
Simulated	Maximum acceleration × g	0.115	0.08	0.022
	Duration [s]	80	80	80

7. Response spectra

7.1. Measures of damage

Various methods have been developed to assess the impact of earthquakes on both linear and non-linear structures, with significant contributions from researchers such as Lin, Mahin, and Grigorio. The pursuit of precision plays a pivotal role in structural analysis, making the utilization of highly sensitive predictive models a matter of significant importance. More specifically, ARMA models are recognized as effective analytical tools for both qualitatively and quantitatively describing the non-stationary nature of input data in structural analysis. Consequently, each acceleration time series under examination is regarded as an outcome arising from a sequence of multiple stochastic processes.

As a result, each acceleration time series being analyzed is considered the outcome of a series of multiple stochastic processes.

Simultaneously, the characterization of ground acceleration time series can be achieved through structural response spectra where a measure of the response damage is graphically represented, where a measure of response damage is plotted as a function of time period.

Single degree of freedom and viscous damping systems are used to calculate these spectra as shown schematically in Fig. 6. It is worth noting that these systems can exhibit either bilinear or degenerate stiffness. This implies that for successful modeling, an integration method must

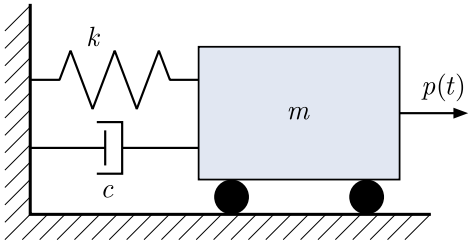

Fig. 6. One-degree-of-freedom system.

be employed that takes linear acceleration into account at each computational step. This approach enables the derivation of spectral responses for the series, as represented by the equation:

$$M\ddot{U}(t) + c\dot{U}(t) + R(u,t) = -M\ddot{U}_g(t), \tag{7.1}$$

where M is the mass, u is the relative displacement of mass, c is the damping coefficient, $\ddot{U}_g$ is the ground acceleration, R is the restoring force.

7.2. Peak displacement ductility

For design, it suffices to consider the maximum response value:

$$U_{\max} = |U_{\max}(t)|\,, \tag{7.2}$$

where $U_{\max}(t)$ represents the maximum displacement during an earthquake, and $U_{\max}$ denotes ultimate deformation capacity under monotonic loading.

Responses $U_{\max}(t)$ are obtained by assuming a linear acceleration at each time step, we make a numerical integration of the general equation.

This function enables us to relate the system's maximum value to its natural oscillation period, facilitating the creation of a spectrum for systems where damping values and the periodic range are the same.

7.3. Hysteretic energy in a normalized form

The hysteretic energy is derived by dividing the dissipation energy by twice the absorbed energy. For structures with hysteretic load-deformation, the dissipation energy is:

$$E_h(t) = \int_0^t R(u,t)\dot{u}(t)\,\mathrm{d}t - E_s(t), \tag{7.3}$$

where $E_s(t)$ is elastic deformation energy:

$$E_s = \frac{1}{2}K_y U_y^2, \tag{7.4}$$

where K_y the stiffness after elasticity, U_y is the initial elastic displacement.

The bilinear model, often used in this context, is defined by three primary parameters: U_y the initial yield displacement; K_1 the initial elastic stiffness; and K_y the post-yielding stiffness. As displacement increases, this model provides the corresponding restoring force:

$$R(u,t) = \begin{cases} R(u,t) = K_1 u(t) & \text{if } U_y \geq u(t), \\ R(u,t) = K_y(u(t) - u_z) & \text{if } U_y < u(t). \end{cases} \tag{7.5}$$

The value u_z represents at the yield envelope intersects the displacement axis. During unloading, stiffness remains at the initial level until the yield envelope is reached.

The normalized hysteric energy is given as follows:

$$E_{NH} = 1 + \frac{E_H}{R_y U_y}, \tag{7.6}$$

where $R_y = K_y U_y$ represents the force at yield, E_H the hysteretic energy resulting from inelastic deformation.

7.4. Application and numerical results

Several ARMA models proved highly suitable for analyzing three distinct time series with varying data points. For the response analysis, damping coefficients (ε) were set to 0.05, and the yield coefficient (Y) was calculated as $Y = R_y/Mg$, ranging from 0.05 to 0.3. The hysteretic energy was computed using alternative output coefficients, and mean displacement ductility was used to establish demand spectra for the hysteretic energy (Brahimi, 2021). Confidence intervals were estimated using standard deviations, and spectral values decreased as the period increased.

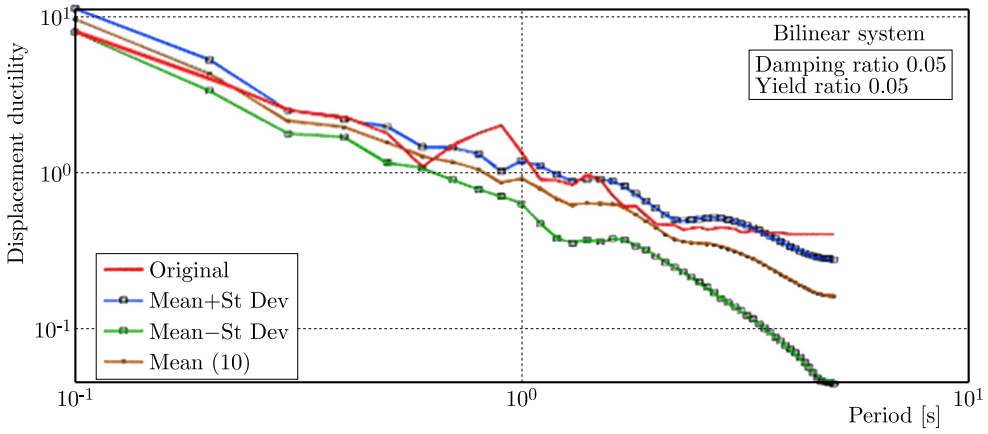

Fig. 7. Displacement ductility in a bilinear system as a function of period for a given damping ratio.

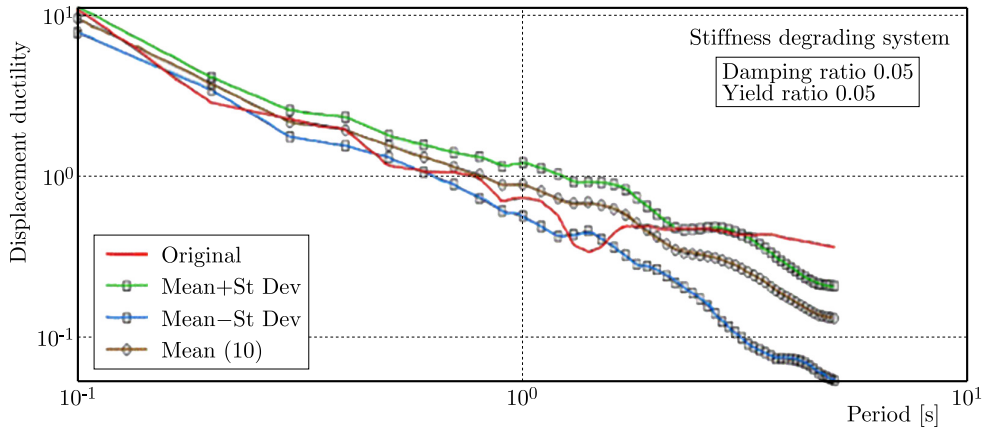

Fig. 8. System for modeling stiffness degradation with respect to displacement ductility.

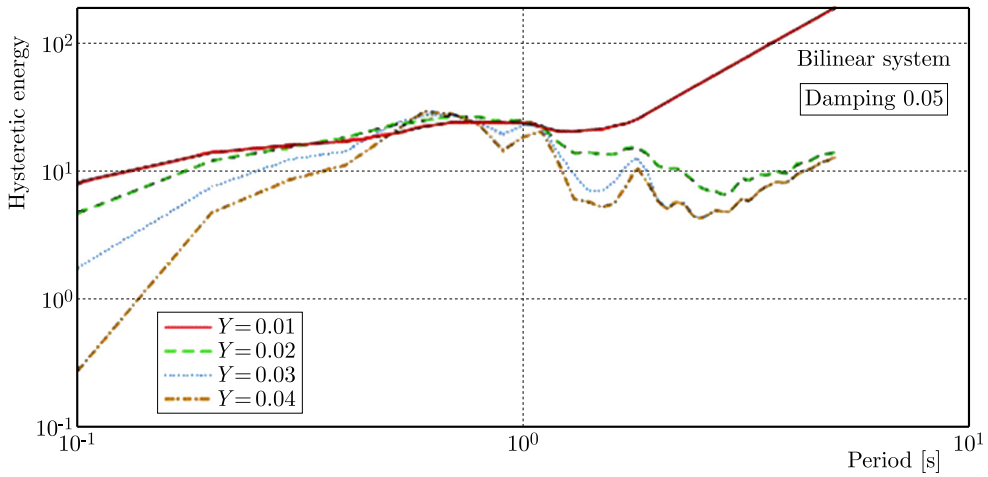

Fig. 9. Impact of the elasticity ratio on hysteretic energy in a bilinear system.

The results, shown in Figs. 7 and 8, reveal a consistent decrease in spectral values with longer periods and similar trends between systems with reduced and bilinear stiffness.

The yield coefficient has been recognized as one of the foremost factors in the structural analysis of nonlinear systems (Brahimi & Smain, 2021), because the initial yield displacement is a prerequisite for the inelastic reaction. Thus, Fig. 9 illustrates classical descriptions of mean displacement ductility for varying yield coefficients, assuming a system with bilinear stiffness and 5 % damping.

8. Conclusions

It has been demonstrated that by applying simulated ARMA processes within a time-domain approach, satisfactory results can be achieved with fewer parameters. The response spectra of simulated earthquakes closely resemble those of real earthquakes, except for long-period events. Studies have revealed a linear relationship between the logarithms of the mean nonlinear response spectrum and the system's natural period, indicating that an increase in the period results in a decrease in the average displacement ductility and hysteretic energy. Specifically, as the logarithm of the system's period increases, the response spectra for displacement, ductility, and hysteretic energy decrease for a given period and damping. The findings in this study, shown in time series form, converge with theoretical results and can be generalized. This could represent a significant advancement in the measurement and monitoring of stability in construction zones. We believe that these results can provide valuable insights for construction companies and society at large.

References

1. Ay, A.M. & Wang, Y. (2014). Structural damage identification based on self-fitting ARMAX model and multi-sensor data fusion. *Structural Health Monitoring*, *13*(4), 445–460. https://doi.org/10.1177/1475921714542891

2. Bodeux, J.B. & Golinval, J.C. (2001). Application of ARMAV models to the identification and damage detection of mechanical and civil engineering structures. *Smart Materials and Structures*, *10*(3), 479–489. https:/doi.org/10.1088/0964-1726/10/3/309

3. Box, G.E., Jenkins, G.M., Reinsel, G.C., & Ljung, G.M. (2015). *Time series analysis: Forecasting and control*. John Wiley & Sons.

4. Brahimi, M. (1989). *The use of ARMA models for earthquake response spectra*. Polytechnic Institute of Brooklyn.

5. Brahimi, T. & Smain, T. (2021). A nonstationary mathematical model for acceleration time series. *Mathematical Modelling of Engineering Problems*, *8*(2), 246–252. https://doi.org/10.18280/mmep.080211

6. Carden, E.P. & Brownjohn, J.M. (2008). ARMA modelled time-series classification for structural health monitoring of civil infrastructure. *Mechanical Systems and Signal Processing*, *22*(2), 295–314. https://doi.org/10.1016/j.ymssp.2007.07.003

7. El-Choum, M.K. (2014). Utilization of ARMA models to measure damage potential in seismic records. In K. Chantawarangul (Ed.), *Sustainable Solutions in Structural Engineering and Construction* (pp. 138–143). Fargo, USA: ISEC Press. http://dx.doi.org/10.14455/ ISEC.res.2014.58

8. Johnson, E.A., Lam, H.F., Katafygiotis, L.S., & Beck, J.L. (2004). Phase I IASC-ASCE structural health monitoring benchmark problem using simulated data. *Journal of Engineering Mechanics*, *130*(1), 3–15. https://doi.org/10.1061/(ASCE)0733-9399(2004)130:1(3)

9. Luo, W.F. & Yu, L. (2017). New damage-sensitive feature for structures with bolted joints. *Journal of Physics: Conference Series*, *842*(1), Article 012083. IOP Publishing. https://doi.org/10.1088/1742-6596/842/1/012083

10. Menasri, A. (2012). *Simulation of strong motion with the ARMA technique* (in French). [Doctoral dissertation, Ecole Nationale Polytechnique].

11. Menasri, A., Brahimi, M., Frank, R., & Bali, A. (2012). ARMA modeling of artificial accelerograms for Algeria. *Applied Mechanics and Materials*, *105–107*, 348–355. https://doi.org/10.4028/www.scientific.net/AMM.105-107.348

12. Nair, K.K., Kiremidjian, A.S., & Law, K.H. (2006). Time series-based damage detection and localization algorithm with application to the ASCE benchmark structure. *Journal of Sound and Vibration*, *291*(1–2), 349–368. https://doi.org/10.1016/j.jsv.2005.06.016

13. Ouzandja, D., Messaad, M., Berrabah, A.T., & Belhrizi, M. (2023). Impact of material nonlinearity of dam-foundation rock system on seismic performance of concrete gravity dams. *Journal of Theoretical and Applied Mechanics*, *61*(1), 49–63. https://doi.org/10.15632/jtam-pl/157571

14. Sakellariou, J.S. & Fassois, S.D. (2006). Stochastic output error vibration-based damage detection and assessment in structures under earthquake excitation. *Journal of Sound and Vibration*, *297*(3–5), 1048–1067. https://doi.org/10.1016/j.jsv.2006.05.009

15. Zhang, Q.W. (2007). Statistical damage identification for bridges using ambient vibration data. *Computers & Structures*, *85*(7–8), 476–485. https://doi.org/10.1016/j.compstruc.2006.08.071

16. Zheng, H. & Mita, A. (2007). Two-stage damage diagnosis based on the distance between ARMA models and pre-whitening filters. *Smart Materials and Structures*, *16*(5), Article 1829. https://doi.org/10.1088/0964-1726/16/5/038

Manuscript received January 22, 2024; accepted for publication December 28, 2024; published online April 24, 2025.

JOURNAL OF THEORETICAL
AND APPLIED MECHANICS
63, 2, pp. 239–249, Warsaw 2025
https://doi.org/10.15632/jtam-pl/199771

RESEARCH ON HYDRODYNAMIC CHARACTERISTICS OF A 200 m × 175 m ANCHORED-OFFSHORE PHOTOVOLTAIC UNDER WIND-WAVE-CURRENT LOADS

Jian CHEN[1], Lv REN[2], Xin JIN[3], Maofeng GONG[4], Jie LIU[5*], Mingming LIU[6]

[1] *PowerChina Hebei Electric Power Design and Research Institute Co., Ltd, Shijiazhuang 050031, China*
[2] *China Renewable Energy Engineering Institute, Beijing 100120, China*
[3] *College of Electronic Engineering, Chengdu University of Information Technology, Chengdu 610225, China*
[4] *School of Automation, Chengdu University of Information Technology, Chengdu 610225, China*
[5] *School of Mechanical Engineering, Sichuan University of Science and Engineering, Yibin 644000, China*
[6] *School of Architecture and Engineering, Liaocheng University, Liaocheng 252000, China*

*corresponding author, *pzhjieliu@126.com*

This paper presents a numerical simulation of an anchored-offshore PV under loads, using SESAM & OrcaFlex for dynamic analysis of the coupled system. It obtains forces, characteristics, and tension, and calculates the PV structure first through SESAM, then substitutes the parameters into OrcaFlex to yield the coupling model. Various conditions are considered to estimate the dynamic characteristics and obtain the operating conditions.

Keywords: hydrodynamic characteristics; response amplitude operator; SESAM; OrcaFlex; anchored offshore photovoltaic.

1. Introduction

With the increasing energy demand, the depletion of fossil energy and greenhouse gas emissions, countries are vigorously promoting the use of renewable energy. Solar energy has become one of the most applicable energy sources (Sahu *et al.*, 2016). In the past decade, the solar photovoltaic (PV) industry has experienced rapid growth and expansion of terrestrial PV due to the need to take up a large amount of land resources and therefore being limited, the floating photovoltaic (FPV) came into being. FPV uses a wide sea surface to install the PV system, with many advantages such as small water area coverage and high power generation efficiency (Vo *et al.*, 2021). According to statistics, less than 1 % of the covered area can meet 25 % of the world's electricity demand (Tina *et al.*, 2018). Moreover, it can integrate complementary wind, wave and tidal energy, which has huge potential for development.

PV power stations commonly adopt the underwater anchoring or shoreline anchoring, including gravity anchors, screw anchors, and pull anchors (Wu *et al.*, 2022), and the mooring system generally employs wire ropes to moor PV arrays to the anchorage points. For reasons of installation convenience, most of the completed FPV projects at home and abroad have adopted the pontoon mounting scheme (Trapani & Redón Santafé, 2015).

Lin and Liu (2019) proposed a new concept of converting a decommissioned floating liquefied natural gas system (FPSO) into an FPV platform. A PV system was designed to power the offshore platform using a frequency domain hydrodynamic analysis of the FPSO to evaluate the effect of tilt angle on energy output. Yan *et al.* (2023) proposed a new modular offshore FPV with numerical simulation and hydrodynamic coupling analysis of a multi-body FPV system. Trapani and Millar (2016) used a computational fluid dynamics (CFD) method to study the kinematic response and mooring tension of a flexible thin film PV system under the action of

regular waves. Ikhennicheu *et al.* (2022) investigated the kinematic performance of small amplitude waves (amplitude <1 m) on a 3×3 array FPV. Sree *et al.* (2022) proposed a methodology combining the numerical simulation and experimental validation for evaluating the kinematic and structural response of modular FPVs under wave excitations. Xu and Wellens (2022) analysed the nonlinear interaction of waves with an offshore FPV system.

FPV systems are growing at an astonishing rate of 133 % per year over the past decade, and the total installed capacity of FPV systems globally exceeded 2.0 GW mark by the end of 2019, and reached 2.6 GW by the end of August 2020 (Kumar *et al.*, 2021). However, the current research is based on the hydrodynamic characteristics of monolithic structures and is dominated by lake and inland river FPV designs, and lacks the analysis of the impact on the marine environment, such as meteorological, hydrodynamic, photothermal, and submarine conditions. There is also no systematic research on the survival and operational performance of FPV power plants at sea conditions (wind, wave and current). In addition, at this stage, FPV power plants use the method of splicing PV modules, and the system's resistance to wind, wave and current performance has not been explored in depth.

In this study, the 200.0 m × 175.0 m offshore FPV system is designed. The calculations refer to the natural conditions of Zhoushan sea area in Zhejiang Province, China, including the local wind, wave and current parameters, and the amplitude response of the overall PV structure under multi-source loading and mooring forces are investigated, and reasonable mooring parameters are determined according to API RP 2SK, and the relevant results can be used for the application of the offshore PV. The results can provide a reference for the application of the offshore PV system.

2. Numerical methodology

Firstly, the PV model is established through SESAM/GeniE, and SESAM/HydroD is to obtain the hydrodynamic parameters of the PV structure (potential flow damping, additional mass, RAO, first-order wave force, and second-order average slow-drift force), and finally, the hydrodynamic parameters are substituted into OrcaFlex and thus yields a coupled floating body-mooring model. The coupled model is used to study the dynamic responses of the positive PV sheet, which would provide a reference for the overall development of the marine PV.

In the coupling calculation of the PV and mooring system, the interaction between the floating body and the slender body structure should be considered in each step of the iterative analysis, and the coupling influence of the floating body and the slender body structure is fully considered in Orcaflex, and the expression of the spatial discrete dynamic equilibrium control equation for the time-domain coupling analysis is as follows:

$$\mathbf{F}^I(\mathbf{r}, \ddot{\mathbf{r}}, t) + \mathbf{F}^D(\mathbf{r}, \dot{\mathbf{r}}, t) + \mathbf{F}^S(\mathbf{r}, t) = \mathbf{F}^E(\mathbf{r}, \dot{\mathbf{r}}, t), \tag{2.1}$$

where $\mathbf{F}^I$, $\mathbf{F}^D$, and $\mathbf{F}^S$ are the inertia force vector, damping force vector, and interaction force vector, respectively, $\mathbf{F}^E$ is the external force vector, $\mathbf{r}$, $\dot{\mathbf{r}}$, and $\ddot{\mathbf{r}}$ are the displacement vector, velocity vector, and acceleration vector of the floating body structure, respectively.

$\mathbf{F}^I$ is expressed as follows:

$$\mathbf{F}^I(\mathbf{r}, \ddot{\mathbf{r}}, t) = \mathbf{M}(\mathbf{r})\ddot{\mathbf{r}}, \tag{2.2}$$

where $\mathbf{M}$ is the mass matrix, including structural mass, fluid mass in the pipe and additional mass.

$\mathbf{F}^D$ is formulated as

$$\mathbf{F}^D(\mathbf{r}, \dot{\mathbf{r}}, t) = \mathbf{C}(\mathbf{r})\dot{\mathbf{r}}, \tag{2.3}$$

where $\mathbf{C}(\mathbf{r})$ is the damping matrix of the system, including the structural and hydrodynamic damping.

$\mathbf{F}^S$ is calculated based on the instantaneous stress results of the unit, and $\mathbf{F}^E$ is mainly derived from the structural gravity, buoyancy, forced displacement, environmental forces, and other specific loads.

Formulas of the wind force and moment for PV structures are, respectively, as follows:

$$F_{XW} = \frac{1}{2} C_{XW} \rho_W V_W^2 A_T, \tag{2.4}$$

$$F_{YW} = \frac{1}{2} C_{YW} \rho_W V_W^2 A_L, \tag{2.5}$$

$$M_{XYW} = \frac{1}{2} C_{XYW} \rho_W V_W^2 A_L L_{BP}, \tag{2.6}$$

where F_{XW}, F_{YW}, and M_{XYW} are the longitudinal wind force, transverse wind force and bow-wake wind moment, respectively, C_{XW}, C_{YW}, and C_{XYW} are, respectively, the longitudinal wind force coefficient, the transverse wind force coefficient and the bow-wake wind moment coefficient, where the wind force coefficient is obtained by referring to the plots in the Oil Companies International Marine Forum [OCIMF] (1994) data, ρ_W is the air density; V_W is the wind speed at 10 metres above the sea level, A_T is the forward wind area, A_L is the lateral wind area, L_{BP} is the length between plumb lines.

The flow rate is modelled using a power function (power law function), as follows:

$$S = S_b + [(S_f - S_b) \times (Z - Z_b)/(Z_f - Z_b)]^{1/7}, \tag{2.7}$$

where S_b and S_f correspond to the bottom flow velocity and surface flow velocity, Z_b is the height of the still water surface, Z_f is the depth of the seabed.

The longitudinal flow force F_{XC}, the transverse flow force F_{XY} and the bow-wake flow moment M_{XYC} for PV structures are, respectively, estimated through the formulas:

$$F_{XC} = \frac{1}{2} C_{XC} \rho_C V_C^2 T B, \tag{2.8}$$

$$F_{YC} = \frac{1}{2} C_{YC} \rho_C V_C^2 T L_{BP}, \tag{2.9}$$

$$M_{XYC} = \frac{1}{2} C_{XYC} \rho_C V_C^2 T L_{BP}^2, \tag{2.10}$$

where C_{XC}, C_{YC}, and C_{XYC} are the longitudinal flow coefficient, transverse flow coefficient, and bow hook moment coefficient, respectively, and the flow coefficients are obtained by referring to the plots in the OCIMF (1994) data; ρ_C is the density of seawater, and V_C is the flow velocity; T is the draught; B is the width.

3. Computational parameters

3.1. Study region and designed cases

The 200.0 m × 175.0 m PV monolithic structure is considered, with the operating environment being designed with reference to the sea conditions in Zhoushan, Zhejiang Province, China. The water depth of $h = 15.0$ m is applied. Three different wave conditions are considered, which are generated by JONSWAP spectra with effective wave heights of 1.5 m, 2.0 m, and 2.5 m, corresponding to wave periods of 5.0 s, 6.0 s, and 7.0 s, as well as three wind speed conditions (10.0 m/s, 20.0 m/s, and 30.0 m/s) and two current conditions (0.5 m/s and 1.0 m/s). A total of 18 operational conditions are simulated, as shown in Table 1.

Table 1. Operational cases in wind-wave-current sea conditions.

No.	Significant wave height [m]	Peak frequency [s]	Flow velocity [m/s]	Wind velocity [m/s]
LC1∼LC3	1.5	5.0	0.5	10.0/20.0/30.0
LC4∼LC6	1.5	5.0	1.0	10.0/20.0/30.0
LC7∼LC9	2.0	6.0	0.5	10.0/20.0/30.0
LC10∼LC12	2.0	6.0	1.0	10.0/20.0/30.0
LC13∼LC15	2.5	7.0	0.5	10.0/20.0/30.0
LC16∼LC18	2.5	7.0	1.0	10.0/20.0/30.0

3.2. Model geometric parameters and modelling

The PV system consists of 100×100 PV basic blocks, which are rigidly connected without considering the influence of mutual movement of structures. The computational model simplifies the PV overall and individual structural forms and ignores the PV detailed structures, thus reducing the mesh quantity, and the PV wet-surface, and the mass model is built by SESAM/GeniE, and the PV model and the individual sheet mesh model are shown in Fig. 1.

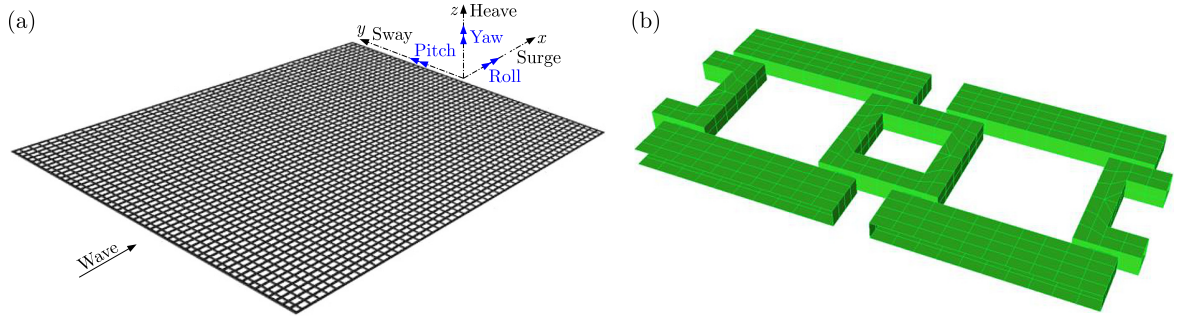

Fig. 1. Model of offshore PV structure: (a) panel model; (b) individual photovoltaic grid models.

Table 2. Overall structure of anchored offshore PV system.

Length [m]	Width [m]	Draft [m]	Discharge [ton]	Centre of gravity height from baseline [m]	Wind area in longitudinal [m^2]	Wind area in transverse [m^2]	Flow area in longitudinal [m^2]	Flow area in transverse [m^2]
200	175	0.2	463	0.2	75.4	21	40	35

The simulation is divided into the static and dynamic analyses. The static analysis considers the average loads of wind, current and drift forces acting on the PV and the mooring cable as well as external loads, and the calculated average offset position of the PV system and the mooring cable tension are used as the starting position for the subsequent dynamic analysis. The dynamic analysis takes into account the dynamic effects of the PV structure, the mooring cable and the external loads to obtain the displacement of the structure and the mooring cable tension.

3.3. Mooring scheme

The PV structure is fixed by mooring positioning, and the seabed is anchored by concrete blocks (the gravity of the concrete blocks is much greater than the tension of the anchor chains). The mooring chain is distributed along the perimeter of the PV, and the anchor chain is set at the chain exit to the anchorage point, with a diameter of 0.04 mm, a length of 32.0 m, and a spacing of 20.0 m, for a total of 40 anchor chains. The parameters of the mooring chain and the deployment are, respectively, shown in Table 3 and Fig. 2.

Table 3. Properties of mooring chains.

Cable length [m]	Diameter [m]	Air quality [kg/m]	Water quality [kg/m]	Axial stiffness [N]	Breaking force [kN]	Drag coefficients	Added mass coefficients
32	0.04	31.8	27.7	1.37e8	1280	(2.6, 2.6, 1.4)	(1.0, 1.0, 0.5)

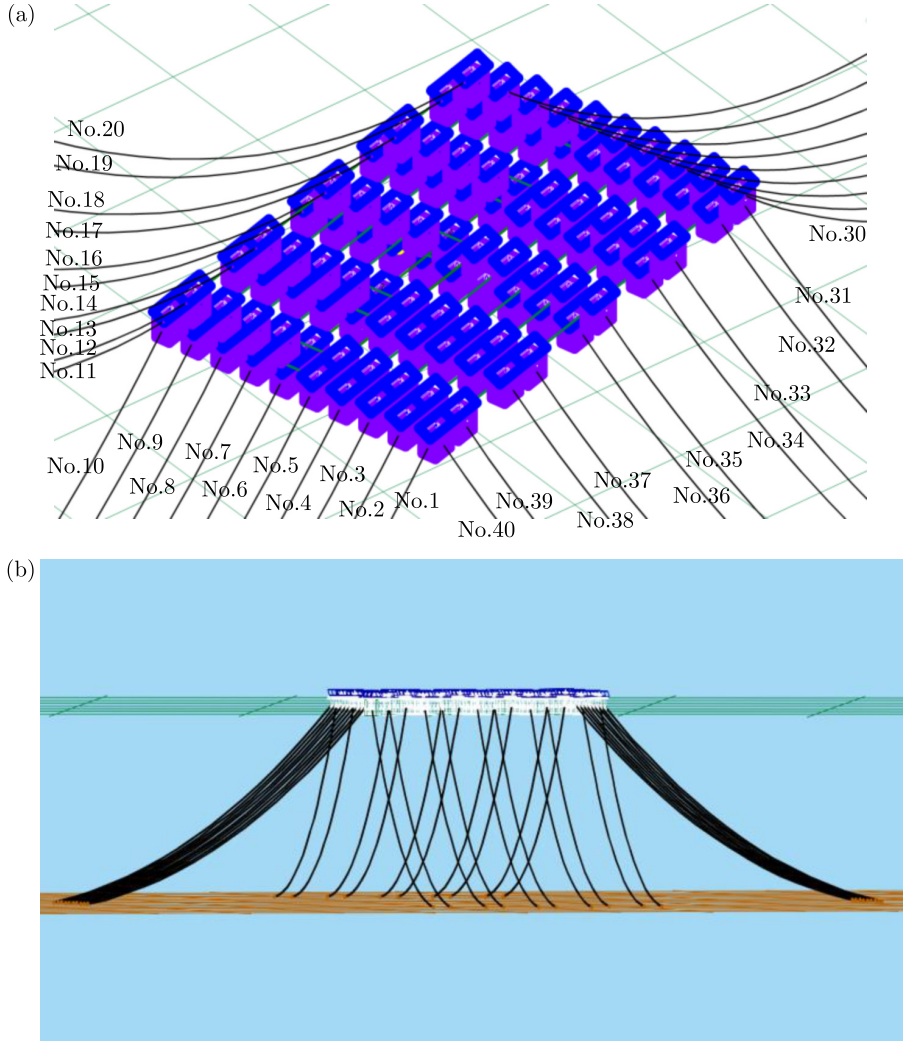

Fig. 2. Schematic map of the mooring chain: (a) over view; (b) front view.

3.4. Safety specification

The main constraints of the coupled dynamic analysis of photovoltaics and mooring chain are the mooring cable tension, the anchor grip, and the float motion response. Since the large long-period slow-drift motion of the float has less impact on the upper PV structure, and the present PV anchoring method is simplified as fixed, the mooring cable tension is the main concern in the calculation.

Minimum Safety Factor for Mooring Cable Referring to API RP 2SK Specification (OCIMF, 1994) and China Classification Society [CCS] (2019) specification require that the mooring cable tension must satisfy a certain safety factor. The ratio of the breaking load of the mooring cable to the maximum design tension represents the safety factor (SF), i.e., SF = breaking load / maximum design tension. The results listed in the paper are that after taking into account the dynamic amplification factor, which is a dynamic calculation, the minimum safety factor for normal operating conditions is set as 1.67.

4. Results and discussion

4.1. Frequency domain characteristics

SESAM is used to carry out the frequency domain characteristics of the PV structure to obtain the hydrodynamic parameters. Regular waves are chosen for the frequency domain calculation, the wave frequency ranges from 0.2 rad/s to 1.8 rad/s with an interval of 0.05 rad/s, and the wave incidence direction ranges from 0° to 180° with an interval of 15°.

The six-degree-of-freedom (surge, sway, heave, roll, pitch, and yaw) response amplitude operators (RAOs) of the PV structure under different wave incidence conditions are illustrated in Fig. 3. From the figure, it can be seen that the RAOs of both surge and sway decrease with the increase of the wave frequency. We can also find that both RAOs are almost identical, which is mainly due to the fact that the PV structure is close to the square; the maximum surge

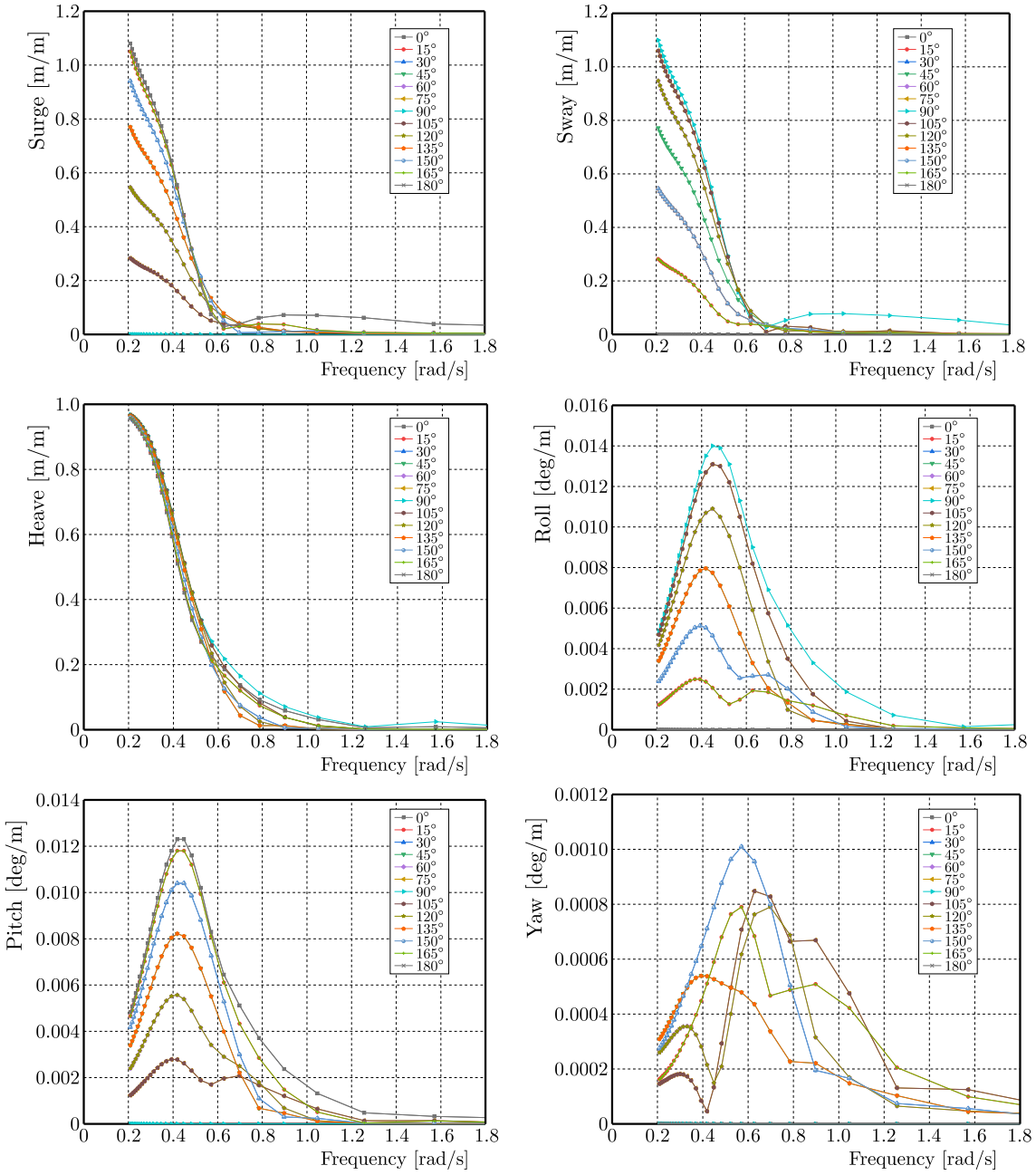

Fig. 3. Variations of response amplitude operator (RAO) with wave frequency under various wave direction angles.

RAO for different wave directions occurs at 0° or 180° wave direction angle, while the maximum sway RAO for different wave directions occurs at 90° wave direction angle. Besides, the surge is sensitive to the low-frequency wave below 0.6 rad/s, and the facing and following waves have the greatest influence on the surge, while the transverse wave has almost no influence. Similar to that of the surge, the sway is also sensitive to the wave frequency of less than 0.6 rad/s. But, contrary to that of the surge, the transverse wave influences on the sway greatly, while the influence of the wave facing and following is weak. In heave motion, the amplitude of each wave angle decreases with the increase of wave frequency, the heave RAOs of all wave directions are almost the same, and no resonance appears. Therefore, the PV structure is not sensitive to the wave resonance frequency.

For both roll and pitch, the RAOs at each wave direction angle show a tendency of increasing and then decreasing with the increasing wave frequency. The sensitive frequency of roll and pitch RAOs corresponds to 0.524 rad/s, where the maximum roll RAO appears at 90° wave direction angle, while the maximum pitch RAO occurs at 0° and 180° wave direction angles. The maximum yaw RAO occurs at 150° wave direction angle, which corresponds to a wave frequency of 0.58 rad/s.

The above discussions reveal that the planar responses are much fierce than the rotational motions, thus the planar motions of the PV structure are the main controlling factor for the tension of the mooring chain.

4.2. Time domain characteristics

The coupled dynamic analysis of moored floating body is based on Orcaflex, the pre-tension of the mooring chain is about 10 tons in the simulation, in which the JONSWAP spectrum is selected to generate random waves. The frequency domain hydrodynamic parameters of the PV structure are substituted into Orcaflex, and the integrated effects of the environmental forces of the wind, wave, and current are considered to carry out the time-domain dynamic analysis under anchored conditions, to obtain the time series of the force acting on the anchored cable. Finally, the maximum tension of the anchored cable and the operational response of the anchored-offshore PV system are obtained according to the 3.0 hours' regression period.

In the calculation, the most dangerous working condition is considered to be the coincident incidence of wind, wave and current, and then the coupled dynamics of the floating body-anchor chain is solved. Reference is made to the API RP 2SK Specification (OCIMF, 1994), and five different wave seeds are calculated, respectively, in the simulation of irregular waves, and the anchored chain tension is chosen as the average value of five runs to reduce the randomness of irregular waves.

For demonstration, the dynamic response of the PV system at a certain time instant is demonstrated in Fig. 4. From this figure, the anchored chain in the environmental incidence

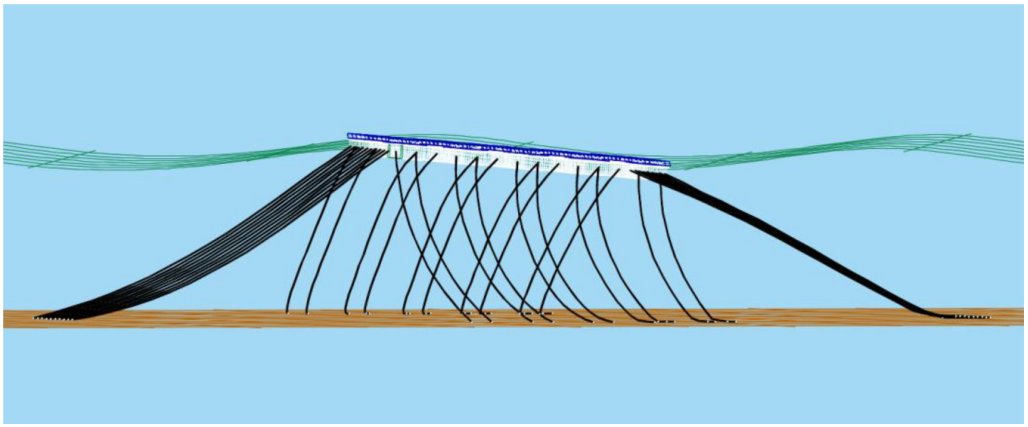

Fig. 4. Schematic map of the dynamic response of the PV system at a certain time instant.

direction is in a tense state, while the anchored chain in the propagation direction is in a relaxed state. Due to the overall rigidity of the PV system, the draft of the PV structure in the environmental incidence direction increases, thus increasing the force on the anchored cable, so the anchored chain is in a tense shape.

Figure 5 shows the time series of the wind force, current force, first order wave force and the second order slow drift force on the PV structure of Case 12. It can be seen from this figure that the PV structure is subjected to the largest first-order wave force with a maximum of about 15000 kN, the wind force is about 5.18 kN, and the second-order wave force of the slow drift approaches 540 kN. The current force is the minimal, being 0.288 kN. Therefore, by comparisons, it can be concluded that the main controlling factor of the system is the first-order wave force, and therefore the design should be focused on considering the effect of its impacts on the mooring equipment.

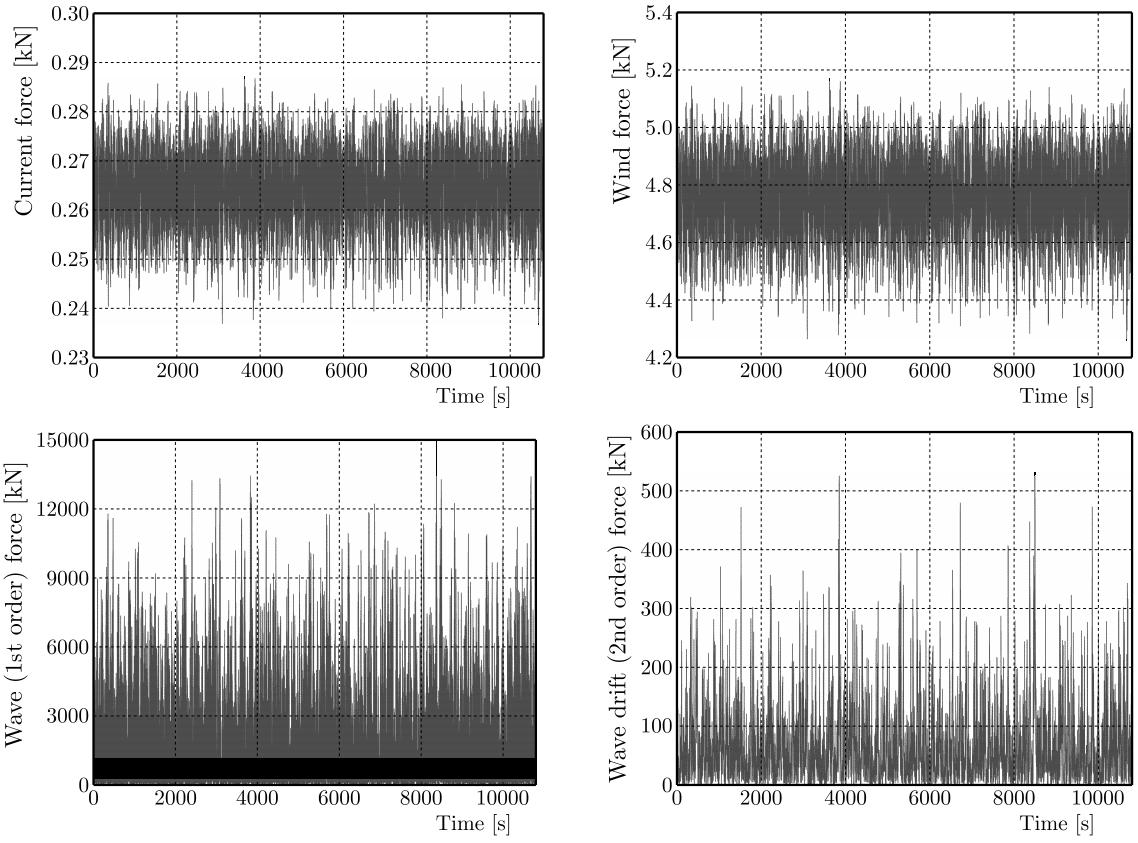

Fig. 5. Time series of current, wind and wave loads on the PV structure.

Table 4 gives the effective tensions of the maximum tension of the anchor chain under five wave seeds with the wave heights of 1.5 m, 2.0 m, and 2.5 m. From this table, it can be seen that the working conditions of LC1 to LC6 with the wave height of 1.5 m, the maximum tension of the anchor cable is 324.0 kN, and the corresponding safety factor is 4.85, which can meet the

Table 4. Maximum tension of cable chains.

Working condition	Mooring chain [kN]						Safety factor
	Seed 1	Seed 2	Seed 3	Seed 4	Seed 5	Mean value	
LC6	202	324	276	233	285	264	4.85
LC12	945	1230	1002	960	923	1012	1.26
LC18	2430	2675	2560	2468	2617	2550	0.5

requirement of the safety factor 1.67; for the working conditions of LC7 to LC12 with the wave height of 2.0 m, the maximum tension of the anchor cable is 1012.0 kN, with the corresponding safety factor being 1.26, which no longer satisfies the safety factor 1.67. As for the working conditions of LC13 to LC18, the wave height being 2.5 m, the maximum anchor cable tension is 2550.0 kN, yielding the safety factor being 0.5, which also does not guarantee the specification requirements. Therefore, the anchored chain with the diameter 40.0 mm cannot meet the safety requirements of 2.0 m and 2.5 m wave height' operation conditions. To meet the operation requirement of 1.67, a cable with a diameter of at least 48.0 mm should be selected for 2.0 m wave height, and for 2.5 m wave height, a cable with a diameter of at least 76.0 mm diameter is needed.

The time series of the maximum dynamic tensions of the anchored cable for LC6, LC12, and LC 18 of the wave seed 2 are shown in Fig. 6. The figure shows that the maximum tension is at the transient stage, which exhibits one or several peaks, and the tension oscillates up and down in a certain equilibrium position, which is consistent with the large-value planar motion of the PV structure.

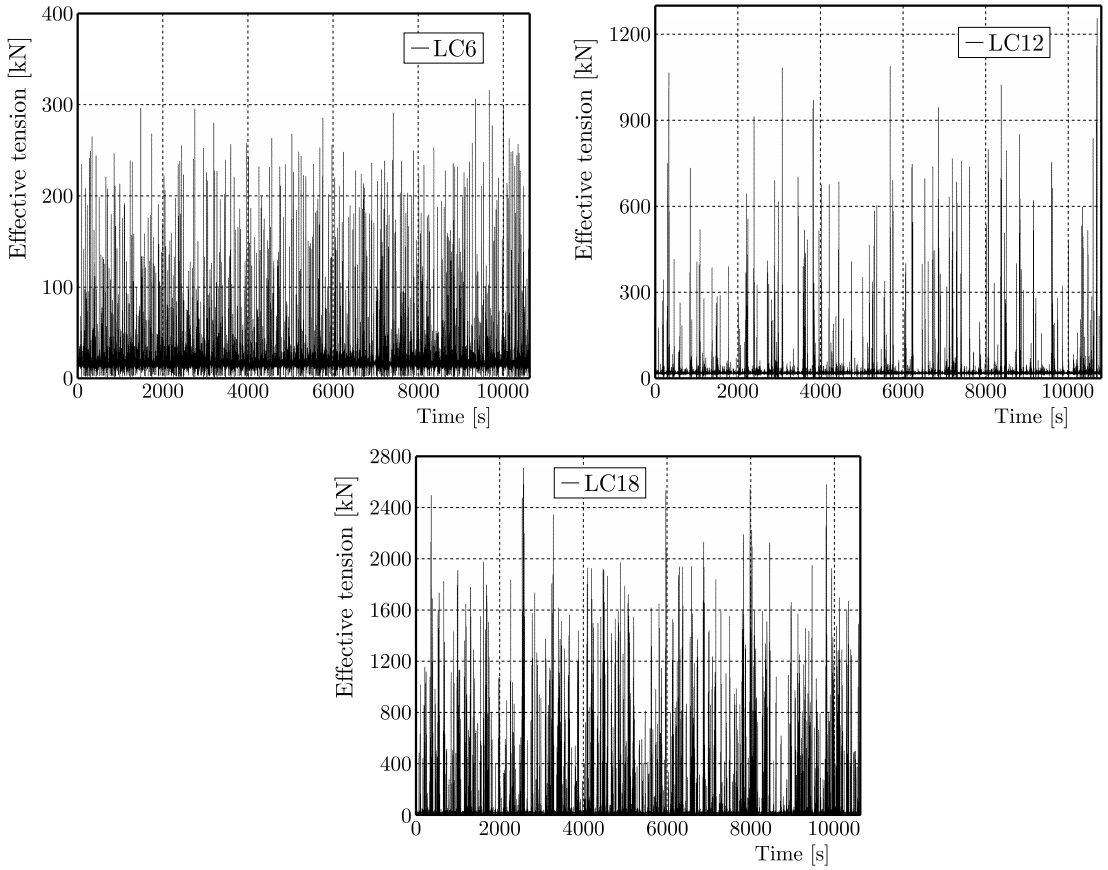

Fig. 6. Time series of anchored cable tension.

5. Conclusions

This study carries out the time-domain coupled dynamic characterization of a 200.0 m × 175.0 m anchored-offshore PV system based on the potential flow theory, and the dynamic response characteristics of the PV structure under the combined effects of wind, wave and current loads are obtained. And, the optimal anchored chain parameters are identified based on the API RP 2SK specification (OCIMF, 1994). The conclusions are as follows:

1) The designed PV structure has no significant wave resonance characteristics. Since the PV structure is close to a square, its transverse and longitudinal oscillation RAOs are

basically the same, and the transverse and longitudinal oscillation RAO trends are also the same. Moreover, since the longitudinal and transverse areas of the PV sheet are large, their frequency domain characteristics show no obvious wave resonance characteristics.

2) Wave load is the main factor affecting the mooring cable tension. Due to the shallow draft and small wind area of the PV, its wind and current loads are significantly smaller than the wave loads, and the wind and current loads have less influence on the dynamic maximum tension of the mooring cable.
3) This design of 40.0 mm anchor chain can meet the operational requirements of working conditions LC1∼LC6, but is invalid for working conditions LC7∼LC18. When the environmental load is 2.0 m wave height, 1.0 m flow velocity, 30.0 m/s wind speed operating conditions, the minimum diameter of the anchored chain should be selected as 48.0 mm; when the environmental load is 2.5 m wave height, 1.0 m flow velocity, 30.0 m/s wind speed operating conditions, the diameter of the anchored chain should be no less than 76.0 mm.

Acknowledgments

The work was supported, in part, by the National Natural Science Foundation of China (grant no. U2342216), Key R&D program of Science & Technology Department of Sichuan Province (grant no. 2024YFHZ0173), Science Foundation of Science & Technology Department of Sichuan Province (grant no. 2023NSFSC0747), and the Ministry of Education Collaborative Education (grant no. 230806521252005, 231006521163646).

References

1. China Classification Society [CCS]. (2019). *Classification specification for offshore mobile platforms.*
2. Ikhennicheu, M., Blanc, A., Danglade, B., & Gilloteaux, J.-C. (2022). OrcaFlex modelling of a multi-body floating solar island subjected to waves. *Energies*, *15*(23), Article 9260. https://doi.org/10.3390/en15239260
3. Kumar, M., Niyaz, H.M., & Gupta, R. (2021). Challenges and opportunities towards the development of floating photovoltaic systems. *Solar Energy Materials and Solar Cells*, *233*, Article 111408. https://doi.org/10.1016/j.solmat.2021.111408
4. Lin, Z. & Liu, X. (2019). Sustainable development of decommisioned FPSO as a floating solar plant – case study of the effects of tilt angle on energy efficiency. *Proceedings of the International Conference on Applied Energy*, Västerås, Sweden (4, Article 0468).
5. Oil Companies International Marine Forum [OCIMF]. (1994). *Prediction of wind and current loads on VLCCs* (2nd ed.). London, England: Witherby.
6. Sahu, A., Yadav, N., & Sudhakar, K. (2016). Floating photovoltaic power plant: A review. *Renewable and Sustainable Energy Reviews*, *66*, 815–824. https://doi.org/10.1016/j.rser.2016.08.051
7. Sree, D.K.K., Law, A.W.K., Pang, D.S.C., Tan, S.T., Wang, C.L., Kew, J.H., Seow, W.K., & Lim, V.H. (2022). Fluid-structural analysis of modular floating solar farms under wave motion. *Solar Energy*, *233*, 161–181. https://doi.org/10.1016/j.solener.2022.01.017
8. Tina, G.M., Cazzaniga, R., Rosa-Clot, M., Rosa-Clot, P. (2018). Geographic and technical floating photovoltaic potential. *Thermal Science*, *22*(Suppl. 3), S831–S841. https://doi.org/10.2298/TSCI170929017T
9. Trapani, K. & Millar, D.L. (2016). Hydrodynamic overview of flexible floating thin film PV arrays. *Proceedings of the 3rd Offshore Energy and Storage Symposium*, Valletta, Malta.
10. Trapani, K. & Redón Santafé, M. (2015). A review of floating photovoltaic installations: 2007–2013. *Progress in Photovoltaics: Research and Applications*, *23*(4), 524–532. https://doi.org/10.1002/pip.2466

11. Vo, T.T.E., Ko, H., Huh, J., & Park, N. (2021). Overview of possibilities of solar floating photovoltaic systems in the offshore industry. *Energies*, *14*(21), Article 6988. https://doi.org/10.3390/en14216988

12. Wu, X., Xiao, W., Yang, L., & Pan, Y. (2022). Research on hydrodynamic characteristics of an offshore flexible floating photovoltaic in waves. *2022 3rd International Conference on Geology, Mapping and Remote Sensing (ICGMRS)*, Zhoushan, China, 841–845. https://doi.org/10.1109/ICGMRS55602.2022.9849362

13. Xu, P. & Wellens, P.R. (2022). Theoretical analysis of nonlinear fluid-structure interaction between large-scale polymer offshore floating photovoltaics and waves. *Ocean Engineering*, *249*, Article 110829. https://doi.org/10.1016/j.oceaneng.2022.110829

14. Yan, C., Shi, W., Han, X., Li, X., & Verma A.S. (2023). Assessing the dynamic behaviour of multi-connected offshore floating photovoltaic systems under combined wave-wind loads: A comprehensive numerical analysis. *Sustainable Horizons*, *8*, Article 100072. https://doi.org/10.1016/j.horiz.2023.100072

Manuscript received April 30, 2024; accepted for publication January 3, 2025; published online March 24, 2025.

JOURNAL OF THEORETICAL
AND APPLIED MECHANICS
63, 2, pp. 251–262, Warsaw 2025
https://doi.org/10.15632/jtam-pl/199928

PERFORMANCE BENEFITS OF VEHICLE AIR SUSPENSION SYSTEM EMPLOYING INERTER ELEMENT

Yujie SHEN*, Jiaheng LIN, Yuqiu XU, Xiaofeng YANG, Yanling LIU

Automotive Engineering Research Institute, Jiangsu University, Zhenjiang 212013, China
*corresponding author, *shenyujie@ujs.edu.cn*

This paper analyzes the performance analysis of vehicle air inerter-spring-damper (ISD) suspension systems. First of all, this paper establishes the air ISD suspension with series-connected inerter and with parallel-connected inerter which are the quarter car model of the two basic vehicle suspension layouts involving an inerter. After that, the primary parameters are optimized through particle swarm optimization by considering the overall performance, including vehicle body acceleration, suspension working space and dynamic tire load. The simulation analysis reveals that all of the dynamic performance indexes of the vehicle air ISD suspension are significantly decreased by comparing to the conventional air suspension. A bench test was carried out to verify that the model assumptions and simplifications are correctly formulated.

Keywords: inerter; vehicle suspension; air suspension; ride comfort.

1. Introduction

The vehicle suspension, a general device situated between the wheel and the axle for the force transmission, which can maintain the vehicle ride comfort and ensuring handling stability. So far, the semi-active suspension (Elahi *et al.*, 2016; Sammier *et al.*, 2003) and active suspension (Cui *et al.*, 2019; Li *et al.*, 2023) systems can be self-adjusted according to changes in driving conditions. Different from the general suspension, the air suspension (Oda & Nishimura, 1970; Quaglia & Sorli, 2001; Shen *et al.*, 2024b) replaces the plate spring in the traditional suspension with the air spring. Due to the nonlinear characteristics of the airbag (Wen *et al.*, 2013), the variable stiffness characteristics of the air spring can be guaranteed, which can improve the ride comfort while ensuring the vehicle handling stability. Li *et al.* (2014) creates the model of interlinked air suspension, confirming that the vehicle's roll angle and vertical vibration will be reduced effectively by using the proposed suspension. However, the air suspension still maintains the "spring-damper" structure of the traditional suspension system, which is still limited in improving the performance of the suspension. With the development of suspension technology, active suspension (Yang *et al.*, 2024) and semi-active suspension (Shen *et al.*, 2024a) has been studied widely. But from the view of energy consumption and reliability, semi-active suspension and active suspension still have a long way to engineering application. From this perspective, it is more reasonable to enhance the suspension performance by using a passive element.

Smith (2002) from Cambridge University first proposed the concept of interter. It represents a departure from the common structure of the traditional suspension "spring-damper". The force applied at both ends of the mechanical element is proportional to the relative accelerations. The application of the inerter to the vehicle suspension, that is, the "inerter-spring-damper" structure (ISD suspension), has pushed the development of the vehicle suspension system to a new platform (Shen *et al.*, 2023a; 2023b; Wang *et al.*, 2024a; 2024b). To date, different realizations of inerter have been developed, including ball-screw inerter (Ma *et al.*, 2021),

rack-and-pinion inerter (Papageorgiou *et al.*, 2009), hydraulic inerter (Wang *et al.*, 2011), electromagnetic mechanism inerter (Gonzalez-Buelga *et al.*, 2015), helical fluid inerter (De Domenico *et al.*, 2019) and living-hinge inerter (John & Wagg, 2019). Seifi and Hassannejad (2022) introduces a novel suspension design featuring inerters and asymmetric dampers, and it is confirmed that the ride comfort and road-holding ability can be improved by using the optimized suspension with inerters and nonlinear dampers.

Currently, there is limited research by scholars on the integration of inerters into suspension systems to improve the air suspension performance. The air suspension of the existing research still maintains the "spring-damper" structure of the traditional suspension system, and the performance of the air suspension with inerter is unknown. In this paper, on the basis of the air suspension, the inerter will be included and the performance of the air ISD suspension will be explored.

The structure of the paper is organized in the following manner: in Section 2, a new air ISD suspension structure is introduced, along with the establishment of the models for air ISD suspension that including both series-connected and parallel-connected inerter. Section 3 employs the particle swarm optimization algorithm to complete the optimization under random road input conditions. In Section 4, the two suspension models will be simulated and analyzed in both the time and frequency domains under various road conditions. In Section 5, the bench test was carried out to verify that the model assumptions and simplifications are correctly formulated in the paper. The paper concludes with a summary in Section 6.

2. Model of the vehicle air ISD suspension

An accurate model that takes into account various connectivity relationships and nonlinear factors is essential for accurately capturing the dynamic response of real vehicles. There are many studies on vehicle suspension performance using a 7 degree-of-freedom (dof) model and even a 14 dof model. However, an accurate model is often too complicated, and there have been studies using a 2 dof model to demonstrate vehicle suspension performance (Shen *et al.*, 2023b). This paper focuses on the general laws of the inerter's benefits on the vehicle vertical dynamics performance. Consequently, this paper considers the nonlinear stiffness feature of the air spring and establishes a 2 dof quarter car ISD suspension model. Among this dynamic model, the car body and wheel are assumed to be rigid bodies with concentrated mass. The inerter, air spring and damper are connected according to series arrangement and parallel arrangement between the sprung mass and unsprung mass. The effect of tire damping is neglected, and the tires are simplified as equivalent springs connected to the road surface. The conventional air suspension model is marked as S_0 and the series-connected air suspension and parallel-connected air suspension are marked as S_1 and S_2, respectively, as shown in Fig. 1.

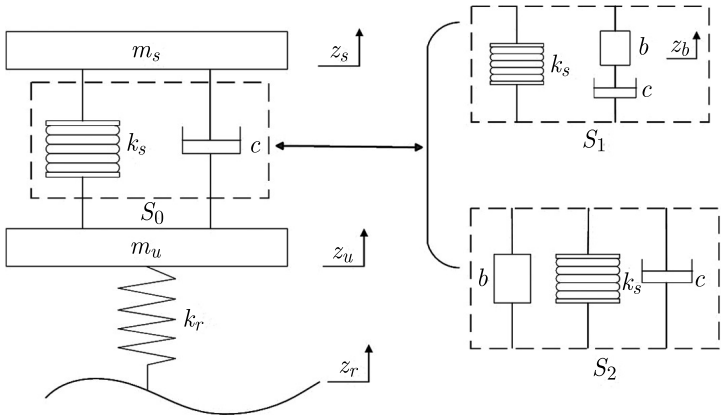

Fig. 1. Vehicle air ISD suspension.

Here, m_s represents the mass of the sprung component, m_u denotes the mass of the unsprung component, k_r represents the stiffness of tire, z_s, z_u, and z_r denotes the vertical displacements of the sprung mass, unsprung mass and road input, respectively.

For a sleeve model air spring with a negligible change in effective area and hysteresis effect, the stiffness of the air spring is formulated as follows:

$$k_s = \frac{np_0}{v_0 - A_e(z_u - z_s)} A_e^2, \tag{2.1}$$

where p_0 represents the initial effective air pressure, v_0 represents the initial volume, A_e represents the effective area and n represents the thermos dynamic coefficient.

There are many realization forms of inerters and different types of inerters have a different mathematical model. But the ideal inerter output force is related with the acceleration between two terminals. Consider the length of this paper, the ideal inerter output force can be summarized as follow:

$$F_b = b\ddot{x}, \tag{2.2}$$

where b represents the inertance with the unit kg, $\ddot{x}$ is the acceleration between two terminals.

The suspension has two basic arrangements, namely series arrangement and parallel arrangement. In this document, the inerter structure is added on the basis of air suspension, and two new structural forms of suspension are constructed, called series-connected air suspension and parallel-connected air suspension with the inerter component, as demonstrated in parts S_1 and S_2 of Fig. 1.

Where b represents the inertance with the unit kg, z_b represents the vertical displacement of the inerter, pertaining to the sprung mass denoted as m_s, based on Newton's laws of motion, the equation is described as follows:

$$m_s\ddot{z}_s + b(\ddot{z}_s - \ddot{z}_b) + k_s(z_s - z_u) = 0. \tag{2.3}$$

For the unsprung mass denoted as m_u, the equation is described as follows:

$$m_u\ddot{z}_u - k_s(z_s - z_u) - c(\dot{z}_b - \dot{z}_u) + k_r(z_u - z_r) = 0. \tag{2.4}$$

At the connection point of the inerter to the damping mechanism, the equation is described as follows:

$$b(\ddot{z}_s - \ddot{z}_b) = c(\dot{z}_b - \dot{z}_u). \tag{2.5}$$

After that, the equations describing the motion of the entire system are as follows:

$$\begin{aligned} m_s\ddot{z}_s + b(\ddot{z}_s - \ddot{z}_b) + k_s(z_s - z_u) &= 0, \\ m_u\ddot{z}_u - k_s(z_s - z_u) - c(\dot{z}_b - \dot{z}_u) + k_r(z_u - z_r) &= 0, \\ b(\ddot{z}_s - \ddot{z}_b) &= c(\dot{z}_b - \dot{z}_u). \end{aligned} \tag{2.6}$$

The S_2 part of Fig. 1 illustrates a quarter car model incorporating an inerter. The inerter is connected in parallel with the damping element in this model. It is intuitively to figure out the motion equation of this system according to the above analysis of the series-connected system.

For the sprung mass denoted as m_s, based on Newton's laws of motion, the equation is described as follows:

$$m_s\ddot{z}_s + b(\ddot{z}_s - \ddot{z}_u) + k_s(z_s - z_u) + c(\dot{z}_s - \dot{z}_u) = 0. \tag{2.7}$$

For the unsprung mass denoted as m_u, the equation is described as follows:

$$m_u\ddot{z}_u - b(\ddot{z}_s - \ddot{z}_u) - k_s(z_s - z_u) - c(\dot{z}_s - \dot{z}_u) + k_r(z_u - z_r) = 0. \tag{2.8}$$

After that, the equations describing the motion of the entire system are as follows:

$$\begin{aligned} m_s\ddot{z}_s + b(\ddot{z}_s - \ddot{z}_u) + k_s(z_s - z_u) + c(\dot{z}_s - \dot{z}_u) &= 0, \\ m_u\ddot{z}_u - b(\ddot{z}_s - \ddot{z}_u) - k_s(z_s - z_u) - c(\dot{z}_s - \dot{z}_u) + k_r(z_u - z_r) &= 0. \end{aligned} \tag{2.9}$$

3. Optimization of the suspension parameters

In the optimization process, the root-mean-square (RMS) values of vehicle body acceleration, suspension working space, and dynamic tire load incorporates the consideration so that the vehicle air ISD suspension can get optimized. It is assumed that the vehicle drives with a speed of v on a Grade C road, with the random road input being characterized as follows:

$$\dot{z}_r(t) = -0.111\left[vz_r(t) + 40\sqrt{G_q(n_0)v}\omega(t)\right], \tag{3.1}$$

where the vertical displacement of the random road input can be expressed as $z_r(t)$, the road roughness can be expressed as $G_q(n_0)$, and the Gaussian white noise with mean value as 0 can be expressed as $\omega(t)$. Here, $G_q(n_0)$ is $256 \times 10^{-6}\,\mathrm{m}^3 \cdot \mathrm{cycle}^{-1}$, v is 20 m/s. Particle swarm optimization (PSO) is a swarm intelligence algorithm, which regards the behavior of optimizing the objective function as the cooperation and competition among individuals in the predatory behavior of birds. During the simulation optimization in this paper, the PSO is adopted.

3.1. Parameters optimization of S_1 and S_2

When using the PSO to determine the optimal parameters of S_1 and S_2, the damping coefficient and the inertance are variables and require optimization, and the rest of the suspension model parameters are provided in Table 1.

Table 1. Parameters of the mature air suspension model.

Parameter name	Value
Sprung mass, m_s	800 kg
Unsprung mass, m_u	100 kg
Stiffness of tire, k_r	243000 N/m
Passive damping coefficient, c_0	2000 Ns/m
Air spring initial air pressure, p_0	188000 Pa
Initial volume of air spring, v_0	0.0116 m^3
Effective area of air spring, A_e	0.0421 m^2
Air polytropic index, n	1

Using S_0 as the comparison object, the optimization objectives include the RMS of the vehicle body acceleration, the suspension working space and the dynamic tire load. A unified objective function is then formulated, and MATLAB/Simulink is employed to determine the optimal solution of this objective function along with its specific parameters.

It should be noted that, under random road inputs, the RMS values for the vehicle body acceleration, the suspension working space, and the dynamic tire load of S_0 are 0.4828 $\mathrm{m/s}^2$, 0.0072 m, 625.16 N, respectively. Establishing a unified objective function is essential, given that the above three performance indexes differ in units and magnitudes. To examine the overall dynamic performances, encompassing ride comfort, handling stability, and driving safety, of the proposed vehicle air ISD suspension, a comprehensive objective is formulated. Divide the three indexes of the suspension with S_1 and the three indexes of S_0 separately, then the unified objective function is the sum of three quotients. The formula for the unified objective function is as follows:

$$f = 0.6 \times J_1/J_{1\mathrm{pas}} + 0.2 \times J_2/J_{2\mathrm{pas}} + 0.2 \times J_3/J_{3\mathrm{pas}}, \tag{3.2}$$

where the fitness function can be expressed as f, J_1, J_2, J_3, respectively, represent the RMS of the body acceleration, the suspension working space and the dynamic tire load of the vehicle air

ISD suspension, while $J_{1\text{pas}}$, $J_{2\text{pas}}$, and $J_{3\text{pas}}$ are the RMS values of the vehicle body acceleration, the suspension working space and the dynamic tire load of S_0, respectively. The penalty rule is established such that, among the RMS values of body acceleration, suspension working space, and dynamic tire load, if any one of these is inferior to the corresponding value of S_0, the penalty value is assigned as 100; otherwise, it is set to 0. Represents the upper and lower limits of parameters to be optimized can be expressed as lb and ub, respectively, given that the actual structure, $lb = [1, 1]$, $ub = [2000, 5000]$.

When the maximum number of iterations is 30, the group size is 10, the inertia coefficient is 0.8, the damping ratio of the inertia coefficient is 0.9, the individual acceleration coefficient c_1 is 1.5, the social acceleration coefficient c_2 is 2. The optimal parameters for S_1 and S_2 are detailed in Table 2.

Table 2. Optimization results of S_1 and S_2.

Suspension	Inertance b [kg]	Damping coefficient c [Ns/m]
S_1	793	3362
S_2	17	3190

4. Dynamic performance analysis

After using the optimized parameters in Section 3, time domain and frequency domain simulations for S_1 and S_2 under various working conditions are conducted so that the improvement of the performance of the air suspension by the inerter can get deeper research.

4.1. Simulation under the random road

Figures 2–4 show the three dynamic performance indexes of S_1 and S_2 compared to S_0 on the random road surface at a speed of 20 m/s, where (a) is the time domain response and (b) is the frequency domain response.

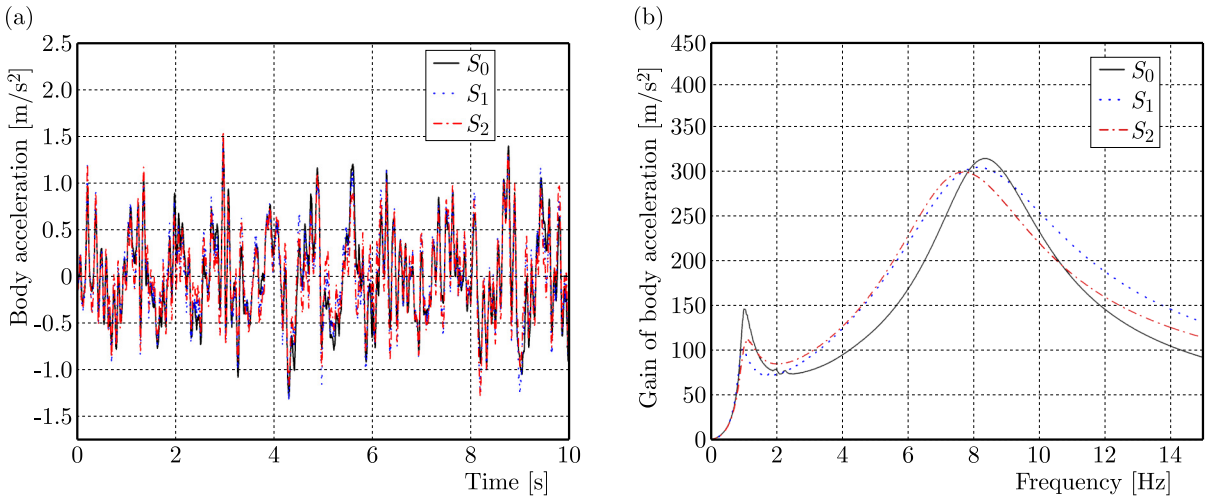

Fig. 2. Responses of vehicle body acceleration under the random road.

Table 3 shows the dynamic performance indexes of S_0, S_1, and S_2 on the random road surface at a speed of 20 m/s.

In the frequency domain responses, as the frequency increases, all the gain value of the three indexes increases first and then decreases in the low frequency band, and have a trend of increas-

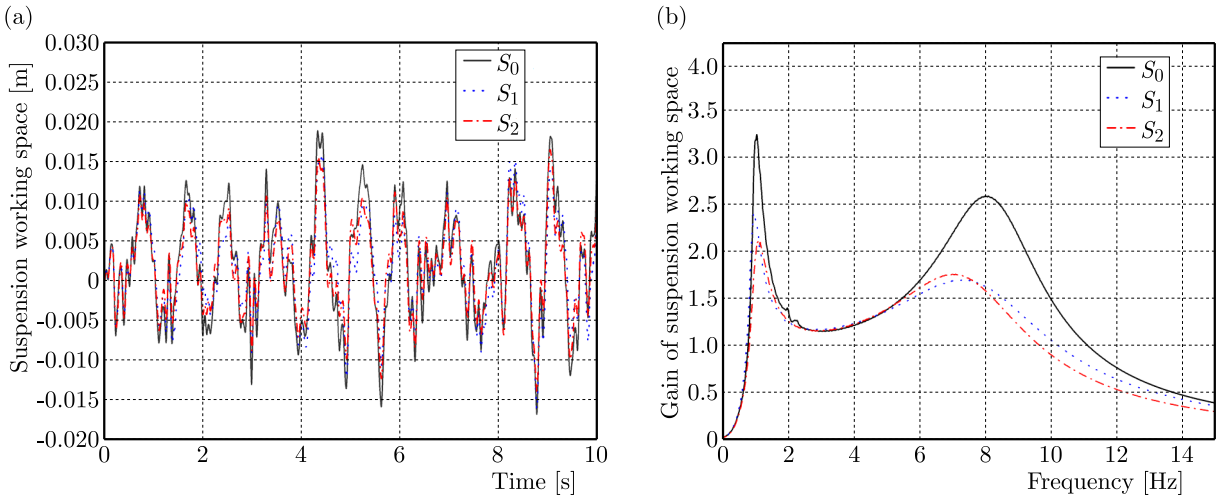

Fig. 3. Responses of suspension working space under the random road.

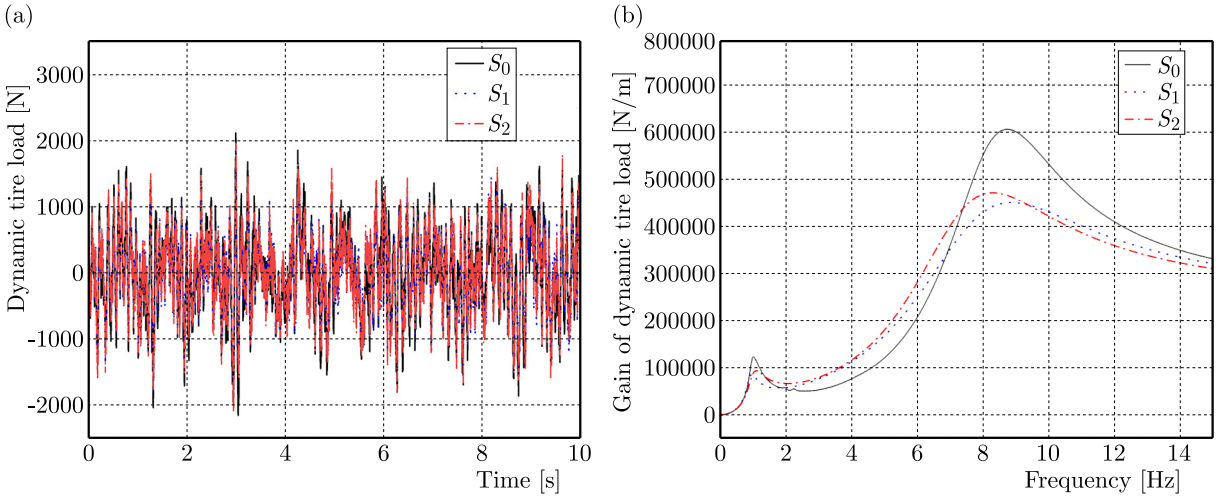

Fig. 4. Responses of dynamic tire load under the random road.

Table 3. Dynamic performance indexes.

Indexes	S_0	S_1	S_2
RMS of body acceleration [m/s^2]	0.48	0.45	0.47
RMS of suspension working space [m]	0.0072	0.0060	0.0058
RMS of dynamic tire load [N]	625	556	589

ing before decreasing in the high frequency band, with each frequency band displaying a peak value. From Fig. 4, for the vehicle body acceleration, the peak of S_1 in the low frequency is obviously lower than S_0, which decreases from 148.4 to 101.7 [(m/s^2)/m], compared with S_2 from 148.4 to 113.9, it has a great improvement of 31.4 %. But for the high frequency peak, the change of both S_1 and S_2 is small, S_1 decreases by 3.6 %, and S_2 decreases by 2.4 %. The performance improvement of the suspension workspace is greater compared to the acceleration of the vehicle body. The low frequency peak of S_1 is reduced from 3.2 to 2.5 (marking a reduction of 21.8 %), the peak of S_2 from 3.3 to 2.1 (marking a reduction of 36.4 %), the high frequency peak of S_1 is reduced from 2.6 to 1.6 (marking a reduction of 38.5 %), and the high frequency peak of S_2 is reduced from 2.6 to 1.8 (marking a reduction of 30.1 %). For the dynamic tire load analysis, the low frequency peak of S_1 is reduced from 124228 to 85080 (marking a reduction of

31.5 %), the peak of S_2 is reduced from 124228 to 95040 (marking a reduction of 23.5 %), the high frequency peak of S_1 is reduced from 610471 to 436081 (marking a reduction of 28.6 %), and the high frequency peak of S_2 is reduced from 610471 to 474744 (marking a reduction of 22.2 %). As can be observed from the above figures and tables that, both of the dynamic performance of S_1 and S_2 are improved compared with S_0. For the time domain, the body acceleration and the dynamic tire load of S_1 are better than S_2, and S_2 is better than S_1 regarding the dynamic performance of the suspension working space. While for the frequency domain, both S_1 and S_2 can make the suspension obtain enhanced dynamic performance, handling stability ride and comfort.

4.2. Time domain analysis under pulse road input

According to the GB5902-86, it is assumed that the vehicle passes through the long-wave soil block at a speed of 10 m/s, which is used as the input of the pulse-type excitation displacement. As the road input is different, if the inertance and the damping coefficient optimized by the random road surface are brought into the pulse road input, there will be a number of dynamic performance deterioration. As a consequence, S_1 and S_2 under the pulse road input are re-optimized using the particle swarm optimization algorithm. For S_1, the optimized inertance coefficient is 485.6 kg, and the damping coefficient is 2238.6 Ns/m. For S_2, the optimized inertance coefficient is 14.9 kg, and the damping coefficient is 1087.9 Ns/m. Figure 5 shows three dynamic performance indexes of S_1 and S_2 compared with S_0 under a pulse input in the time-domain.

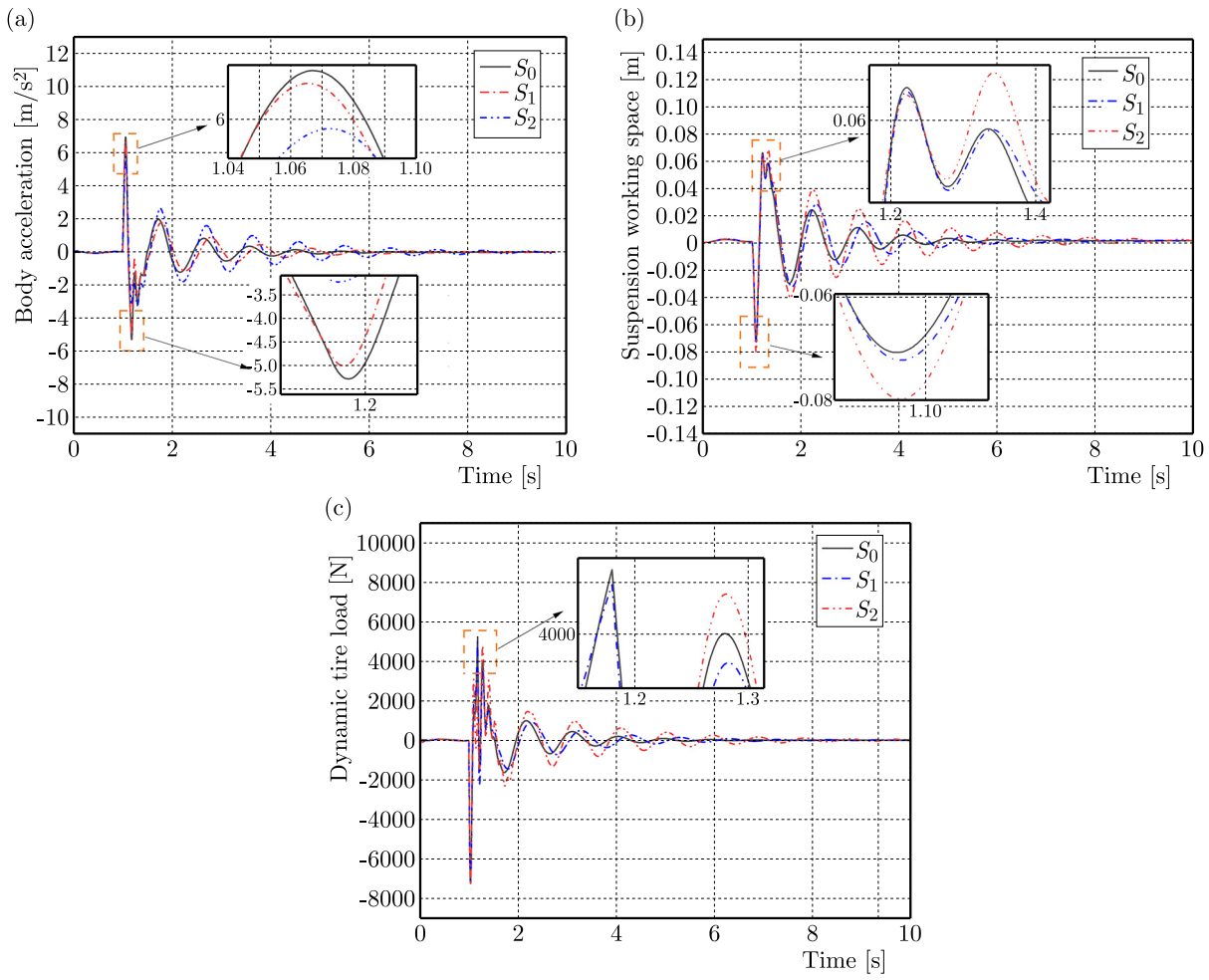

Fig. 5. Dynamic performance indexes under pulsed road.

Table 4 shows the dynamic performance indexes of S_1 and S_2 under a pulse input. The figures and tables clearly show that, compared with S_0, the peak-to-peak (PTP) value of vehicle body acceleration of S1 decreased by 4.1 %, and the PTP value of dynamic tire load decreased by 1.9 %, while the PTP value of body acceleration of S_2 decreased by 26.2 %, and the PTP value of dynamic tire load decreased by 2.5 %. On the contrary, for the suspension working space, S_1 and S_2 are increased slightly. In order to find out the reason, the three-dimensional diagram of S_1 and S_2 is shown. The inertance coefficient is the X-axis, the damping coefficient is the Y-axis, and the PTP values of the three dynamic performances are the Z-axis, so that the PTP values of the three dynamic performances can be clearly observed with the inertance coefficient and damping coefficient.

Table 4. Dynamic performance indexes under pulse input.

Name	S_0	S_1	S_2
PTP of vehicle body acceleration [m/s^2]	12.2	11.7	9.0
PTP of dynamic tire load [N]	12381	12149	12067
PTP of suspension working space [m]	0.1366	0.1373	0.1483

Figures 6–8 show the variation trend of PTP value of the body acceleration, suspension working space and dynamic tire load of S_1 and S_2 with damping coefficient and inertance

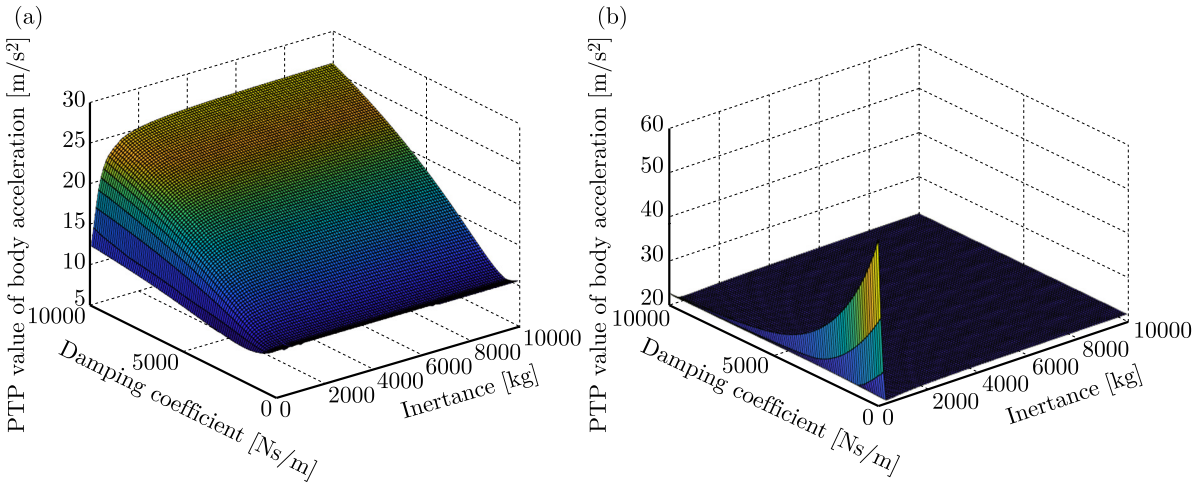

Fig. 6. Change trend of body acceleration under pulse road surface.

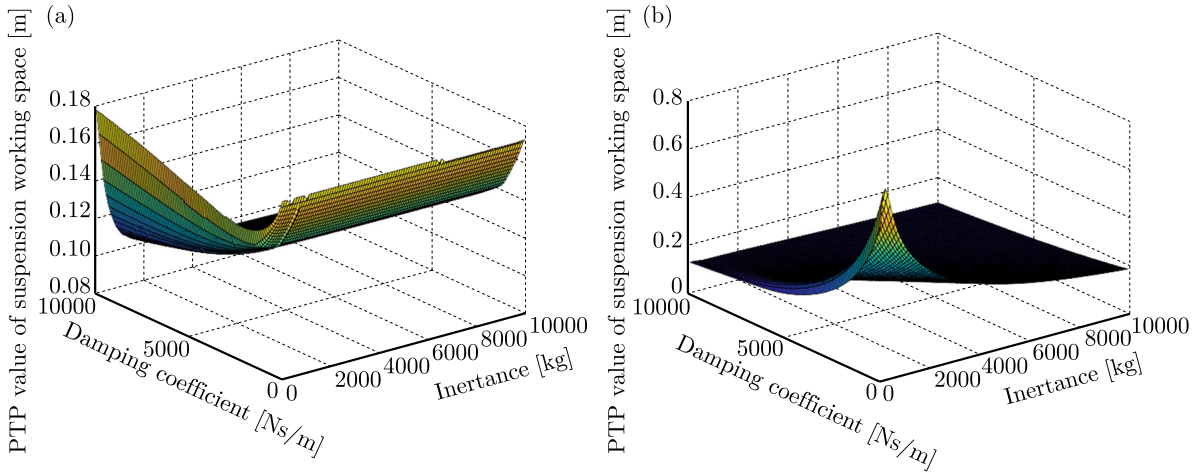

Fig. 7. Change trend of suspension working space under pulse road surface.

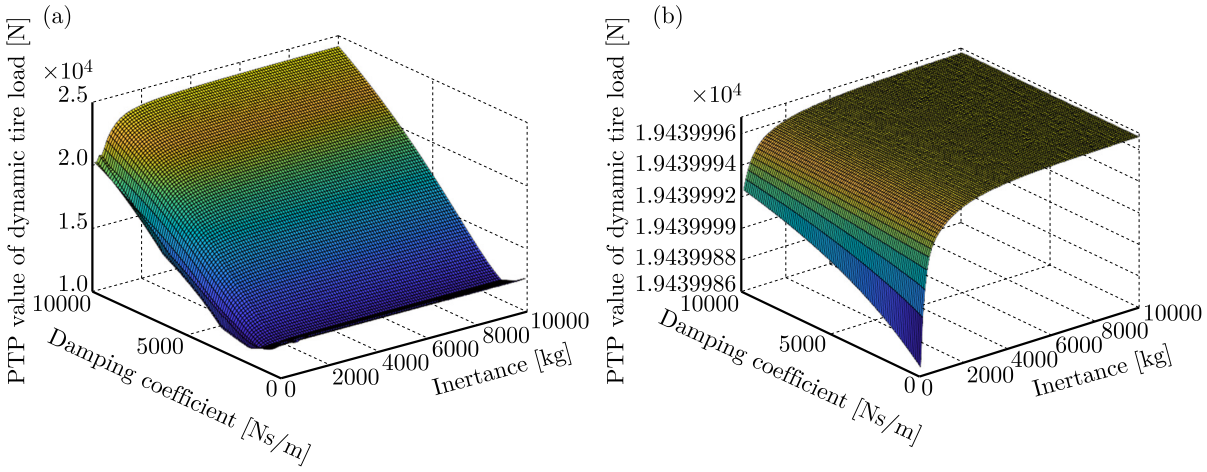

Fig. 8. Change trend of dynamic tire load under pulse road surface.

coefficient compared with the traditional air suspension under a pulse input, where (a) is S_1 and (b) is S_2.

As shown in the above figure, for the S_1, the PTP trend of the dynamic tire load and the body acceleration is basically the same, but the suspension working space is different. Therefore, in the optimization process of this paper, the weight coefficients of body acceleration and dynamic tire load in the fitness function are set to 0.4, and the weight coefficient of suspension working space is set to 0.2, so as to achieve the best overall optimization effect. However, it is obvious that according to the three-dimensional diagram, when the PTP value of body acceleration and dynamic tire load is minimized, the PTP value of suspension working space shows an upward trend. Compared with the traditional air suspension, the dynamic performance of suspension working space is deteriorated, and the expected optimization effect cannot be achieved at the same time. In the S_2 as shown in the figure, the three dynamic performance trends with the inertance coefficient and the damping coefficient are not the same, and the optimal points of the three dynamic performance cannot be achieved in the same place. Therefore, in the process of optimization in this paper, when the PTP value of body acceleration is minimized, the PTP values of dynamic tire load and the suspension working space are not at the lowest point. The PTP value of dynamic tire load is slightly improved compared with the traditional air suspension, while the dynamic performance of suspension workspace is deteriorated.

5. Experimental research

To verify the performance benefits of a vehicle air suspension system employing an inerter, a bench test was carried out to demonstrate the results obtained in Section 4. The overall layout of the bench test is shown in Fig. 9. The suspension parameters are the same as in Table 1 and Table 2. A fluid inerter which can create the damping effect and inertia effect simultaneously was used in this experiment. The suspension structures S_1 and S_2 can achieve by changing the parts inside the fluid inerter as shown in Figs. 9a and 9b.

Taking the C-level random road simulated in Section 4 as the test road input. The test result is shown in Fig. 10 and Table 5.

Table 5. Comparison of RMS of vehicle body acceleration in bench test.

Indexes	S_0	S_1	S_2
RMS of body acceleration [m/s^2]	0.55	0.52	0.54

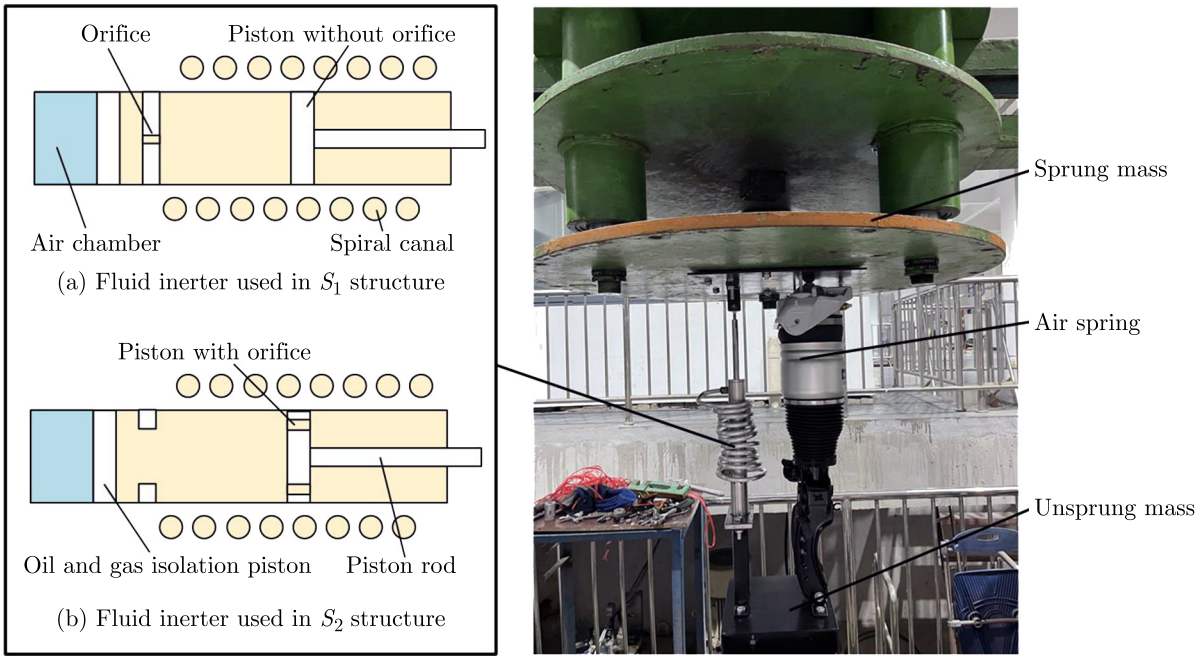

Fig. 9. Overall layout of bench test.

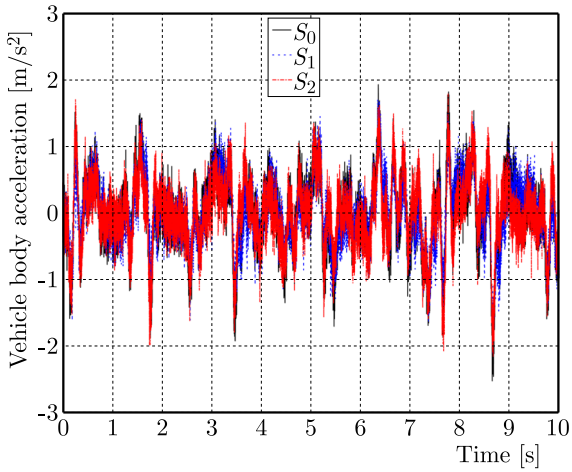

Fig. 10. Test comparison diagram of random road input.

Compared with the S_0 suspension, the RMS value of the body acceleration of the S_1 suspension reduced by 5.5 %, the RMS value of body acceleration of S_2 reduced by 1.8 %. There are some differences between the experimental data and the simulation results, which are initially analysed to be due to the sensor noise interference and system nonlinear factors. However, from the comparison of experimental results, the vibration suppression performances of the S_1 suspension superior to the S_0 suspension and S_2 suspension, which is consistent with the theoretical simulation.

6. Conclusion

This paper researches the performance benefits of the vehicle air suspension system using an inerter. Through designing the quarter car models of the two basic vehicle ISD suspension, the series-connected suspension and the parallel-connected suspension are created. Considering the overall suspension performance, key parameters of the two suspension systems are op-

timized through the PSO. In the time domain and the frequency domain a simulation analysis of the two suspension models was carried out, the findings indicate that, the dynamic performance of the suspension working space, dynamic tire load and body acceleration of the air ISD suspension with an inerter is enhanced, which confirms that the air ISD suspension can enhance the comfortable vehicle ride and the performance of road handling. The bench test was carried out and verified that the model assumptions and simplifications are correctly formulated in the paper.

Acknowledgments

This work was supported by National Natural Science Foundation of China (grant no. 52072157), China Postdoctoral Science Foundation (no. 2024T171048, 2024M753653), Young Elite Scientists Sponsorship Program by CAST (grant no. 2022QNRC001), Qing Lan Project of Jiangsu Province, China.

References

1. Cui, L.F., Xue, X.Y., Le, F.X., Mao, H.P., & Ding, S.M. (2019). Design and experiment of electro hydraulic active suspension for controlling the rolling motion of spray boom. *International Journal of Agricultural and Biological Engineering*, *12*(4), 72–81. https://doi.org/10.25165/j.ijabe.20191204.4648
2. De Domenico, D., Deastra, P., Ricciardi, G., Sims, N.D., & Wagg, D.J. (2019). Novel fluid inerter based tuned mass dampers for optimised structural control of base-isolated buildings. *Journal of the Franklin Institute*, *356*(14), 7626–7649. https://doi.org/10.1016/j.jfranklin.2018.11.012
3. Elahi, H., Israr, A., Khan, M.Z., & Ahmad, S. (2016). Robust vehicle suspension system by converting active & passive control of a vehicle to semi-active control system analytically. *Journal of Automation and Control Engineering*, *4*(4), 300–304. https://doi.org/10.18178/joace.4.4.300-304
4. Gonzalez-Buelga, A., Clare, L.R., Neild, S.A., Burrow, S.G., & Inman, D.J. (2015). An electromagnetic vibration absorber with harvesting and tuning capabilities. *Structural Control and Health Monitoring*, *22*(11), 1359–1372. https://doi.org/10.1002/stc.1748
5. John, E.D. & Wagg, D.J. (2019). Design and testing of a frictionless mechanical inerter device using living-hinges. *Journal of the Franklin Institute*, *356*(14), 7650–7668. https://doi.org/10.1016/j.jfranklin.2019.01.036
6. Li, J.Y., Nie, Z.Y., Chen, Y.F., Ge, D.Q., & Li, M.Q. (2023). Development of boom posture adjustment and control system for wide spray boom. *Agriculture*, *13*(11), Article 2162. https://doi.org/10.3390/agriculture13112162
7. Li, Z.X., Cui, Z., & Li, M. (2014). Modeling of interlinked air suspension and study on its dynamic performance. *Applied Mechanics and Materials*, *494–495*, 163–166. https://doi.org/10.4028/www.scientific.net/AMM.494-495.163
8. Ma, R., Bi, K., & Hao, H. (2021). A novel rotational inertia damper for amplifying fluid resistance: Experiment and mechanical model. *Mechanical Systems and Signal Processing*, *149*, Article 107313. https://doi.org/10.1016/j.ymssp.2020.107313
9. Oda, N. & Nishimura, S. (1970). Vibration of air suspension bogies and their design. *Bulletin of JSME*, *13*(55), 43–50. https://doi.org/10.1299/jsme1958.13.43
10. Papageorgiou, C., Houghton, N.E., & Smith, M.C. (2009). Experimental testing and analysis of inerter devices. *Journal of Dynamic Systems, Measurement, and Control*, *131*(1), Article 011001. https://doi.org/10.1115/1.3023120
11. Quaglia, G. & Sorli, M. (2001). Air suspension dimensionless analysis and design procedure. *Vehicle System Dynamics*, *35*(6), 443–475. https://doi.org/10.1076/vesd.35.6.443.2040
12. Sammier, D., Sename, O., & Dugard, L. (2003). Skyhook and H8 control of semi-active suspensions: Some practical aspects. *Vehicle System Dynamics*, *39*(4), 279–308. https://doi.org/10.1076/vesd.39.4.279.14149

13. Seifi, A. & Hassannejad, R. (2022). Parameters uncertainty in pareto optimization of nonlinear inerter-based suspension system under nonstationary random road excitation. *Proceedings of the Institution of Mechanical Engineers, Part D: Journal of Automobile Engineering*, *236*(12), 2725–2744. https://doi.org/10.1177/09544070211060936

14. Shen, Y.J., Chen, A., Du, F., Yang, X.F., Liu, Y.L., & Chen, L. (2024a). Performance enhancements of semi-active vehicle air ISD suspension. *Proceedings of the Institution of Mechanical Engineers, Part D: Journal of Automobile Engineering*. https://doi.org/10.1177/09544070241233024

15. Shen, Y.J., Hua, J., Fan, W., Liu, Y.L., Yang, X.F., & Chen, L. (2023a). Optimal design and dynamic performance analysis of a fractional-order electrical network-based vehicle mechatronic ISD suspension. *Mechanical Systems and Signal Processing*, *184*, Article 109718. https://doi.org/10.1016/j.ymssp.2022.109718

16. Shen, Y.J., Jia, M.Q., Yang, X.F., Liu, Y.L., & Chen, L. (2023b). Vibration suppression using a mechatronic PDD-ISD-combined vehicle suspension system. *International Journal of Mechanical Sciences*, *250*, Article 108277. https://doi.org/10.1016/j.ijmecsci.2023.108277

17. Shen, Y.J., Qiu, D.D., Yang, X.F., Chen, J.J., Guo, Y., & Zhang, T.Y. (2024b). Vibration isolation performance analysis of a nonlinear fluid inerter-based hydro-pneumatic suspension. *International Journal of Structural Stability and Dynamics*. https://doi.org/10.1142/S0219455426500793

18. Smith, M.C. (2002). Synthesis of mechanical networks: the inerter. *IEEE Transactions on Automatic Control*, *47*(10), 1648–1662. https://doi.org/10.1109/TAC.2002.803532

19. Wang, F.C., Hong, M.F., & Lin, T.C. (2011). Designing and testing a hydraulic inerter. *Proceedings of the Institution of Mechanical Engineers, Part C: Journal of Mechanical Engineering Science*, *225*(1), 66–72. https://doi.org/10.1243/09544062JMES2199

20. Wang, Y., Wang, P., Meng, H., & Chen, L., (2024a). Dynamic performance and parameter optimization of a half-vehicle system coupled with an inerter-based X-structure nonlinear energy sink. *Applied Mathematics and Mechanics*, *45*(1), 85–110. https://doi.org/10.1007/s10483-024-3070-7

21. Wang, Y., Xu, B., & Meng, H. (2024b). Enhanced vehicle shimmy performance using inerter-based suppression mechanism. *Communications in Nonlinear Science and Numerical Simulation*, *130*, Article 107800. https://doi.org/10.1016/j.cnsns.2023.107800

22. Wen, G.L., Lei, Z.H., Yin, J.W., & Yin, H.F. (2013). Cushion characteristics of an omni-directional and multi-chamber airbag (in Chinese). *Journal of Vibration and Shock*, *32*(8), 13–17.

23. Yang, X., Zhang, T., Shen, Y., Liu, Y., Bui, V., & Qiu, D. (2024). Tradeoff analysis of the energy-harvesting vehicle suspension system employing inerter element. *Energy*, *308*, Article 132841. https://doi.org/10.1016/j.energy.2024.132841

Manuscript received February 29, 2024; accepted for publication January 8, 2025; published online March 22, 2025.

JOURNAL OF THEORETICAL
AND APPLIED MECHANICS
63, 2, pp. 263–278, Warsaw 2025
https://doi.org/10.15632/jtam-pl/199924

NUMERICAL STUDY ON MICRO-FRACTURE CHARACTERISTICS OF ROCK UNLOADING FAILURE UNDER HIGH STRESSES AND THE EXPLANATION FOR ROCK BURST

Yuezong YANG*, Anye LI

School of Science, Xi'an University of Architecture and Technology, Xi'an 710055, China
*corresponding author, *yangyuezong@xauat.edu.cn*

The micro-structure of rock essentially affects its macroscopic mechanical behaviors. To investigate the effect of micro-structure on the rock burst, an improved grain-based discretized virtual internal bond (GB-DVIB) model is developed. By the improved GB-DVIB model, different types of mineral grains and grain-boundaries can be generated effectively. A novel parameter calibration method, in which the scanning electron microscope, nano-indentation approach and conventional mechanical tests are utilized synthetically, is proposed. The single face unloading test is simulated to verify the ability of the improved GD-DVIB model to simulate the rock burst. The simulated results show that the the improved GB-DVIB model can simulate the intra- and inter-granular cracking and the main characteristics of the rock unloading failure process. The influence of the specimen size and the micro-structure on the rock burst proneness is investigated. As the height-to-thickness ratio decreases from large to small, the tensile failure characteristics weaken, while the shear failure characteristics enhance, manifested as the tensile-shear transition. With the increase of mineral grain size and heterogeneity, the rock burst proneness is stronger. Compared with the horizontal distribution of mineral grains, the vertical distribution can make the rock burst proneness stronger.

Keywords: grain-based method; unloading failure; micro-cracking process; rock burst.

1. Introduction

With the exploitation and utilization of underground space from shallow to deep, the rock burst is increasingly prominent and seriously threatens the safety of constructors and equipment. At present, the prediction and prevention of the rock burst is difficult to meet the requirements of engineering practice. The underlying reason is that the rock burst mechanism is highly complex and influenced by many factors. The influencing factors of the rock burst can be divided into two main categories, i.e., engineering geological factors and rock properties. The engineering geological factors contain in-situ stress, amplitude and frequency of dynamic disturbance load, unloading rate, temperature and so on. The rock properties contain strength, moisture content, brittleness, structural plane and so on. At the micro-scale, the rock is composed of the mineral grains. The types, content and properties of mineral grains essentially affect the properties of rock (Hofmann *et al.*, 2015). Therefore, to better understand the rock burst mechanism, it is necessary to investigate the rock burst from the point of micro-fracture at the mineral grain scale.

Many experimental studies have been conducted to investigate the micro-fracture characteristics of rock induced by the rock burst. Compared with the micro-fracture of the rock in compression experiments, the percentage of intra-granular cracks is higher and the fracture surface is rougher (He *et al.*, 2011) in rock burst experiments. Huang *et al.* (2012) utilized the triaxial unloading tests to investigate the rock burst, and concluded that with the increase of an unloading rate, the micro-fracture characteristics transform from an intra-granular shear fracture to an inter-granular tensile fracture gradually. Zhao *et al.* (2015) examined the composition

of the rock at the rock burst site, and found that the rock burst is more likely to occur in the hard-brittle rocks with a high degree of crystallization and the dense micro-structure. Su *et al.* (2019) studied the influence of mineral grain size on the rock burst, and found that the coarser mineral grain can make the rock burst proneness stronger. Zheng and Wang (2024) and Jin *et al.* (2024) investigated the influencing factors on the deformation and failure of porous coal, and found that the loading rate, borehole inclination and borehole diameter all have significant influences. These studies contribute to a deeper understanding of the rock burst from the perspective of micro-fracture. However, the rock burst is a violent dynamic fracture process, which brings some difficulties to the observation of the entire micro-fracture process. In this situation, the numerical simulation method is a powerful complement to further study the problem.

So far, many continuum-based numerical methods (Manouchehrian & Cai, 2015) have been adopted to investigate the rock burst. The stress and strain response can be calculated accurately by these methods. However, they have some limitation in fracture simulation, e.g., complicated fracture criterion and remeshing. Compared with these continuum-based methods, the discontinuum-based methods provide an effective and simple method for fracture simulation. The discontinuum-based methods discretize rocks into blocks or particles and connect them through springs or bonds, simulating the fracture process of rocks through the breaking of springs or bonds. The complicated 3D failure problem of material is transferred to the 1D bond rupture. Therefore, the issues of the complicated fracture criterion and re-meshing can be avoided in this method. The discrete element method (DEM) is a commonly used discontinuum-based method that can simulate the collapse of rock masses and the contact and rotation between rock blocks (Cundall, 1988). Procházka (2004) simulated the rock burst using both a hexagonal block and a particle DEM, and found that the hexagonal block DEM is more suitable for simulating crack initiation and propagation, while the particle DEM is more suitable for simulating dynamic failure processes. Vacek *et al.* (2008) used DEM to analyze the stress changes in the surrounding rock before and after tunnel excavation, and successfully simulated the block ejection phenomenon of the rock burst. Zhu *et al.* (2022) used DEM to study the influence of in-situ stress on the rock burst tendency and found that as the burial depth increases, the stress and released elastic strain energy increase, making the rock burst more likely to occur. However, due to the lack of theoretical relationship between macroscopic parameters and microscopic bond parameters, the calibration of microscopic bond parameters in DEM is inconvenient.

The discretized virtual internal bond (DVIB) (Zhang, 2013) model is another discontinuum-based method. This method considers a material to consist of bond cells. Each bond cell can take any geometry with any numbers of bonds, which makes it suitable to represent the micro-structure of geomaterials. Based on the ideal unit cell, the theoretical relationship between macroscopic parameters and microscopic bond parameters is established. Compared with the DEM, the microscopic bond parameters can be calibrated more coveniently in the DVIB model. The two-body potential adopted in DVIB only accounts for the normal interaction between two particles, which leads to an issue of fixed the Poisson ratio. To solve the issue, Zhang *et al.* (2014) proposed the Stillinger–Weber (SW) potential based DVIB (SW-DVIB) model. In this method, a modified SW potential, which is not only related to the normal deformation of bond, but also the bond angles, is embed in the DVIB. However, the realistic micro-structures of rock, e.g., the mineral grain and grain boundaries, have not been sufficiently considered in these DVIB methods. To simulate a microscopic fracture process of rocks more realistically, a grain-based DVIB (GB-DVIB) (Yang & Zhang, 2022) is developed to simulate the micro-structure at the mineral grain scale. A micro-structure generation method based on the Voronoi polygon has been proposed to more realistically represent micro-structure of rock. By this method, mineral grains and grain boundaries can be generated conveniently. The SW-DVIB is adopted to model the mineral grains, and a contact model considering the tension and shear is adopted to model the grain boundaries. However, the GB-DVIB model approximately assumes that the mechanical properties of different mineral grains are consistent.

In this study, the GB-DVIB model is improved. According to the observed types of mineral grains and the measured micromechanical properties, different mineral grains are assigned different mechanical parameters. To facilitate the application of the improved GB-DVIB model, a novel parameter calibration method is proposed. In this method, the scanning electron microscope (SEM), nano-indentation approach and conventional mechanical tests are utilized synthetically. The micro-fracturing process of granite samples in direct tension tests, uniaxial compression tests and confined compression tests are simulated. The simulated results show that the micro-fracture process, such as the inter-grain fracture and intra-grain fracture, is reproduced successfully. Then, the method is used to simulate rock burst. The three stages of the rock burst, i.e., several small grains ejectiong, big fragment falling down and a lot of big fragments ejection, can be reproduced well. The effect of the height-to-thickness ratio and mineral grain size on the rock burst is investigated. The simulated results are basically consistent with the experimental results. The effect of micro-structure on the rock burst is investigated by the simulation of SFUT. The simulated results show that with the increase of mineral grain size and heterogeneity, the rock burst proneness is stronger. Compared with horizontal distribution of mineral grains, the vertical distribution can make the rock burst proneness stronger.

2. Grain-based DVIB model

2.1. Generation of micro-structure

Rock is a combination of mineral grains. Take the granite as an example, as shown in Fig. 1a, the main mineral grains contain the quartz, felspar (plagioclase and potash felspar) and biotite (Su *et al.*, 2019). The Voronoi polygon is highly similar to the micro-structure of rock (Li *et al.*, 2017). A micro-structure generation method based on the Voronoi polygon is proposed to more realistically represent micro-structure of rock. Based on the SEM images, the average mineral grain size and the percentages of different kinds of mineral grains are obtained, and then used as the key parameters to generate the micro-structure of rock by the Voronoi algorithm. Simply put, the employment of the Voronoi algorithm to generate micro-structure in the GB-DVIB model is based on the statistical averaging of real micro-structure in SEM images.

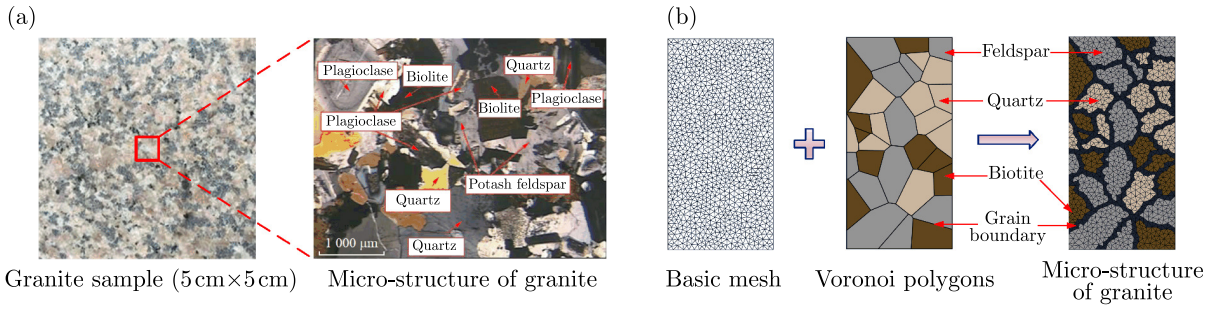

Fig. 1. Generation of micro-structures in GB-DVIB: (a) mineral grain composition of granite; (b) generation process of the micro-structure of granite.

The detailed micro-structure generation process of granite is shown in Fig. 1b. First of all, the basic bond cells and Voronoi polygons are generated by the code of GMesh and MATLAB, respectively. A polygon represents a mineral grain. The edges of polygons represent the grain boundaries. The mineral grain size and the mineral types can be set up according to the actual mineral grains. Different mineral grains are endowed with different mechanical properties. Then, the basic bond cells are covered by Voronoi polygons. If a bond cell is in a Voronoi polygons, the bond cell is defined as grain bond cells. While the bond cells which are cut by the edges of the Voronoi polygons are defined as the interface bond cells. By this method, different mineral grains and grain boundaries can be generated conveniently.

The degree of discretization and types of mesh can affect the calculation results of the GB-DVIB model. The GB-DVIB model is developed based on the DVIB model. The influences of the mesh size on the elastic modulus and the Poisson ratio of materials in the DVIB model is investigated in the previous study (Zhang, 2013). The research results indicate that with the decrease of the mesh size, the calculation error decreases. When the mesh is fine enough, the calculation error is close to zero. The influence of the mesh size on the calculation results of the DVIB model also applies to the GB-DVIB model. In the rock simulation of this study, the average size of the basic mesh is 0.25 mm. Through the verification, the mesh size meets the calculation accuracy requirements.

2.2. SW-DVIB model for mineral grain

The discretized virtual internal bond (DVIB) (Zhang, 2013) model is a developed lattice model by dispersing the continuous virtual internal bond (VIB) (Gao & Klein, 1998). It is composed of unit bond cells. The bond cells can take any geometry with finite micro-bonds, which make the DVIB suitable to represent the micro-structure of geomaterials. Compared with VIB, the individual behavior of every bond is considered in DVIB. Bond potentials are adopted to describe the bond mechanical behavior.

The Stillinger–Weber (SW) potential based DVIB (SW-DVIB) (Zhang *et al.*, 2014) is employed to model mineral grain. Compared with the traditional DVIB, the modified SW potential, which is not only related to the normal deformation of bond, but also the bond angles, is adopted to characterize the bond cell (Fig. 2a). The modified SW potential used for the rock fracture simulation (Zhang *et al.*, 2015) is

$$\Phi_2 = \frac{1}{2}Al_0^2(\widetilde{r}_I - 1)^2, \qquad \Phi_3 = \frac{1}{2}\lambda(\theta_{IJ} - \theta_{IJ0})^2, \tag{2.1}$$

where Φ_2 and Φ_3 are two- and three-body interactions, respectively; A and λ are material parameters, $A = 2V/[N(N-1)l_0^2] \cdot 3E/(1-2\mu)$ and $\lambda = V/[N(N-1)(N-2)] \cdot 9E(1-4\mu)/[2(1+\mu)(1-2\mu)]$; V is the volume of a bond cell; N is the number of bonds in a bond cell; E is the elastic modulus of material; μ is the Poisson ratio; l_0 is the bond length when undeformed; $\widetilde{r}_I$ is the normalized bond length, $\widetilde{r}_I = r_{ij}/l_0$; θ_{IJ} is the bond angle subtended by the bond r_{ij} and r_{ik} in the current configuration, and θ_{IJ0} is the value in the reference configuration.

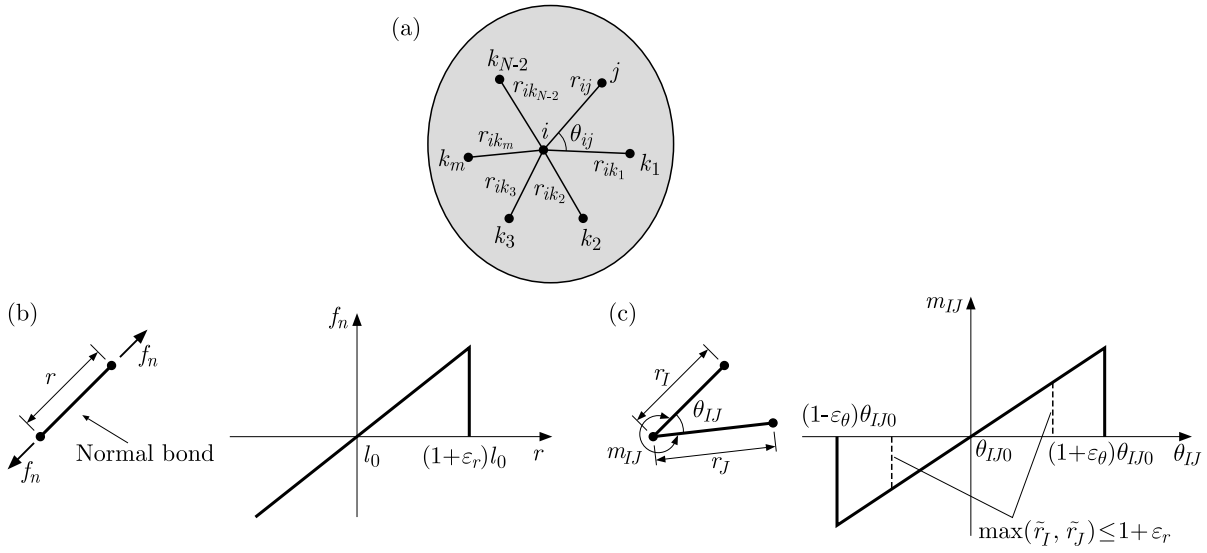

Fig. 2. Modeling mineral grains by SW-DVIB: (a) a bond cell with N particles; (b) normal bond force versus bond length; (c) bond moment versus bond angle.

According to (Zhang *et al.*, 2015), the constitutive relation (Figs. 2b and 2c) of SW-DVIB can be written as

$$\begin{aligned} f_n &= \frac{\partial \Phi_2}{\partial r} = \begin{cases} Al_0(\widetilde{r}-1) & \text{if} \quad \widetilde{r}-1 \le \varepsilon_r, \\ 0 & \text{else}, \end{cases} \\ m_{IJ} &= \frac{\partial \Phi_3}{\partial \theta_{IJ}} = \begin{cases} \lambda(\theta_{IJ}-\theta_{IJ0}) & \text{if} \quad \max(\widetilde{r}_I, \widetilde{r}_J) \le 1+\varepsilon_r \ \text{ and } \ |\theta_{IJ}-\theta_{IJ0}| \le \varepsilon_\theta, \\ 0 & \text{else}, \end{cases} \end{aligned} \tag{2.2}$$

where f_n is the normal bond force, m_{IJ} is the bond moment, ε_r is the critical bond length strain, ε_θ is the critical bond angle strain.

2.3. Modeling grain boundaries

As shown in Fig. 3a, the bond cells cut by the grain boundaries are defined as interface bond cells. In the interface bond cells, the bonds cut by the grain boundaries are defined as interface bonds, while the other bonds are intact bonds. A contact model considering the tension and shear is adopted in these interface bonds. Before the rupture of the interface bonds, they are considered as intact bonds. The contact normal stress and shear stress of these interface bonds are calculated as

$$\sigma_n = \frac{f_{y'}}{A_c^b}, \qquad \tau = \frac{f_{x'}}{A_c^b}, \tag{2.3}$$

where $\left[f_{x'}, f_{y'}\right]^{\mathrm{T}}$ is the contact force vector of the interface bond in the local coordinate, $[f_{x'}, f_{y'}]^{\mathrm{T}} = \mathbf{T}\Sigma\mathbf{f}$, $\mathbf{T}$ is the coordinate transform matrix from the global coordinate to the local one, and $\mathbf{f}$ is the internal force of interface bonds, A_c^b is the equivalent contact area of the interface bond (Fig. 3b), $A_c^b = A/N_{cra}$, A is the sectional area of the interface bond cell, N_{cra} is the number of interface bonds in the interface bond cell.

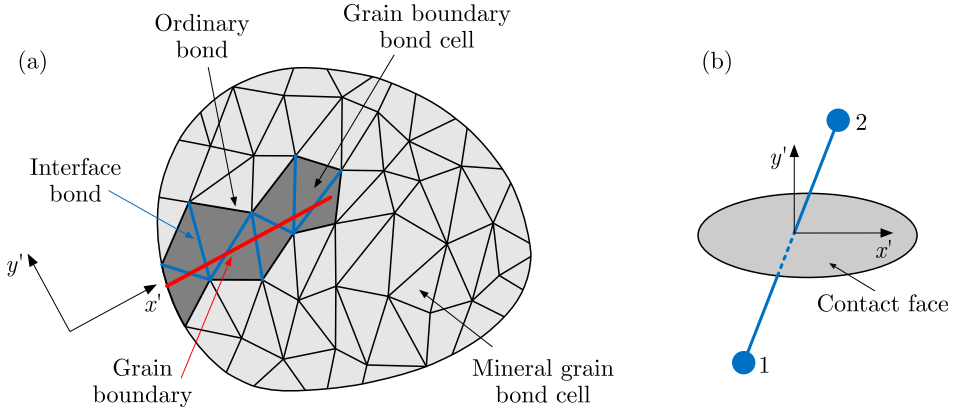

Fig. 3. Grain interface modeling: (a) interface bonds; (b) contact face adjunct to an interface bond.

Once the contact stress satisfied the failure criterion (tension failure or shear failure), the interface bond rupture. The failure criterion is

$$\sigma_n > \overline{\sigma}_n, \qquad \tau > c + \sigma_n \cdot \tan\varphi, \tag{2.4}$$

where $\overline{\sigma}_n$ is the tensile strength of grain boundary, c is the cohesion, φ is the internal friction angle.

3. Parameter calibration

Parameter calibration is a key step in the application of numerical simulation methods. To facilitate the application of the improved GB-DVIB model, a novel parameter calibration

method is proposed. In this method, the scanning electron microscope (SEM), nano-indentation approach and conventional mechanical tests are utilized synthetically.

3.1. Procedure of parameter calibration

The macro-mechanical behaviors of rock are significantly influenced by the types, content and properties of mineral grains. The mineral composition and micro-structure of different rocks vary greatly. Take granite as an example, the procedure of parameter calibration in GB-DVIB is explained. SEM is adopted to analysis the main mineral composition and the average grain size (Zhang *et al.*, 2017). The main minerals of granite contain the quartz, felspar and biotite. The percentages of quartz, felspar and biotite are approximately 30 %, 45 %, and 25 %, respectively (Zhang *et al.*, 2017). The average grain size is 2.23 mm. According to the quantitative relationship between micro-bond parameters and macro-mechanical parameters in DVIB (Zhang, 2013), the mechanical parameters of mineral grains and grain boundaries obtained by the nano-indentation approach (Sun *et al.*, 2020) are used as the initial input parameters. The direct tension tests, uniaxial compression tests and confined compression tests are conducted to obtain the macro-mechanical parameters (Peng *et al.*, 2017a; 2017b). The macro-mechanical parameters include the Young modulus (E), tensile strength (σ_t), uniaxial compressive strength (UCS), and triaxial compressive strengths under different confining pressures.

With the initial input parameters, a series of direct tension tests, uniaxial compression tests and confined compression tests are simulated. The geometries of simulated granite samples are shown in Fig. 4. The height (H) and thickness (T) of the specimen are 100 mm and 50 mm, respectively. By comparing the simulated macro-mechanical behaviors with experimental results, the material parameters are adjusted. The process of parameter adjustment is as follows:

1) the Young modulus of granite (E) is used to calibrate the Young modulus of mineral grains (E_q, E_f, and E_b; where the subscripts q, f, and b represent quartz, feldspar, and biotite, respectively) and the grain boundaries (E_{gb});
2) the tensile strength (σ_t) is used to calibrate the critical bond length strains of mineral grains (ε_{rq}, ε_{rf}, and ε_{rb}) and the tensile strength of grain boundary ($\overline{\sigma}_n$);
3) the UCS is used to calibrate the cohesion of the grain boundary (c) and the Poisson ratios (μ_q, μ_f, and μ_b), and the critical bond angle strain ($\varepsilon_{\theta q}$, $\varepsilon_{\theta f}$, and $\varepsilon_{\theta b}$) of mineral grains;
5) the triaxial compressive strengths under different confining pressures are used to calibrate the internal friction angle of the grain boundary (φ) and the normal and shear stiffness of the crack face (k_n and k_s).

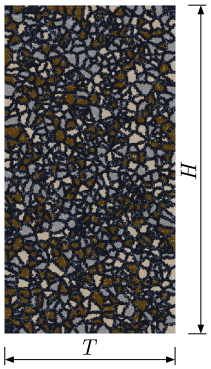

Fig. 4. Geomerty of simulated granite samples.

By repeating the process of parameter adjustment, once the adjusted input parameters can make the simulated results match the experimental results well, the adjusted input parameters can be taken as the calibrated ones. By the aforementioned procedure of parameter calibration, the material parameters are calibrated as

- quartz: $E_q = 20.26\,\text{GPa}$, $\mu_q = 0.15$, $\rho_q = 2650\,\text{kg/m}^3$, $\varepsilon_{rq} = 2.4 \times 10^{-3}$, $\varepsilon_{\theta q} = 1.92 \times 10^{-3}$;
- feldspar: $E_f = 8.45\,\text{GPa}$, $\mu_f = 0.2$, $\rho_f = 2600\,\text{kg/m}^3$, $\varepsilon_{rf} = 3.6 \times 10^{-3}$, $\varepsilon_{\theta f} = 3.06 \times 10^{-3}$;
- biotite: $E_b = 7.11\,\text{GPa}$, $\mu_b = 0.3$, $\rho_b = 2600\,\text{kg/m}^3$, $\varepsilon_{rb} = 4.1 \times 10^{-3}$, $\varepsilon_{\theta b} = 3.28 \times 10^{-3}$;
- grain boundary: $E_{gb} = 7.11\,\text{GPa}$, $\overline{\sigma}_n = 39.75\,\text{MPa}$, $k_n = 10\,\text{MPa}$, $k_s = 1\,\text{kPa}$, $c = 45\,\text{MPa}$, $\varphi = 28°$.

3.2. Direct tension test

The simulated results of direct tension test are shown in Fig. 5. The simulated tensile strength is 10.51 MPa. Compared with the experimental tensile strength (10.1 MPa), the relative error is 4.06 %. The simulated Young modulus is 33.75 GPa. Compared with the experimental Young modulus (35.5 GPa), the relative error is −4.93 %. The simulated micro-fracture process shows that when the axial stress reaches 85 % of the tensile strength, the inter-granular tensile cracks initiate from the center of the sample. With the increase of axial stress, a macroscopic main crack propagates horizontally. Finally, a horizontal macroscopic crack is formed in the middle of the sample. In the process, intra-granular and inter-granular cracks both have been observed. The inter-granular cracks play a predominant role in the tensile failure of rock. The simulated results agree well with the experimental observation (Peng *et al.*, 2017b).

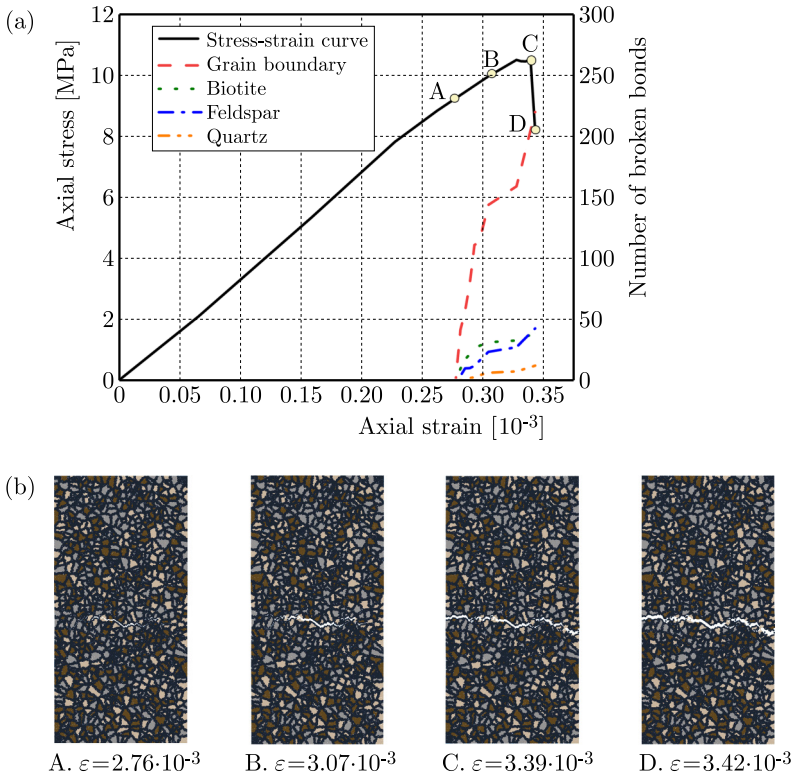

Fig. 5. Simulated results of direct tension tests: (a) stress-strain relationship and evolution of broken bonds; (b) micro-fracture process.

3.3. Uniaxial compression test

The simulated results of uniaxial compression test are shown in Fig. 6. The simulated UCS is 189.03 MPa. Compared with the experimental UCS (184.70 MPa), the relative error is 2.33 %. The simulated micro-fracture process shows that when the axial stress reaches about 60 % of UCS, the inter-granular cracks have been observed firstly. When the axial stress reaches about 70 % of UCS, the intra-granular cracks occur. Due to the initiation, propagation and coalescence of micro-cracks, a macroscopic shear crack propagates from the lower right corner

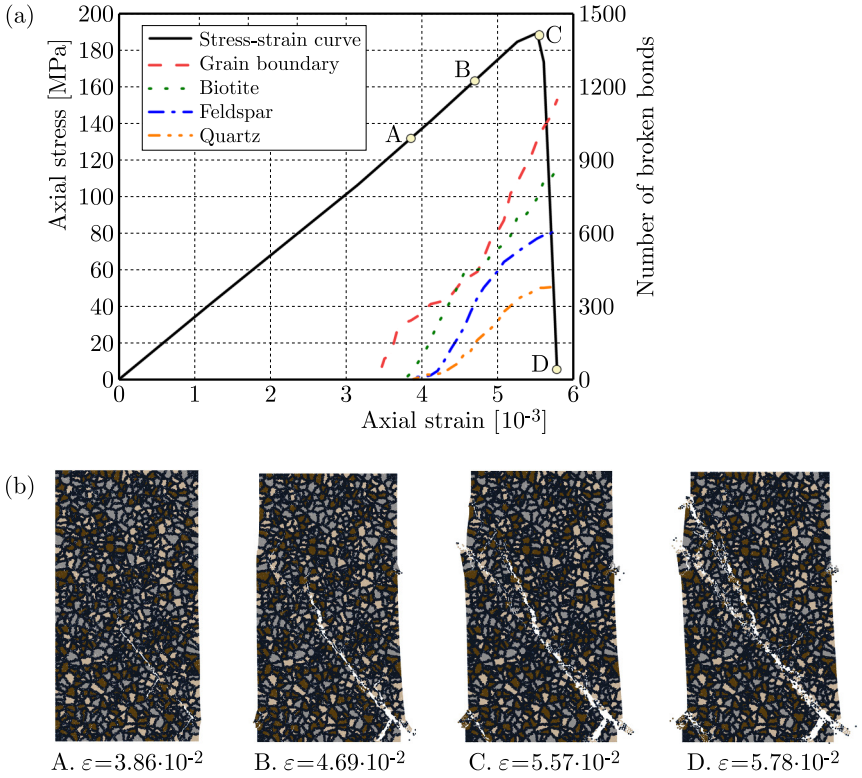

Fig. 6. Simulated results of uniaxial compression tests: (a) stress-strain relationship and evolution of broken bonds; (b) micro-fracture process.

of the sample to the upper left corner. Compared with the direct tension test, the final number of broken bonds and the percentage of intra-granular cracks in uniaxial compression test is larger. The simulation results are in good agreement with the experimental results (Peng *et al.*, 2017b).

3.4. Confined compression test

The simulated results of confined compression test are shown in Fig. 7. As shown in Fig. 7a, with the increase of the confined pressure, the strength of the granite sample increases. Because the friction of the crack face is considered in the improved GB-DVIB model, the residual strength

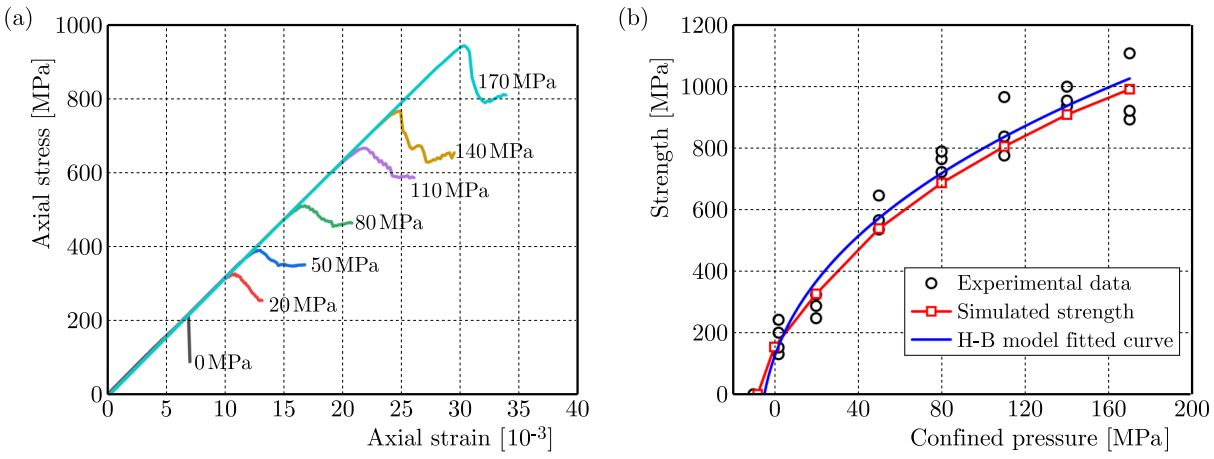

Fig. 7. Simulated results of confined compression tests: (a) stress-strain relationships with different confined pressures; (b) comparison between simulated strength with experimental one (Peng *et al.*, 2017b).

can be reflected well. As shown in Fig. 7b, the Hoek–Brown failure criterion is adopted to fit the experimental data. The fitted UCS and the material parameter m_i are 184.7 MPa and 23.2, respectively (Peng *et al.*, 2017b). The simulated strengths of samples under different confined pressures are almost corresponding to the fitted result. The comparison between the simulated and experimental results shows that the effect of confined pressure on triaxial strength can be reflected by the improved GB-DVIB model.

4. Simulation of rock unloading failure

Before the excavation of tunnel, the rock mass is in a quasi-static triaxial stress state. The excavation of the tunnel makes the rock mass to change from the triaxial stress state to the biaxial or uniaxial stress state, which induces the release of strain energy in rock mass to lead to the rock burst. Based on the evolution of the stress state during the rock burst, the single face unloading test (SFUT) (He *et al.*, 2012; Zhao & He, 2016) has been conducted to investigate the dynamic fracture process of rock during the rock burst.

The SFUT is conducted by a true triaxial testing system. At first, the original triaxial stress state is applied by triaxial loading. Then, one surface of the sample is unloaded abruptly to simulate the excavation (Fig. 8a). In the simulation, the SFUT is simplified as a two-dimensional plane strain problem, as shown in Fig. 8b. The height H of the sample is 150 mm, and the thickness T is 60 mm. A load-unloading path similar to experimental process is adopted. First, the lateral constraints of the left and right boundaries and the axial constraint of the low boundaries is fixed, and displacement loading is applied at the top of the specimen. When the axial stress reaches about 80 % of the UCS of the specimen, the constraint on the right side is suddenly released and the axial load continues to be applied until the final failure of the sample. The application of boundary conditions is completed through a MATLAB code. The calculation process of the main program is implemented by the Intel Parallel Studio solver on Microsoft's Visual Studio platform using the Fortran language. The materials parameters calibrated in Section 3 are adopted in the simulation.

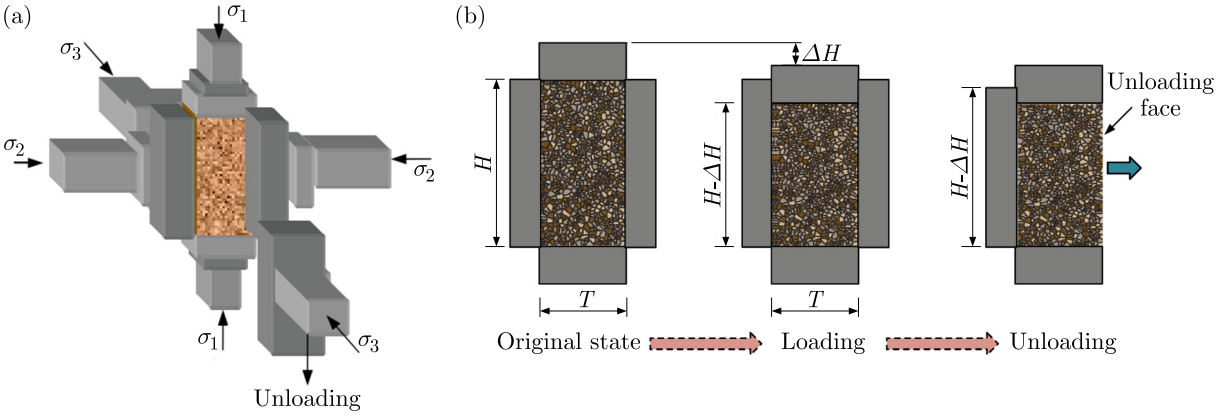

Fig. 8. Geometry and boundary conditions of SFUT: (a) schematic diagram of the SFUT (He *et al.*, 2012); (b) simplified loading-unloading process in simulation.

4.1. Rock failure process in SFUT

To examine the performance of the improved GB-DVIB model in simulating the fracture process of rock during the rock burst, the SFUT is simulated. The simulated results are shown in Figs. 9a and 9b. In the loading stage, the strain energy of the rock sample increases with the increase of axial displacement. In this stage, there are no broken bonds. The release of the constraint of the right boundary makes the strain energy release abruptly, which make several small grains eject from the unloading face. After the unloading point, the broken bonds have

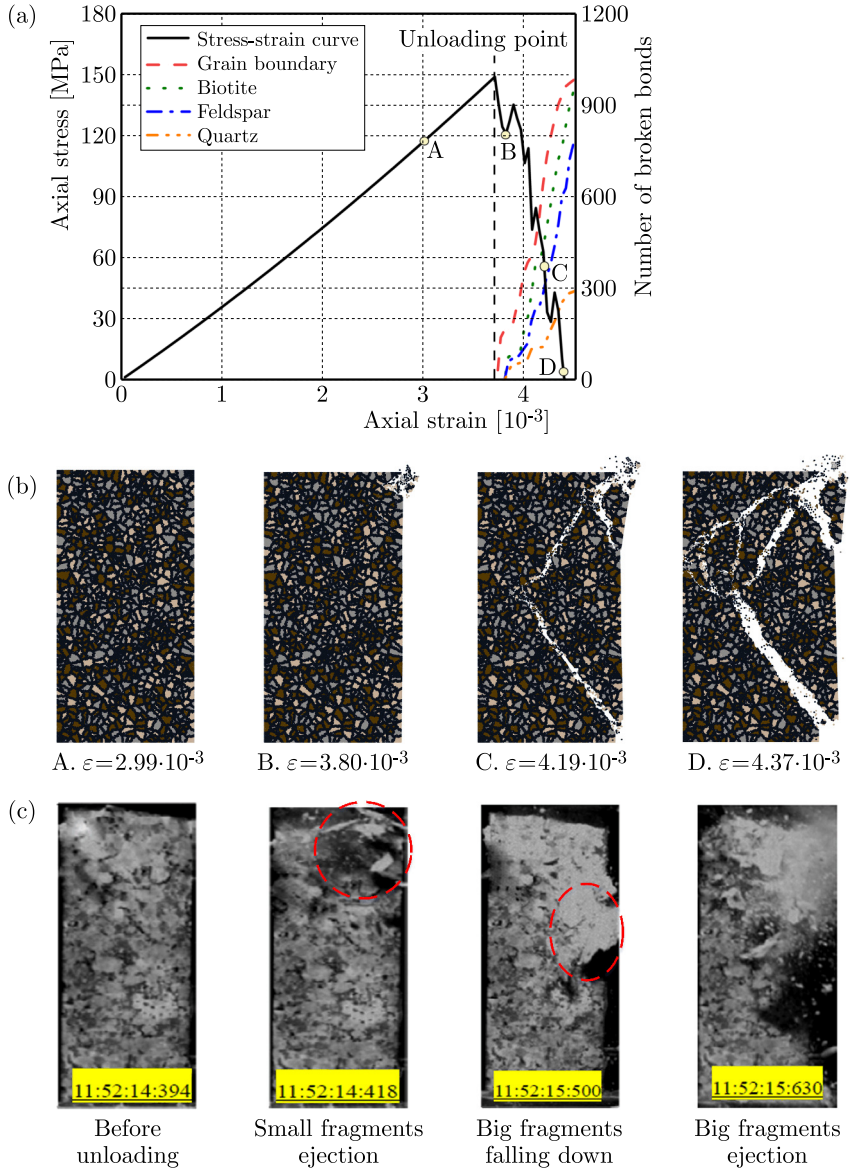

Fig. 9. Comparison between simulated SFUT and experimental results (a) simulated stress-strain relation and evolution of broken bonds; (b) simulated failure process; (c) experimental failure process.

been observed. Then, the application of axial displacement makes a big fragment fall down. Finally, a lot of big fragments eject from the unloading face, which leads to the ultimate failure of the rock sample. The similar failure process of a rock sample during the rock burst has been observed in the SFUT (He *et al.*, 2012), as shown in Fig. 9c. This indicates that the main characteristics of the rock burst process can be captured by the present method.

4.2. Effect of height-to-thickness ratios of specimen

The size effect of rock samples has a significant impact on their strength and failure mode. To investigate the size effect of rock samples on rock unloading failure, SFUTs with different height-to-thickness ratios (H/T) are simulated. In these tests, the H/T of granite sample varies from 5 to 2 with a fixed thickness of 30 mm. As shown in Fig. 10, when $H/T = 5$ and 4, the failure of the sample is mainly caused by splitting, and the tensile failure characteristics are obvious. When $H/T = 3$ and 2, shear cracks propagate from the top and bottom corners of the unloading surface of the specimen, and the shear failure characteristics are obvious. Therefore, as the H/T

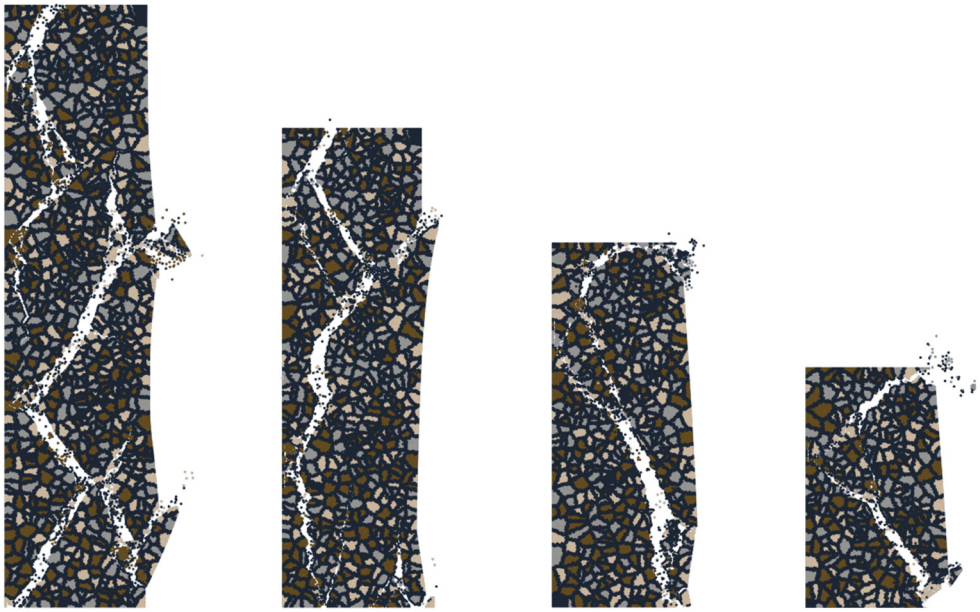

Fig. 10. Simulated fracture patterns of the samples with different H/T.

decreases from large to small, the tensile failure characteristics weaken, while the shear failure characteristics enhance, manifested as the tensile-shear transition. The failure regular pattern is basically consistent with the experimental observation.

The height-to-thickness ratio effect of rock samples is mainly caused by the end friction effect and the number of defects. When the rock sample is short, the stress distribution is relatively uniform due to the end effect, and the sample is basically in a three-dimensional stress state as a whole. In this case, the lateral displacement of the specimen is not significant due to the constraint at the ends, and the failure of the specimen exhibits shear failure. As the height of the specimen increases, the end constraints have little effect on the middle part of the sample, the stress in the middle of the rock sample gradually transitions from a three-dimensional stress state to a one-dimensional stress state. At this point, there will be a significant lateral displacement in the middle of the sample, leading to a significant increase in the tensile stress and resulting in tensile failure. At the same time, as the height of the sample increases, the defects inside the rock intensifies. During the compression process of the specimen, there will be more initiation points and ultimately more complex failure modes.

4.3. Effect of mineral grain size

The mineral grain size has a significant impact on the macroscopic mechanical behavior of rocks. The effect of the mineral grain size on the rock burst is analyzed by four cases with different average mineral grain diameters, namely $D_g = 2.0$, 2.5, 3.0, and 3.5 mm. The simulated results show that with an increase of the mineral grain size, the rock burst is more violent. As shown in Fig. 11, when $D_g = 2.0$ mm, the upper right corner of the specimen was fractured and ejected due to the local stress concentration, and a main crack runs through the lower right corner at an angle of about 60 degrees to the upper left corner. With an increase of the mineral grain size, the degree of fragmentation and dynamic characteristics of the sample have intensified. When $D_g = 3.5$ mm, the right part of the sample splits and pops out as a whole, and the rock is broken into many small pieces in the middle of the sample. Ultimately, a large V-shaped crater is formed. It shoud be noted that the similar experimental results have also been obtained by the physical model test (Su *et al.*, 2019).

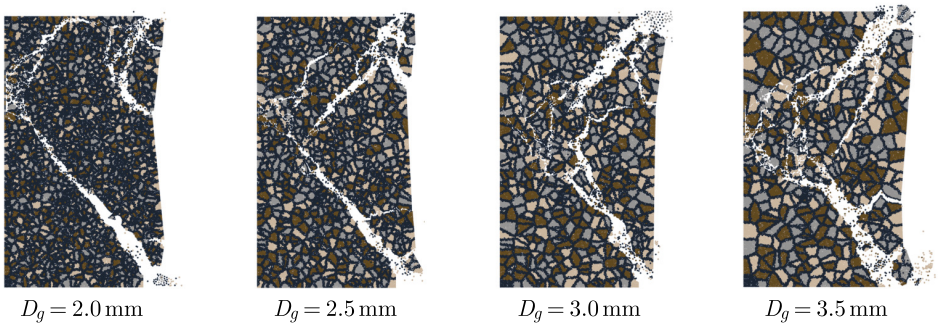

Fig. 11. Failure patterns of granite samples with different grain sizes.

The influence of the mineral grain size on the rock burst is essentially determined by the non-uniformity of the mineral grain distribution. When the mineral grain size is large, the non-uniformity of the mineral grain distribution becomes stronger. During the loading process, the rock is more prone to tensile stress concentration and local accumulation of elastic strain energy. When the local elastic strain energy exceeds the rock bearing limit, it will cause local failure of the specimen, that is, the dissipation of energy is relatively random and dispersed in the spatial and temporal distribution. In this case, the failure of the specimen tends to occur through dynamic failure, namely severe rock ejection phenomenon. When the mineral grain size is small, the non-uniformity of mineral grain distribution becomes weaker. During the loading process, due to the relatively uniform distribution of stress field inside the specimen, the concentration of local tensile stress and elastic strain energy is less likely to occur. As the load increases, the specimen will gradually swell, break, and slide outward, with concentrated and continuous damage locations.

4.4. Effect of mineral grain heterogeneity

The non-uniformity of mineral grains can cause uneven stress distribution, which in turn affects the macroscopic mechanical behavior of rocks. To investigate the effect of mineral grain heterogeneity on the rock burst, two cases with different random distribution of mineral grains are simulated. The average mineral grain diameters in these two cases are both 2.5 mm. The simulated failure patterns are shown in Fig. 12. When mineral grain heterogeneity is strong, two shear cracks initiate from the upper and lower parts of the unloading surface and propagate towards the middle of the specimen, ultimately leading to the overall failure of the specimen and forming a V-shaped crater. When mineral grain heterogeneity is weak, the sample failure is concentrated in the upper right part of the sample, manifested as local splitting of the sample. Therefore, as the mineral grain heterogeneity decreases, the failure area decreases, and the failure pattern exhibits the shear-tension transition. Compared with the homogeneous sample, the rock burst proneness of a heterogeneous sample is stronger.

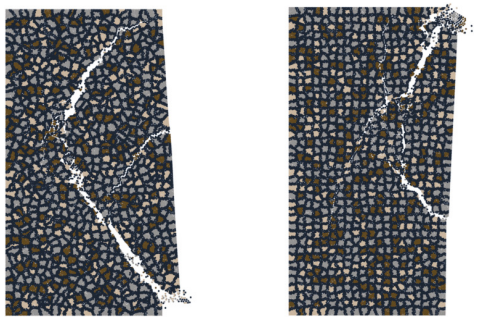

Fig. 12. Failure patterns of granite samples with different gain randomness.

The effect of mineral grain heterogeneity on the rock burst can be further explained by the direction distribution of a mineral grain interface. As shown in Fig. 12, the mineral grain heterogeneity can significantly affect the direction distribution of mineral grain interfaces. When the mineral grain heterogeneity is strong, the direction of mineral grain interfaces is random. However, when the mineral grain heterogeneity is weak, the direction of mineral grain interfaces tends to be vertical and horizontal. Overall, the mechanical properties of mineral grain interfaces are weaker than those of mineral particles. The directional distribution of mineral grains has a significant effect on the failure of rock samples. When the mineral grain heterogeneity is strong, the randomly distributed mineral grain interfaces will fracture and penetrate, ultimately forming two macroscopic shear cracks. When the mineral grain heterogeneity is weak, the vertical mineral grain interfaces are more likely to fracture and ultimately result in splitting failure of the sample.

4.5. Effect of mineral grain directionality

Mineral grains in sedimentary rocks have a certain directionality during the sedimentation process. The directionality of mineral grain greatly influences the anisotropic behavior of the rock sample (Ghazvinian *et al.*, 2014). To investigate the effect of mineral grain directionality on the rock burst, two typical distributions, namely vertical and horizontal distribution, are analyzed. The average mineral grain diameters in the two cases are both 3.0 mm. The simulated failure patterns are shown in Fig. 13. When the mineral grains are arranged vertically, it is discovered that two shear cracks begin at the top and bottom of the unloading surface and move towards the centre of the specimen. This finally causes the specimen to fail completely and leaves a V-shaped crater. The sample failure is centred in the top right portion of the sample and appears as localised splitting when the mineral grains are spread horizontally. The rock burst proneness of the rock sample with vertically distributed mineral grains is stronger than that with horizontally distributed mineral grains.

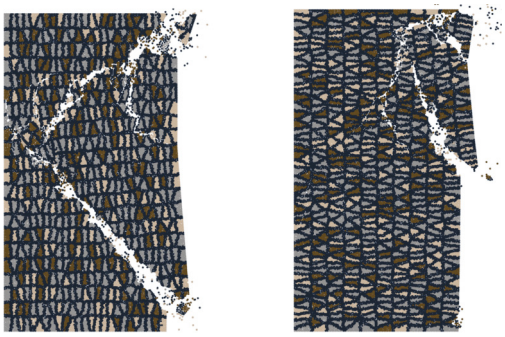

Fig. 13. Failure patterns of granite samples with different grain directionality.

The effect of mineral grain directionality on the rock burst can also be explained by the direction distribution of a mineral grain interface. As shown in Fig. 13, when the mineral grains are distributed vertically, the long side of mineral grains is in the vertical direction, and the short side of mineral grains is in the horizontal direction. In contrast, when the mineral grains are distributed horizontally, the long side and short side of the mineral grains are in the horizontal and vertical directions, respectively. Under the vertical compression load, the vertical interface of mineral particles will undergo tensile failure under the lateral expansion caused by compression, while the horizontal interface will undergo compression without failure. For the vertically distributed mineral grains, the failure of the long side of the mineral grains in the vertical direction can lead to a violent failure of the sample. While, for the horizontally distributed mineral grains, the failure of the short side of the mineral grains in the vertical direction causes weaker failure than vertically distributed mineral grains.

5. Conclusions

The GB-DVIB model is improved to investigate how the micro-structure affects the rock burst. By the improved GB-DVIB model, different types of mineral grains and grain-boundaries can be generated effectively. A novel parameter calibration method, in which the SEM, nano-indentation approach and conventional mechanical tests are utilized synthetically, is proposed. The SFUT is simulated to verify the ability of the improved GD-DVIB to simulate the rock burst. The simulated results show that the improved GB-DVIB model can simulate the intra- and inter-granular cracking and the rock burst process, i.e., small grains ejection, big fragments fall down and a lot of big ejection fragments. The influence of the sample size, the mineral grain size, heterogeneity and distribution directionality on rock unloading failure are investigated.

With the decrease of height-to-thickness ratio of specimen, the rock burst is more violent, and the fracture pattern exhibits the tensile-shear transition. This phenomenon is caused by end effects. With the increase of the mineral grain size, the rock burst is more violent. The underlying reason is that when the mineral grain size is large, the non-uniformity of mineral grain distribution becomes stronger. When the mineral grain heterogeneity is strong or the mineral grains are distributed vertically, the rock burst proneness is stronger. This is because when the mineral grain heterogeneity is strong, the direction of mineral grain interfaces is random, which is more likely to cause shear cracks to occur. While, when the mineral grain heterogeneity is weak, the direction of mineral grain interfaces tends to be vertical and horizontal, which is more likely to cause tensile cracks to occur. For the vertically and horizontally distributed mineral grains, the long and short sides of the mineral grains are in the vertical direction, respectively. The failure of more vertical grain interfaces in rock samples with vertically distributed grains results in a stronger tendency for the rock burst.

In this study, we adopted the Voronoi polygons to generate the micro-structure of rocks. Although the Voronoi polygons can reflect the main characteristics of the rock micro-structure, this is still a statistical averaging method. The micro-structure of rocks obtained through SEM images cannot be fully projected into the numerical model. In future research, we will attempt to generate more realistic micro-structure by projecting the SEM images into the numerical model.

Acknowledgments

This work is supported by the China Postdoctoral Science Foundation (no. 2023MD744236), the Natural Science Basic Research Program of Shaanxi (no. 2024JC-YBQN-0061), the Postdoctoral Research Project of Shaanxi Province (no. 2023BSHEDZZ270), the Special Scientific Research Plan Project of Education Department of Shaanxi Provincial Government (no. 23JK0509), and the Innovation and Entrepreneurship Projects for College Students (no. S202310703047).

References

1. Cundall, P.A. (1988). Formulation of a three-dimensional distinct element model – Part I. A scheme to detect and represent contacts in a system composed of many polyhedral blocks. *International Journal of Rock Mechanics and Mining Sciences & Geomechanics Abstracts*, *25*(3), 107–116. https://doi.org/10.1016/0148-9062(88)92293-0

2. Gao, H. & Klein, P. (1998). Numerical simulation of crack growth in an isotropic solid with randomized internal cohesive bonds. *Journal of the Mechanics and Physics of Solids*, *46*(2), 187–218. https://doi.org/10.1016/S0022-5096(97)00047-1

3. Ghazvinian, E., Diederichs, M.S., & Quey, R. (2014). 3D random Voronoi grain-based models for simulation of brittle rock damage and fabric-guided micro-fracturing. *Journal of Rock Mechanics and Geotechnical Engineering*, *6*(6), 506–521. https://doi.org/10.1016/j.jrmge.2014.09.001

4. He, M., Nie, W., Zhao, Z., & Cheng, C. (2011). Micro- and macro-fractures of coarse granite under true-triaxial unloading conditions (in Chinese). *Mining Science and Technology*, *21*(3), 389–394. https://doi.org/10.1016/j.mstc.2011.05.016

5. He, M., Xia, H., Jia, X., Gong, W., Zhao, F., & Liang, K. (2012). Studies on classification, criteria and control of rockbursts. *Journal of Rock Mechanics and Geotechnical Engineering*, *4*(2), 97–114. https://doi.org/10.3724/SP.J.1235.2012.00097

6. Hofmann, H., Babadagli, T., Yoon, J.S., Zang, A., & Zimmermann, G. (2015). A grain based modeling study of mineralogical factors affecting strength, elastic behavior and micro fracture development during compression tests in granites. *Engineering Fracture Mechanics*, *147*, 261–275. https://doi.org/10.1016/j.engfracmech.2015.09.008

7. Huang, D., Tan, Q., & Huang, R. (2012). Study of micro-mesoscopic characteristics of marble fracture surface and correlation with unloading rock mass strength under high stress and unloading (in Chinese). *Rock and Soil Mechanics*, *33*(Supp. 2), 7–15.

8. Jin, X., Zheng, J., Hua, S., & Tong, X. (2024). Influencing factors of deformation and failure of porous coal under conventional loading. *Facta Universitatis, Series: Mechanical Engineering*. https://doi.org/10.22190/FUME240304036J

9. Li, X.F., Li, H.B., & Zhao, J. (2017). 3D polycrystalline discrete element method (3PDEM) for simulation of crack initiation and propagation in granular rock. *Computers and Geotechnics*, *90*, 96–112. https://doi.org/10.1016/j.compgeo.2017.05.023

10. Manouchehrian, A. & Cai, M. (2015). Simulation of unstable rock failure under unloading conditions. *Canadian Geotechnical Journal*, *53*(1), 22–34. https://doi.org/10.1139/cgj-2015-0126

11. Peng, J., Wong, L.N.Y., & Teh, C.I. (2017a). Influence of grain size heterogeneity on strength and microcracking behavior of crystalline rocks. *Journal of Geophysical Research: Solid Earth*, *122*(2), 1054–1073. https://doi.org/10.1002/2016JB013469

12. Peng, J., Wong, L.N.Y., Teh, C.I., & Li, Z. (2017b). Modeling micro-cracking behavior of Bukit Timah granite using grain-based model. *Rock Mechanics and Rock Engineering*, *51*(1), 135–154. https://doi.org/10.1007/s00603-017-1316-x

13. Procházka, P.P. (2004). Application of discrete element methods to fracture mechanics of rock bursts. *Engineering Fracture Mechanics*, *71*(4–6), 601–618. https://doi.org/10.1016/S0013-7944(03)00029-8

14. Su, G., Chen, G., Hu, X., Mei, S., & Huang, X. (2019). Experimental study on influence of granite grain size on rockburst (in Chinese). *Explosion and Shock Waves*, *39*(12), 66–77. http://dx.doi.org/10.11883/bzycj-2018-0419

15. Sun, C., Li, G., Gomah, M.E., Xu, J., & Rong, H. (2020). Meso-scale mechanical properties of mudstone investigated by nanoindentation. *Engineering Fracture Mechanics*, *238*, Article 107245. https://doi.org/10.1016/j.engfracmech.2020.107245

16. Vacek, J., Vacek, J., & Chocholoušová, J. (2008). Rock burst mechanics: Insight from physical and mathematical modelling. *Acta Polytechnica*, *48*(6), 38–44. https://doi.org/10.14311/1071

17. Yang, Y. & Zhang, Z. (2022). Micro-fracture simulation of rock under unloading condition by grain-based discretized virtual internal bond method. *International Journal of Applied Mechanics*, *14*(1), Article 2250001. https://doi.org/10.1142/S1758825122500016

18. Zhang, F., Guo, H., Zhao, J., Hu, D., Sheng, Q., & Shao, J. (2017). Experimental study of micro-mechanical properties of granite (in Chinese). *Chinese Journal of Rock Mechanics and Engineering*, *36*(2), 3864–3872.

19. Zhang, Z. (2013). Discretized virtual internal bond model for nonlinear elasticity. *International Journal of Solids and Structures*, *50*(22–23), 3618–3625. https://doi.org/10.1016/j.ijsolstr.2013.07.003

20. Zhang, Z., Chen, Y., & Zheng, H. (2014). A modified Stillinger–Weber potential-based hyperelastic constitutive model for nonlinear elasticity. *International Journal of Solids and Structures*, *51*(7–8), 1542–1554. https://doi.org/10.1016/j.ijsolstr.2014.01.003

21. Zhang, Z., Yao, Y., & Mao, X. (2015). Modeling wave propagation induced fracture in rock with correlated lattice bond cell. *International Journal of Rock Mechanics and Mining Sciences*, *78*, 262–270. https://doi.org/10.1016/j.ijrmms.2015.06.006

22. Zhao, F. & He, M.C. (2016). Size effects on granite behavior under unloading rockburst test. *Bulletin of Engineering Geology and the Environment*, *76*(3), 1183–1197. https://doi.org/10.1007/s10064-016-0903-5

23. Zhao, K., Zhao, H., & Jia, Q. (2015). An analysis of rockburst fracture micromorphology and study of its mechanism. *Explosion and Shock Waves*, *35*(6), 913–918. https://doi.org/10.11883/1001-1455(2015)06-0913-06

24. Zheng, J. & Wang, L. (2024). Experimental study on creep loading of porous coal under different influencing factors. *Facta Universitatis, Series: Mechanical Engineering*, *22*(1), 153–163. https://doi.org/10.22190/FUME231205011Z

25. Zhu, B., Fan, J., Shi, X., Liu, P., & Guo, J. (2022). Study on rockburst proneness of deep tunnel under different geo-stress conditions based on DEM. *Geotechnical and Geological Engineering*, *40*(3), 1373–1386. https://doi.org/10.1007/s10706-021-01969-8

Manuscript received August 18, 2024; accepted for publication January 8, 2025; published online March 1, 2025.

JOURNAL OF THEORETICAL
AND APPLIED MECHANICS
63, 2, pp. 279–287, Warsaw 2025
https://doi.org/10.15632/jtam-pl/200054

DESIGN AND EXPERIMENT OF MEMBRANE-TYPE ACOUSTIC METAMATERIALS USED IN EMUs TO CONTROL LOW FREQUENCY NOISE

Peng LIU[1], Hao LIN[2], Pan GAO[1], Pengyi TIAN[1], Chengcheng JIANG[1], Leiming SONG[2*], Xiaoqing DONG[1]

[1] *Locomotive & Car Research Institute, China Academy of Railway Sciences Corporation Limited, Beijing 100081, China*
[2] *School of Mechanical, Electronic and Control Engineering, Beijing Jiaotong University, Beijing 100044, China*
*corresponding author, *lmsong@bjtu.edu.cn*

Acoustic metamaterials, a new type of material with great design flexibility, have been widely studied by scholars in recent decades. For high-speed electric multiple units (EMUs), a membrane-type acoustic metamaterial is used to design a lightweight sound insulation material that adapts to the space requirements within the low frequency range. A theoretical analysis on the membrane-type acoustic metamaterial was carried out. The sound insulation coefficient was calculated. Experimental comparisons were conducted on six different thicknesses of films combined with five types of additional masses. The experimental results verified the sound insulation performance. It has great potential for designing lightweight noise reduction structures.

Keywords: membrane-type acoustic metamaterials; high-speed electric multiple units; low frequency noise; experiment.

1. Introduction

With the increase of train speed, the problem of noise becomes more and more serious. In order to solve the noise problem inside high-speed electric multiple units (EMUs), a large number of control measures are adopted in the design process.

According to the traditional method of sound insulation quality, it is observed that doubling the material mass results in only a 6 dB increase in sound insulation, making it relatively easy to achieve high-frequency sound wave insulation. There are three main types of commonly used sound insulation methods. The first involves using double-layer boards with air or vacuum sandwiched in between to enhance sound reflection and block sound wave propagation for improved insulation. However, this approach increases volume and does not provide ideal acoustic performance for low-frequency bands. The second method entails plate reinforcement to control stiffness and enhance material's sound insulation properties, but it does not effectively control low-frequency noise (Jung *et al.*, 2019). The third method is to lay damping materials or sound-absorbing materials on the surface of panels, which slows down panel structure vibration to achieve the noise reduction function. However, this method increases the structural mass and size and has certain limitations when used under space constraints.

The sound insulation design of the high-speed EMUs primarily incorporates the aforementioned methods, including the utilization of double-layer board materials for vehicle cross-section structure, optimization of vehicle body structure profile parameters, and enhancement of damping for profile and interior panels. Sound insulation treatments are implemented for critical noise sources such as interior flooring (e.g., aluminum honeycomb panels) and traction converter equipment compartments (Lu *et al.*, 2016; Thompson *et al.*, 2015). Nevertheless, components

like interior flooring entail high costs, substantial mass, and intricate designs, resulting in inconvenient maintenance. Furthermore, in order to fulfill the demands for light-weighting, energy efficiency, environmental preservation, and reduction of environmental contamination in vehicles, compromises are made with regards to acoustic design. This leads to a decline in sound insulation performance and presents novel challenges for noise control within the train. Hence, there is a necessity to develop a lightweight structure capable of achieving sound insulation effects (Ho *et al.*, 2003).

The emergence of acoustic metamaterials provides a new approach for the design of low-frequency noise control structures. The localized resonance units (Assouar *et al.*, 2016; Fang *et al.*, 2006) or other characteristic units (Song *et al.*, 2015) contained in acoustic metamaterials can generate extraordinary physical properties such as negative refraction and negative mass density, which offer new solutions to the challenges faced by traditional sound insulation materials in low-frequency sound insulation (Jena *et al.*, 2019; Wang *et al.*, 2019). Liu *et al.* (2000) proposed the concept of local resonant phononic crystals, which used small-sized structures to regulate low-frequency and long-wavelength mechanical waves (Sheng *et al.*, 2003). This design broke through the limitations imposed by traditional laws of mass and created a band gap in the low-frequency range, preventing the propagation of sound waves and providing new ideas for low-frequency vibration and noise control (Ma *et al.*, 2014; Rostami-Dogolsara *et al.*, 2020). In recent years, membrane-type acoustic metamaterials (MAMs) have become hot topics, opening up new chapters for the realization and application of lightweight low-frequency sound insulation materials (Ahluwalia *et al.*, 1985; Kriegsmann *et al.*, 1984).

Research on MAMs can be divided into studies on the acoustical vibration characteristics of thin film structures with or without additional mass. Naify *et al.* (2011; 2012) from the University of Southern California, studied different combinations of thin film unit structures with single or multiple masses added to them, comparing different sound insulation characteristics using the finite element results and impedance tube test results. The results show that this structure had over a five-fold improvement in sound insulation compared to traditional methods, forming multiple peaks at lower frequencies to broaden the soundproofing frequency band. Zhang *et al.* (2013) studied the low-frequency sound insulation performance of thin film acoustic metamaterials with different qualities attached to adjacent units, which was elaborated from both the experimental and finite element aspects. The results show that when the total mass remains unchanged, the film structure with different masses can form multiple sound insulation peaks, and the sound insulation effect is better than that of the film structure with the same mass.

On the other hand, research on MAMs often involves combining thin films with other structures without additional mass. Zhou *et al.* (2019) designed a combination structure of EVA perforation and PI film to study how structural parameters and material parameters affect sound insulation effects. The structure showed improved sound insulation effects within the frequency range of 80 Hz–800 Hz (Zhou *et al.*, 2019; Yoshizawa *et al.*, 2019). Although good sound insulation effects can be achieved with various additional masses or other combined structures, these structures have higher manufacturing costs which are not conducive to practical engineering applications.

The purpose of this article is to study the application of film-type acoustic metamaterials in low-frequency vibration characteristics and propose a method for designing sound insulation structures to address low-frequency noise problems during the operation of high-speed trains. In this article, structural design of the MAMs was conducted, and the characteristic theoretical analysis was carried out in Section 2. The experiment was carried out to verify sound insulation performance of MAMs in Section 3.

This study has the following contributions: the proposed structure consists of a rigid frame, elastic membrane, and additional mass, which form a high sound insulation area in the low-frequency range through local resonance of the unit, thereby achieving sound insulation effects

in this frequency range. Compared with traditional design solutions, this structure is lighter and more compact, providing new ideas for lightweight sound insulation and noise reduction designs for high-speed trains.

2. Structural design and theoretical analysis

The study shows that the interior of train compartment mainly experiences noise generated by wheel-rail excitation during operation (Varanasi *et al.*, 2013; Thompson *et al.*, 2006). As the bogies are distributed at both ends of the train compartment, when the train is running on a straight track, the interior noise exhibits a characteristic where the sound pressure level is greater at the end of the car than in the middle section. The frequency domain characteristics of these two areas of noises are not significantly different.

When the EMUs is traveling at high speed, Fig. 1a demonstrates the comparison of noise spectrum between the end and middle areas of the carriage. It indicates a high energy concentration in the middle and low frequency bands. Specifically, the noise is predominantly distributed within the range of 125 Hz to 2000 Hz. The identification results of interior noise sources indicate that most of them concentrate on floor areas in end sections as shown in Fig. 1b.

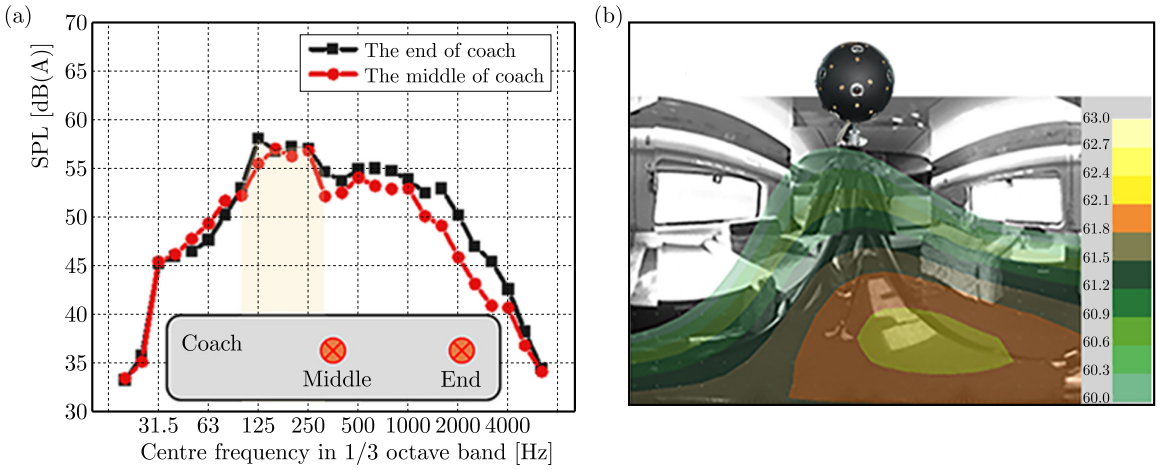

Fig. 1. Noise characteristics inside the EMUs: (a) noise characteristics at the end and middle of the carriage; (b) sound source distribution diagram at the end of the carriage.

According to sound insulation mass laws, achieving good sound insulation effects using traditional methods would require materials with dimensions much larger than those available in the vehicle design space for this frequency range. Therefore, composite materials and structures are used for design purposes; however, this method conflicts with lightweight design concepts and may result in decreased sound insulation effects after weight reduction. The development of MAMs provides a solution to address these issues by utilizing their structural features which can meet design space requirements while achieving good sound insulation effects.

In order to create desired structures, an analysis is conducted on acoustic vibration characteristics of MAMs first. When the thin-film acoustic metamaterial is fixed in the acoustic impedance tube for test measurement, the main distribution state of the internal sound pressure is shown in Fig. 2a. Figure 2b illustrates one type of circular MAMs where orange represents a membrane with radius R_1 and black represents additional mass with radius R_2. To simplify the model, this paper considers the case of vertically incident unit plane waves and focuses on the steady-state response of thin film structures.

For sound waves in a circular tube, rigid boundary conditions are satisfied with zero air velocity at the wall. Due to the symmetry of the structure and acoustic pressure load, only axisymmetric modes of the thin film structure need to be considered.

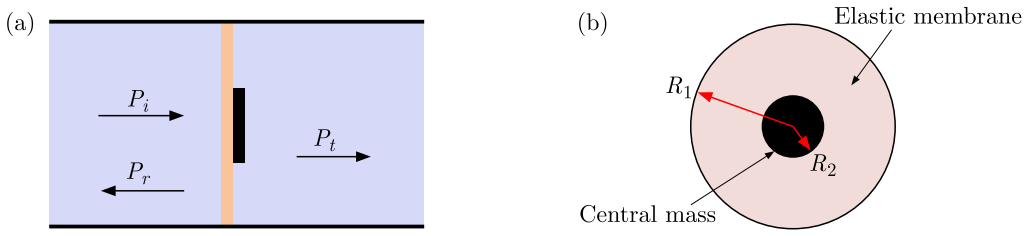

Fig. 2. (a) Schematic diagram of plane wave incident acoustic wave tube; (b) schematic of circular MAMs.

The annular membrane vibrates under acoustic loading as following equation:

$$\Delta P = P_i + P_r - P_t, \tag{2.1}$$

where transmitted sound pressure is P_t, incident sound pressure is P_i, reflected sound pressure is P_r.

In the cylindrical coordinate system, the incident sound pressure is formed by the incident wave and the reflected wave, and is expressed as

$$p_i + p_r = e^{-j\mathbf{k}_a z} + \sum_{n=0}^{\infty} R_n J_0(\mathbf{k}_n r) e^{j\sqrt{\mathbf{k}_a^2 - \mathbf{k}_n^2} z}, \tag{2.2}$$

where J_0 is zero-order Bessel function, $\mathbf{k}_n$ is wave vector, R_n is reflection coefficient, $\mathbf{k}_a$ is wave vector in the air.

Transmitted sound pressure is expressed as follows:

$$p_t = \sum_{n=0}^{\infty} T_n J_0(\mathbf{k}_n r) e^{-j\sqrt{\mathbf{k}_a^2 - \mathbf{k}_n^2} z}, \tag{2.3}$$

where T_n is the transmitted coefficient.

In a circular impedance tube, the propagation of sound pressure satisfies the wave equation. The velocity of the rigid boundary is zero. The continuity condition is that the normal vibration velocity of the air is continuous with the normal vibration velocity of the film.

Since the stiffness of the central mass block is much greater than that of the thin film, its motion can be described by the rigid body translation displacement. The thin film acts as a spring for the central mass, providing a restoring force F.

From the aforementioned analysis, two vibration control equations of the MAMs can be obtained. The first equation is the vibration equation under the acoustic pressure ΔP as follows:

$$-\rho_1 \omega^2 \eta_1 - T\nabla^2 \eta_1 = \Delta p, \tag{2.4}$$

where the surface density of the elastic film is ρ_1, and the transverse vibration displacement under the action of tension T is η_1.

Due to the symmetry of structure and the sound pressure load, the central mass is regarded as a rigid body displacement η_2. Then the motion equation of the mass block is shown in the second vibration control equation:

$$-\pi R_2^2 \omega^2 \rho_2 \eta_2 = \iint \Delta p dS_2 - F, \tag{2.5}$$

where the surface density of the central mass is ρ_2, and the restoring force of the film acting on the central mass is F.

The acoustic transmission coefficient of the structure can be obtained by means of the modal superposition method. The structural vibration displacement can be expressed as

$$\eta(r) = \sum_{m=1} W_m(r) q_m. \tag{2.6}$$

Combined with boundary conditions and continuity conditions, the equation is as follows:

$$p_i - p_r = p_t = j\omega\rho_a c_a \eta, \tag{2.7}$$

where ρ_a and c_a are density and sound speed of air, respectively.

Only a plane wave can propagate to the far field, the far field transmission coefficient is determined by surface displacement of the structure as follows:

$$t_P = |\rho_a c_a \omega \langle\eta\rangle| = \left|\rho_a c_a \omega \frac{\int \eta dS}{S}\right|. \tag{2.8}$$

The sound insulation coefficient is expressed by the following formula:

$$\mathrm{STL} = 20\log_{10}(1/t_P). \tag{2.9}$$

According to Eq. (2.9), the sound insulation coefficient curve of the structure is calculated, as shown in Fig. 3.

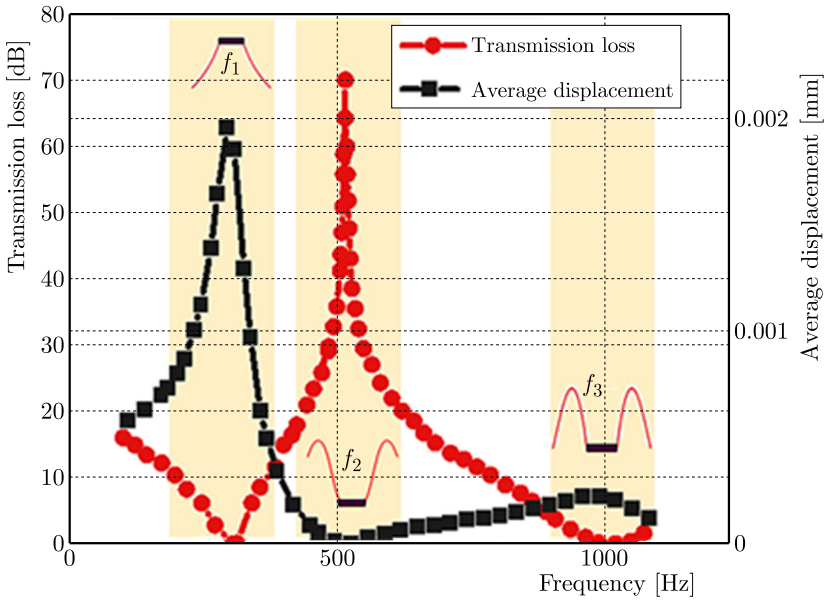

Fig. 3. Structure sound insulation curve and surface mean displacement curve.

In Fig. 3, the small figure is the modal shape of the structure at corresponding frequency points. At the resonance frequency points (f_1, f_3), the sound insulation quantity is very small. It can be seen from Eq. (2.8) that the transmission coefficient is related to the average displacement η of the structure. According to the mean displacement curve, there is a significant displacement of the structure itself at resonance, which means that the sound waves continue to propagate through the structure. When the sound insulation peak occurs at f_2 point, the average displacement of the structure is close to 0, which can be regarded as a rigid body which greatly enhances structural sound insulation performance and reduces the sound transmission coefficient. Therefore, it can be concluded that by adjusting parameters such as radius and surface density of additional mass as well as surface density of thin films, one can design structural sound insulation coefficients accordingly.

3. Experimental analysis

In order to further verify acoustic characteristics under different parameters for this structure, different thicknesses of thin films along with small masses with different sizes and weights are prepared for testing purposes, as shown in Figs. 4a and 4b. By using the acoustic impedance tube to test these structures, the experimental results were compared with calculated results, as shown in Fig. 4c. The presence of additional mass in the composite film structure results in a higher sound insulation performance compared to pure film structures. This is mainly due to the change in modal behavior and the emergence of new axisymmetric modes caused by the presence of additional mass. It also leads to a larger equivalent mass when anti-resonance occurs.

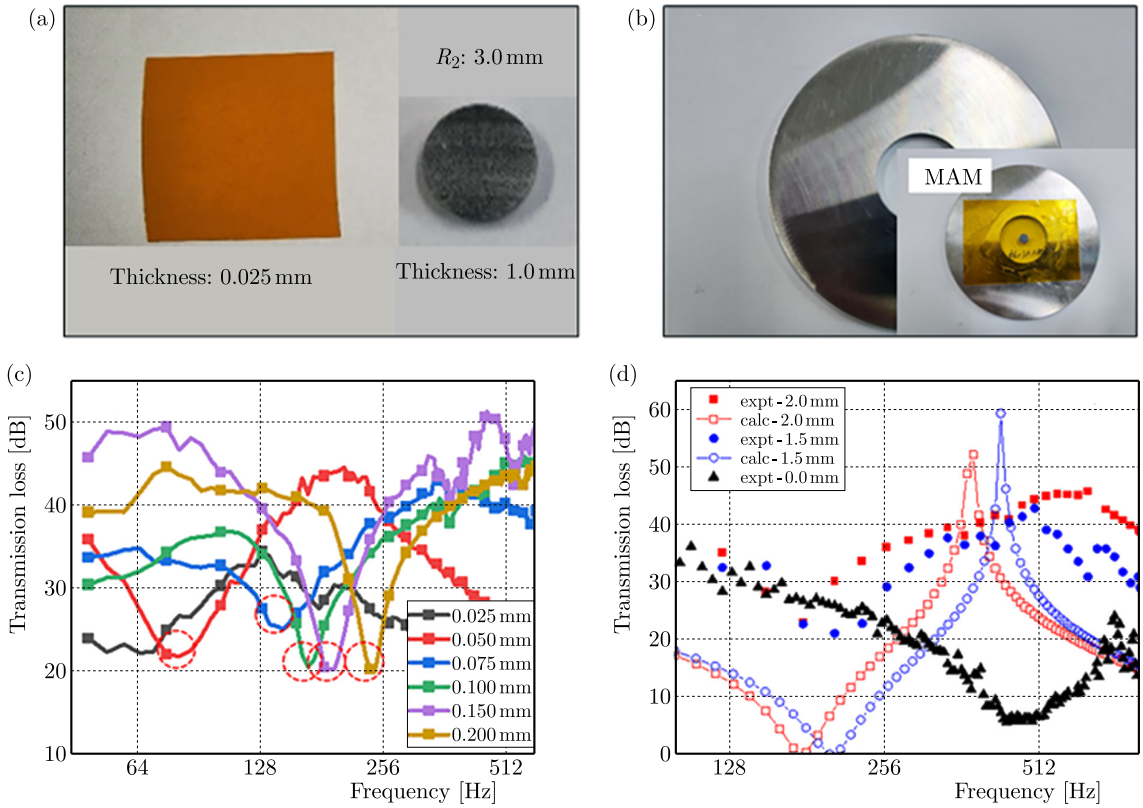

Fig. 4. Experimental results of thin-film acoustic metamaterials: (a) components of thin-film acoustic metamaterials; (b) the prepared acoustic metamaterial cell; (c) sound insulation test results of films of different thicknesses; (d) comparison of experimental and calculated results.

Experimental comparisons were conducted on six different thicknesses of films combined with five types of additional masses, as shown in Fig. 4c. It can be seen that with the increase of film thickness, the first-order resonance frequency (sound insulation valley frequency) of the structure increases. The increase of thin film thickness can be equivalent to the increase of structural stiffness, so that the first-order resonance frequency of the structure increases. On the other hand, increasing the thickness of additional mass enhances the overall equivalent mass of the structure, resulting in lower natural frequencies and shifting sound insulation valley frequencies towards lower frequencies.

By comparing theoretical and experimental data for MAMs and analyzing their design parameters such as film thickness, mass thickness, and radius on sound insulation curves, suitable design parameters are selected for addressing low-frequency noise issues inside high-speed train compartments. Focusing on frequencies below 500 Hz, a structure composed of a 2 mm thick additional mass combined with a 0.1 mm thick film is chosen after screening processes since its sound insulation curve exceeds 30 dB within 125 Hz–500 Hz range, as shown in Fig. 4d.

Incorporating this structure into flat panel noise reduction schemes showed improved sound insulation performance compared to traditional structures, as shown in Fig. 5a. Considering the problem of structural vibration transmission in the practical application process, the vibration state of the surface of the two structures is tested and compared, and there is almost no difference, as shown in Fig. 5b, indicating that the internal metamaterials had little influence on the vibration of the overall structure, and metamaterials mainly played a role in sound insulation.

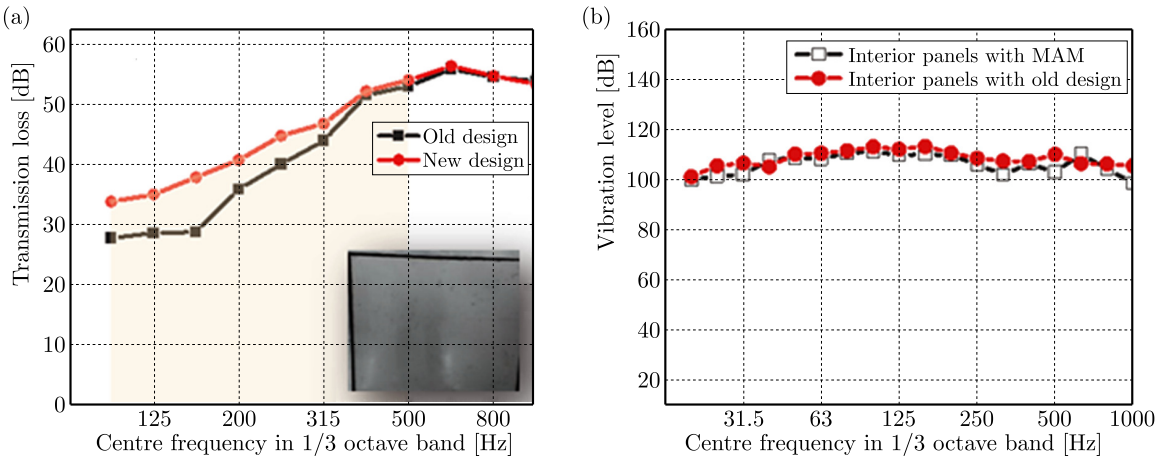

Fig. 5. Noise reduction comparison of different design schemes: (a) sound insulation comparison of design schemes with or without acoustic metamaterials; (b) structural surface vibration comparison of different schemes.

4. Conclusion

In this paper, the acoustic and vibration characteristics of MAMs were studied, leading to the following conclusions.

By designing the characteristics of low frequency sound insulation, a noise reduction structure of composite acoustic metamaterials was proposed to solve the problem of low frequency noise reduction inside high-speed EMUs.

Through theoretical analysis, it can be concluded that by adjusting parameters such as radius and surface density of additional mass as well as surface density of thin films, one can design structural sound insulation coefficients accordingly.

Experimental comparisons were conducted on six different thicknesses of films combined with five types of additional masses. The experimental results verified sound insulation performance of composite acoustic metamaterials. With the increase of film thickness, the first-order resonance frequency of the structure increases. Increasing the thickness of additional mass enhances the overall equivalent mass of the structure, resulting in lower natural frequencies and shifting sound insulation valley frequencies towards lower frequencies.

The MAMs analyzed in this research has already been studied for low frequency noise control. However, it has not been used in high-speed EMUs. The proposed composite acoustic metamaterials only consist of a single mass and a single film structure, which is simple in structure. The plane-type structure can be applied to areas such as vehicle floors, roofs, and side walls in the future. Due to its good acoustic performance, small thickness and mass, it has great potential for designing lightweight noise reduction structures in small design spaces, providing rich ideas for the noise reduction design of high-speed trains.

Acknowledgments

This work was supported by Research on Noise Characteristics of High-Speed EMU Running in Tunnel and Methods of Vibration and Noise Reduction (no. N2023J070), Research on

Vibration and Noise Performance of the EMU in the Middle and Late Life (no. 2021YJ306), Fundamental Research Funds for the Central Universities (no. 2022JBZY028), Science and Technology Research and Development Plan of China National Railway Group Corporation Limited (no. L2022Z002), and Beijing Natural Science Foundation (no. 3244035).

References

1. Ahluwalia, D.S., Kriegsmann, G.A., & Reiss, E.L. (1985). Scattering of low-frequency acoustic waves by baffled membranes and plates. *The Journal of the Acoustical Society of America*, *78*(2), 682–687. https://doi.org/10.1121/1.392437
2. Assouar, B., Oudich, M., & Zhou, X. (2016). Acoustic metamaterials for sound mitigation. *Comptes Rendus. Physique*, *17*(5), 524–532. https://doi.org/10.1016/j.crhy.2016.02.002
3. Fang, N., Xi, D., Xu, J., Ambati, M., Srituravanich, W., Sun, C., & Zhang, X. (2006). Ultrasonic metamaterials with negative modulus. *Nature materials*, *5*(6), 452–456. https://doi.org/10.1038/nmat1644
4. Ho, K.M., Cheng, C.K., Yang, Z., Zhang, X.X., & Sheng, P. (2003). Broadband locally resonant sonic shields. *Applied Physics Letters*, *83*(26), 5566–5568. https://doi.org/10.1063/1.1637152
5. Jena, D.P., Dandsena, J., & Jayakumari, V.G., (2019). Demonstration of effective acoustic properties of different configurations of Helmholtz resonators. *Applied Acoustics*, *155*, 371–382. https://doi.org/10.1016/j.apacoust.2019.06.004
6. Jung, J., Kim, H.G., Goo, S., Chang, K.J., & Wang, S. (2019). Realisation of a locally resonant metamaterial on the automobile panel structure to reduce noise radiation. *Mechanical Systems and Signal Processing*, *122*, 206–231. https://doi.org/10.1016/j.ymssp.2018.11.050
7. Kriegsmann, G.A., Norris, A., & Reiss, E.L. (1984). Acoustic scattering by baffled membranes. *The Journal of the Acoustical Society of America*, *75*(3), 685–694. https://doi.org/10.1121/1.390579
8. Liu, Z., Zhang, X., Mao, Y., Zhu, Y.Y., Yang, Z., Chan, C.T., & Sheng, P. (2000). Locally resonant sonic materials. *Science*, *289*(5485), 1734–1736. https://doi.org/10.1126/science.289.5485.1734
9. Lu, K., Wu, J.H., Guan, D., Gao, N., & Jing, L. (2016). A lightweight low-frequency sound insulation membrane-type acoustic metamaterial. *AIP Advances*, *6*(2), Article 025116. https://doi.org/10.1063/1.4942513
10. Ma, F., Wu, J.H., Huang, M., Fu, G., & Bai, C. (2014). Cochlear bionic acoustic metamaterials. *Applied Physics Letters*, *105*(21), Article 213702. https://doi.org/10.1063/1.4902869
11. Naify, C.J., Chang, C.M., McKnight, G., & Nutt, S.R. (2011). Transmission loss of membrane-type acoustic metamaterials with coaxial ring masses. *Journal of Applied Physics*, *110*(12), Article 124903. https://doi.org/10.1063/1.3665213
12. Naify, C.J., Chang, C.M., McKnight, G., & Nutt, S.R. (2012). Scaling of membrane-type locally resonant acoustic metamaterial arrays. *The Journal of the Acoustical Society of America*, *132*(4), 2784–2792. https://doi.org/10.1121/1.4744941
13. Rostami-Dogolsara, B., Moravvej-Farshi, M.K., & Nazari, F. (2016). Acoustic add-drop filters based on phononic crystal ring resonators. *Physical Review B*, *93*(1), Article 014304. https://doi.org/10.1103/PhysRevB.93.014304
14. Sheng, P., Zhang, X.X., Liu, Z., & Chan, C.T. (2003). Locally resonant sonic materials. *Physica B: Condensed Matter*, *338*(1–4), 201–205. https://doi.org/10.1016/S0921-4526(03)00487-3
15. Song, Y., Feng, L., Wen, J., Yu, D., & Wen, X. (2015). Reduction of the sound transmission of a periodic sandwich plate using the stop band concept. *Composite Structures*, *128*, 428–436. https://doi.org/10.1016/j.compstruct.2015.02.053
16. Thompson, D. & Gautier, P.-E. (2006). Review of research into wheel/rail rolling noise reduction. *Proceedings of the Institution of Mechanical Engineers, Part F: Journal of Rail and Rapid Transit*, *220*(4), 385–408. https://doi.org/10.1243/0954409JRRT79

17. Thompson, D.J., Latorre Iglesias, E., Liu, X., Zhu, J., & Hu, Z. (2015). Recent developments in the prediction and control of aerodynamic noise from high-speed trains. *International Journal of Rail Transportation*, *3*(3), 119–150. https://doi.org/10.1080/23248378.2015.1052996

18. Varanasi, S., Bolton, J.S., Siegmund, T.H., & Cipra, R.J. (2013). The low frequency performance of metamaterial barriers based on cellular structures. *Applied Acoustics*, *74*(4), 485–495. https://doi.org/10.1016/j.apacoust.2012.09.008

19. Wang, Z. & Choy, Y. (2019). Acoustical coupling and radiation control of open cavity using an array of Helmholtz resonators. *Mechanical Systems and Signal Processing*, *130*, 632–648. https://doi.org/10.1016/j.ymssp.2019.05.037

20. Yoshizawa, T., Mochida, T., & Yamazaki, T. (2019). Study of analysis method of interior noise in railway cars by means of ray tracing method. *Mechanical Engineering Journal*, *6*(5), Article 18-00449. https://doi.org/10.1299/mej.18-00449

21. Zhang, Y., Wen, J., Zhao, H., Yu, D., Cai, L., & Wen, X. (2013). Sound insulation property of membrane-type acoustic metamaterials carrying different masses at adjacent cells. *Journal of Applied Physics*, *114*(6), Article 063515. https://doi.org/10.1063/1.4818435

22. Zhou, G., Wu, J., Lu, K., Tian, X., Liang, X., Huang, W., & Zhu, K. (2019). An approach to broaden the low-frequency bandwidth of sound insulation by regulating dynamic effective parameters of acoustic metamaterials. *Journal of Physics D: Applied Physics*, *52*(21), Article 215102. https://doi.org/10.1088/1361-6463/ab07f9

Manuscript received August 3, 2024; accepted for publication January 13, 2025; published online March 25, 2025.

JOURNAL OF THEORETICAL
AND APPLIED MECHANICS
63, 2, pp. 289–306, Warsaw 2025
https://doi.org/10.15632/jtam-pl/200379

GLOBAL BEHAVIORS OF PARAMETERIZED SOLUTION DOMAIN AND BASINS OF ATTRACTION OF STAR HERRINGBONE GEAR TRANSMISSION SYSTEM

He LIN[1,2*], Jiamin GUO[1], Yingjie LI[1], Xiaole CHENG[1], Ling HONG[2]

[1] *School of Mechanical and Electrical Engineering, Xi'an Polytechnic University, Xi'an, 710048, China*
[2] *State Key Laboratory for Strength and Vibration of Mechanical Structures, Xi'an Jiaotong University, Xi'an 710049, China*

*corresponding author, *linhe@xpu.edu.cn*

The analysis of global behaviors is quite essential for the prediction of the potential dynamical vibration of the geared system. A novel meshing stiffness formula approximated to rectangular wave was proposed utilizing an odd harmonic superposition, the distribution maps of the parameterized solution domain and basin of attraction of the star herringbone gear transmission system were calculated containing various periodic regions and then validated. The analysis of the joint probability density indicates that transformations occurred on the portrait structure of attractors during the evolution into chaos. In addition, with discretization techniques and cell mapping methodology, the two-dimensional parameterized solution domain, as well as overall distributions of periodic and chaotic domains hidden in the basins of attraction were identified. Subsequently, the stochasticity of the damping ratio produced in normal distribution is analyzed, which presents that the attractor will experience perturbations before reaching a steady-state, while the periodicity of the attractor is significantly weakened. By the comparison of evolution behaviors, the distributions of periodic basin of attraction have little variations, but it caused some scattered periodic cells which mixed in the original domains, resulting in the deterioration of the steady-state to the system.

Keywords: time-varying meshing stiffness; parameterized solution domain; basin of attraction; joint probability density function; stochasticity.

Nomenclature

b – backlash,
b_c – nominal scale,
c – damping,
k – stiffness,
k_m – average meshing stiffness,
p_{ij} – joint probability density function,
$pi1$, $pi2$ – left and right side of the planetary gear i, respectively,
r – base circle radius,
$r1$, $r2$ – left and right side of ring gear, respectively,
$s1$, $s2$ – left and right side of sun gear, respectively,
u – dimensionless displacement,
u_{sp11}, $\dot{u}_{sp11}$ – dimensionless meshing displacement and velocity, respectively,
x, y – displacement along the X-axis and Y-axis, respectively,
E – amplitude of transmission error,
F – engagement force,
I – rotational inertia,
M – mass,
N_p – number of planetary gears,

T – torque,
U_i – uniformly distributed random number,
α_t, β – pressure and helical angle, respectively,
ε – stiffness fluctuation coefficient,
θ – angular displacement,
ξ – damping ratio,
φ, φ_0 – pressure, helical, phase angle, and initial phase angle, respectively,
ω – meshing frequency,
Θ – point sets.

1. Introduction

The star herringbone gear transmission system belongs to a power split gear dynamical machinery, which is normally applied in the situations that have extremely high-speed or high-power demands, such as warships, airplanes, gas turbines, even heavy machines and so forth. Its power transmission is from the sun gear to the planetary gear then converges by the internal ring gear, which could have remarkable advantages, such as quite high power density and the large transmission ratio. Compared with the planetary gear mechanism, the star herringbone gear transmission system adopts a fixed-axis gear train and possesses even better structural strength (Hong *et al.*, 2022; Arian & Taghvaei, 2021). However, the prominent issues deal with the problem of existing various vibrations on a conventional gear transmission that is also the concern of the technical research topics which the star herringbone gear transmission system encounters, especially the disclosure of its parametric domains and basins of attraction turns out to be particularly crucial for monitoring the dynamical behavior details, identifying the unstable dynamic regions or predicting the evolution processes of vibration more comprehensively (Li *et al.*, 2018).

As for now, many of the literatures regarding a gear system focusing on dynamical investigation can be mainly classified as a local analysis, that is, trying to compute dynamic solutions of the vibration, to analyze the stability of the response or even to study the influence of a parameter on vibrations. This kind of a numerical method has produced rich achievements during the previous exploration of gear dynamics. Wang *et al.* (2020) investigated the vibration of the GTF aero-engine star gear-rotor coupling system, and analyzed the gradual transformation mechanism of the bifurcation phenomenon. Marafona *et al.* (2024) studied the gear design optimization problem to minimize dynamic excitation by implementing the genetic algorithm (GA). Xiang *et al.* (2020) obtained the global bifurcation diagram of multi-stage gear transmission by altering the bifurcation parameter. Tang *et al.* (2020) presented an analytical model of time-varying support stiffness based on the Hertz contact theory, their calculations indicate that the planetary gear system with an external node engagement will enter uncertainties and cause chaos nearby the resonance frequency. Nevertheless, many studies on the excitation behavior of a gear system mainly investigate the primary unidirectional dimension. In the matter of the dynamical modeling of the star herringbone gear transmission system, apart from considering the conventional excitations, such as, the time-varying meshing stiffness and external load fluctuation, then the designated strong nonlinear influencing factor such as backlash has also been taken into account. But diverse excitations are mutually related or coupled with each other to determine the system vibration properties, on the other hand, the stochasticity present in the parameter excitations also has a significant impact on the long-term global behaviors. If one wants to thoroughly figure out the internal mechanism between these factors versus the global evolution of dynamical solutions or clarify the hierarchical domain distribution between excitation channels, the exploration of solution domain will be essential and feasible. The research on the solution domain of the star herringbone gear transmission system mainly focuses on the region of a parametric solution domain and the analysis of the global characteristics of attractors in the basin of attraction,

so as to track the evolutionary behaviors of the attractor and state basins from a given phase space and acquire the spatial microscopic details of global solutions.

In global analysis, the cell mapping technique (Wang *et al.*, 2023; Koh *et al.*, 2021) has been mostly used for the investigation of dynamical issues, as a well-known computation algorithm based on the evolutionary probability vector, it is also suitable for exploring meshed gear-tooth pair dynamics with strong nonlinearity. Besides, it is also able to track out the potential vibration situation of the system due to its ability to comprehensively evaluate the attractive region and the emergence location of chaos. Gyebrószki *et al.* (2017), Ma *et al.* (2020), Yue *et al.* (2019), and Zhang *et al.* (2019) have published relevant researches and applications involving different fields adopting that methodology, and also discussed the development tendency and technical challenges. Tang *et al.* (2011) utilized a graph cell mapping method to achieve the global solution sets of a spur gear system with a single degree of freedom (DOF) earlier. Mo *et al.* (2022) calculated the phase trajectory of the discrete cell on the Poincaré section, and observed the influence of the initial state on dynamic behaviors. Farshidianfar *et al.* (2014) and Saghafi *et al.* (2016) developed the homoclinic bifurcation and chaotic migration of the gear system in the global domain based on the Melnikov method, and accurately predicted the location of the chaotic parameter band. According to the regional discretization investigation, Lin *et al.* (2021) studied the bifurcation evolutions of a power-split gear transmission under multiple dynamical excitations. With the combination of simple cell mapping and the escape time algorithm, Gou *et al.* (2015) captured the variety of coupled vibration information of the torsional vibration gear system on the two-parameter plane.

Advantageous dynamical status conditions are meaningful to improve the stability of various gear transmission systems. In this study, the global nonlinear characteristics of the star herringbone gear transmission system from the view of multiple dimensions have been investigated, the dynamic parameters subjected to stochastic disturbance causing global variational effects were considered as well. Associated with the joint probability density function and the domain discretization technology, the determination criteria of the boundary and domain of attraction are deduced theoretically, the borderline structure and attractor behavior of the solution domain under two parameterized dynamic excitations of speed and input power are computed, and the stability and transition pattern of the attractive domain in the meshing vibration state space are simulated too. The researches show that the vibration sensitivity of the system to the initial states can be weakened and excellent steady-state characteristics can be obtained by reasonable configuring the operating conditions of the initial parameters, thereby providing the reference for the optimization of global domains and resonance parameter designs of the star herringbone gear transmission system.

2. Modeling of the star herringbone gear transmission system

The translational-torsional dynamical model of the star herringbone gear transmission system with backlash is established by employing the lumped mass method, as shown in Fig. 1. Wherein, θ_s, θ_{pi} $(i = 1, 2, 3)$, and θ_r denote the rotational vibration displacements of the sun gear, the i-th planetary gear and the ring gear around the Z-axis direction, respectively; x_s, x_{pi}, x_r, y_s, y_{pi}, and y_r are the translational vibration displacements of the sun gear, the i-th planetary gear and the internal ring gear measured along the X-axis and Y-axis direction, respectively; Fm is the meshing force between the teeth along the line of action. In the model presented in Fig. 1b, the planetary carrier is fixed to the frame without any displacement, so the rotational and translational vibrations of the carrier could be ignored. All herringbone gears in the entire system should be with a standard involute tooth profile, which are regarded as the splicing of two helical gears with opposite helical angle and the same physical property, regardless of the sliding or sliding friction between meshing teeth. Meanwhile, the Euler beam unit is connected between the left and right gear tooth.

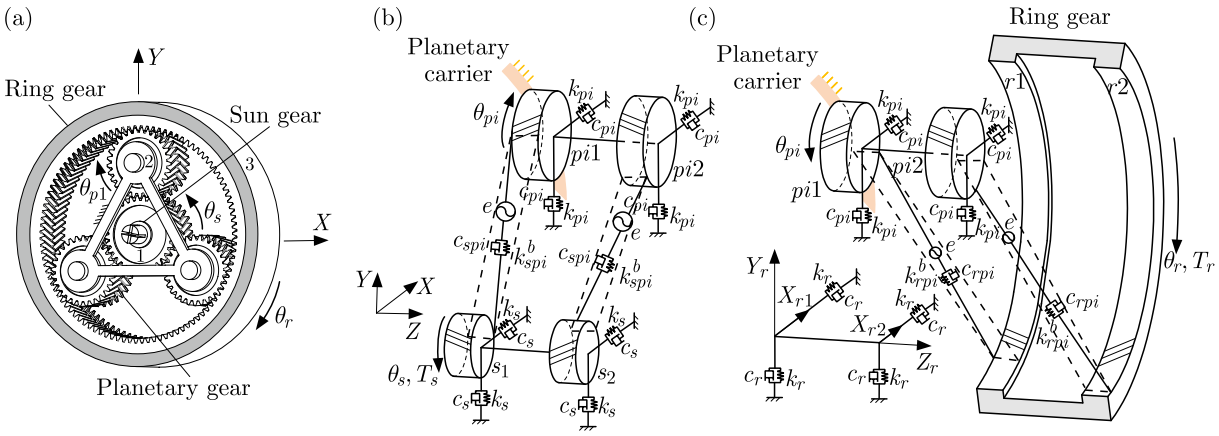

Fig. 1. (a) Dynamic schematics of star herringbone gear transmission system; (b) dynamic model between sun gear and planetary gear; (c) dynamic model between planetary gear and ring gear.

Considering the symmetry in the circumferential of the system, in order to characterize the dynamic details between component gears, the meshing translational-torsional dynamical model shown in Figs. 1b and 1c are established for only one of the planetary gears. The mass nodes $s1$ and $s2$ represent the left and right side of helical teeth of the sun gear, $pi1$ and $pi2$ represent the left side and right side of the planetary gear i ($i = 1, 2, 3$), similarly, $r1$ and $r2$ represent the two side helical teeth of the ring gear, respectively.

In light of the analysis of the gear meshing movement, the dynamical differential governing equations of vibration of the system could be established.

The dynamical differential equations of motion of the left side of the sun gear can be expressed as Eq. (2.1). The dynamical differential equations of motion of the right side of the sun gear can be expressed as Eq. (2.2). The dynamical differential equations of motion of the left side of the planetary gear pi can be expressed as Eq. (2.3). The dynamical differential equations of motion of the right side of the planetary gear pi can be expressed as Eq. (2.4). The dynamical differential equations of motion of the left side of the internal ring gear can be expressed as Eq. (2.5). The dynamical differential equations of motion of the right side of the internal ring gear can be expressed as Eq. (2.6).

$$
\begin{aligned}
I_{s1}\ddot{\theta}_{s1} &= -\sum_{i=1}^{3} F_{spi1}\, r_{s1} \cos\beta_1 + T_s, \\
M_{s1}\ddot{x}_{s1} &= -\sum_{i=1}^{3} F_{spi1} \sin\varphi_{spi} \cos\beta_1 - k_s x_{s1} - c_s \dot{x}_{s1}, \\
M_{s1}\ddot{y}_{s1} &= -\sum_{i=1}^{3} F_{spi1} \cos\varphi_{spi} \cos\beta_1 - k_s y_{s1} - c_s \dot{y}_{s1},
\end{aligned}
\tag{2.1}
$$

$$
\begin{aligned}
I_{s2}\ddot{\theta}_{s2} &= -\sum_{i=1}^{3} F_{spi2}\, r_{s2} \cos\beta_2, \\
M_{s2}\ddot{x}_{s2} &= -\sum_{i=1}^{3} F_{spi2} \sin\varphi_{spi} \cos\beta_2 - k_s x_{s2} - c_s \dot{x}_{s2}, \\
M_{s2}\ddot{y}_{s2} &= -\sum_{i=1}^{3} F_{spi2} \cos\varphi_{spi} \cos\beta_2 - k_s y_{s2} - c_s \dot{y}_{s2},
\end{aligned}
\tag{2.2}
$$

$$
\begin{aligned}
I_{pi1}\ddot{\theta}_{pi1} &= -F_{spi1}\, r_{pi1}\cos\beta_1 + F_{rpi1}\, r_{pi1}\cos\beta_1,\\
M_{pi1}\ddot{x}_{pi1} &= F_{spi1}\sin\varphi_{spi}\cos\beta_1 - F_{rpi1}\sin\varphi_{rpi}\cos\beta_1 - k_{pi}x_{pi1} - c_{pi}\dot{x}_{pi1},\\
M_{pi1}\ddot{y}_{pi1} &= F_{spi1}\cos\varphi_{spi}\cos\beta_1 + F_{rpi1}\cos\varphi_{rpi}\cos\beta_1 - k_{pi}y_{pi1} - c_{pi}\dot{y}_{pi1},
\end{aligned}
\tag{2.3}
$$

$$
\begin{aligned}
I_{pi1}\ddot{\theta}_{pi2} &= -F_{spi2}\, r_{pi2}\cos\beta_2 + F_{rpi2}\, r_{pi2}\cos\beta_2,\\
M_{pi2}\ddot{x}_{pi2} &= F_{spi2}\sin\varphi_{spi}\cos\beta_2 - F_{rpi2}\sin\varphi_{rpi}\cos\beta_2 - k_{pi}x_{pi2} - c_{pi}\dot{x}_{pi2},\\
M_{pi1}\ddot{y}_{pi2} &= F_{spi2}\cos\varphi_{spi}\cos\beta_2 + F_{rpi2}\cos\varphi_{rpi}\cos\beta_2 - k_{pi}y_{pi2} - c_{pi}\dot{y}_{pi2},
\end{aligned}
\tag{2.4}
$$

$$
\begin{aligned}
I_{r1}\ddot{\theta}_{r1} &= -\sum_{i=1}^{3} F_{rpi1}\, r_{r1}\cos\beta_1,\\
M_{r1}\ddot{x}_{r1} &= -\sum_{i=1}^{3} F_{rpi1}\sin\varphi_{spi}\cos\beta_1 - k_s x_{r1} - c_s\dot{x}_{r1},\\
M_{r1}\ddot{y}_{r1} &= -\sum_{i=1}^{3} F_{rpi1}\cos\varphi_{spi}\cos\beta_1 - k_s y_{r1} - c_s\dot{y}_{r1},
\end{aligned}
\tag{2.5}
$$

$$
\begin{aligned}
I_{r2}\ddot{\theta}_{r2} &= -\sum_{i=1}^{3} F_{rpi2}\, r_{r2}\cos\beta_2 + T_r,\\
M_{r2}\ddot{x}_{r2} &= -\sum_{i=1}^{3} F_{rpi2}\sin\varphi_{spi}\cos\beta_2 - k_s x_{r2} - c_s\dot{x}_{r2},\\
M_{r2}\ddot{y}_{r2} &= -\sum_{i=1}^{3} F_{rpi2}\cos\varphi_{spi}\cos\beta_2 - k_s y_{r2} - c_s\dot{y}_{r2}.
\end{aligned}
\tag{2.6}
$$

From Eq. (2.1) to Eq. (2.6), I indicates the rotational inertia; M denotes the equivalent mass, where $M = I/r^2$; β_1 and β_2 are the helical angle of the herringbone gears, assuming that left-hand rotation is positive and right-hand rotation is negative, then there the relationship occurs $\beta_2 = -\beta_1$. F_{spi} is the meshing force between the sun gear and the planetary gear, and F_{rpi} is the meshing force between the planetary gear and the ring gear, given as

$$
\begin{aligned}
F_{spi} &= k_{spi} f\left(x_{spi}, b\right) + c\dot{x}_{spi},\\
F_{rpi} &= k_{rpi} f\left(x_{rpi}, b\right) + c\dot{x}_{rpi},
\end{aligned}
\tag{2.7}
$$

where k_{spi} and k_{rpi} are the meshing stiffness between the sun gear and the planetary gear, and c_{spi}, c_{rpi} are the meshing damping between the planetary gear and the ring gear, respectively; $f(x, b)$ describes the expression of the backlash; b is the backlash; x_{spi} and x_{rpi} are the relative displacements along the line of action between meshing pairs.

Here, we define the time-varying meshing stiffness by an approximate square wave, which can be built by the abbreviated function $k(t)$ and the mean meshing stiffness k_m, when we take the first three orders of j ($j = 1$, $j = 2$, $j = 3$) and draw the superimposed harmonic waveform in Fig. 2a:

$$
k'(t) = \frac{2k_m}{\pi}\left[\sin(\omega t) + \frac{1}{3}\sin(3\omega t) + \ldots + \frac{1}{j}\sin(j\omega t) + \ldots\right],
\tag{2.8}
$$

where $(j = 1, 3, 5, ..., 2n + 1)$, E represents the square wave amplitude. The first three order harmonic waveforms of meshing stiffness can be plotted, respectively, in Fig. 2b.

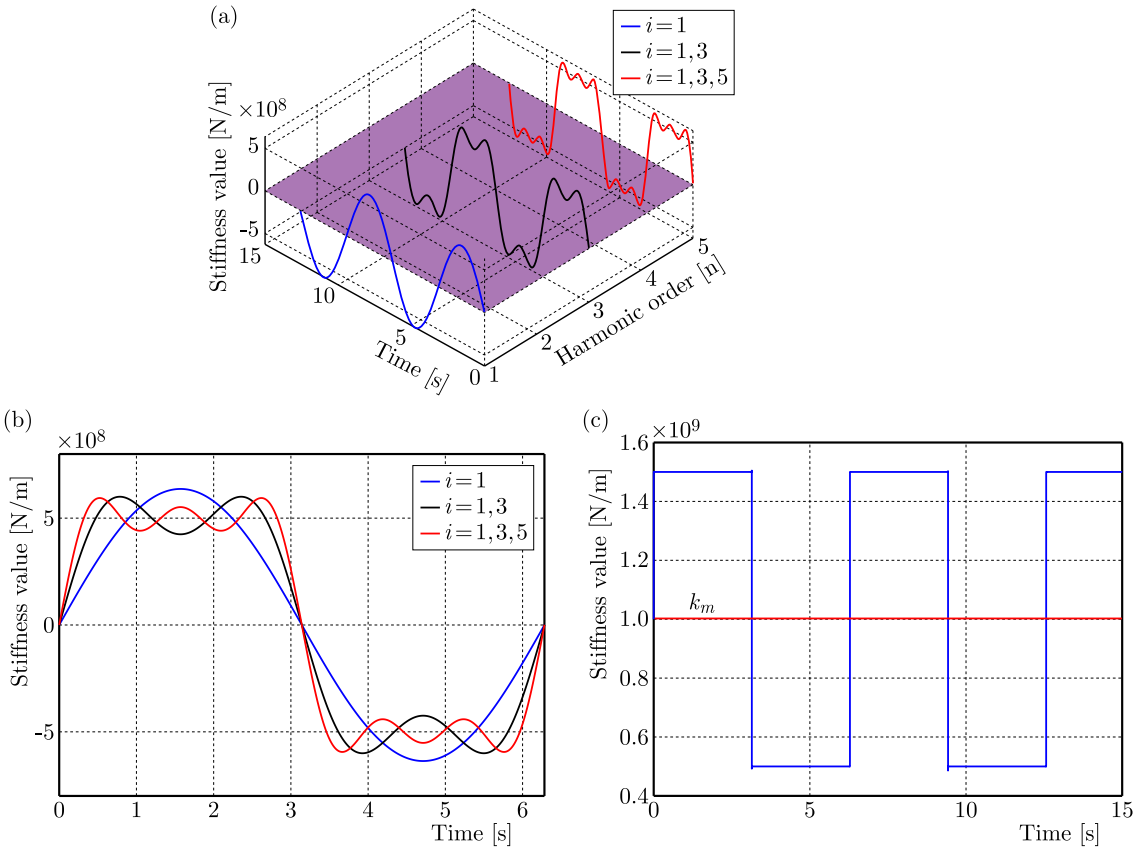

Fig. 2. (a) Superposition of the first three order harmonic waveform of time-varying meshing stiffness; (b) harmonic waveform superposition of the first three orders (1 period); (c) approximate model of the time-varying meshing stiffness.

In Fig. 2c, then the time-varying meshing stiffness of the gear system can be expressed by the Fourier series as

$$k(t) = k_m + \varepsilon k'(t) = k_m + \varepsilon \frac{2k_m}{\pi} \sum_{i=1}^{\infty} \left(\sin\left(\frac{1}{j} \omega t + \varphi_0 \right) \right), \qquad (j = 1, 3, 5, ..., 2n + 1), \quad (2.9)$$

where ω is the meshing frequency, and ε represents the fluctuation coefficient of the time-varying meshing stiffness; φ_0 denotes the initial phase angle, and defines the initial phase angle φ_{spi} and φ_{rpi}, respectively:

$$\begin{aligned} \varphi_{spi} &= \alpha_t - 2\pi(i-1)/N_p, \quad (i = 1, 2, 3), \\ \varphi_{rpi} &= \alpha_t + 2\pi(i-1)/N_p, \quad (i = 1, 2, 3). \end{aligned} \qquad (2.10)$$

The meshing damping related to the meshing stiffness is derived, and given as Eq. (2.11). The nonlinear function of the backlash can be expressed as Eq. (2.12):

$$c_{spi} = 2\xi \sqrt{k_m / M_{esp}}, \qquad (2.11)$$

$$f(x, b) = \begin{cases} x - b/2 & x > b/2, \\ 0 & -b/2 \le x \le b/2, \\ x + b/2 & x < -b/2, \end{cases} \qquad (2.12)$$

where ξ is the meshing damping ratio, M_{esp} denotes the equivalent mass of mating gears between the sun gear and the planetary gear.

Then along the line of action, x_{spi1} and x_{spi2} are the relative meshing displacements between the sun gear and the i-th planetary gear; similarly, x_{rpi1} and x_{rpi2} denote the i-th planetary gear and the ring gear, which can be separately expressed as follows:

$$\begin{aligned}
x_{spi1} &= [(x_{s1} - x_{pi1})\sin\varphi_{spi} + (y_{s1} - y_{pi1})\cos\varphi_{spi} \\
&\quad + (r_{s1}\theta_{s1} + r_{pi1}\theta_{pi1})]\cos\beta_1 - e_{i1}(t), \\
x_{spi2} &= [(x_{s2} - x_{pi2})\sin\varphi_{spi} + (y_{s2} - y_{pi2})\cos\varphi_{spi} \\
&\quad + (r_{s2}\theta_{s2} + r_{pi2}\theta_{pi2})]\cos\beta_2 - e_{i2}(t), \\
x_{rpi1} &= [(x_{pi1} - x_{r1})\sin\varphi_{spi} + (y_{r1} - y_{pi1})\cos\varphi_{spi} \\
&\quad + (r_{r1}\theta_{r1} - r_{pi1}\theta_{pi1})]\cos\beta_1 - e_{i3}(t), \\
x_{rpi2} &= [(x_{pi2} - x_{r2})\sin\varphi_{spi} + (y_{r2} - y_{pi2})\cos\varphi_{spi} \\
&\quad + (r_{r2}\theta_{r2} - r_{pi2}\theta_{pi2})]\cos\beta_2 - e_{i4}(t),
\end{aligned} \tag{2.13}$$

where $e_{ij}(t) = E\sin(\omega t + \varphi_0)$ $(i = 1, 2, 3;\ j = 1, 2, 3, 4)$, $e_{ij}(t)$ is the comprehensive transmission error, and E indicates the amplitude. Taking the second derivative to Eq. (2.13) and substituting it into Eqs. (2.1)–(2.6), then the differential equations adopted for eliminating rigid body displacement can be obtained as follows:

$$\begin{aligned}
\ddot{x}_{spi1} &= \Bigg[(\ddot{x}_{s1} - \ddot{x}_{pi1})\sin\varphi_{spi} + (\ddot{y}_{s1} - \ddot{y}_{pi1})\cos\varphi_{spi} + r_{s1}T_s/I_{s1} \\
&\quad - \sum_{i=1}^{3} F_{spi1}\cos\beta_1/M_{s1} + \cos\beta_1\left(F_{rpi1} - F_{spi1}\right)/M_{pi1}\Bigg]\cos\beta_1 - \ddot{e}_{i1}(t), \\
\ddot{x}_{spi2} &= \Bigg[(\ddot{x}_{s2} - \ddot{x}_{pi2})\sin\varphi_{spi} + (\ddot{y}_{s2} - \ddot{y}_{pi2})\cos\varphi_{spi} \\
&\quad + \left(-\sum_{i=1}^{3} F_{spi2}/M_{s2} + \left(F_{rpi2} - F_{spi2}\right)/M_{pi2}\right)\cos\beta_2\Bigg]\cos\beta_2 - \ddot{e}_{i2}(t), \\
\ddot{x}_{rpi1} &= \Bigg[(\ddot{x}_{pi1} - \ddot{x}_{r1})\sin\varphi_{spi} + (\ddot{y}_{r1} - \ddot{y}_{pi1})\cos\varphi_{spi} \\
&\quad + \left(-\sum_{i=1}^{3} F_{rpi1}/M_{r1} + \left(F_{spi1} - F_{rpi1}\right)/M_{pi1}\right)\cos\beta_1\Bigg]\cos\beta_1 - \ddot{e}_{i3}(t), \\
\ddot{x}_{rpi2} &= \Bigg[(\ddot{x}_{pi2} - \ddot{x}_{r2})\sin\varphi_{spi} + (\ddot{y}_{r2} - \ddot{y}_{pi2})\cos\varphi_{spi} + r_{r1}T_r/I_{r1} \\
&\quad - \sum_{i=1}^{3} F_{rpi2}\cos\beta_2/M_{r2} + \cos\beta_2\left(F_{spi2} - F_{rpi2}\right)/M_{pi2}\Bigg]\cos\beta_2 - \ddot{e}_{i4}(t).
\end{aligned} \tag{2.14}$$

With the help of above expressions, the dynamical equations of the entire system in a unified form after eliminating rotational rigid displacement is simplified as

$$[\mathbf{M}]\,\ddot{\mathbf{X}} + [\mathbf{C}]\,\dot{\mathbf{X}} + [\mathbf{K}]\,\mathbf{f}\,(\mathbf{X}, \mathbf{b}) = \mathbf{F}, \tag{2.15}$$

where $\mathbf{X}$ represents the displacement vector; $\mathbf{M}$, $\mathbf{C}$, $\mathbf{K}$, and $\mathbf{F}$, respectively, indicate the mass matrix, damping matrix, stiffness matrix, and load vector, each of them is given as

$$\mathbf{X} = [x_{spi1},\ x_{spi2},\ x_{rpi1},\ x_{rpi2},\ x_{s1},\ y_{s1},\ x_{s2},\ y_{s2},\ x_{pi1},\ y_{pi1},\ x_{pi2},\ y_{pi2},\ x_{r1},\ y_{r1},\ x_{r2},\ y_{r2}]^{\mathrm{T}}, \tag{2.16}$$

$$\mathbf{M}=\begin{bmatrix}\mathbf{E}_{2\times2} & 0_{2\times2} & \mathbf{A} & -\mathbf{A} & 0_{2\times4}\\ 0_{2\times2} & \mathbf{E}_{2\times2} & 0_{2\times4} & \mathbf{B} & -\mathbf{B}\\ 0_{2\times2} & 0_{2\times2} & \mathbf{m}_1 & 0_{2\times4} & 0_{2\times4}\\ 0_{2\times2} & 0_{2\times2} & \mathbf{m}_2 & 0_{2\times4} & 0_{2\times4}\\ 0_{2\times2} & 0_{2\times2} & 0_{2\times4} & \mathbf{m}_3 & 0_{2\times4}\\ 0_{2\times2} & 0_{2\times2} & 0_{2\times4} & \mathbf{m}_4 & 0_{2\times4}\\ 0_{2\times2} & 0_{2\times2} & 0_{2\times4} & 0_{2\times4} & \mathbf{m}_5\\ 0_{2\times2} & 0_{2\times2} & 0_{2\times4} & 0_{2\times4} & \mathbf{m}_6\end{bmatrix},\qquad \mathbf{A}=\begin{bmatrix}-a_1 & -a_2 & 0 & 0\\ 0 & 0 & -a_3 & -a_4\end{bmatrix},$$

$$\mathbf{m}_1=\begin{bmatrix}m_{s1} & 0 & 0 & 0\\ 0 & m_{s1} & 0 & 0\end{bmatrix},\qquad \mathbf{m}_2=\begin{bmatrix}m_{s2} & 0 & 0 & 0\\ 0 & m_{s2} & 0 & 0\end{bmatrix},$$

$$\mathbf{m}_3=\begin{bmatrix}m_{pi1} & 0 & 0 & 0\\ 0 & m_{pi1} & 0 & 0\end{bmatrix},\qquad \mathbf{m}_4=\begin{bmatrix}m_{pi2} & 0 & 0 & 0\\ 0 & m_{pi2} & 0 & 0\end{bmatrix},$$

$$\mathbf{m}_5=\begin{bmatrix}m_{r1} & 0 & 0 & 0\\ 0 & m_{r1} & 0 & 0\end{bmatrix},\qquad \mathbf{m}_6=\begin{bmatrix}m_{r2} & 0 & 0 & 0\\ 0 & m_{r2} & 0 & 0\end{bmatrix}, \tag{2.17}$$

$$\mathbf{K}\backslash\mathbf{C}=\begin{bmatrix}\mathbf{D}_1 & \mathbf{D}_2 & 0_{2\times2} & 0_{2\times2} & 0_{2\times2} & 0_{2\times2} & 0_{2\times2} & 0_{2\times2}\\ \mathbf{D}_3 & \mathbf{D}_4 & 0_{2\times2} & 0_{2\times2} & 0_{2\times2} & 0_{2\times2} & 0_{2\times2} & 0_{2\times2}\\ \mathbf{D}_5 & 0_{2\times2} & \mathbf{K_s} & 0_{2\times2} & 0_{2\times2} & 0_{2\times2} & 0_{2\times2} & 0_{2\times2}\\ 0_{2\times2} & \mathbf{D}_6 & 0_{2\times2} & \mathbf{K_s} & 0_{2\times2} & 0_{2\times2} & 0_{2\times2} & 0_{2\times2}\\ \mathbf{D}_7 & \mathbf{D}_8 & 0_{2\times2} & 0_{2\times2} & \mathbf{K}_{pi} & 0_{2\times2} & 0_{2\times2} & 0_{2\times2}\\ \mathbf{D}_9 & \mathbf{D}_{10} & 0_{2\times2} & 0_{2\times2} & 0_{2\times2} & \mathbf{K}_{pi} & 0_{2\times2} & 0_{2\times2}\\ 0_{2\times2} & \mathbf{D}_{11} & 0_{2\times2} & 0_{2\times2} & 0_{2\times2} & 0_{2\times2} & \mathbf{K}_r & 0_{2\times2}\\ 0_{2\times2} & \mathbf{D}_{12} & 0_{2\times2} & 0_{2\times2} & 0_{2\times2} & 0_{2\times2} & 0_{2\times2} & \mathbf{K}_r\end{bmatrix}, \tag{2.18}$$

$$\mathbf{F}=\left[\left(r_{s1}T_s\cos\beta_1\right)/I_{s1}\quad 0_{1\times2}\quad \left(r_{s1}T_r\cos\beta_2\right)/I_{r2}\quad 0_{1\times12}\right]^{\mathrm{T}},$$

where

$$\mathbf{D}_1=\begin{bmatrix}\left(\sum_{i=1}^{3}\Gamma_{spi}/m_{s1}+\Gamma_{spi}/m_{pi1}\right)\cos^2\beta_1 & 0\\ 0 & \left(\sum_{i=1}^{3}\Gamma_{spi}/m_{s2}+\Gamma_{spi}/m_{pi2}\right)\cos^2\beta_2\end{bmatrix},$$

$$\mathbf{D}_2=\begin{bmatrix}-\left(\Gamma_{rpi}\cos^2\beta_1\right)/m_{pi1} & 0\\ 0 & -\left(\Gamma_{rpi}\cos^2\beta_2\right)/m_{pi2}\end{bmatrix},$$

$$\mathbf{D}_3=\begin{bmatrix}-\left(\Gamma_{spi}\cos^2\beta_1\right)/m_{pi1} & 0\\ 0 & -\left(\Gamma_{spi}\cos^2\beta_2\right)/m_{pi2}\end{bmatrix},$$

$$\mathbf{D}_4=\begin{bmatrix}\left(\sum_{i=1}^{3}\Gamma_{rpi}/m_{r1}+\Gamma_{rpi}/m_{pi1}\right)\cos^2\beta_1 & 0\\ 0 & \left(\sum_{i=1}^{3}\Gamma_{rpi}/m_{r2}+\Gamma_{rpi}/m_{pi2}\right)\cos^2\beta_2\end{bmatrix},$$

$$\mathbf{D}_5=\begin{bmatrix}\sum_{i=1}^{3}\Gamma_{spi}a_1 & 0\\ \sum_{i=1}^{3}\Gamma_{spi}a_2 & 0\end{bmatrix},\qquad \mathbf{D}_6=\begin{bmatrix}0 & \sum_{i=1}^{3}\Gamma_{spi}a_1\\ 0 & \sum_{i=1}^{3}\Gamma_{spi}a_2\end{bmatrix},\qquad \mathbf{D}_7=\begin{bmatrix}-\Gamma_{spi}a_1 & 0\\ -\Gamma_{spi}a_2 & 0\end{bmatrix},$$

$$\mathbf{D}_8 = \begin{bmatrix} \Gamma_{rpi} b_1 & 0 \\ -\Gamma_{rpi} b_2 & 0 \end{bmatrix}, \qquad \mathbf{D}_9 = \begin{bmatrix} 0 & -\Gamma_{spi} a_3 \\ 0 & -\Gamma_{spi} a_4 \end{bmatrix}, \qquad \mathbf{D}_{10} = \begin{bmatrix} \Gamma_{rpi} b_3 & 0 \\ -\Gamma_{rpi} b_4 & 0 \end{bmatrix},$$

$$\mathbf{D}_{11} = \begin{bmatrix} -\sum_{i=1}^{3} \Gamma_{rpi} b_1 & 0 \\ \sum_{i=1}^{3} \Gamma_{rpi} b_2 & 0 \end{bmatrix}, \qquad \mathbf{D}_{12} = \begin{bmatrix} -\sum_{i=1}^{3} \Gamma_{rpi} b_3 & 0 \\ \sum_{i=1}^{3} \Gamma_{rpi} b_4 & 0 \end{bmatrix},$$

$$\mathbf{K}_s = \Gamma_s \mathbf{E}_{2\times 2}, \qquad \mathbf{K}_{pi} = \Gamma_{pi} \mathbf{E}_{2\times 2}, \qquad \mathbf{K}_r = \Gamma_r \mathbf{E}_{2\times 2},$$

where

$$\mathbf{E}_{2\times 2} = \begin{bmatrix} 1 & 0 \\ 0 & 1 \end{bmatrix},$$

$$a_1 = \sin\varphi_{spi}\cos\beta_1, \quad a_2 = \cos\varphi_{spi}\cos\beta_1, \quad a_3 = \sin\varphi_{spi}\cos\beta_2, \quad a_4 = \cos\varphi_{spi}\cos\beta_2,$$
$$b_1 = \sin\varphi_{rpi}\cos\beta_1, \quad b_2 = \cos\varphi_{rpi}\cos\beta_1, \quad b_3 = \sin\varphi_{rpi}\cos\beta_2, \quad b_4 = \cos\varphi_{rpi}\cos\beta_2.$$

To simplify the computation of aforementioned matrices, the symbol Γ is introduced, Γ would be substituted by stiffness or damping according to Eq. (2.15). The following Eq. (2.19) is demonstrating the substitution of Γ in the matrix $\mathbf{D}_1$ by means of stiffness k_{spi}:

$$\mathbf{D}_1 = \begin{bmatrix} \left(\sum_{i=1}^{3} k_{spi}/m_{s1} + k_{spi}/m_{pi1}\right)\cos^2\beta_1 & 0 \\ 0 & \left(\sum_{i=1}^{3} k_{spi}/m_{s2} + k_{spi}/m_{pi2}\right)\cos^2\beta_2 \end{bmatrix}, \tag{2.19}$$

$$\omega_n = \sqrt{k_m\,(1/M_s + 1/M_{pi})}. \tag{2.20}$$

Additionally, k_s, k_{pi}, and k_r are the support stiffness of the sun gear, planetary gear and ring gear, respectively; similarly, c_s, c_{pi}, and c_r represent their damping correspondingly.

During the numerical computation of Eq. (2.15), a dimensionless operation is required to avoid the convergence problem due to the huge differences in the order of magnitude of the polynomial coefficient. Therefore, the dimensionless nominal scale parameter is defined as Eq. (2.20), where M_s and M_{pi} indicate the equivalent masses of the sun gear and the planetary gear, separately. Once the nominal time scale ω_n and displacement scale b_c, $b_c = 100 \times 10^{-6}$ m are defined, then the time τ, vibration displacement u and backlash $\overline{b}$ with normalized dimensions can be derived as $\tau = \omega_n t$, $u(\tau) = x(t)/b_c$, and $\overline{b} = b/b_c$.

3. Global behaviors of parameterized solution domain and basins of attraction

3.1. Solutions inside the parameterized plane

The followings and Table 1 provide the essential dynamical parameters of the star herringbone gear transmission system. For instance, the amount of planetary gears is 3; all the gear modulus is 4 mm; the installation angle α_{pi} $(i = 1, 2, 3)$ of each planetary gear is 0, $2\pi/3$, and $4\pi/3$; the normal pressure angle α_n is 20°, and the base helical angle β_b is 22.5°. The mean stiffness km is 2×10^9 N/m; the support stiffness k is 1×10^6 N/m; the stiffness fluctuation coefficient ε is 0.1; the meshing damping ratio ξ is 0.1; the power is 3000 kW, and the backlash b is set 0.1 mm.

The two-dimensional parametric domain is composed of the horizontal parameter μ_j $(j = 1, 2, ..., j)$ and the vertical parameter λ^i $(i = 1, 2, ..., i)$, both directions are discretized into a certain number of cells, c_{ij} represents a single cell (see Fig. 3). Next, combining with Eq. (3.1) and adopting the Runge–Kutta method to compute the dynamical differential equations in Eq. (2.20). Parameterized cells that have the same periodic solution constitute a periodic domain

Table 1. Partial major parameters of the gears.

	Sun gear	Planetary gear	Ring gear
Number of teeth Z	36	32	100
Mass m [kg]	5.30	4.50	16.08
Moment of interia I [kg · m^2]	0.0226	0.0149	0.6564

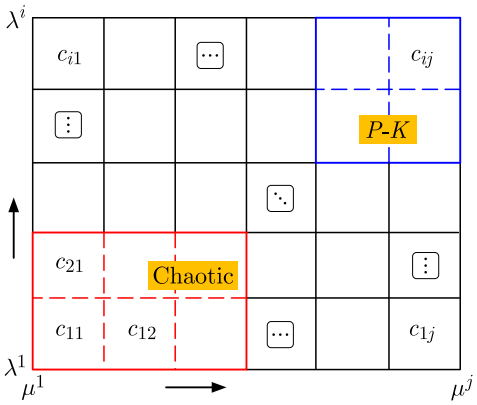

Fig. 3. Cell discretization of two-dimensional parametric domain.

of period-K (P-K), K is the periodic state, and called P-K motion. Similarly, chaotic solution can also be calculated.

In global analysis of the parameterized plane, each discretized cell represents an exact value of an excitation parameter for numerical calculation, and the initial state (0, 0) is brought into the differential equations of motion. The mapping iteration starts from time $\tau = 0$, and 4 adjacent mapping points of the attractor in state space are extracted from the Poincaré section, then compared with the criteria value of $\varepsilon_1 = 1.0 \times 10^{-3}$, and $\varepsilon_2 = 1.0 \times 10^{-4}$, respectively, here the ε_2 determines the periodic state of the attractor domains in calculation.

For point sets $\Theta \in R^n$, n is the dimension of the system, and Θ is the set of all points on the Poincaré section achieved by mappings. Assuming $X(i)$ is one of the points in the Θ, accordingly, $X^{(i)} \in P$ $(i = 1, 2, ..., k)$, k is the quantity of points in the set Θ. Here, Y is another point on the Poincaré section, and Y_j $(j = 1, 2, ..., n)$ is the j-th component of Y, then we can define the 2-norm between point Y and point set Θ as

$$\rho(Y, \Theta) = \min\left(\operatorname{dis}(Y, X^{(i)})\right), \qquad i = 1, 2, ..., k, \tag{3.1}$$

where

$$\operatorname{dis}(Y, X^{(i)}) = \max\left|Y_j - X_j^{(i)}\right|, \qquad j = 1, 2, ..., n. \tag{3.2}$$

If point Y and the point set Θ satisfy the following expression, $\rho(Y, \Theta) < \varepsilon$.

Consequently, it can be determined that point Y falls within the domain of attraction composed of the point set A. If the $\rho(Y, \Theta) < \varepsilon$ is still not satisfied, that means there might exist a chaotic attractor under the present parameter. To ensure that result, preset 5 extra mappings to the potential chaotic attractor.

In Fig. 4, which is divided into 300×300 regular cells in the parameterized plane, after discretization and iteration, the two-dimensional solution domains could be plotted out. The distribution of various dynamic parameter domains is identified with the aid of series of discrete cells. One can clearly see that the period-doubling bifurcation imbedded in the parametric plane, which is presented while the rotational speed raises from 4000 rpm to 20000 rpm.

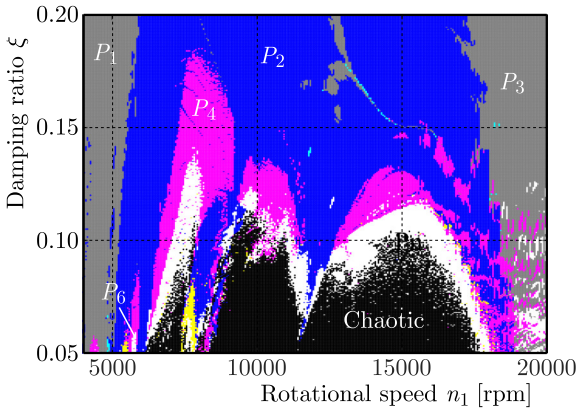

Fig. 4. Two-dimensional plane of parameterized solution domain.

A parametric cell at (8000, 0.15) is select from Fig. 4 and its phase portrait and the Poincaré diagram are computed as shown in red color in Fig. 5. Then chaotic attractor is also analyzed in the same way, at this point, the phase trajectory in chaotic state exhibits a little bit local repeated with winding, and the fractal characteristic of the mapping points on the Poincaré section are obvious. The period-4 attractor now with slightly larger size maintains a certain distance away from the chaotic attractor. That implies the period-4 attractor will move down if the speed or damping ratio varies properly into the chaotic domain. Accordingly, on the selection of parameters from solution cells, a chaotic vibration can be also eliminated by driving into the periodic domains.

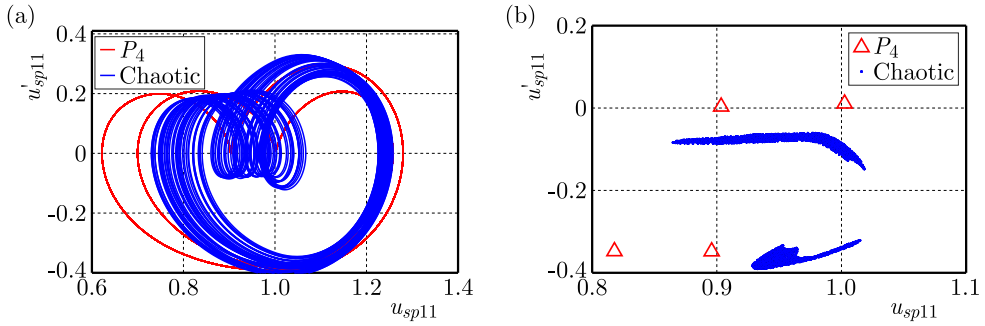

Fig. 5. (a) Phase portrait and (b) Poincaré section of attractors.

One of the global analysis is to study the movement behaviors of the attractor. The projection of the phase trajectory will play a major role. Next, to explore the behavior of the attractor transformation by using the joint probability density function $P(X, Y)$. We define the two-dimensional discrete variable (X, Y), all possible points in the target region Ω could be defined by (x, y), then it has Eq. (3.3).

In the study of the star herringbone gear transmission system, the joint distribution of two-dimensional discrete variables is defined as Eq. (3.4):

$$P((X,Y) \in \Omega) = \iint_A f(x,y), \qquad \text{for all} \quad \Omega, \tag{3.3}$$

$$p_{ij} = P\{X = u_{sp11}, Y = \dot{u}_{sp11}\}. \tag{3.4}$$

Then, by using the Monte Carlo method (Dreeben *et al.*, 1998) the joint probability density function is calculated. For the period-4 attractor, the vertical peak representing the probability density of the attractor at the intersection of the Poincaré section. In Fig. 6, four convex peaks

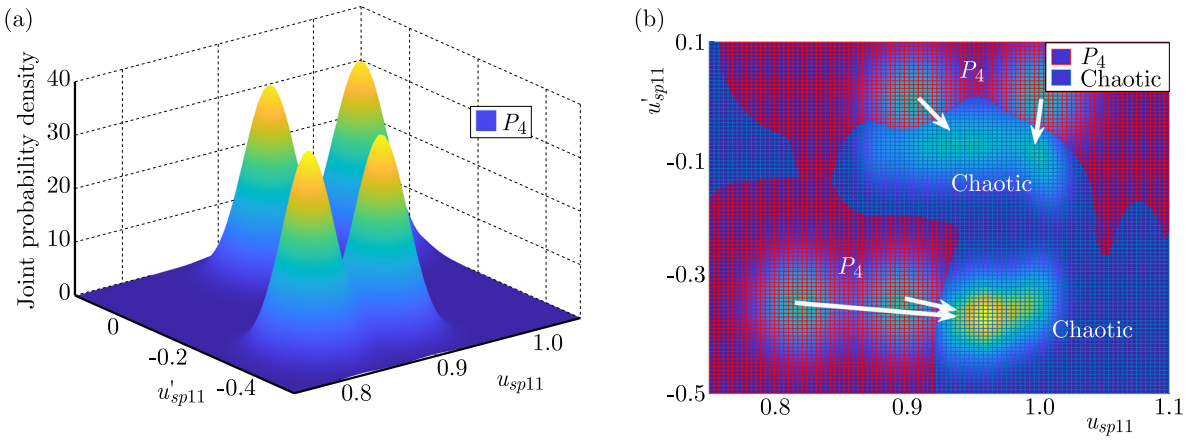

Fig. 6. (a) Joint probability density of period-4 attractor; (b) the evolution of attractor from period-4 to chaos.

between each of them are almost equal proving that this attractor has only four harmonic periods and no other coexisting attractors. Afterwards, as the damping ratio decreases to 0.05, we see the period-4 attractor has started to move down and approach to the chaotic attractor gradually.

3.2. Validation of parameterized solution domains

The local domain of interest which consists of speed and power with the finite field of [4000, 20000] × [1500, 4000]. The solutions reveal information on the steady-state oscillations in a more overall way on the plane (Fig. 7), and mainly including period-1, period-2, period-4, multi-period, and chaotic parameterized regions. The various regions suggest the differences of steady-state result if under excitation, particularly, more uncertainties will appear adjacent to the borderline. During the increasing of horizontal speed, the periodic state changes frequently, which indicates the system behavior is sensitive to the variation of the sun gear velocity, however, while in the vertical direction at 4000 r/min, the dynamic domain seems to keep period-1 motion with the increase of power.

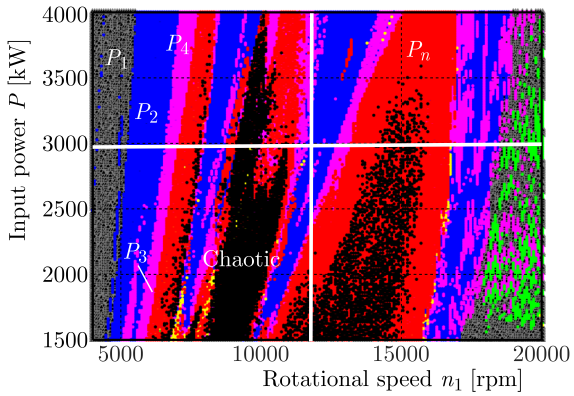

Fig. 7. Parameterized solution domain with speed and power.

The validation to the global parameterized results is carried out along the horizontal and vertical bifurcation process. In Fig. 8, these two bifurcation routes are following the white lines in Fig. 7 at 3000 kW and 11500 rpm, respectively. Evolutionary phenomena such as period doubling, chaos, as well as disturbances, is consistent with the parameterized solutions. Where the fluctuation weakens along the horizontal axis in the bifurcation diagram. Accordingly, the vibration and stability of the system could be globally predicted and improved by properly adjusting the dynamical parameters.

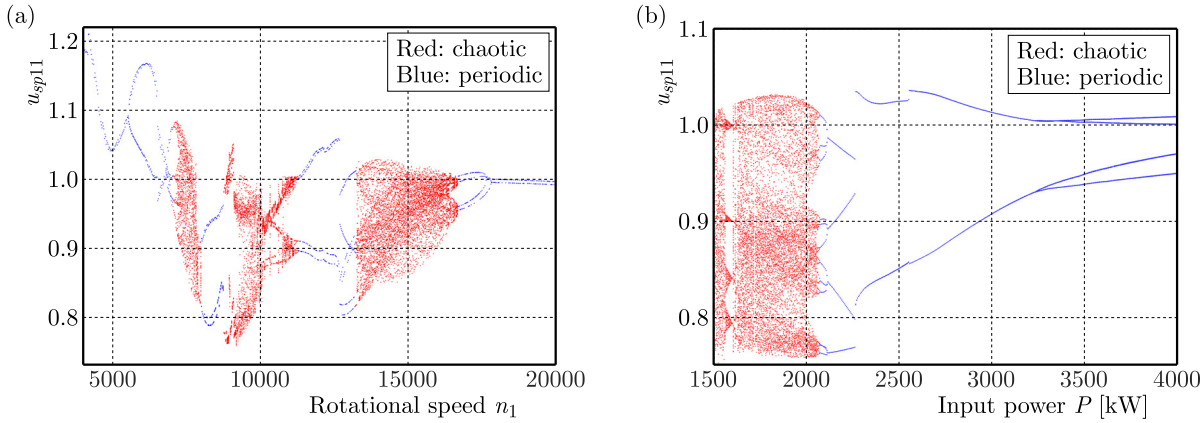

Fig. 8. Bifurcation evolution process with respect to (a) speed and (b) input power.

3.3. Fundamentals of attraction solution

The calculation of global domains associates with a couple of methods, as the continuous target parametric domain or state space are discretized into a series of cell units by the regional discretization technology combined with cell mappings. When subdividing the selected region, the reasonable number of cells can be set depending on the numerical accuracy and computational efficiency.

Define a simple cell mapping C, where the cell Z^* satisfying $Z^* = C(Z^*)$, and Z^* is called the fixed cell of the geared system, let C_m represents the cell mapping iterated m times, and C_0 refers to the self-map. If there are another cells $Z^*(j)$, $j \in \{K\}$, and K $(K \geq 2)$ denotes the total amount, which satisfies the relationships:

$$Z^*(m+1) = C^m\left(Z^*(1)\right), \qquad m \in \{K-1\}, \tag{3.5}$$

$$Z^*(1) = C^K\left(Z^*(1)\right). \tag{3.6}$$

Then Z^* is said to constitute the periodic solution of period K, and each cell $Z^*(j)$ is a periodic cell with the period K. In order to strengthen the identification, such cells are called P-K cells. For example, a monocycle solution is a stable cell, which is called P_1 cell. Figure 9 exhibits a system with two periodic solutions, Z_1 is the first periodic solution with one period, Z_2, Z_3, and Z_4 finally go toward the second periodic solution with a period of 3.

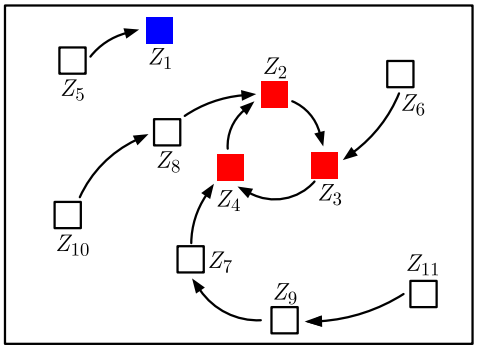

Fig. 9. Convergence of mapping cells in dynamical system.

When the initial state is discretized, the global domain of attraction with oscillation details can be computed by analyzing the evolution of cells, these computations often take a lot

of time due to the 14 degrees of freedom contained in our system. Note that, if in the solutions a cell (μ^i, λ^j) shows different periodic property with its neighbors (μ^{i+1}, λ^j), (μ^i, λ^{j+1}), and $(\mu^{i+1}, \lambda^{j+1})$, that means the current cell (μ^i, λ^j) is located on the border of the domain. Hence, the above technique is able to compute the borderline of different domains as well.

3.4. Evolution behaviors of basin of attraction

3.4.1. Global behaviors without stochasticity

The global behaviors inside a state space reveal the vibration evolution of the system under initial conditions. Cells are calculated individually on the region of $[-1, 1] \times [1, 1]$. In Fig. 10, the state domain consists of period-2, period-4, and multi-periodic basins. The proportion of period-2 state cells in the whole domain continues to reach to 34 %, and the number of period-4 cells amount to 12393, accounting for 30 %. The period-2 basin of attraction is still expanding, and the chaotic domain has completely degenerated into the multi-periodic basin of attraction and period-4 basin of attraction, then the system is mainly covered by period-2 and period-4 basins of attraction, accounting for as high as 64 %, which further decreases the sensitivity to the initial status parameters.

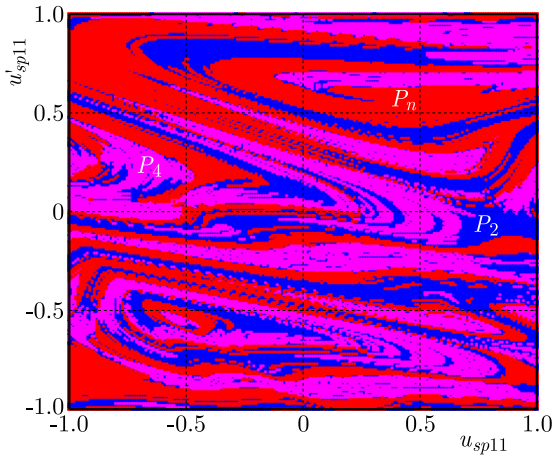

Fig. 10. Basin of attraction without stochasticity when $\xi = 0.1$.

Take the altered parameters set as $n1 = 9000$ rpm, $\xi = 0.1$, $b = 1$. Select and verify one of the state cells at the location of $[x, \dot{x}] = [0.8, -0.07]$ (see Fig. 10). In Fig. 11, the portrait of the attractor in black is stable, while in red is still evolving. Thus, the phase trajectory and Poincaré mapping points double affirm that the responses of the system coming into period-2 state in the end, while the black dots reveal that the period-2 phase portrait has stabilized after entering a steady-state. At this point, the attractor is stable.

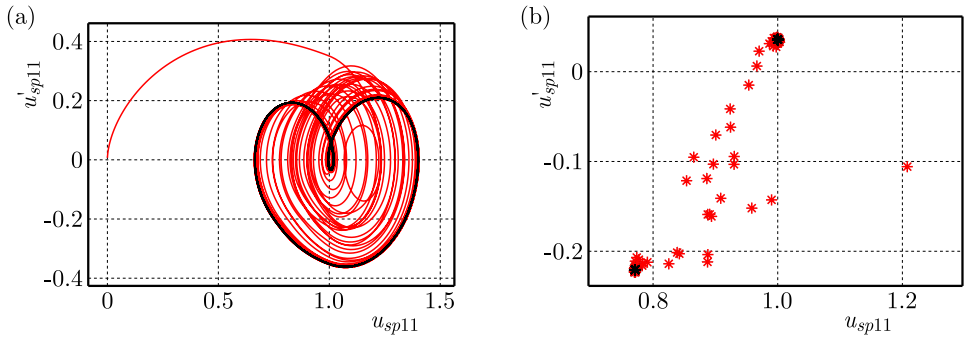

Fig. 11. Period-2 attractor without stochasticity when $\xi = 0.1$: (a) phase portrait; (b) Poincaré section.

3.4.2. Global behaviors under stochasticity

In terms of the global basins of attraction with stochasticity, which is to be compared. The basic value of the stochastic term is from the original excitation. First of all, the damping ratio ξ is selected as the stochastic parameter, and one may generate the stochastic number that corresponds to the normal distribution. Then, the necessity is to determine whether the stochastic factor η is within the upper and lower limits of the fluctuations of the analyzed parameter. Once satisfied, the stochastic number is taken as the current excitation and assigned to the parameter. If not, a normal distribution stochastic number will be regenerated again for judgment to guarantee satisfying the critical values. Subsequently, the dynamic response of the stochastic nonlinear system during meshing period is carried out.

By employing the central limit theorem (CLT) to define the meshing damping ratio ξ as a normal distribution $\xi \sim N\ (0.1,\ 0.00022)$ for a system under stochastic excitation, then ξ has the upper and lower maximum of excitations as 0.1006 and 0.0994 following the criterion of 3σ in normal distribution. Generated normal distribution of a pseudo-random damping ratio parameter could be plotted as in Fig. 12.

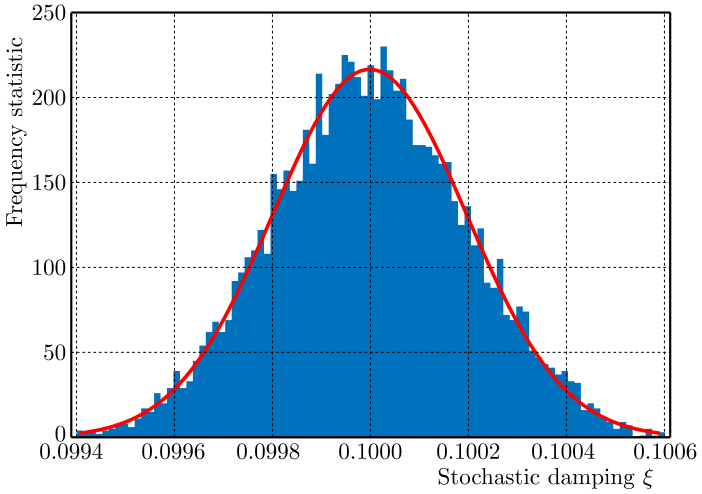

Fig. 12. Normal distribution of stochastic damping ratio.

Here, the computing formula of stochastic damping ratio ξ could be expressed as

$$\xi = 0.1 + 0.0002 \left\{ \frac{\sum_{i=1}^{n} U_i - n/2}{\sqrt{n/12}} \right\}, \quad \left\{ \frac{\sum_{i=1}^{n} U_i - n/2}{\sqrt{n/12}} \right\} \sim N\,(0,\ 1)\,, \tag{3.7}$$

where U_i is a uniformly distributed random number, and $U_i \sim U\ (0,\ 1)$, n represents the total amount of U_i. The global basins of attraction are calculated as shown in Fig. 13. The state domain mainly consists of period-2, period-4, and multi-period attraction domains. The proportion of period-2 attraction domain state cells in the entire space is 33 %, while the proportion of period-4 and period-6 attraction domain cells is about 31 %. Among them, the number of period-6 cells is 57, accounting only for 0.14 %. Compared to Fig. 10, where without stochasticity on the damping ratio, although there no significant change occurs to the proportion of periodic attractors in the entire domains, due to the mutual abrupt transitions between period-2, period-4, and multi-period attractors, the number of boundary cells gradually increases, and the basin of attraction begins to turn into chaos together with more scattered period-2 cells. Additionally, a boundary between the adjacent attraction domain is suffering interference, and the vibration of the boundary cell changes frequently indicating instability. The system becomes sensitive to the initial state, and the global attraction domains develop slightly deteriorated.

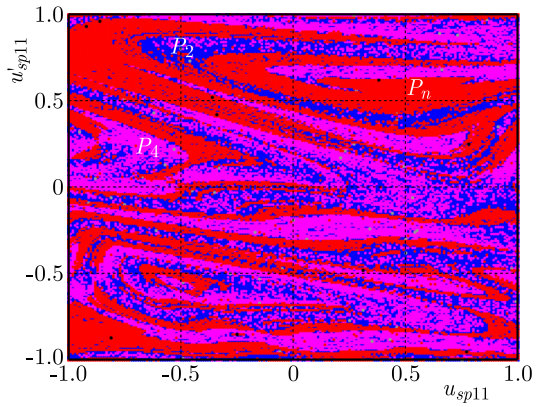

Fig. 13. Basin of attraction under stochasticity when $\xi \sim N$ (0.1, 0.00022).

The concerned state cell still at [0.8, −0.07] under stochasticity is calculated and shown in Fig. 14. From the view of structural perspective, the period-2 phase portrait and Poincaré mappings exhibit small fluctuations gradually, and it is noteworthy that the vibration of the system tends to converge towards the two fix points especially with certain oscillations on the Poincaré section in the final stage.

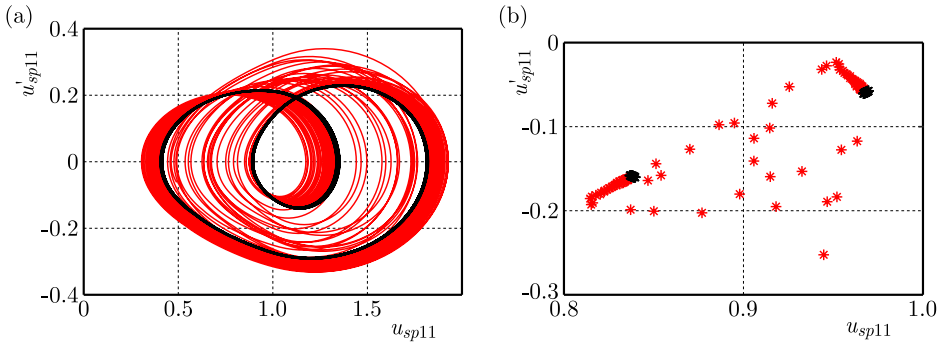

Fig. 14. Period-2 attractor under stochasticity when $\xi \sim N$ (0.1, 0.00022): (a) phase portrait; (b) Poincaré section.

By comparing the attractors and their joint probability density distribution (Figs. 15 and 16), we found while the damping ratio is subjected to stochastic excitation, the geometric structure of the trajectory still remains in the period-2 state without much movements, but shrinks significantly in size. Meanwhile, the periodic intensity of the attractor weakens too much, and the phase portrait loosened up and dispersibility stands out. It demonstrates that stochasticity of the damping ratio could minimize the vibration stability, while their impact on the period state is not validated through this comparison.

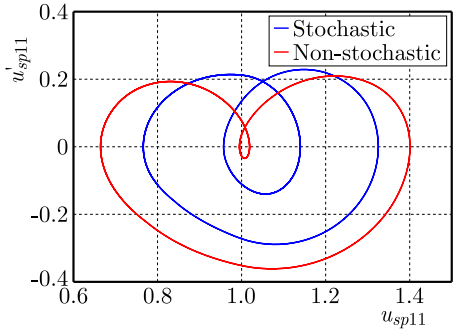

Fig. 15. Evolution transformations of period-2 attractor.

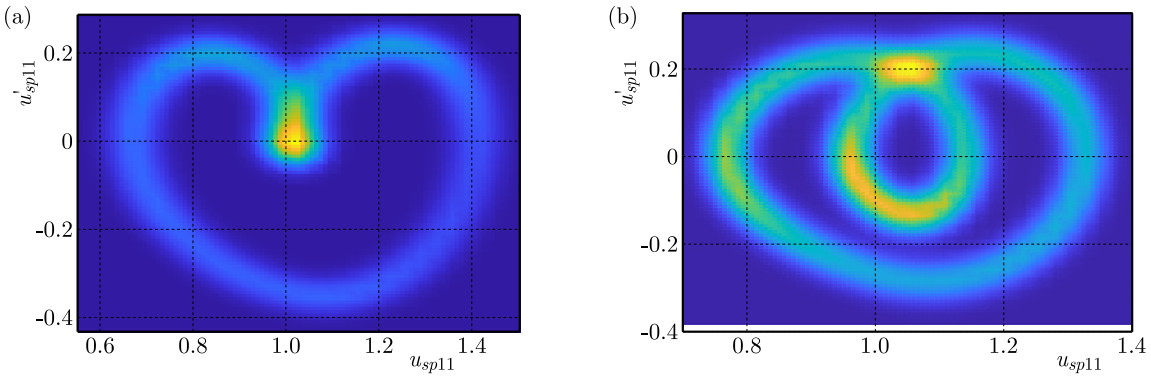

Fig. 16. Comparisons of joint probability density of period-2 attractor: (a) without stochasticity; (b) under stochasticity.

4. Conclusions

1) A novel meshing stiffness expression approximated to a rectangular wave was proposed utilizing odd harmonic superposition, the distribution map of parameterized solution domain and the evolutions of basin of attraction subjected to two dimensional excitations were identified. The period-doubling bifurcation route was detected and verified in accordance with the bifurcation region.
2) The evolution of the geometric feature of attractors was performed associated with the joint probability density function. The phase portrait scatters during period-4 attractor going into a chaotic state, simultaneously, the Poincaré section transformed from the previous 4 point sets down to a chaotic segment fractal point groups, which causes the shift and converge occurred on attractors.
3) The global two-dimensional parameterized solution domain was calculated out, and the overall distribution patterns of periodic and chaotic cell domains on parametric planes such as speed and the damping ratio were achieved. The verification for the solution domains was confirmed correctly by means of the bifurcation diagram.
4) The period-2 attractor experienced resonance while reaching the stable state under stochastic fluctuations that in normal distribution influences on the damping ratio, the periodicity of the attractor was significantly weakened. By the comparison of the behaviors of the basin of attraction, the distributions of each periodic domain inside the overall domain keeps barely transforms, but it generates more scattered periodic cells mixed in the original domains, resulting in the deterioration of the steady-state of the system.

Acknowledgments

This work is supported by the National Natural Science Foundation of China (grant no. 51805402; 11972274), the Natural Science Foundation of Shaanxi Province (no. 2019JQ-851).

References

1. Arian, G. & Taghvaei, S. (2021). Dynamic analysis and chaos control of spur gear transmission system with idler. *European Journal of Mechanics – A/Solids*, *87*, Article 104229. https://doi.org/10.1016/j.euromechsol.2021.104229
2. Dreeben, T.D. & Pope, S.B. (1998). Probability density function/Monte Carlo simulation of near-wall turbulent flows. *Journal of Fluid Mechanics*, *357*, 141–166. https://doi.org/10.1017/S0022112097008008
3. Farshidianfar, A. & Saghafi, A. (2014). Global bifurcation and chaos analysis in nonlinear vibration of spur gear systems. *Nonlinear Dynamics*, *75*(4), 783–806. https://doi.org/10.1007/s11071-013-1104-4

4. Gou, X.F., Zhu, L.Y., & Chen, D.L. (2015). Bifurcation and chaos analysis of spur gear pair in two-parameter plane. *Nonlinear Dynamics*, *79*(3), 2225–2235. https://doi.org/10.1007/s11071-014-1807-1
5. Gyebrószki, G. & Csernák, G. (2017). Clustered Simple Cell Mapping: An extension to the Simple Cell Mapping method. *Communications in Nonlinear Science and Numerical Simulation*, *42*, 607–622. https://doi.org/10.1016/j.cnsns.2016.06.020
6. Hong, J., Yang, Z.F., Sun, B., Song, Z., & Ma, Y. (2022). Influence of local rotary inertia on the dynamic properties of rotor systems (in Chinese). *Journal of Aerospace Power*, *37*(4), 673–683. http://doi.org/10.13224/j.cnki.jasp.20210579
7. Koh, D., Anderson, R.L., & Bermejo-Moreno, I. (2021). Cell-mapping orbit search for mission design at ocean worlds using parallel computing. *The Journal of the Astronautical Sciences*, *68*(1), 172–196. https://doi.org/10.1007/s40295-021-00251-6
8. Li, Z.G., Jiang, J., Li, J., Hong, L., & Li, M. (2018). A subdomain synthesis method for global analysis of nonlinear dynamical systems based on cell mapping. *Nonlinear Dynamics*, *95*(1), 715–726. https://doi.org/10.1007/s11071-018-4592-4
9. Lin, H., Hong, L., & Liu, X. (2021). Global characteristics of solution domain and attraction domain in power split gear transmission parameter space (in Chinese). *Journal of Vibration Engineering*, *34*(2), 235–242.
10. Ma, S.C., Ning, X., & Wang, L. (2020). Dynamic analysis of stochastic friction systems using the generalized cell mapping method. *Computer Modeling in Engineering & Sciences*, *122*(1), 49–59. https://doi.org/10.32604/cmes.2020.06911
11. Marafona, J.D.M., Carneiro, G.N., Marques, P.M.T., Martins, R.C., António C.C., & Seabra, J.H.O. (2024). Gear design optimization: Stiffness *versus* dynamics. *Mechanism and Machine Theory*, *191*, Article 105503. https://doi.org/10.1016/j.mechmachtheory.2023.105503
12. Mo, S., Zhang, Y., Luo, B., Bao, H., Cen, G., & Huang, Y. (2022). The global behavior evolution of non-orthogonal face gear-bearing transmission system. *Mechanism and Machine Theory*, *175*, Article 104969. https://doi.org/10.1016/j.mechmachtheory.2022.104969
13. Saghafi, A. & Farshidianfar, A. (2016). An analytical study of controlling chaotic dynamics in a spur gear system. *Mechanism and Machine Theory*, *96*(Part 1), 179–191. https://doi.org/10.1016/j.mechmachtheory.2015.10.002
14. Tang, J.Y., Xiong, X.B., & Chen S.Y. (2011). Analysis of global character of single degree of freedom nonlinear gear system based on digraph cell mapping method (in Chinese). *Journal of Mechanical Engineering*, *47*(5), 59–65.
15. Tang, X., Bao, H.Y., Lu, F.X., & Jin, G. (2020). Nonlinear dynamic analysis of planetary gear train system with meshing beyond pitch point. *Transactions of Nanjing University of Aeronautics and Astronautics*, *37*(6), 884–897.
16. Wang, S.Y. & Zhu, R.P. (2020). Nonlinear torsional dynamics of star gearing transmission system of GTF gearbox. *Shock and Vibration*, *2020*(1), Article 6206418. https://doi.org/10.1155/2020/6206418
17. Wang, X., Jiang, J., Hong, L., Zhao, A., & Sun, J.Q. (2023). Radial basis function neural networks solution for stationary probability density function of nonlinear stochastic systems. *Probabilistic Engineering Mechanics*, *71*, Article 103408. https://doi.org/10.1016/j.probengmech.2022.103408
18. Xiang, L., Deng, Z.Q., & Hu, A.J. (2020). Dynamical analysis of planetary gear transmission system under support stiffness effects. *International Journal of Bifurcation and Chaos*, *30*(6), Article 2050080. https://doi.org/10.1142/S0218127420500807
19. Yue, X.L., Xu, Y., Xu, W., & Sun, J.Q. (2019). Probabilistic response of dynamical systems based on the global attractor with the compatible cell mapping method. *Physica A: Statistical Mechanics and its Applications*, *516*, 509–519. https://doi.org/10.1016/j.physa.2018.10.034
20. Zhang, W., Han, B.B., Li, X., Sun, J.Q., & Ding, Q. (2019). Multiple-objective design optimization of squirrel cage for squeeze film damper by using cell mapping method and experimental validation. *Mechanism and Machine Theory*, *132*, 66–79. https://doi.org/10.1016/j.mechmachtheory.2018.10.010

Manuscript received March 12, 2024; accepted for publication January 22, 2025; published online April 22, 2025.

JOURNAL OF THEORETICAL
AND APPLIED MECHANICS
63, 2, pp. 307–329, Warsaw 2025
https://doi.org/10.15632/jtam-pl/200383

BIFURCATION CHARACTERISTICS AND CONTROL OF FRICTION SELF-EXCITED VIBRATION SYSTEM OF COKE PUSHING

Junjun CHEN*, Bing XU, Ge YAN

School of Automation and Software Engineering, Shanxi University, Taiyuan 030031, China
*corresponding author, *chenjunjun7505179@163.com*

There are typical friction self-excited vibration phenomena such as stick-slip and flutter in the working process of a coke pushing device. For the purpose of studying the vibration mechanism, a mechanical model of friction self-excited vibration of a double-mass-conveyor belt is established based on the Stribeck friction effect. Mass 1 and mass 2 are used to represent the part entering the carbonization room and the part outside the carbonization room, and the stability and bifurcation characteristics of the two masses are studied. The results show that the critical instability velocity and bifurcation velocity of the two masses are the same. Then the linear and nonlinear state feedback controller is designed to control the velocity bifurcation points and limit cycles of the coke pushing system. The numerical simulation results show that the appropriate selection of linear gain can reduce the bifurcation velocity and ensure the stability of the system at low velocity, and the appropriate selection of nonlinear gain can reduce the amplitude of the limit cycle and reduce the intensity of self-excited vibration of the coke pushing device.

Keywords: self-excited vibration; friction model; coke pushing system; bifurcation; linear and nonlinear state feedback.

1. Introduction

The mechanical device studied in this paper is a kind of coke pushing device, its function is to push coke out of the carbonization chamber (Chen *et al.*, 2019; 2020). In the process of pushing red coke out of the carbonization chamber, the coke pushing rod entering the carbonization chamber contacts the ground through the sliding shoe to form sliding friction. In the process of pushing coke, there is strong and complicated friction between the sliding shoe and the carbonizing chamber floor. Through the monitoring of the production process, we can see that there is an obvious flutter phenomenon when pushing the coke. Moreover, the vibration exhibits typical friction-induced vibration. Usually, the unwanted vibrations will cause wear of the contacting parts, surface damage, fatigue damage and noise, and it also will have a great impact on working performance, operation reliability, and service life of the coke pushing device.

We often find friction-induced vibrations in mechanical systems and in daily life, such as squeaky windshield wipers, the sound of certain arcuate instruments, the flutter of machine tools, the brake noise of automobile and stick-slip vibration of drill pipe (Kinkaid *et al.*, 2003). In the field of engineering, many scholars and engineers have conducted in-depth research on automobile braking noise. Of course, many published papers have also investigated various dynamic behaviours of friction-excited systems. Popp *et al.* (1995) investigated discrete and continuous models including stick-slip motion and bifurcation and demonstrated chaotic phenomena. Elmaian *et al.* (2014) described three modes of motion, stick, slip and separation in a three-degree-of-freedom (3-DOF) model incorporating friction-induced vibration. Zhang *et al.* (2018) introduced a flexible pin-on-disc system to reveal the process of generating noise in friction con-

tact, and researched the periodic friction coefficient effect on the features of time-varying squeal. Kruse *et al.* (2015) studied the influence of joints on the dynamic characteristics of a friction-induced flutter system. Brunetti *et al.* (2016) established a periodic modular lumped model to study its dynamic properties. Pilipchuk *et al.* (2015) studied the non-stationary mechanism of a 2-DOF braking model in the vibration caused by friction. The results show that the responses of the system change qualitatively as the velocity of the belt decreases. Wei *et al.* (2019) simulated a brake system with a 3-DOF mechanical model, and indicated bifurcation and chaotic phenomena. Denimal *et al.* (2020) proposed a new method to determine the degree of influence of unstable modes in a nonlinear self-excited vibration response, and which is also used to estimate the limit cycle. Lima and Sampaio (2020) analyzed a multi-physical system with stick-slip oscillation in the interaction of mechanical subsystem and electromagnetic subsystem. Papangelo *et al.* (2018) found that there were several local vibration states in the weakly coupled friction-excited oscillator chain. Von Wagner *et al.* (2007) analyzed the stability characteristics of the oscillating disc brake model. Sui and Ding (2018) studied the instability of the pad in the motion interaction of the disc and carried out the random analysis. Li *et al.* (2018) and Wang *et al.* (2020) verified experimentally the low degree of freedom models simulated numerically, and the friction-induced vibration of the system on the real test bench. Liu and Ouyang (2020) investigated the friction-induced vibration of a new model consisting of 5-DOF mass oscillating band including various nonlinearities. Without doubt, 1-DOF mechanical models containing mass blocks and constant velocity belts have been widely used to study vibration mechanism caused by friction (Wang *et al.*, 2022). A great deal of research has also been done on the sources of nonlinearity in friction-induced vibration problems, such as the nonlinearity of the contact stiffness, non-smooth characteristics such as stick-slip and contact/separation. However, there is a lack of comprehensive analysis of the effects of various nonlinearities on friction-induced self-excited vibration.

After in-depth research, three main mechanisms by which friction drives oscillations have been proposed. One of the main mechanisms is the Stribeck effect which is characterized by velocity weakening characteristics. In contrast, two other widely investigated mechanisms are called model-coupling and sprag-slip instability. We already know that friction-induced vibration is unacceptable in many systems. And rich dynamic behaviours often appear in friction-induced vibration. Saha *et al.* (2016) experimentally studied a test device representing a friction-induced system with 1-DOF and showed the properties of bifurcations related to friction instability of the system. Veraszto and Stepan (2017) investigated stability and bifurcation behaviours in digital and Saha *et al.* (2016) mentioned a continuous systems on the basis of 1-DOF nonlinear mechanical model. It is also necessary to effectively control the dynamic behaviours caused by friction vibration. In recent years, there have been many papers on how to control the friction-induced vibration. Nonlinear state feedback control is one of the control methods, which can realize the precise control of the system by feeding the state of the system back to the controller. When controlling a frictional self-excited vibration system, the output of the nonlinear state feedback controller is a nonlinear function of the system state, which can be designed according to the characteristics and control objectives of the system. By selecting suitable nonlinear functions, the system can maintain good control performance under various working conditions, and has strong robustness to the change of system parameters and external interference. Different active and passive vibration control methods were proposed in literature. Adaptive control is a widely used method in the control system, which can realize the stability control of the system when the system parameters are unstable or uncertain. The basic principle of adaptive control is to realize the stability control of the system by estimating the uncertain parameters online and adjusting the control coefficient in time. This involves establishing the mathematical model of the system, using the parameter estimation and control algorithm to realize real-time adjustment of the dynamic characteristics of the system. Of course, the technical challenges of adaptive control include model stability and robustness, real-time performance, and accuracy of param-

eter estimation. Robust control is also a frequently used control method that aims to design a control system that can maintain stability and performance in the face of model uncertainties, external perturbations, and parameter changes. H_∞ control theory is one of the most commonly used methods in robust control. The controller is designed by optimizing the H_∞ norm of the control system, which represents the maximum gain of the system from input to output and is used to measure the system's ability to suppress disturbances. Robust control is an important branch of the modern control theory, which is very important to solve the uncertainty problem in complex systems. By understanding and applying the robust control theory, the performance and reliability of the system in the face of uncertainty can be improved. The linear and nonlinear state feedback is a combination of linear and nonlinear state feedback control. The theory of linear state feedback control is mature, easy to implement, and very effective for linear systems and linear parts of nonlinear systems. Nonlinear state feedback control is suitable for nonlinear systems and can provide better control performance and robustness.

However, few scholars have studied the bifurcation characteristics of the pushing coke and how to control the vibration of this device. Therefore in this paper, a 2-DOF mass-on-conveyor belt model including friction-induced vibration is proposed, and the bifurcation characteristics and control methods of pushing coke are studied. The dual-mass conveyor system is also very widely used in practical applications, such as the security conveyor of airport railway stations, the conveyor belt of beverage production companies to transmit beverage bottles, and the carton production transmission belt. In the field of industry and agriculture, there is also the improvement of the dual-mass conveyor model to transport the whole bag of cement, the whole bag of rice, the whole packing box, and other items from a low place to a certain height according to the inclination angle. Without doubt, studying the friction-induced vibration of pushing coke has good theoretical and engineering value for manufacturers.

The organizational structure of the paper is arranged as follows. In Section 2, a dynamic model of friction self-excited vibration of a double-mass-conveyor belt is established according to the working characteristics of pushing coke. In Section 3, the stability and bifurcation characteristics of the coke pushing system are analyzed by the theoretical calculation and numerical simulation. Then the linear and nonlinear state feedback controller is put forward to control the bifurcation behavior of the system in Section 4. The linear gain is used to control the change of the bifurcation velocity point, and the nonlinear gain is used to control the size of the limit cycle of the coke pushing system. The research conclusions of this paper are drawn in Section 5.

2. Establishment of mechanical model of coke pushing system

The device of pushing coke is a specific actuator to push the red coke out of the carbonization chamber. Its main structure includes a coke pushing ram, a rack and pinion transmission mechanism, a sliding shoe, a coke pushing head and several supporting rollers. The specific structure of the device of pushing coke is shown in Fig. 1. The device is a large mechanical equipment, in which the length of the pushing ram is nearly 30 meters and the weight is about 40 tons. Due to high temperature and closed coke pushing environment, it is very difficult to carry out experimental researches on such a large equipment.

The establishment of the mechanical model of the system can well reveal the dynamic characteristics of the coke pushing device in theory, which is helpful to further study the self-excited vibration of the device and provide theoretical support for engineering application. In order to study the complex dynamic phenomena during the operation of the coke pushing device, considering the fact that the ram of pushing coke is partly in the carbonization chamber and partly in the carbonization outdoor during the operation of pushing coke, based on the Stribeck friction effect (Thomsen & Fidlin, 2003), the double mass-conveyor belt friction self-excited vibration model is established in Fig. 2.

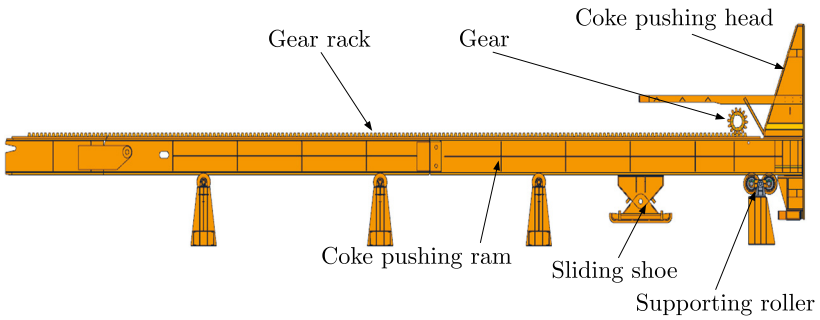

Fig. 1. Main structure of coke pushing device.

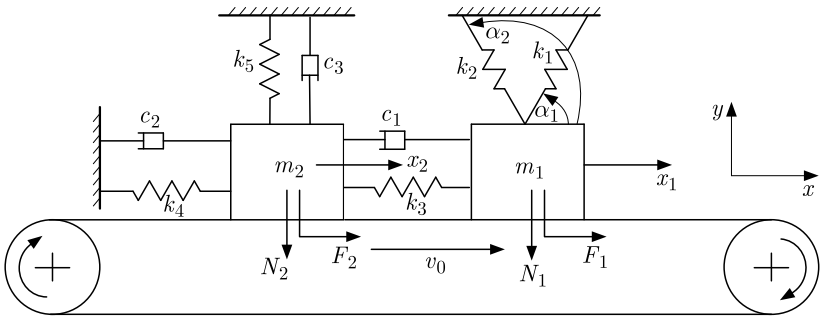

Fig. 2. Mechanical model of coke pushing friction self-excited vibration system.

The conveyor belt moves continuously and unidirectionally with velocity v_0, the part of the coke pushing ram entering the carbonization chamber is represented by mass m_1, while the part of the coke pushing ram outside the carbonization chamber is represented by mass m_2. The positive pressures of m_1 and m_2 applied on the conveyor belt are N_1 and N_2, respectively. The friction forces generated by positive pressures are F_1 and F_2, respectively. The displacement of m_1 and m_2 driven by friction is x_1 and x_2, respectively, and where k_i $(i = 1, ..., 5)$ is the stiffness coefficient, c_1 and c_2 represent the damping coefficients of the system. The differential equation of coke pushing system is

$$\begin{aligned} F_1 &= m_1\ddot{x}_1 + c_1(\dot{x}_1 - \dot{x}_2) + k_3(x_1 - x_2) + k_2 x_1 \cos^2\alpha_2 - k_1 x_2 \cos^2\alpha_1, \\ F_2 &= m_2\ddot{x}_2 + c_2\dot{x}_2 + k_4 x_2 - c_1(\dot{x}_1 - \dot{x}_2) - k_3(x_1 - x_2). \end{aligned} \tag{2.1}$$

In Eq. (2.1), friction F_1 and F_2 are calculated using the Stribeck friction model (Thomsen & Fidlin, 2003), and the expression is

$$\begin{aligned} F_i &= \mu(v_r)N_i, \\ \mu(v_r) &= -\mu_s \operatorname{sgn}(v_r) + \frac{3(\mu_s - \mu_m)}{2v_m} v_r - \frac{(\mu_s - \mu_m)}{2v_m^3} v_r^3, \\ v_r &= \dot{x}_i - v_0, \qquad i = 1, 2, \end{aligned} \tag{2.2}$$

where v_r is the relative sliding velocity between the mass and the conveyor belt, μ_s is the coefficient of static friction, μ_m is the coefficient of dynamic friction, v_m represents the running velocity of the system corresponding to the minimum coefficient of dynamic friction, N_i is the positive pressure originates in the mass and the conveyor belt, and μ represents the friction coefficient of the Stribeck model.

Let $\omega = \sqrt{k_4/m_2}$, $L = N_2/k_3$, the following dimensionless variables are obtained:

$$\begin{aligned}
&\tau = \omega t, && X_1 = x_1 k_3/N_2, && X_2 = x_2 k_3/N_2,\\
&\xi_1 = m_1\omega^2/k_3, && \xi_2 = m_2\omega^2/k_3, && a_1 = c_1\omega/k_3,\\
&a_2 = c_2\omega/k_3, && \beta = N_1/N_2, && \beta_1 = k_4/k_3,\\
&\beta_2 = k_1\cos^2\alpha_1/k_3, && \beta_3 = k_2\cos^2\alpha_2/k_3, && V_0 = \upsilon_0/\omega L,\\
&\dot{X}_1 = \mathrm{d}X_1/\mathrm{d}\tau, && \dot{X}_2 = \mathrm{d}X_2/\mathrm{d}\tau,
\end{aligned} \tag{2.3}$$

where τ means the dimensionless time, X_1 means the dimensionless displacement of mass m_1, and $\dot{X}_1$ means the dimensionless velocity of mass m_1. X_2 means the dimensionless displacement of mass m_2, and $\dot{X}_2$ means the dimensionless velocity of mass m_2. By introducing the aforementioned dimensionless variables, the dimensionless motion equation of the system is obtained:

$$\begin{aligned}
\beta\mu_1 &= \xi_1\ddot{X}_1 + a_1(\dot{X}_1 - \dot{X}_2) + (1 - \beta_2 + \beta_3)X_1 - X_2,\\
\mu_2 &= \xi_2\ddot{X}_2 + a_2\dot{X}_2 - a_1(\dot{X}_1 - \dot{X}_2) - X_1 + (1 + \beta_1)X_2.
\end{aligned} \tag{2.4}$$

Among which,

$$\mu_i = -\mu_s\,\mathrm{sgn}(\dot{X}_i - V_0) + \frac{3(\mu_s - \mu_m)}{2\upsilon_m}(\dot{X}_i - V_0) - \frac{(\mu_s - \mu_m)}{2\upsilon_m^3}(\dot{X}_i - V_0)^3, \qquad i = 1, 2. \tag{2.5}$$

Based on the simplification method in ordinary differential equations, the normal high-order differential equations can be simplified into equivalent first-order differential equations to analyze and calculate more conveniently. Let: $X_1 = Y_1$, $\dot{X}_1 = Y_2$, $X_2 = Y_3$, $\dot{X}_2 = Y_4$, we can get the first order differential equations:

$$\begin{aligned}
\dot{Y}_1 &= Y_2, \qquad \dot{Y}_2 = \frac{-a_1(Y_2 - Y_4) - (1 - \beta_2 + \beta_3)Y_1 + Y_3 + \beta\mu_1}{\xi_1},\\
\dot{Y}_3 &= Y_4, \qquad \dot{Y}_4 = \frac{-a_2Y_4 + a_1(Y_2 - Y_4) + Y_1 - (1 + \beta_1)Y_3 + \mu_2}{\xi_2}.
\end{aligned} \tag{2.6}$$

3. Analysis of bifurcation behaviors of the coke pushing system

When the velocity of the transmission belt in the system reaches a certain value, the mass will meet the static equilibrium state under the interaction of friction and restoring force. At the moment, the system satisfies $X_1' = 0$, $X_2' = 0$, and the sign function of the friction coefficient of the Stribeck model in Eq. (2.2) is $\mathrm{sgn}(\upsilon_r) = -1$. According to the actual data obtained from the production of the enterprise and the actual test of the coke pushing operation site, the coefficient of static friction, the coefficient of dynamic friction, and the running velocity of the system under condition of the minimum dynamic friction coefficient are, respectively, set as $\mu_s = 0.8$, $\mu_m = 0.6$, $\upsilon_m = 0.45$.

Based on the Lyapunov stability theory, the equilibrium point stability of the coke pushing system is analyzed. When $Y_2 = 0$, $Y_4 = 0$, the equilibrium point of the system can be obtained from Eq. (2.6):

$$\begin{aligned}
Y_{10} &= \frac{-\beta(1 + \beta_1)\mu_1 - \mu_2}{-(1 + \beta_1)(1 - \beta_2 + \beta_3) + 1}, && Y_{20} = 0,\\
Y_{30} &= (1 - \beta_2 + \beta_3)\frac{-\beta(1 + \beta_1)\mu_1 - \mu_2}{-(1 + \beta_1)(1 - \beta_2 + \beta_3) + 1} - \beta\mu_1, && Y_{40} = 0.
\end{aligned} \tag{3.1}$$

By moving the system's equilibrium point to the zero point, the equations can be obtained:

$$Y_1 = \widehat{Y}_1 + Y_{10}, \qquad Y_2 = \widehat{Y}_2, \qquad Y_3 = \widehat{Y}_3 + Y_{30}, \qquad Y_4 = \widehat{Y}_4. \tag{3.2}$$

The disturbance equation of the original system is

$$\begin{aligned} \dot{\widehat{Y}}_1 &= \widehat{Y}_2, \qquad \dot{\widehat{Y}}_2 = \frac{-a_1(Y_2 - Y_4) - (1 - \beta_2 + \beta_3)\widehat{Y}_1 + \widehat{Y}_3 + \beta\mu_1}{\xi_1}, \\ \dot{\widehat{Y}}_3 &= \widehat{Y}_4, \qquad \dot{\widehat{Y}}_4 = \frac{-a_2 Y_4 + a_1(Y_2 - Y_4) + \widehat{Y}_1 - (1 + \beta_1)\widehat{Y}_3 + \mu_2}{\xi_2}. \end{aligned} \tag{3.3}$$

In which,

$$\begin{aligned} \mu_1 &= -\mu_s \operatorname{sgn}(Y_2 - V_0) + \frac{3(\mu_s - \mu_m)}{2\upsilon_m}(Y_2 - V_0) - \frac{(\mu_s - \mu_m)}{2\upsilon_m^3}(Y_2 - V_0)^3, \\ \mu_2 &= -\mu_s \operatorname{sgn}(Y_4 - V_0) + \frac{3(\mu_s - \mu_m)}{2\upsilon_m}(Y_4 - V_0) - \frac{(\mu_s - \mu_m)}{2\upsilon_m^3}(Y_4 - V_0)^3. \end{aligned} \tag{3.4}$$

By the Taylor series expansion on the right side of Eq. (3.3) and omitting the second and above terms, we can get the first-order approximate equations of the coke pushing system. When $\widehat{Y}_1 = 0$, $\widehat{Y}_2 = 0$, $\widehat{Y}_3 = 0$, $\widehat{Y}_4 = 0$, the Jacobian matrix of the first-order differential equations of the coke pushing system relative to the variables $\widehat{Y}_1$, $\widehat{Y}_2$, $\widehat{Y}_3$, $\widehat{Y}_4$ can be obtained from Eq. (3.3) as follows:

$$\mathbf{A} = \begin{bmatrix} 0 & 1 & 0 & 0 \\ a_{21} & a_{22} & \dfrac{1}{\xi_1} & \dfrac{a_1}{\xi_1} \\ 0 & 0 & 0 & 1 \\ \dfrac{1}{\xi_2} & \dfrac{a_1}{\xi_2} & a_{43} & a_{44} \end{bmatrix}. \tag{3.5}$$

In which,

$$\begin{aligned} a_{21} &= \frac{\beta_2 - \beta_3 - 1}{\xi_1}, \qquad a_{22} = \frac{-a_1 + 0.67 - 3.3V_0^2}{\xi_1}, \\ a_{43} &= -\frac{1 + \beta_1}{\xi_2}, \qquad a_{44} = \frac{-a_1 - a_2 + 0.67 - 3.3V_0^2}{\xi_2}. \end{aligned} \tag{3.6}$$

The system's dimensionless parameters are set to: $\xi_1 = \xi_2 = 0.1$, $a_1 = a_2 = 0.01$, $\beta = 1$, $\beta_1 = 1.5$, $\beta_2 = \beta_3 = 0.01$. Substituting the above parameters into Eq. (3.5), the corresponding characteristic equation of matrix $\mathbf{A}$ is

$$\begin{aligned} |\lambda\mathbf{E} - \mathbf{A}| = \lambda^4 &+ (66V_0^2 - 13.1)\lambda^3 + (1089V_0^4 - 432.3V_0^2 + 77.89)\lambda^2 \\ &+ (1155V_0^2 - 232)\lambda + 150 = 0. \end{aligned} \tag{3.7}$$

The system's critical instability velocity $V_c = 0.45$ can be obtained by solving the formula $66V_0^2 - 13.1 = 0$ using the Routh criterion. When the coke driving velocity is higher than this value, the pushing device operates stably. When the coke driving velocity is lower than this value, the pushing device operates unstably and is more prone to self-excited vibration.

In the purpose of verifying the correctness of the theoretical calculation results, the established friction self-excited vibration system is numerically simulated at different driving velocities. The velocity values are 0.425, 0.435, 0.45, and 0.465, respectively. The simulated phase diagrams and the corresponding displacement curves are shown in Figs. 3 and 4.

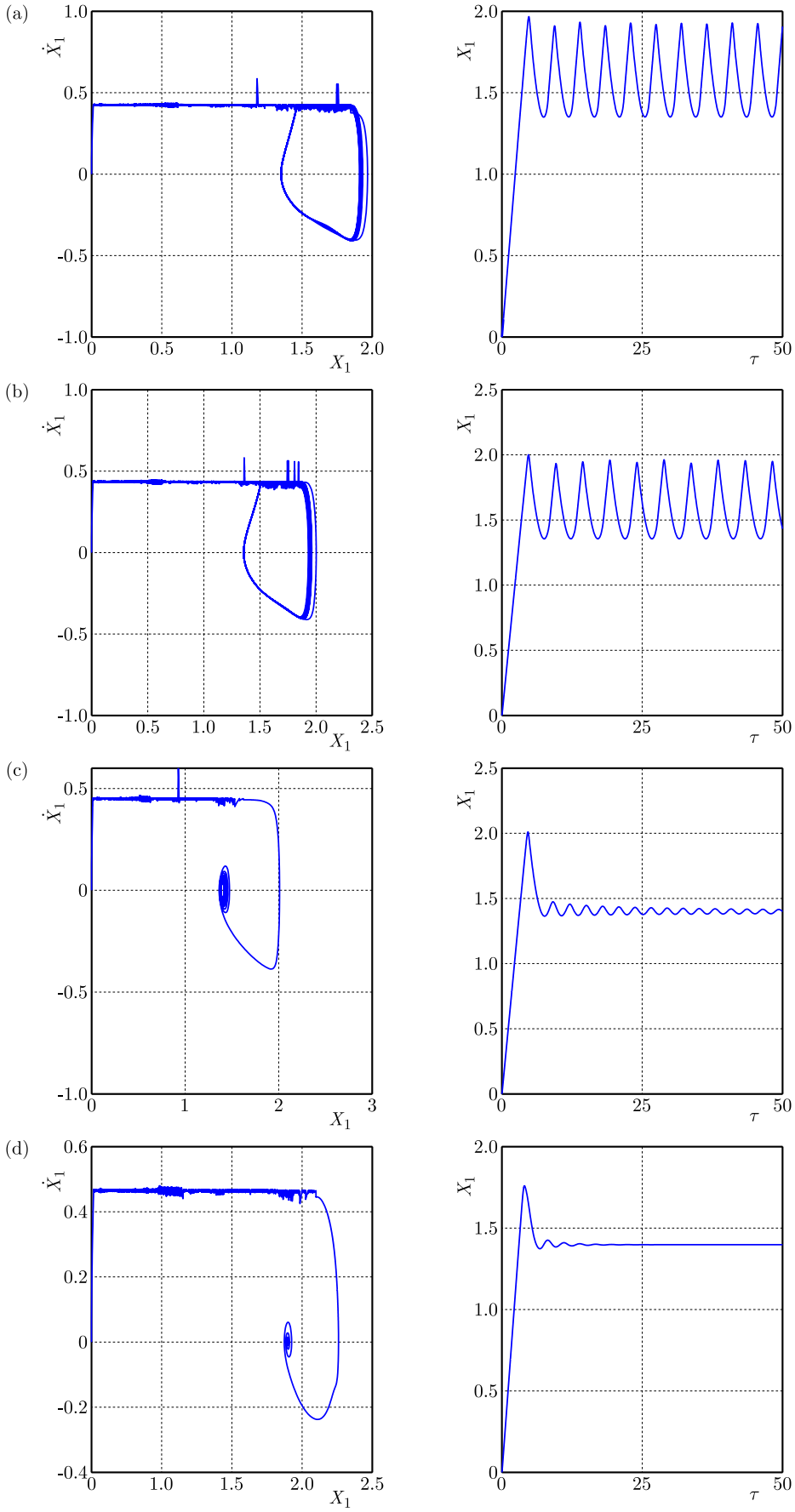

Fig. 3. Simulation phase diagrams and displacement curve diagrams of mass 1 under different driving velocities: (a) $V_0 = 0.425$; (b) $V_0 = 0.435$; (c) $V_0 = 0.45$; (d) $V_0 = 0.465$.

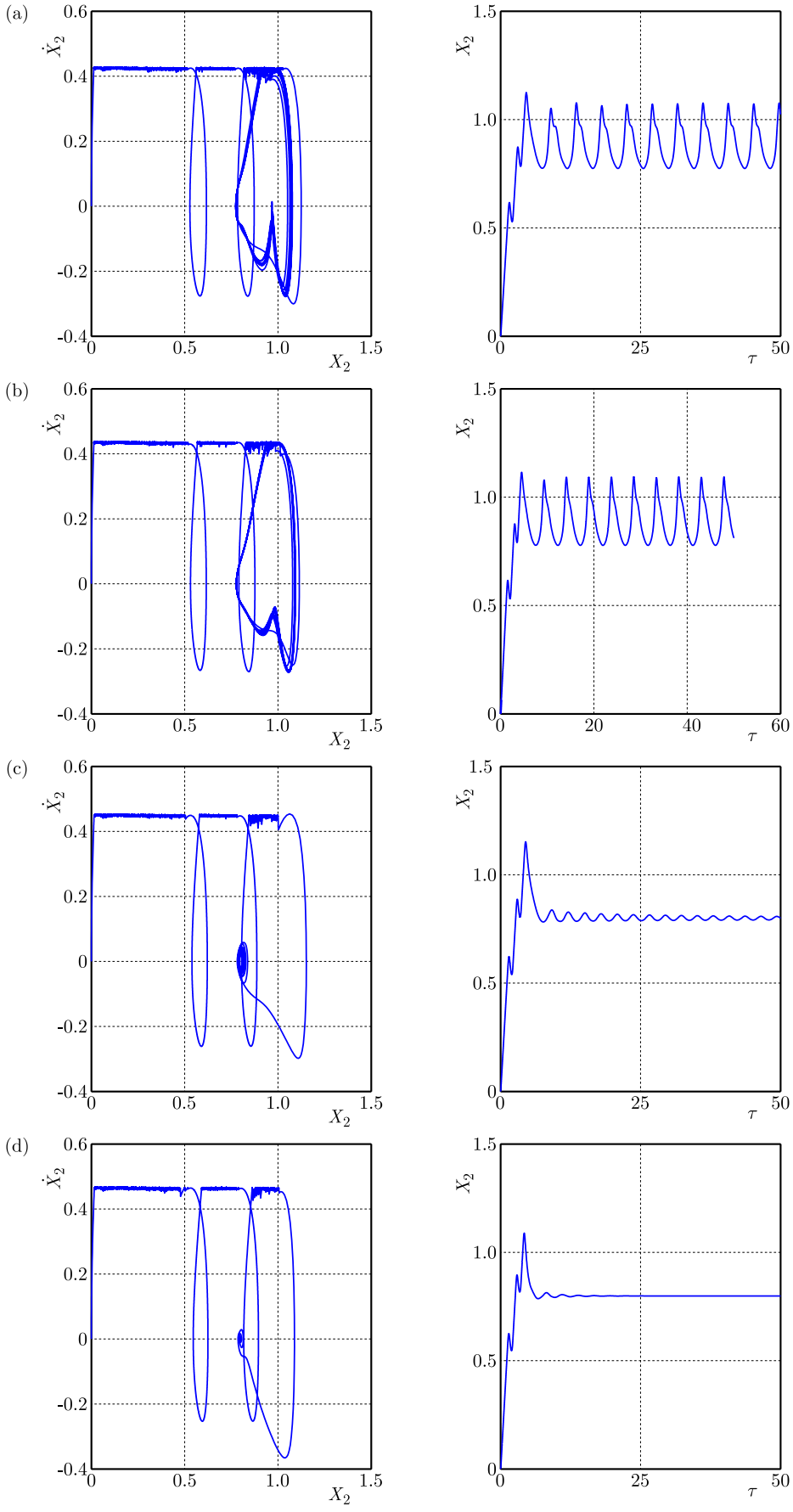

Fig. 4. Simulation phase diagrams and displacement curve diagrams of mass 2 under different driving velocities: (a) $V_0 = 0.425$; (b) $V_0 = 0.435$; (c) $V_0 = 0.45$; (d) $V_0 = 0.465$.

We can see from Fig. 3 and Fig. 4 that when the operating velocity of the device is lower than 0.45, the amplitude of the limit cycle is relatively large, and the equilibrium point of the coke pushing system is in an unstable state. When the operating velocity of the device exceeds 0.45, the amplitude of the limit cycle decreases rapidly, and the equilibrium point of the coke pushing system is in a stable state. It can be seen that in the process of increasing the velocity of the system, the equilibrium point changes from unstable to stable. From the stability analysis of the system, it can be seen that when the driving velocity is 0.45, the Hopf bifurcation phenomenon begins to appear in the system. In order to intuitively show the Hopf bifurcation type of the coke pushing system, the system's bifurcation diagram with the change of the driving velocity is obtained by numerical calculations.

Of course, there are also factors such as friction, damping, or system inertia that can have an impact on bifurcation points and stability. When considering bifurcation cases, such as the transition of a system from rest to motion. The bifurcation point appears when the static friction force is just overcome, and the bifurcation point will change accordingly when the friction factor changes. In the process of motion, friction acts as damping. If the friction factor is large, the stability of the system will be enhanced. As the damping increases, the dynamic behavior of the system changes. The bifurcation point occurs at the transition from undamped periodic motion to damped decayed motion. When the damping exceeds a certain critical value, the properties of the equilibrium point of the system will change and bifurcation will occur. In the case of a two-mass-spring-damping system, the natural frequency of the system changes when one of the masses is changed. The bifurcation point is related to the natural frequency of the system, and the change of mass will lead to the change of the modal characteristics of the system. The amount of inertia (mass) affects how quickly the system responds to external forces. The greater inertia makes the system more difficult to accelerate or slow down. From a stability point of view, systems with high inertia may be less likely to quickly deviate from their equilibrium state when subjected to external disturbances. In general, changes in the parameters of friction, damping and inertia of the system have complex effects on the bifurcation point and stability. They interact with each other, and in different physical systems, the specific manifestation and degree of these effects will vary depending on the specific structure and dynamics of the system. In engineering and physics research, the effects of these parameters on system performance need to be carefully analyzed in order to optimize the system design and control.

The coke pushing device studied in this paper is a practical device, which has been installed and calculated in advance. In actual use, according to the different production stages of the coke pushing device starting from the empty stroke to the coke pushing operation process, the most significant change in system parameters is the operating velocity of the coke pushing device. According to the field observation, it is found that when the coke pushing device starts to push coke, the running velocity of the device will decrease rapidly, resulting in a strong vibration phenomenon, so this paper chooses the sensitive parameter of coke pushing velocity as the bifurcation parameter according to the actual working condition. The controller design is also mainly to solve the vibration control problem caused by the velocity change.

The system's simulation parameters are set as follows: $\mu_s = 0.8$, $\mu_m = 0.6$, $\upsilon_m = 0.45$, $\xi_1 = \xi_2 = 0.1$, $a_1 = a_2 = 0.01$, $\beta = 1$, $\beta_1 = 1.5$, $\beta_2 = \beta_3 = 0.01$. The bifurcation diagrams of the system with respect to the driving velocity are shown in Fig. 5.

It can be found from the bifurcation diagrams that when the velocity is less than 0.45, the system's equilibrium point is in an unstable state, and the motion form is quasi-periodic motion. When the velocity is greater than 0.45, the system's equilibrium point is in a stable state, and each bifurcation diagram appears as a single-valued curve. This indicates that the equilibrium point of the coke pushing system will gradually transit from an unstable to a stable state as the system's velocity increases. When the driving velocity increases to 0.45, the system begins to exhibit the supercritical Hopf bifurcation. Therefore, in the purpose of improving the stability of the coke pushing device and reduce the intensity of the friction self-excited vibration of the

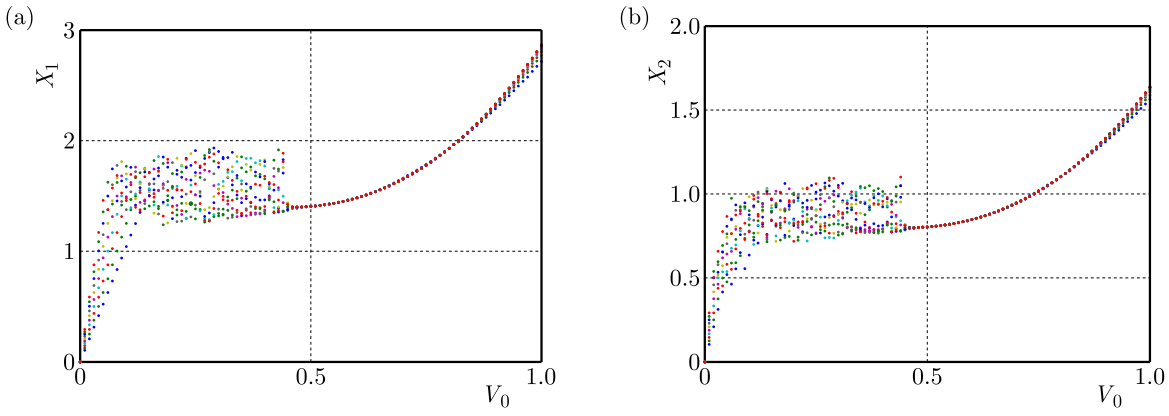

Fig. 5. System's bifurcation diagrams along with the driving velocity: (a) bifurcation diagram of mass 1 with respect to the driving velocity; (b) bifurcation diagram of mass 2 with respect to the driving velocity.

device, a linear and nonlinear state feedback controller is introduced at the critical bifurcation velocity of 0.45 to control the coke pushing system.

4. Research on the bifurcation control of coke pushing system

4.1. Research on linear state feedback control

Let $\mu_s = 0.8$, $\mu_m = 0.6$, $\upsilon_m = 0.45$, $\xi_1 = \xi_2 = 0.1$, $a_1 = a_2 = 0.01$, $\beta = 1$, $\beta_1 = 1.5$, $\beta_2 = \beta_3 = 0.01$. Applying the linear feedback control to the coke pushing system (Eq. (2.6)), it can be obtained that:

$$\begin{aligned} \dot{Y}_1 &= Y_2, \qquad \dot{Y}_2 = -0.1(Y_2 - Y_4) - 10Y_1 + 10Y_3 + 10\mu_1 + k_1 Y_2, \\ \dot{Y}_3 &= Y_4, \qquad \dot{Y}_4 = -0.2Y_4 + 0.1Y_2 + 10Y_1 - 25Y_3 + 10\mu_2. \end{aligned} \tag{4.1}$$

Here, $\mu_1 = 0.8 + 0.67(Y_2 - V_0) - 1.1(Y_2 - V_0)^3$, $\mu_2 = 0.8 + 0.67(Y_4 - V_0) - 1.1(Y_4 - V_0)^3$, k_1 is the linear gain of the designed controller, $k_1 \neq 0$, the introduction of the linear part of the controller does not change the equilibrium point of the original system. When the friction force takes only the linear part, the expressions of friction coefficients are, respectively, simplified as: $\mu_1 = 0.67(Y_2 - V_0) - 3.3V_0^2 Y_2$, $\mu_2 = 0.67(Y_4 - V_0) - 3.3V_0^2 Y_4$. When V_0 is 0.45, the Jacobian matrix of the linear part of system (Eq. (4.1)) at the equilibrium point is

$$\mathbf{A} = \begin{bmatrix} 0 & 1 & 0 & 0 \\ -10 & k_1 - 0.0825 & 10 & 0.1 \\ 0 & 0 & 0 & 1 \\ 10 & 0.1 & -25 & -0.1825 \end{bmatrix}. \tag{4.2}$$

The characteristic equation of matrix $\mathbf{A}$ is

$$\lambda^4 + (0.265 - k_1)\lambda^3 + (35.005 - 0.1825k_1)\lambda^2 + (1.8875 - 25k_1)\lambda + 150 = 0. \tag{4.3}$$

In order to satisfy the Routh–Hurwitz stability criterion and ensure that the roots of the characteristic Eq. (4.3) all have negative real parts, then

$$\begin{aligned} &0.265 - k_1 > 0, \qquad 35.005 - 0.1825k_1 > 0, \qquad 1.8875 - 25k_1 > 0, \\ &(0.265 - k_1)(35.005 - 0.1825k_1) - (1.8875 - 25k_1) > 0, \\ &(0.265 - k_1)(35.005 - 0.1825k_1)(1.8875 - 25k_1) - (1.8875 - 25k_1)^2 - 150(0.265 - k_1)^2 > 0, \end{aligned} \tag{4.4}$$

that is

$$\begin{aligned} &k_1 < 0.265, \qquad k_1 < 191.808, \qquad k_1 < 0.0755, \\ &k_1 < 0.745 \qquad \text{or} \qquad k_1 > 54.342, \\ &k_1 < 0.028 \qquad \text{or} \qquad 1.267 < k_1 < 20.99. \end{aligned} \tag{4.5}$$

In summary, $k_1 \in (-\infty, 0) \cup (0, 0.028)$.

To verify the correctness of the theoretical calculation, V_0 is set to 0.45 and the other parameters remain unchanged. The k_1 is set to -0.1, -0.5, -0.8, respectively, and the system (Eq. (4.1)) is simulated and analyzed. The phase diagrams and time-domain displacement waveform diagrams are shown in Figs. 6 and 7.

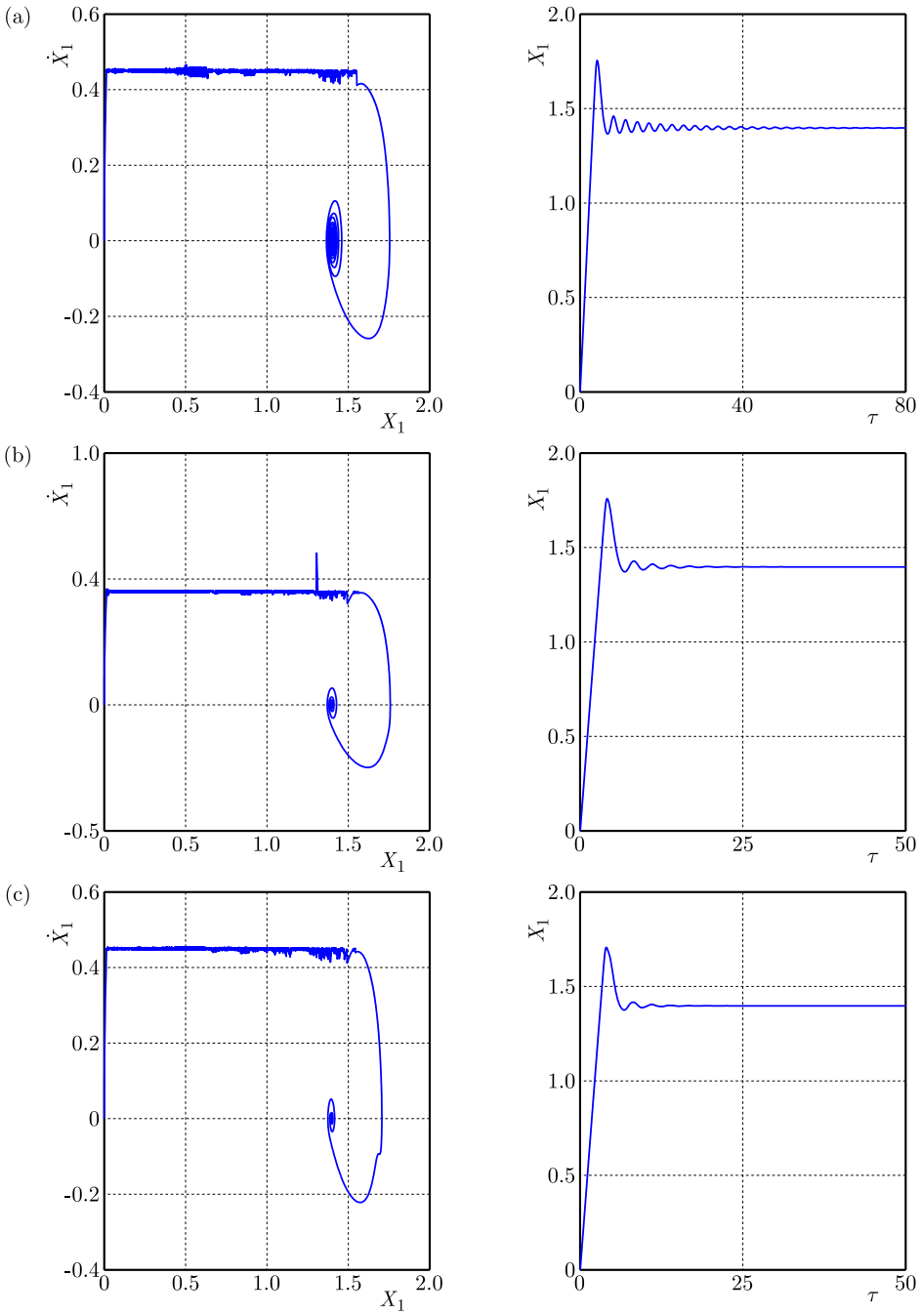

Fig. 6. Phase diagrams and the corresponding displacement curves of mass 1 when the linear gain k_1 takes different values: (a) $k_1 = -0.1$; (b) $k_1 = -0.5$; (c) $k_1 = -0.8$.

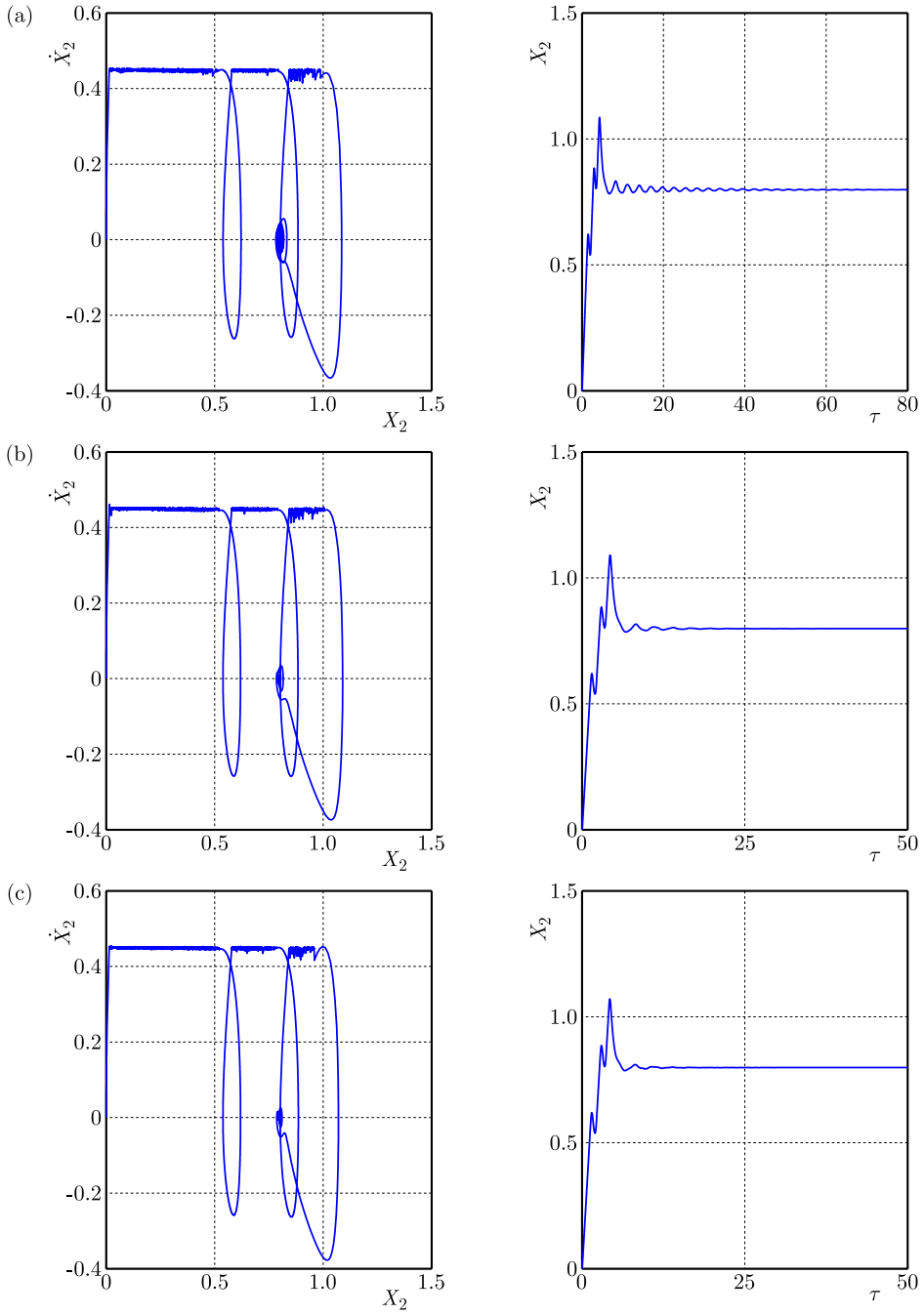

Fig. 7. Phase diagrams and the corresponding displacement curves of the mass 2 when the linear gain k_1 takes different values: (a) $k_1 = -0.1$; (b) $k_1 = -0.5$; (c) $k_1 = -0.8$.

From the simulation results of Fig. 6 and Fig. 7, it can be clearly seen that when the linear gain k_1 takes -0.1, -0.5, -0.8, compared with the phase diagrams and displacement curve diagrams without control (Figs. 3c and 4c), the limit cycle disappears and the system stabilizes to the equilibrium point after the control is applied. It can be seen that when the appropriate parameter k_1 is selected, the Hopf bifurcation phenomenon can be eliminated near the original bifurcation point, the Hopf bifurcation point is changed, the supercritical Hopf bifurcation occurs in advance, and the motion stability of pushing coke is improved. Meanwhile, the simulation results from Fig. 3 to Fig. 7 show that the bifurcation points of the critical velocity of mass 1 and mass 2 are the same, and the change trends of the motion affected by the velocity are the same, and the motions are also carried out according to the similar trend after being controlled,

which indicates that after controlling mass 1, mass 2 can be affected synchronously with mass 1. Limited in space, we only study the influence of the controller on mass 1.

For the purpose of studying the influence of different values of k_1 on the Hopf bifurcation point, the values of other parameters remain unchanged, V_0 is set to 0.44 and 0.43, k_1 is set to -0.1, -0.8, -1.4, respectively, and the system (Eq. (4.1)) is simulated and analyzed. The phase diagrams and time-domain displacement waveform diagrams are shown in Figs. 8 and 9, respectively.

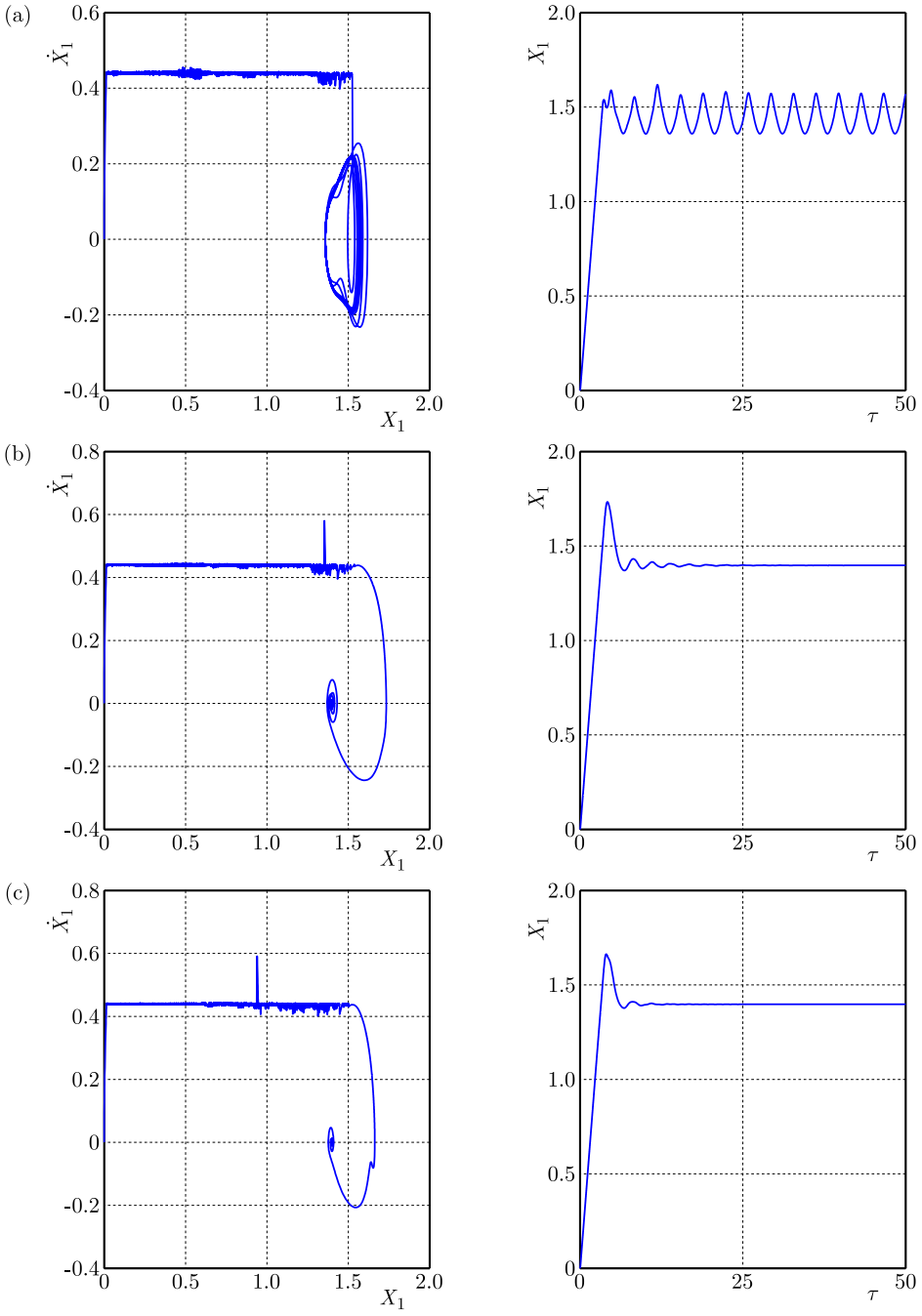

Fig. 8. Phase diagrams and corresponding displacement curves of mass 1 when V_0 is 0.44 and linear gain k_1 is different: (a) $k_1 = -0.1$; (b) $k_1 = -0.8$; (c) $k_1 = -1.4$.

Through the analysis of the simulation results in Fig. 8a, we can intuitively find that when V_0 is 0.44 and k_1 is -0.1, the Hopf bifurcation behavior of the system is not eliminated. Compared with Fig. 6a, it can be seen that when k_1 is -0.1, the bifurcation velocity of the coke pushing

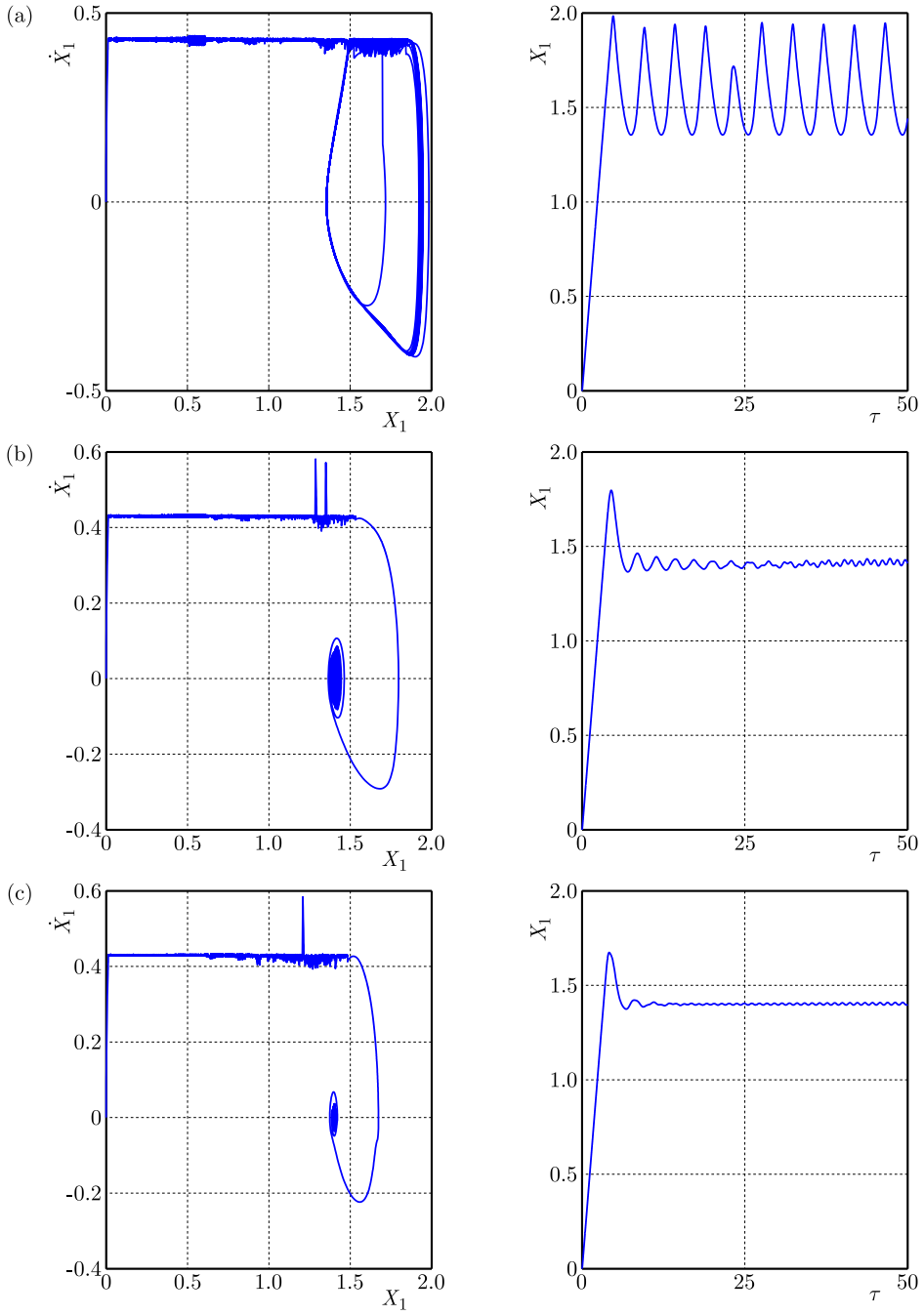

Fig. 9. Phase diagrams and corresponding displacement curves of mass 1 when V_0 is 0.43 and linear gain k_1 is different: (a) $k_1 = -0.1$; (b) $k_1 = -0.8$; (c) $k_1 = -1.4$.

system can be advanced from 0.45 to 0.44. As the value of k_1 continues to decrease, the system gradually stabilizes to the equilibrium point, and the Hopf bifurcation behavior of the system disappears. Comparing Fig. 8b and 8c with Fig. 9b and 9c, we can find that when k_1 is -0.8, -1.4, the bifurcation velocity of the coke pushing system can be advanced from 0.45 to 0.43. The simulation analysis results in Fig. 9 show that with the decrease of k_1, the control effect on the coke pushing system is more and more significant, but the bifurcation behavior of the system is not eliminated. This shows that to a certain extent, selecting a smaller k_1 value is conducive to reducing the critical bifurcation velocity of the coke pushing system, and then to achieve the stable operation of the coke pushing device at a lower operating velocity and reduce the possibility of self-excited vibration.

4.2. Research on nonlinear state feedback control

The linear part of the controller can control the change of the bifurcation point of the system, thus, the motion state of the system can be well improved. However, the linear part of the controller has no effective control effect on the limit cycle. Cui *et al.* (2012) show that the design of a suitable nonlinear state controller can effectively reduce the amplitude of the limit cycle, so as to control the amplitude of the periodic solution generated by the bifurcation. In view of this, this section studies the influence of nonlinear state feedback control on the vibration amplitude of the self-excited vibration system.

Let $\mu_s = 0.8$, $\mu_m = 0.6$, $\upsilon_m = 0.45$, $\xi_1 = \xi_2 = 0.1$, $a_1 = a_2 = 0.01$, $\beta = 1$, $\beta_1 = 1.5$, $\beta_2 = \beta_3 = 0.01$. By applying nonlinear feedback control to the coke pushing system (Eq. (2.6)), we can obtain:

$$\begin{aligned} \dot{Y}_1 &= Y_2, \qquad \dot{Y}_2 = -0.1(Y_2 - Y_4) - 10Y_1 + 10Y_3 + 10\mu_1 + k_2 Y_2^3, \\ \dot{Y}_3 &= Y_4, \qquad \dot{Y}_4 = -0.2Y_4 + 0.1Y_2 + 10Y_1 - 25Y_3 + 10\mu_2. \end{aligned} \tag{4.6}$$

Here, $\mu_1 = 0.8 + 0.67(Y_2 - V_0) - 1.1(Y_2 - V_0)^3$, $\mu_2 = 0.8 + 0.67(Y_4 - V_0) - 1.1(Y_4 - V_0)^3$, k_2 is the nonlinear gain of the designed controller, $k_2 \neq 0$, and the introduction of the nonlinear part of the controller does not change the equilibrium point of the original system. When the friction force is only a linear part, the friction coefficient expressions are simplified as: $\mu_1 = 0.67(Y_2 - V_0) - 3.3V_0^2 Y_2$, $\mu_2 = 0.67(Y_4 - V_0) - 3.3V_0^2 Y_4$. Then system (Eq. (4.6)) can be written as follows:

$$\dot{\mathbf{Y}} = \mathbf{B}\mathbf{Y} + \mathbf{C}\mathbf{Q}. \tag{4.7}$$

When V_0 is 0.45, the expressions of matrices $\mathbf{B}$, $\mathbf{Y}$, $\mathbf{C}$, and $\mathbf{Q}$ are

$$\mathbf{B} = \begin{bmatrix} 0 & 1 & 0 & 0 \\ -10 & -0.0825 & 10 & 0.1 \\ 0 & 0 & 0 & 1 \\ 10 & 0.1 & -25 & -0.1825 \end{bmatrix}, \tag{4.8}$$

$$\mathbf{Y} = [\, Y_1 \;\; Y_2 \;\; Y_3 \;\; Y_4 \,]^{\mathrm{T}}, \tag{4.9}$$

$$\mathbf{C} = [\, 0 \;\; 1 \;\; 0 \;\; 0 \,]^{\mathrm{T}}, \tag{4.10}$$

$$\mathbf{Q} = [k_2 Y_2^3]. \tag{4.11}$$

The characteristic equation corresponding to the matrix $\mathbf{B}$ is

$$\lambda^4 + 0.265\lambda^3 + 35.0051\lambda^2 + 1.8875\lambda + 150 = 0. \tag{4.12}$$

According to Eq. (4.12), the characteristic roots of the system are $\lambda_1 = -0.0112 + 2.2361i$, $\lambda_2 = -0.0112 - 2.2361i$, $\lambda_3 = -0.1213 + 5.4758i$, $\lambda_4 = -0.1213 - 5.4758i$. The eigenvector matrix corresponding to the characteristic roots is

$$\begin{aligned} \mathbf{D} &= [\, v_1 \;\; v_2 \;\; v_3 \;\; v_4 \,] \\ &= \begin{bmatrix} -0.0018 - 0.3651i & -0.0018 + 0.3651i & 0.0009 + 0.0803i & 0.0009 - 0.0803i \\ 0.8165 & 0.8165 & -0.4400 - 0.0048i & -0.4400 + 0.0048i \\ -0.0001 - 0.1826i & -0.0001 + 0.1826i & -0.0036 - 0.1606i & -0.0036 + 0.1606i \\ 0.4083 + 0.0018i & 0.4083 - 0.0018i & 0.8798 & 0.8798 \end{bmatrix}. \end{aligned} \tag{4.13}$$

Let $\mathbf{Y} = \mathbf{TU}$, where the matrices $\mathbf{T}$ and $\mathbf{U}$ are

$$\mathbf{T} = [\operatorname{Re} v_3, -\operatorname{Im} v_3, \operatorname{Re} v_1, -\operatorname{Im} v_1] = \begin{bmatrix} 0.0009 & -0.0803 & -0.0018 & 0.3651 \\ -0.44 & 0.0048 & 0.8165 & 0 \\ -0.0036 & 0.1606 & -0.0001 & 0.1826 \\ 0.8798 & 0 & 0.4083 & -0.0018 \end{bmatrix}, \tag{4.14}$$

$$\mathbf{U} = [\, U_1 \;\; U_2 \;\; U_3 \;\; U_4 \,]^{\mathrm{T}}. \tag{4.15}$$

Then the system (Eq. (4.7)) can be reduced to the following form:

$$\begin{aligned} \dot{U}_1 &= -0.1201U_1 - 5.4756U_2 + G_1(U_1, U_2, U_3, U_4, k_2), \\ \dot{U}_2 &= 5.4760U_1 - 0.1224U_2 + G_2(U_1, U_2, U_3, U_4, k_2), \\ \dot{U}_3 &= -0.0115U_3 - 2.2359U_4 + G_3(U_1, U_2, U_3, U_4, k_2), \\ \dot{U}_4 &= 2.2363U_3 - 0.0110U_4 + G_4(U_1, U_2, U_3, U_4, k_2), \end{aligned} \tag{4.16}$$

where G_1, G_2, G_3, G_4 are expressed as

$$\begin{aligned} G_1(U_1, U_2, U_3, U_4, k_2) &= -0.4547k_2(-0.44U_1 + 0.0048U_2 + 0.8165U_3)^3, \\ G_2(U_1, U_2, U_3, U_4, k_2) &= -0.0131k_2(-0.44U_1 + 0.0048U_2 + 0.8165U_3)^3, \\ G_3(U_1, U_2, U_3, U_4, k_2) &= 0.9798k_2(-0.44U_1 + 0.0048U_2 + 0.8165U_3)^3, \\ G_4(U_1, U_2, U_3, U_4, k_2) &= 0.0031k_2(-0.44U_1 + 0.0048U_2 + 0.8165U_3)^3. \end{aligned} \tag{4.17}$$

The stability index σ_2 of the Hopf bifurcation in Eq. (4.18) can be calculated by substituting Eq. (4.17) into Appendix or the formulas in (Liu & Tang, 2008; Hassard, 1981):

$$\begin{aligned} \sigma_2 &= 2\operatorname{Re}\left\{ \frac{g_{20}g_{11} - 2\left|g_{11}\right|^2 - \frac{1}{3}\left|g_{02}\right|^2}{2\omega_0} i + \frac{g_{21}}{2} \right\} \\ &= \operatorname{Re}\left\{k_2(0.0012i + 0.029)\right\} = 0.029k_2. \end{aligned} \tag{4.18}$$

When $k_2 < 0$, $\sigma_2 < 0$, the Hopf bifurcation stability of the coke pushing system can be guaranteed. Next, the numerical calculation method is used to study the influence of the change of the nonlinear gain k_2 on the size of the limit cycle. The purpose is to determine a reasonable parameter range to improve the working condition of the coke pushing system, so as to reduce the self-excited vibration phenomenon of the pushing coke process.

For research on the influence of k_2 on the motion state of the coke pushing device at different velocities, the V_0 is set as 0.44, 0.43, 0.42, and the k_2 is set as -1, -10, and -20, respectively, for simulation analysis. The phase diagrams and displacement curves of the system are shown in Figs. 10–12.

From Figs. 10–12, it can be seen that the nonlinear gain k_2 can effectively control the limit cycle amplitude of the system. From the phase diagrams, it is found that with the continuous decrease of the nonlinear gain k_2, the overall trend of the limit cycle amplitude of the coke pushing system is gradually reduced. From the displacement curves, it is found that the displacement fluctuation amplitude is also gradually reduced, indicating that the control effect is more obvious during the decrease of the nonlinear gain k_2. Comparing with Fig. 10, Fig. 11, and Fig. 12, we can also see that when the nonlinear gain k_2 takes the same value, the closer the driving velocity is to the bifurcation velocity 0.45, the more significant the nonlinear gain control effect is.

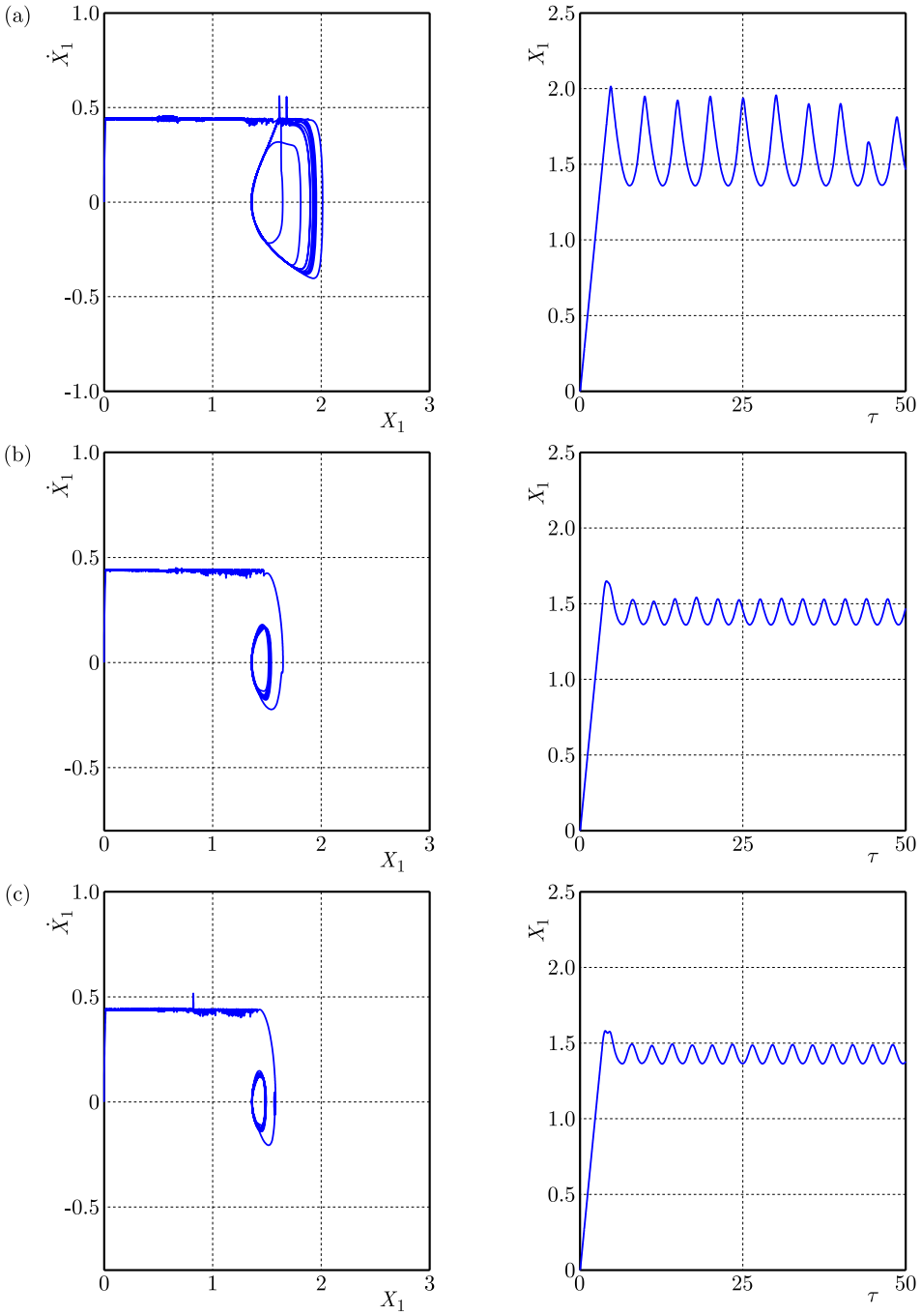

Fig. 10. Phase diagrams and the corresponding displacement curves when V_0 is 0.44 and nonlinear gain k_2 is set as different values: (a) $k_2 = -1$; (b) $k_2 = -10$; (c) $k_2 = -20$.

Therefore, the reasonable selection of nonlinear gain can effectively reduce the amplitude of the limit cycle, and then reduce the self-excited vibration of the pushing coke process.

To characterize the effect of simultaneous control of linear and nonlinear parts of the controller proposed in this article, the linear gain k_1 is taken as -0.8, and the nonlinear gain k_2 is taken as -10. Then the motion behaviour of the coke pushing device under different running velocities is controlled. For an intuitive comparison with Figs. 3a to 3c, the driving velocity V_0 of the system is set to 0.425, 0.435, and 0.45, respectively, on the basis of other parameters unchanged. The coke pushing system is numerically simulated, and the obtained phase diagrams and the corresponding displacement curves are shown in Fig. 13.

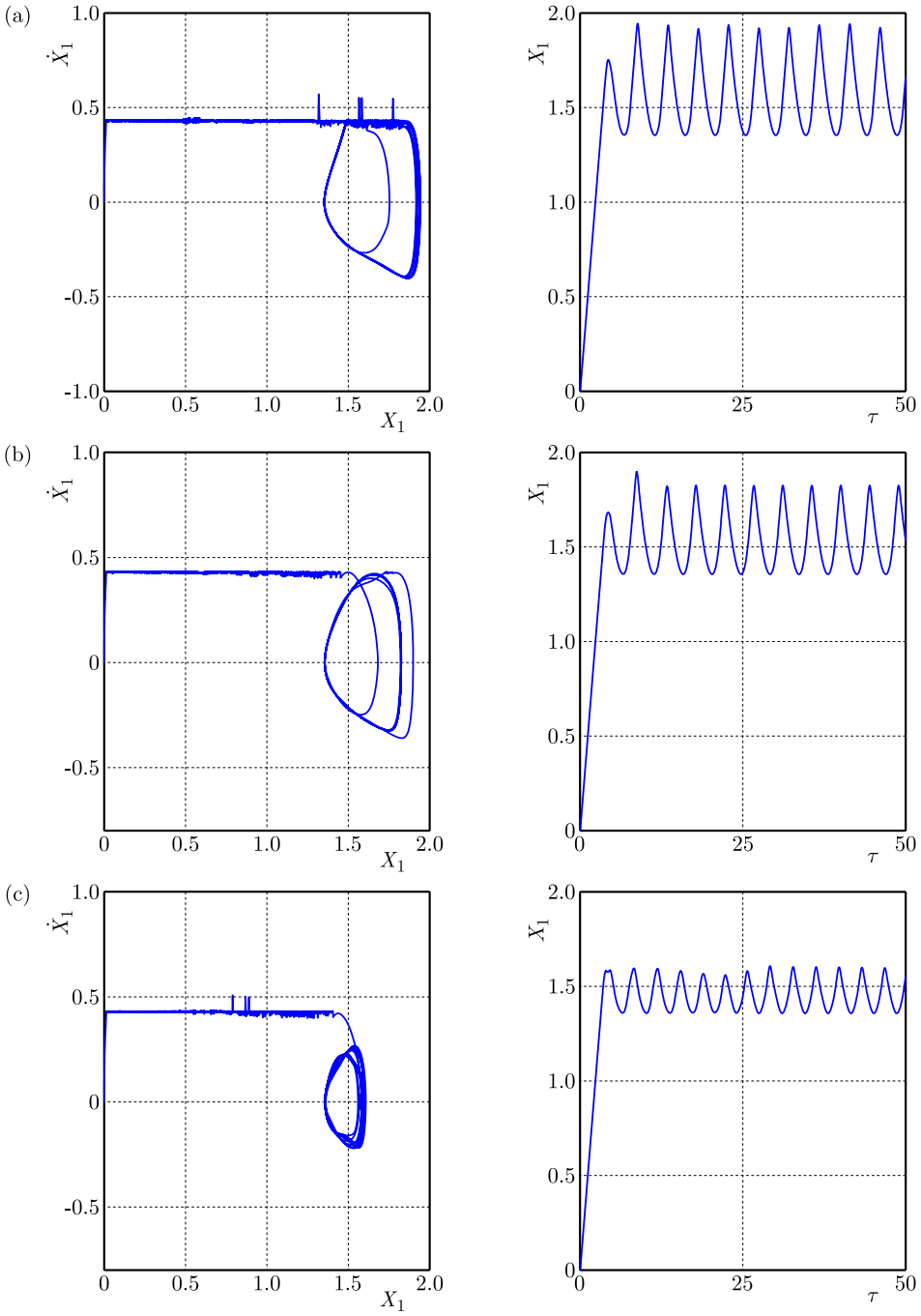

Fig. 11. Phase diagrams and the corresponding displacement curves when V_0 is 0.43 and nonlinear gain k_2 is set as different values: (a) $k_2 = -1$; (b) $k_2 = -10$; (c) $k_2 = -20$.

From the phase diagrams and displacement curve diagrams of Fig. 13, we can see that the motion state of the coke pushing system is obviously improved after the controller is applied. By comparing Fig. 13a and Fig. 3a, it can be clearly observed that the vibration amplitude of the system is significantly reduced after the controller designed in this paper is applied. The comparison result of Fig. 13b and Fig. 3b indicates that the vibration amplitude of the coke pushing system is greatly reduced after applying the controller designed in this paper, but the bifurcation phenomenon of the system is not eliminated. By comparing Fig. 13c and Fig. 3c, it is found that the limit cycle disappears and the coke pushing system stabilizes to the equilibrium point after applying the controller designed in this paper. On the whole, the control effect on the

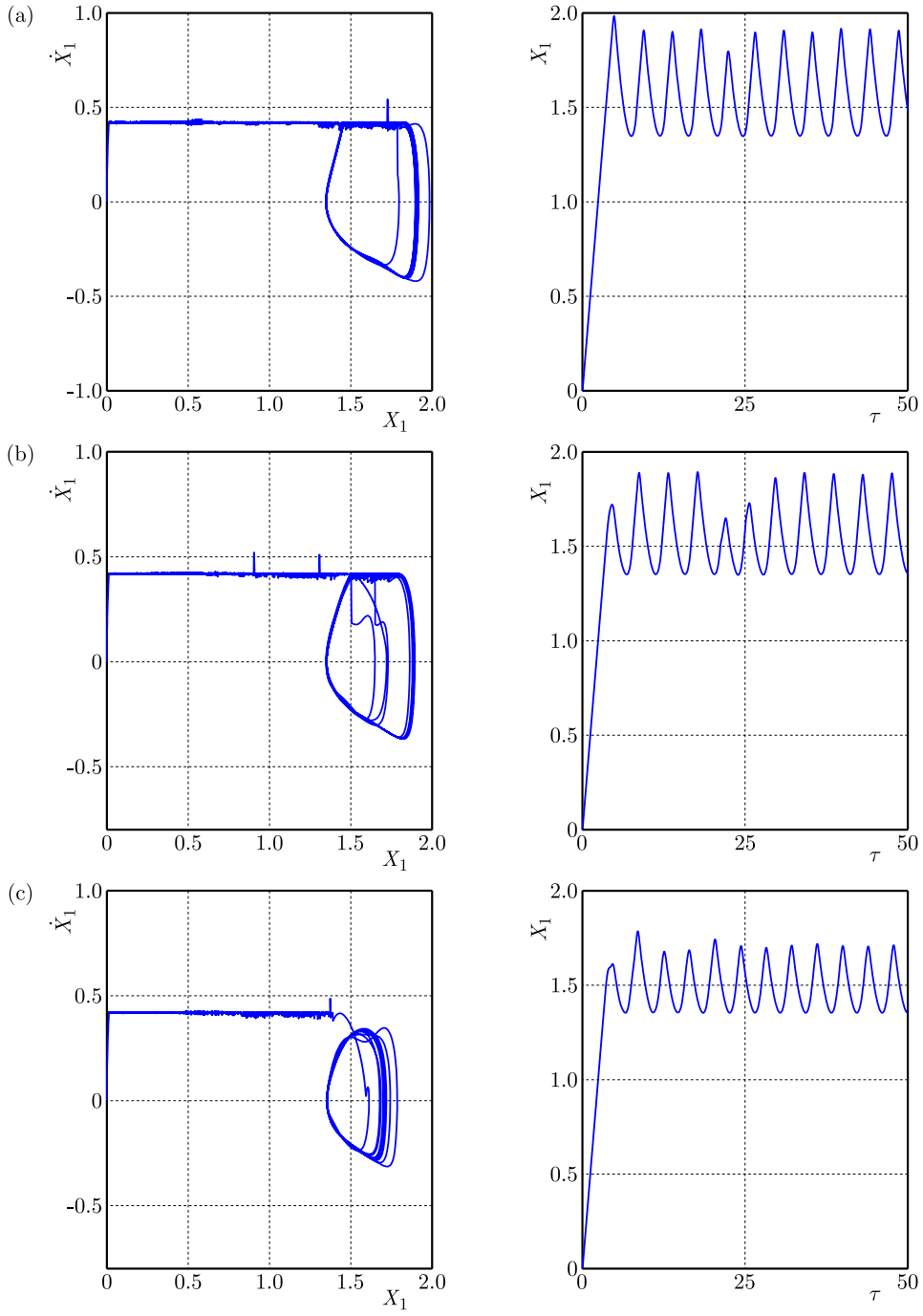

Fig. 12. Phase diagrams and the corresponding displacement curves when V_0 is 0.42 and nonlinear gain k_2 is set as different values: (a) $k_2 = -1$; (b) $k_2 = -10$; (c) $k_2 = -20$.

coke pushing system is more obvious when the driving velocity is closer to the critical bifurcation point, which is consistent with the previous results when linear gain and nonlinear gain acting alone.

5. Conclusions

According to the fact that part of the coke rod is located in the carbonization room and part is located outside the carbonization room, the frictional self-excited vibration model of the double-mass-conveyor belt is established to study the friction-induced vibration characteristics

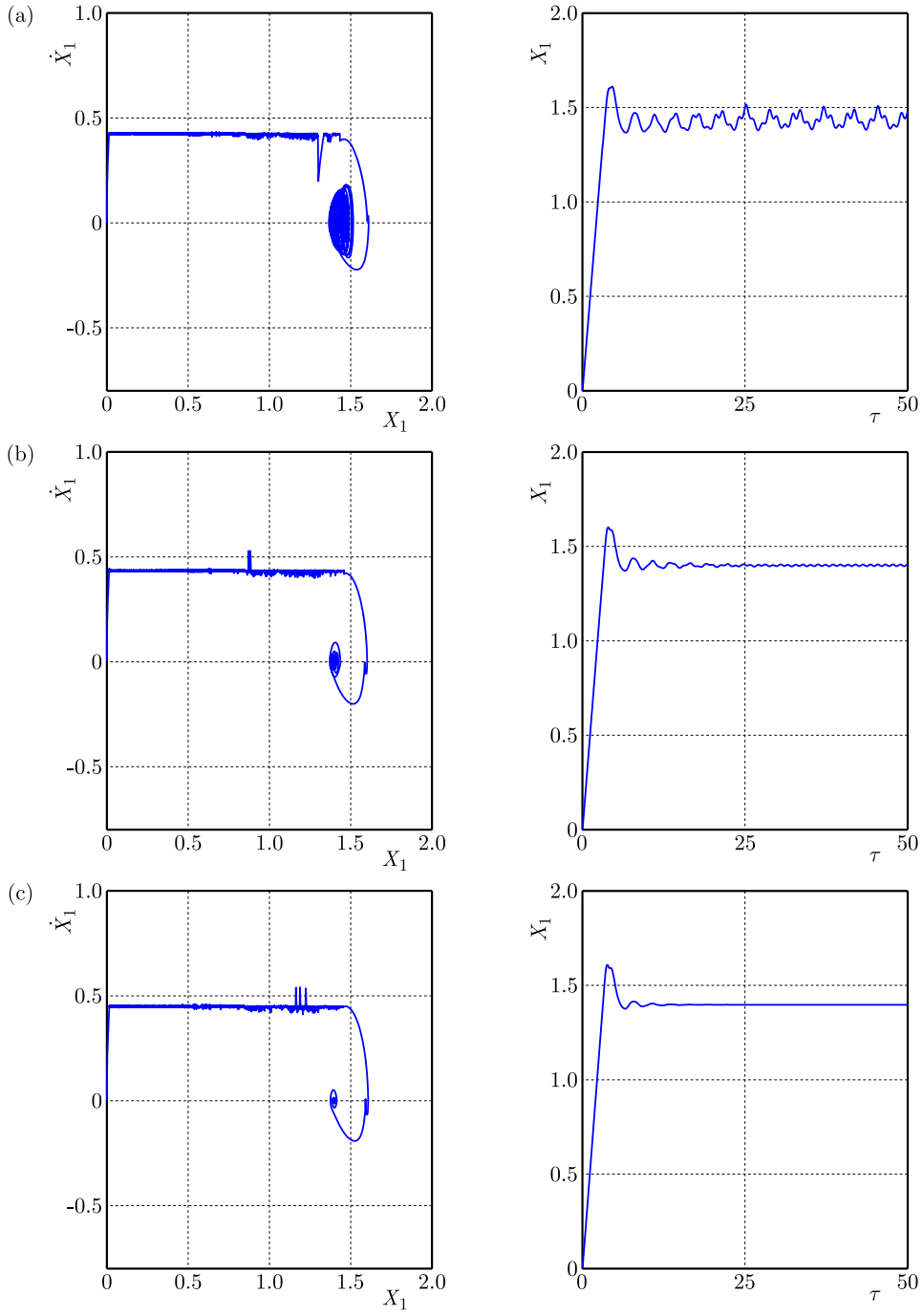

Fig. 13. Comprehensive control effect of the controller designed in this paper when V_0 takes different values: (a) $V_0 = 0.425$; (b) $V_0 = 0.435$; (c) $V_0 = 0.45$.

of pushing coke progress. The critical instability velocity of the coke pushing system is obtained by theoretical calculations and verified by numerical simulation. Then, the bifurcation characteristics of the system are analyzed, and the linear and nonlinear state feedback controllers are proposed to control the bifurcation behaviours of the system. Numerical simulation shows the effectiveness of the control effect. The specific conclusions are as follows:

– The newly established dynamic model of the system divides the coke pushing system into two bodies, which can better simulate the running state of the coke pushing device, that is, the part that enters the carbonization room and the part that stays outside the carbonization room.

– Both the critical instability velocity and bifurcation velocity of the coke pushing system are 0.45. When the driving velocity exceeds this value, the system is stable to the equilibrium point. When the driving velocity does not reach this value, the coke pushing system is in an unstable state and the self-excited vibration phenomenon is easy to occur. When the drive velocity reaches 0.45, the system begins to appear the supercritical Hopf bifurcation.
– The linear gain of the designed controller has an important effect on the Hopf bifurcation point of the coke pushing system. Choosing a smaller linear gain can reduce the Hopf bifurcation velocity and help the system work stably at a lower velocity. The nonlinear gain of the designed controller has an important effect on the limit cycle of the coke pushing system. The smaller nonlinear gain can reduce the amplitude of the limit cycle of the system, and then alleviate the friction self-excited vibration of the system.

Appendix. Coefficients in Eq. (4.18)

$$g_{20} = \frac{1}{4}\left\{\frac{\partial^2 G_1}{\partial U_1^2} - \frac{\partial^2 G_1}{\partial U_2^2} + 2\frac{\partial^2 G_2}{\partial U_1 \partial U_2} + i\left[\frac{\partial^2 G_2}{\partial U_1^2} - \frac{\partial^2 G_2}{\partial U_2^2} - 2\frac{\partial^2 G_1}{\partial U_1 \partial U_2}\right]\right\},$$

$$g_{11} = \frac{1}{4}\left\{\frac{\partial^2 G_1}{\partial U_1^2} + \frac{\partial^2 G_1}{\partial U_2^2} + i\left[\frac{\partial^2 G_2}{\partial U_1^2} + \frac{\partial^2 G_2}{\partial U_2^2}\right]\right\},$$

$$g_{02} = \frac{1}{4}\left\{\frac{\partial^2 G_1}{\partial U_1^2} - \frac{\partial^2 G_1}{\partial U_2^2} - 2\frac{\partial^2 G_2}{\partial U_1 \partial U_2} + i\left[\frac{\partial^2 G_2}{\partial U_1^2} - \frac{\partial^2 G_2}{\partial U_2^2} + 2\frac{\partial^2 G_1}{\partial U_1 \partial U_2}\right]\right\},$$

$$g_{21} = G_{21} + 2G_{110}^1\omega_{11}^1 + G_{101}^1\omega_{20}^1 + 2G_{110}^2\omega_{11}^2 + G_{101}^2\omega_{20}^2,$$

where

$$G_{21} = \frac{1}{8}\left\{\frac{\partial^3 G_1}{\partial U_1^3} + \frac{\partial^3 G_1}{\partial U_1 \partial U_2^2} + \frac{\partial^3 G_2}{\partial U_1^2 \partial U_2} + \frac{\partial^3 G_2}{\partial U_2^3} + i\left[\frac{\partial^3 G_2}{\partial U_1^3} + \frac{\partial^3 G_2}{\partial U_1 \partial U_2^2} - \frac{\partial^3 G_1}{\partial U_1^2 \partial U_2} - \frac{\partial^3 G_1}{\partial U_2^3}\right]\right\},$$

$$G_{110}^1 = \frac{1}{2}\left\{\frac{\partial^2 G_1}{\partial U_1 \partial U_3} + \frac{\partial^2 G_2}{\partial U_2 \partial U_3} + i\left[\frac{\partial^2 G_2}{\partial U_1 \partial U_3} - \frac{\partial^2 G_1}{\partial U_2 \partial U_3}\right]\right\},$$

$$G_{110}^2 = \frac{1}{2}\left\{\frac{\partial^2 G_1}{\partial U_1 \partial U_4} + \frac{\partial^2 G_2}{\partial U_2 \partial U_4} + i\left[\frac{\partial^2 G_2}{\partial U_1 \partial U_4} - \frac{\partial^2 G_1}{\partial U_2 \partial U_4}\right]\right\},$$

$$G_{101}^1 = \frac{1}{2}\left\{\frac{\partial^2 G_1}{\partial U_1 \partial U_3} - \frac{\partial^2 G_2}{\partial U_2 \partial U_3} + i\left[\frac{\partial^2 G_2}{\partial U_1 \partial U_3} + \frac{\partial^2 G_1}{\partial U_2 \partial U_3}\right]\right\},$$

$$G_{101}^2 = \frac{1}{2}\left\{\frac{\partial^2 G_1}{\partial U_1 \partial U_4} - \frac{\partial^2 G_2}{\partial U_2 \partial U_4} + i\left[\frac{\partial^2 G_2}{\partial U_1 \partial U_4} + \frac{\partial^2 G_1}{\partial U_2 \partial U_4}\right]\right\},$$

$$\omega_{11}^1 = -\frac{1}{4\lambda_3(V_c)}\left[\frac{\partial^2 G_3}{\partial U_1^2} + \frac{\partial^2 G_3}{\partial U_2^2}\right],$$

$$\omega_{11}^2 = -\frac{1}{4\lambda_4(V_c)}\left[\frac{\partial^2 G_4}{\partial U_1^2} + \frac{\partial^2 G_4}{\partial U_2^2}\right],$$

$$\omega_{20}^1 = \frac{1}{4(2i\omega_0 - \lambda_3(V_c))}\left[\frac{\partial^2 G_3}{\partial U_1^2} - \frac{\partial^2 G_3}{\partial U_2^2} - 2i\frac{\partial^2 G_3}{\partial U_1 \partial U_2}\right],$$

$$\omega_{20}^2 = \frac{1}{4(2i\omega_0 - \lambda_3(V_c))}\left[\frac{\partial^2 G_4}{\partial U_1^2} - \frac{\partial^2 G_4}{\partial U_2^2} - 2i\frac{\partial^2 G_4}{\partial U_1 \partial U_2}\right].$$

The derivatives of the above are all at zero point, and the bifurcation parameter is the bifurcation value.

Acknowledgments

The authors gratefully acknowledge the financial support by the Basic Research Program of Shanxi Province of China (grant no. 20210302124203).

References

1. Brunetti, J., Massi, F., D'Ambrogio, W., & Berthier, Y. (2016). A new instability index for unstable mode selection in squeal prediction by complex eigenvalue analysis. *Journal of Sound and Vibration*, *377*, 106–122. https://doi.org/10.1016/j.jsv.2016.05.002
2. Chen, J., Sun, H., Gao, H., Fan, Y., & Xu, B. (2019). Modeling, stability and stick-slip behaviour analysis of coke pushing system. *Tribology International*, *136*, 105–113. https://doi.org/10.1016/j.triboint.2019.03.057
3. Chen, J., Sun, H., Jiao, T., Liu, Z., & Xu, B. (2020). Stick-slip vibration analysis and vibration frequency extraction of coke pushing system. *Engineering Failure Analysis*, *108*, Article 104325. https://doi.org/10.1016/j.engfailanal.2019.104325
4. Cui, Y., Liu, S., & Ge, X. (2012). Amplitude control of limit cycle from Hopf bifurcation in the Langford system (in Chinese). *Acta Physica Sinica*, *61*(10), Article 100202. https://doi.org/10.7498/aps.61.100202
5. Denimal, E., Sinou, J.J., & Nacivet, S. (2020). Generalized Modal Amplitude Stability Analysis for the prediction of the nonlinear dynamic response of mechanical systems subjected to friction-induced vibrations. *Nonlinear Dynamics*, *100*(4), 3121–3144. https://doi.org/10.1007/s11071-020-05627-1
6. Elmaian, A., Gautier, F., Pezerat, C., & Duffal, J.M. (2014). How can automotive friction-induced noises be related to physical mechanisms?. *Applied Acoustics*, *76*, 391–401. https://doi.org/10.1016/j.apacoust.2013.09.004
7. Hassard, B.D., Kazarinoff, N.D., & Wan Y.-H. (1981). Theory and applications of Hopf bifurcation. New York, Cambridge University Press.
8. Kinkaid, N.M., O'Reilly, O.M., & Papadopoulos, P. (2003). Automotive disc brake squeal. *Journal of Sound and Vibration*, *267*(1), 105–166. https://doi.org/10.1016/S0022-460X(02)01573-0
9. Kruse, S., Tiedemann, M., Zeumer, B., Reuss, P., Hetzler, H. & Hoffmann, N. (2015). The influence of joints on friction induced vibration in brake squeal. *Journal of Sound & Vibration*, *340*, 239–252. https://doi.org/10.1016/j.jsv.2014.11.016
10. Li, Z., Wang, X., Zhang, Q., Guan, Z., Mo, J.L., & Ouyang, H. (2018). Model reduction for friction-induced vibration of multi-degree-of-freedom systems and experimental validation. *International Journal of Mechanical Sciences*, *145*, 106–119. https://doi.org/10.1016/j.ijmecsci.2018.06.039
11. Lima, R. & Sampaio, R. (2020). Stick-slip oscillations in a multiphysics system. *Nonlinear Dynamics*, *100*(3), 2215–2224. https://doi.org/10.1007/s11071-020-05677-5
12. Liu, N. & Ouyang, H. (2020). Friction-induced vibration considering multiple types of nonlinearities. *Nonlinear Dynamics*, *102*(4), 2057–2075. https://doi.org/10.1007/s11071-020-06055-x
13. Liu, S.H. & Tang, J.S. (2008). Anti-control of Hopf bifurcation at zero equilibrium of 4D Qi system (in Chinese). *Acta Physica Sinica*, *57*(10), 6162–6168. https://doi.org/10.7498/APS.57.6162
14. Papangelo, A., Hoffmann, N., Grolet, A., Stender, M., & Ciavarella, M. (2018). Multiple spatially localized dynamical states in friction-excited oscillator chains. *Journal of Sound and Vibration*, *417*, 56–64. https://doi.org/10.1016/j.jsv.2017.11.056
15. Pilipchuk, V., Olejnik, P., & Awrejcewicz, J. (2015). Transient friction-induced vibrations in a 2-DOF model of brakes. *Journal of Sound and Vibration*, *344*, 297–312. https://doi.org/10.1016/j.jsv.2015.01.028

16. Popp, K., Hinrichs, N., & Oestreich, M. (1995). Dynamical behaviour of a friction oscillator with simultaneous self and external excitation. *Sādhanā*, *20*(2–4), 627–654. https://doi.org/10.1007/BF02823210

17. Saha, A., Wahi, P., & Bhattacharya, B. (2016). Characterization of friction force and nature of bifurcation from experiments on a single-degree-of-freedom system with friction-induced vibrations. *Tribology International*, *98*, 220–228. https://doi.org/10.1016/j.triboint.2016.02.006

18. Sui, X. & Ding, Q. (2018). Instability and stochastic analyses of a pad-on-disc frictional system in moving interactions. *Nonlinear Dynamics*, *93*(3), 1619–1634. https://doi.org/10.1007/s11071-018-4280-4

19. Thomsen, J.J. & Fidlin, A. (2003). Analytical approximations for stick-slip vibration amplitudes. *International Journal of Non-Linear Mechanics*, *38*(3), 389–403. https://doi.org/10.1016/S0020-7462(01)00073-7

20. Veraszto, Z. & Stepan, G. (2017). Nonlinear dynamics of hardware-in-the-loop experiments on stick–slip phenomena. *International Journal of Non-Linear Mechanics*, *94*, 380–391. https://doi.org/10.1016/j.ijnonlinmec.2017.01.006

21. von Wagner, U., Hochlenert, D., & Hagedorn, P. (2007). Minimal models for disk brake squeal. *Journal of Sound and Vibration*, *302*(3), 527–539. https://doi.org/10.1016/j.jsv.2006.11.023

22. Wang, Q., Wang, Z.W., Mo, J.L., & Zhang, L. (2022). Nonlinear behaviors of the disc brake system under the effect of wheel-rail adhesion. *Tribology International*, *165*, Article 107263. https://doi.org/10.1016/j.triboint.2021.107263

23. Wang, X.C., Huang, B., Wang, R.L., Mo, J.L., & Ouyang, H. (2020). Friction-induced stick-slip vibration and its experimental validation. *Mechanical Systems and Signal Processing*, *142*, Article 106705. https://doi.org/10.1016/j.ymssp.2020.106705

24. Wei, D., Song, J., Nan, Y., & Zhu, W. (2019). Analysis of the stick-slip vibration of a new brake pad with double-layer structure in automobile brake system. *Mechanical Systems and Signal Processing*, *118*, 305–316. https://doi.org/10.1016/j.ymssp.2018.08.055

25. Zhang, L., Wu, J., & Meng, D. (2018). Transient analysis of a flexible pin-on-disk system and its application to the research into time-varying squeal. *Journal of Vibration and Acoustics*, *140*(1), Article 011006. https://doi.org/10.1115/1.4037468

Manuscript received September 13, 2024; accepted for publication January 22, 2025; published online April 8, 2025.

JOURNAL OF THEORETICAL
AND APPLIED MECHANICS
63, 2, pp. 331–348, Warsaw 2025
https://doi.org/10.15632/jtam-pl/200390

NUMERICAL SIMULATION STUDY ON CONTINUOUS SPAN VARIABLE CROSS-SECTION ARCHED ROOF

Qing ZHANG[1], Miao PENG[1*], Ji YAO[1], Yu ZHOU[2], Jianfeng HUANG[3]

[1] *Faculty of Civil Engineering and Mechanics, Kunming University of Science and Technology, Kunming 650500, China*
[2] *Yunnan Earthquake Engineering Research Center, Kunming 650228, China*
[3] *College of Civil Engineering and Architectural, Beibu Gulf University, Qinzhou 535011, China*
[*]corresponding author, *miaopeng@stu.kust.edu.cn*

Arched roofs are commonly utilized in various large-scale facilities for their remarkable stability and safety. With the advent of arched roofs featuring variable rise heights, there is a lack of research on wind pressure distribution and shape coefficients for these newer designs. This paper fills this gap by using the computational fluid dynamic (CFD) method on a continuous-span arched roof with different rise height, and valuable results have been obtained.

Results indicate that there will be significant positive pressure in the fence under different wind directions, while the maximum negative pressure and maximum velocity will occur in areas with significant changes in the cross-section of the fence structure. Except for the 90° wind direction, where the roof is primarily affected by positive pressure, the roof structure experiences a large area of negative pressure under other wind directions. The shape coefficients are negative and stable in wind directions of 0° and 180°. The coefficients under the 90° wind direction are all positive values, with slight drastic changes. Under wind directions of 45° and 135°, the variation of the shape coefficient is complex, with positive and negative values appearing. The influence of structural characteristics and size effects on the performance of the building roof is significant. The cantilevered structure of the roof can weaken the disturbance after the incoming flow impacts the building and the diffusion of the wake. Meanwhile, the changes in the size effect of the roof structure can lead to complex pressure distributions and shape coefficient values. The series of results indicate that the building's roof has good performance, with its wavy structure effectively reducing the pressure exerted by the incoming flow, ensuring safe operation. It is worth noting that there is always an area with a significant change in cross-sectional area in the fence structure under different wind directions, which tends to be subjected to greater negative pressure and requires more attention.

Keywords: wind pressure coefficient; shape coefficient; continuous variable cross-section arched roof; realizable k-ε turbulence models; turbulent intensity.

1. Introduction

1.1. Research review

Large-span steel roof structures are particularly susceptible to wind forces. The impact of wind on the integrity and longevity of these roofs is a significant concern (Li *et al.*, 2007; Tian *et al.*, 2021). Arched roofs are known for their stability and safety under diverse wind conditions, although the complexity of calculating wind effects on their surfaces and their three-dimensional aspects is notable (Li *et al.*, 2010; Sun & Zhang, 2020; Tian *et al.*, 2021). Many scholars have conducted research on this type of roof.

Esfeh *et al.* (2021) numerically assessed the influence of wind direction on the ventilation capabilities of arched roofs with openings, highlighting the potential for reducing ventilation costs. Pagnini *et al.* (2022) used both numerical methods and wind tunnel tests to determine mean and peak wind coefficients on the inner and outer surfaces of arched canopies and suggested

zoning approaches. Tian *et al.* (2021) proposed peak external wind pressure coefficients and more defined wind load zones for roof structures, informed by the updated wind load standards (JGJ/T 481-2019, 2020) and extensive wind tunnel data. Kim *et al.* (2019) measured wind pressure data for different roof styles and validated numerical simulations, finding the large eddy simulation (LES) particularly precise for predicting wind-related values for both single and multi-span arched roofs. Based on the EN 1991-1-4, Blackmore and Tsokri (2006) conducted wind tunnel studies to analyze wind coefficient patterns on arched roofs facing various wind directions and sizes, providing detailed regional categorizations and coefficient summaries to address gaps in existing guidelines, as illustrated in Fig. 1.

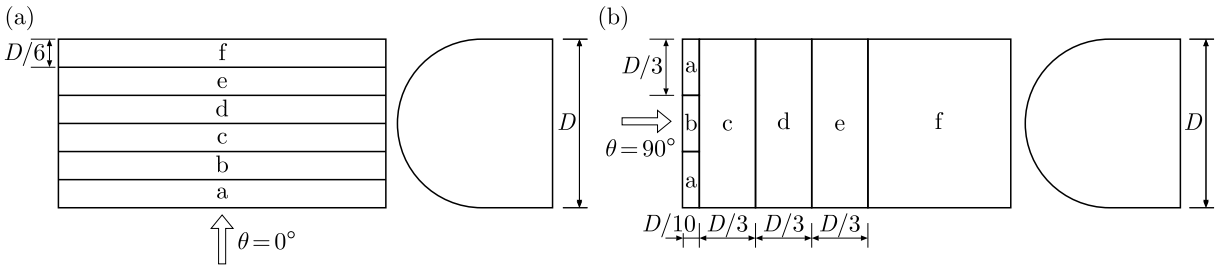

Fig. 1. Roof zoning of BRE wind tunnel test: (a) 0° wind direction; (b) 90° wind direction.

Li *et al.* (2006) explored the effects of different wind directions and conditions on the surface pressures of arched roofs with varying length-to-span ratios, noting the impact of the Reynolds number. Del Coz Díaz *et al.* (2013) conducted the computational fluid dynamics (CFD) analysis on large-span arched roof buildings under wind loading, evaluated roof wind pressure on arched roofs under wind loading, confirming that the results were in line with specifications and highlighting the need to consider localized suction effects in design. Paluch *et al.* (2003) studied the alterations in wind pressure and coefficients due to the addition of canopies to arched roofs, observing the differential effects of axial and vertical flows. Wang *et al.* (2023) numerically assessed the wind pressure coefficient variations in large-span industrial facilities, emphasizing the role of wind direction and terrain roughness.

1.2. Study purpose

The above researches have thoroughly explored the wind pressure dynamics of arched roofs. Recently, there has been a growing trend in the construction of large-span athletic facilities that feature arched roofs with varying cross-sections, a design that harmoniously blends aesthetic appeal with functional utility. Despite this, existing international standards (JGJ/T 481-2019, 2020) have not adequately addressed the study of wind pressure coefficients or form factors for these types of roofs, indicating a gap in the research for such coverings.

In response, this paper employs CFD to examine the wind field characteristics of a continuous span arched roof with a variable cross-section (discussed in Subsection 2.1). It analyzes the flow field dynamics, wind pressure, and form factor distributions across the roof under various wind orientations.

2. Method, setting and verification

2.1. Geometry and computational domain

Currently, numerical simulations are increasingly being used to examine the performance and flow patterns of building structures under wind action. This method can conduct the comprehensive analysis and evaluation of the building prior to construction, which can save costs.

The parameters for the numerical simulation are derived from a large venue located in Dali, Yunnan Province, China with the length, width and height parameters shown in Table 1. As shown in Fig. 2b, the building roof is symmetrical on both sides, with a shape similar to the wings of a butterfly and a narrow front (60.7 m) and wide back (89 m) shape. The structure of the roof is like rolling waves, undulating up and down (hereinafter referred to as a wavy roof), mainly composed of 4 peaks and 3 troughs as shown in Fig. 2e. As shown in Fig. 2c, it can be seen that the height of the peak is constantly changing. Furthermore, it is worth noting that the roof of the building is larger than the fence structure, which results in some areas of the wave peaks becoming cantilever structure.

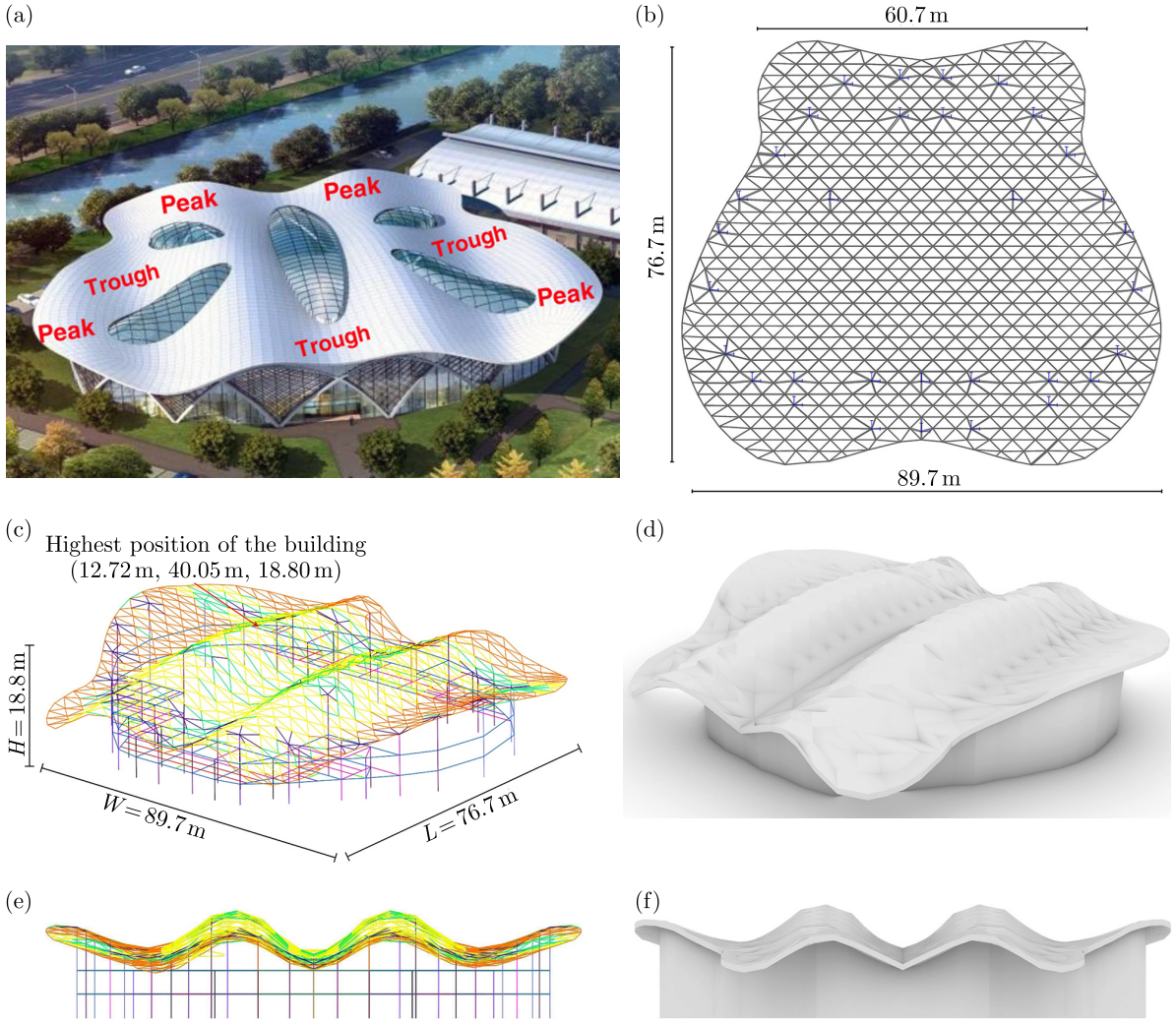

Fig. 2. Rendering, model diagram and dimensions.

Table 1. Model size.

Parameters	Length L [m]	Width W [m]	Height H [m]
Size	76.7	89.7	18.8

It is crucial to ensure that the analysis model remains unaffected by the flow field's inlet and outlet boundaries, while also maintaining similarity between the numerical model and the real-world counterpart. Additionally, it is essential to mitigate the impact of blockage effects, which is achieved through the following equation:

$$\delta = A/A_0, \tag{2.1}$$

where A and A_0 denote the areas of the model and the computational domain, respectively. The ratio is known as the blockage ratio, should be less than 5 %. Furthermore, it is necessary to ensure an adequate distance between the model and the computational boundaries. The height of the computational domain should exceed the model's height by at least 2 to 2.5 times, and the width should be at least 6 times greater than the model's width. The distance separating the inlet and outlet of the computational domain should be a minimum of 5 times the height of the model (Esfeh *et al.*, 2021; Wang *et al.*, 2023; Zhang *et al.*, 2021).

Building on the preceding analysis, the computational domain is established with a height of $5H$ (94 m), width to $6.2W$ (556.14 m) and length to 348.5 m. The model is $5H$ from the inlet, $10H$ from the outlet, which ensure the full development of the flow field. Based on the above settings, the blockage rate meets the requirements, as shown in Table 2. In addition, a body of influence has been set up near the model to encrypt the mesh near the model in the Subsection 2.3. The configuration of the computational domain is depicted in Fig. 3.

Table 2. Blockage rate of different wind directions.

Wind directions	A [m^2]	A_0 [m^2]	Blockage rate [%]
0°/180°	1686.36	52277.16	3.23
45°/135°	2218.80	62207.65	3.57
90°	1441.96	33717.80	4.28

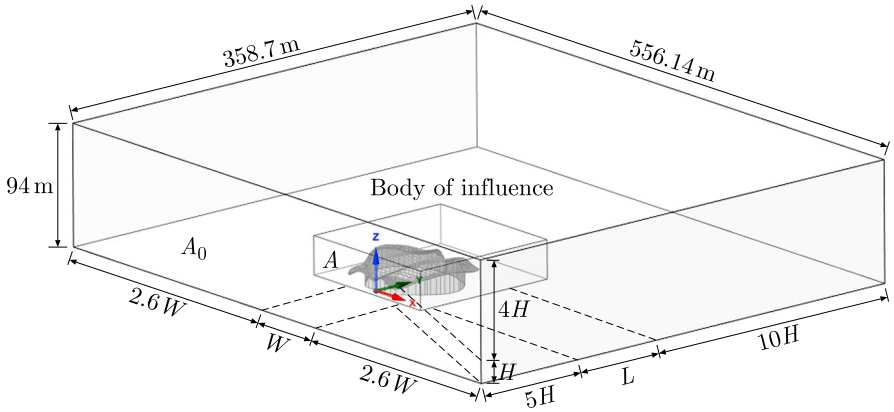

Fig. 3. Computational domain.

2.2. Turbulence model and boundary conditions

The Reynolds number (Re, a ratio of inertial force to viscous force) is an important parameter for determining the fluid state near buildings. The Reynolds number is determined by:

$$\mathrm{Re} = \frac{UL}{v}, \tag{2.2}$$

where U is the wind of building height, which is 8 m/s, v is the kinematic viscosity of the wind, which is 1.48×10^{-5} m^2/s at standard conditions, L is the characteristic length. The calculated Re is 5.4×10^5, indicating that the flow field near a building roof is in a turbulent state.

To efficiently simulate turbulent flows, different turbulence modeling approaches have been developed, including direct numerical simulation (DNS), LES, and the Reynolds-averaged Navier–Stokes (RANS) methods. Among these, DNS and LES are computationally intensive and require significant resources, limiting their widespread use in engineering applications. The RANS method is the most commonly used in practice due to its ability to produce satisfactory

results with reasonable computational efficiency under appropriate parameter selections (del Coz Díaz *et al.*, 2013; Meng *et al.*, 2018; Zhang *et al.*, 2021).

The instantaneous equations are given as follows:

$$\frac{\partial \rho}{\partial t} + \nabla \cdot [\rho(\overline{v} - v_r)] = 0, \tag{2.3}$$

$$\frac{\partial}{\partial t}(\rho \overline{v}) + \nabla \cdot [\rho \overline{v}(\overline{v} - v_r)] = -\nabla \cdot \overline{p} I + \nabla \cdot \left(T - \rho \overline{v'v'}\right) + f_b, \tag{2.4}$$

where ρ is the density of air, which is taken as $1.225\,\mathrm{kg/m^3}$.

The realizable k-ε turbulence model is known for its effectiveness in simulating fluid flows in numerical simulations, particularly in scenarios involving rapid strain, streamline curvature, flow separation, reattachment, and recirculation. Consequently, this turbulence model was selected for the numerical simulation (Meng *et al.*, 2018; Zhang *et al.*, 2021). The governing equations for this model are presented in Eqs. (2.5) and (2.6):

– k-equation:

$$\frac{\partial(\rho k)}{\partial t} + \frac{\partial}{\partial x_k}(\rho k u_k) = \frac{\partial}{\partial x_k}\left[\left(\mu + \frac{\mu_t}{\sigma_k}\right)\frac{\partial k}{\partial x_k}\right] + G_k + G_b - \rho\varepsilon - Y_M + S_k, \tag{2.5}$$

– ε-equation:

$$\frac{\partial(\rho\varepsilon)}{\partial t} + \frac{\partial(\rho\varepsilon u_k)}{\partial x_k} = \frac{\partial}{\partial x_k}\left[\left(\mu + \frac{\mu_t}{\sigma_\varepsilon}\right)\frac{\partial \varepsilon}{\partial x_k}\right] + \rho C_1 S\varepsilon - \rho C_2 \frac{\varepsilon^2}{k + \sqrt{\nu\varepsilon}} + C_{1\varepsilon}\frac{\varepsilon}{k} C_{3\varepsilon} G_b + S_\varepsilon, \tag{2.6}$$

$$\frac{U(z)}{U_H} = \left(\frac{z}{z_H}\right)^{\alpha}. \tag{2.7}$$

The characteristics of the incoming flow are of significant importance. Considering the specific circumstances, national standards, and relevant references, this study establishes the ground roughness coefficient as category IV, in accordance with GB 50009-2012 (2012). To represent the wind speed profile Eq. (2.7) (refer to Fig. 4a) is utilized, taking into account the inflow conditions of the atmospheric boundary layer wind. $U(z)$ denotes the wind speed at height z, U_H is the wind speed at the building height of $z_H = 18.8\,\mathrm{m}$, set as $8\,\mathrm{m/s}$, and α represents the wind profile coefficient, set as 0.27.

Turbulent intensity I serves as a crucial parameter that influences the dynamics of wind flow during separation events and is incorporated into numerical simulations through Eq. (2.8) (refer to Fig. 4b). In this context, z_G means gradient wind height, set as $550\,\mathrm{m}$, and the turbulence intensity at the building height of 18.8 m is specified as 0.295:

$$I = 0.1\left(\frac{z}{z_G}\right)^{-\alpha-0.05}. \tag{2.8}$$

Turbulent kinetic energy k and turbulent dissipation rate ε are calculated using Eqs. (2.9) and (2.10), as illustrated in Figs. 4c and 4d, respectively. Notably, a in Eq. (2.9) is a constant that depends on the standard deviations of turbulent fluctuations and is assigned a value of 1.0 for this numerical simulation:

$$k(z) = a\left(I(z) \cdot U(z)\right)^2, \tag{2.9}$$

$$\varepsilon = \frac{k^{1.5} \cdot C_u^2}{0.07 L_u}. \tag{2.10}$$

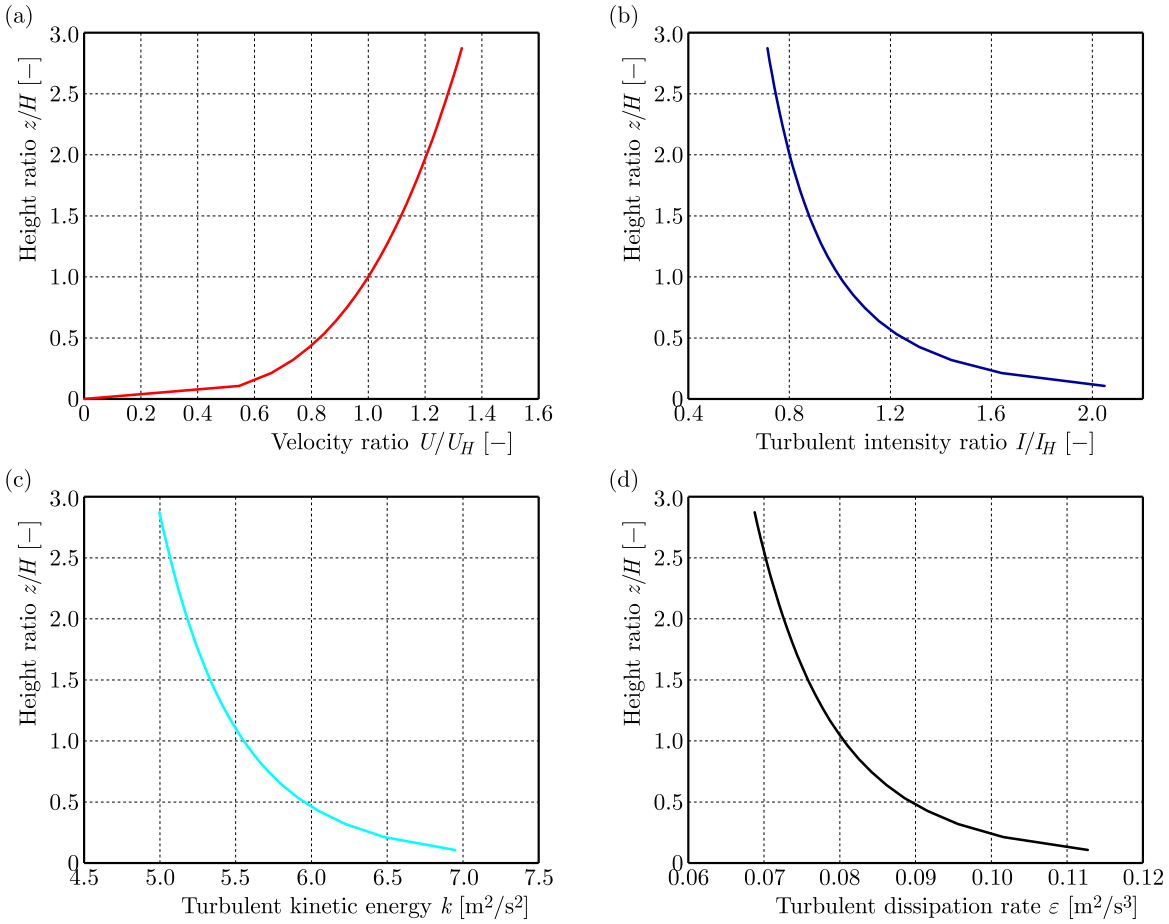

Fig. 4. Profiles of: (a) wind speed; (b) turbulent intensity; (c) turbulent kinetic energy, and (d) turbulence dissipation rate. Note: H signifies the height of the model, and I_H denotes the turbulence intensity at the building height.

The turbulence dissipation rate equation involves a characteristic length of the computational domain, L_u is the characteristic length of a computational domain, set as 18.8 m. C_u is an empirical constant, set as 0.09.

The boundary conditions are defined as depicted in Fig. 5. As previously discussed, the velocity-inlet is characterized by an exponential wind speed profile, the outlet boundary is designated as a pressure-outlet, and the surfaces of the building and the computational domain are treated as frictionless-walls. The simulation employs the SIMPLEC algorithm and a second-order upwind scheme for discretizing momentum, turbulent kinetic energy, and turbulent dissipation rate (del Coz Díaz *et al.*, 2013; Meng *et al.*, 2018). Convergence of the simulation reaches

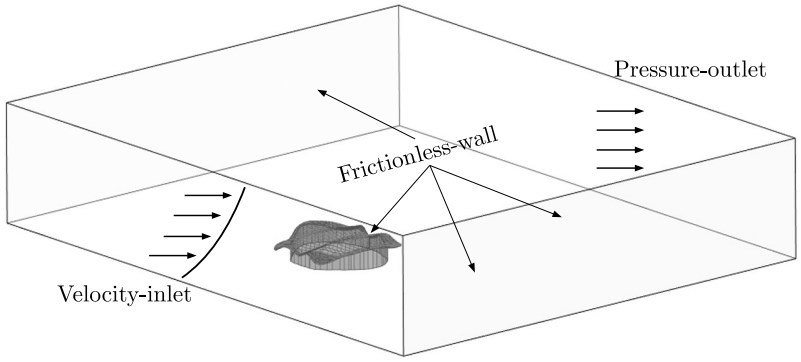

Fig. 5. Boundary conditions.

is assumed when the residual of continuity, the momentum of x, y, z, k, ε equations decrease below 10^{-6}.

2.3. Grid division and verification

The flow conditions on the model roof are intricate and necessitate a refined mesh. Consequently, the rate of mesh growth near the model's wall is adjusted to 1.15 times to maintain a seamless transition between the mesh and the model. Furthermore, the grid height of the initial layer is meticulously chosen to guarantee that the value of y^+ is less than 1 (Esfeh *et al.*, 2021; Meng *et al.*, 2018; Zhang *et al.*, 2021). The grid layout is illustrated in Fig. 6a.

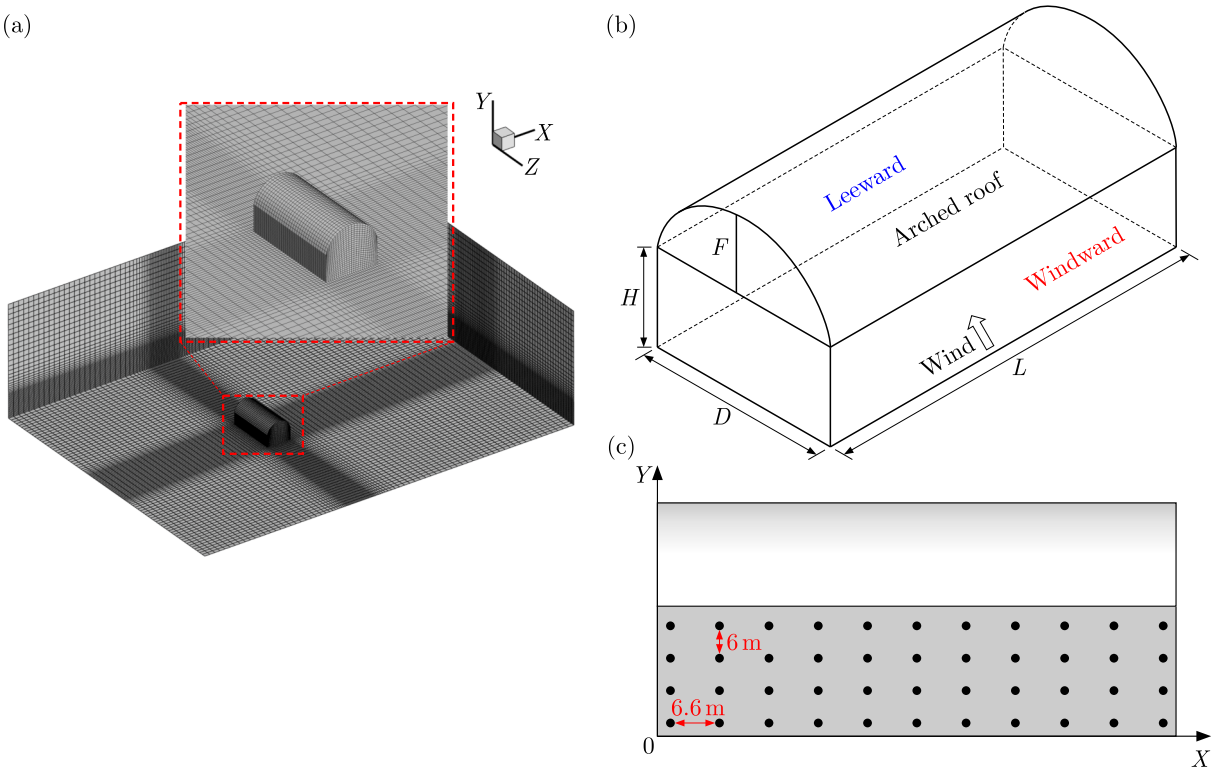

Fig. 6. (a) Grid partitioning and refinement; (b) standardized arched roof model; (c) setting of measuring points.

The codes do not provide the standard values for the shape coefficient of such roofs. So, we selected an arched roof in the codes (JGJ/T 481-2019, 2020) that is similar to the research object of this article. As shown in Fig. 6b, the roof parameters are $L/D = 2$, $F/D = 0.25$, calculating the coefficients on the windward and leeward surfaces and compare them with the standard values for verification based on 5 different grids. Also, the 5 grid size settings are shown in Table 3.

Table 3. Dimensions of 5 grids.

Mesh type	Mesh number	Minimum size	Minimum volume [m^3]
Grid-1	15543	0.07235L	38.05
Grid-2	49392	0.05605L	10.76
Grid-3	128478	0.03620L	3.79
Grid-4	247848	0.02630L	1.55
Grid-5	357048	0.01975L	0.74

The operation is as follows, set measurement points on the windward and leeward sides, as shown in the Fig. 6c. Set a measuring point at an interval of 6.6 m in the X-direction and a measuring point at an interval of 6 m in the Y-direction. There is a total of 88 measuring points. Wind pressure coefficients are calculated through Eq. (2.11). And use Eq. (2.12) to calculate the shape coefficient:

$$C_{pi} = \frac{P_i - P_\infty}{\frac{1}{2}\rho U_\infty^2}, \tag{2.11}$$

$$\mu_{si} = C_{pi}\left(\frac{z_H}{z_i}\right)^{2a}, \tag{2.12}$$

$$\mu_s = \frac{\sum_{i=1}^{n} \mu_{si} A_i}{\sum_{i=1}^{n} A_i}, \tag{2.13}$$

$$\gamma = \frac{|\mu_s - \mu_{s,\text{standard}}|}{\mu_{s,\text{standard}}}, \tag{2.14}$$

where C_{pi} is the wind pressure coefficient of a specific point i, P_i represents the wind pressure, P_∞ is the static pressure at the reference height, U_∞ is wind speed at the reference height, μ_{si} is the local shape coefficient of measuring points, and μ_s is the mean shape coefficient, $\mu_{s,\text{standard}}$ is the standard values from codes, z_H and z_i is the height of the building height and measuring points, A_i is the area of measuring points.

As indicated in Table 4, it is evident that the μ_s on both the windward and leeward sides of the roof decrease progressively and converge towards the standard values as the grid is refined. Figure 7a illustrates the discrepancy between the CFD results and the codes (JGJ/T 481-2019, 2020).

Table 4. Results under 5 different grids.

μ_s	Grid number				
	Grid-1	Grid-2	Grid-3	Grid-4	Grid-5
Windward side	1.52	1.06	0.85	0.74	0.74
Standard	+0.80				
Leeward side	−0.55	−0.46	−0.36	−0.42	−0.37
Standard	-0.40				

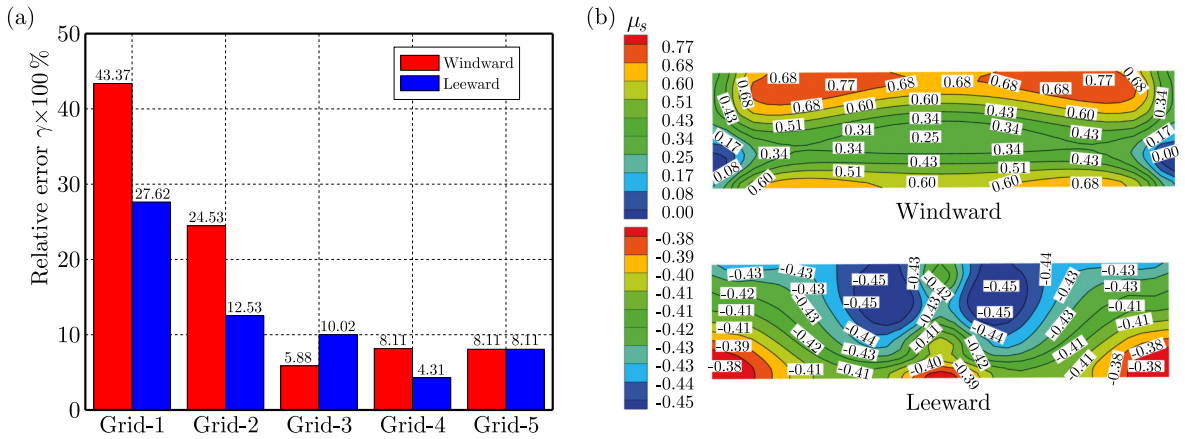

Fig. 7. (a) Deviation of shape coefficient under 5 grid models; (b) local shape coefficient of windward and leeward under Grid-4.

As the number of grid cells rises, it becomes clear that the absolute deviation between the calculated results and the actual values diminishes. The results from Grid-4 and Grid-5 exhibit a trend towards stability, with the absolute deviation dropping below 10 %. Given that Grid-4 has a lower grid count and demands fewer computational resources, it is selected as the standard for the grid division in the subsequent analysis.

2.4. CFD verification

Select the same model as in Subsection 2.3 and use the same method to calculate the shape coefficients of the roof to verify the feasibility of CFD method. Figure 8 shows the wind zone method and measurement points set on the roof. The mean shape coefficients of the 3 zones were obtained by calculating the local shape coefficient. The results are shown in Fig. 9.

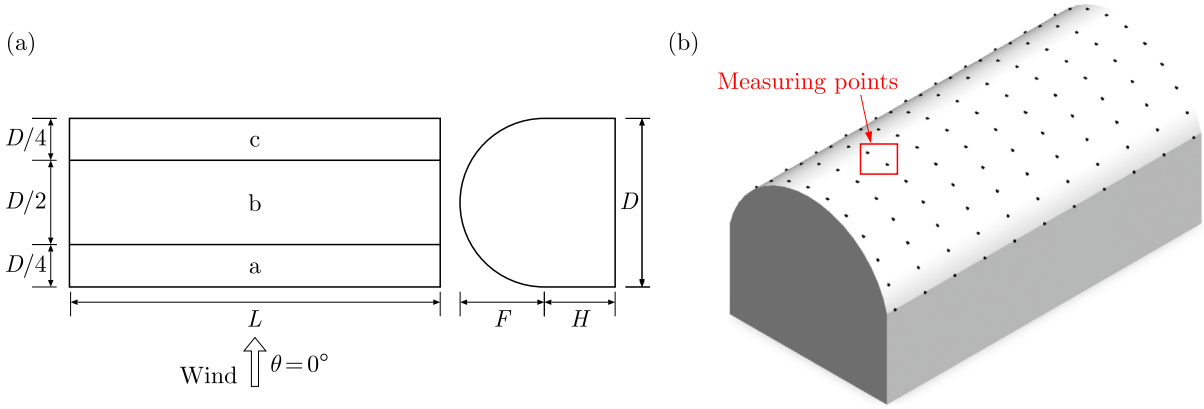

Fig. 8. (a) Standardized roof zoning; (b) measuring points settings.

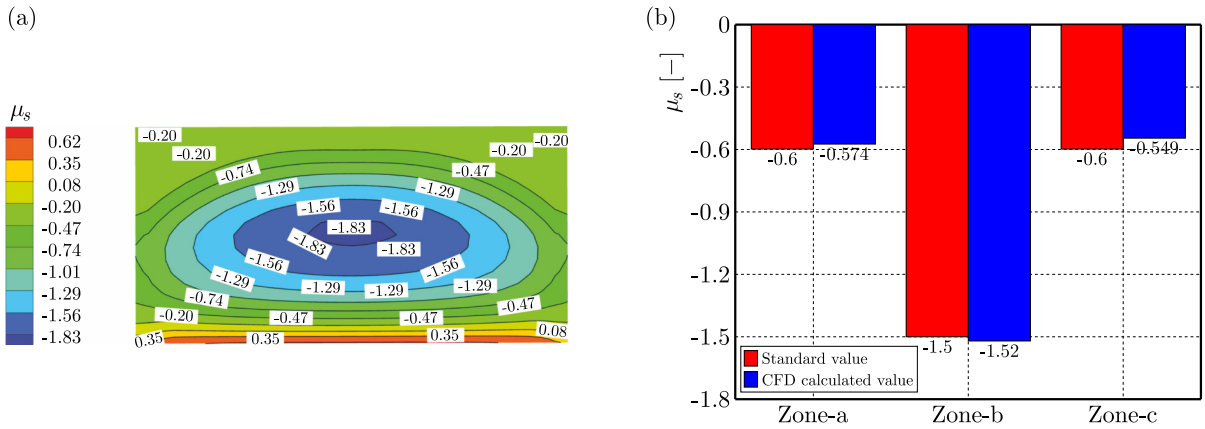

Fig. 9. (a) Local shape coefficient of arched roof; (b) mean shape coefficient of different zones.

It can be seen that under the above settings and the grid division, the deviation between the shape coefficient and the standard value is small, it indicates that the above settings and grid division are credible. In the following numerical simulation, the same settings, the grid division will be used.

3. Results and discussion

Based on codes (JGJ/T 481-2019, 2020), we selected 5 wind directions (0°, 45°, 90°, 135°, and 180°) for numerical simulation of the research object in this paper.

As shown in Fig. 10, the construction is divided into parts as shown in Fig. 10a, namely: peaks-A, B, C, D and trough-A, B, C. As shown in Fig. 10b, the model is divided into grids

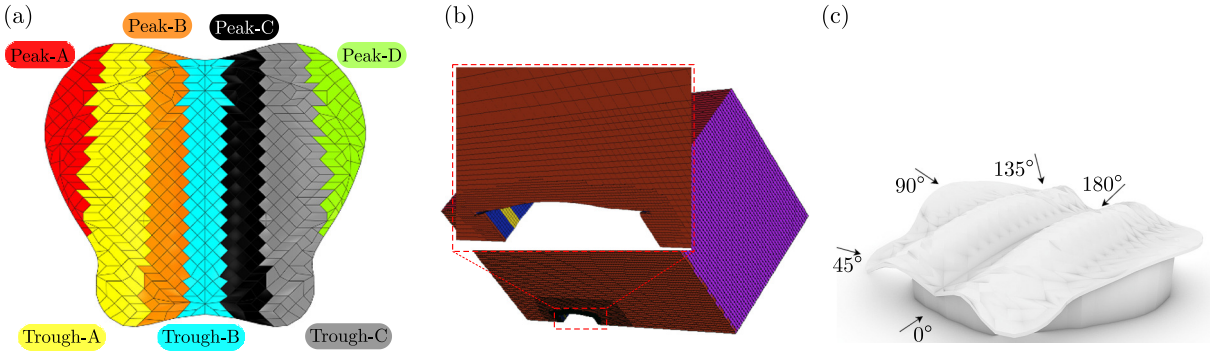

Fig. 10. (a) Roof zoning and naming; (b) grid area of roof and BOI; (c) wind directions.

according to the model in Grid 4. Measurement points are also set on the model roof before calculation. Table 5 lists the coordinates of roof measurement points. The setting of wind directions is shown in Fig. 10c. Coordinates of roof structure monitoring points (m).

Table 5. Coordinates of roof measurement points.

Positions	Measuring point 1			Measuring point 2			Measuring point 3			Measuring point 4			Measuring point 5		
	x	y	z	x	y	z	x	y	z	x	y	z	x	y	z
Peak-A	−36.45	63.54	17.93	−43.19	43.44	16.33	−36.18	29.51	17.73	−42.17	10.91	17.33	−40.82	3.75	17.52
Trough-A	−26.43	68.87	9.89	−28.45	45.44	12.34	−26.68	20.26	12.18	−13.22	11.37	11.31	−15.49	2.89	10.52
Peak-B	−14.28	69.13	17.22	−15.24	48.97	16.15	−13.59	31.03	16.08	−13.22	11.37	17.57	−14.49	2.89	16.92
Trough-B	0	67.35	10.52	0	52.63	12.07	0	31.73	9.64	0	11.37	8.72	0	2.89	9.92
Peak-C	14.28	69.13	17.14	15.24	48.97	16.28	13.59	31.03	16.07	13.22	11.37	17.45	14.49	2.89	17.02
Trough-C	26.43	69.13	9.88	27.66	45.77	12.16	27.5	20.2	12.13	13.22	11.37	11.31	15.49	2.89	10.52
Peak-D	36.45	63.54	17.93	43.19	43.44	16.33	36.18	29.51	17.73	42.17	10.91	17.33	40.82	3.75	17.52

3.1. Velocity and wind pressure distribution

As shown in Table 6, the peak velocity is the lowest under the 0° wind direction and the highest under the 45° wind direction. The maximum positive pressure occurs at the 90° wind directions and the maximum negative pressure occurs at the 45° wind direction.

Table 6. Velocity and pressure.

Wind directions	Peak wind speed [m/s]	Peak maximum pressure [Pa]	Trough minimum pressure [Pa]
0°	13.93	9.63	−120.77
45°	18.36	19.96	−228.13
90°	15.91	75.33	−65.13
135°	16.17	46.72	−120.77
180°	13.85	35.53	−77.48

Under the 0° wind direction, Figs. 11a and 11b show that the windward surface of the fence is first impacted by the incoming flow, which then quickly passes along the fence, reaching maximum velocity at the largest cross-section of the fence. Correspondingly, Figs. 11c and 11d show that there is a larger negative pressure at this location, indicating a transition from positive to negative pressure on the fence. In the vertical direction, as seen in Fig. 11b, the incoming flow does not undergo significant rotational disturbance on the roof due to the presence of

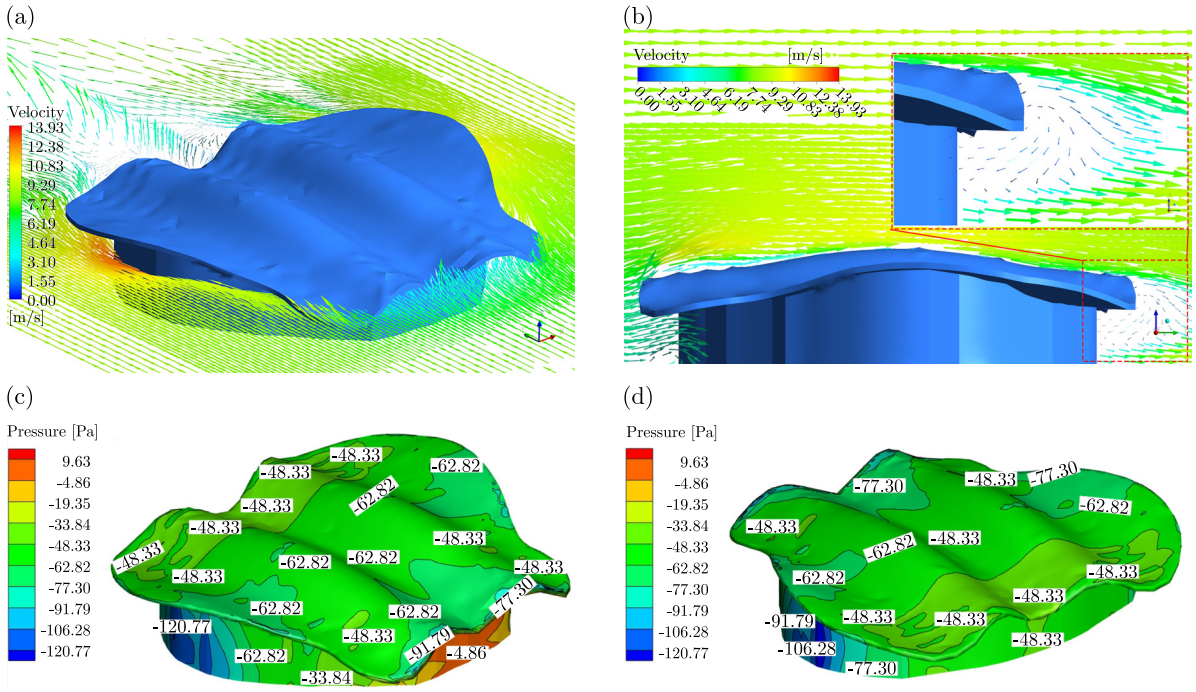

Fig. 11. (a)–(b) Velocity vector; (c)–(d) contours of wind pressure under 0° direction.

the variable cross-section arch roof, but instead rapidly moves towards the rear of the model along the direction of the incoming flow, effectively reducing the impact of the incoming flow and preventing strong airflow rotation at the roof tail, resulting in relatively smaller negative pressures.

Under the 45° wind direction, the interaction between the incoming flow and the building is significantly intensified. As shown in Fig. 12a, the disturbance of the incoming flow at the fence is greater compared to the 0° wind direction. Figure 12b shows that there are higher wind

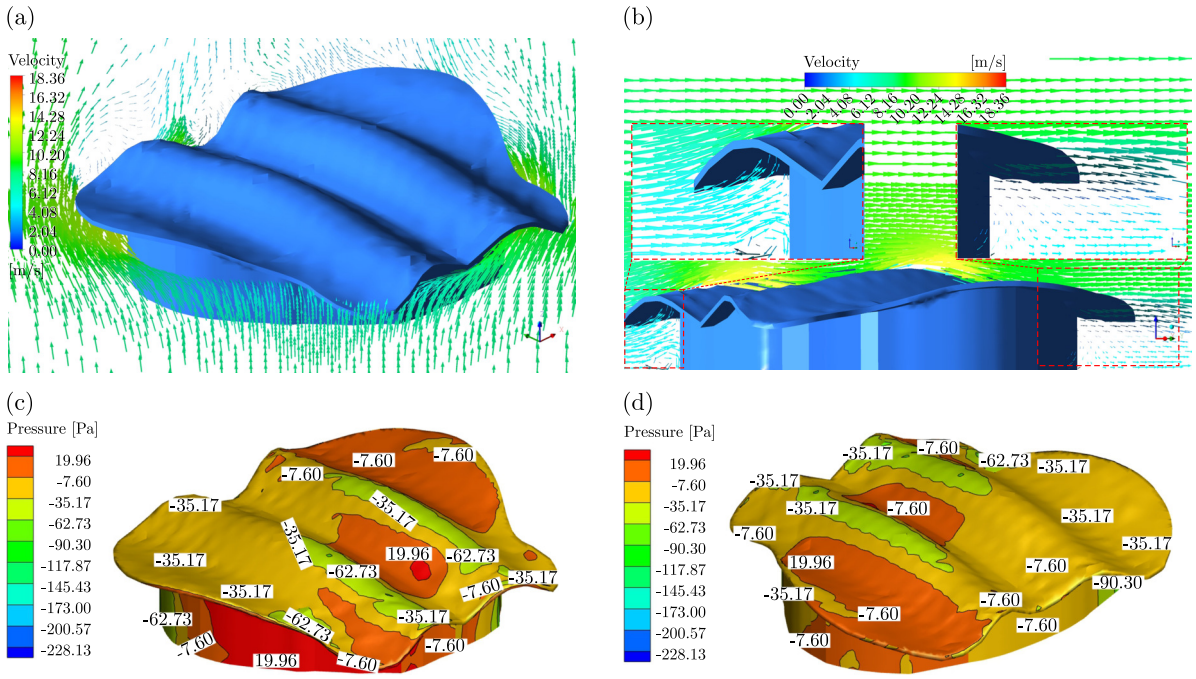

Fig. 12. (a)–(b) Velocity vector; (c)–(d) contours of wind pressure under 45° direction.

speeds at the peak-A and B of the roof since the incoming flow does not pass directly over the variable cross-section roof in the span direction but instead moves laterally through the wavy structure. Figures 12c and 12d indicate that there is a larger area of negative pressure at these locations. However, there is no significant airflow disturbance at peak-D and the trailing edge of the building after the impact of the airflow is weakened by peak-A, B, and trough-A. Comparing Figs. 12c and 12d, it can be observed that the suction force on the roof at peak-A, B, C, and D gradually decreases, and there is a region of positive pressure at trough B, indicating that the airflow changes over the roof are more complex under the 45° wind direction.

The 90° and 45° wind directions share similarities. Figures 13a and 13b reveal that there is a significant airflow rotation at trough-A and B under the 90° wind direction, with a larger rotation area at trough-A and a smaller one at trough-B. Figures 13c and 13d show that the strong impact also results in positive pressure in this area. While at trough-C, there is no significant airflow disturbance, and the flow quickly passes over the roof. The roof pressure under the 90° wind direction shows a large area of positive pressure, with relatively higher peak positive pressures. This is because the 90° wind direction represents the most distinct structural feature of the roof, causing the incoming flow to be most obstructed as it passes over the roof. Additionally, the larger positive pressures on the roof appear at the ends of the building, which is the result of the interaction between the flow fields near the fence and at the ends of the roof.

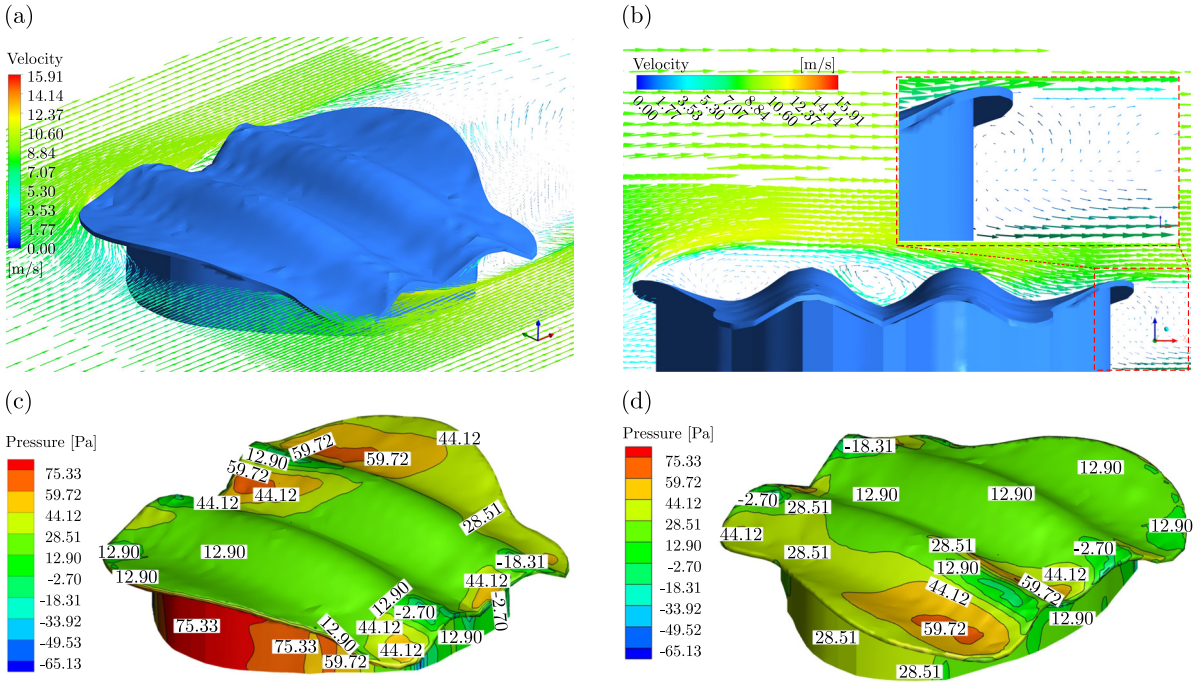

Fig. 13. (a)–(b) Velocity vector; (c)–(d) contours of wind pressure under 90° direction.

Under the 135° wind direction, the velocity changes around the roof are similar to those in a wind direction of 45°, with peak-A, B, and C mainly experiencing negative pressure, peak-D mainly experiencing positive pressure and all three troughs are mainly under positive pressure. As shown in Fig. 10a, the roof structure is narrower at the front and wider at the back. Therefore, under the 45° wind direction, the structural features along the direction of the incoming flow increase, the rise height of a roof is increasing continuedly, the obstruction to incoming flow is increasing. Conversely, under the 135° wind direction, the structural features decrease along the flow direction, resulting in decreasing obstruction. Thus, under the 45° wind direction, the roof experiences larger areas and values of negative pressure and smaller areas and values of positive pressure, while the opposite is true under the 135° wind direction.

The velocity situation under the 180° wind direction is similar to 0° wind direction, with little difference in the peak velocities and their locations. As previously analyzed, compared to the 0° wind direction where the roof width gradually increases, both the peak velocity and the suction force on the roof under the 180° wind direction are smaller than those under the 0° wind direction, due to the structural features of the building under the 180° wind direction gradually decreasing.

In summary, there will be significant changes in wind speed and roof pressure or the building will experience greater pressure when the incoming flow passes through the building, if the structural features of the building decrease. The results from Figs. 11 to 14 indicate that the flow fields near the ends of the building are more complex, showing more complex situations in the roof pressure. Additionally, the parts of the roof that first contact the incoming flow will experience greater suction or smaller pressure, and as the incoming flow develops, the suction gradually decreases or the pressure gradually increases.

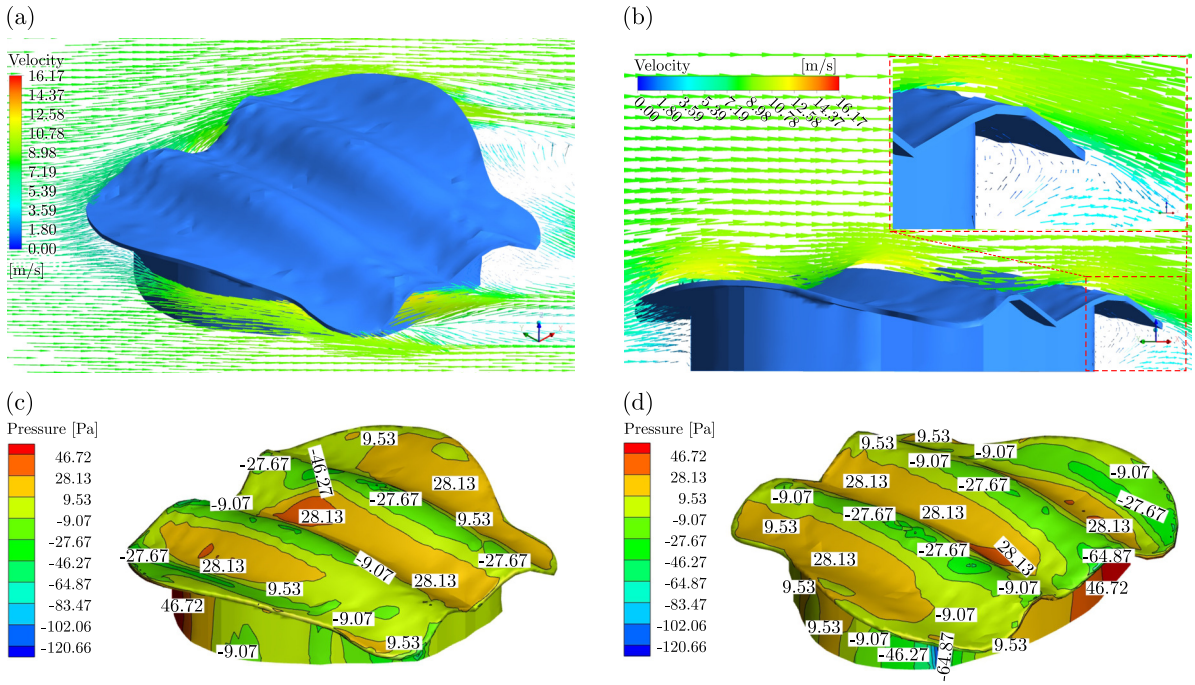

Fig. 14. (a)–(b) Velocity vector; (c)–(d) contours of wind pressure under 135° direction.

In Subsection 2.1 of this paper, it is mentioned that the building roof has actually a portion of the cantilevered structure. Wang *et al.* (2023) point out: "The size effect modifies the distribution of the pressure field within the columnar vortex at the leading edge of the windward side". It can be seen that the structural characteristics of the building play an important role in protecting the roof from the velocity vector diagram. As shown in Fig. 9, there will be rotation and vortices, and the disturbance of this part of the airflow will result in a large area of negative pressure at the top of the roof, ultimately affecting the distribution of the roof's shape coefficients after the incoming flow contacts the roof and the fence structure. The cantilevered structure of this building effectively weakens this phenomenon. From part (b) of Figs. 11–15, it can be seen that after the windward side contacts, the produced rotation and vortices are small, such as under the 0° and 180° directions, or vortices appear, but these vortices do not develop to affect the roof structure area, such as under the 90° and 45° wind directions due to the cantilevered structure. The wake region is also the same, where the wake rotation is limited under the cantilevered structure. Both structural characteristics and size effects affect the wind pressure characteristics of a building's roof, and the design structure of this building demonstrates good superiority.

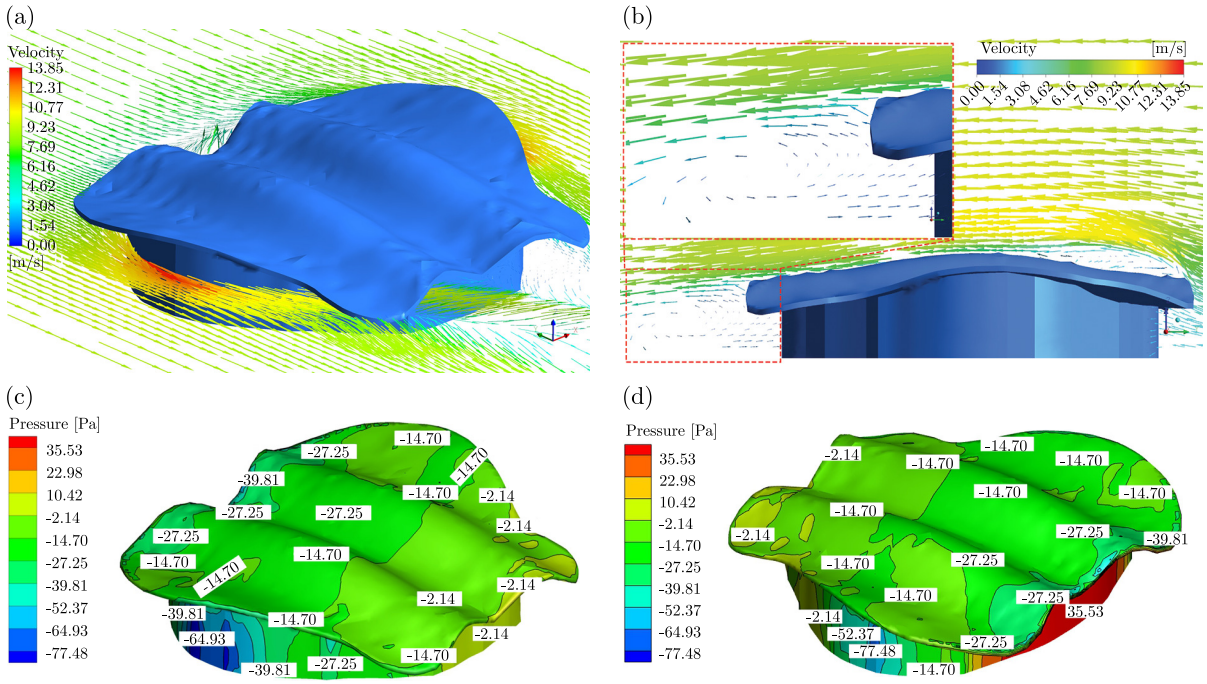

Fig. 15. (a)–(b) Velocity vector; (c)–(d) contours of wind pressure under 180° direction.

Blackmore and Tsokri (2006) imply that for arched roofs, "The suctions on the central roof zones are highly dependent on the position along the roof", which is fully confirmed in the research object of this paper. For example, as shown in Fig. 12c, a small area and small positive pressure appear in the region trough-B and the peak-C under the 45° wind direction. Subsequently, the pressure changes to a large area of negative pressure near the maximum rise height, and then as the rise height decreases, the negative pressure value on the roof increases, indicating that the suction force on the roof decreases. However, the pressure changes on the roof are more severe and are also more affected by adjacent roof structures in continuous-span buildings unlike single-span structures, which is different from the literature.

3.2. Wind pressure coefficient and mean shape coefficient

Based on the calculation results, wind pressure coefficients and mean shape coefficients for the building surface were calculated using Eq. (2.11), Eq. (2.12), and Eq. (2.13), respectively, and the results were visualized in contour maps. The results are presented in Table 7, Fig. 16, and Fig. 17.

Table 7. Mean shape coefficients.

Zone	Wind directions				
	0°	45°	90°	135°	180°
Peak-A	−1.78621	−0.94503	0.342702	−0.70617	−0.98657
Trough-A	−2.19161	−0.72146	0.639788	0.898425	−1.38848
Peak-B	−1.64519	−1.26795	0.534423	0.649691	−1.29938
Trough-B	−1.96209	−0.04145	1.105404	0.994864	−1.35412
Peak-C	−1.60694	−1.36378	0.655461	−0.623750	−1.31092
Trough-C	−2.16317	−0.24185	1.142049	0.188102	−1.37046
Peak-D	−1.78401	−0.23856	1.120191	0.238559	−0.98535

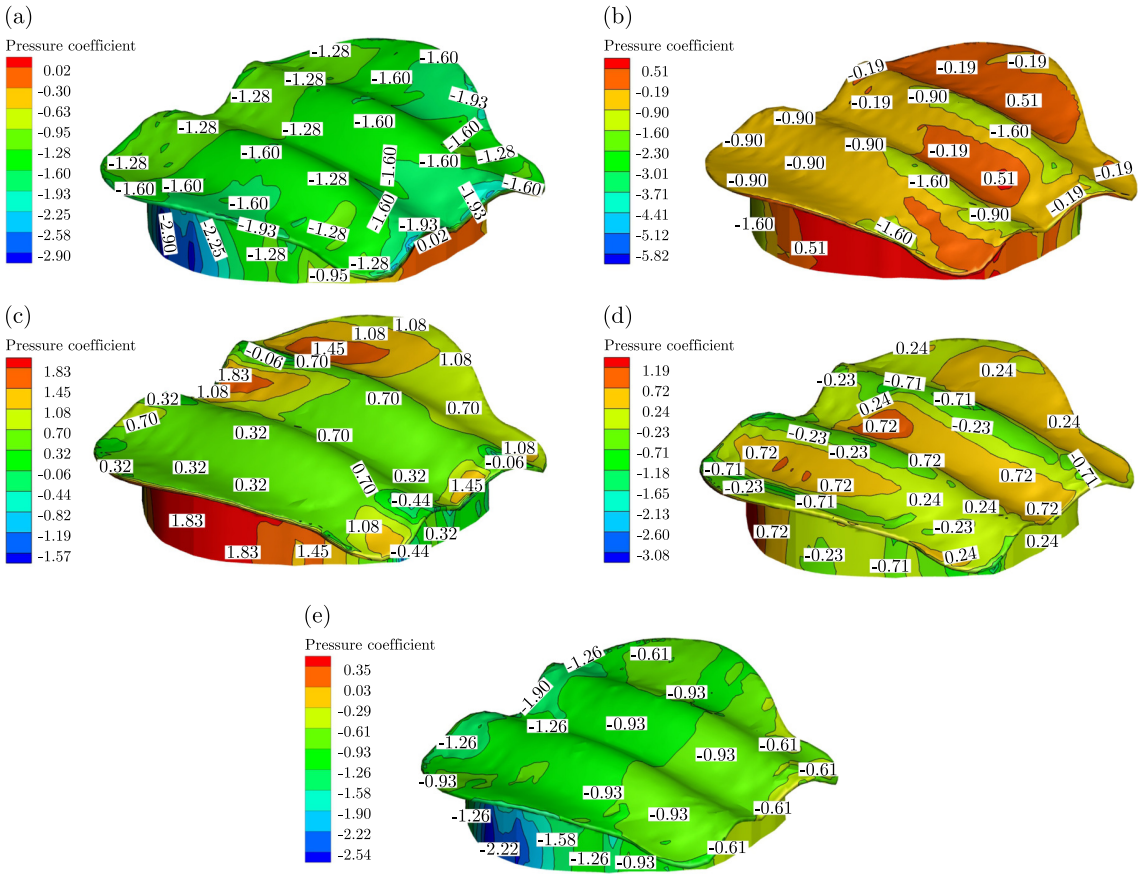

Fig. 16. Wind pressure coefficient of different wind directions: (a) 0°; (b) 45°; (c) 90°; (d) 135°; (e) 180°.

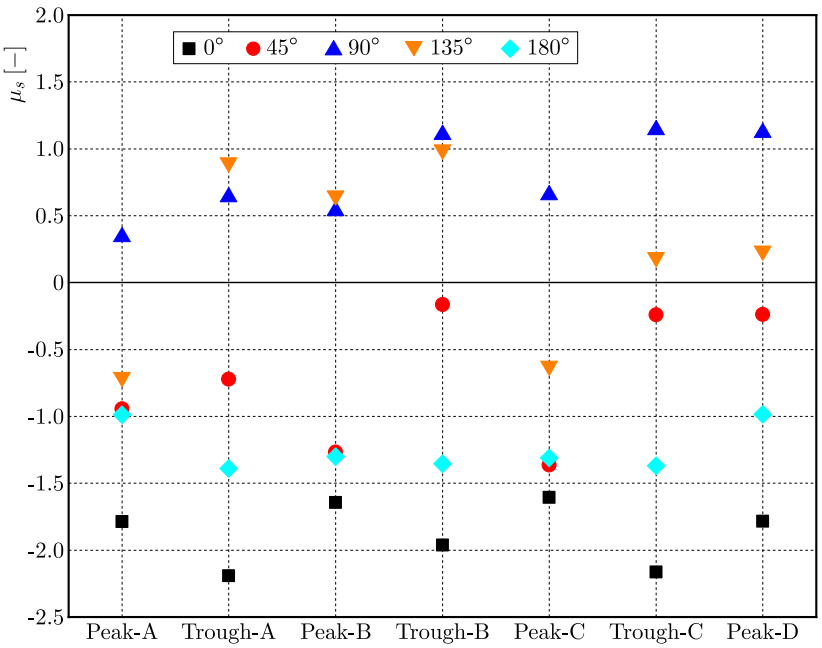

Fig. 17. Mean shape coefficient of roof area under different wind directions.

Both large positive and small negative wind pressure coefficients appeared at the cantilever structure of the roof among the five wind directions. For the roof structure, only under the 90° wind direction did a large area of positive wind pressure coefficients appear, while under the other wind directions, the roof wind pressure coefficients were mainly negative. These results

indicate that the roof is mainly acted upon by suction, with the pressure acting mainly on the windward side of the roof cantilever.

From Table 7 and Fig. 17, it can be seen that the wind pressure coefficients are relatively stable under the 0° and 180° wind directions, with values distributed around −2.0 and −1.25, respectively. The shape coefficients under the 180° wind direction are greater than those under the 0° wind direction in all areas, indicating that the suction force on the roof under the 180° wind direction is less than that under the 0° condition. This is because under the 180° wind direction, the roof windward surface area is larger, receiving a greater impact from the incoming flow, and the building cantilever withstands a larger positive pressure, which also greatly weakens the incoming flow. The force on the roof also decreases after the incoming flow is weakened by the windward surface, resulting in a smaller suction force on the roof under the 180° wind direction, which corresponds to Figs. 16a and 16b.

As for the 45° and 135° wind directions, the shape coefficients have larger fluctuations, especially under the 135° wind direction, where the roof shape coefficients are more complex, with both positive and negative values. Specifically, under the 135° wind direction, Fig. 17 shows that in addition to the shape coefficients at peak-A and C being negative, the values of the shape coefficients in the other areas are all positive. Under the 45° wind direction, the fluctuations are slightly reduced, with the roof shape coefficients being negative and larger in value than under the 135° wind direction. This is because the suction force on the roof is relatively small.

It can be seen that under the 135° wind direction, the structural features of the roof decrease along the incoming flow direction, leading to a more complex flow field and changes in roof wind pressure and shape coefficients. Under the 45° wind direction, the structural features of the roof gradually increase, and the wavy roof plays a greater role in guiding the flow after the incoming flow passes through the windward side, resulting in larger wind pressure coefficients and shape coefficients at peak-D and trough-C.

There is a large area of positive wind pressure coefficients and shape coefficients under the 90° wind direction with only a small part of negative wind pressure coefficients at the ends of the roof structure, compared to other wind directions. Combining Fig. 13b, it can be seen that under the 90° wind direction, the building impedes the incoming flow to a greater extent, and there is a significant degree of rotation and disturbance when the wind flows perpendicular to the wavy roof, causing the roof to be acted upon by positive pressure. It is worth noting that although the impediment to the incoming flow is significant, the wavy roof structure causes the incoming flow to weaken rapidly, the roof does not receive a large positive pressure.

4. Conclusion

This paper focuses on a CFD simulation of a continuous-span building with a variable-section arch-shaped roof as the main structure, analyzing its flow field characteristics, wind pressure distribution, wind pressure coefficients, and shape coefficients under different wind directions. The findings provide guidance for the wind resistance design and subsequent safety maintenance of such buildings. The main conclusions are as follows:

1) Under different wind directions, the fence of building experiences significant positive pressures, the maximum negative pressure and maximum velocity appear at the transition points of the fence structure's cross-section under different directions. Except for the 90° wind direction, where the roof is primarily acted upon by positive pressure, the roof structure experiences a large area of negative pressure under other wind directions, which is due to the maximum obstruction of the wave-shaped structure of the roof being perpendicular to the wind direction.
2) Along the symmetric direction of the building under various wind directions, both the wind pressure coefficients and the mean shape coefficients tend to be evenly distributed.

Under oblique winds, i.e., at 45° and 135° wind directions, the wind pressure coefficients and mean shape coefficients on the roof change complexly, with smaller negative wind pressure coefficients appearing at the areas of the roof that firstly come into contact with the incoming flow, and some positive shape coefficients can also appear at the highest point of the roof's rise. Under the 90° wind direction the roof mainly experiences positive wind pressure coefficients, with positive shape coefficients, indicating that the roof is mainly acted upon by positive pressure.

3) The influence of structural characteristics and size effects is the most significant part of the results, mainly divided into two points: firstly, the cantilevered structure of the roof plays a weakening role on the incoming flow and wake diffusion, which can reduce the pressure on the roof. Secondly, the influence of size effect changes produced by the flow passing over the roof.
4) It is important to note that the above results require further verification through wind tunnel tests or on-site measurements. In future research, the authors will consider these two methods, which can provide a more comprehensive study of the building. Additionally, wind resistance design of structures includes the calculation of many important parameters; the authors hope to analyze these parameters in future calculations.

References

1. Blackmore, P.A. & Tsokri, E. (2006). Wind loads on curved roofs. *Journal of Wind Engineering and Industrial Aerodynamics*, *94*(11), 833–844. https://doi.org/10.1016/j.jweia.2006.06.006
2. del Coz Díaz, J.J., García Nieto, P.J., Vilán Vilán, J.A., Alvarez Rabanal, F.P., Navarro-Manso, A., & Alonso-Martínez, M. (2013). Nonlinear analysis of the pressure field in industrial buildings with curved metallic roofs due to the wind effect by FEM. *Applied Mathematics and Computation*, *221*, 202–213. https://doi.org/10.1016/j.amc.2013.06.067
3. Esfeh, M.K., Sohankar, A., Shahsavari, A.R., Rastan, M.R., Ghodrat, M., & Nili, M. (2021). Experimental and numerical evaluation of wind-driven natural ventilation of a curved roof for various wind angles. *Building and Environment*, *205*, Article 108275. https://doi.org/10.1016/j.buildenv.2021.108275
4. GB 50009-2012 (2012). *Load code for the design of building structures*. China Architecture & Building Press.
5. JGJ/T 481-2019 (2020). *Standard for wind loads on roof structures*. Ministry of Housing and Urban-Rural Development of the People's Republic of China, Beijing.
6. Kim, R., Lee, I., Yeo, U., & Lee, S. (2019). Estimating the wind pressure coefficient for single-span greenhouses using an large eddy simulation turbulence model. *Biosystems Engineering*, *188*, 114–135. https://doi.org/10.1016/j.biosystemseng.2019.10.009
7. Li, F., Ni, Z., & Shen, S. (2007). Characteristics of wind pressure on typical roofs under different terrain conditions (in Chinese). *Journal of Building Structures*, *28*(1), 119–124. https://doi.org/10.14006/j.jzjgxb.2007.01.017
8. Li, Y., Hu, W., & Wang, L. (2010). State-of-art: wind tunnel investigation on wind pressure distribution of large-span spatial structures with typical shapes (in Chinese). *Acta Aerodynamica Sinica*, *28*(1), 32–38.
9. Li, Y., Yukio, T., & Shen, Z. (2006). Wind tunnel test for wind pressure distribution characteristics of cylindrical shells (in Chinese). *Journal of Tongji University (Natural Science)*, *34*, 1457–1464.
10. Ma, R. & He, M. (2006). Discussion on concept design of long span special steel roof structures (in Chinese). *Journal of Building Structures*, *27*(4), 61–64. https://doi.org/10.14006/j.jzjgxb.2006.04.009
11. Meng, F.Q., He, B.J., Zhu, J., Zhao, D.X., Darko, A., & Zhao, Z.Q. (2018). Sensitivity analysis of wind pressure coefficients on CAARC standard tall buildings in CFD simulations. *Journal of Building Engineering*, *16*, 146–158. https://doi.org/10.1016/j.jobe.2018.01.004

12. Pagnini, L., Torre, S., Freda, A., & Piccardo, G. (2022). Wind pressure measurements on a vaulted canopy roof. *Journal of Wind Engineering and Industrial Aerodynamics*, *223*, Article 104934. https://doi.org/10.1016/j.jweia.2022.104934

13. Paluch, M.J., Loredo-Souza, A.M., & Blessmann, J. (2003). Wind loads on attached canopies and their effect on the pressure distribution over arch-roof industrial buildings. *Journal of Wind Engineering and Industrial Aerodynamics*, *91*(8), 975–994. https://doi.org/10.1016/S0167-6105(03)00047-3

14. Sun, W. & Zhang, Q. (2020). Universal equivalent static wind loads of fluctuating wind loads on large-span roofs based on compensation of structural frequencies and modes. *Structures*, *26*, 92–104. https://doi.org/10.1016/j.istruc.2020.04.008

15. Tian, Y., Guan, H., Shao, S., & Yang, Q. (2021). Provisions and comparison of Chinese wind load standard for roof components and cladding. *Structures*, *33*, 2587–2598. https://doi.org/10.1016/j.istruc.2021.06.011

16. Wang, Y., Liu, H., Lei, M., Chen, Z., Tse, T.K.T., Li, C.Y., & Fu, Y. (2023). Aerodynamic analysis of an ultra-long and ultra-wide industrial building under wind loading: Insights into flow dynamics and pressure distribution characteristics. *Journal of Building Engineering*, *76*, Article 107144. https://doi.org/10.1016/j.jobe.2023.107144

17. Zhang, G., Zhang, Q., Fan, F., & Shen, S. (2021). Numerical simulations of snowdrift characteristics on multi-span arch roofs. *Journal of Wind Engineering and Industrial Aerodynamics*, *212*, Article 104593. https://doi.org/10.1016/j.jweia.2021.104593

Manuscript received May 10, 2024; accepted for publication January 22, 2025; published online April 5, 2025.

JOURNAL OF THEORETICAL
AND APPLIED MECHANICS
63, 2, pp. 349–361, Warsaw 2025
https://doi.org/10.15632/jtam-pl/200621

DIFFRACTION OF PLANE *P*-WAVE BY AN UNDERWATER TUNNEL

Jia HA, Guochao LI*, Mingjian YU, Chong NIU, Wanwan FU

Yellow River Engineering Consulting Co., Ltd., Zhengzhou 450003, China
*corresponding author, *algcycg@163.com*

In this investigation, the traditional seismic response problem of tunnels in single-phase and saturated soil under the incidence of plane waves is extended to the ground motion problem considering the overlying water. Firstly, the site model of underwater tunnel under plane *P*-wave incidence is established. Then, the influence of thermal physical parameters such as incident angle, incident frequency and porosity on the ground motion of an underwater tunnel is studied using the Fourier–Bessel series expansion method of the wave function, which provides a reasonable explanation for the ground motion of an underwater site.

Keywords: saturated soil; underwater tunnel; scattering; plane *P*-wave; wave propagation.

1. Introduction

As a result of the scarcity of land resources, many cities began to focus on constructing underground facilities. With the construction of ocean engineering, an increasing number of scholars have begun to pay attention to the study of the effect of ground motion on underwater sites. The underwater tunnel is a significant transport terminal-junction. If damaged by the earthquake, it would inevitably cause significant property damage. The essence of the research on the impact of the underwater tunnel on ground motion is to examine the diffraction of the elastic wave, which can simulate the influence of seismic waves on various linear structures. Accordingly, it is significant to investigate the diffraction of seismic waves by underwater tunnels and to examine the influence of topographic conditions on ground motion and the ground motion of underground sites considering local geological structures.

Currently, many scholars have conducted the analysis and research on seismic response problems and achieved important scientific research results. Pao and Mow pioneered the use of the wave function expansion method to investigate the DSCF of a hole in the whole space under seismic wave incidence (Achenbach, 1973). Subsequently, Lee and Karl (1992) extended the method to half space and investigated the analytical solution of plane wave diffraction through a cavity. Luco and de Barros (1994) obtained the two-dimensional response of a circular cavity in a viscoelastic half-space under the action of plane *P*-wave, *SH*-wave, *SV*-wave, and the Rayleigh wave based on the two-dimensional Green's function and the indirect boundary integral method. Gomes *et al.* (2015) investigated the scattering of seismic waves by a circular tunnel in two layers of linear elastic soil using the finite element method. Liang *et al.* (2023) investigated the scattering of plane *SH*-waves by a circular tunnel in a nonlocal fractional-order viscoelastic half-space by using the complex variable function method.

However, the contents of the above research are the scattering law in the single-phase foundation, without considering the influence of other factors in soil. In fact, owing to the presence of groundwater and air, the state of soil is closer to saturated or unsaturated soil. Subsequently, on the basis of the Biot theory of porous media (Biot *et al.*, 1956a; 1956b), the diffraction of

elastic waves in saturated soil sites has been extensively investigated. Kattis *et al.* (2003) used the boundary integral method to solve the scattering problem of elastic waves by lining and unlined caverns in a saturated full space. Xu *et al.* (2019) investigated the diffraction of a plane wave by a lining tunnel on the basis of the nonlocal Biot theory. Liu *et al.* (2017) made use of the indirect boundary element method (IBEM) to investigate the diffraction for the plane P-wave by a tunnel. Ding *et al.* (2020) gave the analytical solution of the seismic response of lining tunnels under P-wave incidence. Ba *et al.* (2022) used IBEM to investigate the diffraction of a tunnel in a layered site. Xiang *et al.* (2024) investigated the seismic response of the water-rich tunnel under P-wave incidence. Tan *et al.* (2020) used the wave function expansion method to investigate the scattering problem of a plane dilatational wave disturbed by a lined tunnel with an imperfect interface embedded in an infinite unsaturated poro-elastic solid. Yue and Liu (2023) solved the scattering problem of P- and SV-waves by lining tunnels in unsaturated soil using the method of complex variable function. Zhao *et al.* (2024) investigated the scattering of plane P-waves by unlined and single-layer lined tunnels in unsaturated soils using the Fourier–Bessel expansion method of wave functions. The diffraction of local topography under plane wave incidence has been widely investigated (Ma *et al.*, 2023). The above research shows that the diffraction of local topography in porous elastic media is quite different in single-phase media. Therefore, the multiphase effect of soil cannot be ignored in the investigation of seismic response.

It can be seen that the diffraction of plane waves by a single-layer soil foundation has been widely investigated, but there are few investigations on underwater sites. Therefore, it is of engineering significance to research the diffraction of elastic waves by tunnels in underwater saturated soil sites. On the basis of the Biot theory of saturated porous elastic medium, the diffraction law for the P-wave around the underwater tunnel is investigated using the Fourier–Bessel series expansion method of the wave function. Through numerical examples, the effect of incident wave frequency, angle, porosity and buried depth on the displacement amplitude of dynamic stress concentration factor at the water-soil interface and tunnel surface in the underwater tunnel is analyzed.

2. Materials and methods

The underwater tunnel site model is shown in Fig. 1, using the rectangular coordinate system and cylindrical coordinate. The radius and buried depth for the tunnel are a and d, respectively, and the thickness of the water layer is h. The soil medium is saturated porous medium.

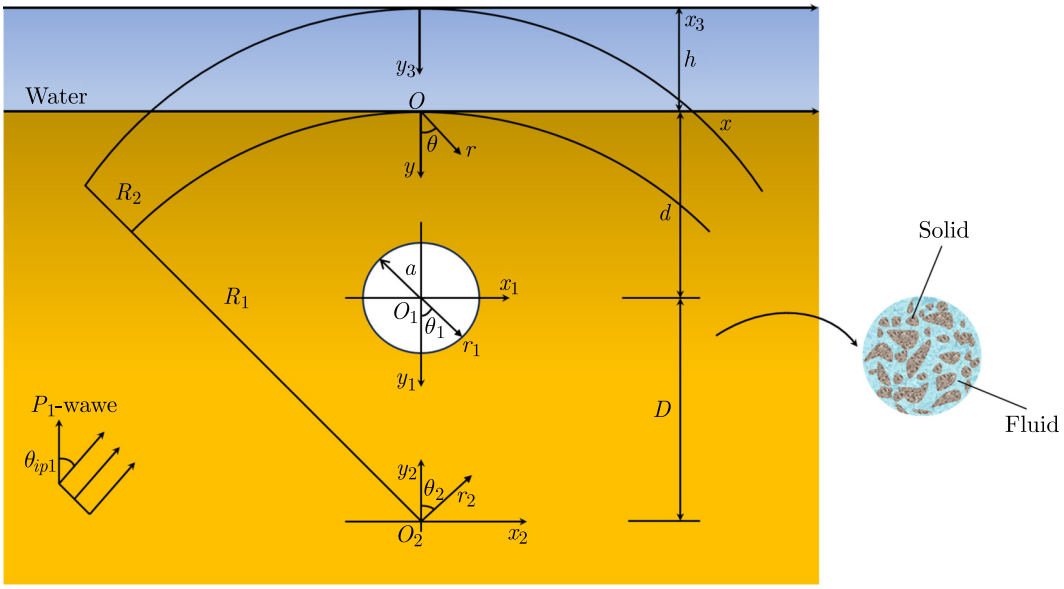

Fig. 1. Model of circular underwater tunnel site.

The constitutive equation and motion equation for the fluid are as follows:

– the constitutive equation:

$$-P_W = K_W \nabla \cdot \mathbf{U}_W, \tag{2.1}$$

– motion equation:

$$K_W \nabla\nabla \cdot \mathbf{U}_W = \rho_W \ddot{\mathbf{U}}_W, \tag{2.2}$$

where P_W is the hydrodynamic pressure of water; K_W denotes the bulk modulus of water; ρ_W denotes the density of water; $\mathbf{U}_W$ denotes the displacement vector of water.

The displacement vector $\mathbf{U}_W$ of the water layer can be written as

$$\mathbf{U}_W = \nabla \varphi_W. \tag{2.3}$$

Equations (2.1) and (2.2) could be expressed by potential functions:

$$-P_W = K_W \nabla^2 \varphi_W, \tag{2.4}$$

$$K_W \nabla^2 \varphi_W = \rho_W \ddot{\varphi}_W^2. \tag{2.5}$$

The wave velocity and wave number of a compression wave in the water layer could be written as

$$c_W = \sqrt{K_W / \rho_W}, \tag{2.6}$$

$$k_W = 2\pi f \sqrt{\rho_W / K_W}. \tag{2.7}$$

For the establishment of the wave equation of saturated soil, referring to the modified Biot model proposed by Zhou *et al.* (2013), which ignores the mass coupling coefficient and considers the compressibility of soil particles and pore fluid, the wave equation of saturated soil is derived from the basic equation of homogeneous saturated porous media.

The wave equation of saturated soil is

$$\mu \nabla^2 u^s + \operatorname{grad}\left[(\mu + \lambda + \alpha^2 M)\theta\right] - \operatorname{grad}(\alpha M \zeta) = \rho \ddot{u}^s + \rho^f \ddot{u}^f, \tag{2.8}$$

$$\operatorname{grad}(\alpha M \theta - M\zeta) = \rho^f \ddot{u}^s + m\ddot{u}^f + b\dot{u}^f. \tag{2.9}$$

According to the Helmholtz vector decomposition theorem, the displacement vector in saturated soil could be expressed as

$$u^s = \nabla \varphi_s + \nabla \times \psi_s, \qquad u^f = \nabla \varphi_f + \nabla \times \psi_f. \tag{2.10}$$

In saturated soil, there are two kinds of compression wave P-waves and one kind of shear wave SV-wave. When P-wave is incident, the circular frequency is ω and the incident angle is θ_{ip1}. The incident wave could be indicated as

$$\varphi_i^\iota(x, y) = A_{ip1}^\iota \exp\left[\mathrm{i}k_{ip1}(x \sin\theta_{ip1} - y \cos\theta_{ip1}) - \mathrm{i}\omega t\right], \tag{2.11}$$

where k_{ip1} is the wave number of P_1-wave, $i = \sqrt{-1}$. $\exp(\mathrm{i}\omega t)$ is left out for simplicity, the aforementioned equations could be expressed as

$$\varphi_i^\iota(x, y) = A_{ip1}^\iota \exp\left[\mathrm{i}k_{ip1}(x \sin\theta_{ip1} - y \cos\theta_{ip1})\right]. \tag{2.12}$$

P-wave will produce reflected P_1-, P_2-, and SV-waves at the water-soil interface, and produce the transmitted P-wave and reflected P-wave in the water. The wave potential functions could be written as

– in saturated soil:

$$\varphi_{rp1}^{\iota}(x,y) = A_{rp1}^{\iota} \exp\left[\mathrm{i}k_{rp1}(x\sin\theta_{rp1} + y\cos\theta_{rp1})\right], \tag{2.13}$$

$$\varphi_{rp2}^{\iota}(x,y) = A_{rp2}^{\iota} \exp\left[\mathrm{i}k_{rp2}(x\sin\theta_{rp2} + y\cos\theta_{rp2})\right], \tag{2.14}$$

$$\psi_{rs}^{\iota}(x,y) = B_{rs}^{\iota} \exp\left[\mathrm{i}k_{rs}(x\sin\theta_{rs} + y\cos\theta_{rs})\right], \tag{2.15}$$

where k_{rp1}, k_{rp2}, and k_{rs} represent the wavenumbers of reflected P_1-, P_2-, and S-wave, respectively; θ_{rp1}, θ_{rp2}, and θ_{rs} represent the reflection angles. A_{rp1}^{ι}, A_{rp2}^{ι}, and B_{rs}^{ι} represent the amplitude for the reflected waves in ι phase media and $\delta_{L1} = A_{rp1}^{f}/A_{rp1}^{s}$, $\delta_{L2} = A_{rp2}^{f}/A_{rp2}^{s}$.

– in the water layer:

a) transmission P-wave:

$$\varphi_{i}^{w}(x,y) = A_{tp}^{w} \exp\left[\mathrm{i}k_{w}(x_3\sin\theta_{w} - y_3\cos\theta_{w})\right], \tag{2.16}$$

b) reflected P-wave:

$$\varphi_{rp}^{w}(x,y) = A_{rp}^{w} \exp\left[\mathrm{i}k_{rp}(x_3\sin\theta_{w} + y_3\cos\theta_{w})\right], \tag{2.17}$$

where A_{tp}^{w} and A_{rp}^{w} are the amplitude coefficients of the transmitted and the reflected P-waves, respectively, k_w is the wave number of the P-wave in the water, θ_w is the reflection angle of the P-wave in the water layer.

For the convenience of analysis, it can be expressed as follows in cylindrical coordinates:

$$\varphi_{1}^{\iota}(r_1,\theta_1) = A_{ip1}^{\iota} \exp\left(\mathrm{i}dk_{ip1}\cos\theta_{ip1}\right) \exp\left[-\mathrm{i}k_{ip1}r_1\cos(\theta_1 + \theta_{ip1})\right], \tag{2.18}$$

$$\varphi_{rp1}^{\iota}(r_1,\theta_1) = A_{rp1}^{\iota} \exp\left(-\mathrm{i}dk_{rp1}\cos\theta_{rp1}\right) \exp\left[\mathrm{i}k_{rp1}r_1\cos(\theta_1 - \theta_{rp1})\right], \tag{2.19}$$

$$\varphi_{rp2}^{\iota}(r_1,\theta_1) = A_{rp2}^{\iota} \exp\left(-\mathrm{i}dk_{rp2}\cos\theta_{rp2}\right) \exp\left[\mathrm{i}k_{rp2}r_1\cos(\theta_1 - \theta_{rp2})\right], \tag{2.20}$$

$$\psi_{rs}^{\iota}(r_1,\theta_1) = B_{rs}^{\iota} \exp\left(-\mathrm{i}dk_{rs}\cos\theta_{rs}\right) \exp\left[\mathrm{i}k_{rs}r_1\cos(\theta_1 - \theta_{rs})\right], \tag{2.21}$$

$$\varphi_{i}^{w}(x,y) = A_{ip}^{w} \exp\left[\mathrm{i}k_{w}(d+h)\cos\theta_{w}\right] \exp\left[-\mathrm{i}k_{w}\cos(\theta_1 + \theta_{w})\right], \tag{2.22}$$

$$\varphi_{r}^{w}(x,y) = A_{rp}^{w} \exp\left[\text{-}\mathrm{i}k_{w}(d+h)\cos\theta_{w}\right] \exp\left[\mathrm{i}k_{w}\cos(\theta_1 - \theta_{w})\right]. \tag{2.23}$$

The aforementioned equation is expanded into the Fourier–Bessel series form:

$$\varphi_{i+rp1}^{\iota}(r_1,\theta_1) = \sum_{n=0}^{\infty} J_n(k_{ip1}r_1)(C_{01,n}\cos n\theta_1 + D_{01,n}\sin n\theta_1), \tag{2.24}$$

$$\varphi_{rp2}^{\iota}(r_1,\theta_1) = \sum_{n=0}^{\infty} J_n(k_{rp2}r_1)(C_{02,n}\cos n\theta_1 + D_{02,n}\sin n\theta_1), \tag{2.25}$$

$$\varphi_{rp3}^{\iota}(r_1,\theta_1) = \sum_{n=0}^{\infty} J_n(k_{rp3}r_1)(C_{03,n}\cos n\theta_1 + D_{03,n}\sin n\theta_1), \tag{2.26}$$

$$\varphi_{i+r}^{w}(r_1,\theta_1) = \sum_{n=0}^{\infty} J_n(k_{w}r_1)(C_{04,n}\cos n\theta_1 + D_{04,n}\cos n\theta_1). \tag{2.27}$$

There are scattered P_1-, P_2-, and SV-waves caused by the tunnel in the saturated soil layer, and scattered P_1-, P_2-, and SV-waves caused by the large arc approximation. The scattered wave

field in a half space could be represented by the Fourier–Bessel series. In the r_1-θ_1 coordinate system, since the scattered wave fields generated by large arcs satisfy the Sommerfeld condition at infinity, their potential functions can be written as the Fourier–Bessel series:

– in saturated soil:

$$\varphi_{dp1}^{\iota}(r_1,\theta_1)=\sum_{n=0}^{\infty}H_n^{(1)}(k_{rp1}r_1)\left(C_{11,n}^{(1)}\cos n\theta_1+D_{11,n}^{(1)}\sin n\theta_1\right), \tag{2.28}$$

$$\varphi_{dp2}^{\iota}(r_1,\theta_1)=\sum_{n=0}^{\infty}H_n^{(1)}(k_{rp2}r_1)\left(C_{12,n}^{(1)}\cos n\theta_1+D_{12,n}^{(1)}\sin n\theta_1\right), \tag{2.29}$$

$$\psi_{ds}^{\iota}(r_1,\theta_1)=\sum_{n=0}^{\infty}H_n^{(1)}(k_{rs}r_1)\left(C_{14,n}^{(1)}\sin n\theta_1+D_{14,n}^{(1)}\cos n\theta_1\right), \tag{2.30}$$

where $J_m(\ )$ and $H_n^{(1)}(\ )$ are the Bessel functions and the Hankel functions, respectively.

The aforementioned equations are established in the (r_1,θ_1) coordinate system, it cannot satisfy the boundary conditions of the water-soil interface and the water layer surface. In this research, the water-soil interface and the free surface of the water layer are simulated by using an arc centred on O_2 (as shown in Fig. 1). Accordingly, the solution in the research is the approximate analytical solution. The research proves that: if the radius of the arc R is sufficiently large ($R>50a$), the error of the calculation result is rather small, and the appropriate result could be obtained.

In the r_2-θ_2 coordinate system, the potential function of the wave generated by the large arc boundary is expressed as follows:

– in saturated soil:

$$\varphi_{ap1}^{\iota}(r_2,\theta_2)=\sum_{m=0}^{\infty}J_m(k_{rp1}r_2)\left(C_{21,n}^{(2)}\cos m\theta_2+D_{21,n}^{(2)}\sin m\theta_2\right), \tag{2.31}$$

$$\varphi_{\mathrm{ap2}}^{\iota}(r_2,\theta_2)=\sum_{m=0}^{\infty}J_m(k_{rp2}r_2)\left(C_{22,n}^{(2)}\cos m\theta_2+D_{22,n}^{(2)}\sin m\theta_2\right), \tag{2.32}$$

$$\psi_{as}^{\iota}(r_2,\theta_2)=\sum_{m=0}^{\infty}J_m(k_{rs}r_2)\left(C_{24,n}^{(2)}\sin m\theta_2+D_{24,n}^{(2)}\cos m\theta_2\right), \tag{2.33}$$

– in the water layer:

$$\varphi_{a1}^{w}(r_2,\theta_2)=\sum_{m=0}^{\infty}J_m(k_wr_2)\left(C_{31,m}^{(2)}\cos m\theta_2+D_{31,m}^{(2)}\sin m\theta_2\right), \tag{2.34}$$

$$\varphi_{a2}^{w}(r_2,\theta_2)=\sum_{m=0}^{\infty}H_m(k_wr_2)\left(C_{32,n}^{(2)}\cos m\theta_2+D_{32,n}^{(2)}\sin m\theta_2\right). \tag{2.35}$$

The total wave potential function can be expressed as follows:

– in saturated soil:

$$\varphi^{\iota}=\varphi_{ip1}^{\iota}+\varphi_{rp1}^{\iota}+\varphi_{rp2}^{\iota}+\varphi_{dp1}^{\iota}+\varphi_{dp2}^{\iota}+\varphi_{ap1}^{\iota}+\varphi_{ap2}^{\iota}, \tag{2.36}$$

$$\psi^{\iota}=\psi_{rs}^{\iota}+\psi_{ds}^{\iota}+\psi_{as}^{\iota}, \tag{2.37}$$

– in the water layer:

$$\varphi^{w}=\varphi_{i}^{w}+\varphi_{r}^{w}+\varphi_{a1}^{w}+\varphi_{a2}^{w}. \tag{2.38}$$

Before introducing the boundary conditions, it is necessary to use the Graf addition formula to unify the coordinates for the wave functions:

$$C_n\left(kr_2\right)\left\{\begin{array}{c}\cos n\theta_2\\ \sin n\theta_2\end{array}\right\}=\sum_{m=-\infty}^{m=+\infty}C_{m+n}\left(kD\right)J_m\left(kr_1\right)\left\{\begin{array}{c}\cos m\theta_1\\ \sin m\theta_1\end{array}\right\}, \tag{2.39}$$

where D is the distance from O_1 point to O_2 point, as shown in Fig. 1, $C_n(\ )$ can be $J_n(\ )$ function or $H_n^{(1)}(\ )$ function.

Therefore, the coordinate transformation of Eqs. (2.28)–(2.43) can be obtained:

$$\varphi_{dp1}^{\iota}(r_2,\theta_2)=\sum_{m=0}^{\infty}J_m(k_{rp1}r_2)\left(C_{11,n}^{(2)}\cos m\theta_2+D_{11,n}^{(2)}\sin m\theta_2\right), \tag{2.40}$$

$$\varphi_{dp2}^{\iota}(r_2,\theta_2)=\sum_{m=0}^{\infty}J_m(k_{rp2}r_2)\left(C_{12,n}^{(2)}\cos m\theta_2+D_{12,n}^{(2)}\sin m\theta_2\right), \tag{2.41}$$

$$\psi_{ds}^{\iota}(r_2,\theta_2)=\sum_{m=0}^{\infty}J_m(k_{rs}r_2)\left(C_{14,n}^{(2)}\sin m\theta_2+D_{14,n}^{(2)}\cos m\theta_2\right), \tag{2.42}$$

$$\varphi_{ap1}^{\iota}(r_1,\theta_1)=\sum_{n=0}^{\infty}J_n(k_{rp1}r_1)\left(C_{21,n}^{(1)}\cos n\theta_1+D_{21,n}^{(1)}\sin n\theta_1\right), \tag{2.43}$$

$$\varphi_{ap2}^{\iota}(r_1,\theta_1)=\sum_{n=0}^{\infty}J_n(k_{rp2}r_1)\left(C_{22,n}^{(1)}\cos n\theta_1+D_{22,n}^{(1)}\sin n\theta_1\right), \tag{2.44}$$

$$\psi_{as}^{\iota}(r_1,\theta_1)=\sum_{n=0}^{\infty}J_n(k_{rs}r_1)\left(C_{24,n}^{(1)}\sin n\theta_1+D_{24,n}^{(1)}\cos n\theta_1\right), \tag{2.45}$$

$$\varphi_{a1}^{w}(r_1,\theta_1)=\sum_{n=0}^{\infty}J_n(k_wr_1)\left(C_{31,n}^{(1)}\cos n\theta_1+D_{31,n}^{(1)}\sin n\theta_1\right), \tag{2.46}$$

$$\varphi_{a2}^{w}(r_1,\theta_1)=\sum_{m=0}^{\infty}J_m(k_wr_1)\left(C_{32,m}^{(1)}\cos m\theta_1+D_{32,m}^{(1)}\sin m\theta_1\right), \tag{2.47}$$

where

$$\left[\begin{array}{c}C_{11,m}^{(2)}\\ C_{12,m}^{(2)}\\ D_{13,m}^{(2)}\end{array}\right]=\sum_{n=0}^{\infty}\left[\begin{array}{ccc}F2_{nm}^{+}(k_{rp1}D) & & \\ & F2_{nm}^{+}(k_{rp2}D) & \\ & & F2_{nm}^{+}(k_{rs}D)\end{array}\right]\left[\begin{array}{c}C_{11,n}^{(1)}\\ C_{12,n}^{(1)}\\ D_{13,n}^{(1)}\end{array}\right], \tag{2.48}$$

$$\left[\begin{array}{c}D_{11,m}^{(2)}\\ D_{12,m}^{(2)}\\ C_{13,m}^{(2)}\end{array}\right]=\sum_{n=0}^{\infty}\left[\begin{array}{ccc}F2_{nm}^{-}(k_{rp1}D) & & \\ & F2_{nm}^{-}(k_{rp2}D) & \\ & & F2_{nm}^{-}(k_{rs}D)\end{array}\right]\left[\begin{array}{c}D_{11,n}^{(1)}\\ D_{12,n}^{(1)}\\ C_{13,n}^{(1)}\end{array}\right], \tag{2.49}$$

$$\left[\begin{array}{c}C_{21,n}^{(1)}\\ C_{22,n}^{(1)}\\ C_{31,n}^{(1)}\\ C_{32,n}^{(1)}\\ D_{23,n}^{(1)}\end{array}\right]=\sum_{n=0}^{\infty}\left[\begin{array}{ccccc}F1_{nm}^{+}(k_{rp1}D) & & & & \\ & F1_{nm}^{+}(k_{rp2}D) & & & \\ & & F1_{nm}^{+}(k_wD) & & \\ & & & F1_{nm}^{+}(k_wD) & \\ & & & & F1_{nm}^{+}(k_{rs}D)\end{array}\right]\left[\begin{array}{c}C_{21,m}^{(2)}\\ C_{22,m}^{(2)}\\ C_{31,m}^{(1)}\\ C_{32,m}^{(1)}\\ D_{23,m}^{(2)}\end{array}\right], \tag{2.50}$$

$$\begin{bmatrix} D_{21,n}^{(1)} \\ D_{22,n}^{(1)} \\ D_{31,n}^{(1)} \\ D_{32,n}^{(1)} \\ C_{23,n}^{(1)} \end{bmatrix} = \sum_{n=0}^{\infty} \begin{bmatrix} F1_{nm}^{-}(k_{rp1}D) & & & & \\ & F1_{nm}^{-}(k_{rp2}D) & & & \\ & & F1_{nm}^{-}(k_wD) & & \\ & & & F1_{nm}^{-}(k_wD) & \\ & & & & F1_{nm}^{-}(k_{rs}D) \end{bmatrix} \begin{bmatrix} D_{21,m}^{(2)} \\ D_{22,m}^{(2)} \\ D_{31,m}^{(1)} \\ D_{32,m}^{(1)} \\ C_{23,m}^{(2)} \end{bmatrix}, \tag{2.51}$$

where

$$F1_{nm}^{\pm}(kD) = \frac{1}{2}\varepsilon_n[J_{n+m}(kD) \pm (-1)^m J_{n-m}(kD)],$$

$$F2_{nm}^{\pm}(kD) = \frac{1}{2}\varepsilon_m[H_{m+n}(kD) \pm (-1)^n H_{m-n}(kD)].$$

This research assumes that the surface and the tunnel surface are permeable boundaries, and the boundary conditions are as follows:

– on the surface of the water $y = 0$:

$$\sigma_{rr}^{w} = 0, \tag{2.52}$$

– on the tunnel surface $r_1 = a$:

$$\sigma_{rr}^{S} = 0, \qquad \sigma_{r\theta}^{S} = 0, \qquad \sigma_{rr}^{L} = 0, \tag{2.53}$$

– at the soil-water interface $r_2 = R_1$:

$$(1-n)u_r^S + nu_r^L = u_r^w, \qquad \sigma_{rr}^S + \sigma_{rr}^L = -\sigma_{rr}^w, \qquad \sigma_{rr}^L = -n\sigma_{rr}^w, \quad \sigma_{r\theta}^S = 0. \tag{2.54}$$

Bringing Eq. (2.46) and Eq. (2.47) into the boundary condition (2.52):

$$\sum_{m=0}^{\infty} \begin{bmatrix} E_{11}^{w(1)}(m,R_2) & E_{12}^{w(2)}(m,R_2) \end{bmatrix} \begin{Bmatrix} C_{31,m}^{(2)} \\ C_{32,m}^{(2)} \end{Bmatrix} \{\cos m\theta_2\} + \sum_{m=0}^{\infty} \begin{bmatrix} E_{21}^{w(1)}(m,R_2) & E_{22}^{w(2)}(m,R_2) \end{bmatrix} \begin{Bmatrix} D_{31,m}^{(2)} \\ D_{32,m}^{(2)} \end{Bmatrix} \{\sin m\theta_2\} = \{0\}. \tag{2.55}$$

Bringing Eq. (2.28)–(2.30) and Eq. (2.43)–(2.53) into the boundary condition (2.53):

$$\sum_{m=0}^{\infty} \begin{bmatrix} U_{111}^{s(3)}(n,a) & U_{112}^{s(3)}(n,a) & U_{113}^{s(3)+}(n,a) \\ U_{211}^{s(3)-}(n,a) & U_{212}^{s(3)-}(n,a) & U_{213}^{s(3)}(n,a) \\ U_{311}^{s(3)}(n,a) & U_{312}^{s(3)}(n,a) & 0 \end{bmatrix} \begin{Bmatrix} C_{11,n}^{(1)} \\ C_{12,n}^{(1)} \\ C_{13,n}^{(1)} \end{Bmatrix} \begin{Bmatrix} \cos n\theta_1 \\ \sin n\theta_1 \\ \cos n\theta_1 \end{Bmatrix}$$

$$+ \sum_{m=0}^{\infty} \begin{bmatrix} U_{111}^{s(1)}(n,a) & U_{112}^{s(1)}(n,a) & U_{113}^{s(1)+}(n,a) \\ U_{211}^{s(1)-}(n,a) & U_{212}^{s(1)-}(n,a) & U_{213}^{s(1)}(n,a) \\ U_{311}^{s(1)}(n,a) & U_{312}^{s(1)}(n,a) & 0 \end{bmatrix} \begin{Bmatrix} C_{21,n}^{(1)} + C_{01,n} \\ C_{22,n}^{(1)} + C_{02,n} \\ C_{23,n}^{(1)} + C_{03,n} \end{Bmatrix} \begin{Bmatrix} \cos n\theta_1 \\ \sin n\theta_1 \\ \cos n\theta_1 \end{Bmatrix}$$

$$+ \sum_{m=0}^{\infty} \begin{bmatrix} U_{111}^{s(3)}(n,a) & U_{112}^{s(3)}(n,a) & U_{113}^{s(3)-}(n,a) \\ U_{211}^{s(3)+}(n,a) & U_{212}^{s(3)+}(n,a) & U_{213}^{s(3)}(n,a) \\ U_{311}^{s(3)}(n,a) & U_{312}^{s(3)}(n,a) & 0 \end{bmatrix} \begin{Bmatrix} D_{11,n}^{(1)} \\ D_{12,n}^{(1)} \\ D_{13,n}^{(1)} \end{Bmatrix} \begin{Bmatrix} \sin n\theta_1 \\ \cos n\theta_1 \\ \sin n\theta_1 \end{Bmatrix}$$

$$+ \sum_{m=0}^{\infty} \begin{bmatrix} U_{111}^{s(1)}(n,a) & U_{112}^{s(1)}(n,a) & U_{113}^{s(1)}\text{-}(n,a) \\ U_{211}^{s(1)+}(n,a) & U_{212}^{s(1)+}(n,a) & U_{213}^{s(1)}(n,a) \\ U_{311}^{s(1)}(n,a) & U_{312}^{s(1)}(n,a) & 0 \end{bmatrix} \begin{Bmatrix} D_{21,n}^{(1)} + D_{01,n} \\ D_{22,n}^{(1)} + D_{02,n} \\ D_{23,n}^{(1)} + D_{03,n} \end{Bmatrix} \begin{Bmatrix} \sin n\theta_1 \\ \cos n\theta_1 \\ \sin n\theta_1 \end{Bmatrix} = \begin{Bmatrix} 0 \\ 0 \\ 0 \end{Bmatrix}. \tag{2.56}$$

Bringing Eqs. (2.31)–(2.33) and Eqs. (2.40)–(2.42) into the boundary condition (2.54):

$$\sum_{m=0}^{\infty}\begin{bmatrix} E_{111}^{(s1)} & E_{112}^{(s1)} & E_{113}^{(s1)+} \\ E_{211}^{(s1)} & E_{212}^{(s1)} & E_{213}^{(s1)+} \\ E_{311}^{(s1)} & E_{312}^{(s1)} & 0 \\ E_{411}^{(s1)+} & E_{412}^{(s1)+} & E_{413}^{(s1)} \end{bmatrix}\begin{Bmatrix} C_{11,m}^{(2)}+C_{21,m}^{(2)} \\ C_{12,m}^{(2)}+C_{22,m}^{(2)} \\ C_{13,m}^{(2)}+C_{23,m}^{(2)} \end{Bmatrix}\begin{bmatrix} \cos m\theta_2 \\ \cos m\theta_2 \\ \cos m\theta_2 \\ \sin m\theta_2 \end{bmatrix}$$
$$+\sum_{m=0}^{\infty}\begin{bmatrix} E_{111}^{(s1)} & E_{112}^{(s1)} & E_{113}^{(s1)-} \\ E_{211}^{(s1)} & E_{212}^{(s1)} & E_{213}^{(s1)-} \\ E_{311}^{(s1)} & E_{312}^{(s1)} & 0 \\ E_{411}^{(s1)-} & E_{412}^{(s1)-} & E_{413}^{(s1)} \end{bmatrix}\begin{Bmatrix} D_{11,m}^{(2)}+D_{21,m}^{(2)} \\ D_{12,m}^{(2)}+D_{22,m}^{(2)} \\ D_{13,m}^{(2)}+D_{23,m}^{(2)} \end{Bmatrix}\begin{bmatrix} \sin m\theta_2 \\ \sin m\theta_2 \\ \sin m\theta_2 \\ \cos m\theta_2 \end{bmatrix}$$
$$+\sum_{m=0}^{\infty}\begin{bmatrix} V_{111}^{(s1)} \\ V_{211}^{(s1)} \\ V_{311}^{(s1)} \\ 0 \end{bmatrix}\left\{C_{31,m}^{(2)}\right\}\begin{bmatrix} \cos m\theta_2 \\ \cos m\theta_2 \\ \cos m\theta_2 \\ \sin m\theta_2 \end{bmatrix}+\sum_{m=0}^{\infty}\begin{bmatrix} V_{111}^{(s1)} \\ V_{211}^{(s1)} \\ V_{311}^{(s1)} \\ 0 \end{bmatrix}\left\{D_{31,m}^{(2)}\right\}\begin{bmatrix} \sin m\theta_2 \\ \sin m\theta_2 \\ \sin m\theta_2 \\ \cos m\theta_2 \end{bmatrix}$$
$$+\sum_{m=0}^{\infty}\begin{bmatrix} V_{111}^{(s2)} \\ V_{211}^{(s2)} \\ V_{311}^{(s2)} \\ 0 \end{bmatrix}\left\{C_{32,m}^{(2)}\right\}\begin{bmatrix} \cos m\theta_2 \\ \cos m\theta_2 \\ \cos m\theta_2 \\ \sin m\theta_2 \end{bmatrix}+\sum_{m=0}^{\infty}\begin{bmatrix} V_{111}^{(s2)} \\ V_{211}^{(s2)} \\ V_{311}^{(s2)} \\ 0 \end{bmatrix}\left\{D_{32,m}^{(2)}\right\}\begin{bmatrix} \sin m\theta_2 \\ \sin m\theta_2 \\ \sin m\theta_2 \\ \cos m\theta_2 \end{bmatrix}=\begin{Bmatrix} 0 \\ 0 \\ 0 \\ 0 \end{Bmatrix}, \quad (2.57)$$

where $i = 1$ and 3, $C_n^{(i)}$ is $J_n(x)$ and $H_n^{(1)}(x)$.

The coefficients can be obtained by combining Eqs. (2.55), (2.56), and (2.57).

3. Verification

Converting frequency into dimensionless frequency:

$$\eta = 2a/\lambda_\beta. \quad (3.1)$$

The astringency for the displacement field series could be determined in accordance with the Cauchy criterion:

$$e(n; r_1, \theta_1) = |u(n+1; r_1, \theta_1) - u(n; r_1, \theta_1)|. \quad (3.2)$$

You (2005) investigated the diffraction of P-wave by underground tunnels. For the purpose of validating the result of this research, the underwater tunnel model is degraded to an underground tunnel model in saturated soil. The detailed parameters are shown in (You, 2005), and compared to the displacement derived by You using the IBEM. It could be found out from Fig. 2a that the data is rather consistent, verifying the correctness of the solutions in this research.

In order to further verify the solution of this paper, the underwater tunnel is degraded into a saturated soil depression terrain, and compared with the surface displacement amplitude obtained by Ba (2006) using the large arc assumption. It can be seen from Fig. 2b that the two are in good agreement, which further verifies the correctness of the results in this paper.

If $R = 10^7 a$ it is ample to satisfy the accuracy requirements. The relationship between the error e and the truncation term number n is computed. Figure 3 shows the relationship from the x-, y-direction displacement error e_x, e_y to the n. To satisfy $e_x < 10^{-6}$, in Figs. 3a and 3b, n satisfies $n \geq 14$ and $n \geq 15$, respectively. To sum up, the number of astringency terms of the series is $n_c = 15$.

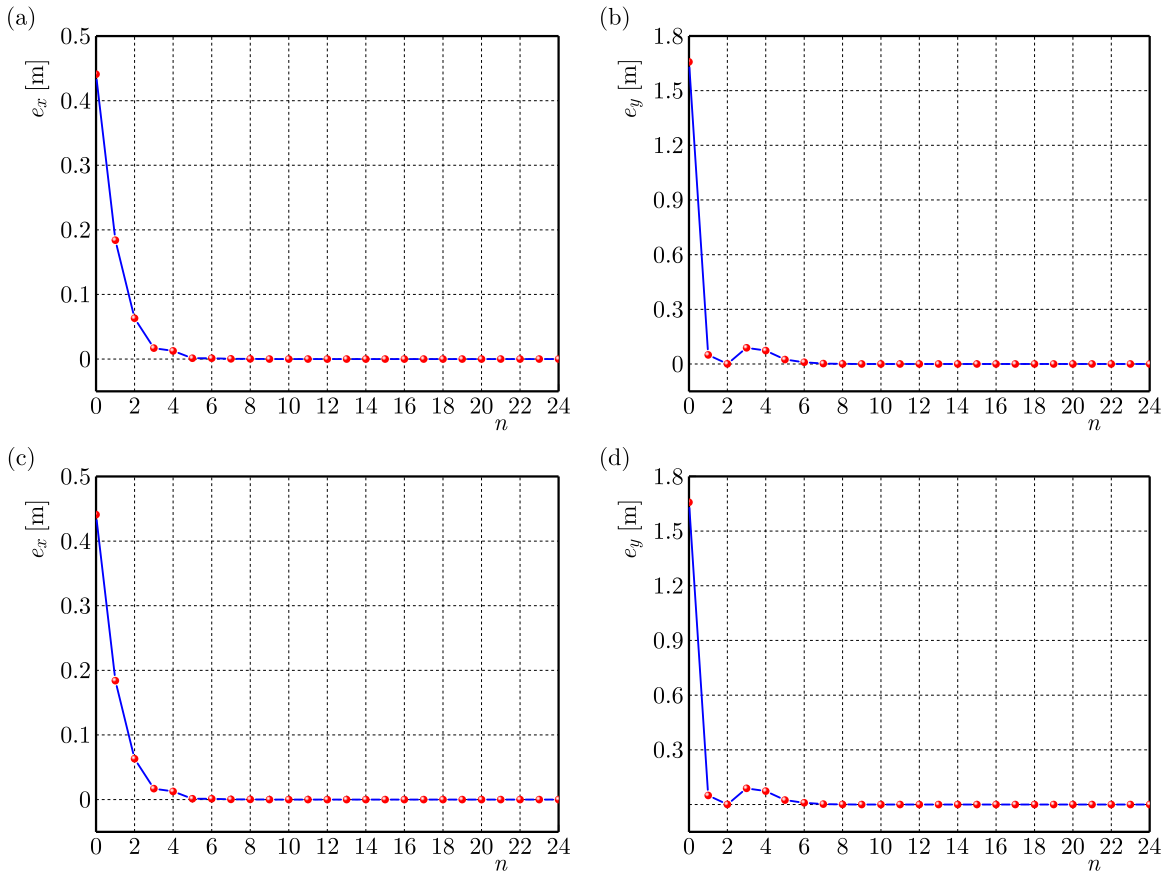

Fig. 2. Curve of error: (a) e_x ($x = 0$, $y = d$); (b) e_y ($x = 0$, $y = d$); (c) e_x ($x = \pm a$, $y = 0$); (d) e_x ($x = \pm a$, $y = 0$).

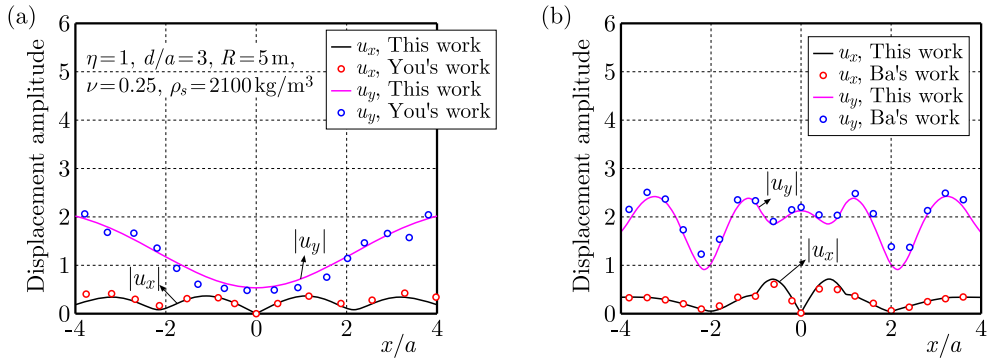

Fig. 3. Curve of comparative verification.

4. Analysis

The parameters (Zhang *et al.*, 2024) chosen in this research are exhibited in Table 1, the tunnel radius $a = 5$ m.

4.1. Impact of incident frequency on the diffraction of wave

Figure 4 shows the variety curves of the displacement amplitude at the water-soil interface and the DSCF of the tunnel surface when the incident angle $\theta_{ip1} = 30°$ and the incident wave frequencies are $\eta = 0.5$, 1, 2, respectively. It can be found out from the figure that the complex degree of the spatial pattern for the displacement increases along the frequency. The reason is

Table 1. Physical parameters.

Material parameters	Magnitude
Porosity n	0.3
Soil particle density ρ^S [kg/m^3]	2650
Liquid density ρ^L [kg/m^3]	1000
Bulk modulus of soil particles K_s [GPa]	36
Bulk modulus of liquid K_f [GPa]	2
Solid skeleton bulk modulus K [MPa]	43.6
Intrinsic permeability of the soil k [m^2]	3×10^{-13}
Viscosity coefficient of solid η^b [Pa · s]	1×10^{-3}
Permeability coefficient k^b [Pa · s]	1×10^{-10}
Lamé constant λ_S [MPa]	26.2
Lamé constant μ_S [MPa]	26.1

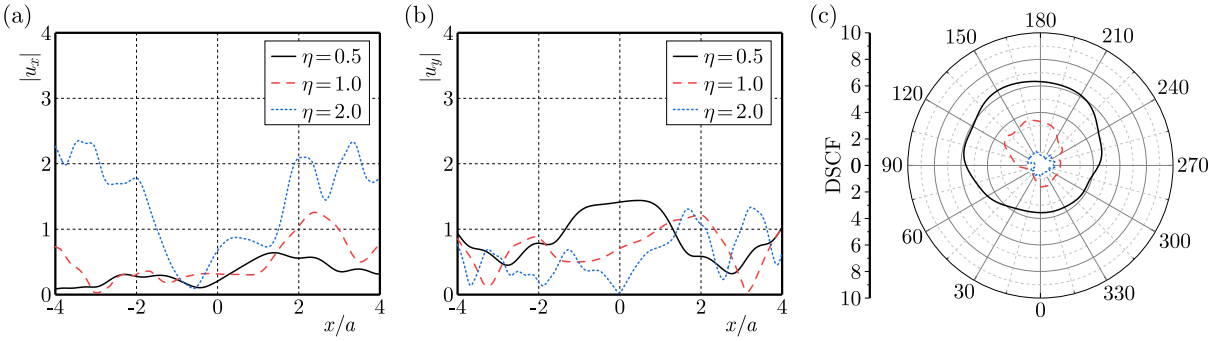

Fig. 4. Curves of displacement amplitude and DSCF at water-soil interface changing with frequency: (a) $|u_x|$; (b) $|u_y|$; (c) DSCF.

that when η is low, the incident wavelength is far above the tunnel radius, and it is insensitive to small terrain changes. Furthermore, the displacement on the left side changes more complexly than it does on the right side. The reason for this is the tunnel leading to the production of scattered waves. The left side of the tunnel reflects the wave. Scattering waves interfere with each other, causing energy convergence, so that the displacement curve at the water-soil interface appears as crests and valleys, exhibiting the characteristics of stationary waves (Cao & Lee, 1990; Lee & Cao, 1989; Lee & Karl, 2014). As the frequency increases, the number of crests and valleys in the figures increases, and the displacement alters more sharply, which shows that the interference effect of the wave is enhanced. As the frequency increases, the DSCF on the tunnel surface gradually decreases, and its distribution becomes more complex.

4.2. Impact of incident angle on the diffraction of wave

Figure 5 gives the displacement amplitude at the water-soil interface and the DSCF curve of the tunnel surface when the incident angle $\theta_{ip1} = 0°$, 30°, 60°, and incident frequency $\eta = 1$. It can be seen from the figures that when $\theta_{ip1} = 0°$, the displacement is symmetrical about $x = 0$. As the θ_{ip1} increases, the displacement on the left side changes more complexly than on the right one. Moreover, as the incident angle increases, both horizontal and vertical displacements as well as the peak value of DSCF decrease.

4.3. Impact of porosity on the diffraction of wave

Figure 6 illustrates the displacement and DSCF curves as the incident wave frequency is $\eta = 1$ and the porosity $n = 0.1$, 0.2, 0.3 gradually increases.

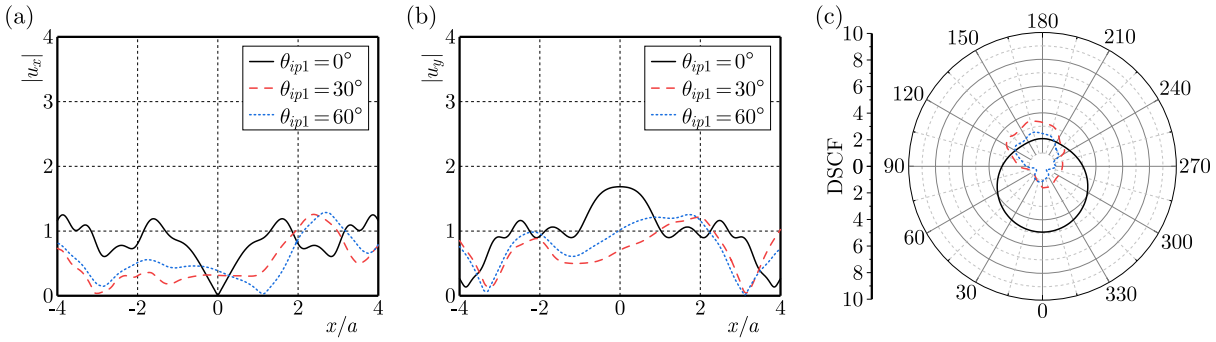

Fig. 5. Curves of displacement amplitude and DSCF at water-soil interface changing with angle: (a) $|u_x|$; (b) $|u_y|$; (c) DSCF.

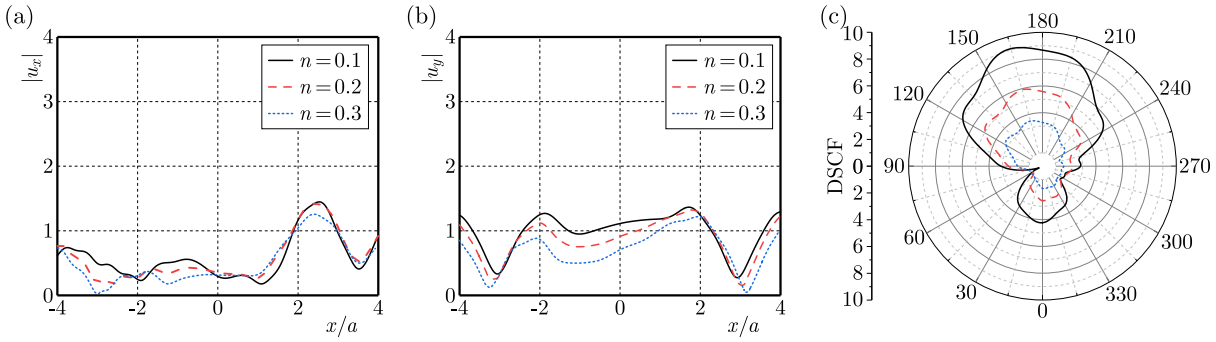

Fig. 6. Curves of displacement amplitude and DSCF at water-soil interface changing with porosity: (a) $|u_x|$; (b) $|u_y|$; (c) DSCF.

It can be found from the figures that as the porosity increases, the displacement at the water-soil interface, as well as the DSCF of the tunnel surface decreases.

4.4. Impact of incident frequency on the diffraction of wave

Figure 7 shows the displacement and DSCF curves when the buried depth is $d/a = 2$, 5, 10 in the case of $\theta_{ip1} = 30°$ and $\eta = 1$.

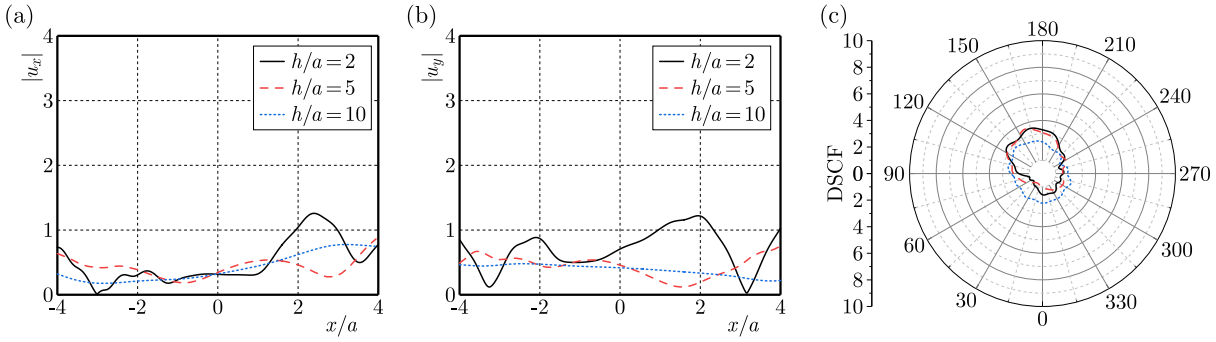

Fig. 7. Curves of displacement amplitude and DSCF at water-soil interface changing with burial depth: (a) $|u_x|$; (b) $|u_y|$; (c) DSCF.

With the increase of buried depth, the displacement at the water-soil interface decreases. However, the impact of the buried depth on the peak value of DSCF on the tunnel surface is not significant, and the DSCF at the top of the tunnel decreases as the buried depth increases. The DSCF at the bottom of the tunnel increases along with the buried depth.

5. Conclusion

Based on the Biot theory, the solution for P-wave scattering by underwater tunnel is given using the Fourier–Bessel series expansion. By numerical examples, the effect of incident angle, frequency, porosity and buried depth on displacement amplitude and dynamic stress concentration factor at the water-soil interface in the underwater tunnel is examined. The research indicates that:

1) The frequency has a considerable influence on the displacement at the water-soil interface and DSCF of the tunnel surface. The complex degree of the spatial pattern for the displacement increases along the incident frequency. The displacement amplitude inside the tunnel and at the water-soil interface on the left side changes greatly. It is extremely necessary to consider the impact of the incident wave frequency on the diffraction of the elastic wave in the underwater tunnel.
2) As the incident angle amplifies, the displacement on the left side changes more complexly compared to the right side, and the displacement amplitude and the peak value for DSCF decrease.
3) As the porosity amplifies, the displacement amplitude at the water-soil interface and the DSCF of the tunnel surface decrease.
4) The displacement amplitude at the water-soil interface decreases with the buried depth increase. The DSCF at the top of the tunnel decreases as the buried depth increases, and the DSCF at the bottom side increases with the increase of buried depth.

References

1. Achenbach, J.D. (1973). [Review of the book *Diffraction of Elastic Waves and Dynamic Stress Concentrations*, by Y.H. Pao & C.C. Mow]. *Journal of Applied Mechanics*, *40*, 872. https://doi.org/10.1115/1.3423178
2. Ba, Z. (2006). *Scattering of P and SV waves by canyons and tunnels in saturated half-space*. Tianjin University.
3. Ba, Z., Sang, Q., & Liang, J. (2022). Seismic analysis of a lined tunnel in a multi-layered TI saturated half-space due to qP1- and qSV-waves. *Tunnelling and Underground Space Technology*, 119, Article 104248. https://doi.org/10.1016/j.tust.2021.104248
4. Biot M.A. (1956a). Theory of propagation of elastic waves in a fluid-saturated porous solid. I. Low-frequency range. *The Journal of the Acoustical Society of America*, *28*(2), 168–178. https://doi.org/10.1121/1.1908239
5. Biot M.A. (1956b). Theory of propagation of elastic waves in a fluid-saturated porous solid: II. Higher frequency range. *The Journal of the Acoustical Society of America*, *28*(2), 179–191. https://doi.org/10.1121/1.1908241
6. Cao, H. & Lee, V.W. (1990). Scattering and diffraction of plane P waves by circular cylindrical canyons with variable depth-to-width ratio. *Soil Dynamics and Earthquake Engineering*, *9*(3), 141–150. https://doi.org/10.1016/S0267-7261(09)90013-6
7. Ding, H., Tong, L.H., Xu, C., & Hu, W. (2020). Aseismic performance analysis of composite lining embedded in saturated poroelastic half space. *International Journal of Geomechanics*, *20*(9), Article 04020156. https://doi.org/10.1061/(ASCE)GM.1943-5622.0001787
8. Gomes, R.C., Gouveia, F., Torcato, D., & Santos, J. (2015). Seismic response of shallow circular tunnels in two-layered ground. *Soil Dynamics and Earthquake Engineering*, *75*, 37–43. https://doi.org/10.1016/j.soildyn.2015.03.012
9. Kattis, S.E., Beskos, D.E., & Cheng, A.H.D. (2003). 2D dynamic response of unlined and lined tunnels in poroelastic soil to harmonic body waves. *Earthquake Engineering and Structural Dynamics*, *32*(1), 97–110. https://doi.org/10.1002/eqe.216

10. Lee, V.W. & Cao, H. (1989). Diffraction of SV waves by circular canyons of various depths. *Journal of Engineering Mechanics*, *115*(9), 2035–2056. http://doi.org/10.1061/(ASCE)0733-9399(1989)115:9(2035)

11. Lee, V.W. & Karl, J. (1992). Diffraction of *SV* waves by underground, circular, cylindrical cavities. *Soil Dynamics & Earthquake Engineering*, *11*(8), 445–456. https://doi.org/10.1016/0267-7261(92)90008-2

12. Lee, V.W. & Liu, W.Y. (2014). Two-dimensional scattering and diffraction of P- and SV-waves around a semi-circular canyon in an elastic half-space: An analytic solution via a stress-free wave function. *Soil Dynamics and Earthquake Engineering*, *63*, 110–119. https://doi.org/10.1016/j.soildyn.2014.02.005

13. Liang, Y., Zhou, F., Cao, X., Wang, L., Liu, H., & Zhu, S. (2023). Scattering of plane SH waves by a circular tunnel in nonlocal fractional-order viscoelastic half-space. *Soil Dynamics and Earthquake Engineering*, *170*, Article 107934. https://doi.org/10.1016/j.soildyn.2023.107934

14. Liu, Z., Ju, X., Wu, C., & Liang, J. (2017). Scattering of plane P_1 waves and dynamic stress concentration by a lined tunnel in a fluid-saturated poroelastic half-space. *Tunnelling and Underground Space Technology*, *67*, 71–84. https://doi.org/10.1016/j.tust.2017.04.017

15. Luco, J.E. & de Barros, F.C.P. (1994). Dynamic displacements and stresses in the vicinity of a cylindrical cavity embedded in a half-space. *Earthquake Engineering and Structural Dynamics*, *23*(3), 321–340. https://doi.org/10.1002/eqe.4290230307

16. Ma, Q., Zhou, F.X., Shao, S.J., Shao, S., & Zhang, M. (2023). Diffraction of plane P waves by a circular-arc canyon in an unsaturated poroelastic half-space. *Soil Dynamics and Earthquake Engineering*, 174, Article 108163. https://doi.org/10.1016/j.soildyn.2023.108163

17. Tan, Y., Yang, M., & Li, X. (2020). Dynamic response of a circular lined tunnel with an imperfect interface embedded in the unsaturated poroelastic medium under P wave. *Computers and Geotechnics*, *122*, Article 103514. https://doi.org/10.1016/j.compgeo.2020.103514

18. Xiang, G.L., Tao, M., Zhao, R., Zhao, H., Memon, M.B., & Wu, C. (2024). Dynamic response of water-rich tunnel subjected to plane P wave considering excavation induced damage zone. *Underground Space*, *15*, 113–130. https://doi.org/10.1016/j.undsp.2023.08.010

19. Xu, C.J., Ding, H.B., Tong, L.H., Luo, W.J., & Wang, N. (2019). Scattering of a plane wave by shallow buried cylindrical lining in a poroelastic half-space. *Applied Mathematical Modelling*, *70*, 171–189. https://doi.org/10.1016/j.apm.2019.01.029

20. You, H.B. (2005). *Elastic wave scattering by a canyon or tunnel in layered saturated half space* (in Chinese). Tianjin University.

21. Yue, C. & Liu, Q. (2023). Dynamic response of a shallow lined circular tunnel by incident P1 and SV waves in an unsaturated half-plane. *Tunnelling and Underground Space Technology*, *141*, Article 105364. https://doi.org/10.1016/j.tust.2023.105364

22. Zhang, J.L., Ma, Q., & Jiang, H.P. (2024). Study on the transmission and reflection of P1 wave at the interface between saturated soil and saturated frozen soil medium (in Chinese). *Rock and Soil Mechanics*, *45*(10), 1–14.

23. Zhao, S. & Ma, Q. (2024). Diffraction of plane P waves by a circular unlined tunnel in an unsaturated poroelastic half-space. *Journal of Vibration Engineering & Technologies*, *12*(Suppl. 2), 1501–1519. https://doi.org/10.1007/s42417-024-01487-w

24. Zhao, S., Ma, Q., & Zhang, W.Y. (2024). Diffraction of plane P-waves by a single-layer lined tunnel in an unsaturated poroelastic half-space. *Mechanics of Solids*, *59*(1), 496–520. https://doi.org/10.1134/S0025654424600041

25. Zhou, F.X., Lai, Y.M., & Song, R.X. (2013). Propagation characteristics of plane wave in non-homogeneously saturated soils (in Chinese). *Science China Press*, *43*(2), 131–140.

Manuscript received September 27, 2024; accepted for publication January 29, 2025; published online March 24, 2025.

JOURNAL OF THEORETICAL
AND APPLIED MECHANICS
63, 2, pp. 363–374, Warsaw 2025
https://doi.org/10.15632/jtam-pl/200944

STUDY ON NOISE CONTROL OF TUNABLE FLUID-SOLID COUPLED PHONONIC CRYSTAL STRUCTURES IN THE CONTEXT OF ENCLOSED FISH FARMS

Denghui QIAN*, Jiawei ZHUANG, Shengke ZHANG

School of Naval Architecture & Ocean Engineering, Jiangsu University of Science and Technology, Zhenjiang 212100, Jiangsu, China

*corresponding author, *dhqian@just.edu.cn*

Identifying innovative strategies to mitigate underwater noise, which exerts a wide array of detrimental effects on fish physiology, behavior, biodiversity, and entire aquatic ecosystems, presents a significant scientific challenge in the conservation of marine environments. The sources of underwater noise are well-documented and encompass marine transportation, geological exploration, and various industrial activities in marine environments. In addressing these concerns, we propose a solid cylindrical structure of fluid-solid coupled phononic crystals that leverages the local resonance mechanism. The finite element method is employed to analyze the bandgap characteristics and acoustic transmission loss of the finite periodic structure. Furthermore, we investigate the influence of structural parameters on the attenuation frequency range of the bandgap. Building on this analysis, we design a hollow cylindrical structure of fluid-solid coupled phononic crystals, which demonstrates superior sound insulation performance for frequencies below 300 Hz. Additionally, we propose filling the hollow cylinders with fluid to modulate the bandgap of the structure. This study introduces an innovative approach to controlling underwater noise and modulating the phononic crystal bandgap, providing essential insights into the preservation of aquatic ecosystems and mitigating the detrimental influence of underwater noise on marine organisms.

Keywords: phononic crystals; fluid-solid coupling; underwater noise; enclosed fish farm; transmission curve.

1. Introduction

In recent years, intensified human exploration of the oceans has escalated anthropogenic activities in the marine environment, leading to increased underwater noise that adversely affects the health and behavior of numerous fish and marine mammals. High-frequency noise can induce short-term changes in physiological parameters such as oxygen consumption, cortisol, glucose, and lactic acid levels in fish (Herbert-Read *et al.*, 2017), thereby altering their swimming speed, depth, and direction, ultimately impacting fish shoals. Low-frequency noise compromises the auditory sensitivity of fish (Zhan *et al.*, 2023), resulting in temporary or permanent shifts in their auditory thresholds. Prolonged exposure to high-intensity low-frequency noise can impair species identification, reproductive behaviors, and population communication in fish. Li *et al.* (2022) monitored underwater environmental noise at a depth of 35 meters and concluded that wind on the sea surface is the primary factor influencing frequencies above 500 Hz, whereas, for frequencies below 500 Hz, human navigation activities are the predominant factor. Consequently, an increasing number of researchers are concentrating on anthropogenic low-frequency noise, as its impact on fish has emerged as a serious ecological concern.

Ocean noise primarily comprises natural background noise from wind, waves, tides, rainfall, and earthquakes; biological noise from fish movements, feeding, and mating; and anthropogenic noise (Lu *et al.*, 2024; Huang *et al.*, 2023). Anthropogenic noise encompasses marine shipping (Helal *et al.*, 2024), geological exploration, sonar (Fan *et al.*, 2017), as well as industrial and

construction activities in marine environments. Owing to the properties of sound in water – such as rapid propagation speed, low transmission loss, and extended transmission distance – industrial activities like piling (Jia *et al.*, 2024), dredging, offshore wind turbine operation (Zhang *et al.*, 2017), and underwater blasting can generate noise that affects areas ranging from 100 meters to over 1000 meters from the source (Zhang *et al.*, 2012).

Numerous studies have investigated the effects of low-frequency noise on fish physiology, behavior, and population dynamics. Shi *et al.* (2010) examined the impact of ship noise on cortisol levels in large yellow croaker, finding a significant increase in blood cortisol levels under ship noise exposure. Ye *et al.* (2023) studied the effects of low-frequency vibration stimuli on the behavior and physiology of large yellow croaker and discovered that the fish exhibited heightened sensitivity to 200 Hz vibration stimuli. Lin *et al.* (2020) investigated the impact of ship noise sound pressure levels on the behavior of juvenile large yellow croakers, revealing that increasing sound pressure levels intensified stress avoidance behaviors. Crovo *et al.* (2015) discovered that the auditory thresholds of blacktail shiner significantly increased across various noise frequencies when exposed to traffic road noise.

As human activities in the ocean continue to escalate, noise from diverse sources has become increasingly prevalent. Implementing effective control measures for underwater noise is imperative to prevent irreversible damage to fish diversity and underwater ecosystems. Noise arises from the propagation effects of elastic waves within structures and the coupling interactions between these waves and media such as air and water. In recent decades, the concept of phononic crystals has invigorated the study of elastic wave propagation characteristics in the field of physics (Wu *et al.*, 2016a; 2016b; Yin *et al.*, 2022). The bandgap properties of phononic crystals effectively suppress the propagation of elastic waves within the bandgap range, offering novel approaches for underwater noise reduction.

Li *et al.* (2024) focused on the wooden frame structure of high-speed train floors and designed a hybrid structure combining wooden frames with phononic crystals, leveraging the phononic crystal theory. They conducted a systematic analysis of the bandgap characteristics and sound insulation performance of the phononic crystal structure. Liu *et al.* (2023) designed the Helmholtz-type phononic crystal featuring an adjustable cavity structure. Yao *et al.* (2021) proposed the smooth finite element calculation method for two-dimensional fluid/solid phononic crystals and validated it through multiple two-dimensional phononic crystal examples. Jiang *et al.* (2009) developed an underwater sound-absorbing material composed of locally resonant phononic woodpile. Theoretical and experimental results demonstrated that the locally resonant phononic woodpile exhibited excellent sound absorption properties due to the synergy of locally resonant unit structures and multi-scale woodpile structures. Wang *et al.* (2022) tackled the challenge of low-frequency sound absorption in acoustic coatings by developing a composite structure that integrates locally resonant structures within the cavity coating.

In summary, this paper addresses the challenge of underwater anthropogenic noise adversely affecting fish diversity and underwater ecosystems by designing a solid cylindrical structure of fluid-solid coupled phononic crystals leveraging the local resonance mechanism. The bandgap characteristics and acoustic transmission loss of the finite periodic structure were analyzed using the finite element method, and the impact of structural parameters on the bandgap attenuation frequency range was investigated. Building on this analysis, a hollow cylindrical structure of fluid-solid coupled phononic crystals was designed. It is proposed to fill the hollow cylinders with fluid to modulate the bandgap of the structure, offering a novel approach for underwater noise control and phononic crystal bandgap regulation.

2. Model and calculation method

Based on the mechanism of local resonance phononic crystal bandgap formation, this paper establishes a fluid-solid coupled phononic crystal solid cylinder unit cell model, utilizing water

as the base material, as illustrated in Fig. 1a. Building on this foundation, a novel fluid-solid coupled phononic crystal hollow cylinder unit cell model is designed by perforating the scatterer, as depicted in Fig. 1b. Fixed constraint conditions are applied at the bottom of the cylinder to better match the structure's application environment. The geometric and material parameters of the structural model are detailed in Tables 1 and 2. Figure 2 presents a schematic diagram of the arrangement of the fluid-solid coupled phononic crystal structure in an enclosure fishery. The fluid-solid coupled phononic crystal structures are periodically arranged on a steel plate, with their bases secured to the plate. The steel plate can be attached to the four pile centers of the enclosure fishery using clamps.

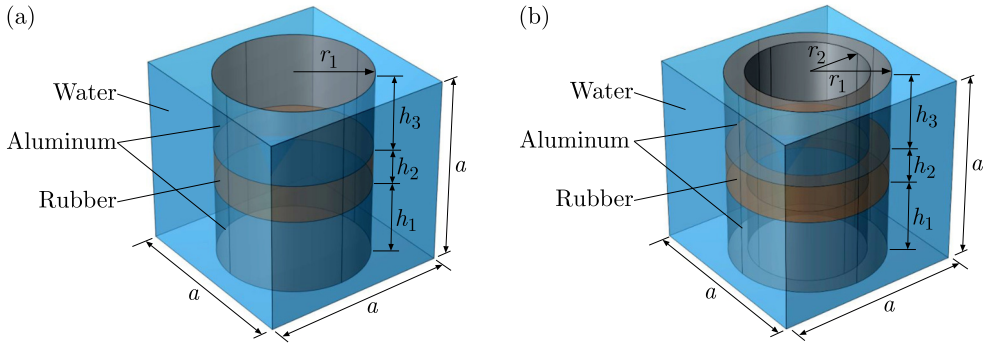

Fig. 1. Single-cell model of fluid-solid coupled phononic crystals: (a) solid cylinder; (b) hollow cylinder.

Table 1. Material parameters.

Material	Density [kg/m^3]	Young's modulus [GPa]	Poisson's ratio	Velocity [m/s]
Aluminum	2700	70	0.33	–
Rubber	1100	1.49e-3	0.49	–
Water	1000	–	–	1490

Table 2. Structural parameters.

Parameter [m]	a	h_1	h_2	h_3	r_1	r_2
Value	1	0.4	0.2	0.4	0.4	0.3

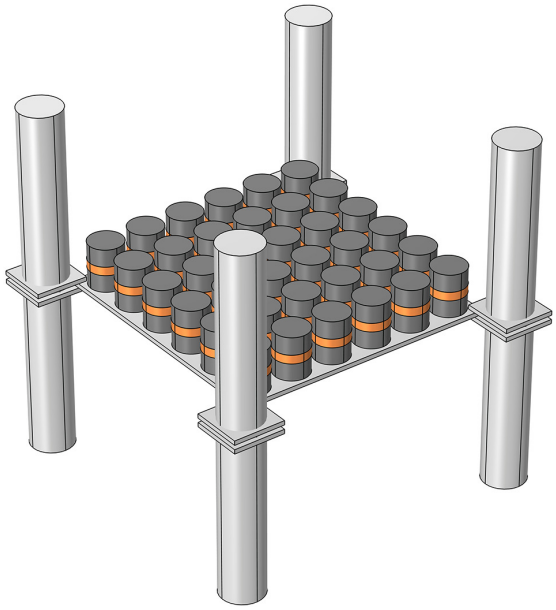

Fig. 2. Schematic arrangement of fluid-solid coupled phononic crystal structure.

Drawing on the propagation characteristics of elastic waves in phononic crystals and the periodicity theory, this paper employs the finite element method for calculations by applying Floquet periodic boundary conditions on the unit cell boundaries and introducing the Bloch wave vector **k** for solutions. These computations are performed using COMSOL Multiphysics. The discrete form of the phononic crystal unit cell characteristic equation is given as

$$(\mathbf{K} - \omega^2 \mathbf{M}) \cdot \mathbf{u} = 0, \tag{2.1}$$

where **K** represents the stiffness matrix, **M** denotes the mass matrix, **u** signifies the displacement matrix of the unit cell. Mechanical waves propagate as vector waves (transverse and longitudinal) in solids, whereas in fluids, they propagate solely as longitudinal waves. Therefore, when calculating the band structure of fluid-solid coupled phononic crystals, it is imperative to partition the fluid and solid domains and apply appropriate boundary conditions at the fluid-solid interface. At the fluid-solid interface, the normal displacement and force must be continuous:

$$U_s \cdot \mathbf{n} = U_f \cdot \mathbf{n}, \qquad p \cdot \mathbf{n} = \sigma \cdot \mathbf{n}, \tag{2.2}$$

where U_s and U_f represent the displacements in the solid and fluid, respectively, **n** denotes the normal vector at the fluid-solid interface, p signifies the fluid pressure at the interface, σ is the stress tensor of the solid at the interface:

$$U_s(r + a) = e^{i(k \cdot a)} U_s(r), \qquad p(r + a) = e^{i(k \cdot a)} p(r). \tag{2.3}$$

In a two-dimensional phononic crystal, $\mathbf{r}(x, y)$ denotes the position vector, and $\mathbf{k}(x, y)$ represents the wave vector. By integrating the characteristic equation with boundary conditions, the eigenfrequencies can be determined for a given wave vector **k**. In COMSOL, scanning the wave vector **k** along the boundary of the irreducible Brillouin zone yields the band structure diagram of the phononic crystal.

3. Numerical results and analysis

3.1. Band structure and transmission curve of the fluid-solid coupled phononic crystal solid cylinder structure

Figure 3a illustrates the band structure of the fluid-solid coupled phononic crystal solid cylinder structure, with the material and geometric parameters of the unit cell detailed in Tables 1 and 2, respectively. To validate the accuracy of the band structure diagram, Fig. 3b presents the acoustic transmission loss curve for the finite periodic structure. The unit cells are arranged

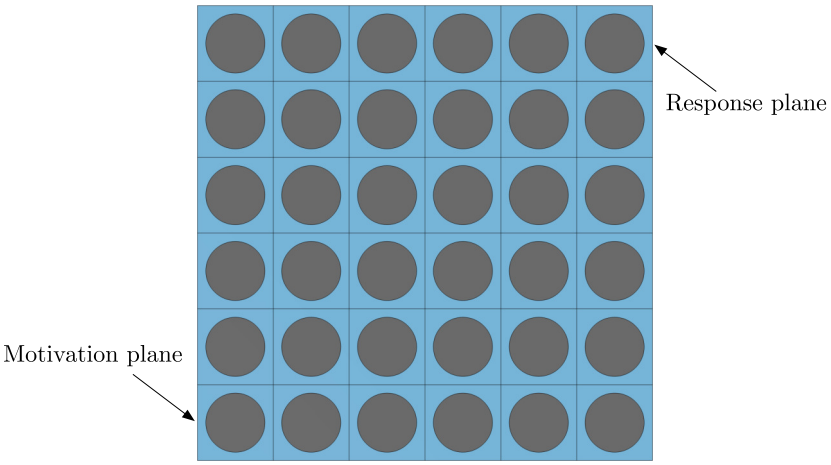

Fig. 3. Finite element calculation model.

in a square lattice periodic configuration horizontally to form a two-dimensional fluid-solid coupled phononic crystal structure with six periods, as depicted in Fig. 3. The background pressure field serves as the incident acoustic excitation, with a sound pressure amplitude of 1 Pa. The sound wave is incident perpendicularly onto the phononic crystal structure as a plane wave, and the response is measured at the diagonal of the incident end.

Figure 4a reveals that the first complete bandgap range of the fluid-solid coupled phononic crystal solid cylinder structure spans from 17.8 Hz to 46 Hz, while the second bandgap range extends from 126 Hz to 153.1 Hz. It is noteworthy that numerous flat bands exist within the second bandgap; these are local resonance bands and do not impact the structural bandgap. Figure 4b indicates that elastic waves propagate in the finite periodic structure with significant sound insulation effects in the ranges of 17.8 Hz–46 Hz and 126 Hz–153.1 Hz, particularly in the range of 17.8 Hz–46 Hz, where the sound insulation level can reach up to 168 dB. The sound attenuation frequency range aligns with the bandgap frequency range of the infinite periodic structure depicted in Fig. 4a. To further elucidate the bandgap formation mechanism, characteristic modes at the beginning and end frequencies of the bandgap are analyzed, as shown in Fig. 5.

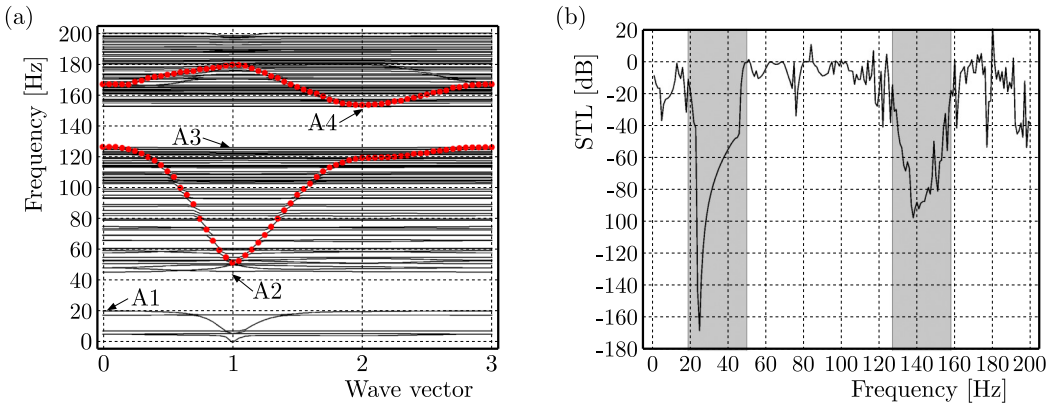

Fig. 4. Band structure (a) and sound transmission loss (b) of solid cylinder structure of fluid-solid coupled phononic crystals.

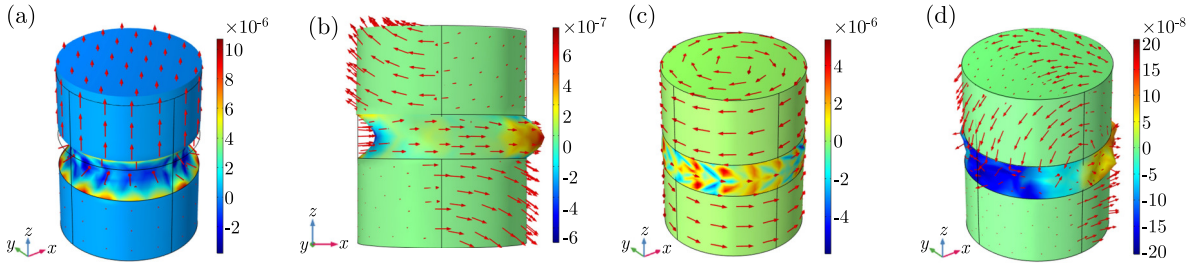

Fig. 5. Vibration modal diagrams: (a) A1; (b) A2; (c) A3; (d) A4.

The vibration modes depicted in Fig. 5 indicate that in mode A1, the rubber and the upper aluminum column in the scatterer vibrate longitudinally along the z-axis, while the lower aluminum column remains stationary. Modes A2 and A4 belong to the same vibration mode, exhibiting torsional vibration of the hard scatterer aluminum in the x-, z-plane attributed to the fixed constraint at the bottom of the column. In mode A3, the hard scatterer exhibits torsional vibration in the x-, z-plane without movement in the z-direction. The upper and lower aluminum columns undergo torsional vibrations in opposite directions, achieving dynamic equilibrium. When elastic waves propagate through this structure, these vibration modes couple to form two vibration bandgaps, 17.8 Hz–46 Hz and 126 Hz–153.1 Hz.

To further illustrate the attenuation characteristics of this structure, Fig. 6a presents the sound pressure distribution for the finite periodic fluid-solid coupled phononic crystal solid cylinder structure at a frequency within the bandgap attenuation range. A sound pressure of 1 Pa is applied in the x-direction on the excitation surface, with a plane wave incident perpendicularly to the structure at a frequency of $f = 46$ Hz. Figure 6a demonstrates that when excitation is applied to one side of the structure, the sound wave cannot propagate through it, resulting in significant attenuation of the sound pressure on the response surface located on the opposite side compared to the excitation surface. In contrast, Fig. 6b illustrates the sound pressure distribution for the structure at a frequency outside the bandgap attenuation range, with a selected frequency of $f = 51$ Hz. It is evident that when excitation is applied to one side of the structure, the sound wave propagates effectively through the structure without any attenuation.

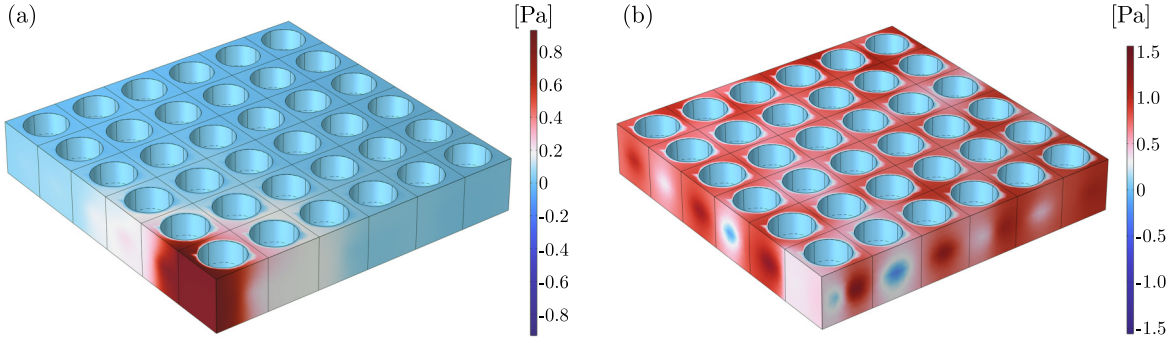

Fig. 6. Sound pressure diagrams of solid cylinder structures of finite-period fluid-solid coupled phononic crystals with frequencies falling in (a) the bandgap ($f = 46$ Hz) and (b) the non-bandgap ($f = 51$ Hz) attenuation band.

3.2. Influence of structural parameters on the bandgap attenuation range of the solid cylinder structure

The parameters used for the calculations align with those presented in Fig. 1a and are detailed in Tables 1 and 2. The lattice constant a, the radius of the solid cylinder r_1, and the thickness of the intermediate rubber layer h are chosen as influencing parameters. Since the total height of the column must remain constant according to the control variable method, the analysis of the thickness h of the intermediate rubber layer is adjusted to the proportion of the rubber layer within the column. These parameters are utilized to investigate the influence of structural geometric parameters on the starting frequency, cutoff frequency, and bandwidth of the bandgap attenuation range. For clarity in this section, SF denotes the starting frequency, CF denotes the cutoff frequency, and W denotes the bandgap width. More specifically, SF-1 and SF-2 denote the starting frequencies of the first and the second bandgaps, respectively; CF-1 and CF-2 denote the cutoff frequencies of the first and second bandgaps, respectively; and W-1 and W-2 denote the widths of the first and second bandgaps, respectively.

For the fluid-solid coupled phononic crystal solid cylinder structure, as illustrated in Figs. 7a and 7b, increasing the lattice constant keeps the starting frequency of the first bandgap attenuation range nearly constant, while slightly decreasing the starting frequency of the second bandgap attenuation range. The cutoff frequencies of both the first and second bandgap attenuation ranges exhibit an upward trend. Consequently, as the lattice constant increases, the widths of both bandgaps expand. Increasing the radius of the solid cylinder reveals that the starting frequency of the first bandgap attenuation range slightly increases, whereas the starting frequency of the second bandgap attenuation range slightly decreases. The cutoff frequencies of both the first and second bandgap attenuation ranges decrease. Therefore, the widths of both bandgaps demonstrate a decreasing trend, as shown in Figs. 7c and 7d. Figures 7e and 7f illustrate that

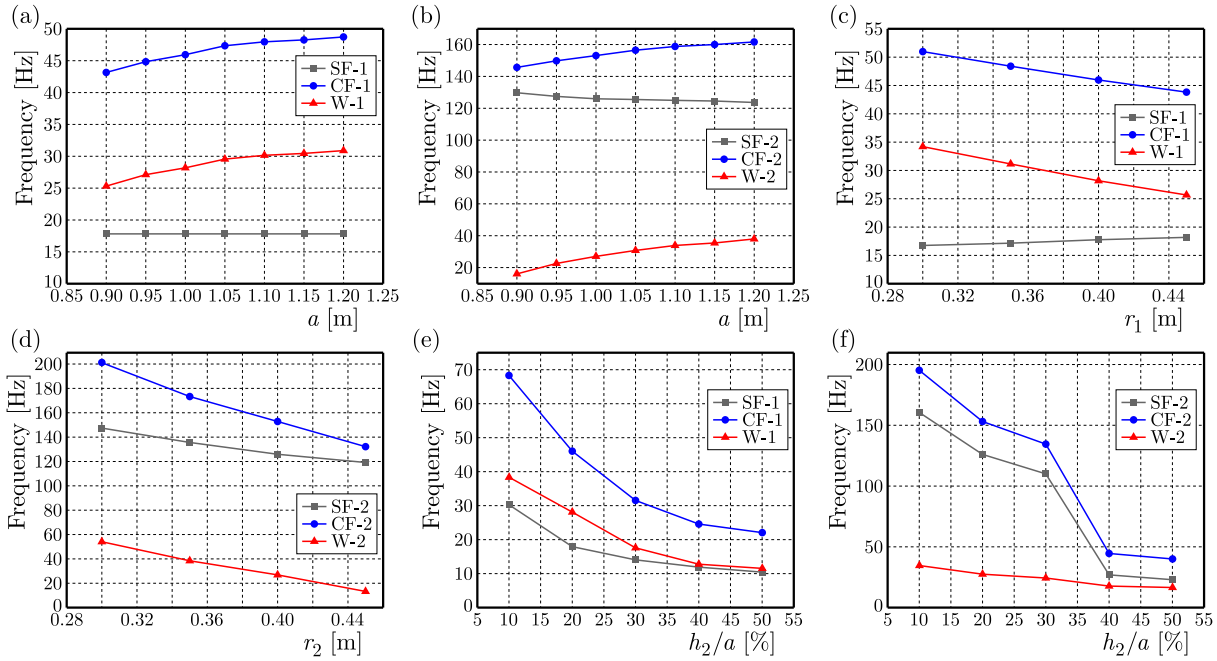

Fig. 7. Influence law of structural parameters on the bandgap attenuation band of solid cylinder structures.

the proportion of the rubber layer significantly impacts the bandgap attenuation range. As the proportion of the rubber layer in the solid cylinder gradually increases, the starting and cut-off frequencies of both the first and second bandgap attenuation ranges decrease significantly, along with the widths of both bandgaps. It is important to note that when the proportion of the rubber layer exceeds 30 %, the attenuation range of the second bandgap significantly decreases.

3.3. Band structure and transmission curve of the fluid-solid coupled phononic crystal hollow cylinder structure

Figure 8a illustrates the band structure of the fluid-solid coupled phononic crystal hollow cylinder structure, with the material and geometric parameters of the unit cell detailed in Tables 1 and 2. To validate the accuracy of the band structure diagram, Fig. 8b presents the acoustic transmission loss curve for the finite periodic structure. The unit cells are arranged in a square lattice periodic configuration horizontally to form a two-dimensional fluid-solid coupled

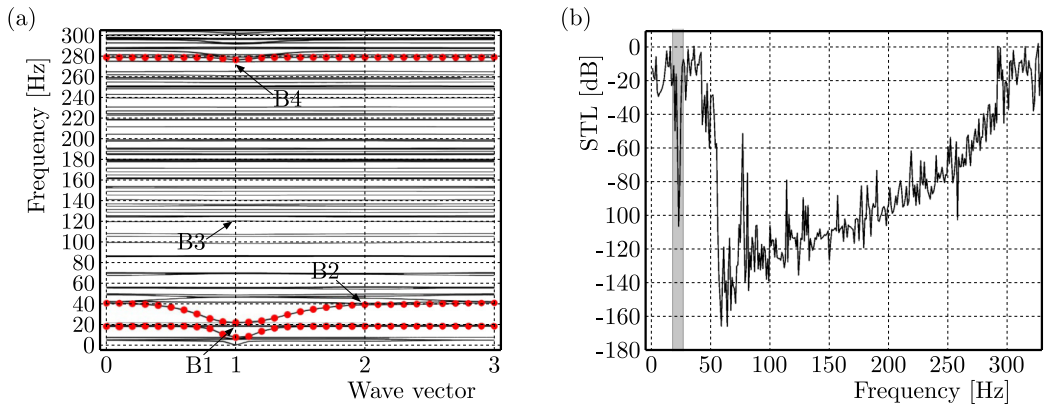

Fig. 8. Band structure (a) and sound transmission loss (b) of hollow cylinder structure of fluid-solid coupled phononic crystals.

phononic crystal structure with six periods. The background pressure field serves as the incident acoustic excitation, with a sound pressure amplitude of 1 Pa. The sound wave is incident perpendicularly onto the phononic crystal structure as a plane wave, and the response is measured at the diagonal of the incident end.

Figure 8a shows that the first complete bandgap range of the fluid-solid coupled phononic crystal hollow cylinder structure spans from 18 Hz to 21.8 Hz, while the second bandgap range extends from 46.3 Hz to 275.4 Hz. Although many flat bands exist within the second bandgap, their impact on the structural bandgap is negligible. Figure 8b indicates that when elastic waves propagate in the finite periodic structure, significant sound insulation occurs in the ranges of 18 Hz–21.8 Hz and 46.3 Hz–275.4 Hz. The sound attenuation frequency range aligns with the complete bandgap opening frequency range of the infinite periodic structure depicted in Fig. 8a. Within the bandgap range illustrated in Fig. 8, the fluid-solid coupled phononic crystal hollow cylinder structure exhibits no intrinsic modes. To further elucidate the mechanism of bandgap formation, characteristic modes at the starting and cutoff frequencies of the bandgap are analyzed, as shown in Fig. 9.

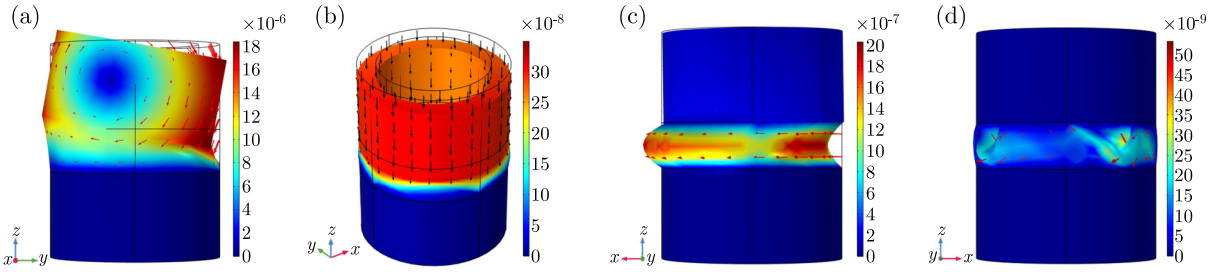

Fig. 9. Vibration modal diagrams: (a) B1; (b) B2; (c) B3; (d) B4.

The vibration modes shown in Fig. 9 reveal that in mode B1, the scatterer undergoes torsional vibration, with the lower aluminum column remaining stationary due to the fixed constraint at the bottom of the column, while the rubber and upper aluminum column undergo torsional vibration in the y-, z-plane. In mode B2, the rubber and upper aluminum column in the scatterer vibrate longitudinally along the z-axis, while the lower aluminum column remains stationary. In mode B3, the rubber and upper aluminum column in the scatterer vibrate laterally in the x-, y-plane, while the lower aluminum column remains stationary. Mode B4 involves torsional vibration of the scatterer, with the middle rubber layer undergoing torsional vibration in the x-, y-plane and very slight movement in the z-direction. B4 corresponds to a point at the cutoff frequency of the flat bandgap, as shown in Fig. 9d. The displacement field at mode B4 is much smaller compared to other modes, indicating that at point B4, the structure is nearing equilibrium, and the local resonance mode will no longer be excited, thus closing the bandgap. When elastic waves propagate in this structure, these vibration modes couple to form two vibration bandgaps, 18 Hz–21.8 Hz and 46.3 Hz–275.4 Hz. The hollow cylinder structure can form an improved low-frequency bandgap, which, compared to a solid cylinder structure of the same size, widens the low-frequency bandgap, enhances sound insulation, and better achieves low-frequency broadband noise reduction.

To further illustrate the attenuation characteristics of this structure, Fig. 10a shows the sound pressure distribution for the finite periodic fluid-solid coupled phononic crystal solid cylinder structure at a frequency within the bandgap attenuation range. A sound pressure of 1 Pa is applied in the x-direction on the excitation surface, with a plane wave incident perpendicularly to the structure at a frequency of $f = 84$ Hz. Figure 10a demonstrates that when the excitation is applied to one side of the structure, the sound wave cannot propagate through it, resulting in significant attenuation of the sound pressure on the response surface located on the opposite side compared to the excitation surface. In contrast, Fig. 10b illustrates the sound pressure distri-

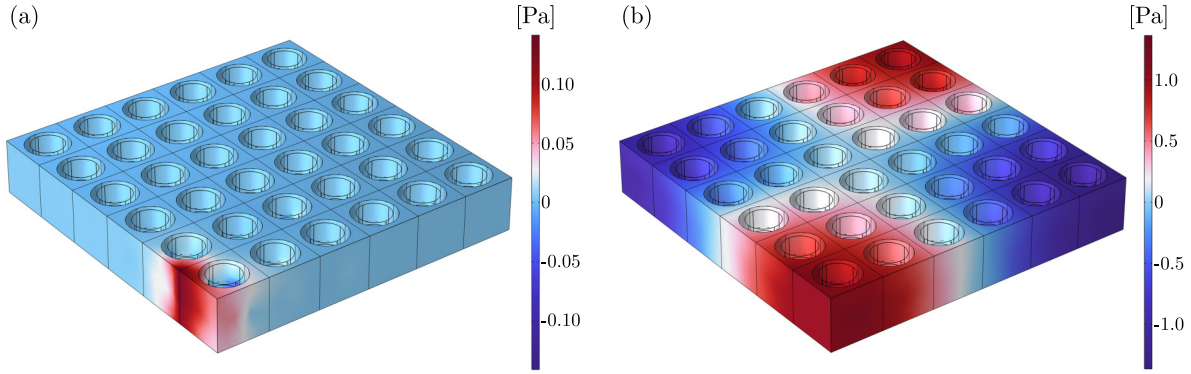

Fig. 10. Sound pressure diagrams of hollow cylinder structures of finite-period fluid-solid coupled phononic crystals with frequencies falling in (a) the bandgap ($f = 84\,\mathrm{Hz}$) and (b) the non-bandgap ($f = 16\,\mathrm{Hz}$) attenuation band.

bution for the structure at a frequency outside the bandgap attenuation range, with a selected frequency of $f = 16\,\mathrm{Hz}$. It is evident that when the excitation is applied to one side of the structure, the sound wave propagates effectively through the structure without any attenuation.

3.4. Influence of structural parameters on the bandgap attenuation range of the hollow cylinder structure

The parameters used for the calculations align with those shown in Fig. 1b and are detailed in Tables 1 and 2. Subsection 3.2 of this paper has already examined the influence of the basic structural parameters of the fluid-solid coupled phononic crystal solid cylinder on the bandgap attenuation range, so it will not be reiterated here. In the fluid-solid coupled phononic crystal hollow cylinder, the aperture r_2 is selected as the influencing parameter to investigate the impact of structural geometric parameters on the starting frequency, cutoff frequency, and bandwidth of the bandgap attenuation range.

For the fluid-solid coupled phononic crystal hollow cylinder structure, as the aperture radius increases, as shown in Fig. 11a, the starting frequency of the first bandgap attenuation range remains nearly constant, while the cutoff frequency decreases slightly, resulting in a narrower first bandgap. Figure 11b indicates that the starting frequency of the second bandgap attenuation range decreases slightly, while the cutoff frequency increases significantly, leading to a substantial widening of the second bandgap.

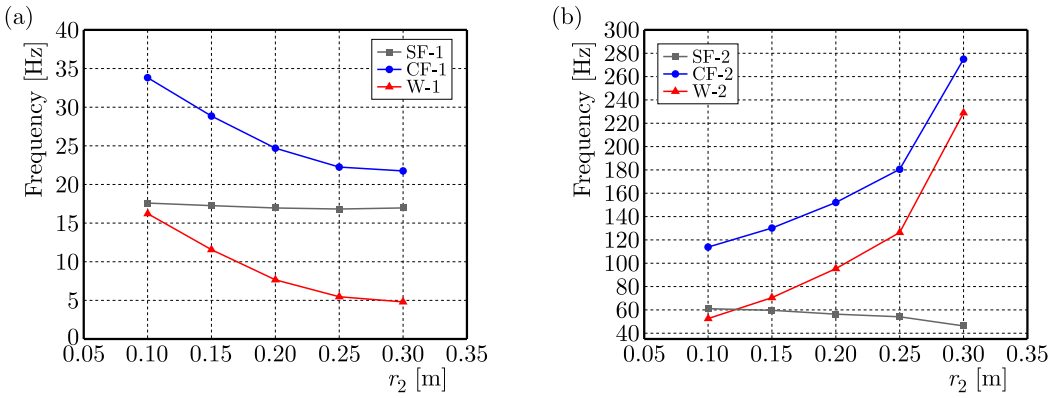

Fig. 11. Influence law of structural parameters on the bandgap attenuation band of hollow cylinder structures.

3.5. Optimization of the fluid-solid coupled phononic crystal hollow cylinder structure

The previous analysis examined the influence of structural parameters on the bandgap attenuation range of fluid-solid coupled phononic crystal solid and hollow cylinder structures, concluding that altering structural parameters allows control over the attenuation range to target specific frequency ranges. Although this method effectively controls the propagation of elastic waves, altering structural parameters is cumbersome and not economical. In contrast, filling the hollow cylinder structure of fluid-solid coupled phononic crystals with fluid can achieve tunability of the elastic wave bandgap. We investigated the impact of the fluid fill height in the hollow cylinder structure on the bandgap attenuation range. The parameters used for the calculations align with those shown in Fig. 1b and are detailed in Tables 1 and 2.

As shown in Fig. 12, filling the hollow cylinder with fluid up to 0.4 m lowered the bandgap attenuation range by 2.6 Hz, while the center frequency of the bandgap decreased by 15.3 %. When the fluid fill height in the hollow cylinder is between 0.4 m and 0.6 m, the starting frequency of the first bandgap remains essentially unchanged, while the cutoff frequency exhibits an increasing trend. When the fluid fill height in the hollow cylinder exceeds 0.6 m, the starting frequency of the first bandgap decreases by 2.2 Hz, and the cutoff frequency increases by 14.2 Hz, thereby widening the bandgap by 16.4 Hz, or 56.6 %. Therefore, through the study of fluid filling in the fluid-solid coupled phononic crystal hollow cylinder structure, we have demonstrated that fluid filling can be used to control the transmission of elastic waves within a specific frequency range, thus adjusting the position of the bandgap attenuation range.

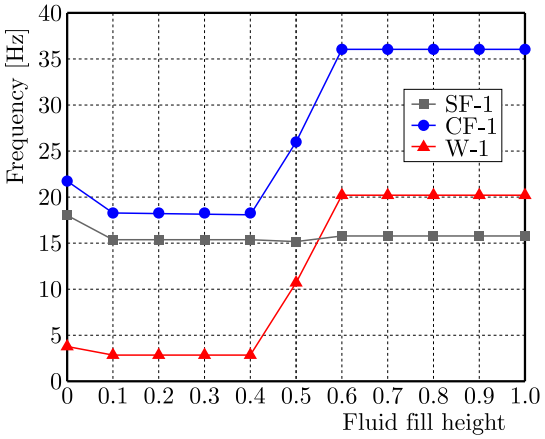

Fig. 12. First bandgap attenuation band and bandgap width versus fluid fill height.

4. Conclusion

As human activities in the ocean continue to intensify, anthropogenic underwater noise has had a profound impact on fish biodiversity and marine ecosystems. This paper addresses the influence of underwater noise on the aquaculture of marine enclosed fisheries and introduces a fluid-solid coupled phononic crystal solid cylinder structure, leveraging the local resonance mechanism inherent in phononic crystals. The band structure and acoustic transmission loss curve of the finite periodic structure were computed utilizing the finite element method, facilitating a comprehensive study of its bandgap characteristics. Building upon this, a fluid-solid coupled phononic crystal hollow cylinder structure was proposed. The bandgap characteristics of fluid-solid coupled solid and hollow cylinder structures were compared and analyzed, and the effects of various structural parameters on the bandgap attenuation range of the fluid-solid coupled phononic crystal structure were meticulously examined. Furthermore, the study proposed filling the fluid-solid coupled phononic crystal hollow cylinder structure with fluid to modulate the low-frequency bandgap. The primary conclusions are as follows:

- Analysis of the band structure and acoustic transmission loss curve revealed that the fluid-solid coupled phononic crystal solid cylinder structure, utilizing water as the matrix and solid composite materials as scatterers, can form a low-frequency bandgap and exhibits excellent sound insulation properties, thereby effectively controlling the propagation of underwater noise.
- Comparative analysis of the bandgap characteristics between the fluid-solid coupled phononic crystal solid cylinder structure and the hollow cylinder structure indicated that the hollow cylinder structure can establish a superior low-frequency bandgap. Compared to the solid cylinder structure of equivalent dimensions, the hollow cylinder structure significantly broadens the low-frequency bandgap, enhances sound insulation, achieves superior low-frequency broadband noise reduction, and is more lightweight and cost-effective.
- By infusing the fluid-solid coupled phononic crystal hollow cylinder structure with fluid, the transmission of elastic waves within a specified frequency range can be controlled, thereby adjusting the position of the bandgap attenuation range and enhancing the structure's applicability across various marine noise environments.

The fluid-solid coupled phononic crystal column structure presented in this study exhibits outstanding sound insulation capabilities for noise frequencies below 300 Hz in marine environments. This structure holds significant promise in mitigating the harmful effects of anthropogenic underwater noise on fish physiology, behavior, and populations, thereby enhancing the health of the aquatic ecosystem and safeguarding fish biodiversity.

Acknowledgments

This research was supported by the National Natural Science Foundation of China (no. 52301373), the Young Elite Scientists Sponsorship Program by CAST (2022QNRC001) and the Natural Science Foundation of Jiangsu Higher Education Institutions of China (no. 22KJB580005).

References

1. Crovo, J.A., Mendonça, M.T., Holt, D.E., & Johnston, C.E. (2015). Stress and auditory responses of the otophysan fish, *Cyprinella venusta*, to road traffic noise. *PLoS One*, *10*(9), Article e0137290. https://doi.org/10.1371/journal.pone.0137290
2. Fan, L., Zhang, L., Chen, D., Liu, G., & Wang, C. (2017). Research method about flow-induced noise in the bow of underwater vehicles (in Chinese). *Ship Science and Technology*, *39*(13), 48–53.
3. Herbert-Read, J.E., Kremer, L., Bruintjes, R., Radford, A.N., & Ioannou, C.C. (2017). Anthropogenic noise pollution from pile-driving disrupts the structure and dynamics of fish shoals. *Proceedings of the Royal Society B: Biological Sciences*, *284*(1863), Article 20171627. https://doi.org/10.1098/rspb.2017.1627
4. Huang, H., Yang, Y., Ruan, H., & Weng, J. (2023). Study about the correlation of very low frequency ocean noise with wind (in Chinese). *Journal of Applied Oceanography*, *42*(2), 255–263. https://doi.org/10.3969/J.ISSN.2095-4972.2023.02.009
5. Jia, F., He, R., & Xiang, Y. (2024). Experimental study of underwater noise HSD noise mitigation device for offshore wind turbine piles (in Chinese). *Marine Environmental Science*, *43*(3), 407–416.
6. Jiang, H., Wang, Y., Zhang, M., Hu, Y., Lan, D., Zhang, Y., & Wei, B. (2009). Locally resonant phononic woodpile: A wide band anomalous underwater acoustic absorbing material. *Applied Physics Letters*, *95*(10), Article 104101. https://doi.org/10.1063/1.3216805
7. Li, H., Cao, X., Shi, G., Zhang, X., Song, G., & Zhang, X. (2024). Research on sound insulation of floor support layer of high-speed trains based on phonon crystal (in Chinese). *Noise and Vibration Control*, *44*(1), 220–225.

8. Li, H., Guo, X., Song, G., Jia, Y., & Ma, L. (2022). Estimating the sound speed of the surface layer of the seabed using ocean ambient noise in shallow water (in Chinese). *Acta Acustica*, *47*(3), 348–355.

9. Lin, T., Liu, X., Wang, C., & Zhang, D. (2020). Effects of ship noise pressure level on swimming, feeding behaviors and immuno-physiological indicators of *Larimichthys crocea* juveniles (in Chinese). *Marine Fisheries*, *42*(1), 61–72.

10. Liu, H., Zhao, J., Yao, H., Han, D., Zhang, X., Wang, C., & Zhang, G. (2023). Bandgaps of a Helmholtz-type phononic crystal with adjustable chamber (in Chinese). *Journal of Synthetic Crystals*, *52*(4), 590–597.

11. Lu, Z., Zhu, X., Du, X., & Li, J. (2024). Development and prospect of deep-sea environmental noise monitoring technology (in Chinese). *Earth Science*, *49*(6), 2120–2130. http://doi.org/10.3799/dqkx.2023.162

12. Shi, H., Jiao, H., You, Z., Wang, Y., Li, S., Xu, J., & Yang, J. (2010). The effect of ship noise on the secretion of cortisol in *Lateolabrax japonicus* and *Pseudosciaena crocea* (in Chinese). *Acta Ecologica Sinica*, *30*(14), 3760–3765.

13. Wang, J., Zhou, H., & Zhang, J. (2022). Optimization design of low frequency sound absorption performance of local resonant cavity coating (in Chinese). *Ship Science and Technology*, *44*(22), 43–49.

14. Wu, J., Bai, X., Xiao, Y., Geng, M., Yu, D., & Wen, J. (2016a). Low frequency band gaps and vibration reduction properties of a multi-frequency locally resonant phononic plate (in Chinese). *Acta Physica Sinica*, *65*(6), Article 064602. http://doi.org/10.7498/aps.65.064602

15. Wu, J., Ma, F., Zhang, S., & Shen, L. (2016b). Application of acoustic metamaterials in low-frequency vibration and noise reduction (in Chinese). *Journal of Mechanical Engineering*, *52*(13), 68–78.

16. Yao, L., Xu, J., Jiang, G., & Wu, F. (2021). Band structure calculation of 2D fluid/solid and solid/fluid phononic crystal using a modified smoothed finite element method with fluid–solid interaction. *Ultrasonics*, *110*, Article 106267. https://doi.org/10.1016/j.ultras.2020.106267

17. Helal, K.M., Fragasso, J., & Moro, L. (2024). Effectiveness of ocean gliders in monitoring ocean acoustics and anthropogenic noise from ships: A systematic review. *Ocean Engineering*, *295*, Article 116993. https://doi.org/10.1016/j.oceaneng.2024.116993

18. Ye, L., Liu, Y., Liu, Y., Guo, J., & Yin, L. (2023). Study on behavior and physiology of low frequency vibration for *Larimichthys crocea* (in Chinese). *Fishery Modernization*, **50**(6), 1–8. https://doi.org/10.3969/j.issn.1007-9580.2023.06.001

19. Yin, J., Cai, L., Fang, X., Xiao, Y., Yang, H., Zhang, H., Zhong, J., Zhao, H., Yu, D., & Wen, J. (2022). Review on research progress of mechanical metamaterials and their applications in vibration and noise control (in Chinese). *Advances in Mechanics*, *52*(3), 508–586. http://doi.org/10.6052/1000-0992-22-005

20. Zhan, H., Li, X., Ni, M., Zhang, Z., Da, W., Wang, Y., Liu, Z., Liu, Y., He, C., Shi, X., & Liu, G. (2023). Research status and prospect of noise effect on fish (in Chinese). *Journal of Hydroecology*, *44*(6), 142–147.

21. Zhang, G., Gu, X., Xing, B., & Han, J. (2012). The classification and the impact of marine environment noise on marine animals (in Chinese). *Journal of Dalian Ocean University*, *27*(1), 89–94. https://doi.org/10.3969/j.issn.1000-9957.2012.01.018

22. Zhang, W., Yang, H., Ding, J., & Ji, X. (2017). The applicability research of offshore wind farm underwater noise propagation model (in Chinese). *Marine Sciences*, *41*(7), 78–86.

Manuscript received July 29, 2024; accepted for publication February 6, 2025; published online April 10, 2025.

JOURNAL OF THEORETICAL
AND APPLIED MECHANICS
63, 2, pp. 375–385, Warsaw 2025
https://doi.org/10.15632/jtam-pl/200939

DAMAGE MECHANISM AND AMPLIFICATION EFFECT OF COMPRESSION FAILURE IN SOFT ROCK WITH INITIAL CRACKS

Senyuan WEN[1], Chaoyi LIAO[2], Shitao YAN[3], Ning LIANG[4*], Tao JIN[4]

[1] *Guangxi Road And Bridge Engineering Group Co., Ltd, Nanning, China*
[2] *Transportation Comprehensive Administrative Law Enforcement Bureau of Guangxi Zhuang Autonomous Region, Nanning, China*
[3] *College of Road and Bridge Engineering, Guangxi Transport Vocational and Technical College, Nanning, China*
[4] *College of Civil and Architectural Engineering, Guangxi University of Science and Technology, Liuzhou, China*
*corresponding author, *liangn5@126.com*

This study presents an approach for characterizing the path of strength failure in pre-cracked soft rocks using the Weibull distribution. Based on the energy obtained from experiments, the damage propagation mechanism and energy dissipation mode of soft rocks were studied. The results indicate that the damage of soft rock forms a diffusion path starting from the two ends of the prefabricated crack, following a characterization model of the Weibull distribution. The dissipation and mutation of energy are the key factors related to the overall instability of the soft rock, and a damage amplification effect area of the soft rock is formed around the prefabricated cracks.

Keywords: soft rock; prefabricated crack; damage; energy characteristics; amplification effect.

1. Introduction

The distribution of soft rocks is extremely extensive worldwide, making these areas important locations for human activities and ecological preservation. In major engineering projects such as excavation in soft rock tunnels, the protection of soft rock slopes, and the reinforcement of foundations, an accurate analysis of the deformation and failure mechanism of soft rocks can provide important guidance for construction methods. The composition and arrangement of soft rock minerals, the initial damage degree, the compressive strength of the rock mass, and the crack pattern collectively determine the overall stability of soft rocks.

Based on the scientific and practical engineering problems aforementioned, many researchers have conducted studies on the failure mechanism of the soft rocks. The difference between the internal friction angle of the soft rock and the cohesive force of particles determines its own elastic modulus and mechanical properties, ultimately leading to different characteristics during its failure (Majedi *et al.*, 2021; Zhang *et al.*, 2022b). Researchers have investigated the correlation between the internal structure and mechanical properties of the soft rock based on the content and particle characteristics of its different components. With the continuous exacerbation of damage, the cracks in soft rocks generate and expand, ultimately leading to a decrease in mechanical performance (Liu *et al.*, 2023; Efimov, 2018). Significant research achievements have been made in relation to the uniaxial compression failure of soft rocks, providing a theoretical basis and experimental methods for the study of damage paths in soft rocks.

The existence of prefabricated cracks usually affects the degradation path and degree of soft rock, and newly generated microcracks mainly occur at both ends of prefabricated cracks (Yuan *et al.*, 2022; Li *et al.*, 2023). Meanwhile, comparing prefabricated cracks at different angles, it was found that the larger the inclination angle, the greater the elastic energy storage of the rock sample. The overall failure mode of rock samples also varies with the angle of

prefabricated cracks (Pan *et al.*, 2023; Zhou *et al.*, 2024). Through numerical experiments, the dynamic process of crack propagation and changes in stress intensity factors can be fully analyzed. The friction coefficient and bonding mode between particles are important physical quantities for the mesoscopic parameters of the soft rock, playing a major role in their mechanical properties (Riazi *et al.*, 2023; Wang *et al.*, 2021; Alenizi *et al.*, 2024). These research findings highlight the impact of pre-cracked soft rocks on the failure process, indicating that initial damage is a disadvantageous factor for soft rock disasters. However, most of the existing research results have focused on the qualitative and variation patterns of prefabricated cracks.

Researchers have also attempted to analyze the evolution of soft rock damage by using quantitative characterization methods. For example, a characterization model of the damage path of the soft rock can be achieved based on the number of sound emissions, energy density, and CT scans. The damage mechanism of soft rock was inferred based on the three-dimensional reconstruction image (Faisal *et al.*, 2017; Gautam *et al.*, 2021; Al-Marzougi, 2018). By utilizing ultrasonic and digital image correlation technologies, the internal pore distribution and stress-strain behavior on the outer surface of soft rocks can be effectively reflected. Ultimately, this enables a quantitative characterization of the three-dimensional space of soft rocks (Abbas *et al.*, 2022; Zhang *et al.*, 2022a; Tian *et al.*, 2024). Therefore, combining qualitative analysis with quantitative characterization is one of the more advantageous methods for studying the failure of soft rocks.

In conclusion, in relation to the existing research results, most studies focus on the analysis of soft rock failure characteristics and physical damage quantities. A series of complex changes triggered by soft rock damage still require further exploration of the related key issues. For example, establishing damage characterization models for soft rocks with different prefabricated crack angles can better predict the failure patterns of rock masses. Therefore, this article focuses on the above issues and presents numerical simulation experiments investigating the compression failure of soft rocks containing prefabricated cracks. The changes in the mechanical and physical parameters of soft rock failure are analyzed based on the experimental results. Based on the internal particle contact and arrangement patterns during the failure process of soft rocks, the study aims to investigate its damage amplification effect.

2. Materials and methods

2.1. Selection of numerical modes

In order to ensure the authenticity of numerical simulations, some parameters can be obtained through indoor experiments. This study focuses on the mudstone sandstone, conducting uniaxial compression failure tests by preparing rock samples with different prefabricated cracks. The experiment adopts a displacement-controlled loading method with a loading speed of 0.03 mm/min. As shown in Fig. 1, the minerals of this type of rock are mainly quartz, feldspar, and mud calcium cement, with a natural density of 2.23 g/cm^3 and an elastic modulus of 4.274 GPa. The rock sample is a standard cylinder with a bottom diameter of 50 mm and a height of 100 mm. The prefabricated crack is semi-transparent; its length, width, and depth dimensions are 10 mm, 2 mm, and 25 mm, respectively. The angle between the prefabricated crack and the horizontal direction is 0°, 15°, 30°, 45°, 60°, 75°, and 90°, respectively.

Fig. 1. Soft rock samples.

2.2. Determination of mesoscopic parameters in numerical experiments

PFC6.0 software was used for the simulations. In order to better simulate the real situation of particles inside the soft rock, the particles in this numerical experiment were all bonded in a parallel manner. In the numerical parallel bonding experiment, the parameters of the specimen include its density and elastic modulus. The mesoscopic parameters of particles include particle size ratio n, linear contact modulus E_c, parallel bonding modulus $\overline{E}_c$, normal bonding strength σ_c, tangential bonding strength τ_c, friction coefficient μ, and stiffness ratio n_k. The parameters of the sample were obtained in indoor experiments, and the mesoscopic parameters of the particles refer to the method introduced by Xiao *et al.* (2019). In order to ensure that the numerical simulation is similar to the indoor experiments, various mesoscopic parameters are continuously fine-tuned. The final parameters used for numerical experiments are shown in Table 1.

Table 1. Values of mesoscopic parameters in numerical experiments.

n	E_c [Pa]	$\overline{E}_c$ [Pa]	τ_c [Pa]	$\overline{\tau}_c$ [Pa]	μ	n_k	n
1.66	1.025E9	6.952E9	3.529E6	7.261E6	0.563	1.356	1.66

2.3. Particle contact model for numerical experiments

In numerical experiments, the connection properties between particles will affect the final accuracy of the calculation results. The interior of the soft rock can generally be divided into two categories, one of which is minerals without cementation, i.e., skeletal particles. These types of particles are relatively stable and do not have adhesive properties. Skeleton particles are usually rigidly connected, and only normal and tangential forces are transmitted between particles. The other category is minerals with cementation, i.e., clay particles. These types of particles have a relatively large composition inside soft rocks and usually play a cementing role between skeleton particles. When clay particles are connected or are inserted between clay particles and skeleton particles, normal force, tangential force, and torque can be transmitted between particles. In addition, these types of particles can maintain their stable state and prevent sliding and loss between particles.

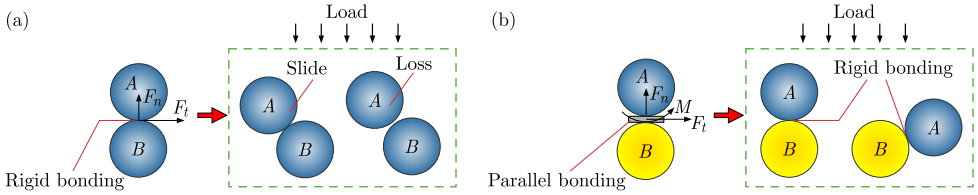

Fig. 2. Particle contact model: (a) rigid connection; (b) parallel bonding.

2.4. Numerical testing methods

This numerical experiment takes the results obtained from indoor experiments as a reference and tries to match them as closely as possible. Based on the mesoscopic parameters obtained above, numerical experiments were modeled and solved using different initial conditions for prefabricated cracks. The experiment is divided into three steps:

– Establishment of the model: the initial physical parameters are defined to form the basic properties of particle flow operations. The number of particles in this experiment is 10000, which meets the numerical test requirements. Based on the contact between particles, as well as between particles and walls, the position of the particles is continuously adjusted until the entire model finally reaches a stable state. For uniaxial compression, after the model is built, the wall on the outer surface of the specimen can be removed to ensure that the confining pressure during the numerical test is kept at zero. After particle generation, prefabricated cracks can form inside the particles. The models of the sample are shown in Fig. 3.

– The bonding properties of particles: particle mesoscopic parameters are set and the parallel bonding properties between particles are repeatedly adjusted. Due to the need to track the cracking between particles in numerical experiments, a measurement circle was added to this experiment, which was used to monitor the deformation and failure displacement of rock samples, and can also track the generation and propagation of cracks. Finally, the fish scripting language was used to set the particle bonding attributes.
– Apply loads and export results: according to the established axial wall model, a displacement-controlled loading method was adopted with a loading speed of 0.03 mm/min. During the loading process, the program recorded the stress and strain data of the specimen in real time, as well as recording the relevant physical quantities of the crack.

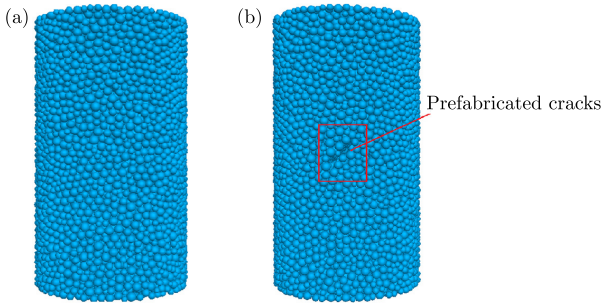

Fig. 3. Sample model for numerical simulation:
(a) no prefabricated crack; (b) including prefabricated crack.

3. Results

3.1. Compressive strength of rock samples with different prefabricated cracks

According to the results of the numerical experiments, the stress-strain curves of different rock samples during the loading process are shown in Fig. 4. In the initial loading stage, as the load increases, the internal particles of the rock sample are continuously compressed. At this point, the rock sample is similar to an isotropic material, and the stress-strain curve exhibits good linear characteristics. When the load reaches the compressive strength of the rock sample, the stress-strain curve loses its original linear variation characteristics and suddenly shows a sharp downward trend. At this point, the rock samples exhibit obvious brittle failure, and their ability to resist external loads becomes weaker. The compressive strength of rock samples with prefabricated cracks is mostly lower than that of rock samples without prefabricated cracks. The larger the angle of the prefabricated crack, the greater the compressive strength of the rock sample. It can be seen that the inclination angle and distribution of the damage location are the key factors affecting the compressive strength of rock samples.

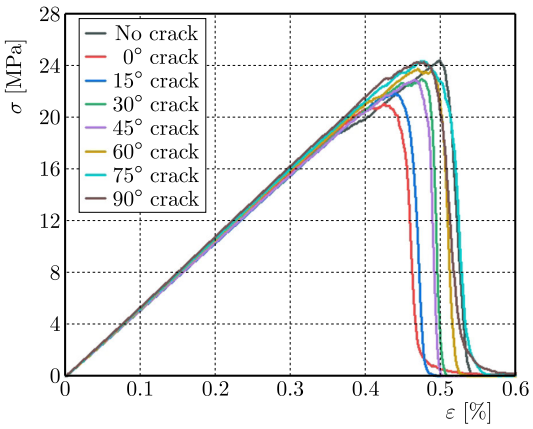

Fig. 4. Stress-strain curves of rock samples with different prefabricated cracks.

3.2. Morphological failure characteristics of rock samples with different prefabricated cracks

Figure 5 shows the final morphology of the rock samples under compression failure. It can be seen that the final failure of the rock sample occurs with the generation of the main crack, and a shear plane is formed along the direction of the main crack. For rock samples containing prefabricated cracks, newly generated cracks start from the two endpoints of the prefabricated cracks and propagate along the direction of the inclination angle. The cracks in rock samples

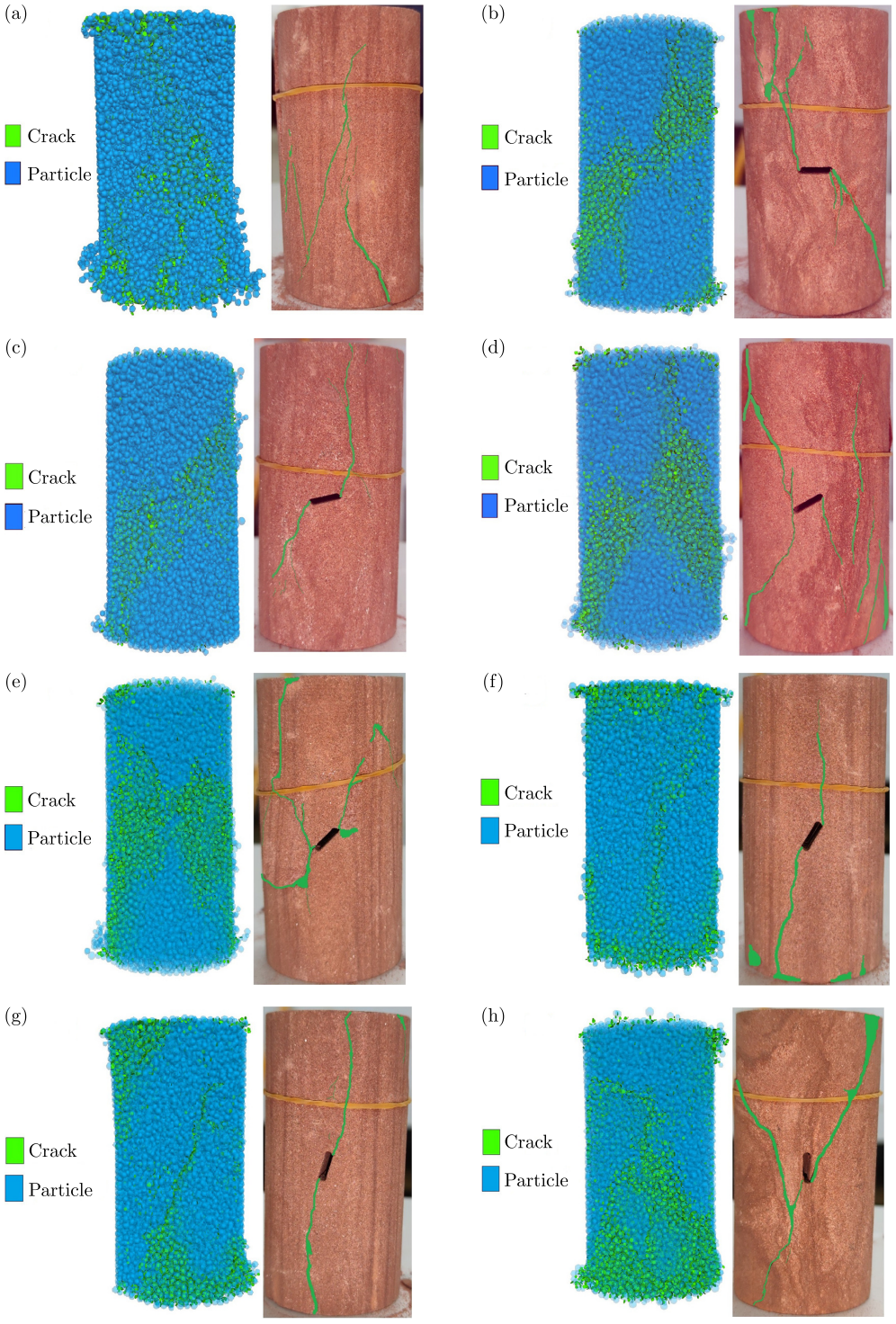

Fig. 5. Final failure mode of rock samples: (a) no crack; (b) 0° crack; (c) 15° crack; (d) 30° crack; (e) 45° crack; (f) 60° crack; (g) 75° crack; (h) 90° crack.

without prefabricated cracks are mainly in the vertical direction. Therefore, the initial damage of the rock sample not only affects the compressive strength of the rock mass, but also guides the failure mode of the rock mass. Meanwhile, for discrete materials such as soft rocks, when the shear plane continues to evolve, the rock mass will exhibit sudden characteristic changes. These sudden changes are the result of the accumulation of internal damage along the main direction in the soft rock.

3.3. Energy characterization of damage process in soft rock with different prefabricated cracks

Assuming that the soft rock and external loading jointly form a complete closed system, it can be considered that the system has no energy exchange with the outside world. From the previous analysis, it can be seen that the soft rock is in the initial stage of particle compaction during loading. For soft rocks, during the compression failure process, there is a continuous exchange of dissipated energy and strain energy. If U represents the total energy input of the loading part to the soft rock, then

$$U = \alpha U_d + \beta U_e, \tag{3.1}$$

where U_d and U_e are the dissipated energy, storage energy, and strain energy of the soft rock, respectively; α and β are the reduction coefficients of energy, which are related to prefabricated cracks and represent different initial damage levels of the soft rock. During uniaxial compression, the rock sample is only subjected to axial stress and the radial stress is 0. Therefore, in the initial stage of loading, there is basically no energy dissipation in the rock sample, and the vast majority is stored as axial strain energy:

$$U = \beta \int_0^{\varepsilon} \sigma \, \mathrm{d}\varepsilon_e, \tag{3.2}$$

where σ is the stress, ε is the total strain, and ε_e is the unit strain. According to the experimental results, it can be seen that when the external load does not reach the compressive strength of the rock sample, the stress-strain curve exhibits obvious linear characteristics. At this point, the rock sample can be approximated as an isotropic material and satisfies Hooke's law. Therefore, the strain energy stored in rock samples can be expressed as follows:

$$U_e = \beta \cdot \frac{1}{2}\sigma \, \mathrm{d}\varepsilon_e = \beta \cdot \frac{1}{2}\sigma\varepsilon = \beta \cdot \frac{E}{2} \cdot \varepsilon^2, \tag{3.3}$$

where E is the elastic modulus of the soft rock. According to Eq. (3.3), the accumulation of energy in rock samples comes from the application of loads. At this point, the rock sample converts external loads into strain energy and continuously completes the storage. When the load reaches the compressive strength of the rock sample, the stored strain energy of the rock sample reaches its maximum value, which is inevitably accompanied by the release of energy. Therefore, after the peak strength, the rock sample releases strain energy in the form of dissipated energy.

The total energy curves of different pre-cracked rock samples during the loading process are shown in Fig. 6. In the initial stage of loading, as the load continues to increase, the strain of the rock sample also increases. The strain and strain energy stored in rock samples follow a quadratic exponential distribution. When the load exceeds the compressive strength of the rock sample, the total energy of the rock sample reaches a stable state, and the rock sample exhibits a sudden failure characteristic. This is due to the strain energy being converted into dissipated energy in a short period of time. The release of dissipated energy in rock samples leads to rapid brittle failure.

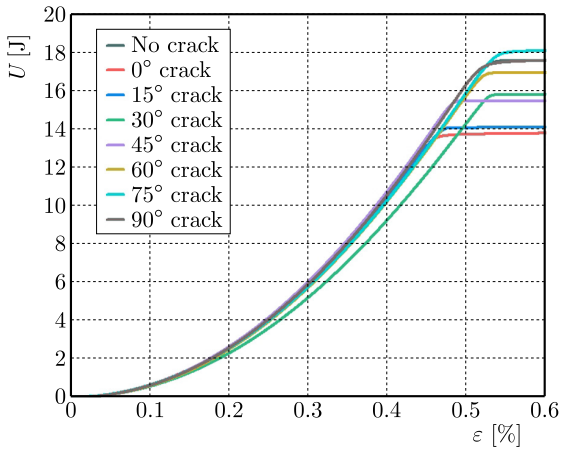

Fig. 6. Total energy curves of different pre-cracked rock samples during loading.

4. Discussion

4.1. Distribution characterization model of soft rock damage caused by different prefabricated cracks

For soft rock, its internal structure is complex and uneven. The Weibull distribution can effectively describe this random strength characteristic, and the parameters in its probability density function can reflect the physical and mechanical properties of the soft rock, such as material uniformity, defect distribution, etc. By assuming that the strength of the soft rock follows the Weibull distribution, it can better capture the laws of strength changes in the soft rock under different prefabricated crack conditions, and more accurately predict the failure mode and mechanical behavior of the soft rock.

As a discrete medium, the soft rock is initially distributed with pores and fractures of varying sizes. Therefore, the rock sample exhibits varying degrees of initial damage, and the presence of prefabricated cracks determines the different states of initial damage. Assuming that the strength of the soft rock follows the Weibull distribution, the relevant probability density function $P(\varepsilon)$ is as follows:

$$P(\varepsilon) = \frac{m}{F}\left(\frac{\varepsilon}{F}\right)^{m-1} \exp\left[-\left(\frac{\varepsilon}{F}\right)^{m}\right], \tag{4.1}$$

where ε represents the strain of the soft rock, while m and F represent the Weibull distribution parameters – these represent the physical and mechanical properties of the soft rock. The ratio of the number of microelements N_e that cause failure in the soft rock to the total number of microelements N in the soft rock is defined as the damage variable, which can be expressed as follows:

$$D = \frac{N_e}{N} = \frac{\int_0^{\varepsilon} NP(x)\,\mathrm{d}x}{N} = \frac{N\left\{1-\exp\left[-\left(\frac{\varepsilon}{F}\right)^{m}\right]\right\}}{N} = 1-\exp\left[-\left(\frac{\varepsilon}{F}\right)^{m}\right]. \tag{4.2}$$

According to the acoustic emission results obtained from numerical experiments, it can be seen that the amount of ringing is mostly concentrated near the peak stress, and the amount of ringing in other processes is very small. The entire acoustic emission curve shows a clear peak and a sharp decline on both sides. This distribution feature is very similar to the damage variable characterization equation aforementioned. If the damage distribution of the acoustic emission curve is similar to that of a rock sample, the characterization equation of the fitted acoustic emission ringing number N is as follows:

$$N = D_0 + a \cdot \exp\left[\frac{(\varepsilon_c-\varepsilon)^2}{2b^2}\right], \tag{4.3}$$

where D_0 is the initial damage value, ε_c is the peak strain, ε is the strain, and a and b are the distribution parameters, respectively. Therefore, the related parameters of different pre-cracked soft rock damage fitted by the above equation are shown in Table 2.

Table 2. Values of mesoscopic parameters in numerical experiments.

Parameter	No crack	0°	15°	30°	45°	60°	75°	90°
D_0	0.052	0.046	0.047	0.050	0.047	0.045	0.069	0.043
ε_c	0.517	0.453	0.461	0.488	0.482	0.499	0.517	0.501
a	19.954	21.174	22.542	19.032	24.137	19.953	18.874	12.957
b	0.005	0.005	0.004	0.004	0.004	0.006	0.005	0.005

According to the data in Table 2, it can be seen that different prefabricated cracks have varying degrees of influence on the initial damage, peak strain, and distribution parameters of the soft rock. In addition, the peak strain without prefabricated cracks is larger than that with prefabricated cracks. This indicates that soft rocks with a smaller amount of initial damage have a stronger strain capacity and a greater compressive performance. The peak strain of the soft rock with 0° prefabricated cracks is the smallest. This result has also been validated in numerical simulation and indoor experiments.

4.2. Amplification criteria of soft rock damage caused by different prefabricated cracks

According to the experimental results and the comprehensive analysis above, the application of load causes the soft rock to absorb a large amount of energy and store it inside the rock mass. This causes the continuous adjustment of the internal structure of the soft rock. A nonlinear dynamic mechanism is formed between the soft rock and the external loads. The fluctuation and mutation of energy ultimately cause an amplification effect of soft rock damage, leading to the overall failure of the soft rock. At this point, the soft rock exhibits a strong damage amplification effect, and its internal particles continuously recombine. The damage and failure process of rock samples without prefabricated cracks and with 45° prefabricated cracks is illustrated in Figs. 7 and 8.

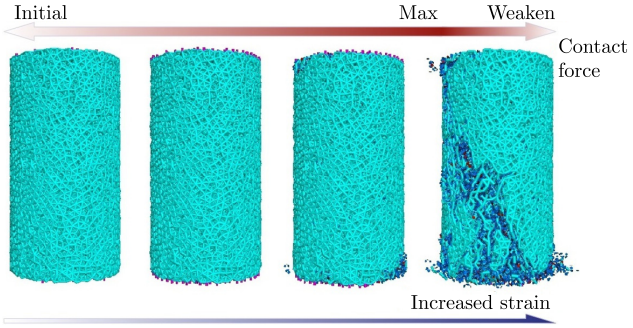

Fig. 7. Particle contact force during damage process of rock samples without prefabricated cracks.

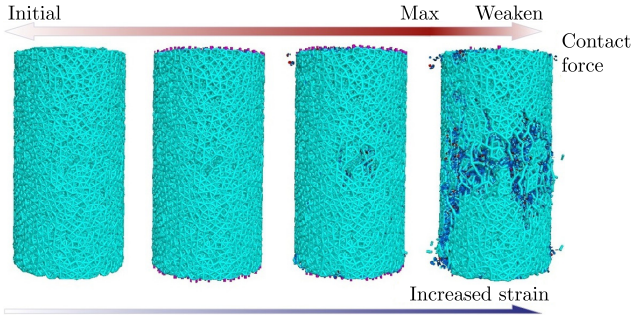

Fig. 8. Particle contact force during damage process of 45° pre-cracked rock samples.

When the load continues to increase, the contact force between particles reaches the limit state, and the bearing capacity of particles cannot resist more loads. Figure 9 shows the damage amplification effect model of the internal structure of soft rocks. At this point, the particles inside the rock sample mainly reflect two possible adjustment forms. One form transfers the load to nearby particles, whereby the connections between nearby particles become tighter. Another form involves the connection performance between particles being disrupted, resulting in the release of load and the formation of local damage. When the vast majority of particles inside the rock sample reach the limit state of bearing capacity, these tightly connected particles instantaneously fail, releasing the load they bear. At this point, it is the concentrated manifestation of the amplification effect of rock damage, which is the key node for the overall failure of the soft rock.

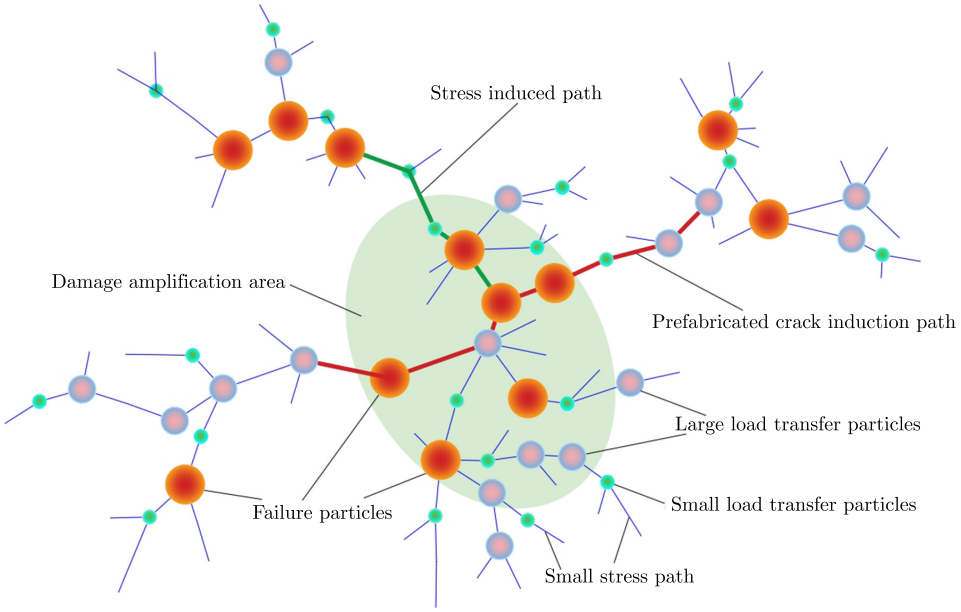

Fig. 9. Damage amplification effect model for the internal structure of soft rocks.

4.3. Exploration of numerical simulation on soft rock damage path and amplification effect

Numerical simulation can deeply explore the mechanical behavior and damage evolution process of the soft rock under different prefabricated crack conditions. Więckowski (2004) introduced the application of the material point method in large strain industrial and geomechanical problems. Similar to the research content of this article, both emphasize the relationship between the microstructure and the macroscopic mechanical response of materials. Sokołowski and Kamiński (2018) used the stochastic finite element method (SFEM) to study the mechanical properties of composite materials with defects. This is consistent with the method used in this article to consider the influence of prefabricated cracks on the mechanical properties of soft rocks, which focuses on the impact of internal defects or damage on the overall performance of the material. In addition, some researchers (Riazi *et al.*, 2023; Sun *et al.*, 2023; Wu *et al.*, 2023) found, through particle flow software or XFEM methods, that the pre-splitting angle of rocks has a significant impact on the mechanical properties and crack propagation of the model. This complements the research presented in this article, emphasizing the advantages of numerical simulation in revealing the internal mechanical mechanisms of rocks.

5. Conclusions

This article proposes a method that uses the Weibull distribution to characterize the strength failure path of pre-fractured soft rock, and studies the damage propagation mechanism and en-

ergy dissipation mode of the soft rock based on numerical and indoor experiments. The dissipation and mutation of energy have been identified as key factors in the overall instability of the soft rock, and it has been found that there is a damage amplification effect zone around prefabricated cracks. The research conclusions are as follows:

- At the initial stage of loading, the stress-strain curves of different pre-fractured soft rocks exhibit good linear characteristics. After the peak stress, the curve becomes dispersed. The compressive strength of soft rock decreases with the decrease in the precast crack angle. The damage of the soft rock propagates along the direction of prefabricated cracks.
- Soft rocks exhibit evolution laws of energy absorption, dissipation, and abrupt changes during compression. The damage changes in the soft rock follow the Weibull distribution, exhibiting obvious nonlinear and non-equilibrium phase transition characteristics. The smaller the angle of prefabricated cracks, the lower the peak stress of the soft rock. This indicates a faster failure rate and more pronounced brittle characteristics, revealing the key role of energy dissipation and abrupt changes in overall instability.
- The damage and destruction of soft rocks have a significant amplification effect, which is a concentrated manifestation of their internal particle connections and continuous adjustments. The load is transmitted or released by particles inside the soft rock, ultimately forming a damage amplification effect zone of overall failure. Elucidating the relationship between soft rock damage, internal particle connection adjustment, and load transfer and release provides a new perspective for the stability analysis of soft rock engineering.

Acknowledgments

This research was supported by the Guangxi Science and Technology Program (no. AD23026265, no. AD21220126), the Scientific Research Basic Ability Improvement Project of Young and Middle-aged Teachers in Guangxi Colleges and Universities (no. 2022KY1140).

References

1. Abbas, H.A., Mohamed, Z., & Mohd-Nordin, M.M. (2022). Characterization of the body wave anisotropy of an interbedded sandstone-shale at multi orientations and interlayer ratios. *Geotechnical and Geological Engineering*, *40*(7), 3413–3429. https://doi.org/10.1007/s10706-022-02096-8
2. Alenizi, F.A., Mohammed, A.H., Alizadeh, S.M., Gohari, O.M., & Motahari, M.R. (2024). Appraisal of rock dynamic, physical, and mechanical properties and forecasting shear wave velocity using machine learning and statistical methods. *Journal of Applied Geophysics*, *223*, Article 105216. https://doi.org/10.1016/j.jappgeo.2023.105216
3. Al-Marzouqi, H. (2018). Digital rock physics: Using CT scans to compute rock properties. *IEEE Signal Processing Magazine*, *35*(2), 121–131. https://doi.org/10.1109/MSP.2017.2784459
4. Efimov, V.P. (2018). Features of uniaxial compression failure of brittle rock samples with regard to grain characteristics. *Journal of Mining Science*, *54*(2), 194–201. https://doi.org/10.1134/S1062739118023545
5. Faisal, T.F., Awedalkarim, A., Chevalier, S., Jouini, M.S., & Sassi, M. (2017). Direct scale comparison of numerical linear elastic moduli with acoustic experiments for carbonate rock X-ray CT scanned at multi-resolutions. *Journal of Petroleum Science and Engineering*, *152*, 653–663. https://doi.org/10.1016/j.petrol.2017.01.025
6. Gautam, P.K., Dwivedi, R., Kumar, A., Verma, A.K., Singh, K.H., & Singh, T.N. (2021). Damage characteristics of Jalore granitic rocks after thermal cycling effect for nuclear waste repository. *Rock Mechanics and Rock Engineering*, *54*(1), 235–254. https://doi.org/10.1007/s00603-020-02260-7
7. Li, B., He, Y.Z., Li, L., Zhang, J.X., Shi, Z., & Zhang, Y.P. (2023). Damage evolution of rock containing prefabricated cracks based on infrared radiation and energy dissipation. *Theoretical and Applied Fracture Mechanics*, *125*, Article 103853. https://doi.org/10.1016/j.tafmec.2023.103853

8. Liu, J., Wang, B., Wang, Y.S., Shi, L., Xie, X.K., & Lan, J. (2023). Experimental study on a granular material-filled lining in a high ground-stress soft-rock tunnel. *Applied Sciences*, *13*(24), Article 13326. https://doi.org/10.3390/app132413326

9. Majedi, M.R., Afrazi, M., & Fakhimi, A. (2021). A micromechanical model for simulation of rock failure under high strain rate loading. *International Journal of Civil Engineering*, *19*(5), 501–515. https://doi.org/10.1007/s40999-020-00551-2

10. Pan, X.W., Wan, L., Jiang, T., Jia, Y.C., & Zhang, S. (2023). Experimental study on strength and failure characteristics of mortar specimens with prefabricated cracks under uniaxial and triaxial stress. *Frontiers in Materials*, *10*, Article 1287623. https://doi.org/10.3389/fmats.2023.1287623

11. Riazi, E., Yazdani, M., & Afrazi, M. (2023). Numerical study of slip distribution at pre-existing crack in rock mass using extended finite element method (XFEM). *Iranian Journal of Science and Technology, Transactions of Civil Engineering*, *47*(4), 2349–2363. https://doi.org/10.1007/s40996-023-01051-8

12. Sokołowski, D. & Kamiński, M. (2018). Computational homogenization of carbon/polymer composites with stochastic interface defects. *Composite Structures*, *183*, 434–449. https://doi.org/10.1016/j.compstruct.2017.04.076

13. Sun, X., Li, W., Zhang, C., Zhang, G., & Xia, Z. (2023). Mechanical behaviors and fracture characteristics of sandstone combinations with different pre-crack angles. *KSCE Journal of Civil Engineering*, *27*(12), 5388–5400. https://doi.org/10.1007/s12205-023-1941-8

14. Tian, H., Shu, X., Chen, W., Tan, X., Yang, D., & Tian, Y. (2024). Impact of structural anisotropy on compressive creep behaviors of composite rocks based on digital image correlation technology. *Bulletin of Engineering Geology and the Environment*, *83*(8), Article 299. https://doi.org/10.1007/s10064-024-03792-w

15. Wang, H., Wang, Y.Y., Yu, Z.Q., & Li, J.G. (2021). Experimental study on the effects of stress-induced damage on the microstructure and mechanical properties of soft rock. *Advances in Civil Engineering*, *2021*(1), Article 6696614. https://doi.org/10.1155/2021/6696614

16. Więckowski, Z. (2004). The material point method in large strain engineering problems. *Computer Methods in Applied Mechanics and Engineering*, *193*(39–41), 4417–4438. https://doi.org/10.1016/j.cma.2004.01.035

17. Wu, Y., Ma, D.D., Hu, X.J., Hao, Y., Liu, C.H., & Zhou, H.Y. (2023). Numerical simulation on the mechanical and fracture behavior of bedding argillaceous sandstone containing two pre-existing flaws. *Theoretical and Applied Fracture Mechanics*, *127*, Article 104047. https://doi.org/10.1016/j.tafmec.2023.104047

18. Xiao, Z.Q., Wang, X., Tang, D.S., Dong, Q.Y., Jiang, Y.N., Yang, K., Cao, T.T., & Deng, Z. (2019). Microscopic fabric characteristics of typical red soft rock in Badong Formation under uniaxial compression test (in Chinese). *Coal Geology & Exploration*, *47*(6), 103–114.

19. Yuan S.X., Jiang, T., Lei, J.H., & Cui, C.H. (2022). Experimental study on fracture characteristics of rock-like material with prefabricated cracks under compression shear. *Scientific Reports*, *12*(1), Article 2809. https://doi.org/10.1038/s41598-022-06712-8

20. Zhang, K., Jiang, Z., Liu, X.H., Zhang, K., & Zhu, H. (2022a). Quantitative characterization of the fracture behavior of sandstone with inclusions: Experimental and numerical investigation. *Theoretical and Applied Fracture Mechanics*, *121*, Article 103429. https://doi.org/10.1016/j.tafmec.2022.103429

21. Zhang, W., Zhao, T., & Yin, Y. (2022b). Prefabricated fractured rock under stepwise loading and unloading. *Journal of Theoretical and Applied Mechanics*, *60*(1), 167–179. https://doi.org/10.15632/jtam-pl/145582

22. Zhou, J., Wang, K.Z., Zhou, W.D., Yao, Y.L., & Xie, T. (2024). Uniaxial compressive damage characteristics of rock-like materials with prefabricated conjugate cracks. *Applied Sciences*, *14*(2), Article 20823. https://doi.org/10.3390/app14020823

Manuscript received November 4, 2024; accepted for publication February 6, 2025; published online April 10, 2025.

JOURNAL OF THEORETICAL
AND APPLIED MECHANICS
63, 2, pp. 387–399, Warsaw 2025
https://doi.org/10.15632/jtam-pl/201245

VIBRATION ANALYSIS AND CONTROL OF 2SPS+SR SUSPENSION SEAT FOR IMPROVING VEHICLE RIDE COMFORT

Bijuan YAN*, Haiqing ZHANG, Yihang GENG, Wenjun ZHANG

Taiyuan University of Science and Technology, 030024, Taiyuan, Shanxi, China
*corresponding author, *tyustybj@tyust.edu.cn*

In order to minimize three-dimensional vibrations and improve the ride comfort of a construction vehicle, the 2-spherical-prismatic-spherical+spherical-revolute (2SPS+SR) parallel suspension seat is examined. The dynamic differential equations of the seven degree-of-freedom (DOF) vehicle and the seat model are derived. Under E-, F-, and G-level roads (classified based on standard or index, e.g., ISO 8608, for road roughness), the dynamic responses of the 2SPS+SR seat are analyzed. The simulation results indicate that the seat comfort performance using fuzzy-PID control is enhanced by 40.91 %, 19.84 %, and 36.40 %, which are compared with PID under E-, F-, and G-level roads, respectively.

Keywords: construction vehicle; 2SPS+SR seat suspension; ride comfort; fuzzy-PID.

1. Introduction

Construction vehicles play an important role for assisting employees and increasing their work efficiency in modern economic development. However, they often travel or work on off-roads, the working environments are very poor. Mechanical vibrations in different directions from the source of vibration are transmitted to the drivers through the tires, vehicle suspensions, suspension cab and seat (Yan *et al.*, 2022). The operators react to the unwanted vibrations due to psychological and physiological reasons. The relevant studies in (Desai *et al.*, 2021) show that humans respond differently to vibrations of different frequencies. At the same time, the vibration frequency of vehicles is also located between 0 Hz–20 Hz. Therefore, these vibrations cause adverse health effects for drivers to a certain extent and reduce the service life of vehicle components. So, reducing the vibrations of construction vehicles especially in the low frequency range has become a research hotspot in recent years.

Nowadays, the seat suspension systems are widely used to attenuate whole-body vibration exposure on drivers. For example, Deng *et al.* (2022) investigated a seat suspension installed with rotary magnetorheological dampers to avoid end-stop impact. The negative-stiffness-structure seat suspensions are designed to further ameliorate the vehicle ride quality for different vibration conditions (Ni *et al.*, 2023). Tan *et al.* (2021) used an air suspension system to improve the ride comfort of buses. However, considering that the seated human body is sensitive to the pitch vibration of vehicles, the parallel mechanisms have been applied to vehicle seats to achieve multi-dimensional vibration reduction from the cab to the driver (Sun *et al.*, 2023). For example, Zhang *et al.* (2015) proposed a 3-revolute-prismatic-cylindrical (3-RPC) parallel mechanism combined with energy dissipation components to achieve multi-dimensional vibration reduction. Wu *et al.* (2011) proposed a three-translation parallel mechanism which can make the human body have a better ride comfort.

On the other hand, the seat suspension systems could be classified into three types including passive, semi-active and active suspensions from the view of control modes. Early researches mainly focused on the passive seat suspension, but its damping performance is unsatisfactory

once the vehicle working conditions change. Therefore, in order to solve the above questions, the semi-active and active control become more and more popular. For example, Abdul Zahra and Abdalla (2020) use the combination of fuzzy super twisting sliding mode concept (FSTSMC) and PID controller to improve the comfort of the driver under random road. Khan *et al.* (2016) established an active controller of vehicle suspension systems. With the development of magnetorheological (MR), semi-active suspensions using these smart materials are used and studied by many researchers. For example, Zhang and Zhao (2017) proposed a semi-active car seat suspension with MR damper, and compared three control methods of fuzzy sliding mode controller with expansion factor (FSMCEF), PID, and SMC. Jain *et al.* (2020) proposed a semi-active seat suspension based on MR dampers. Maciejewski *et al.* (2020) analyzed an active vibration damping system with a seated human body. And a new control strategy for permanent magnet synchronous motors is proposed. Based on the mathematical model of mass-spring-damper (MSD) system, Maciejewski *et al.* (2020) proposed the horizontal seat suspension system using sliding mode control (SMC) strategy. It can be seen from the above-mentioned documents that most on current research seat suspensions are based on road vehicles such as automobiles, there are few studies about "off-road" construction vehicles.

Based on the above researches, this paper studies the vibration-reducing performance of the kind of 2SPS+SR parallel suspension seat. In order to verify its three-directional movements, the single-open-chain theory is used to obtain the position and orientation characteristics (POC) set of the seat. The motion differential equations of the seven-DOF vehicle and three-DOF 2SPS+SR suspension seat is established. A fuzzy PID controller that applies the seat acceleration variables as feedback signals is proposed, which can control the vertical, fore-aft and lateral vibration of the vehicle. And the vibration reduction performance of the seat suspension and the ride comfort of the drivers under different control and different roads are compared.

2. Physical model of 2SPS+SR seat suspension

2.1. Structure of 2SPS+SR seat suspension

As is shown in Fig. 1, the new 2SPS+SR parallel seat suspension is equipped with three evenly distributed limbs, in which two limbs are composed of moving and spherical pairs

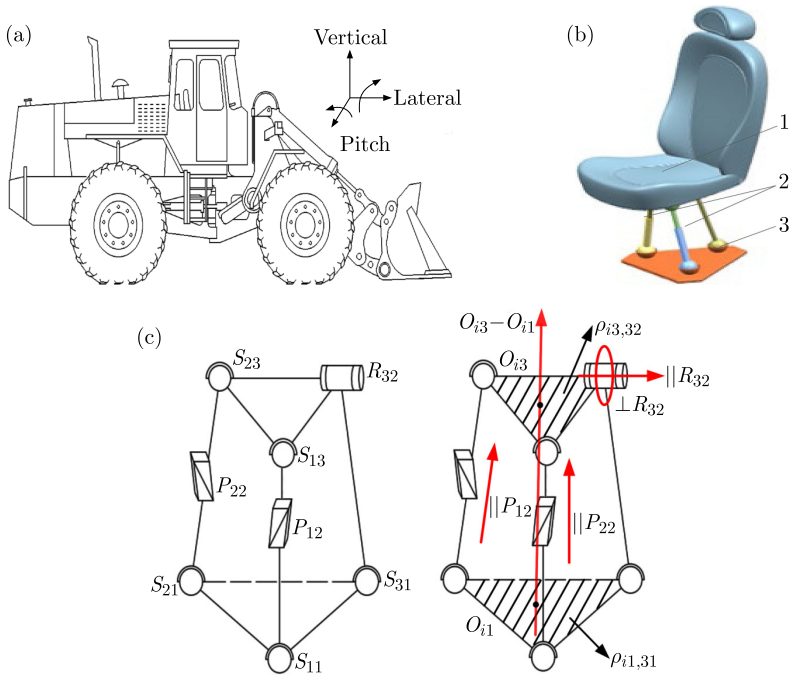

Fig. 1. 2SPS+SR seat suspension of construction vehicle: (a) construction vehicle; (b) seat model (1 – seat, 2 – moving pair, 3 – rotary pair); (c) 2SPS+SR parallel structure.

$\{-S_{i1}-P_{i2}-S_{i3}-\}$ $(i=1,2)$ and the other limb consists of spherical and rotary pairs $\{-S_{31}-R_{32}-\}$. Here, S stands for spherical pair, P is moving pair, and R is rotary pair.

2.2. Vertical-pitch-lateral movement verification

Based on the single-open-chain theory (Yang, 2012), POC sets of the limbs $\{-S_{i1}-P_{i2}-S_{i3}-\}$ $(i=1,2)$ are is described as follows:

$$M_{bi} = \begin{bmatrix} t^1(\parallel P_{i2}) \\ r^0 \end{bmatrix} \cup \begin{bmatrix} t^2(\perp\rho_{i3,32}) \\ r^3(O_{i3}) \end{bmatrix} \cup \begin{bmatrix} t^2(\perp\rho_{i1,3i}) \\ r^3(O_{i1}) \end{bmatrix}$$
$$= \begin{bmatrix} t^1(\parallel P_{i2}) \cup \{t^2(\perp\rho_{i3,32}) \cup \{t^2(\perp\rho_{i1,31}\}\} \\ r^3(O_{i3-i1}) \end{bmatrix}, \qquad i=1,2 \tag{2.1}$$

where $t^1(\parallel P_{i2})$ represents a movement which is parallel to the P_{i2} axis, $t^2(\perp\rho_{i3,32})$ denotes two movements which are perpendicular to the $\rho_{i3,32}$ direction, $t^2(\perp\rho_{i1,3i})$ denotes two movements of the chain end which are perpendicular to the vector $\rho_{i1,3i}$, and $r^3(O_{i3}–O_{i1})$ shows that there are three rotations which are perpendicular to the axis $O_{i3}–O_{i1}$.

The POC set of the $\{-S_{31}-R_{32}-\}$ chain are defined as follow:

$$M_{b1} = \begin{bmatrix} t^1(\perp R_{32}) \\ r^1(\parallel R_{32}) \end{bmatrix} \cup \begin{bmatrix} t^0 \\ r^2(O_{31}) \end{bmatrix} = \begin{bmatrix} t^1(\perp R_{32}) \\ r^2(O_{31}) \end{bmatrix}, \tag{2.2}$$

where $t^1(\perp R_{32})$ denotes one movement of the chain end which is vertical to the axis R_{32}, $r^2(O_{31})$ is chosen for two rotations which are vertical to the axis O_{31}.

Therefore, the POC set of the whole 2SPS+SR parallel seat suspension is obtained:

$$M_{Pa} = \begin{bmatrix} [t^1(\perp R_{32}) \cap [t^1(\perp P_{12}) \cup t^2(\perp\rho_{13,32})] \cap [t^1(\perp P_{22}) \cup t^2(\perp\rho_{23,32})] \\ [r^2(O_{31})] \cap [r^3(O_{13-11})] \cap [r^3(O_{23}-O_{21})] \end{bmatrix}$$
$$= \begin{bmatrix} [t^1(\perp R_{32})] \cap [t^1(\perp P_{12})] \cup [t^2(\perp\rho_{13,32})] \cap [t^1(\perp P_{22})] \cup [t^2(\perp\rho_{23,32})] \\ [r^1(\parallel (O_{13}-O_{11}))] \cup [r^1(\parallel (O_{23-21}))] \cup [r^1(\parallel (O_{11},O_{21},O_{31}))] \end{bmatrix}. \tag{2.3}$$

As can be seen from Eq. (2.3), the POC set of the new type 2SPS+SR parallel seat suspension has three independent elements, and it could realize the desired three-dimensional vertical-pitch-lateral movements. As a results, the seat suspension structure is feasible and reasonable. Figure 2 shows the 2SPS+SR parallel seat suspension.

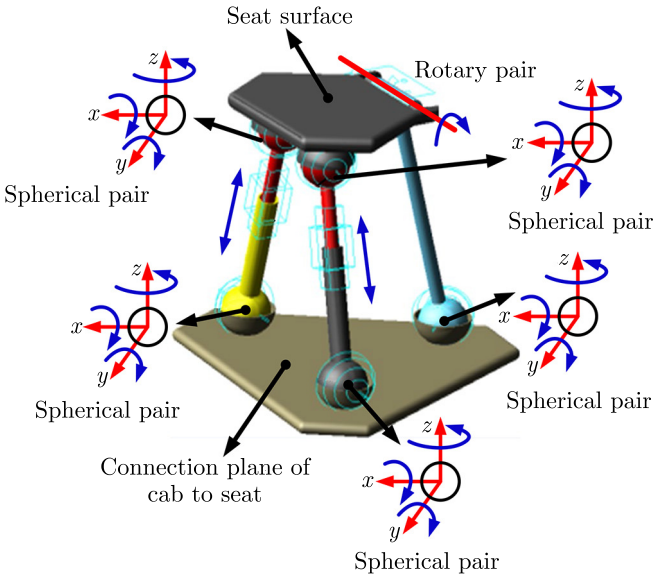

Fig. 2. 2SPS+SR parallel seat suspension.

3. Mathematical model of seat suspension

3.1. Seven degree-of-freedom vehicle model

In this paper, the seven DOF model (depicted in Fig. 3) is used to evaluate the ride comfort of the proposed 2SPS+SR parallel seat suspension. In Fig. 3, m_s and m_{wi} $(i = 1, 2, 3, 4)$ are the mass for the vehicle body and the i-th mass of wheel axles, m_s is the unsprung mass, m_{wi} $(i = 1, 2, 3, 4)$ is the i-th sprung mass, respectively; c_i and k_i $(i = 1, 2, 3, 4)$ denote damping and stiffness coefficients for the vehicle suspensions; c_{ti} and k_{ti} $(i = 1, 2, 3, 4)$ represent the damping and stiffness of tires, a and b are the distances of unsprung masses to the center of gravity of the axles, f and d are the distances between the center of the vehicle body and the front or rear axles; z_{si} and z_{ui} $(i = 1, 2, 3, 4)$ are the vertical displacements of the four support points on vehicle body and suspension systems (base), z_{gi} is the i-th road excitations; z_s, θ, ϕ are the vibration outputs of the vehicle body.

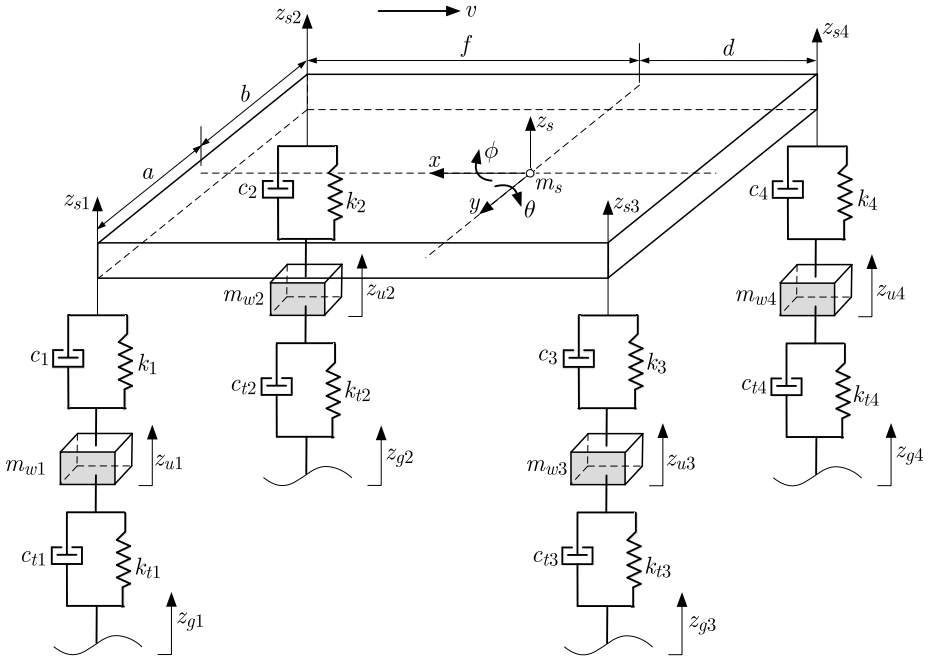

Fig. 3. Seven-DOF vehicle model.

The vertical displacement of the four support points on the vehicle body z_{si} $(i = 1, 2, 3, 4)$ could be obtained by:

$$\begin{aligned} z_{s1} &= z_s + f\theta + a\phi, \qquad & z_{s2} &= z_s + f\theta - b\phi, \\ z_{s3} &= z_s - d\theta + a\phi, \qquad & z_{s4} &= z_s - d\theta - b\phi. \end{aligned} \tag{3.1}$$

The mathematical model that describes a vertical motion of the vehicle body can be written as follows:

$$\begin{aligned} m_s\ddot{z}_s + k_1(z_{s1} - z_{u1}) + c_1(\dot{z}_{s1} - \dot{z}_{u1}) + k_2(z_{s2} - z_{u2}) + c_2(\dot{z}_{s2} - \dot{z}_{u2}) \\ + k_3(z_{s3} - z_{u3}) + c_3(\dot{z}_{s3} - \dot{z}_{u3}) + k_4(z_{s4} - z_{u4}) + c_4(\dot{z}_{s4} - \dot{z}_{u4}) = 0. \end{aligned} \tag{3.2}$$

And the differential equation of the vehicle unit in the pitch direction is established:

$$\begin{aligned} I_{yy}\ddot{\theta} - k_1(z_{s1} - z_{u1}) \cdot f - c_1(\dot{z}_{s1} - \dot{z}_{u1}) \cdot f - k_2(z_{s2} - z_{u2}) \cdot f - c_2(\dot{z}_{s2} - \dot{z}_{u2}) \cdot f \\ + k_3(z_{s3} - z_{u3}) \cdot d + c_3(\dot{z}_{s3} - \dot{z}_{u3}) \cdot d + k_4(z_{s4} - z_{u4}) \cdot d + c_4(\dot{z}_{s4} - \dot{z}_{u4}) \cdot d = 0. \end{aligned} \tag{3.3}$$

The roll movement differential equation is expressed by using the following relation:

$$I_{xx}\ddot{\phi} + k_1(z_{s1} - z_{u1}) \cdot a + c_1(\dot{z}_{s1} - \dot{z}_{u1}) \cdot a - k_2(z_{s2} - z_{u2}) \cdot b - c_2(\dot{z}_{s2} - \dot{z}_{u2}) \cdot b + k_3(z_{s3} - z_{u3}) \cdot a + c_3(\dot{z}_{s3} - \dot{z}_{u3}) \cdot a - k_4(z_{s4} - z_{u4}) \cdot b - c_4(\dot{z}_{s4} - \dot{z}_{u4}) \cdot b = 0. \quad (3.4)$$

In addition, the vertical movement differential equations of four unsprung masses of the vehicle body are obtained as follows:

$$\begin{aligned} &m_{w1}\ddot{z}_1 + k_1(z_{u1} - z_{s1}) + c_1(\dot{z}_{u1} - \dot{z}_{s1}) + k_{t1}(z_{u1} - z_{g1}) + c_{t1}(\dot{z}_{u1} - \dot{z}_{g1}) = 0, \\ &m_{w2}\ddot{z}_2 + k_2(z_{u2} - z_{s2}) + c_2(\dot{z}_{u2} - \dot{z}_{s2}) + k_{t2}(z_{u2} - z_{g2}) + c_{t2}(\dot{z}_{u2} - \dot{z}_{g2}) = 0, \\ &m_{w3}\ddot{z}_3 + k_3(z_{u3} - z_{s3}) + c_3(\dot{z}_{u3} - \dot{z}_{s3}) + k_{t3}(z_{u3} - z_{g3}) + c_{t3}(\dot{z}_{u3} - \dot{z}_{g3}) = 0, \\ &m_{w4}\ddot{z}_4 + k_4(z_{u4} - z_{s4}) + c_4(\dot{z}_{u4} - \dot{z}_{s4}) + k_{t4}(z_{u4} - z_{g4}) + c_{t4}(\dot{z}_{u4} - \dot{z}_{g4}) = 0. \end{aligned} \quad (3.5)$$

Substituting Eq. (3.1) to Eqs. (3.2)–(3.5), the seven DOF vehicle model is obtained as follows:

$$m_s\ddot{z}_s + (c_1 + c_2 + c_3 + c_4)\dot{z}_s + (c_1f + c_2f - c_3d - c_4d)\dot{\theta} + (c_1a - c_2b + c_3a - c_4b)\dot{\phi} - c_1\dot{z}_{u1} - c_2\dot{z}_{u2} - c_3\dot{z}_{u3} - c_4\dot{z}_{u4} + (k_1 + k_2 + k_3 + k_4)z_s + (k_1f + k_2f - k_3d - k_4d)\theta + (k_1a - k_2b + k_3a - k_4b)\phi - k_1z_{u1} - k_2z_{u2} - k_3z_{u3} - k_4z_{u4} = 0, \quad (3.6)$$

$$I_{yy}\ddot{\theta} + (-c_1f - c_2f + c_3d + c_4d)\dot{z}_s + (-c_1f^2 + c_2f^2 - c_3d^2 - c_4d^2)\dot{\theta} + (-c_1af + c_2bf + c_3ad - c_4bd)\dot{\phi} + fc_1\dot{z}_{u1} + fc_2\dot{z}_{u2} - c_3d\dot{z}_{u3} - c_4d\dot{z}_{u4} + (-k_1f - k_2f + k_3d + k_4d)z_s + (-k_1f^2 - k_2f^2 - k_3d^2 - k_4d^2)\theta + (-k_1fa + k_2bf - k_3ad - k_4bd)\phi + fk_1z_{u1} + fk_2z_{u2} - dk_3z_{u3} - dk_4z_{u4} = 0, \quad (3.7)$$

$$I_{xx}\ddot{\phi} + (c_1a - c_2b + c_3a - c_4b)\dot{z}_s + (c_1fa - c_2fb - c_3da + c_4db)\dot{\theta} + (c_1a^2 + c_2b^2 + c_3a^2 + c_4b^2)\dot{\phi} - c_1a\dot{z}_{u1} + c_2b\dot{z}_{u2} - c_3a\dot{z}_{u3} + c_4b\dot{z}_{u4} + (k_1a - k_2b + k_3a - k_4b)z_s + (k_1fa - k_2fb - k_3da + k_4db)\theta + (k_1a^2 + k_2b^2 + k_3a^2 + k_4b^2)\phi - k_1az_{u1} + k_2bz_{u2} - k_3az_{u3} + k_4bz_{u4} = 0, \quad (3.8)$$

$$m_{w1}\ddot{z}_1 - c_1\dot{z}_s - c_1f\dot{\theta} - c_1a\dot{\phi} + (c_1 + c_{t1})\dot{z}_{u1} - k_1z_s - k_1f\theta - k_1a\phi + (k_1 + k_{t1})z_{u1} = k_{t1}z_{g1} + c_{t1}\dot{z}_{g1}, \quad (3.9)$$

$$m_{w2}\ddot{z}_2 - c_2\dot{z}_s - c_2f\dot{\theta} + c_2b\dot{\phi} + (c_2 + c_{t2})\dot{z}_{u2} - k_2z_s - k_2f\theta + k_2b\phi + (k_2 + k_{t2})z_{u2} = k_{t2}z_{g2} + c_{t2}\dot{z}_{g2}, \quad (3.10)$$

$$m_{w3}\ddot{z}_3 - c_3\dot{z}_s + c_3d\dot{\theta} - c_3a\dot{\phi} + (c_3 + c_{t3})\dot{z}_{u3} - k_3z_s + k_3d\theta - k_3a\phi + (k_3 + k_{t3})z_{u3} = k_{t3}z_{g3} + c_{t3}\dot{z}_{g3}, \quad (3.11)$$

$$m_{w4}\ddot{z}_4 - c_4\dot{z}_s + c_4d\dot{\theta} + c_4b\dot{\phi} + (c_4 + c_{t4})\dot{z}_{u4} - k_4z_s + k_4d\theta + k_4b\phi + (k_4 + k_{t4})z_{u4} = k_{t4}z_{g4} + c_{t4}\dot{z}_{g4}. \quad (3.12)$$

3.2. Seat suspension analytical model

In this paper, the three-dimensional vertical-pitch-lateral vibration of the vehicle body is taken as the excitation at the base of a seat suspension. At the same time, the MR dampers (MRD) are adopted in the limbs $\{-S_{i1}-P_{i2}-S_{i3}-\}$ $(i = 1, 2)$. Therefore, the seat suspension analytical model is built in the Fig. 4, where k_{12} and k_{13} denote the spring constant, c_{12} and c_{13} are the damping coefficients of the damper, F_i $(i = 12, 13)$ are the forces when the semi-active control is employed; x_r, θ_z, and Φ_z represent the vertical, pitch and roll output at the seat's center of mass; x_{02}, x_{03} are the vibration input of the limbs $\{-S_{i1}-P_{i2}-S_{i3}-\}$ $(i = 1, 2)$, and x_{12}, x_{13} are their vibration output; m_r is the occupant mass. The main parameters of seat suspension are given in Table 1.

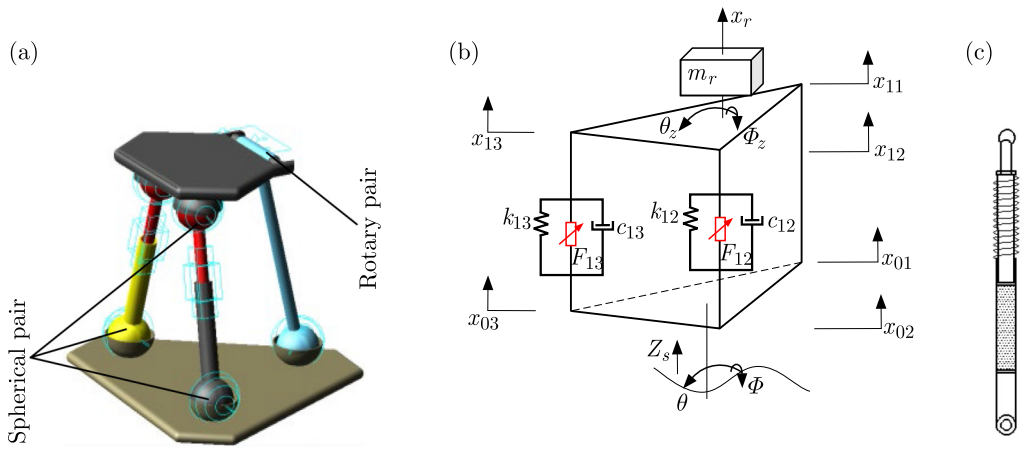

Fig. 4. 2SPS+SR parallel seat suspension: (a) seat suspension; (b) analytical model; (c) MRD.

Table 1. Main parameters of seat suspension.

Parameter description	Unit	Value
Occupant mass, m_r	Kg	75
Vehicle body mass, m_s	Kg	34000
Wheel axles mass	Kg	60
Tire stiffness	N/m	3.2e5
Vehicle suspension stiffness	N/m	4.95e4
Vehicle suspension damping	Ns/m	2250
Seat suspension stiffness	N/m	200
Seat suspension damping	Ns/m	0.6

According to Newton's law, the differential equation of the suspension seat is shown as follows:

$$m_r\ddot{x}_r = k_{12}(x_{02} - x_{12}) + c_{12}(\dot{x}_{02} - \dot{x}_{12}) + k_{13}(x_{03} - x_{13}) + c_{13}(\dot{x}_{03} - \dot{x}_{13}) - F_{12} - F_{13}, \tag{3.13}$$

$$I'_{yy}\ddot{\theta}_z = -[k_{12}(x_{02} - x_{12}) + c_{12}(\dot{x}_{02} - \dot{x}_{12}) - F_{12}]\frac{1}{2}r + [k_{13}(x_{03} - x_{13}) + c_{13}(\dot{x}_{03} - \dot{x}_{13}) - F_{13}]\frac{1}{2}r, \tag{3.14}$$

$$I'_{xx}\ddot{\phi}_z = [k_{12}(x_{02} - x_{12}) + c_{12}(\dot{x}_{02} - \dot{x}_{12}) - F_{12}]\frac{\sqrt{3}}{2}r + [k_{13}(x_{03} - x_{13}) + c_{13}(\dot{x}_{03} - \dot{x}_{13}) - F_{13}]\frac{\sqrt{3}}{2}r, \tag{3.15}$$

where I'_{yy} and I'_{xx} are the moment of inertia in the roll and pitch directions of the seat surface.

4. Fuzzy-PID control

A Fuzzy-PID controller is used to adjust the movement of the 2SPS+SR parallel suspension seat in real time, which is shown in Fig. 5. A commonly used fuzzy control system in this paper includes two-inputs and three-outputs, which takes the systematic error e and the error rate ec as input variables; e stands for the error between the actual acceleration a and the desired acceleration a_0 of the seat. And three-output variables are the automatic quantify factors of

proportional integral, and differential parameters k_p, k_i, and k_d. For the PID controller, its output u is defined as

$$u = k_p(a_0 - a) + k_i \int (a_0 - a)\,\mathrm{d}t + k_d \frac{\mathrm{d}}{\mathrm{d}t}(a_0 - a), \tag{4.1}$$

where

$$a_0 - a = e, \qquad \frac{\mathrm{d}}{\mathrm{d}t}(a_0 - a) = ec.$$

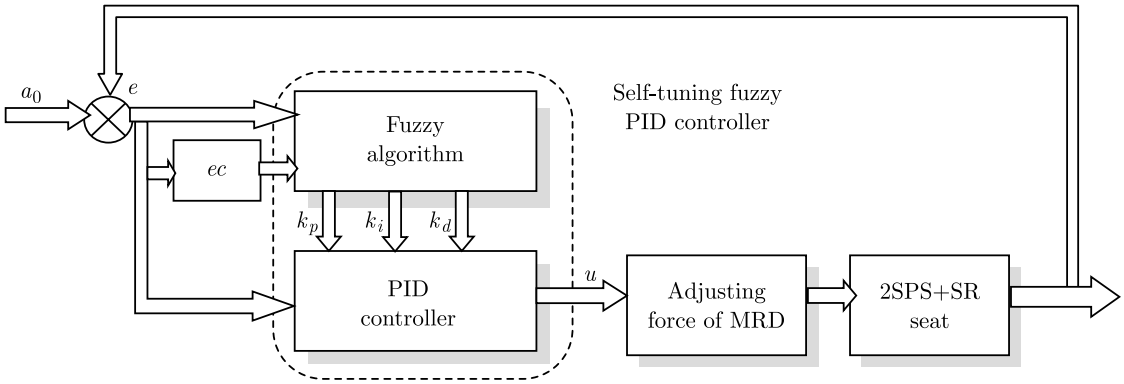

Fig. 5. Block diagram of self-tuning fuzzy-PID controller.

Tables 2–4 give the derived rule-bases. The fuzzy language is: NB – negative big, NM – negative medium, NS – negative small, ZE – zero, PS – positive small, PM – positive medium, PB – positive big. The physical domains of e and ec are $[-4, 4]$, and the domains of k_p, k_i, and k_d are $[-1, 1]$. The Gaussian membership function is used, and the control rule is the IF-Then. There are 49 rules to describe the relationship of the input and output numerical values in this article.

Table 2. Fuzzy control rule-base for k_d.

e	ec						
	NB	NM	NS	ZE	PS	PM	PB
NB	PS	PS	ZE	ZE	ZE	PM	PB
NM	NS	NS	NS	NS	ZE	NS	PM
NS	NB	NM	NM	NS	ZE	PS	PM
ZE	NB	NM	NM	NS	ZE	PS	PM
PS	NB	NM	NS	NS	ZE	PS	PS
PM	NM	NS	NS	NS	ZE	PS	PS
PB	PS	ZE	ZE	ZE	ZE	PB	PB

Table 3. Fuzzy control rule-base for k_i.

e	ec						
	NB	NM	NS	ZE	PS	PM	PB
NB	NB	NB	NB	NM	NM	ZE	ZE
NM	NB	NB	NM	NM	NS	ZE	ZE
NS	NM	NM	NS	NS	ZE	PS	PS
ZE	NM	NS	NS	ZE	PS	PM	PM
PS	NS	NS	ZE	PS	PS	PM	PM
PM	ZE	ZE	PS	PM	PM	PB	PB
PB	ZE	ZE	PS	PM	PM	PB	PB

Table 4. Fuzzy control rule-base for k_p.

e	ec						
	NB	NM	NS	ZE	PS	PM	PB
NB	PB	PB	PM	PM	PS	PS	ZE
NM	PB	PB	PM	PM	PS	ZE	ZE
NS	PM	PM	PM	PS	ZE	NS	NM
ZE	PM	PS	PS	ZE	NS	NM	NM
PS	PS	PS	ZE	NS	NS	NM	NM
PM	ZE	ZE	NS	NM	NM	NM	NB
PB	ZE	NS	NS	NM	NM	NB	NB

5. Simulation results and analysis

5.1. Vibration analysis on different road surfaces

When the vehicle is driven at a speed of 10 km/h, the simulation results for varying road surfaces and different controllers are shown in Figs. 6–8. At the same time, Table 5 shows root-mean-square (RMS) accelerations of the suspension. Figures 6–8 denote the fore-aft, lateral and vertical directions, respectively.

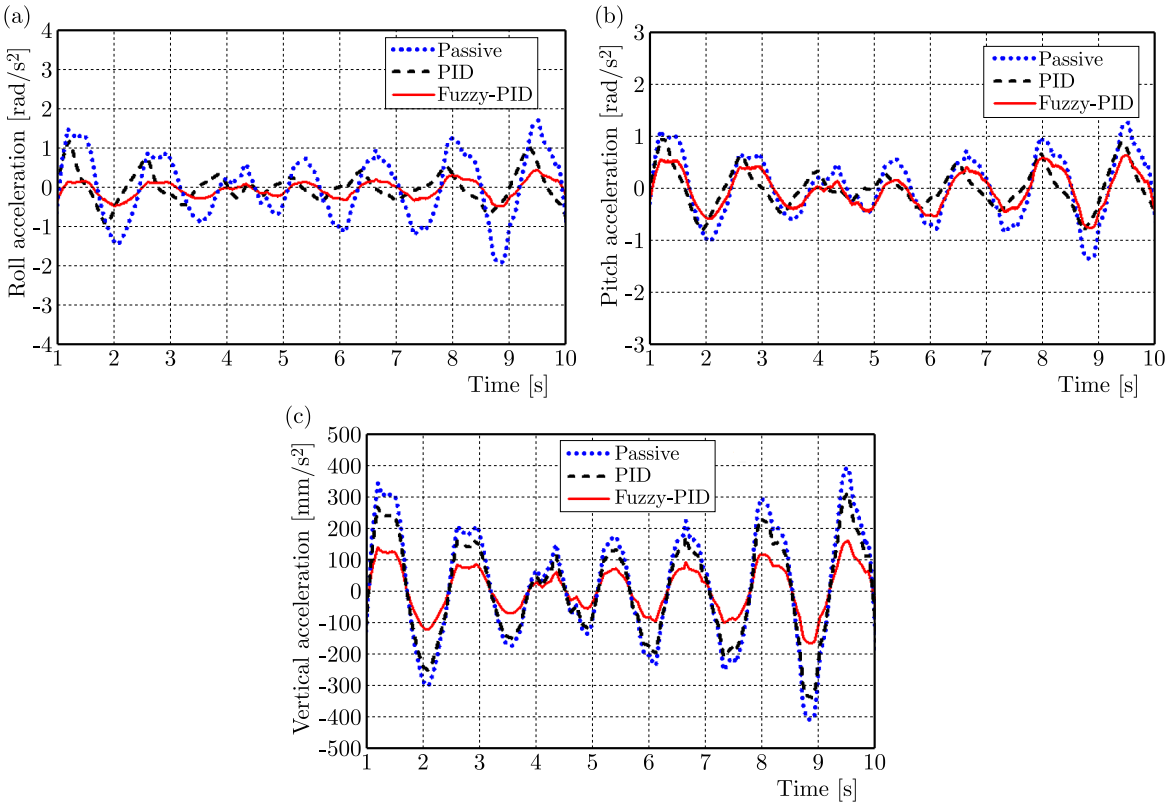

Fig. 6. Acceleration curves of seat under different control modes on E-level road: (a) roll; (b) pitch; (c) vertical.

A PID controller is developed in order to illustrate the improvement of the proposed fuzzy-PID. It can be seen from Figs. 6–8 that compared with the passive suspension seat, the PID and fuzzy-PID control suspension seat can effectively mitigate the vibrations.

In summary, the RMS accelerations of the 2SPS+SR seat using the fuzzy-PID controller in lateral, fore-aft and vertical directions are 0.149 rad/s^2, 0.195 rad/s^2, and 0.041 m/s^2 when the

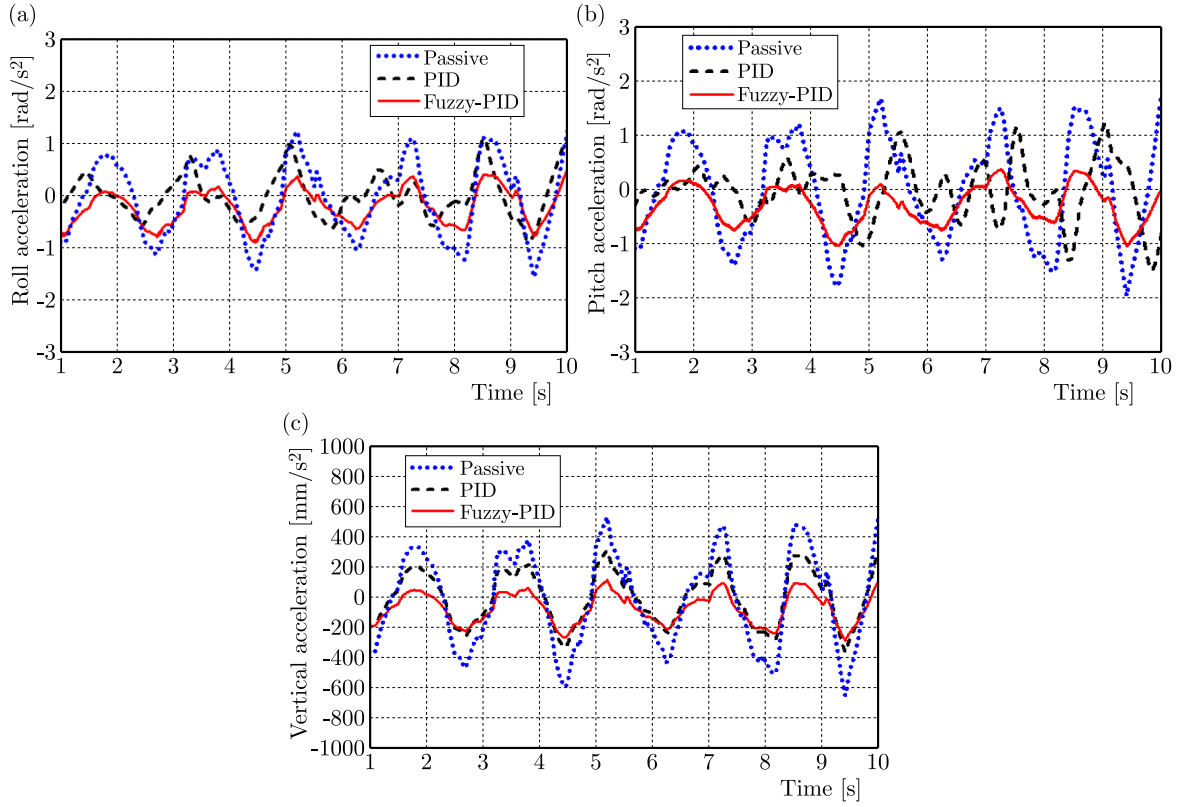

Fig. 7. Acceleration curves of seat under different control modes on F-level road: (a) roll; (b) pitch; (c) vertical.

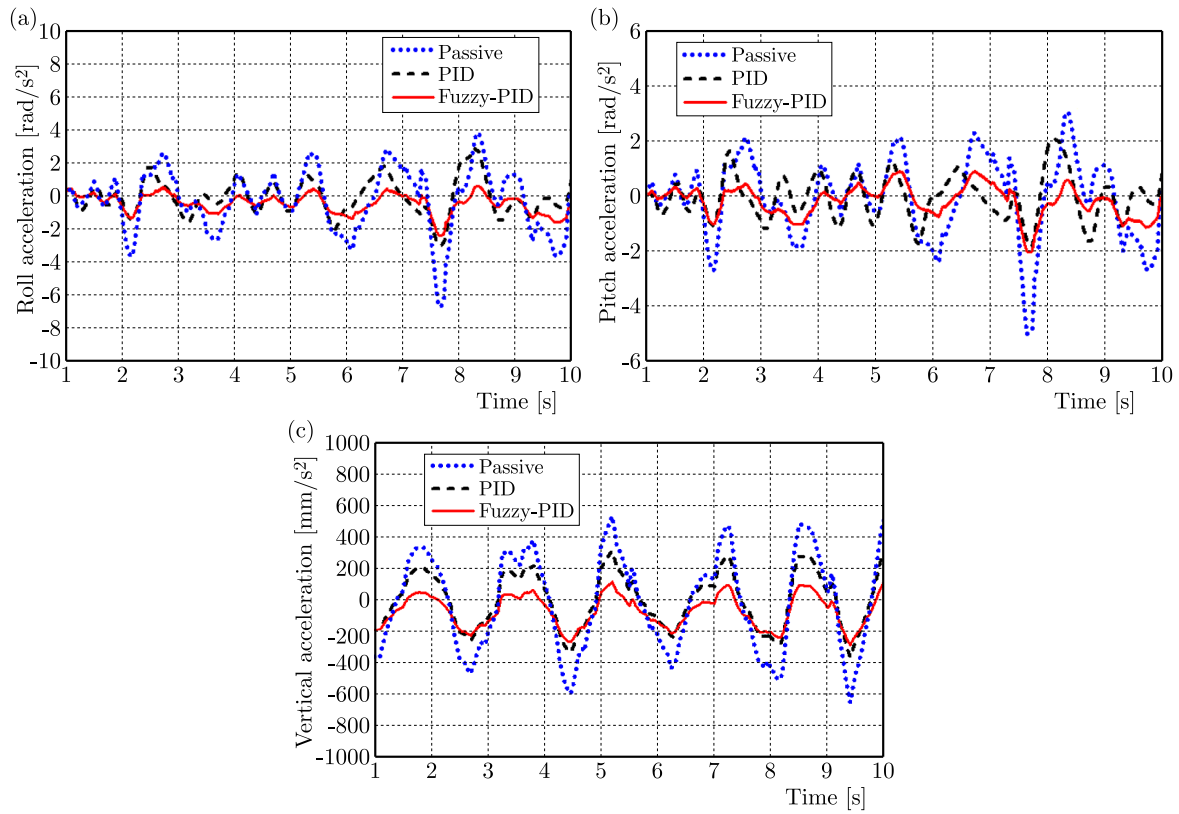

Fig. 8. Acceleration curves of seat under different control modes on G-level road: (a) roll; (b) pitch; (c) vertical.

vehicle is driven on E-class road. At the same time, the RMS accelerations using a simple PID controller are 0.255 rad/s^2, 0.236 rad/s^2, and 0.084 m/s^2, respectively. Similarly, for the F-class road, the acceleration responses using fuzzy-PID are 0.238 rad/s^2, 0.250 rad/s^2, and 0.072 m/s^2. And for the big excitation amplitude of the G-class road, the acceleration using the fuzzy-PID controller are 0.618 rad/s^2, 0.349 rad/s^2, and 0.163 m/s^2. Therefore, the fuzzy-PID provides better control effects than PID at this time.

Based on Table 5, it can be calculated that improvements of acceleration performance under different roads by the PID and fuzzy-PID controllers. The calculation results are shown in Fig. 9.

Table 5. Comparison of RMS accelerations for different roads and controllers.

Road	Modes	Lateral (a_{xw}) [rad/s^2]	Longitudinal (a_{yw}) [rad/s^2]	Vertical (a_{zw}) [m/s^2]
E	Passive	0.469	0.339	0.105
	PID	0.255	0.236	0.084
	Fuzzy-PID	0.149	0.195	0.041
F	Passive	0.763	0.446	0.145
	PID	0.262	0.373	0.083
	Fuzzy-PID	0.238	0.250	0.072
G	Passive	1.844	0.912	0.267
	PID	0.702	0.540	0.169
	Fuzzy-PID	0.618	0.349	0.163

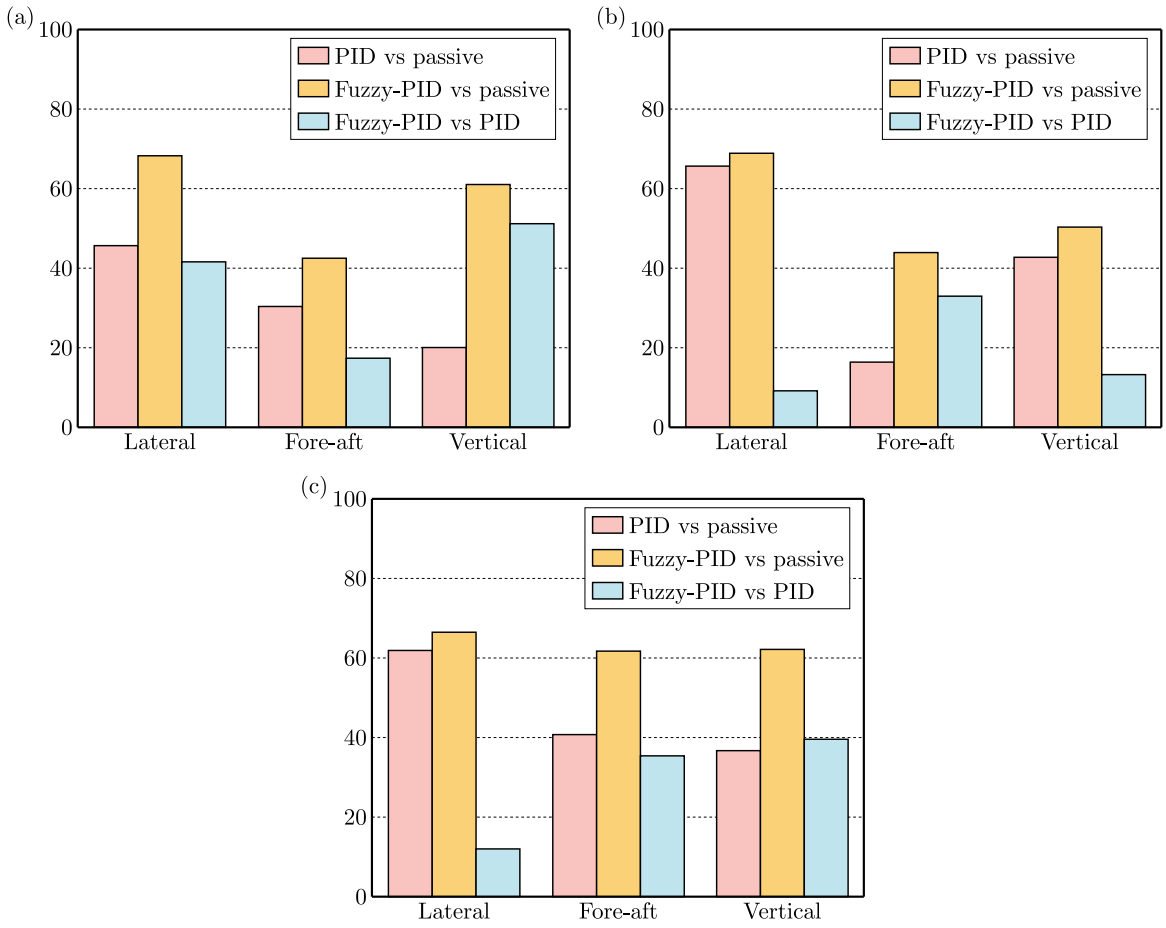

Fig. 9. RMS acceleration reduction – passive vs PID vs fuzzy-PID: (a) E-level road; (b) F-level road; (c) G-level road.

From Fig. 9, it could be known that the fuzzy-PID controller reduces the RMS accelerations by 68.23 %, 42.48 %, 60.95 % from those of a passive system in lateral, fore-aft and vertical directions under E-level road. The RMS accelerations of the PID system reduce 45.62 %, 30.38 %, and 20 % than those of the passive system. More importantly, the accelerations are successfully controlled by the proposed fuzzy-PID controller, which decrease 41.57 %, 17.3 %, and 51.19 % compared with those of the PID controller. Similarly, under F-class road, the fuzzy-PID controller reduces the RMS accelerations by 9.16 %, 32.98 %, 13.25 % from those of the PID controller in lateral, fore-aft and vertical directions. Under G-class road, the acceleration improvements can also be seen, the reductions of the fuzzy-PID system are 11.97 %, 35.37 %, and 39.52 % than those of PID controller. In sum, the fuzzy-PID could obviously reduce the acceleration amplitudes when compared with the PID one.

5.2. Ride comfort analysis of 2SPS+SR seat

The international standard ISO 2361-1997(E) is a general standard for vibration. Considering that the vehicle is subjected to vibration from three different directions, the total weighted acceleration RMS for the three axial directions is given as follows:

$$a_V = [1.4a_{xw}^2 + 1.4a_{yw}^2 + a_{zw}^2]^{1/2}, \tag{5.1}$$

where values of a_{xw}, a_{yw}, and a_{zw} from Table 5.

The weighted vibration level formula is obtained as

$$L_{av} = 20\lg(a_v/a_0), \qquad a_0 = 10^{-6}\,\mathrm{m/s^2}. \tag{5.2}$$

Table 6 shows the relationship between the weighted RMS value of acceleration, weighted vibration level, and human subjective feelings given by (ISO 2631-1, 1997) standard.

In order to further verify the damping effect of the 2SPS+SR suspension seat, the total weighted RMS of acceleration and the weighted vibration level are calculated based on the above Subsection 5.1 analysis results under different control modes. The computation results are shown in Tables 6–8.

Table 6. Comfort level under E-class road.

Modes	a_v [m/s^2]	L_{av} [dB]	Comfort level
Passive	0.159	104	Comfortable
PID	0.110	101	Comfortable
Fuzzy-PID	0.065	96	Comfortable

Table 7. Comfort level under F-class road.

Modes	a_v [m/s^2]	L_{av} [dB]	Comfort level
Passive	0.186	105	Comfortable
PID	0.126	102	Comfortable
Fuzzy-PID	0.101	100	Comfortable

Table 8. Comfort level under G-class road.

Modes	a_v [m/s^2]	L_{av} [dB]	Comfort level
Passive	0.409	112	Comfortable
PID	0.250	108	Comfortable
Fuzzy-PID	0.159	103	Comfortable

Through comparison of Tables 6–8 with international standards (ISO 2631-1, 1997), it could be known that the total weighted RMS of acceleration and the weighted vibration level using

a passive system are slightly larger than 0.315 m/s^2 and 110 dB, whose ride is "discomfortable". When the PID controlled suspension are installed in the seat, the ride is "not discomfort" when the vehicles driving under E- and F-class roads, but the L_{av} is equal to 108 dB and it is very close to the 110 dB on G-class roads. This phenomenon is caused owing to its fixed PID gains. When the 2SPS+SR seat controlled by the fuzzy-PID, the ride is 'not discomfort' when driving on E-, F-, G-class roads. As compared to the passive control and the PID control, the fuzzy-PID control leads to better vibration suppression.

6. Conclusions

In this paper, based on the single-open-chain theory, vertical-pitch-lateral movements are verified of the new type 2SPS+SR suspension seat. And the motion differential equations of the seven-DOF vehicle and three-DOF 2SPS+SR suspension seat are established, the proposed fuzzy-PID controller is designed for the semi-active suspension seat to obtain self-tuning of the gain parameters.

The simulation results prove that, the RMS accelerations of the 2SPS+SR seat using the fuzzy-PID controller in lateral, fore-aft and vertical directions are 0.149 rad/s^2, 0.195 rad/s^2, and 0.041 m/s^2 under the E-class road condition and the RMS accelerations under the F-class road are 0.238 rad/s^2, 0.250 rad/s^2, and 0.072 m/s^2, and the RMS accelerations under the G-class road are 0.618 rad/s^2, 0.349 rad/s^2, and 0.163 m/s^2, respectively. The fuzzy-PID controller can get better vibration-reducing effects than the PID system. The comfort levels are computed at the same time and a successful improvement could also be seen when the fuzzy-PID controller is adopted.

Acknowledgments

The authors would like to thank the Graduate Student Research Innovation Program of Shanxi Province (grant no. 2024KY644) for their support.

References

1. Abdul Zahra, A.K. & Abdalla, T.Y. (2020). Design of fuzzy super twisting sliding mode control scheme for unknown full vehicle active suspension systems using an artificial bee colony optimization algorithm. *Asian Journal of Control*, *23*(4), 1966–1981. https://doi.org/10.1002/asjc.2352
2. Deng, L., Sun, S., Christie, M., Ning, D.H., Jin, S., Du, H., Zhang, S. & Li, W. (2022). Investigation of a seat suspension installed with compact variable stiffness and damping rotary magnetorheological dampers. *Mechanical Systems and Signal Processing*, *171*, Article 108802. https://doi.org/10.1016/j.ymssp.2022.108802
3. Desai, R., Guha, A., & Seshu, P. (2021). Modelling and simulation of active and passive seat suspensions for vibration attenuation of vehicle occupants. *International Journal of Dynamics and Control*, *9*(4), 1423–1443. https://doi.org/10.1007/s40435-021-00788-2
4. International Organization for Standardization. (1997). *Mechanical vibration and shock – Evaluation of human exposure to whole-body vibration – Part 1: General requirements* (ISO Standard No. 2631-1:1997). https://www.iso.org/standard/7612.html
5. Jain, S., Saboo, S., Pruncu, C.I., & Unune, D.R. (2020). Performance investigation of integrated model of quarter car semi-active seat suspension with human model. *Applied Sciences*, *10*(9), Article 3185. https://doi.org/10.3390/app10093185
6. Jereczek, B., Maciejewski, I., Krzyzynski, T., & Krolikowski, T. (2023). Implementation of the SMC control strategy to an active horizontal seat suspension system. *Procedia Computer Science*, *225*, 3527–3535. https://doi.org/10.1016/j.procs.2023.10.348
7. Khan, L., Qamar, S., & Khan, U. (2016). Adaptive PID control scheme for full car suspension control. *Journal of the Chinese Institute of Engineers*, *39*(2), 169–185. https://doi.org/10.1080/02533839.2015.1091427

8. Maciejewski, I., Zlobinski, M., Krzyzynski, T., & Glowinski, S. (2020). Vibration control of an active horizontal seat suspension with a permanent magnet synchronous motor. *Journal of Sound and Vibration*, *488*, Article 115655. https://doi.org/10.1016/j.jsv.2020.115655

9. Ni, D.K., Van Liem, N., & Li, S.M. (2023). Performance analysis of the seat suspension using different models of the optimal negative-stiffness-structures. *Proceedings of the Institution of Mechanical Engineers, Part D: Journal of Automobile Engineering*, *237*(6), 1313–1326. https://doi.org/10.1177/09544070221091040

10. Sun, C., Liu, C., Zheng, X., Wu, J., Wang, Z.M., & Qiu, Y. (2023). An analytical model of seated human body exposed to combined fore-aft, lateral, and vertical vibration verified with experimental modal analysis. *Mechanical Systems and Signal Processing*, *200*, Article 110527. https://doi.org/10.1016/j.ymssp.2023.110527

11. Tan, V.V., Hung, T.M., & Sename, O. (2021). An investigation into the ride comfort of buses using an air suspension system. *International Journal of Heavy Vehicle Systems*, *28*(2), 184–205. https://doi.org/10.1504/IJHVS.2021.115595

12. Wu, W.G., Ma, L.Z., Yang, Q.Z., & Chen, X.X. (2011). 3-D vibration isolation of vehicle seat based on parallel mechanism (in Chinese). *Transactions of the Chinese Society of Agricultural Machinery*, *42*(6), 23–27.

13. Yan, B.J., Liu, Z.K., Zhang, W.J., & Liu, S.Z. (2022). Dynamic characteristics analysis of tubular stand-off layer sandwiched structure used in driving sprocket. *International Journal of Heavy Vehicle Systems*, *29*(2), 163–179. https://doi.org/10.1504/IJHVS.2022.125316

14. Yang, T.L. (2012). Theory and application of robot mechanism topology (in Chinese). Beijing: Science Press.

15. Zhang, J.H., Xu, Z.Y., Li, D.S., & Liu, H. (2015). Research on vibration damping device of vehicle seat based on 3-RPC parallel mechanism (in Chinese). *Mechanical Design*, *32*(2), 26–31.

16. Zhang, N. & Zhao, Q. (2017). Fuzzy sliding mode controller design for semi-active seat suspension with neuro-inverse dynamics approximation for MR damper. *Journal of Vibroengineering*, *19*(5), 3488–3511. https://doi.org/10.21595/jve.2017.17654

Manuscript received May 25, 2024; accepted for publication February 10, 2025; published online April 14, 2025.

JOURNAL OF THEORETICAL
AND APPLIED MECHANICS
63, 2, pp. 401–414, Warsaw 2025
https://doi.org/10.15632/jtam-pl/201984

DIMENSIONAL SYNTHESIS OF SUSPENSION SYSTEM OF WHEEL-LEGGED MOBILE ROBOT†

Przemysław SPERZYŃSKI*, Jacek BAŁCHANOWSKI

Wrocław University of Science and Technology, Faculty of Mechanical Engineering
Division of Fundamentals of Machine Design and Mechatronic Systems, Wrocław, Poland
*corresponding author, *przemyslaw.sperzynski@pwr.edu.pl*

This paper presents a method for selecting the common dimensions of the limb mechanism of a wheel-legged mobile robot. A synthesis task was formulated that divided it into partial stages. The solution was searched using a genetic algorithm. This accelerated the dimension selection process. The algorithm operated on integers, which made it possible to establish the accuracy of the sought basic dimensions of the limb mechanism. The objective of the synthesis was achieved, obtaining the assumed characteristics of wheel movement using the available drives. Finally, further aspects of the design of the limb mechanism of the wheel-legged mobile robot which need to be studied are presented.

Keywords: dimensional synthesis; genetic algorithm; wheel-legged robot.

1. Introduction

Wheel-legged mobile robots are hybrid systems which allow efficient movement on flat terrain and walking to overcome obstacles. The wheel suspension in the robot is a complex mechanism which needs to enable the wheel to be operated in such a way as to ensure driving (rolling and turning of the wheel – two degrees of freedom) and walking (lifting and extending of the wheel – two degrees of freedom). As a result of research work at the Wrocław University of Science and Technology, at the Faculty of Mechanical Engineering, a wheel-legged robot was developed which has four limbs enabling the above-mentioned wheel movements (Fig. 1a) (Gronowicz *et al.*, 2014).

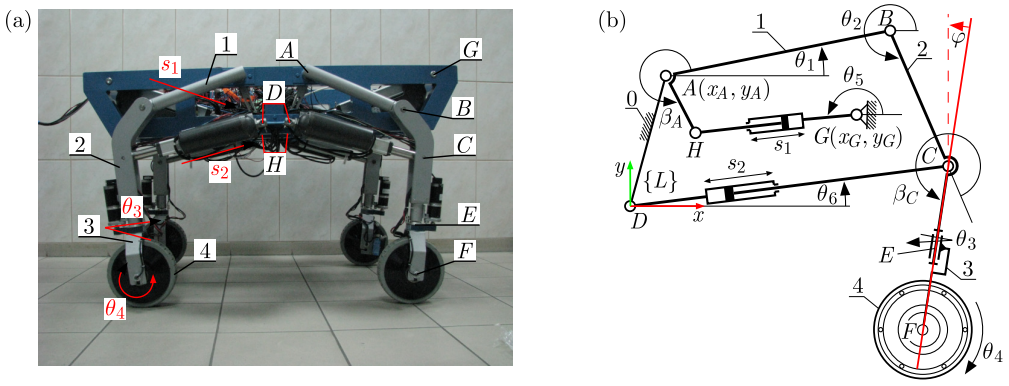

Fig. 1. (a) Prototype of the wheel-legged robot; (b) kinematic scheme of the limb.

†This article was presented at the 5th Polish Congress of Mechanics and 25th International Conference on Computer Methods in Mechanics (PCM-CMM), Gliwice, Poland, September 4–7, 2023.

The aim of this paper is to present the developed method for the dimensional synthesis of a limb, which allows dimensions to be selected to ensure that the lifting motion of the wheel centre follows a trajectory close to the vertical section. The innovation of the wheel suspension used in the robot lies in the fact that, by selecting the appropriate dimensions of the system's elements, the vertical movement of the wheel can be realised using only the lifting drive, with the wheel extension drive inactive. The disadvantage of the designed limb mechanism is the tilt of the steering wheel axis away from the vertical. This tilt can cause control problems when driving. The developed geometrical synthesis method focuses on minimising the steering axis tilt angle while maintaining a rectilinear trajectory of the wheel centre.

2. Material and methods

The task of dimensional synthesis of kinematic systems is to determine the linear and angular dimensions of the elements so as to obtain the assumed law of motion of the mechanism. This is most often assumed by defining such groups of tasks as driving the elements through predefined positions, assuming relative positions of selected moving elements or realising a specific shape of the trajectory of a selected point. The geometric synthesis methods that have been developed use various algorithms or mathematical tools, and recent years have seen significant progress in the application of new methods in this area. Optimisation methods, developed on the basis of new research in artificial intelligence, are increasingly being used. A wide range of techniques for dimensional synthesis have already been explored (Kang *et al.*, 2022). These methods include, among others, fuzzy logic, neural networks (Asaeikheybari *et al.*, 2017; Malarczyk *et al.*, 2023), optimisation algorithms such as ant algorithms, simulated annealing, or genetic algorithms (GA) (Buśkiewicz, 2019; Hernández *et al.*, 2021; Shinde *et al.*, 2017; Wu *et al.*, 2020). The latter method is increasingly used due to its ease of implementation. The above-mentioned methods are replacing the classical deterministic methods concerning the optimisation problem. One reason for their use is the generally lower computational complexity (undoubtedly an advantage of the method) resulting from the fact that there is no need to calculate the derivatives of the objective function (as in the case of the Newton–Raphson algorithm).

2.1. Diagram of the robot limb

The limb of the designed wheel-legged robot has four degrees of freedom. Two of these are responsible for the movements needed to drive the robot using the wheels – that is, wheel turning and rolling. The other two movements are wheel levelling forced by actuator s_1 and walking motion forced by actuator s_2 (Fig. 1b). The main advantage of the presented limb mechanism is that the wheel movements needed to level the platform during uneven travel are performed using the levelling drive s_1, with the gait drive s_2 deactivated, fixed at a position s_2 equal to $s_{2\text{lev}}$.

The stepping motion is performed by s_2 drive. By varying its length CD, the centre of the wheel F moves along an arc with centre at point B and radius BF. The wheel turning axis is located in the mechanism action plane along the section CF. This position of the axis results in the rotation of the wheel not changing the position of the wheel centre F. The choice of the geometry of the limb mechanism of the wheel-legged robot affects the inclination of the axis of the CF segment to the vertical. In the driving mode, where s_2 drive is in a fixed position, CF element is inclined in relation to the vertical axis by an angle φ (Fig. 1b). It makes maintaining a stable track difficult. The present work focusses mainly on determining the geometry of the robot suspension mechanism so that the CF segment is vertical ($\varphi = 0$) during the movement of the wheel responsible for levelling the platform.

The common dimensions of the limb mechanism are the linear and angular dimensions of the individual elements, but also s_1 and s_2 drives mounting points and their range of motion. As for the mechanism shown (Fig. 1), 12 parameters have to be selected. These are: the lengths of

actuators s_1, s_2, the ranges of movement of the actuators Δs_1, Δs_2, the lengths of the elements FC, CB, AB, AH, the positions of points A – x_A, y_A, D – x_D, y_D, and the angles β_A, β_C.

2.2. Dimensional synthesis assumptions

The main objective of the synthesis is to achieve the assumed rectilinear trajectory of motion of the wheel centre – point F, forced by the movement of one drive s_1. With this movement, the drive s_2 is to be inactive, fixed at a certain length $s_2 = s_{2\text{lev}}$ (Fig. 2).

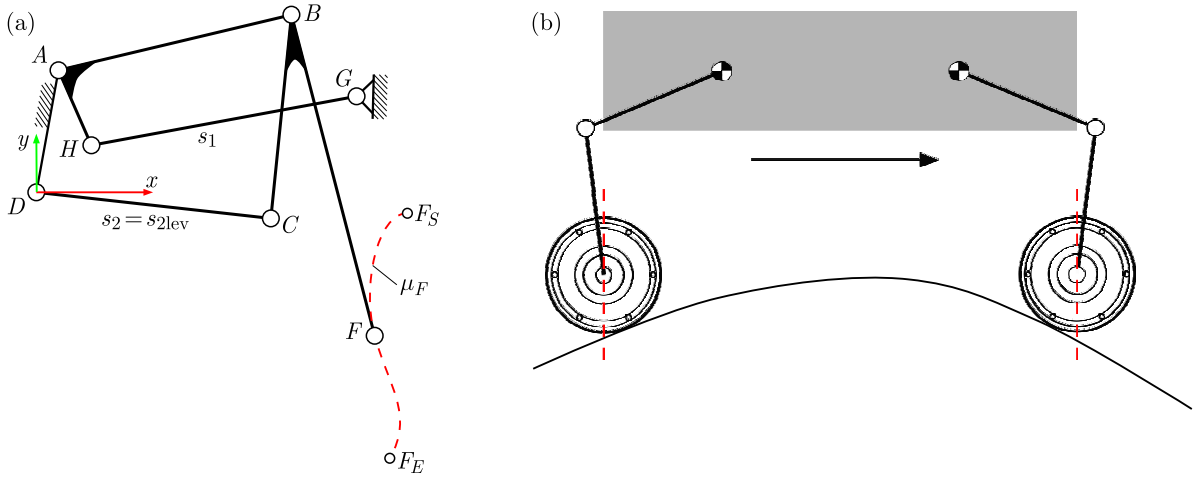

Fig. 2. (a) Wheel trajectory used to level the platform; (b) during driving on uneven terrain.

Next, to obtain the proper driving properties of the robot, it is necessary to ensure that the angle φ of orientation of the steering axis is as close to zero as possible (Fig. 3). It is undesirable for this angle to be negative (Fig. 3b).

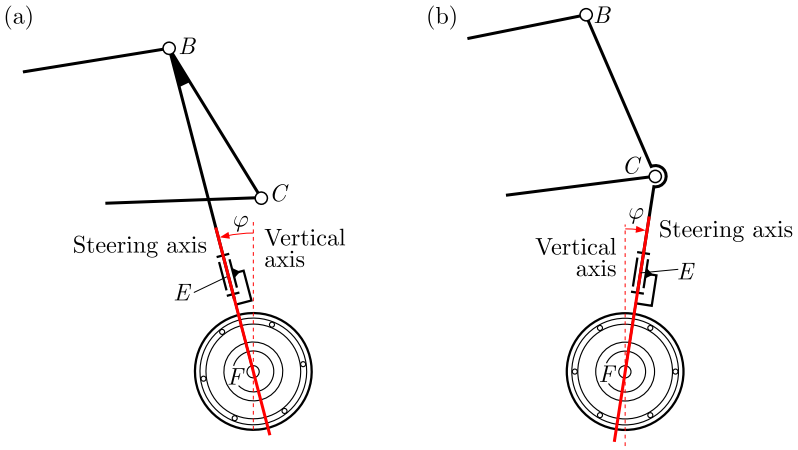

Fig. 3. Angle φ of orientation of the steering axis: (a) positive; (b) negative.

Moreover, when the gait drive s_2 is activated, the resulting limb workspace must be large enough to allow the wheel to move above the steps of a standard staircase. The most desirable case here is to obtain such a zone, which would include the profiles of two consecutive stairs (Fig. 4).

Meeting all the presented requirements is a complex task. The elaborated synthesis method consists in defining a dimension selection procedure and a set of criteria to obtain a solution that meets the requirements. The paper presents a synthesis scheme that focuses on each individual task set for the robot's suspension mechanism. At each stage of the presented synthesis method,

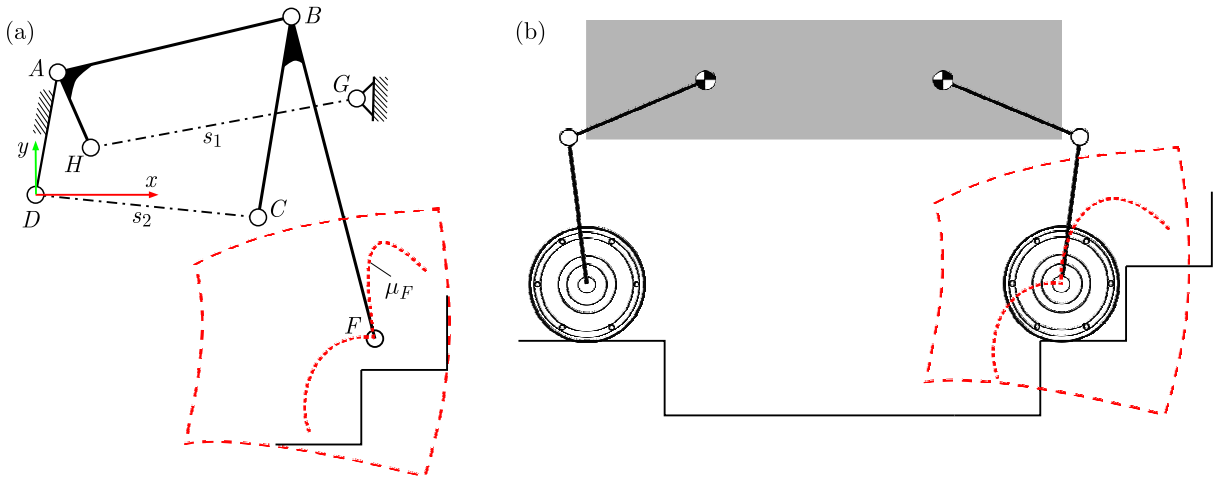

Fig. 4. (a) Robot's limb workspace, (b) while overcoming the steps.

optimization criteria focusing on single kinematic characteristics of the limb mechanism were established.

2.3. Dimensional synthesis algorithm

It was assumed that the dimensional synthesis would be divided into subtasks of basic dimension selection. The presented method allows the selection of two chosen parameters of the limb mechanism at each stage with an assumed single optimisation objective. As a result, the objective function of each stage can be visualised by plotting the area dependent on the two sought parameters.

2.3.1. Orientation angle of the steering axis orientation angle φ

The first task focuses on determining the angle φ of the steering axis orientation during wheel movement along the levelling trajectory (with the s_2 drive locked). The angle φ is given by the relation expressed by the angle of inclination of the CF segment:

$$\varphi = \theta_2 + \beta_C + 90^\circ, \tag{2.1}$$

where angle θ_2 is the orientation angle of element 2, defined as the deviation of segment BC from the horizontal (Fig. 5a).

In this stage of the synthesis, a vertical path μ_F of movement of the wheel centre F along a straight line segment from point F_S to point F_E is assumed (Fig. 5b). The parameters sought are the length CF and the x_F coordinate of the points of the vertical segment F_S–F_E. Selecting these values with the assumed μ_F motion path will determine the angles θ_6 and θ_2.

To determine the profiles of these angles, the length s_2 of the gait actuator CD is equal to the midpoint value within the range of motion $s_{2\text{lev}}$. This is a predetermined value at which the limb moves in a levelling mode. The optimization task is to achieve a constant value of the orientation angle φ of the wheel axis, which is equal to zero. The objective functions were constructed based on the angle φ and defined by the following equation:

$$f_{1\text{TARGET}}(CF, x_F) = \sum_i \text{rms}\left(\varphi_i\right), \tag{2.2}$$

where the function rms determines the root mean square error of the discretely defined φ angle profile. The assumed trajectory μ_F is divided into **n** points F_i (x_{F_i}, y_{F_i}) for $i = 1, ..., n$ (where

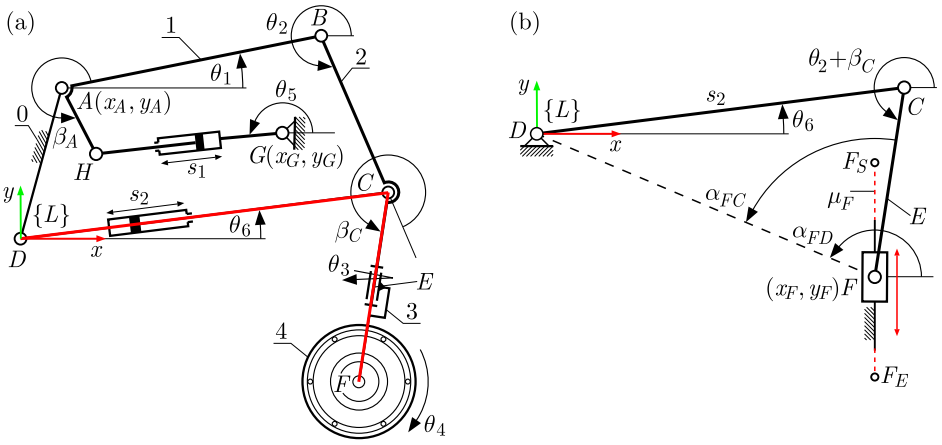

Fig. 5. (a) Selection of parameters defining the steering axis angle; (b) kinematics parameters defining φ angle.

$F_1 = F_S$ and $F_n = F_E$) and the inclination angles θ_6 and θ_2 of the two-link CD and CF mechanism are determined at each of the assumed points F_i. The orientation $\theta_2 + \beta_C$, defining the inclination angle φ of the CF link, is calculated based on the following equation:

$$\theta_2 + \beta_C = \alpha_{FD} - \alpha_{FC} + \pi, \tag{2.3}$$

where α_{FD} represents the inclination of the FD segment at the given point F_i, and α_{FC} is the internal angle of the FDC triangle (Fig. 5b). The orientation of the FD segment, with the wheel centre F fixed at a specific position, is defined by:

$$\alpha_{FD} = \arctan \frac{y_D - y_{F_i}}{x_D - x_{F_i}}, \tag{2.4}$$

the inner angle α_{FC} of the FDC triangle was determined from the analogous relationship:

$$\alpha_{FC} = \arctan \frac{\sin \alpha_{FC}}{\cos \alpha_{FC}}, \tag{2.5}$$

where the cosine of the angle α_{FC} of the FDC triangle is determined from the cosine theorem:

$$\cos(\alpha_{FC}) = \frac{\Delta}{2 \cdot CF \cdot DF}, \tag{2.6}$$

where $\Delta = CF^2 + DF^2 - CD^2$ and the sine of the angle α_{FC} is calculated based on the trigonometric identity:

$$\sin(\alpha_{FC}) = \frac{\sqrt{(2 \cdot CF \cdot DF)^2 - \Delta^2}}{2 \cdot CF \cdot DF}. \tag{2.7}$$

In this way, for the assumed n positions of point F, the characteristics of α_{FD} from Eq. (2.4) and α_{FC} from Eq. (2.5) are obtained. By substituting them into Eq. (2.3) and then into Eq. (2.1), n values of the angle φ are determined. The calculated angles α_{FD} and α_{FC} define the positions of point C_i corresponding to the assumed positions of the wheel centre F_i:

$$(x_{C_i}, y_{C_i})^{\mathrm{T}} = (x_{F_i}, y_{F_i})^{\mathrm{T}} + CF \cdot (\cos(\alpha_{F_iD} - \alpha_{F_iC}), \sin(\alpha_{F_iD} - \alpha_{F_iC}))^{\mathrm{T}}, \tag{2.8}$$

which is essential for the subsequent synthesis step.

To search for the parameters CF and x_F that define the criterion $f_{1\mathrm{TARGET}}$ (Eq. (2.2)), a genetic algorithm was employed. The input data for the algorithm include the number of

sought parameters, their value ranges, and the optimisation goal function. This concise set of information allows the search for solutions to commence. Initially, the algorithm randomly generates solution sets, which are then evaluated based on the specified criterion. Subsequently, in the algorithm main loop, the drawn sets are subjected to certain modifications. The algorithm usually terminates after a specified number of steps or when the discovered solutions do not differ significantly between iterations. To set the resolution of the achieved dimensions, the defined parameter ranges were discretised with a specified distribution. The algorithm operates with integer variables that define the dimension values within the chosen range.

2.3.2. Trace of point B in the BC suspension arm

The next synthesis step involves selecting the geometry of element 2. The sought parameters are the BC segment and the angle β_C (Fig. 6a). The motion of the mechanism is driven by the movement of the wheel centre F along the prescribed trajectory μ_F. When determining the length of the BC segment and the angle β_C, the trajectory of point B is obtained (Fig. 6b), which undergoes further evaluation in subsequent synthesis steps.

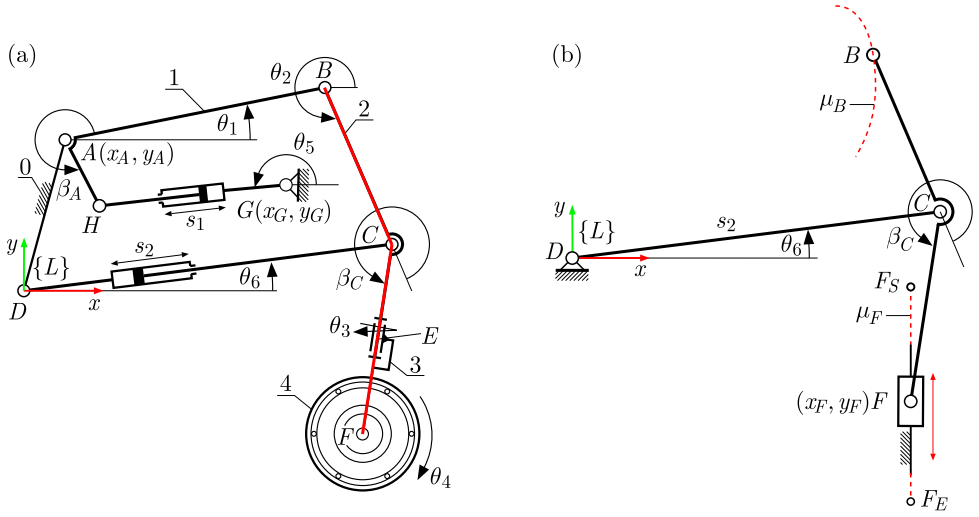

Fig. 6. (a) Selection of coupler parameters; (b) BC length and angle β_C, which determines the trajectory of point B.

The position of point B is given by the following relation:

$$(x_{B_i}, y_{B_i})^{\mathrm{T}} = (x_{C_i}, y_{C_i})^{\mathrm{T}} - BC \cdot (\cos(\theta_2), \sin(\theta_2))^{\mathrm{T}}, \tag{2.9}$$

where the angle θ_2 is determined from relation (2.3), and the position of point C is determined based on Eq. (2.8).

Point B is the point of the upper suspension arm, which has a fixed rotation centre at point A. The search criteria for the parameters BC and β_C were defined to ensure that the trajectory of point B, denoted as μ_B, closely approximates an arc. Determining the parameters of the arc (radius and centre) that approximate the μ_B trace will provide a solution to the search for point A of the suspension arm mount and its AB length. Finding the relationship that defines the curvature of the path μ_B passing through the specified points B_i was the next step in the synthesis.

2.3.3. Curvature of the point B trajectory

In the next step of the synthesis, the curvature of the trajectory of point B was determined. In the previous step, a set of B_i points corresponding to the assumed positions of the centre

of the wheel centre F_i was obtained. A spline defined from a group of third-degree polynomials was drawn for each segment $\langle B_i, B_{i+1}\rangle$ through the B_i points (Fig. 7).

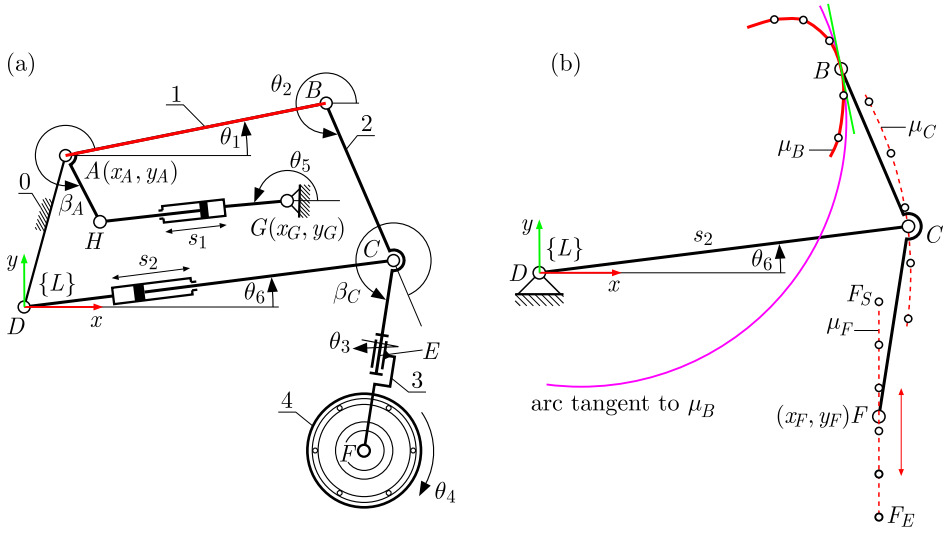

Fig. 7. (a) Upper arm parameters; (b) based on the curvature of the trace of point B.

The equation of the curve μ_B depending on the parameter u, taking values in the interval $u \in \langle 0, 1\rangle$, passing through the given points B_i was divided into segments. Each point B_i was assigned a value of the parameter u equal to u_i. The equation of the curve between two consecutive points B_i and B_{i+1} is expressed as follows:

$$\begin{aligned} x_{B_i}(u) &= p_{x3i}(u-u_i)^3 + p_{x2i}(u-u_i)^2 + p_{x1i}(u-u_i) + p_{x0i} \\ y_{B_i}(u) &= p_{y3i}(u-u_i)^3 + p_{y2i}(u-u_i)^2 + p_{y1i}(u-u_i) + p_{y0i} \end{aligned} \quad \text{for } u \in \langle u_i, u_{i+1}\rangle, \tag{2.10}$$

where the parameters u_i were determined by dividing the interval of the u values into n-equal intervals ($u_i = i/n$), and the coefficients p_{xji}, p_{yji} defined a polynomial for the parameter u from the interval $\langle u_i, u_{i+1}\rangle$. For the pair of points B_i and B_{i+1}, separate polynomial equations defined by the coefficients p_{xji} and p_{yji} were determined. For a parameter u equal to u_i, the determined parametric curve is to pass through the defined point B_i. This determines the parameters p_{x0i} and p_{y0i}, which are equal to the coordinates of the B_i points:

$$p_{x0i} = x_{B_i}, \qquad p_{y0i} = y_{B_i}. \tag{2.11}$$

The successive p_{xji} coefficients were determined so that the functions $x_{B_i}(u)$ were of class C2. The need to obtain the continuity of the first- and second-order derivatives of the parametric functions with respect to the parameter u made it possible to determine the succeeding equations:

$$\begin{aligned} &x_{B_i}(u = u_{i+1}) = x_{B_{i+1}}(u = u_{i+1}), \\ &\frac{\mathrm{d}x_{B_i}}{\mathrm{d}u}(u = u_{i+1}) = \frac{\mathrm{d}x_{B_{i+1}}}{\mathrm{d}u}(u = u_{i+1}), \qquad \frac{\mathrm{d}^2x_{B_i}}{\mathrm{d}u^2}(u = u_{i+1}) = \frac{\mathrm{d}^2x_{B_{i+1}}}{\mathrm{d}u^2}(u = u_{i+1}). \end{aligned} \tag{2.12}$$

Parameters p_{yji} were determined from analogous boundary conditions for the functions $y_{B_i}(u)$. The derivative of the polynomial equations of the parametric equation $x_{B_i}(u)$ is defined by the following equation:

$$\begin{aligned} \frac{\mathrm{d}x_{B_i}}{\mathrm{d}u} &= 3 \cdot p_{x3i}(u-u_i)^2 + 2 \cdot p_{x2i}(u-u_i) + p_{x1i}, \\ \frac{\mathrm{d}^2x_{B_i}}{\mathrm{d}u^2} &= 6 \cdot p_{x3i}(u-u_i) + 2 \cdot p_{x2i}. \end{aligned} \tag{2.13}$$

The tangent vector $\mathbf{t}_i$ to the parametric trajectory μ_B at point B_i was obtained from the first derivative of the polynomial equation:

$$\mathbf{t}_i = (p_{x1i}, p_{y1i})^{\mathrm{T}}. \tag{2.14}$$

The normal vector $\mathbf{n}_i$ rotated to the tangent by $\pi/2$ was determined from the second derivative:

$$\mathbf{n}_i = (2p_{x2i}, 2p_{y2i})^{\mathrm{T}}. \tag{2.15}$$

The tangent and normal vectors to the resulting approximated trajectory of point B allowed the curvature κ of the trace μ_B to be determined at the given points B_i:

$$\kappa = 2\frac{p_{x1i}p_{y2i} - p_{y1i}p_{x2i}}{(p_{x1i}^2 + p_{y1i}^2)^{3/2}}. \tag{2.16}$$

2.3.4. Centre of point B trajectory curvature

The consequence of determining the curvature of the trace of point B is to write a circle tangent to the trace at the given point B_i. The radius of the circle r, tangent to the trace of point B, is equal to the inverse of the curvature κ, $r = 1/\kappa$. By determining the circles tangent to the trajectory μ_B for each point B_i, the set of points A_i forming the trace μ_A of the centre of curvature of the trace of point B was attained (Fig. 8).

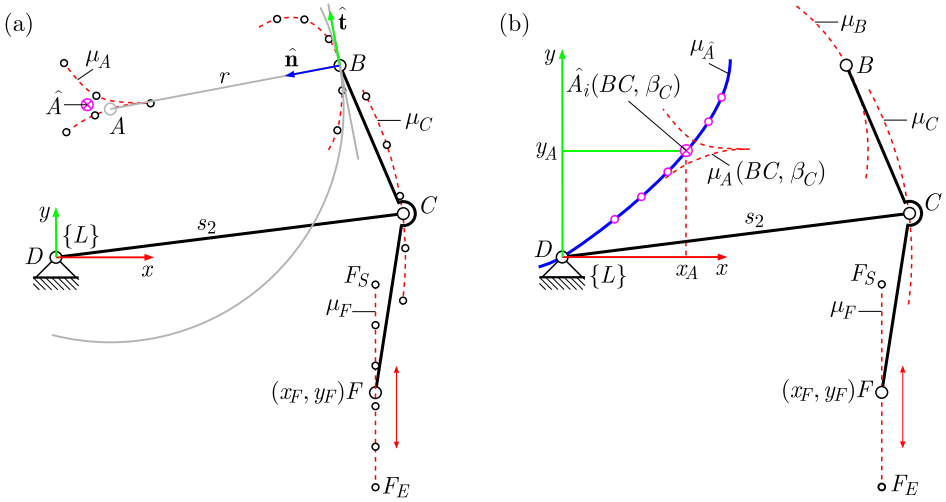

Fig. 8. (a) Point A trajectory, which is the centre of the B trace curvature κ; (b) $\mu_{\widehat{A}}$ trace of points $\widehat{A}$ corresponding to various values of BC and β_C parameters.

The trajectory μ_A of the determined centre of curvature of the trajectory μ_B composed of the points A_i is evaluated. The closer the determined trace μ_B approaches the curve, the more the points A_i will be concentrated around a single point $\widehat{A}$ $(\widehat{x}_A, \widehat{y}_A)$. The objective function was determined as follows:

$$f_{2\mathrm{TARGET}}(BC, \beta_C) = \sum_i \sqrt{(x_{A_i} - \widehat{x}_A)^2 + (y_{A_i} - \widehat{y}_A)^2}, \tag{2.17}$$

where $(\widehat{x}_A, \widehat{y}_A)$ is a point with mean coordinates from the positions of the points A_i – the centre of curvature of the trace μ_B.

A genetic algorithm was run looking for the dimensions of element 2, length BC and angle β_C, given the objective function $f_{2\mathrm{TARGET}}$ (2.17) for a fixed length $BC \neq 0$. The search was for a value of angle β_C such that the trajectory μ_A of the centre of curvature of the trace μ_B is centred

around a single point. There are two points fixed to the element 2: C and F, whose trajectory has a constant trace curvature κ. Curvature of point C equals to $\kappa = 1/CD$, while F has zero curvature of the trace since it moves along a straight-line segment μ_F. The solution is sought where point B will be distant from point C and the centre of the curvature of the trace μ_B of point B will be located above point D. Performing the search for values in the range of the parameter BC resulted in obtaining a set of solutions of the position of the point $\widehat{A}(BC)$ depending on the assumed values of BC. This set was arranged in a specific curve $\mu_{\widehat{A}}$ marked in blue (Fig. 8).

On the basis of the obtained $\mu_{\widehat{A}}$ curve, the attachment point A of member 1 was determined. The design conditions defined the maximum allowed distance between point A and point D along the Y-axis. Taking the height of point A – parameter y_A, the x_A position of point A was read off from the obtained $\mu_{\widehat{A}}$ curve.

2.3.5. Levelling drive parameters s_1

In the next stage of the synthesis, the range of rotation of the rocker arm AB was determined from the orientation of section AB_1 (the highest point B_i corresponding to the given point F_S) and the orientation of section AB_n (the lowest point B_i corresponding to the given point F_E). It was assumed that, in the midpoint position AB_{mid} between AB_1 and AB_n, the levelling drive s_1 will take the value $s_{1\text{mid}}$ and be positioned at a right angle to the crank AH. Mounting point G will therefore be placed on the line μ_{G1}, perpendicular to AB_{mid} (Fig. 9).

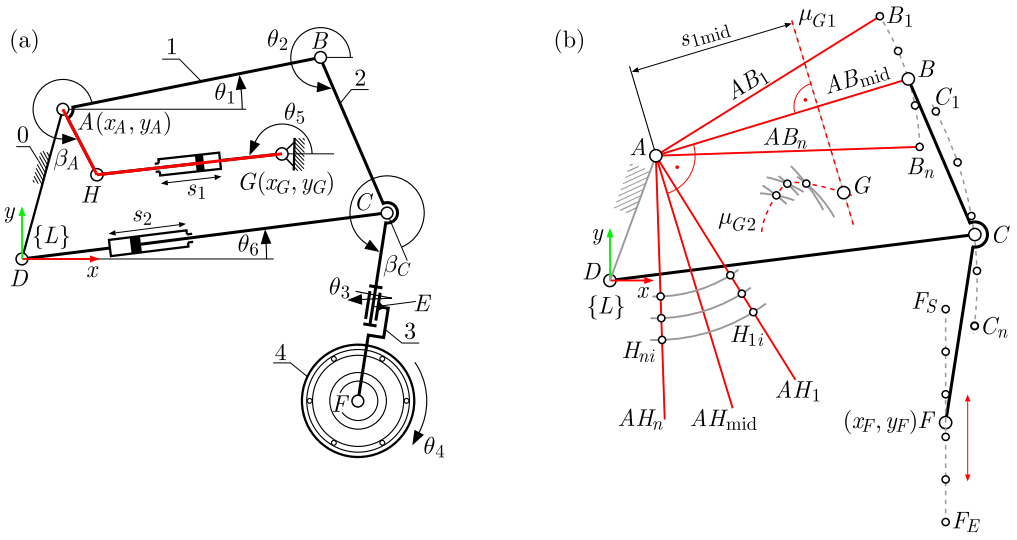

Fig. 9. (a) Lever AH and levelling drive parameters; (b) curves μ_G determining position of point G.

The initial positions H_{1i} and the final positions H_{ni} of point H were determined for a fixed length AH_i and the range of angular movement of element 1 taken from points B_1 and B_n. The position of point G_i (corresponding to the fixed value of AH_i) was determined at the intersection of circles of minimum and maximum actuator extension radius s_1 drawn from points H_{1i} and H_n. Taking successive values of AH_i from the adopted AH length range, the trace μ_{G2} of point G was obtained from the G_i points. The intersection of this trace with the previously determined straight line μ_{G1} gives the solution to determine the mounting point G of the levelling drive s_1.

2.3.6. Limb mechanism workspace

The developed method of dimensional synthesis allows one to obtain the geometry of the robot limb mechanism. The boundary of the working zone defined by the set of all positions of

the centre of the wheel F was determined by fixing the positions of this point at given positions of the levelling drives s_1 and the walking drive s_2. The beginning of the curve is at point F corresponding to the configuration of the mechanism defined by the minimum positions of the levelling drive $s_1 = s_{\min}$ and the walking drive $s_2 = s_{\min}$. The s_2 drive values were successively increased up to the maximum extension value $s_2 = s_{\max}$. The levelling drive s_2 was then tilted to the value $s_2 = s_{\max}$. This resulted in obtaining the upper and right limits of the workspace. The lower limit was obtained by fixing the position of the F point by changing the stepping drive s_2 to the minimum value $s_2 = s_{\min}$. In the last step, by reversing the levelling drive s_1 to the boundary curve of the minimum value $s_1 = s_{\min}$, the workspace boundary curve was closed (Fig. 10).

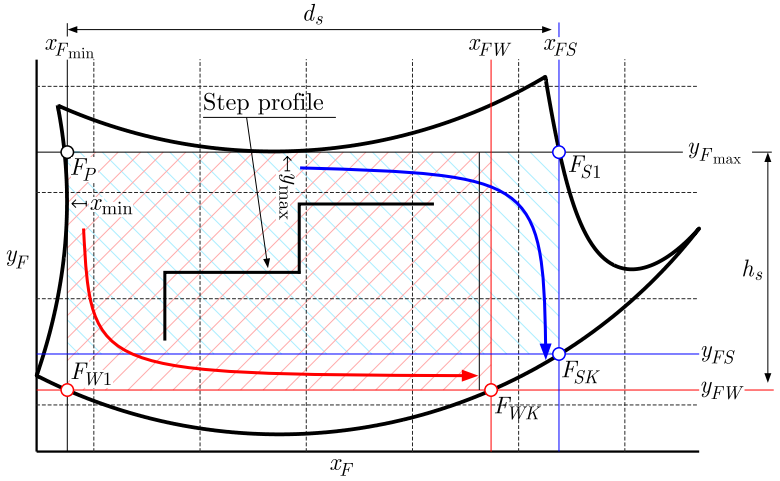

Fig. 10. Analysis of the workspace of the mechanism.

The assumptions made in the introduction determine that the resulting zone should encompass a rectangle twice the height and width of a standard staircase (Fig. 10). A horizontal tangent to the upper boundary of the workspace of the limb was defined and a vertical tangent to the left boundary of the workspace were defined. The intersection of these tangents gives the initial vertex of the rectangle inscribed in the workspace of the robotic limb. The intersection of the horizontal tangent with the right boundary gives the point F_{S1}, and the vertical line drawn from it gives the vertex F_{SK}. Whereas the intersection of the vertical tangent with the lower boundary of the workspace gives the point F_{W1}, and the horizontal line guided from it gives the vertex F_{WK}. The rectangle defined on the vertices (F_P, F_{SK}) has the maximum width d_s from the F_P point. On the other hand, a rectangle defined on the vertices (F_P, F_{WK}) is characterised by the maximum height h_s.

In such rectangles of height h_s and length d_s within the boundaries of the workspace, the profile of the staircase can be entered by checking the dimensions of the zone.

3. Results

The developed method of dimensional synthesis enabled obtaining a new limb mechanism of a wheel-walking robot. Starting from certain assumptions by performing the successive steps of the presented synthesis method, the basic dimensions of the mechanism were achieved.

In the dimensions of the first step, the CF and the position of the F-point trajectory x_F were determined for the assumed length of the walking actuator s_2 and the height of the centre of the rectilinear trajectory of the wheel centre (y_{FS}, y_{FE}). The length of the s_2 actuator was set at the value of the centre of the $s_{2\text{mid}}$ actuator, $CD = 0.425\,\text{m}$. Next, the range of motion of the wheel level was set to $0.3\,\text{m}$, from the initial value of $y_{FS} = -0.025\,\text{m}$ to the final value of

$y_{FE} = -0.325\,\text{m}$. The parameters sought were the length of CF in the range (0.2 m; 0.5 m) and the position of the set trajectory x_F in the range (0.35 m; 0.55 m). The set trajectory was divided into 10 points F_i. The plane of the objective function as a function of the search parameters CF and x_F was plotted, and the course of the angle φ of the orientation of the CF member uniformly distributed around the search value zero was obtained (Fig. 11).

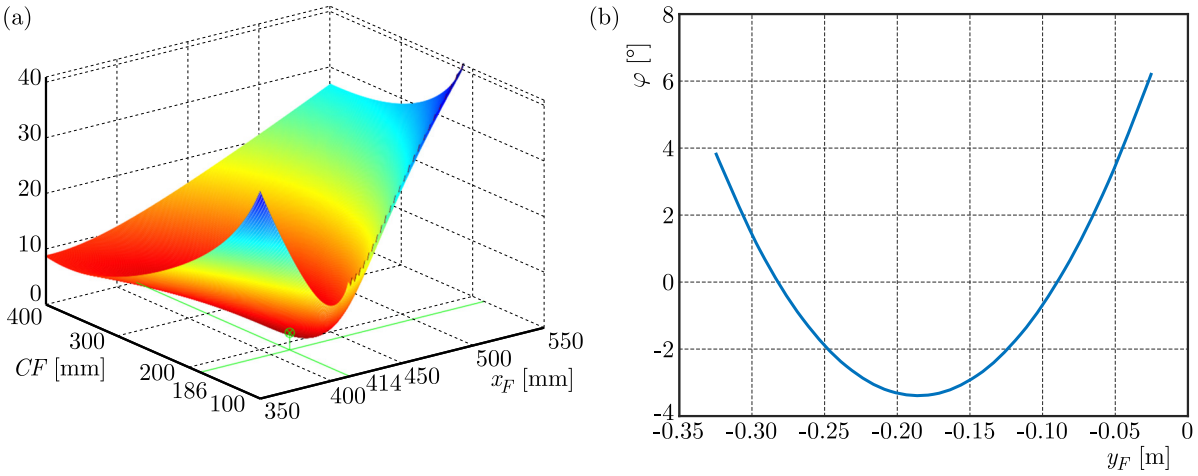

Fig. 11. (a) $f_{1\text{TARGET}}$ target function dependent on CF parameters and x_F position; (b) obtained φ angle.

The trace $\mu_{\widehat{A}}$ of the point $\widehat{A}$ was then determined. The range of BC length values (from 0.001 m to 0.3 m) was assumed, and the corresponding value of β_C in the range (90°, 270°) was searched for, for which the μ_A trace of the centre of curvature of the μ_B trace was centered at a single point $\widehat{A}$. The search was carried out using the genetic algorithm and the objective function $f_{2\text{TARGET}}$ (2.17). Taking BC values from a fixed range, the trajectory of the point $\widehat{A}$ (curve $\mu_{\widehat{A}}$ in blue – Fig. 12a) was determined. The maximum height between points A and D was set to 0.1 m. The coordinates of the control arm mount are equal to the intercept of the horizontal straight line $y_A = 0.1\,\text{m}$ and the $\mu_{\widehat{A}}$ curve (Fig. 12a).

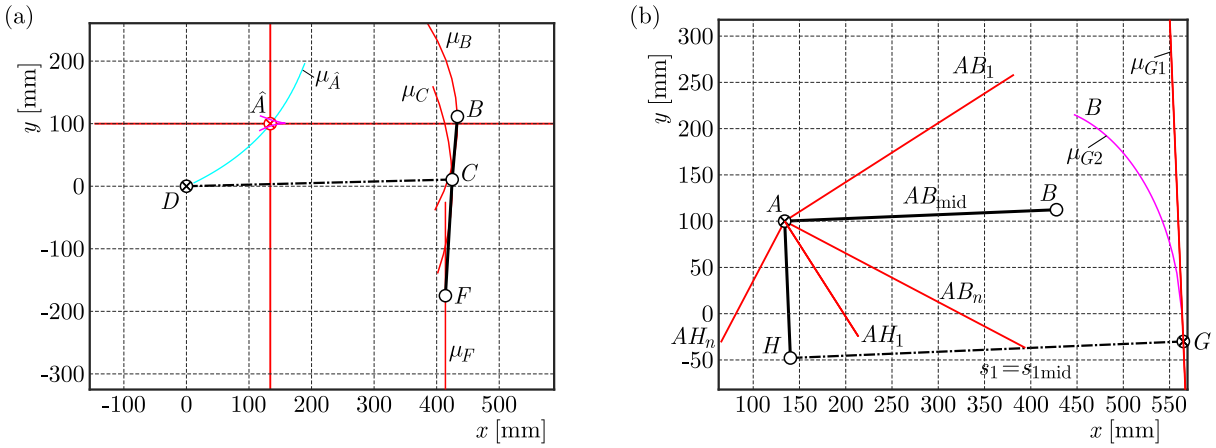

Fig. 12. (a) Trajectory $\mu_{\widehat{A}}$ of AB suspension arm 1 mount; (b) levelling drive s_1 mount point parameters.

In the next step of the synthesis, the parameters of the AH arm and the mounting of the levelling drive s_1 were determined according to the established method (Fig. 12b). The middle length of the levelling actuator $s_{1\text{mid}}$ was assumed to be equal to 0.425 m. The line μ_{G1}

was drawn perpendicular to the section AB in the AB_{mid} orientation at a distance $s_{1\text{mid}}$ from point A. Subsequently, for the determined lever lengths $AH_i \in \langle 0.1; 0.3\rangle$ m, the initial positions H_{1i} and final H_{ni} of the H point were obtained, corresponding to the orientation of element 1 in the AB_1 and AB_n positions. At the intersection of the circle with center H_{1i} and radius $s_{1\,\min}$ and the circle with center H_{ni} and radius $s_{1\,\max}$, points G_i corresponding to the assumed length AH_i were gained. The trace μ_{G2} was carried out through the G_i points. The intersection of this trace μ_{G2} with the line μ_{G1} set the location of point G at $(-0.03\,\text{m};\ 0.565\,\text{m})$.

The trajectory of the centre of the μ_F wheel was obtained for the dimensions of the mechanism chosen in this way. The rotation of element 1 from orientation AB_1 to AB_n was assumed with a fixed stepping drive s_2 of 0.425 m (Fig. 13a). The size of the workspace of the mechanism was analysed with the proposed rectangle inscription method. The result was a rectangle with height h_s equal to 0.231 m and width d_s equal to 0.402 m (Fig. 13). This makes it possible to estimate the size of the obstacle the robot will be able to overcome.

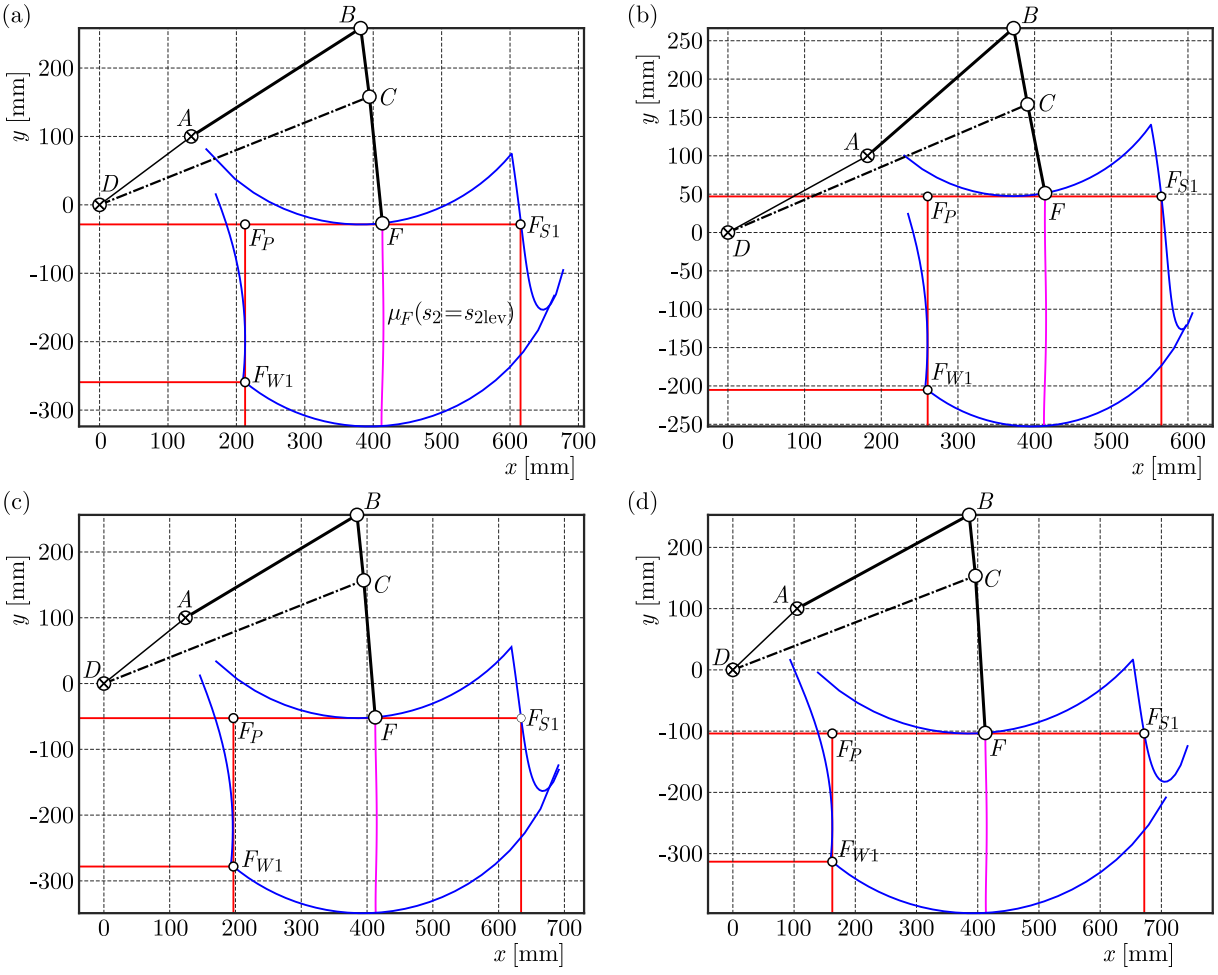

Fig. 13. Solutions obtained by the presented synthesis method for different assumed levels of the *FS* and *FE* wheel.

The synthesis of the limb mechanism was performed for different initial values of the trajectory level y_{FE} and y_{SE} and is shown in Fig. 13. The synthesis steps described were performed for the specified actuator length $s_{2\text{lev}} = 0.425$ m and for four ranges of the height of the wheel centre motion trajectory μ_F. In addition to the presented case ($y_{F1} \in \langle -0.325; -0.025\rangle$ m), three additional ranges of wheel centre motion were assumed in the following intervals: $y_{F2} \in \langle -0.25; 0.05\rangle$ m, $y_{F3} \in \langle -0.35; -0.05\rangle$ m, and $y_{F4} \in \langle -0.4; -0.1\rangle$ m (Figs. 13b–d).

The basic dimensions obtained for the limb mechanism are collected in Table 1.

Table 1. Basic dimensions of the limb mechanism obtained by the proposed synthesis method.

No.	x_F [m]	CF [m]	BC [m]	β_C [°]	AB [m]	x_A [m]	AH [m]	y_G [m]	x_G [m]	h_s [m]	d_s [m]
1	0.416	0.186	0.101	−1.4	0.294	0.134	0.148	−0.03	0.565	0.231	0.402
2	0.414	0.118	0.101	0.8	0.253	0.182	0.125	0.009	0.615	0.251	0.305
3	0.414	0.209	0.1	−1.1	0.304	0.124	0.153	−0.04	0.553	0.224	0.438
4	0.414	0.257	0.1	−2.3	0.32	0.105	0.162	−0.052	0.533	0.209	0.508

4. Conclusions

This paper presents the fundamentals of the method of dimensional synthesis of the wheel-legged robot limb. The presented method for selecting basic dimensions of the mechanism requires determining the motion of the wheel (μ_F trace) and the orientation angle φ of the turning axis. The synthesis procedure is divided into stages in which at most two parameters are searched for. This allows visualisation of the adopted objective functions. The method uses a genetic algorithm operating on integer variables. This makes it possible to significantly speed up the search. In addition, it is possible to determine the accuracy of the searched parameter values. This is extremely helpful in the later stage of the assembly of the limb mechanism, where one has a strictly defined manufacturing technology.

The synthesis method resulted in the geometry of the limb mechanism of the wheel-legged robot that meets the adopted assumptions. The expected characteristics of the steering axis angle φ were obtained, the trace of which is close to the assumed constant value equal to zero. The trajectory of the centre of the wheel when the stepping drive is locked in the $s_2 = s_{2\text{lev}}$ position is quasi-rectilinear. The determined boundaries of the working zone cover the area into which it is possible to write the profile of a standard-sized staircase. Adopting the principle that the target functions depend on at most two parameters in each step of the synthesis allows their visualization and helps interpret the results. At the stage of searching for the wishbone attachment – point A, a trajectory of the point $\widehat{A}$ clustering a set of points A_i for different determined lengths of the BC segment was obtained. The approximate trajectory $\mu_{\widehat{A}}$ is a third-order polynomial curve. To determine the parameters of this polynomial, a minimum of five positions of points $\widehat{A}_i$ must be derived, which speeds up the dimension selection process.

The adopted method of dimensional synthesis of the limb has been divided in a way that allows it to be modified within one step of dimension selection, without affecting the other steps. The paper presents the case of searching for a rectilinear trajectory needed in the task of levelling a robot platform. It is possible to perform a synthesis for other assumed trajectories of wheel centre motion. The described method is based on the description of the μ_B trajectory using splines. If the spline description is changed, the curvature κ of the μ_B trace and the trace of the centre of curvature μ_A will change as a result. In the next stage of the dimension selection study, it is worth investigating the method of approximating an arc based on a set of B_i points. In this case, the determined arc parameters directly define the length AB and the position of point A without determining the curvature κ.

The presented method of dimensional synthesis provided an acceptable solution to the task of selecting the basic dimensions of the mechanism. Dividing the method into steps allows changes to the method within a given synthesis step. The developed synthesis method can be easily modified by changing the optimisation objective function or the algorithm used to find the optimal solution of the dimensions of limb mechanisms having different structures.

References

1. Asaeikheybari, G., Lafmejani, A.S., Kalhor, A., & Masouleh, M.T. (2017). Dimensional synthesis of a four-bar linkage mechanism via a PSO-based Cooperative Neural Network approach. In *2017 Iranian Conference on Electrical Engineering (ICEE)* (pp. 906–911), Tehran, Iran. https://doi.org/10.1109/IranianCEE.2017.7985168
2. Buśkiewicz J. (2019). The optimum distance function method and its application to the synthesis of a gravity balanced hoist. *Mechanism and Machine Theory*, *139*, 443–459. https://doi.org/10.1016/j.mechmachtheory.2019.05.006
3. Gronowicz, A., Sperzyński, P., Szrek, J., & Jakubiak, J. (2014). Wheel-legged robot – construction and obstacle detection sensors. In V. Petuya, C. Pinto, & E.C. Lovasz (Eds.), *Mechanisms and Machine Science: Vol. 17. New Advances in Mechanisms, Transmissions and Applications* (pp. 191–198). Springer. https://doi.org/10.1007/978-94-007-7485-8_24
4. Hernández, A., Muñoyerro, A., Urízar, M., & Amezua, E. (2021). Comprehensive approach for the dimensional synthesis of a four-bar linkage based on path assessment and reformulating the error function. *Mechanism and Machine Theory*, *156*, Article 104126. https://doi.org/10.1016/j.mechmachtheory.2020.104126
5. Kang, Y.-H., Lin, J.-W., & You, W.-C. (2022). Comparative study on the synthesis of path-generating four-bar linkages using metaheuristic optimization algorithms. *Applied Sciences*, *12*(15), Article 7368. https://doi.org/10.3390/app12157368
6. Malarczyk, M., Kaczmarczyk, G., Szrek, J., & Kaminski, M. (2023). Internet of Robotic Things (IoRT) and metaheuristic optimization techniques applied for wheel-legged robot. *Future Internet*, *15*(9), Article 303. https://doi.org/10.3390/fi15090303
7. Shinde, A.S., Kulkarni, S.A., & Shete, S.S. (2017). Dimensional synthesis of mechanism using genetic algorithm. *International Journal of Current Engineering and Technology*, *7*(4), 1572–1580.
8. Wu, H., Li, X., & Yang, X. (2020). Dimensional synthesis for multi-linkage robots based on a niched Pareto genetic algorithm. *Algorithms*, *13*(9), Article 203. https://doi.org/10.3390/a13090203

Manuscript received April 10, 2024; accepted for publication February 17, 2025; published online April 22, 2025.

JOURNAL OF THEORETICAL
AND APPLIED MECHANICS
63, 2, pp. 415–430, Warsaw 2025
https://doi.org/10.15632/jtam-pl/202022

CREEP TEST AND CONSTITUTIVE MODEL FOR GRANITE WITH DIFFERENT WATER CONTENT AFTER HIGH TEMPERATURE COOLING

Guang-Chao ZHANG[1,2], Zhao-Teng JI[1,2], Jun-Yan SU[1], Wu-Kui DAI[1], Jian-Jun YANG[1,2*]

[1] *China Northeast Architectural Design & Research Institute Co., Ltd, Shenyang 110055, Liaoning, China*
[2] *ZJDS Geotechnical Engineering Co., Ltd, Shenyang 110055, Liaoning, China*

*corresponding author, *jianjunyang147@163.com*

Granite was selected as the test specimen to carry out the rock triaxial compression creep test under different water content after high temperature cooling. The creep rate at low stress levels includes deceleration creep rate and steady creep rate. The new damage variable can not only describe the physical damage of the crack growth under the action of temperature, but also characterize the mechanical damage of the specimen under the action of loading. A new damage creep model was obtained by modifying the Burgers model. The research can provide ideas for the support of a high and steep slope.

Keywords: high temperature; water content; granite; high and steep slope; damage model.

1. Introduction

Minerals are one of the important resources in the world, which is related to the long-term development and security of a country (Diederichs *et al.*, 2004). The problem of open-pit slope directly affects the economic benefit of open-pit mining and the safety of production (Abbas *et al.*, 2023; Bandis *et al.*, 1983). Open-pit slope excavation has the following characteristics:

- the construction objects of high and steep open-air slopes were mainly granite, igneous rock or metamorphic rock, whose compressive strength was generally above 80 MPa;
- the ambient temperature of deep-buried rock was generally higher than 100°;
- the deep buried rock mass near the water table in the high and steep open-air slope was often affected by the high temperature and groundwater, resulting in the rock mass failure and further affecting the stability of the slope.

Therefore, the study of rock mechanical properties after high temperature cooling is of great significance for slope stability research.

In resource exploitation and underground engineering construction, it is inevitable to encounter a high temperature environment (Diederichs *et al.*, 2004). For example, the development and utilization of high-temperature rock mass, deep underground disposal of high-level nuclear waste, deep mining of mine rock mass, underground coal gasification, stability of the surrounding rock wall of ultra-deep drilling and other related rock mechanics engineering all involve the influence of high temperature on rock. Uniaxial compression tests were carried out on shale samples with different bedding angles after heat treatment at different temperatures. Acoustic emission monitoring was used to analyze crack propagation. Uniaxial compressive strength tests of sandstone at different temperatures were carried out to explore the mechanical response of sandstone to significant temperature changes (Ranjith *et al.*, 2012). The above research mainly analyses the physical and mechanical properties of rocks from the perspective of temperature,

but does not consider the damage and failure of rocks under the coupling effect of temperature and water.

Research and analysis of rock damage characteristics under different factors were mainly conducted through damage models. To describe the damage degree of physical and mechanical properties of granite after natural cooling at a high temperature treatment and the impact of a high temperature treatment on physical and mechanical properties of rock, research on damage variables by domestic and foreign scholars mainly include: mass damage variable $D(m)$ (Lin *et al.*, 2022), volume damage variable $D(v)$ (Liu *et al.*, 2020b), density damage variable $D(\rho)$ (Ahmed *et al.*, 2020), longitudinal wave velocity damage variable $D(P)$ (Gao *et al.*, 2020), porosity damage variable $D(\Phi)$ (Cao *et al.*, 2024), uniaxial compressive strength $D(\mathrm{UCS})$ (Shao *et al.*, 2022), and shear modulus damage variable $D(G)$ (Hamdi *et al.*, 2011) were used as heat treatment damage parameters. The above studies lack the analysis of rock damage model under the coupling effect of water content and temperature.

In the deep formation environment of a high and steep slope, rock was often in the alternating environment of high temperature and cold water, so it was necessary to study the damage and fracture of rock formation. In this study, the triaxial compression creep test of granite with different water content under high temperature cooling was carried out. The creep characteristics, damage variables and failure modes were analyzed, and the damage index of rock at a high temperature and water content was mainly analyzed. Aiming at the deficiency of a single damage variable, a new coupled damage index was constructed to characterize the comprehensive damage characteristics. Based on the component combination theory, a new damage rheological model describing the whole process of rock creep was obtained by connecting the accelerating element with the Burgers model describing the decay and stability stages of rock. The model has the advantages of fewer parameters and accurate calculation. The research can also provide theoretical support for the stability analysis of high and steep open-air slopes.

2. Test procedures and methodology

2.1. Rock material and test specimen

The study site was selected from the slope of the Huabei granite open pit in Hunyuan County, Shanxi Province, and the granite samples were prepared according to the standards of the International Association of Rock Mechanics (Peellage *et al.*, 2024). The sample is a cylinder with a diameter of 50 mm and a height of 100 mm, the end surface roughness is less than 0.5 mm (Fig. 1a). There are four main water-bearing states of deep rock mass samples: dry state, natural state, natural water-saturated state, and fully water-saturated state. The production process of samples with different water content states is as follows:

- dry state specimen: the drying test is to obtain the rock sample without water. The specimen is placed in the drying box at 100° for 24 h, weighed after taking it out, and then placed in the drying box again for heating and weighing again. If the weight does not change, the drying test ends; if the weight changes, the drying test continues until the weight of the rock sample does not change;
- natural state specimen: the raw rock specimen is cut according to the above size;
- natural saturated state specimen: the specimen was immersed in pure water, the specimen was taken out after 24 h, the surface moisture was wiped with a wet towel, and it is still put back in the water container after weighing, and then weighed once every 24 h until the quality difference between the two times does not exceed 0.01 g;
- fully saturated state specimen: the specimen is placed in a vacuum saturated water instrument and weighed every 24 h until the mass difference between the two is within 1 %. The results show that the water content of dry, natural, naturally saturated and fully saturated granite specimens is 0, 0.5 %, 1.0 %, and 2.0 %, respectively.

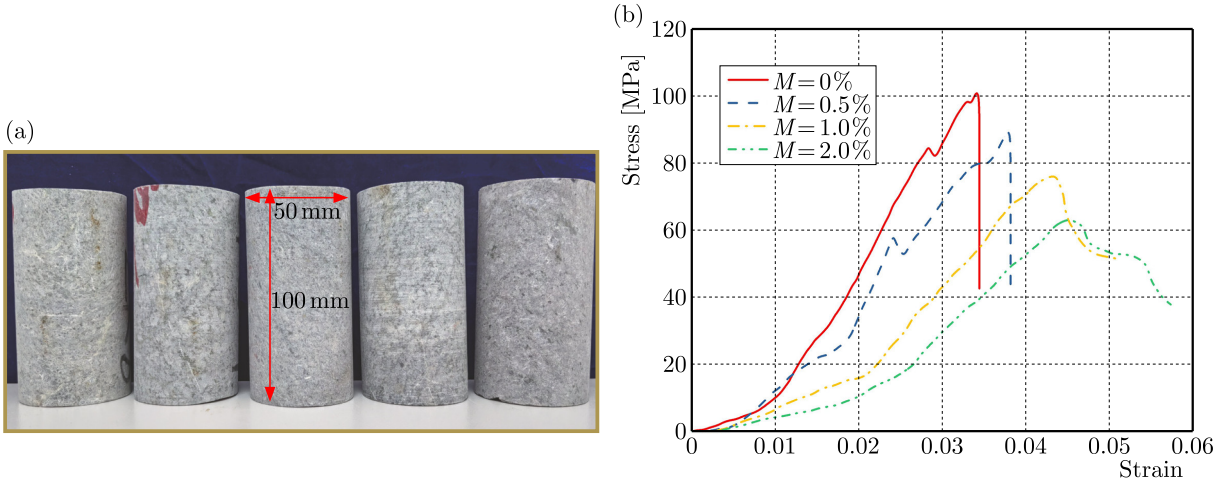

Fig. 1. (a) Granite specimen; (b) stress-strain curves of rocks with different water content.

To determine the stress level of granite creep test under different water content, uniaxial compression tests were carried out on specimens with different water content, as shown in Fig. 1b.

When the water content is low ($M = 0\,\%$ and $M = 0.5\,\%$), due to no water filling or less water filling in the initial pores of the granite, the bonding between the sample particles is strong, resulting in the deformation of the granite sample in the pre-peak stage is almost linear elastic, without obvious plastic deformation, showing significant brittle failure. In the naturally saturated state ($M = 1.0\,\%$), the compaction stage of the granite sample is relatively long, and before the peak stress, due to the water entering the pores of the specimen, the bonding between the particles is weakened, and the specimen has a significant plastic deformation, this has been verified by relevant literature (Liu *et al.*, 2020a). In the failure stage after the peak, the stress-strain curve shows a stepped stress drop. When the water content is high ($M = 2.0\,\%$), the weakening effect of water is the most obvious in the whole deformation and failure process, which makes the deformation of the granite sample larger. The stress-strain curve is convex shortly after loading, and the duration of the linear elastic deformation stage is relatively short. In the pre-peak stage, there is significant plastic deformation, and even a yield platform appears in the completely saturated state. In addition, the density, longitudinal wave velocity, elastic modulus and tensile strength of the granite are $2.592\,\mathrm{g\cdot cm^{-3}}$, $3260\,\mathrm{m\cdot s^{-1}}$, 46.5 GPa, and 5.42 MPa, respectively. In this experiment, the longitudinal wave velocity of rock was measured by the ZT801 rock mass parameter tester.

2.2. Experimental setup and test plan

The stress level and stress state of rock in the deep rock mass are different from that of rock in the surface layer. To make the test conditions more realistic, the test scheme is set from the mechanical state of rock and the occurrence conditions of confining pressure, high temperature and water content are considered. The test equipment used mainly includes:

- rapid heating box type electric furnace, which can perform high temperature heat treatment of the specimen, the maximum heating temperature of the equipment can reach 1600°, and the temperature control accuracy is 1°;
- vacuum water filling device, the device is mainly used for vacuum water filling treatment of granite specimens, in which the pumping rate is 1 l/s, the limit vacuum is 6×10^{-2} Pa, and the vacuum pump power is 150 W;
- the test equipment used was the MTS815.02 rock test system. Its maximum confining pressure was 100 MPa, and the precise range of force measurement was $-1\,\%\sim+1\,\%$.

The triaxial creep test steps of granite under different water content after high temperature cooling are shown as follows (Fig. 2): first of all, the horse boiler was used for high temperature heat treatment of granite samples, the temperature control rate is 5 °/min, and when it reaches 200°, it is maintained at a constant temperature for 24 h, and then the power supply of the heating furnace was turned off, so that the rock samples were naturally cooled to normal temperature in the furnace. The research object is the slope of the west side of the North China open-pit mine. The open-pit mine was mined to 1850 m, and the formation temperature was about 200°. Therefore, 200° was selected as the temperature of the test specimen. Then, the method in Subsection 2.1 was adopted to treat the granite specimens cooled at high temperature with different water content. The water content of the specimens was mainly obtained by calculating the mass of the specimens before and after filling with water. Finally, the triaxial creep test was carried out on the specimen. First, the granite specimen after the above treatment was sealed and placed in the triaxial compression test instrument. Then the confining pressure value of 30 MPa was applied at the loading rate of 0.5 MPa/min and kept stable, and finally the axial load was applied step by step until the specimen was damaged. The granite in the stratum slope environment was in the high ground stress environment, and the deep rock body was subjected to the vertical stress caused by the overlying rock body weight and the tectonic stress caused by the surrounding geological environment (Lemaitre, 1985). Considering the granite density and sampling depth, the triaxial compression confining pressure was 30 MPa, while the axial stress level was obtained by dividing the peak stress into five grades.

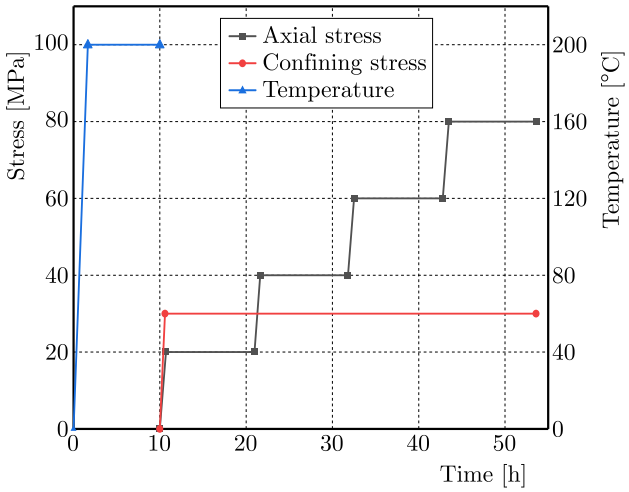

Fig. 2. Stress path.

3. Analysis of test results

3.1. Creep curve

Under the action of external force, the granite sample was compressed in the step creep test, and the tiny cracks and defects among the crystal particles in the sample due to the action of high temperature were further expanded. The low stress level will cause the internal cracks of the specimen to be crowded and closed. Under the action of external forces, the specimen will produce elastic deformation in a short time and gradually stabilize. This process takes a relatively small amount of time, but it is an important stage for the initiation of microcracks in the specimen. With the gradual stability of the internal stress distribution, the specimen enters the creep deformation stage (Fig. 3). At high stress levels, the specimen mainly deforms non-uniformly, which is manifested in two parts: on the one hand, the displacement dominated by high temperature, which is embodied in the expansion of macroscopic cracks. On the other hand, the pore water pressure further increases the crack expansion rate under load.

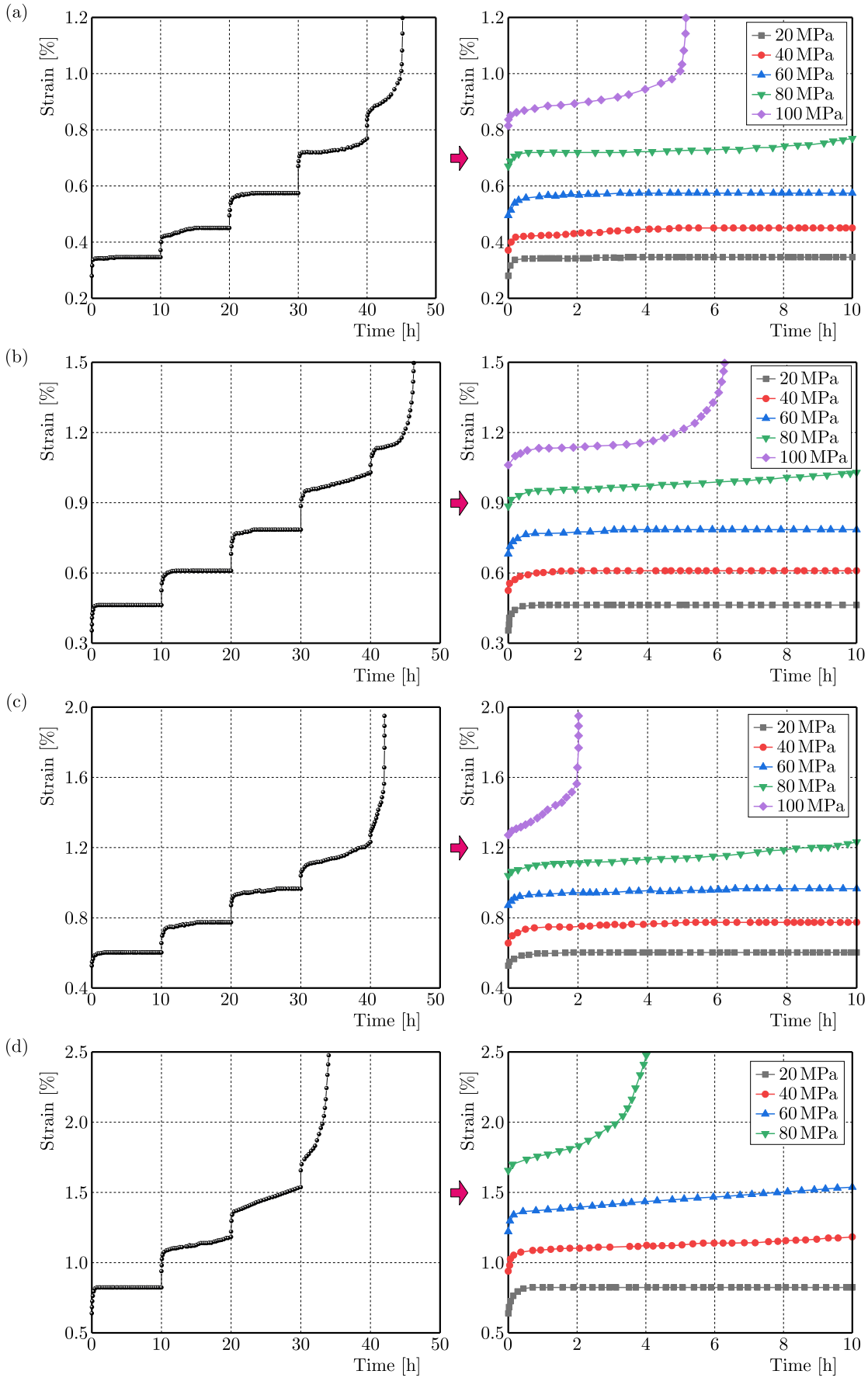

Fig. 3. Creep curve of granite under different water content after high temperature cooling: (a) $M = 0\,\%$; (b) $M = 0.5\,\%$; (c) $M = 1.0\,\%$; (d) $M = 2.0\,\%$.

With the increase of water content, the bonding between the particles inside the specimen gradually weakens, resulting in the decline of the specimen's resistance to external loads, which is reflected in the gradual increase of the peak strain of granite. It is worth explaining that when the water content reaches the state of full water, the granite specimen will be destroyed at the medium stress level. This further shows that the failure of the specimen is closely related to the water content.

3.2. Creep rate

Creep rate is an index to measure the creep deformation speed of rock, and represents the change rate of rock creep deformation with time. According to the changing trend, the creep rate curve can be divided into three stages under the constant stress: decelerating creep rate, steady creep rate and accelerating the creep rate. When $M = 0\,\%$, the curve belongs to the typical three-stage change, while the creep rate curve under other water content is more complicated (Fig. 4). In the deceleration creep rate stage, the creep rate decreases from the highest value to 0 in a very short time, which is mainly the result of the resistance of the internal adhesion of the specimen to the external load. As the internal stress and external load gradually tend to be stable, the corresponding creep rate curve is also maintained at about 0. With the increase of stress level, two stages of decay creep rate and stable creep rate repeatedly appear in the creep rate curve. When the specimen reaches the final failure stress, the appearance of instantaneous macroscopic failure indicates that the specimen has a large displacement and

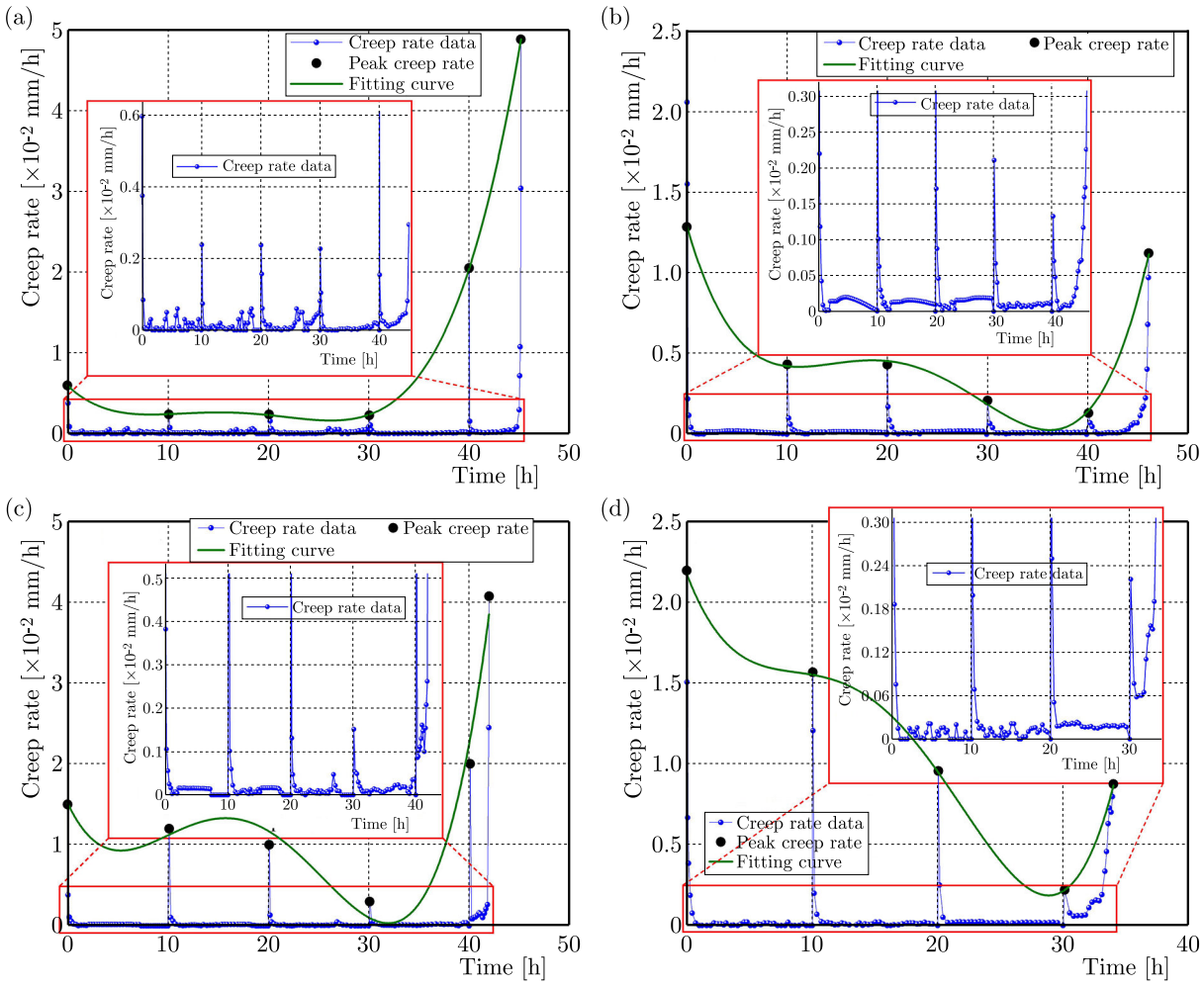

Fig. 4. Creep rate of granite under different water content after high temperature cooling: (a) $M = 0\,\%$; (b) $M = 0.5\,\%$; (c) $M = 1.0\,\%$; (d) $M = 2.0\,\%$.

deformation in a short time, which is manifested as a large increase in creep rate. This stage is called the accelerated creep rate.

In addition, the maximum local strain rate is different in the decay stage under different stress levels. Through fitting, it is found that the variation trend satisfies the polynomial function (Table 1). This further shows that the creep deformation curve of granite is related to the stress level and satisfies a certain function change law.

Table 1. Fitting results of creep rate curve.

Water content [%]	$d\varepsilon/dt = A_0 + A_1 \times t + A_2 \times t^2 + A_3 \times t^3 + A_4 \times t^4$					R^2
	A_0	A_1	A_2	A_3	A_4	
$M = 0$	0.60	−0.12	0.01	-5.86×10^{-4}	8.85×10^{-6}	0.999
$M = 0.5$	1.29	−0.21	0.02	-6.26×10^{-4}	7.12×10^{-6}	0.993
$M = 1.0$	1.51	−0.26	0.04	1.74×10^{-3}	2.50×10^{-5}	0.910
$M = 2.0$	2.17	−0.20	0.03	-1.37×10^{-3}	2.23×10^{-5}	0.996

3.3. Failure mode of specimens

Figure 5 shows the failure characteristics and fracture modes of granite under different water content. In dry environment, granite has typical brittleness characteristics, and the fracture mode is mainly tensile fracture. With the expansion and development of secondary cracks at the end of the specimen and the main tensile crack, the overall integrity of the granite specimen is good. The reason is that under the action of high temperature, the internal water content of granite is 0, the cementation between specimen particles is increased, and high temperature can improve the thermal expansion effect of rock particles. In the natural state, the fracture expansion of granite is mainly of tensile type, and some shear types appear in the micro-fracture concentration area, which may be due to the fracture of the internal crack of the specimen due to water erosion under the natural state, and the stress concentration phenomenon of the crack tip is intensified by the external load.

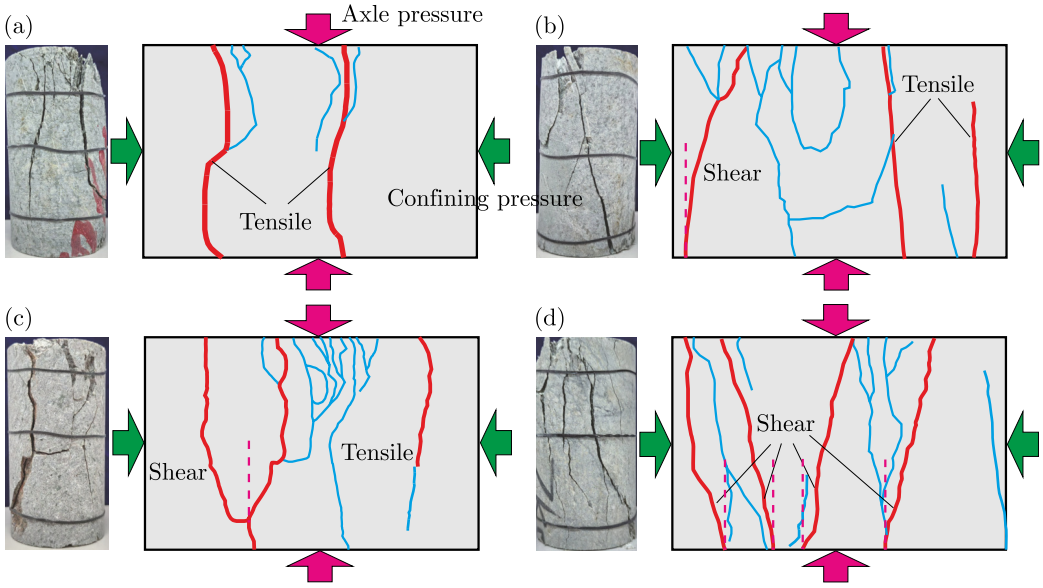

Fig. 5. Compressive failure modes of granite with different water content after high temperature cooling.

When the specimen is subjected to triaxial compression under naturally saturated water, the corresponding failure mode changes from tensile under low water content to shear under high

water content. The shear crack is approximately "Y" type and accompanied by the appearance of concentrated micro-cracks, while the tensile crack, as a secondary crack, fails to penetrate the specimen axially. Finally, the failure mode of the specimen in the fully saturated state is shear fracture, and the fracture degree of the specimen is the highest, which indicates that the cementation between the specimen particles attenuates the fastest under the high water content, and the secondary cracks can penetrate the specimen.

4. Damage creep model

4.1. Damage state variable

In this study, the damage mainly includes thermal expansion damage caused by high temperature cooling, microfissure expansion damage caused by different water conditions, and coupling damage caused by two factors under load.

(1) Temperature damage: the degradation effect of temperature on rock is mainly manifested in two aspects. First, the thermal stress generated by the temperature increase is applied to the internal structure of rock, resulting in the increase of micropore cracks. Second, the increase of temperature changes the arrangement structure of crystals or particles inside the rock, which is manifested as a softening of mechanical properties. Therefore, the temperature damage can be defined by the ratio of rock elastic modulus under different temperatures (Pudasaini & Krautblatter, 2021):

$$D = 1 - \frac{\sigma_T}{\sigma_0}, \tag{4.1}$$

where σ_T and σ_0 are the peak stress of the rock after high temperature and normal temperature (22°), respectively.

It can be seen from the previous analysis that the elastic modulus is related to temperature. Therefore, the elastic modulus is selected as the thermal damage variable in this study to describe the influence of temperature on rock bearing performance, and the thermal damage variable generated by temperature is defined as (Fig. 6)

$$D_T = aT^3 + bT^2 + cT + d, \tag{4.2}$$

where a, b, c, and d are equation coefficients.

(2) Water content damage: under the influence of different water content, pores and cracks in the rock mass expand and penetrate under the action of repeated frost heave, forming more holes and hindering the propagation of P-wave. The wave velocity decreases gradually with the increase of water content, which indicates that the rock sample structure tends to be stable gradually (Shukla *et al.*, 2009). Therefore, the longitudinal wave velocity can be used to characterize the rock damage characteristics under different water content:

$$D_p = 1 - \frac{P_w}{P_0}, \tag{4.3}$$

where P_w is the longitudinal wave velocity of the rock under different water content, P_0 is the longitudinal wave velocity of the dry specimen. Taking the elastic modulus of granite as the damage variable, the damage variable of the elastic modulus of rock under the action of water was obtained as follows (Singh *et al.*, 2018):

$$D_e = 1 - \frac{E_w}{E_0}, \tag{4.4}$$

where E_w is the elastic modulus of the specimen under different water content, and E_0 is the elastic modulus of the dry specimen.

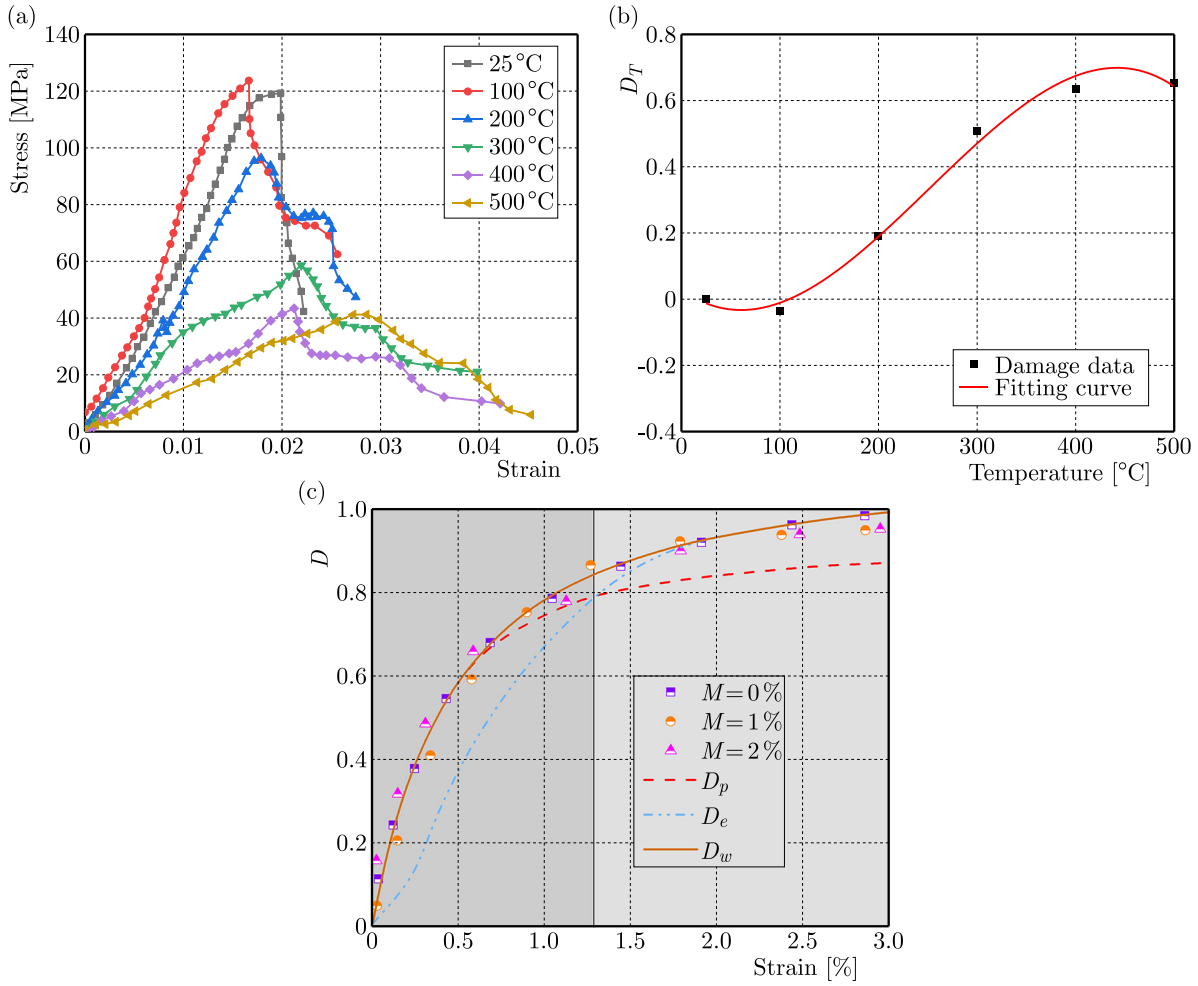

Fig. 6. (a) Stress-strain curves of granite at different temperatures; (b) temperature damage variable curve; (c) granite damage variable curve under different water content.

As a damage variable, the longitudinal wave velocity can only be used to gauge the change of the physical properties of the rock. Similarly, the elastic modulus in the mechanical properties of the rock as a damage variable index lacks the macroscopic physical properties of the specimen, and there are errors in the characterization of the damage variables by the two factors (Fig. 6c). Among them, the damage variable of wave velocity can only reflect the characteristics of the damage variable at the early stage, while the damage variable of elastic modulus mainly represents the damage variable at the later stage. Therefore, this study combines two factors to construct a new type of damage variable:

$$D_w = \xi D_p + \psi D_e = \xi \left(1 - \frac{P_w}{P_0}\right) + \psi \left(1 - \frac{E_w}{E_0}\right), \tag{4.5}$$

where ζ and ψ are water content damage parameters. The new water content damage variable can better reflect the variation trend of damage variable under the low stress level and the high stress level.

(3) Coupled damage variables: according to the extended strain equivalence principle, the damage caused by a high temperature is taken as the first damage state, and the total damage caused by a high temperature and water content is taken as the second damage state. Then the damage constitutive relationship of rock mass after high temperature cooling can be expressed as follows (Weibull, 1951):

$$\begin{aligned}\sigma_1 &= E_0\varepsilon_1(1-D)+\mu(\sigma_2+\sigma_3),\\ \sigma_2 &= E_0\varepsilon_2(1-D)+\mu(\sigma_1+\sigma_3),\\ \sigma_3 &= E_0\varepsilon_3(1-D)+\mu(\sigma_1+\sigma_2),\end{aligned} \tag{4.6}$$

where σ_i and ε_i are principal nominal stress and nominal strain; E_0 is the elastic modulus of intact rock; μ is Poisson's ratio of rock mass; D is the total damage variable of rock mass. It is assumed that N, N_T, N_w, N_1, and N_2 are the total number of microelements, the number of high temperature damaged microelements, the number of water damaged microelements, the number of high temperature and water coupled damaged microelements, and the number of undamaged microelements, respectively. High temperature initial damage D_T can be defined as the ratio of the number of high temperature damage particles to the total number of particles:

$$D_T = \frac{N_T}{N}. \tag{4.7}$$

Rock mass is further damaged under the action of different water content, and the load damage variable D_w of rock mass is defined as

$$D_w = \frac{N_w - N_1}{N - N_T}. \tag{4.8}$$

The final damage degree of rock mass is defined as the total damage variable D of rock mass with different water content under high temperature cooling:

$$D = \frac{N_w - N_1 + N_T}{N}. \tag{4.9}$$

Bring Eqs. (4.2), (4.5), (4.7), and (4.8) into Eq. (4.9) to get:

$$\begin{aligned}D = D_T + D_w - D_wD_T = D_T + (1-D_T)D_w = (aT^3+bT^2+cT+d)\\ + (1-aT^3-bT^2-cT-d)\left[\xi\left(1-\frac{P_w}{P_0}\right)+\psi\left(1-\frac{E_w}{E_0}\right)\right].\end{aligned} \tag{4.10}$$

4.2. Coupling damage model

4.2.1. Burgers model and accelerate body

(1) The Burgers model (Fig. 7a): the constitutive equation of the Burgers model can be obtained as follows:

$$\sigma_0 + \left(\frac{\eta_1}{E_0}+\frac{\eta_1\eta_2}{E_1}\right)\dot{\sigma}_0 + \frac{\eta_1\eta_2}{E_0E_1}\ddot{\sigma}_0 = \eta_1\dot{\varepsilon} + \frac{\eta_1\eta_2}{E_1}\ddot{\varepsilon}, \tag{4.11}$$

where σ_0 and ε are the total stress and strain of the model; E_i and η_i are the elastic and viscosity parameters, respectively.

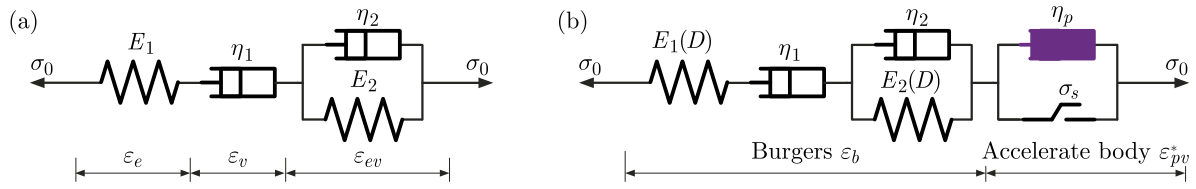

Fig. 7. (a) Schematic diagram of the Burgers model components; (b) schematic diagram of optimizing the Burgers model based on damage variables.

The total axial stain of the Burgers model includes elastic, viscous, and elastoviscous bodies:

$$\varepsilon = \varepsilon_e + \varepsilon_v + \varepsilon_{ve}. \tag{4.12}$$

The Laplace transform of Eq. (4.12) is obtained (Davies *et al.*, 2000):

$$\widetilde{\varepsilon}_e(s) + \widetilde{\varepsilon}_v(s) + \widetilde{\varepsilon}_{ve}(s) = \frac{\sigma_0}{E_1 s} + \frac{\sigma_0}{\eta_1 s^2} + \frac{\sigma_0}{(E_2 + \eta_2 s)s}, \tag{4.13}$$

where $\widetilde{\varepsilon}$ is the Laplace variation of ε and s is the complex variable of the Laplace transform space.

Applying the inverse Laplace transformation to Eq. (4.13), the creep equation of the Burgers model can be calculated by:

$$\varepsilon = \frac{\sigma_0}{E_1} + \frac{\sigma_0}{\eta_1} t + \frac{\sigma_0}{E_2}\left[1 - \exp\left(-\frac{E_2}{\eta_2} t\right)\right]. \tag{4.14}$$

(2) The accelerate body: the nonlinear acceleration element essentially describes the macroscopic displacement of rock, and the microscopic manifestation of the macroscopic displacement is the compaction, expansion and development of micro-cracks, and the expansion of micro-cracks is controlled by external loads. Therefore, the nonlinear accelerating body is closely related to the external load, and the content of the specimen under the low stress load mainly shows the compaction and slow expansion of micro-cracks, while the rapid expansion of micro-cracks under the high stress level gradually changes into macroscopic cracks. The deformation rate of the nonlinear accelerating element per unit time shows a nonlinear change characteristic, which belongs to the exponential function series. The constitutive equation of the viscosity coefficient evolution of the nonlinear accelerating element with time is defined as (Fig. 7b):

$$\dot{\varepsilon} = \frac{\eta_p}{p} \exp^{pt}, \tag{4.15}$$

where η_p and p are the accelerate body parameters. Therefore, the nonlinear acceleration element was controlled by the critical stress σ_s, and the corresponding creep equation is as follows:

$$\varepsilon = \begin{cases} 0 & (\sigma_0 \le \sigma < \sigma_s), \\ \dfrac{\sigma - \sigma_s}{\eta_p} \exp^{pt} & (\sigma \ge \sigma_s), \end{cases} \tag{4.16}$$

where σ_s is the long-term strength.

4.2.2. Damage model

The corresponding constitutive equation is as follows:

$$\frac{\ddot{\sigma}}{E_1(1-D)} + \left(\frac{1}{\eta_2} + \frac{E_2}{E_1\eta_2} + \frac{1}{\eta_1} + \frac{pe^{pt}}{\eta_p}\right)\dot{\sigma} + \left(1 + \frac{E_2}{\eta_2}\right)\frac{pe^{pt}}{\eta_p}(\sigma - \sigma_s) + \frac{E_2}{\eta_2}\int \frac{pe^{pt}}{\eta_p}(\sigma - \sigma_s)\,\mathrm{d}t = \frac{E_2}{\eta_2}\dot{\varepsilon} + \ddot{\varepsilon}. \tag{4.17}$$

Based on the above relation, we can derive a creep equation of the damage model:

– when $\sigma_0 \le \sigma < \sigma_s$, the damage model is transformed into the Burgers model to describe the decay and steady stages of the rock:

$$\varepsilon = \frac{\sigma_0}{E_1(1-D)} + \frac{\sigma_0}{\eta_1} t + \frac{\sigma_0}{E_2(1-D)}\left[1 - \exp\left(-\frac{E_2}{\eta_2} t\right)\right], \tag{4.18}$$

– when $\sigma \geq \sigma_s$, the damage model can describe the whole creep stage of the specimen:

$$\varepsilon = \frac{\sigma_0}{E_1(1-D)} + \frac{\sigma_0}{\eta_1}t + \frac{\sigma_0}{E_2(1-D)}\left[1 - \exp\left(-\frac{E_2}{\eta_2}t\right)\right] + \frac{\sigma - \sigma_s}{\eta_p}\exp^{pt}. \tag{4.19}$$

The compression test of granite with different water content under high temperature cooling meets the three-way stress state, which accords with the actual engineering state. Therefore, the three-dimensional damage constitutive model of granite with different water content is shown as follows:

$$\varepsilon_i = \begin{cases} \frac{\sigma_1+2\sigma_3}{9K} + \frac{\sigma_1-\sigma_3}{3G_1(1-D)} + \frac{\sigma_1-\sigma_3}{3\eta_1}t + \frac{\sigma_1-\sigma_3}{3G_2(1-D)}\left[1 - \exp\left(-\frac{G_2}{\eta_2}t\right)\right] & (\sigma < \sigma_s), \\ \frac{\sigma_1+2\sigma_3}{9K} + \frac{\sigma_1-\sigma_3}{3G_1(1-D)} + \frac{\sigma_1-\sigma_3}{3\eta_1}t + \frac{\sigma_1-\sigma_3}{3G_2(1-D)}\left[1 - \exp\left(-\frac{G_2}{\eta_2}t\right)\right] + \frac{\sigma_1-\sigma_3-\sigma_s}{\eta_p}e^{pt} & (\sigma \geq \sigma_s). \end{cases} \tag{4.20}$$

4.3. Model validation analysis

Combined with the creep test results of granite under different water content after high temperature cooling, the L-M nonlinear optimization algorithm was adopted to optimize and fit the material parameters by using the optimization software 1stOpt, and the parameters of the nonlinear damage constitutive model in this study were obtained.

Figure 8 shows the comparison of the test and fitting results of granite creep curve under different water content. It can be seen from the figure that the prediction results of damage

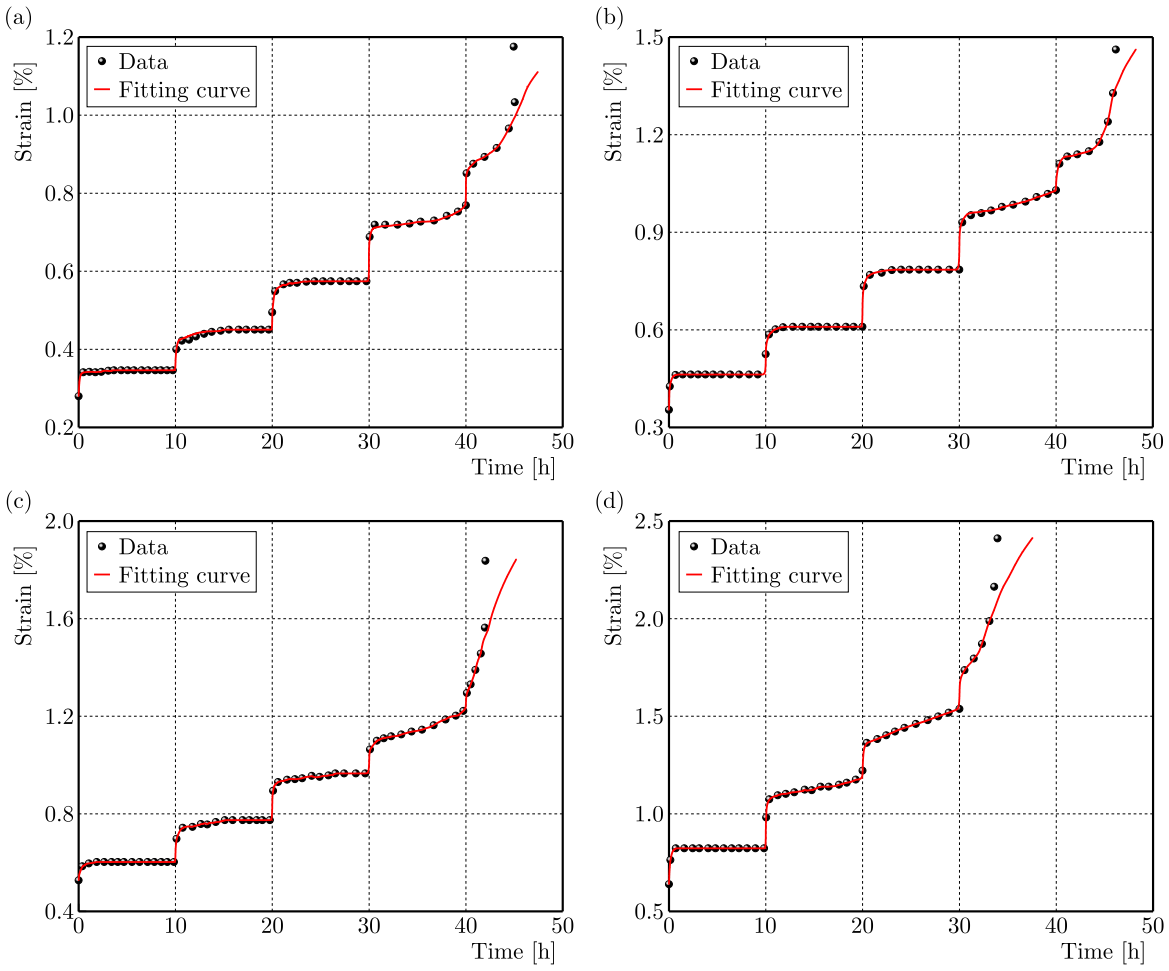

Fig. 8. Fitting curves under different water content:
(a) $M = 0\,\%$; (b) $M = 0.5\,\%$; (c) $M = 1.0\,\%$; (d) $M = 2.0\,\%$.

creep model are consistent with the general trend of test results, which can reflect the creep characteristics of granite. At the same time, there is a certain degree of error between the fitting results and the test results, but the error between them is relatively small, which indicates the accuracy of the prediction results of the model.

5. Discussion

The creep deformation and failure process of granite with different moisture content under high temperature cooling is essentially a thermal (temperature) → flow (water) → solid (rock) coupling problem (Fig. 9). First, water transfers heat in the form of thermal convection, while temperature transfers high temperature to water supply through the thermal conduction effect. Secondly, based on the theory of thermal expansion, high temperature applies thermal stress to the rock, while granite stores the heat under temperature action in the form of strain energy in the specimen (Pathiranagei & Gratchev, 2022). Then the water flows into the micro-pores and micro-cracks, and the micro-cracks of the samples are cracked under the action of external loads, while the micro-cracks of the rock samples are characterized by the crack opening and porosity.

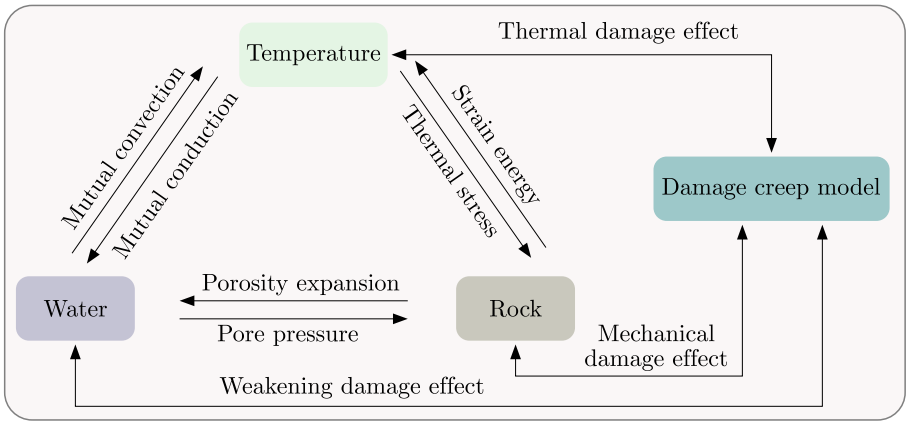

Fig. 9. Coupling schematic diagram of rock, water, and temperature.

Finally, temperature, water and rock together constitute the damage creep model, in which temperature is connected to the damage model through the thermal damage effect, water influences the creep model by weakening the damage effect, and rock specimens feedback the constitutive model through the mechanical damage effect. Specifically, the effect of water content on the mechanical properties of granite is mainly reflected in the peak stress, peak strain and elastic modulus. Figure 10 shows the variation of peak stress, peak strain and elastic modulus of granite samples with water content.

The peak stress of granite samples has a good linear relationship with water content, and the peak stress decreases with the increase of water content. This is because the water content will further increase the proportion of water in the pores of the specimen, and the cementation between granite particles will be gradually eroded, resulting in a decline in the resistance to external loads, and thus a downward trend in the peak stress. The peak strain of granite samples increases with the increase of water content, and its linear characteristics are obvious, which indicates that the increase of water content can improve the plastic characteristics of rock. From the perspective of elastic modulus, with the increase of water content, the elastic modulus presents a decreasing trend, and its decreasing curve conforms to the exponential function, which indicates that the change of water content can affect the mechanical properties of rock, but the influence on the stiffness of rock is non-linear.

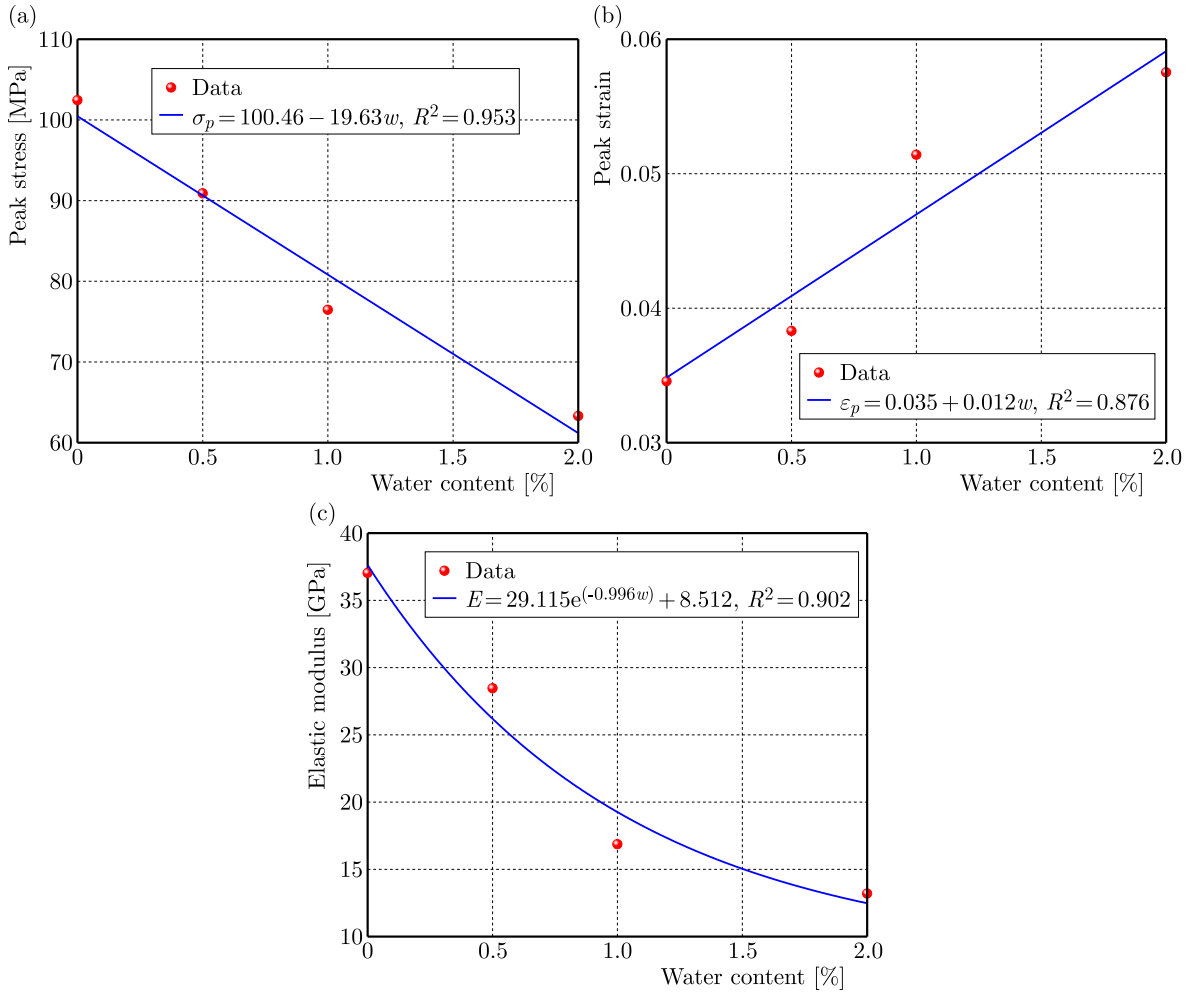

Fig. 10. Curve of mechanical properties of granite with water content: (a) peak stress; (b) peak strain; (c) elastic modulus.

6. Conclusions

Triaxial compression creep tests were carried out on granite at a high temperature and water content, the creep characteristics, failure modes and constitutive models were analyzed. Relevant conclusions are shown as follows:

- the curve of granite with different water content at a high temperature cooling has typical creep characteristics, in which the peak stress gradually decreases with the increase of water content, and the peak strain shows an opposite trend;
- the failure mode of the dry specimen at a high temperature is mainly tensile fracture, and with the increase of water content, the fracture mode changes from tensile crack to shear crack, and the granite in the fully saturated state shows shear failure;
- the damage creep model not only considers the damage factors such as high temperature and water content, but also connects the acceleration element in series. The model can well describe the whole process of creep damage of granite with different water content at a high temperature cooling.

References

1. Abbas, H.A., Mohamed, Z., & Kudus, S.A. (2023). Deformation behaviour, crack initiation and crack damage of weathered composite sandstone-shale by using the ultrasonic wave and the acoustic

emission under uniaxial compressive stress. *International Journal of Rock Mechanics and Mining Sciences*, *170*, Article 105497. https://doi.org/10.1016/j.ijrmms.2023.105497

2. Ahmed, Z., Wang, S., Hashmi, M.Z., Zishan, Z., & Chengjin, Z. (2020). Causes, characterization, damage models, and constitutive modes for rock damage analysis: a review. *Arabian Journal of Geosciences*, *13*(16), Article 806. https://doi.org/10.1007/s12517-020-05755-3

3. Bandis, S.C., Lumsden, A.C., & Barton, N.R. (1983). Fundamentals of rock joint deformation. *International Journal of Rock Mechanics and Mining Sciences & Geomechanics Abstracts*, *20*(6), 249–268. https://doi.org/10.1016/0148-9062(83)90595-8

4. Cao, H., Zhu, D., Bao, T., Sun, P., Li, J., & Erneste, H. (2024). Applicability of rock damage model based on power law distribution. *Acta Geophysica*, *72*(5), 3021–3036. https://doi.org/10.1007/s11600-023-01260-9

5. Davies, M.C.R., Hamza, O., Lumsden, B.W., & Harris, C. (2000). Laboratory measurement of the shear strength of ice-filled rock joints. *Annals of Glaciology*, *31*, 463–467. https://doi.org/10.3189/172756400781819897

6. Diederichs, M.S., Kaiser, P.K., & Eberhardt, E. (2004). Damage initiation and propagation in hard rock during tunnelling and the influence of near-face stress rotation. *International Journal of Rock Mechanics and Mining Sciences*, *41*(5), 785–812. https://doi.org/10.1016/j.ijrmms.2004.02.003

7. Gao, W., Chen, X., Hu, C., Zhou, C., & Cui, S. (2020). New damage evolution model of rock material. *Applied Mathematical Modelling*, *86*, 207–224. https://doi.org/10.1016/j.apm.2020.05.002

8. Hamdi, E., Romdhane, N.B., & Le Cléac'h, J.M. (2011). A tensile damage model for rocks: Application to blast induced damage assessment. *Computers and Geotechnics*, *38*(2), 133–141. https://doi.org/10.1016/j.compgeo.2010.10.009

9. Lemaitre, J. (1985). A continuous damage mechanics model for ductile fracture. *Journal of Engineering Materials and Technology*, *107*(1), 83–89. https://doi.org/10.1115/1.3225775

10. Lin, H., Feng, J., Cao, R., & Xie, S. (2022). Comparative analysis of rock damage models based on different distribution functions. *Geotechnical and Geological Engineering*, *40*(1), 301–310. https://doi.org/10.1007/s10706-021-01899-5

11. Liu, G., Huang, X., & Pang, J. (2020a). The uniaxial creep characteristics of red sandstone under dry-wet cycles. *Advances in Civil Engineering*, *2020*(1), Article 8841773. https://doi.org/10.1155/2020/8841773

12. Liu, L., Ji, H., Elsworth, D., Zhi, S., Lv, X., & Wang, T. (2020b). Dual-damage constitutive model to define thermal damage in rock. *International Journal of Rock Mechanics and Mining Sciences*, *126*, Article 104185. https://doi.org/10.1016/j.ijrmms.2019.104185

13. Pathiranagei, S.V. & Gratchev, I. (2022). Coupled thermo-mechanical constitutive damage model for sandstone. *Journal of Rock Mechanics and Geotechnical Engineering*, *14*(6), 1710–1721. https://doi.org/10.1016/j.jrmge.2022.02.010

14. Peellage, W.H., Fatahi, B., & Rasekh, H. (2024). Stiffness and damping characteristics of jointed rocks under cyclic triaxial loading subjected to prolonged cyclic loading. *International Journal of Fatigue*, *181*, Article 108121. https://doi.org/10.1016/j.ijfatigue.2023.108121

15. Pudasaini, S.P. & Krautblatter, M. (2021). The mechanics of landslide mobility with erosion. *Nature Communications*, *12*, Article 6793. https://doi.org/10.1038/s41467-021-26959-5

16. Ranjith, P.G., Viete, D.R., Chen, B.J., & Perera, M.S.A. (2012). Transformation plasticity and the effect of temperature on the mechanical behaviour of Hawkesbury sandstone at atmospheric pressure. *Engineering Geology*, *151*, 120–127. https://doi.org/10.1016/j.enggeo.2012.09.007

17. Shao, J., Zhang, W., Wu, X., Lei, Y., & Wu, X. (2022). Rock damage model coupled stress–seepage and its application in water inrush from faults in coal mines. *ACS Omega*, *7*(16), 13604–13614. https://doi.org/10.1021/acsomega.1c07087

18. Shukla, S.K., Gupta, S.K., & Sivakugan, N. (2009). Active earth pressure on retaining wall for c-ϕ soil backfill under seismic loading condition. *Journal of Geotechnical and Geoenvironmental Engineering*, *135*(5), 690–696. https://doi.org/10.1061/(ASCE)GT.1943-5606.0000003

19. Singh, A., Kumar, C., Kannan, L.G., Rao, K.S., & Ayothiraman, R. (2018). Estimation of creep parameters of rock salt from uniaxial compression tests. *International Journal of Rock Mechanics and Mining Sciences*, *107*, 243–248. https://doi.org/10.1016/j.ijrmms.2018.04.037

20. Weibull, W. (1951). A statistical distribution function of wide applicability. *Journal of Applied Mechanics*, *18*(3), 293–297. https://doi.org/10.1115/1.4010337

Manuscript received September 3, 2024; accepted for publication February 18, 2025; published online April 24, 2025.

JOURNAL OF THEORETICAL
AND APPLIED MECHANICS
63, 2, pp. 431–442, Warsaw 2025
https://doi.org/10.15632/jtam-pl/202721

EFFECT OF WATER CONTENT ON THE MECHANICAL BEHAVIOR AND ENERGY EVOLUTION OF SOFT ROCK UNDER UNIAXIAL COMPRESSION

Yang LIU[1]*, Hongjun LI[2]

[1] *School of Architectural Engineering, Sichuan Polytechnic University, Deyang, 618000, China*
[2] *China Anergy Group Third Engineering Bureau Co. Ltd., Chengdu 610036, China*

*corresponding author, *201911601006@stu.hebut.edu.cn*

To investigate the influence of water content on the mechanical behavior and the energy evolution law of soft rocks, uniaxial compression tests were carried out on soft rock samples prepared from rock-like materials with different water contents. The test results suggest that under uniaxial compression conditions, as the water content of the soft rock samples increases, the failure pattern is single axial splitting failure (ASF), axial splitting local expansion mixed failure and single local expansion failure (LEF), respectively. The uniaxial compressive strength (UCS) exhibits an exponential decrease, while the elastic modulus displays a linear decline. Additionally, the axial peak strain initially declines and then increases. The total and elastic energies increase exponentially, whereas the dissipated energy decreases linearly. Elastic energy as a percentage of total energy decreases, while dissipated energy as a percentage of total energy increases.

Keywords: soft rock; water content; mechanical behavior; energy evolution.

1. Introduction

Soft rocks are widely distributed in nature and are frequently found in all types of geological engineering. In accordance with the definition set forth by the International Society of Rock Mechanics (ISRM), soft rocks are classified as a group of rocks with a uniaxial compressive strength (UCS) falling between 0.5 MPa and 25 MPa (Cripps & Moon, 1990), such as mudstone, muddy siltstone, muddy mineral rock and so on. Soft rocks usually have mechanical and physical characteristics such as low strength, loose structure (low density), water swelling by absorption, and disintegration by dehydration. The mineral composition (comprising a significant proportion of hydrophilic minerals) and structural characteristics of soft rocks have been demonstrated to be influenced by water, which plays an important role in determining their mechanical behavior (Vásárhelyi, 2005; Vásárhelyi & Ván, 2006; Ciantia *et al.*, 2015; Cherblanc *et al.*, 2016). Nevertheless, water is frequently present during construction in a multitude of soft rock strata. Such circumstances may be exemplified by open-pit mining operations conducted under conditions of heavy precipitation, the construction of reservoir slopes, and the excavation of tunnels in rock strata with the elevated water content.

The influence of water on the mechanical behavior of soft rocks has been the subject of study by a number of scholars. However, the majority of these studies have concentrated on saturated soft rocks and the effects of dry-wet cycles on them. He *et al.* (2021) studied the damping behavior of soft rock by cyclic loading tests, they found that as the stress amplitude decreased, the moisture content had a lesser effect on the dynamic shear modulus and a greater effect on the damping parameters. Li *et al.* (2023) studied the mechanical deformation characteristics of the clay-red stratum soft rock mixture before and after wetting by using a large-scale triaxial test.

They found that wetting led to a decrease in the shear strength and critical strain of the samples, and a decrease in the critical internal friction angle and tangent modulus, which intensified the crushing of the rock blocks. Liu *et al.* (2024) studied the micro-pore dissolution mechanism and macroscopic mechanical behavior of red-bed soft rock by the dry-wet cycle method and a series of uniaxial compression tests. Their results showed that with an increase in the number of dry-wet cycles, the macroscopic failure mode changes from brittle splitting failure to ductile conical failure under the action of the axial load. Zhang *et al.* (2024) studied the mechanism and influence on red-bed soft rock disintegration durability of particle roughness based on the experiment and fractal theory, they found that the roughness decreases with increasing dry-wet cycles, but increases with decreasing particle size. Yu *et al.* (2023) studied the disintegration mechanism of the soft rock due to water intrusion based on the discrete element method, their results showed that the breaking force and the residual strength coefficient of the complete sample exhibit an exponential attenuation relationship with the increase of water content. Fu *et al.* (2021) used the nuclear magnetic resonance (NMR) technology to visualize and quantify the dynamics of water infiltration and distribution in initially unsaturated sandstone. They found that the strength and Young's modulus of sandstones decrease as a function of increasing water saturation.

The deformation and damage evolution processes in rock are accompanied by energy conversion, including the accumulation, dissipation, and release of energy (Xie *et al.*, 2009; Huang & Li, 2014; Chen *et al.*, 2017). Currently, the energy evolution during rock damage can be obtained from the calculation of its stress-strain curve or from the analysis of the collected signals of acoustic emission. Gao *et al.* (2020) investigated the energy evolution characteristics, and identified the damage and crack propagation thresholds based on the uniaxial loading-unloading experiments for five types of rocks. They found that the evolution characteristics of the strain energy rates can be easily identified by the crack propagation thresholds. Gong *et al.* (2021) proposed a theoretical method for characterising the damage of intact rocks under uniaxial compression conditions based on the linear energy dissipation law and the energy dissipation coefficient, they found that with the linear energy storage law serving as a theoretical basis, the peak dissipated strain energy in a rock damage expression under uniaxial compression can be accurately calculated. Meng *et al.* (2023) studied the effects of cyclic loading and unloading rates on the energy evolution of rocks with different lithology, they found that the energy of all rock samples increased nonlinearly with the increase in axial stress, and the elastic energy increased gradually first and subsequently rapidly with the increase in the axial stress. Xi *et al.* (2023) studied the transient process of the mechanical response and energy conversion of rocks with different lithologies under impact loading, their results showed that the fracture energy of the rock increases as the strain rate increases.

The objective of this study was to investigate the effect of water on the mechanical behavior and energy evolution of soft rock. To this end, uniaxial compression tests were performed on soft rock samples with the different water content. A correlation was identified between mechanical parameters, including UCS, elastic modulus and peak strain, and the water content of the soft rock samples. The evolution laws of total energy, elastic energy and dissipated energy in soft rock with varying water contents were investigated. The findings of this study can provide the theoretical guidance on the construction and maintenance of projects in water-bearing soft rock strata.

2. Test methods

2.1. Sample preparation

Despite the prevalence of soft rocks in nature, the preparation of standard cylindrical samples with a specific water content remains a challenging endeavour. This is due to the fact that natural soft rocks lose their structural integrity rapidly upon contact with water, leading to

the formation of fissures when dehydrated. Rock-like materials have been widely used in rock mechanical behavior tests as well as model tests (Luo *et al.*, 2023; Liu *et al.*, 2023a; 2023b). For example, Liu *et al.* (2023a) investigated the compression characteristics of fractured soft rock and its Mohr–Coulomb criterion by means of soft rock samples prepared from rock-like materials. Therefore, in this study, rock-like materials were used to prepare standard soft rock samples with the specific water content. As shown in Fig. 1, the rock-like material consists of quartz sand, kaolin, gypsum, 42.5 normal silicate cement, barite powder, and water. Barite powder and quartz sand were used as the coarse aggregate, and gypsum, kaolin, and cement were used as the binder. The barite powder can effectively improve the sample density, gypsum can effectively prevent the rapid solidification of the mixed mortar, and kaolin can appropriately increase the plasticity of the sample. In order to prepare soft rock samples whose mechanical properties are highly similar to those of the real soft rock (mudstone), a lot of attempts were made on the mass ratio of the rock-like materials in the preliminary stage. By constantly adjusting the proportion of rock-like materials, the soft rock samples with mechanical properties highly similar to those of the real soft rock (mudstone) were finally obtained. The mass ratio of the rock-like materials used to prepare the soft rock samples is shown in Table 1. According to the ISRM (Fairhurst & Hudson 1999), the standard cylinder soft rock samples of 50 mm × 100 mm (diameter × height) are prepared and the basic mechanical parameters of the prepared soft rock samples are shown in Table 2.

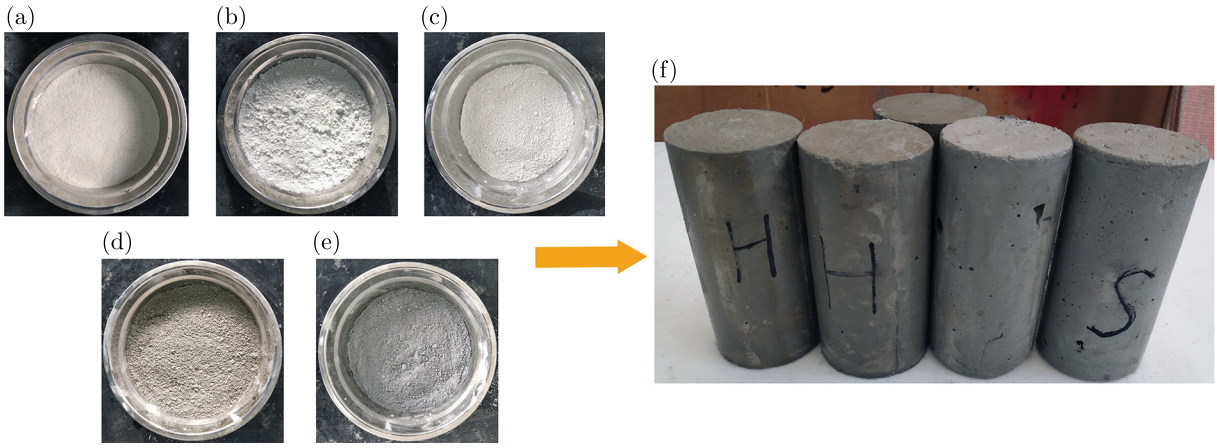

Fig. 1. Rock-like materials for the preparation of soft rock and partially prepared soft rock samples: (a) quartz sand; (b) kaolin; (c) gypsum; (d) cement; (e) barite powder.

Table 1. Material ratios for the preparation of the soft rock.

Type	Quartz sand	Barite powder	Cement	Gypsum	Kaolin	Water-binder ratio
Ratio	0.75	0.25	1.5	0.45	0.35	0.40

Table 2. Basic mechanical parameters of the prepared soft rock samples (dry).

Mechanical parameters	Uniaxial compression strength [MPa]	Tensile strength [MPa]	Elasticity modulus [GPa]	Poisson's ratio	Cohesive force [kN]	Internal friction angle [°]
Value	18.68	2.14	3.68	0.22	2.42	15.23

2.2. Test equipment

Uniaxial compression tests were carried out by the MTS-793 rock mechanics testing machine (Fig. 2) with an axial force loading range of −200 kN to +200 kN, and the accuracy of axial force data collection is 0.001 kN, the accuracy of axial deformation data collection is 0.001 mm.

Fig. 2. MTS-793 rock mechanics testing machine.

2.3. Test procedure

The specific procedure of uniaxial compression test for soft rock with different water content was as follows:

Step 1: The prepared soft rock samples were subjected to drying in an oven at a temperature of 110 °C for a period of 24 hours. Following this, the mass of the samples was measured, resulting in a value designated M_d. Subsequently, the dried samples were saturated with water under vacuum after standing at room temperature, resulting in a saturated water content of 14 % for the soft rock samples.

Step 2: The saturated soft rock samples were placed in an oven at 60 °C and removed at 2-minute intervals to determine their mass, M_w. Therefore, the real-time water content of the soft rock samples can be calculated by Eq. (2.1). When the water content of the soft rock samples was determined, a thin and uniform layer of silicone oil was applied to the surface to prevent the moisture from changing over a short period of time.

$$\omega_t = \frac{M_w - M_d}{M_d} \times 100\,\%, \tag{2.1}$$

where ω_t is the water content of the soft rock samples, M_w is the mass of water-bearing soft rock samples, M_d is mass of dried soft rock samples.

Step 3: Soft rock samples with specified water contents were loaded into the MTS-793 rock mechanics testing machine, and axial load was applied at a static loading rate of 0.01 mm/min until the samples failed. To guarantee the precision of the test data, three samples of soft rock were tested for each water content level.

3. Test results

3.1. Stress-strain curves

The uniaxial compressive stress-strain curves of soft rock samples with different water contents are shown in Fig. 3. The water content has a significant effect on the trend of stress-strain curves of soft rock samples. The evolution of uniaxial compressive stress-strain curves of soft rock samples can be generally divided into four stages: the plastic deformation stage, the elastic

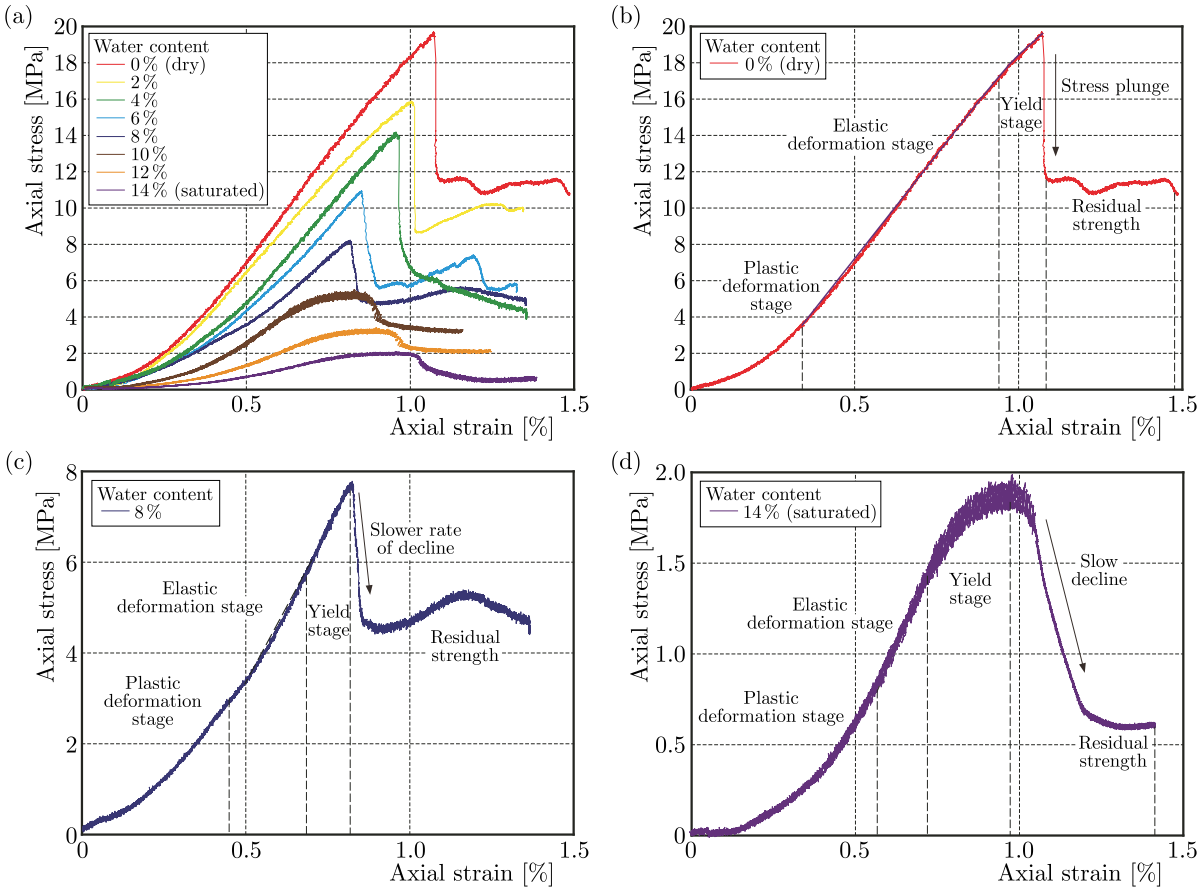

Fig. 3. Uniaxial compressive stress-strain curves of soft rock samples with different water contents.

deformation stage, the yielding stage and the residual stress stage (Fig. 3a). As the water content of the soft rock samples increases, the proportions of the plastic deformation and yielding stages of the stress-strain curve increase, while the proportion of the elastic deformation stage decreases (Figs. 3b–3d). Furthermore, as the water content of the soft rock samples increases, after the peak axial stress of failure is reached, the rate of decrease of axial stress decreases, but the percentage of decrease increases. For example, when the water content of the soft rock sample is 0 % (dry), after reaching the peak axial stress, its axial stress decreases instantaneously and sharply. The axial stress decreased from 19.64 MPa to 11.61 MPa, a reduction of 40.87 % (Fig. 3b). When the water content of the soft rock sample is 14 % (saturated), the axial stress decreases slowly after the peak axial stress is reached. The axial stress decreased from 1.94 MPa to 0.69 MPa, a reduction of 64.35 % (Fig. 3d).

3.2. Peak stress, elastic modulus and peak strain

The relationship between peak stress, elastic modulus, peak strain and water content of soft rock is shown in Fig. 4. The water content has a significant effect on the peak stress (UCS), elastic modulus and axial peak strain of soft rock. As shown in Fig. 4a, the uniaxial compressive strength of soft rock samples decreases with increasing the water content and their relationship can be fitted well by an exponential function. The average UCS was 18.99 MPa when the water content of the soft rock samples was 0 % (dry), and 1.95 MPa when the water content of the soft rock samples was 14 % (saturated). When the water content of the soft rock samples increased from 0 % (dry) to 8 %, the UCS decreased by an average of 21.64 % for every 2 % increase in the water content, while when the water content of the soft rock samples increased from 8 % (dry) to 14 %, the uniaxial compressive strength decreased by an average of 29.01 % for every 2 %

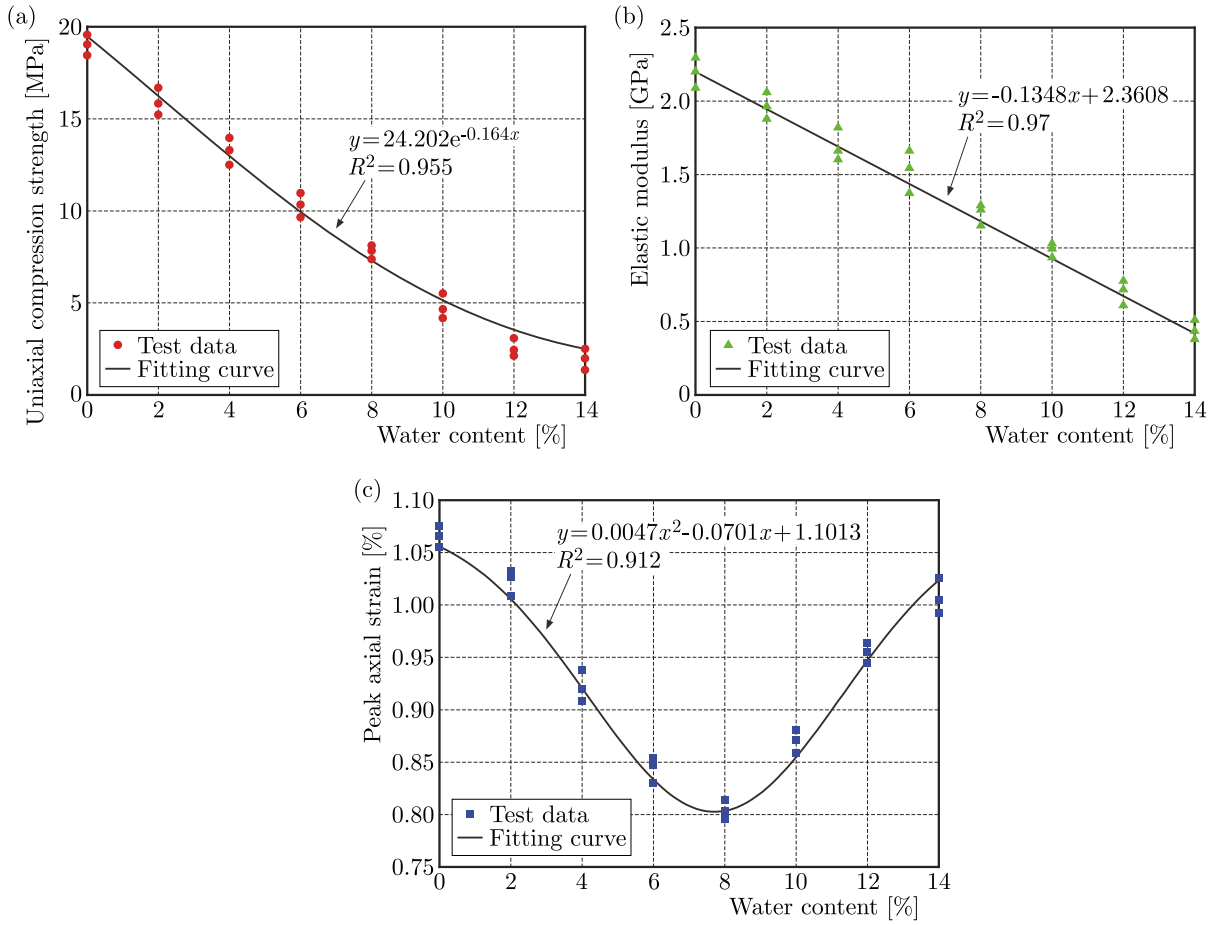

Fig. 4. Relationship between peak stress, elastic modulus, peak strain and water content of soft rock.

increase in the water content. The decrease in UCS increased significantly with the increase in water content of the soft rock samples. As shown in Fig. 4b, the elastic modulus of soft rock samples decreases linearly with increasing water content. With each 2 % increase in the water content of the soft rock samples, the elastic modulus decreased on average by 0.25 GPa. As shown in Fig. 4c, the peak axial strain of soft rock samples first decreases and then increases with increasing water content. The relationship between peak axial strain and the water content can be fitted well by a quadratic function. When the water content of a soft rock samples is low, it has a strong load-bearing capacity, its peak axial strain is larger, and it is mainly elastic deformation. However, as the water content of the soft rock samples increases, the bearing capacity decreases, but the deformation increases and is mainly plastic.

3.3. Ultimate failure pattern

Ultimate failure patterns of soft rock samples with different water contents under uniaxial compression tests are shown in Fig. 5. With the gradual increase of the water content of the soft rock samples, their ultimate failure patterns under uniaxial compression conditions changed from single axial splitting failure (ASF) to mixed ASF and the local expansion failure (LEF) and then to single LEF. As shown in Figs. 5a and 5b, when the water content of the soft rock samples is 0 % (dry) and 2 %, the initial cracks sprout at the end of the sample and then developed towards the other end, its width gradually becomes narrower, and the failure pattern is dominated by ASF. As shown in Figs. 5c–5f, when the water content of the soft rock samples was 4 %, 6 %, 8 %, and 10 %, LEF occurred at one end of the sample (about one-third of the total length of the sample), while the other end of the sample remained ASF. The LEF is manifested

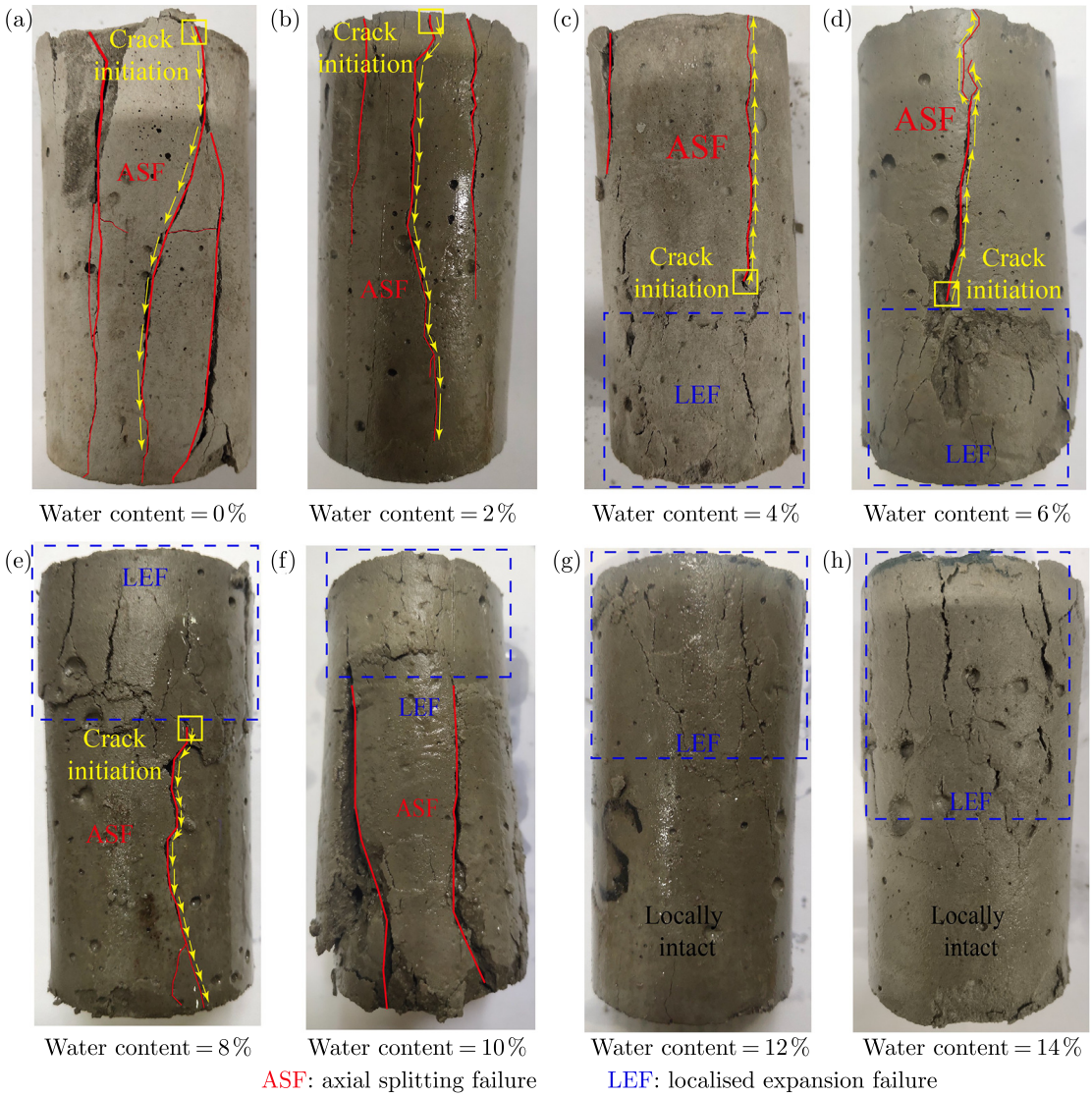

Fig. 5. Ultimate failure patterns of soft rock samples with different water contents.

as a circumferential increase in the volume of the sample and is accompanied by a small number of micro-cracks. Meanwhile, the initial cracks of ASF sprout at the interface of local expansion failure and then develop towards the other end of the sample. As shown in Figs. 5g and 5h, when the water content of the soft rock samples is 12 % and 14 %, the ultimate failure pattern of the samples is dominated by local expansion failure. In addition, the extent of LEF of the soft rock samples increased from one-third to two-thirds of their total length as the water content increased.

4. Energy conversion

4.1. Calculation of energy

The energy composition of the soft rock sample under uniaxial compression is shown schematically in Fig. 6. The total input energy (U) of a rock sample under uniaxial compression consists of the elastic energy (U_e) and the dissipated energy (U_d). The total input energy (U) is the work done on the rock sample by the external load applied by the rock mechanics testing machine, which can be obtained by calculating the total area of the stress-strain curve (given by the area

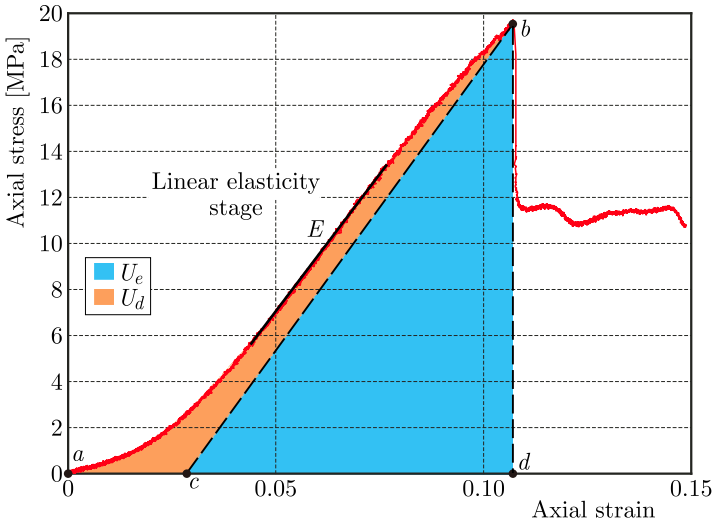

Fig. 6. Stress-strain curve and strain energy.

of figure described by points *abd*, see Fig. 6). The elastic energy (U_e) is the energy stored by the elastic deformation of the rock sample during compression deformation (given by the area of the figure described by points *cbd*, see Fig. 6), and the dissipated energy (U_d) is the energy dissipated by the plastic deformation of the rock sample during compression deformation (given by the area of figure described by points *abc*, see Fig. 6). Therefore, the total energy, elastic energy and dissipated energy are calculated as shown in Eq. (4.1), respectively (Xie *et al.*, 2009; Huang & Li, 2014; Chen *et al.*, 2017):

$$U = \int_a^d \sigma_a d\varepsilon_a, \qquad U_e = \frac{1}{2E}\sigma_a^2, \qquad U_d = U - \frac{1}{2E}\sigma_a^2, \tag{4.1}$$

where σ_a is the axial stress, ε_a is the axial strain, E is the elastic modulus.

4.2. Energy evolution

Energy evolution laws of soft rock samples with different water contents under uniaxial compression tests are shown in Fig. 7. The energy evolution process of a soft rock sample is closely related to its specific deformation pattern. The elastic and dissipated energies represent the elastic and plastic deformation of the soft rock sample, respectively. The total energy is defined as the total work done by the rock mechanics testing machine and therefore exhibits a rapid increase. In contrast, the evolutionary law of the elastic and dissipated energies is contingent upon the deformation pattern that occurs in the soft rock sample. In the absence of water in the soft rock sample (i.e., when it is dry), both the total and elastic energies evolve in a similar manner, exhibiting a rapid increase with increasing axial strain. However, the rate of increase in dissipated energy is slow with increasing axial strain (Fig. 7a). When the water content of the soft rock sample is 8 %, the evolution trends of the total and elastic energies remain generally consistent and continue to increase rapidly as the axial strain increases. However, there is a notable discrepancy between the two energies, with the elastic energy displaying a greater increase than the total energy. Concurrently, the dissipated energy increases gradually initially and then remains constant with increasing axial strain (Fig. 7b). At a water content of 14 % in the soft rock sample, the total energy increases rapidly with increasing axial strain. The elastic energy increases rapidly and then levels off, while the dissipation energy increases slowly and then rapidly (Fig. 7c).

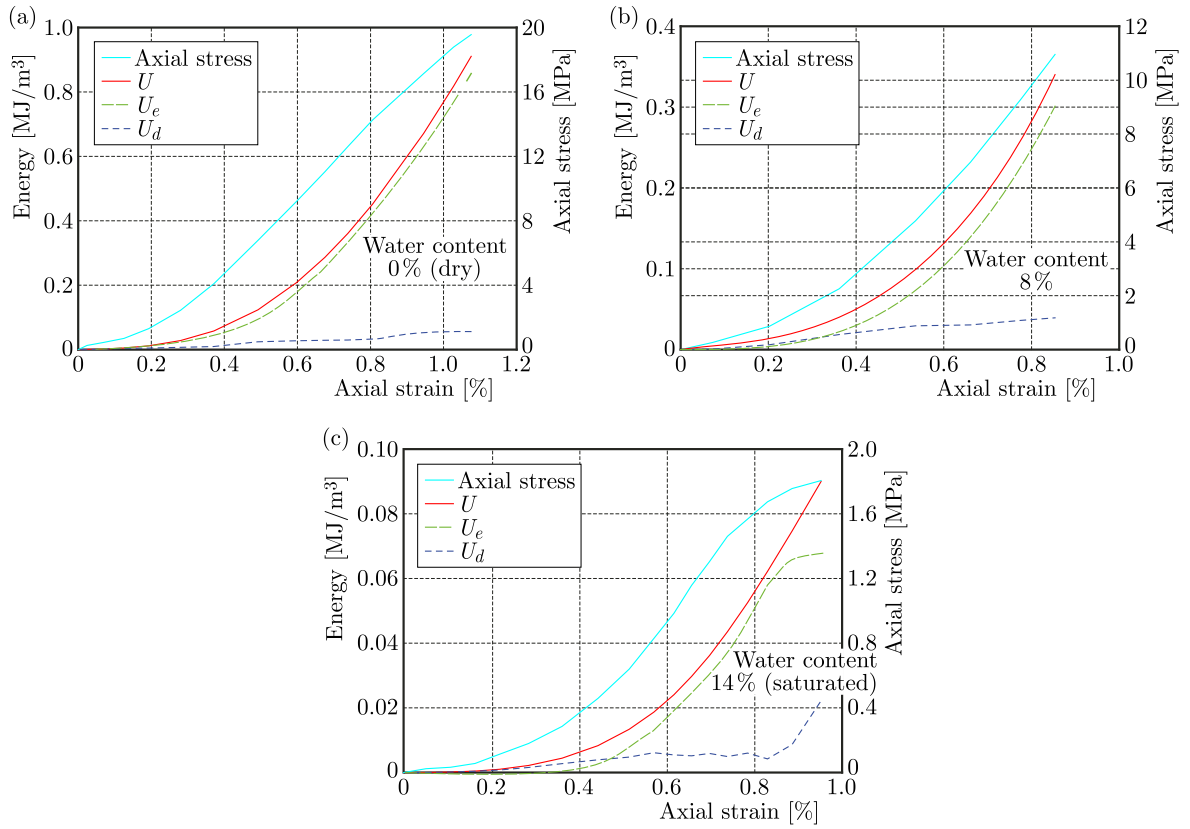

Fig. 7. Energy evolution laws of soft rock samples with different water contents under uniaxial compression tests.

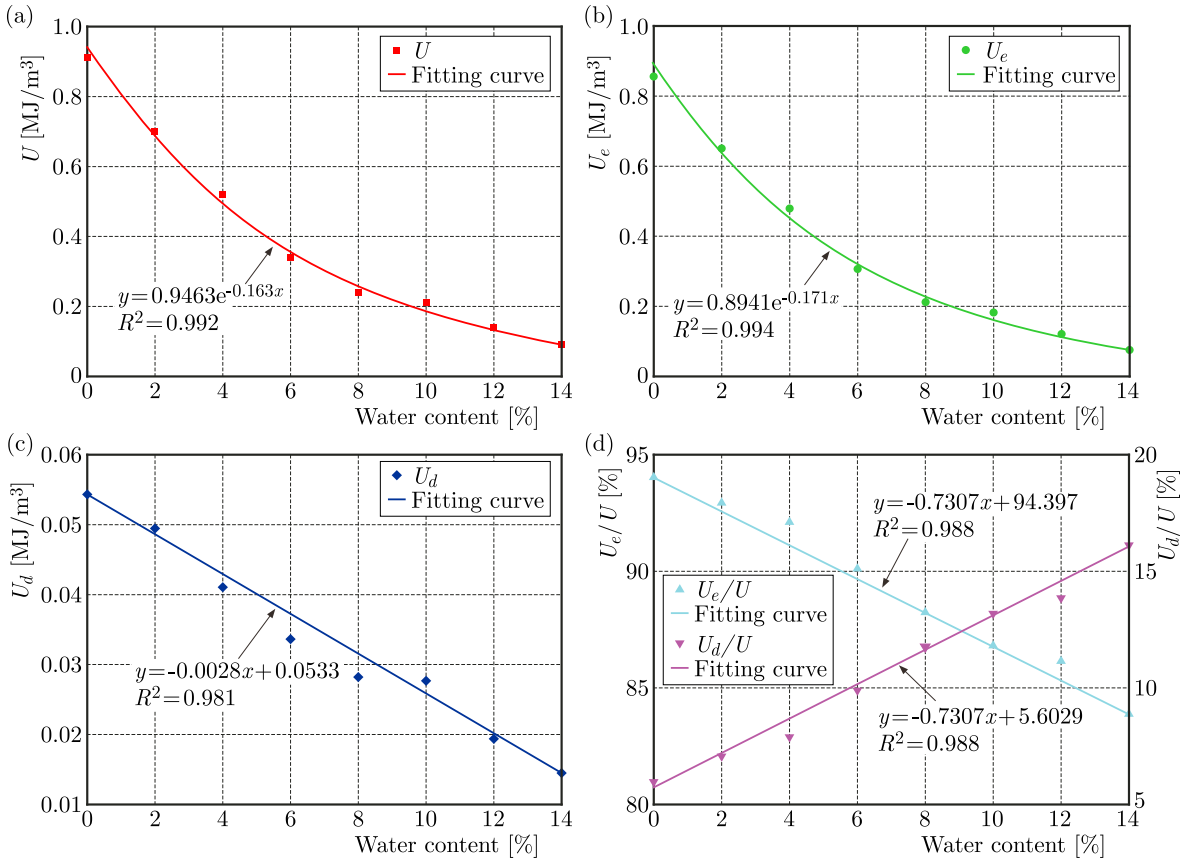

Fig. 8. Relationship between total energy, elastic energy, dissipated energy, and percentage water content.

4.3. Characteristics of energy at UCS

The relationship between total energy, elastic energy, dissipated energy and percentage water content at UCS for soft rock samples is shown in Fig. 8. It can be seen from Figs. 8a and 8b, with the increase of water content of soft rock samples, the total energy and elastic energy are gradually reduced, and the change rule can be well fitted by the exponential function. Meanwhile, as shown in Fig. 8c, the dissipated energy decreases linearly with the increase of water content of soft rock samples. Moreover, as illustrated in Fig. 8d, the proportion of elastic energy in the total energy tends to decrease linearly with increasing water content in the soft rock samples, while the dissipated energy proportion shows a linear increase. This suggests that as the water content of the soft rock sample increases, there is an accompanying increase in plastic deformation and a decrease in elastic deformation during the process of compressive deformation. The dissipation of input energy occurs predominantly through plastic deformation, with a lesser degree of energy storage occurring in the elastic deformation phase.

5. Discussion

Numerous studies have shown that the water content leads to significant changes in the mechanical behavior of soft rocks mainly due to the physical-chemical effect and the mechanical effect (Liu *et al.*, 2021; Wasantha & Ranjith, 2014). The micrographs of the soft rock under dry and saturated conditions are presented in Fig. 9. When the soft rock is in a dry state, the surface of the sample displays a structurally compact appearance with a reduced number of micro-cracks. However, when the soft rock is in a saturated state, its structure becomes looser, and a considerable number of micro-cracks are evident. The increased plasticity of the soft rock samples during compressive deformation is attributed to the loosened structure and the elevated number of micro-cracks. This provides an explanation as to why the dissipated energy as a percentage of the total energy in uniaxial compression conditions of soft rock increases with increasing water content.

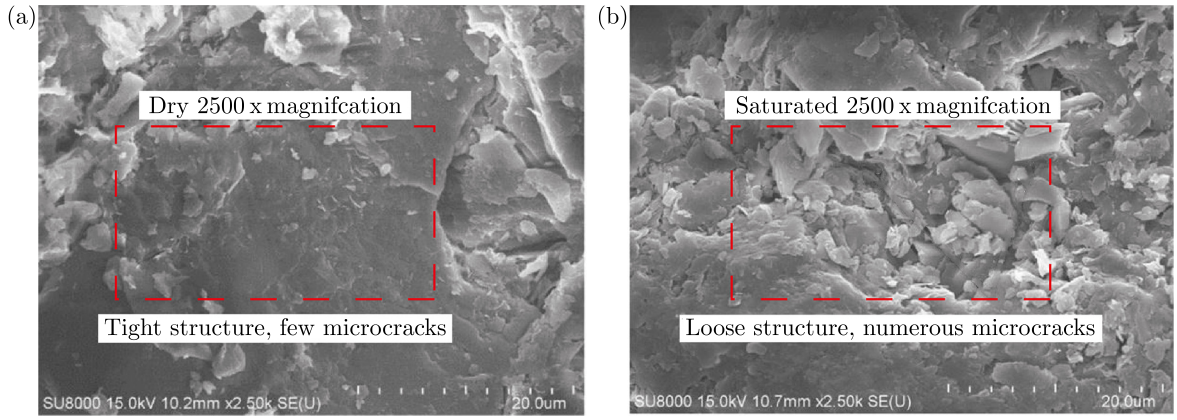

Fig. 9. Scanning electron microscopy images of dry and saturated soft rock (Liu *et al.*, 2021).

6. Conclusion

By conducting uniaxial compression tests on soft rock samples prepared from rock-like materials with the different water content, this study investigated the effect of water content on the strength, deformation, failure pattern, and energy evolution law of soft rock samples. The main conclusions are summarized as follows:

1) The UCS exhibits an exponential function-decreasing trend, while the elastic modulus demonstrates a linear decrease as the water content of the soft rock samples increases.

The peak axial strain initially exhibits a decline, followed by an uptick. Its correlation with the water content can be effectively captured by a quadratic function.

2) The water content has a significant effect on the failure pattern of soft rock samples under the uniaxial compression condition. With the increase of water content, the failure pattern is single ASF, axial splitting local expansion mixed failure and single LEF, respectively.
3) As the water content of the soft rock sample increases, both the total input energy and the elastic energy exhibit an exponential function that demonstrates a decreasing trend, while the dissipated energy displays a linear decreasing trend. Furthermore, as the water content of the soft rock samples increases, the proportion of elastic energy in the total energy decreases linearly, while the proportion of dissipated energy in the total energy increases linearly.

Acknowledgments

This work is supported by the Graduate Student Innovation Foundation of Hebei Province (grants no. CXZZBS2022034).

References

1. Chen, Z.Q., He, C., Wu, D., Xu, G.W., & Yang, W.B. (2017). Fracture evolution and energy mechanism of deep-buried carbonaceous slate. *Acta Geotechnica*, *12*(6), 1243–1260. https://doi.org/10.1007/s11440-017-0606-5

2. Cherblanc, F., Berthonneau, J., Bromblet, P., & Huon, V. (2016). Influence of water content on the mechanical behaviour of limestone: role of the clay minerals content. *Rock Mechanics and Rock Engineering*, *49*(6), 2033–2042. https://doi.org/10.1007/s00603-015-0911-y

3. Ciantia, M.O., Castellanza, R., Crosta, G.B., & Hueckel, T. (2015). Effects of mineral suspension and dissolution on strength and compressibility of soft carbonate rocks. *Engineering Geology*, *184*, 1–18. https://doi.org/10.1016/j.enggeo.2014.10.024

4. Cripps, J.C. & Moon, C.F. (1990). The Engineering Geology of Weak Rock, *Leeds University Press.*

5. Fairhurst, C.E. & Hudson, J.A. (1999). Draft ISRM suggested method for the complete stress-strain curve for intact rock in uniaxial compression. *International Journal of Rock Mechanics and Mining Sciences*, *36*(3), 279–289. https://doi.org/10.1016/S0148-9062(99)00006-6

6. Fu, T.F., Xu, T., Heap, M.J., Meredith, P.G., Yang, T.H., Mitchell, T.M., & Nara, Y. (2021). Analysis of capillary water imbibition in sandstone via a combination of nuclear magnetic resonance imaging and numerical DEM modeling. *Engineering Geology*, *285*, Article 106070. https://doi.org/10.1016/j.enggeo.2021.106070

7. Gao, L., Gao, F., Zhang, Z.Z., & Xing, Y. (2020). Research on the energy evolution characteristics and the failure intensity of rocks. *International Journal of Mining Science and Technology*, *30*(5), 705–713. https://doi.org/10.1016/j.ijmst.2020.06.006

8. Gong, F.Q., Zhang, P.L., Luo, S., Li, J.C., & Huang, D. (2021). Theoretical damage characterisation and damage evolution process of intact rocks based on linear energy dissipation law under uniaxial compression. *International Journal of Rock Mechanics and Mining Sciences*, *146*, Article 104858. https://doi.org/10.1016/j.ijrmms.2021.104858

9. He, M.M., Zhang, Z.Q., & Li, N. (2021). Experimental investigation and empirical model to determine the damping and shear stiffness properties of soft rock under multistage cyclic loading. *Soil Dynamics and Earthquake Engineering*, *147*, Article 106818. https://doi.org/10.1016/j.soildyn.2021.106818

10. Huang, D. & Li, Y.R. (2014). Conversion of strain energy in Triaxial Unloading Tests on Marble. *International Journal of Rock Mechanics & Mining Sciences*, *66*, 160–168. https://doi.org/10.1016/j.ijrmms.2013.12.001

11. Li, S.Q., Yang, Z.P., Gao, Y.H., Liu, H., Liu, X.R., & Jin, X.G. (2023). Wetting deformation characteristics of soil–rock mixture considering the water-disintegration of red stratum soft rock. *Acta Geotechnica*, *19*(7), 4381–4397. https://doi.org/10.1007/s11440-023-02162-2

12. Liu, C.D., Cheng, Y., Jiao, Y.Y., Zhang, G.H., Zhang, W.S., Ou, G.Z., & Tan, F. (2021). Experimental study on the effect of water on mechanical properties of swelling mudstone. *Engineering Geology*, *295*, Article 106448. https://doi.org/10.1016/j.enggeo.2021.106448

13. Liu, H.D., Liu, J.J., Zhang, S.Y., Feng, L.Y., & Qiu, L. (2023a). Experimental study on compression characteristics of fractured soft rock and its Mohr-Coulomb criterion. *Theoretical and Applied Fracture Mechanics*, *125*, 103820. https://doi.org/10.1016/j.tafmec.2023.103820

14. Liu, X.C., Huang, F., Zheng, A.C., & Hu, X.T. (2024). Micro-dissolution mechanism and macro-mechanical behavior of red-bed soft rock under dry-wet cycle. *Materials Letters*, *362*, Article 136220. https://doi.org/10.1016/j.matlet.2024.136220

15. Liu, Y., Huang, D., Peng, J.B., & Guo, Y.Q. (2023b). Analysis of the effect of rock layer structure on the toppling failure evolution of soft-hard interbedded anti-dip slopes. *Engineering Failure Analysis*, *145*, Article 107005. https://doi.org/10.1016/j.engfailanal.2022.107005

16. Luo, P.K., Li, D.Y., Ma, J.Y., Zhou, A.H., & Zhang, C.X. (2023). Experimental investigation on mechanical properties and deformation mechanism of soft-hard interbedded rock-like material based on digital image correlation. *Journal of Materials Research and Technology*, *24*, 1922–1938. https://doi.org/10.1016/j.jmrt.2023.03.145

17. Meng, Q.B., Liu, J.F., Pu, H., Huang, B.X., Zhang, Z.Z., & Wu, J.Y. (2023). Effects of cyclic loading and unloading rates on the energy evolution of rocks with different lithology. *Geomechanics for Energy and the Environment*, *34*, Article 100455. https://doi.org/10.1016/j.gete.2023.100455

18. Vásárhelyi, B. (2005). Statistical analysis of the influence of water content on the strength of the miocene limestone. *Rock Mechanics and Rock Engineering*, *38*(1), 69–76. https://doi.org/10.1007/s00603-004-0034-3

19. Vásárhelyi, B. & Ván, P. (2006). Influence of water content on the strength of rock. *Engineering Geology*, *84*(1–2), 70–74. https://doi.org/10.1016/j.enggeo.2005.11.011

20. Wasantha, P.L.P. & Ranjith, P.G. (2014). Water-weakening behavior of Hawkesbury sandstone in brittle regime. *Engineering Geology*, *178*, 91–101. https://doi.org/10.1016/j.enggeo.2014.05.015

21. Xi, Y., Wang, H.Y., Li, J., Jiang, H.L., & Fan, L.F. (2023). Transient process of mechanical response and energy conversion of rocks with different lithologies under impact loading. *Geoenergy Science and Engineering*, *228*, Article 211978. https://doi.org/10.1016/j.geoen.2023.211978

22. Xie, H.P., Li, L.Y., Peng, R.D., & Ju, Y. (2009). Energy analysis and criteria for structural failure of rocks. *Journal of Rock Mechanics and Geotechnical Engineering*, *1*(1), 11–20. https://doi.org/10.3724/SP.J.1235.2009.00011

23. Yu, H.T., Liu, Z.B., Zhang, Y., Luo, T.Y., Tang, Y.S., Zhang, Q.S., & Wang, Y.T. (2023). The disintegration mechanism analysis of soft rock due to water intrusion based on discrete element method. *Computers & Geosciences*, *171*, Article 105289. https://doi.org/10.1016/j.cageo.2022.105289

24. Zhang, G.D., Ling, S.X., Liao, Z.X., Xiao, C.J., & Wu, X.Y. (2024). Mechanism and influence on red-bed soft rock disintegration durability of particle roughness based on experiment and fractal theory. *Construction and Building Materials*, *419*, Article 135504. https://doi.org/10.1016/j.conbuildmat.2024.135504

Manuscript received June 4, 2024; accepted for publication March 7, 2025; published online April 15, 2025.

JOURNAL OF THEORETICAL
AND APPLIED MECHANICS
63, 2, pp. 443–455, Warsaw 2025
https://doi.org/10.15632/jtam-pl/203595

EXPERIMENTAL STUDY ON MECHANICAL PROPERTIES OF RED SANDSTONE UNDER CYCLIC LOAD AFTER DRY-WET CYCLES

Hongjun LI[1], Baoyun ZHAO[2*], Liyun ZHANG[3], Hang ZOU[4]

[1] *China Anergy Group Third Engineering Bureau Co.Ltd., Chengdu 610036, China*
[2] *School of Civil and Hydraulic Engineering, Chongqing University of Science and Technology, Chongqing 401331, China*
[3] *Finance Bureau of Korla City, Bazhou 841000, Xinjiang, China*
[4] *Chongqing Industry Polytechnic College, Chongqing 401120, China*
*corresponding author, *baoyun666@cqust.edu.cn*

This study investigates the mechanical properties of red sandstone in the Three Gorges Reservoir area under cyclic loading after dry-wet cycles. Results show that the first five cycles significantly affect the dry mass, with a 1.16 % decrease. Under the same cyclic loads, peak stress decreases with increasing dry-wet cycles, and stress-strain curves exhibit hysteresis loops. Elastic modulus increases in stages with the stress amplitude, with the first five cycles having the most significant impact. These findings offer crucial theoretical guidance for safeguarding hazardous slopes within the drawdown zone of the Three Gorges Reservoir.

Keywords: dry-wet cycle; red sandstone; mechanical properties; cyclic loading.

1. Introduction

The bank's rock slopes have undergone varying intensities of dry-wet cycles resulting from periodic fluctuations in reservoir water levels (Liu *et al.*, 2022; Zhao *et al.*, 2017; Akcanca & Aytekin, 2014). The rock engineering of reservoir banks, such as bank slope roads and bridge foundations, is often affected by cyclic loads caused by vehicle vibrations. The rock slope engineering on the reservoir bank may be affected by dynamic loads, such as earthquakes and blasting, following the dry-wet cycle. Therefore, investigating the mechanical properties of rocks under cyclic loading after undergoing dry-wet cycles is of preeminent importance.

Repeated dry-wet cycles degrade the mechanical properties of rocks, resulting in deformation and eventual failure of the rock mass (Huang *et al.*, 2022). In the past few decades, extensive experimental studies have focused on examining how dry-wet cycles affect the weakening of different rock types (Huan *et al.*, 2024; Cao *et al.*, 2022; Wang *et al.*, 2023). Ma *et al.* (2022) found that the uniaxial compressive strength (UCS) of sandstone decreases by 4.58 % in a single dry-wet cycle and by 18.35 % after 20 cycles. Hu *et al.* (2022) observed a reduction in the quality, hardness, and surface gloss of coal samples, alongside an increase in surface roughness after 50 dry-wet cycles. Zheng *et al.* (2023) noted that the elastic modulus, cohesion, and friction of argillaceous sandstone significantly deteriorated during the initial dry-wet cycles, followed by a gradual decline after 10 cycles. Furthermore, utilizing the energy dissipation theory, Chen *et al.* (2019) discovered that rock energy dissipation progressively increased with the number of dry-wet cycles. The energy evolution of rock samples is categorized into the initial dissipation energy stage, stable dissipation energy growth stage, dissipation energy acceleration stage, and dissipation energy surge stage. Liu *et al.* (2019) based their research on thermodynamics and energy dissipation principles to formulate damage evolution equations for red sandstone subjected to various dry-wet cycles.

Since 2005, numerous researchers have conducted studies investigating the impact of cyclic loadings on the fatigue properties of rocks. A series of fatigue tests have been performed to examine fatigue and energy dissipation in materials such as sandstone (Zhao *et al.*, 2023; 2024), marble (Wang *et al.*, 2021), granite (Zhou *et al.*, 2021), and other materials (Zhou *et al.*, 2023). In the field of rock fatigue characteristics, factors such as loading frequency, temperature, stress amplitude, and cycle number have been identified as significantly impacting the strength of rock masses during cyclic loading and unloading tests. In the domain of energy dissipation, researchers utilize the internal elastic energy principle of rocks to analyze energy evolution trends under fatigue loading. Li *et al.* (2023) demonstrated that the total energy involved in the energy transformation process encompasses both elastic energy, representing elastic deformation, and dissipated energy, which accounts for anchor deformation, fracture propagation, and plastic damage. Gao *et al.* (2022) discovered that the elastic strain and elastic energy density increase linearly with deviatoric stress and are proportional to confining pressure and loading rate. Conversely, the irreversible strain and dissipated energy density increase exponentially with the deviatoric stress.

In summary, extensive research has been conducted on the effects of dry-wet cycles on the mechanical properties of rocks, as well as on the cyclic loading mechanical properties of rocks, yielding significant and valuable findings. This paper focuses on the rock slopes within the fluctuating zone of the Three Gorges Reservoir as the primary research subject. Considering the actual environmental conditions of the slope, this study explores the mechanical characteristics of red sandstone under cyclic loading following various numbers of dry-wet cycles. Cyclic loading tests were performed on representative red sandstone samples from the selected site, and a detailed analysis of energy dissipation in the sandstone samples was conducted.

2. Sample preparation and dry-wet cycle test

2.1. Red sandstone sample preparation

The samples were collected from the slope area with fluctuating water levels of the Three Gorges Reservoir in Chongqing, China (Chen *et al.*, 2023), which consisted of typical red sandstone. The test samples exhibited a dense structure with coarser mineral particles, a flesh-red color, and a density of approximately 2380 kg/m^3. Following the methodology proposed by the International Society for Rock Mechanics (ISRM) (Fairhurst & Hudson, 1999), all tested sandstone samples were cylindrical, with a diameter of approximately 50 mm and a length of 100 mm (see Fig. 1).

Fig. 1. Red sandstone samples.

2.2. Dry-wet cycle test

2.2.1. Testing procedure

To thoroughly investigate the effects of dry-wet cycles on the physical properties of red sandstone, five groups with varying numbers of dry-wet cycles were established (Zhao *et al.*, 2021), specifically 0, 10, 20, 30, and 40 cycles. The processed samples were initially dried in a dry-

ing oven at temperatures ranging from 105 °C to 110 °C for 12 hours. After a slight cooling to room temperature, the samples were subsequently placed in a vacuum saturation instrument for 12 hours to achieve saturation. This drying and saturation process was alternately repeated until the desired number of cycles was attained (see Fig. 2 for an illustration of the testing apparatus). Additionally, the samples were weighed after each drying and saturation cycle.

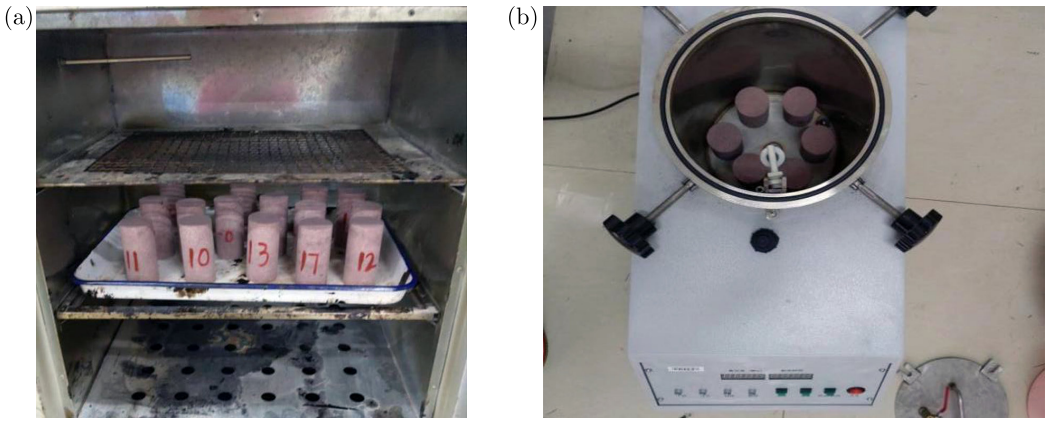

Fig. 2. Dry and wet cycle test apparatus: (a) drying box; (b) vacuum saturating instrument.

2.2.2. Change in law of dried and saturated mass

Figure 3 illustrates the mass of red sandstone after different dry and wet cycles. It can be observed that the curve of the dried mass no longer exhibits discernible changes after 5 cycles of the wet and dry decrease. It is important to note that the mass of the dried sample without a dry-wet cycle was 453.70 g. After 5 cycles, it decreased to 448.40 g, representing a decrease of 1.16 % compared to the initial mass. Subsequently, the mass of the dried sample showed no significant change. Conversely, the curve of the saturated mass increased rapidly after 5 dry and wet cycles and then reached a relatively steady state. Figure 3 illustrates that the initial 5 dry-wet cycles had a significant impact on the mass of sandstone.

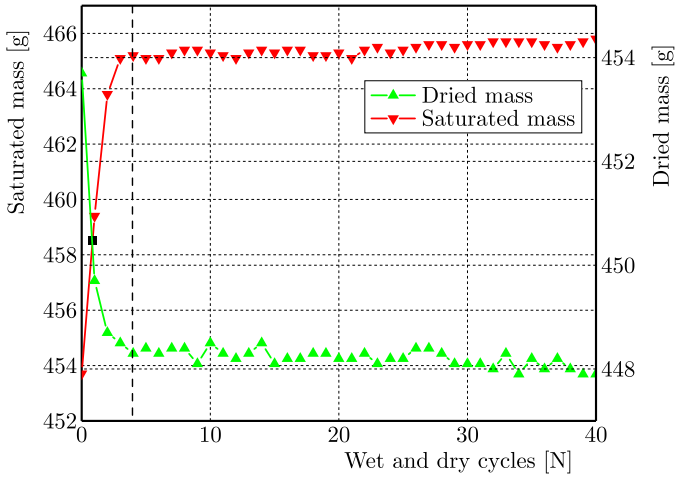

Fig. 3. Mass change of red sandstone under dry-wet cycle.

3. Cyclic loading and unloading tests on red sandstone after dry-wet cycles

3.1. Method of cyclic loading and unloading test

Building upon previous findings regarding the behavior of dried and saturated mass, this study employed red sandstone samples subjected to 0, 5, and 10 dry-wet cycles to perform uni-

axial cyclic loading and unloading tests. The lower limit of cyclic load stress was set at 5 MPa, while the upper limits were 10 MPa, 15 MPa, 20 MPa, 25 MPa, 30 MPa, 40 MPa, and 45 MPa, respectively. In other words, the stress amplitudes were 5 MPa, 10 MPa, 15 MPa, 20 MPa, 25 MPa, 30 MPa, 35 MPa, and 40 MPa, respectively. The loading frequency was 0.02 Hz and there were 10 loading and unloading cycles under the same stress amplitude. Upon completion of the loading and unloading cycles, a loading rate of 0.05 mm/min was applied continuously until the sample failure occurred. The detailed loading and unloading procedure is illustrated in Fig. 4.

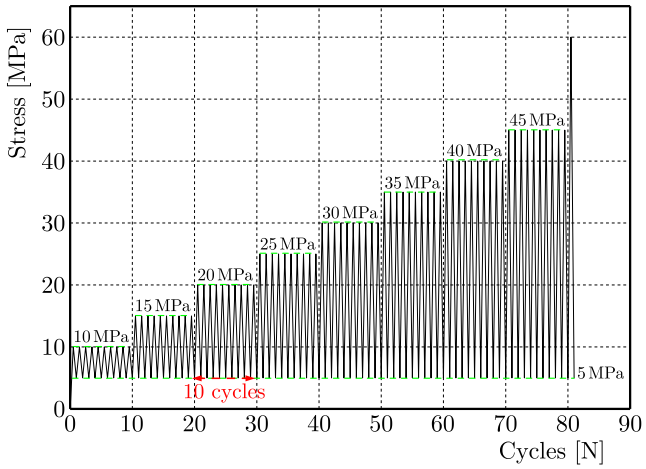

Fig. 4. Diagram of cyclic loading and unloading modes.

3.2. Testing equipment

The TFD-2000 microcomputer servo-controlled rock triaxial testing machine is utilized in the test, as shown in Fig. 5 (Li *et al.*, 2024). This equipment serves as the primary testing apparatus for evaluating the mechanical properties of materials such as rock and cement. It can be employed in various tests, including rock uniaxial compression test, triaxial compression test, and corresponding creep tests. The testing machine has a maximum axial compressive force of 2000 kN, with a force measurement error range of ±0.5 %. During testing, data on stress, strain, force, and displacement were automatically collected by microcomputers, recorded, and analyzed in real time.

Fig. 5. TFD-2000 microcomputer servo-controlled rock triaxial testing machine.

3.3. Stress-strain curve of red sandstone

Figure 6 illustrates the cyclic loading and unloading stress-strain curve of the red sandstone after undergoing dry-wet cycles. Under identical stress amplitudes, the hysteresis loops of the

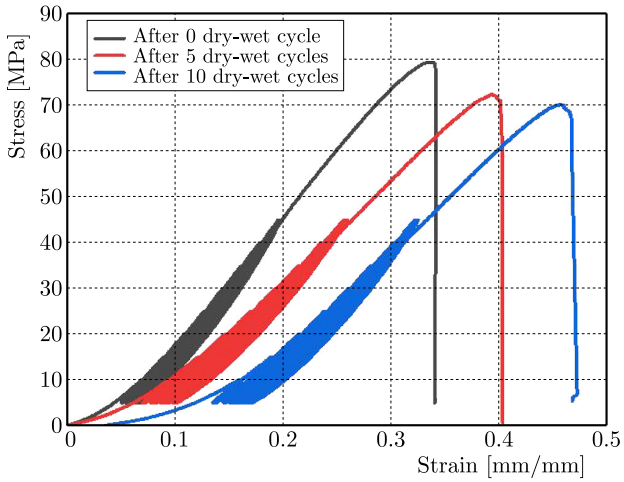

Fig. 6. Uniaxial stress-strain curves of red sandstone under different loading cycles after dry-wet cycles.

stress-strain curves for red sandstone samples exhibit a "sparse-to-dense" development pattern, with the area of the hysteresis loops gradually decreasing until reaching a stable state. Additionally, Fig. 6 shows that the slope of the stress-strain curve for red sandstone decreases as the number of dry-wet cycles increases, while the axial strain concurrently increases.

Figure 7 presents a comparison between the cyclic stress–strain curves of red sandstone and the uniaxial stress–strain curves of samples subjected to different dry-wet cycles. Figure 7 clearly demonstrates that the strength of red sandstone samples subjected to dry-wet cycles is significantly lower than that of samples without such cycles. The increases in lateral and axial strains due to dry-wet cycles can be attributed to the weakening of the rock strength caused by the accumulation of fatigue damage. As the stress amplitude increases, both lateral and axial strains of red sandstone also increase. Under identical stress conditions, axial strain is greater than lateral strain. The increase in axial strain is more pronounced at low stress amplitudes, whereas the opposite occurs at high stress amplitudes as the stress amplitude continues to rise.

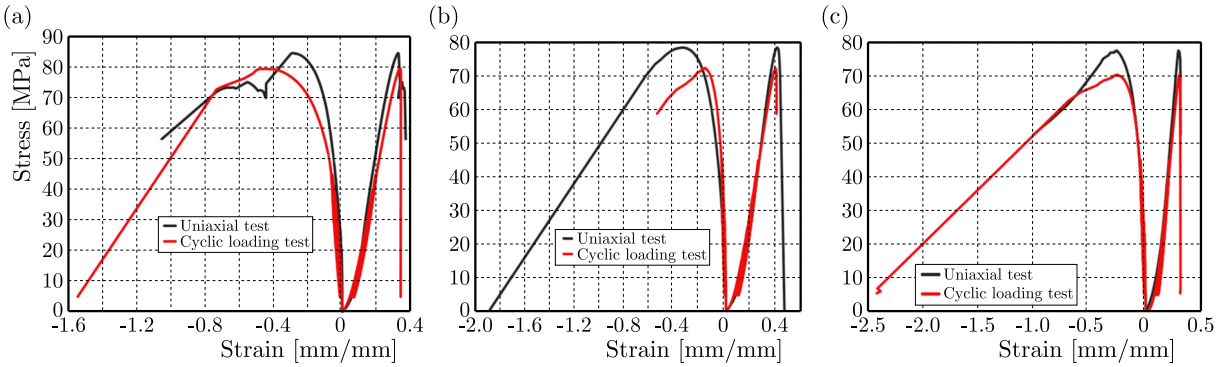

Fig. 7. Stress-strain curves of red sandstone under uniaxial cyclic loading after different dry-wet cycles: (a) 0 dry-wet cycle; (b) 5 dry-wet cycles; (c) 10 dry-wet cycles.

Figure 8 illustrates the comparison of the peak stress during the loading cycle of specimens after various dry-wet cycles with their uniaxial compressive strength (UCS). It is evident that the peak strength of both samples types decreases with the number of dry-wet cycles, mirroring the decrease in UCS. The decreasing trend of the peak stress during cyclic loading and unloading is more pronounced compared to UCS. This phenomenon suggests that cyclic loading intensified the internal damage within the rock, leading to its deteriorated state. Figure 8 shows that the initial strength of red sandstone samples is 84.48 MPa without cyclic loading. After undergoing

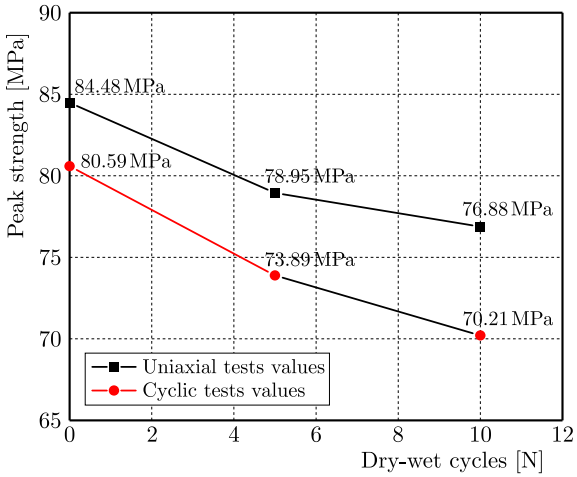

Fig. 8. Comparison of peak strength between conventional uniaxial results and uniaxial cyclic loading results.

5 dry-wet cycles, the strength decreases to 78.95 MPa, and further decreases to 76.88 MPa after 10 dry-wet cycles. Compared to the initial state, peak stress reductions were 6.55 % and 9.63 %, respectively. The peak stress of samples was significantly reduced under loading cycles of varying amplitudes, from 80.59 MPa after zero dry-wet cycles to 73.89 MPa after five cycles and further to 70.21 MPa after ten cycles. Compared to uniaxial strength under static loading conditions, the peak stress of red sandstone samples decreased by 4.60 %, 6.41 %, and 8.68 % after cyclic loading and unloading. According to statistical results, peak stress decreases with an increasing number of dry-wet cycles, with the most significant reduction occurring within the first 5 cycles.

3.4. Law of elastic modulus change

The elastic modulus is a critical parameter for evaluating the mechanical properties of rock. According to the "Regulation for Testing the Physical and Mechanical Properties of Rock – Part 19: Test for Determining the Deformability of Rock in Uniaxial Compression" (DZ/T 0276.19-2015), the elastic modulus for each load cycle is calculated using Eq. (3.1):

$$E = \frac{\sigma_{\max} - \sigma_{\min}}{\varepsilon_{\max} - \varepsilon_{\min}}, \tag{3.1}$$

where E is the elastic modulus (in MPa); $\sigma_{\max}$ is the maximum axial stress in each cycle (in MPa); $\sigma_{\min}$ is the minimum axial stress in each cycle; $\varepsilon_{\max}$ is the maximum axial strain, and $\varepsilon_{\min}$ is the minimum axial strain, respectively.

Using Eq. (3.1), the elastic modulus of the sample under different stress amplitudes after various dry-wet cycles was calculated, as presented in Table 1.

Figure 9 shows the variation of the elastic modulus of the red sandstone during different loading and unloading cycles after different dry-wet cycles. It is evident that there is a gradual increase in the overall elastic modulus. At relatively small stress amplitudes, the elastic modulus of the samples fluctuates with an increasing number of loading cycles. When the stress amplitude increases to 5 MPa–20 MPa, the change in elastic modulus becomes less significant with an increasing number of cyclic loading cycles. Additionally, Fig. 9 shows that the modulus of elasticity of rock samples decreases after being subjected to varying degrees of dry-wet cycles. The elastic modulus decreased significantly after the first 5 cycles, with a smaller decrease from cycles 5 to 10 compared to the initial five cycles.

Figure 10 illustrates the variation of the average modulus of elasticity at different stress amplitude values with the number of dry-wet cycles. It is evident that during the dry-wet cycles, the average modulus of the samples gradually decreases with an increasing number of

Table 1. Elastic modulus of red sandstone with different stress amplitudes after undergone different dry-wet cycles.

Mechanical parameters	Stress amplitude [MPa]	Dry and wet cycles [N]		
		0	5	10
Modulus of elasticity [GPa]	5–10	9.50	5.34	4.83
	5–15	10.26	6.75	5.76
	5–20	10.89	7.69	6.90
	5–25	11.35	8.17	7.76
	5-30	11.60	8.57	8.19
	5–35	11.98	9.31	8.64
	5–40	12.12	9.93	9.01
	5–45	12.23	10.72	9.42

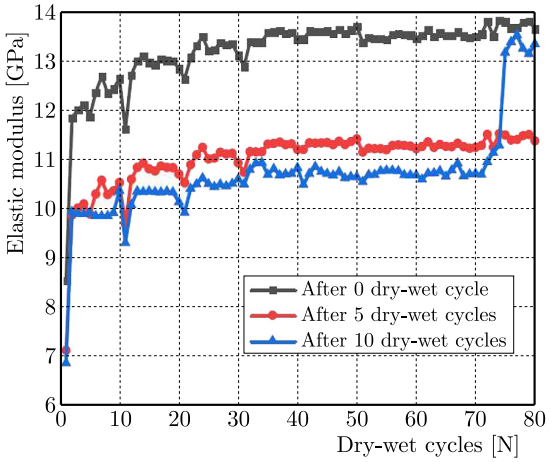

Fig. 9. Elastic modulus of red sandstone after different dry-wet cycle.

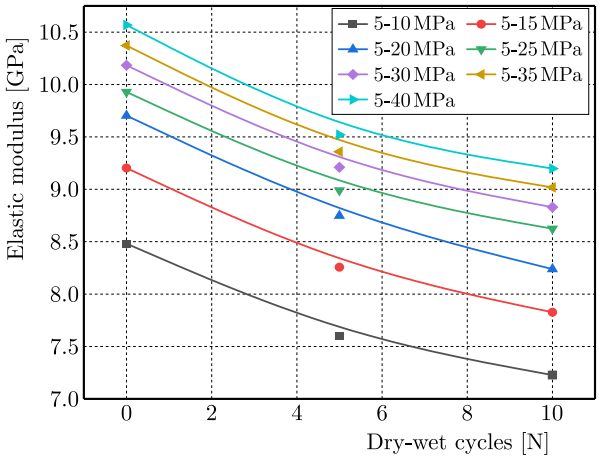

Fig. 10. Curve of elastic modulus vs dry-wet cycle under different cyclic loading.

cycles, a trend that can be expressed using a secondary function. Samples subjected to 5 dry-wet cycles experienced an average decrease in modulus from 42.37 % to 27.56 % compared to samples not subjected to dry-wet cycles. In summary, the initial five dry-wet cycles had the most significant effect on the average elastic modulus of red sandstone samples, closely mirroring the degradation of sample mass during various dry-wet cycles.

Figure 11 shows that the average elastic modulus of red sandstone samples increases with stress amplitude values. However, the growth rate exhibits a gradual slowing trend. The increase in average elastic modulus is most significant at lower stress amplitudes due to the gradual closure of internal cracks under relatively lower stress amplitudes, resulting in a greater increase in stiffness and elastic modulus. As the cyclic stress amplitude value increases, cyclic loading gradually initiates fatigue damage to the samples, leading to the formation of numerous new cracks. Consequently, the stiffness of the rock decreases gradually, and the growth rate of the elastic modulus slows down progressively. The elastic modulus of red sandstone exhibited a significant increase (25.72 % to 76.31 %) when the stress amplitude was elevated from 5 MPa to 40 MPa. This increase was more pronounced at relatively low stress amplitudes (0 MPa to 5 MPa), and the rate of increase slowed as the stress amplitude reached 5 MPa to 30 MPa.

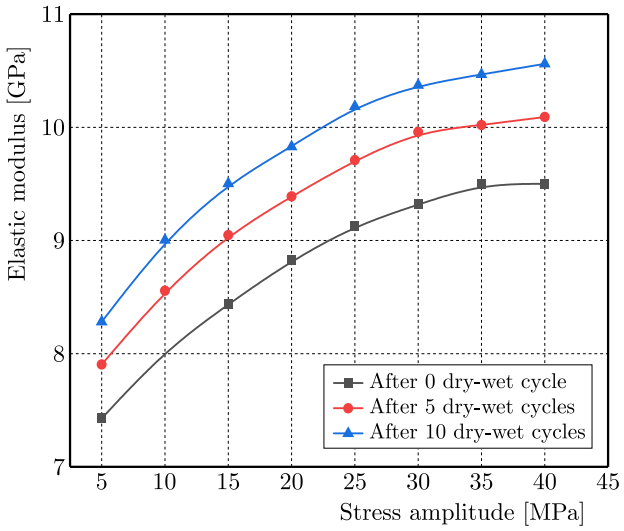

Fig. 11. Curve of elastic modulus vs stress amplitude.

3.5. Failure mode analysis of red sandstone

Figure 12 illustrates the failure modes of sandstone samples subjected to cyclic loading and unloading after a series of dry and wet cycles.

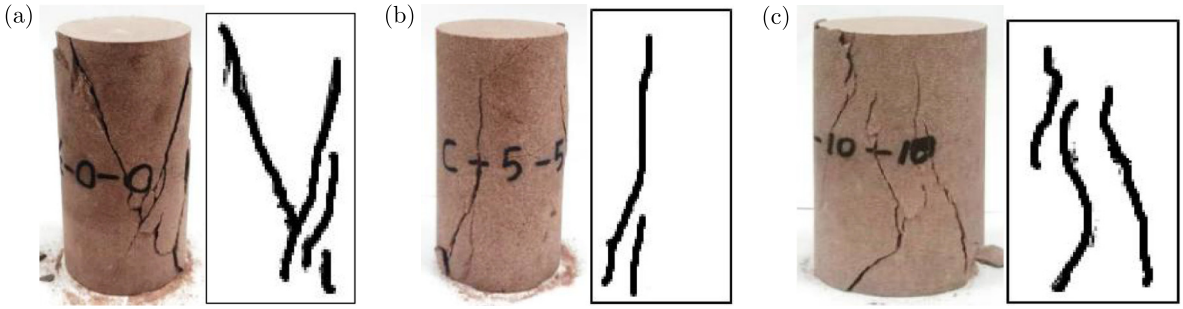

Fig. 12. Uniaxial cyclic load failure mode of red sandstone after different dry-wet cycles: (a) 0 dry-wet cycle; (b) 5 dry-wet cycles; (c) 10 dry-wet cycles.

Figure 12 shows that the failure mode under uniaxial cyclic loading and unloading was primarily splitting failure accompanied by shear failure, differing from the failure modes observed in uniaxial compression tests. The failure mode of red sandstone was predominantly splitting failure throughout the entire specimen. It was also observed that the degree of splitting was greater under cyclic loading due to a significant increase in micro-fractures, volume expansion, and local fractures. This phenomenon becomes increasingly apparent as the number of dry-wet

cycles increases. Additionally, Fig. 12 shows that as the number of dry-wet cycles increases, rock samples become more fragmented, and the number of macro-fractures also rises. Furthermore, as the number of dry-wet cycles increases, the number of through-cracks rapidly escalates.

4. Energy dissipation characteristics

External work is the primary factor contributing to rock failure during rock mechanics experiments (Zhao *et al.*, 2023). Throughout the loading and unloading phases, it is assumed that no heat exchange occurs between the rock sample and its surrounding environment. According to the first law of thermodynamics, the work done by external forces constitutes the total input energy, and the individual energy components can be expressed as

$$U_i = U_{ei} + U_{di}, \tag{4.1}$$

where U_i is the input energy of the i-th cycle, U_{ei} is the elastic energy of the i-th cycle, U_{di} is the dissipated energy of the i-th cycle.

Figure 13 illustrates the schematic diagram of energy calculation under cyclic loading and unloading conditions. The input energy, elastic energy, and dissipated energy of the i-th cycle can be obtained by integrating the loading and unloading sections of the stress-axial strain curve, respectively, as depicted in Eqs. (4.2)–(4.4) (Zhao *et al.*, 2023):

$$U_i = \int_{\varepsilon^l_{\min(2)}}^{\varepsilon^l_{\max}} \mathrm{d}\varepsilon \int_{\sigma_{\min}}^{\sigma_{\max}} f(\sigma_1)\,\mathrm{d}\sigma, \tag{4.2}$$

$$U_{ei} = \int_{\varepsilon^l_{\min(1)}}^{\varepsilon^l_{\max}} \mathrm{d}\varepsilon \int_{\sigma_{\min}}^{\sigma_{\max}} f(\sigma_2)\,\mathrm{d}\sigma, \tag{4.3}$$

$$U_{di} = U_i - U_{ei}, \tag{4.4}$$

where $\sigma_{\max}$ and $\sigma_{\min}$ are the maximum and minimum loading stress, $f(\sigma 1)$ is the equation of loading curve of the i-th cycle, $f(\sigma 2)$ is the equation of unloading curve of the i-th cycle, $\varepsilon^l_{\max}$, $\varepsilon^l_{\min(1)}$, and $\varepsilon^l_{\min(2)}$ are the axial strains at different loading and unloading points of the i-th cycle, respectively.

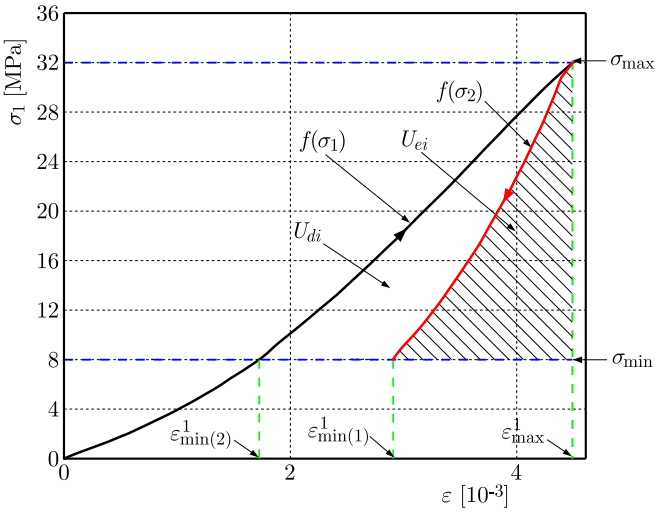

Fig. 13. Schematic diagram of sandstone energy calculation under cyclic loading and unloading condition.

The dissipated energy of sandstone under different loading and unloading after various dry-wet cycles is shown in Fig. 14. It can be observed that dissipated energy increases in stages with rising stress amplitudes. Figure 15 illustrates the variation in dissipated energy between dry-wet cycles under different loading cycles, while Fig. 16 depicts the correlation between dissipated energy and stress amplitudes. It is evident from Fig. 15 that dissipated energy increases logarithmically with the increasing number of dry-wet cycles. From the 0th cycle to the 10th cycle, the dissipated energy under stress amplitudes of 5 MPa, 10 MPa, 15 MPa, 20 MPa, 25 MPa, 30 MPa, 35 MPa, and 40 MPa increased by 138.21 %, 101.48 %, 91.74 %, 83.86 %, 78.90 %, and 65.78 %, respectively. This indicates that the dissipated energy release by the samples accelerates most significantly after five dry-wet cycles. As the number of dry-wet cycles continues to increase, the growth of dissipated energy gradually stabilizes. Throughout the entire process of cyclic loading and unloading of red sandstone, the force applied by the testing machine induces strain, comprising both elastic and plastic strains. The plastic strain escalates with an increasing number of cycles, leading to irreversible permanent deformation of the sample. During cyclic loading, the testing machine causes irreversible damage to the sample, with damage accumulating internally until the rock is ultimately destroyed. From energy Eqs. (4.1)–(4.4), it is evident that the dissipated energy in red sandstone is directly proportional to stress amplitude. As the stress amplitude increases, the dissipated energy also increases. In other words, the energy required

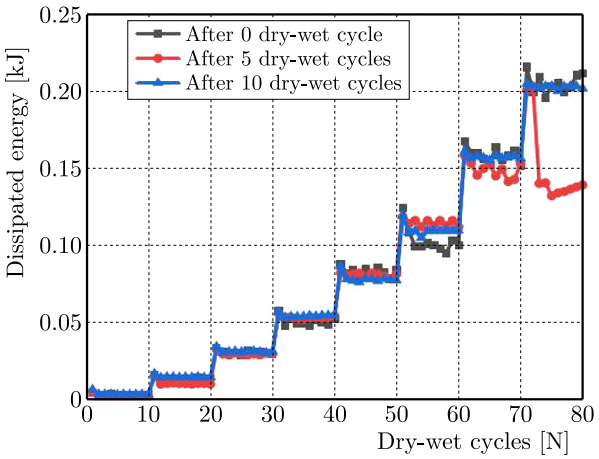

Fig. 14. Curve of the dissipated energy vs loading cycles.

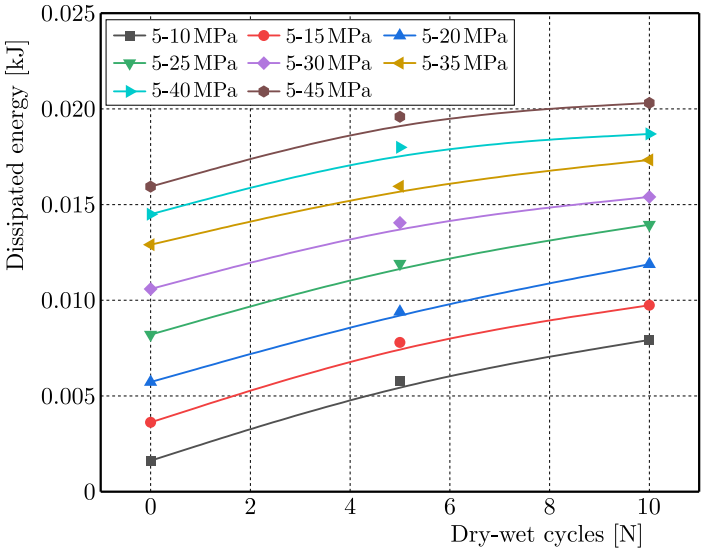

Fig. 15. Curve of the dissipated energy vs dry-wet cycles under different loading cycles.

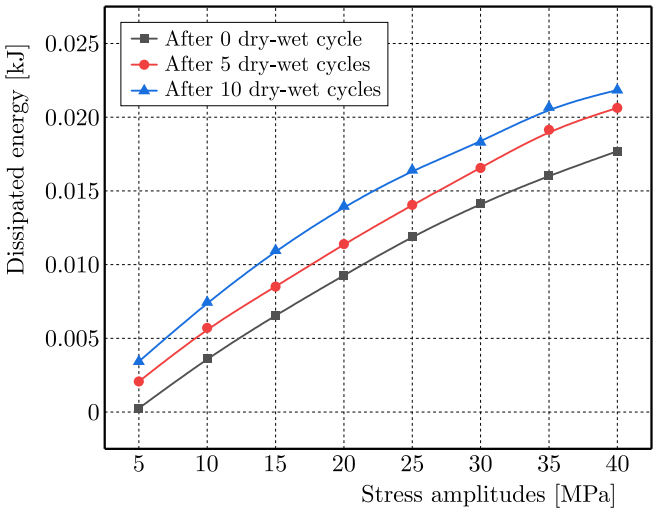

Fig. 16. Curve of the dissipated energy vs stress amplitudes.

to connect the pores and cracks in the rock increases, leading to faster damage and failure, ultimately resulting in a shorter fatigue life of the rock.

Figure 16 illustrates the variation in the dissipated energy law with stress amplitudes at different stress amplitude levels. It can be clearly observed that the dissipated energy of the red sandstone increased with the rise in stress amplitudes. It was found that the dissipated energy increased slowly with stress amplitudes, and a higher number of dry-wet cycles leads to relatively higher dissipated energy under the same stress amplitudes.

5. Conclusion

This research paper assesses the cyclic loading mechanical features and failure patterns of red sandstone after exposure to wet dry-wet cycles. The study aimed to evaluate the degradation of strength parameters, such as peak strength and elastic modulus. Additionally, the energy dissipation characteristics of the samples under cyclic loading were examined, yielding the following primary findings:

The initial 5 dry-wet cycles had a remarkable impact on the sandstone's physical and mechanical properties. The sandstone's mass decreased by 1.16 % after five cycles, and the average elastic modulus of samples under cyclic loads with different stress amplitudes dropped from 42.37 % to 27.56 %, showing that these initial cycles significantly affected the mass and elastic modulus, paralleling the degradation trend during dry-wet cycling.

As the number of dry-wet cycles increased, the stress-strain curve of red sandstone changed notably. The peak stress of samples was substantially reduced under different loading amplitudes, decreasing by 8.31 % after five cycles and 12.88 % after ten cycles. Meanwhile, the primary failure mode of specimens was splitting damage accompanied by partial shear damage.

The dissipated energy demonstrated a clear growth pattern. It increased in stages with the rise of stress amplitudes and logarithmically with the number of dry-wet cycles. From the 0th to the 10th cycle, under stress amplitudes ranging from 5 MPa to 40 MPa, the dissipated energy registered increases between 65.78 % and 138.21 %.

These findings are of paramount importance in comprehending the alterations in the mechanical properties and failure patterns of red sandstone as it undergoes cyclic loading and unloading processes after being subjected to various dry-wet cycles. This understanding provides theoretical guidance for the protection of hazardous slopes in the drawdown zone of the Three Gorges Reservoir.

Acknowledgments

The authors would like to thank the editors and anonymous referees for detailed and valuable suggestions that helped to improve the original manuscript to its present form.

This research was funded by the National Natural Science Foundation of China (grant no. 41302223), the Scientific and Technological Research Program of Chongqing Municipal Education Commission (grant no. KJZD-K2021 01505).

References

1. Akcanca, F. & Aytekin, M. (2014). Impact of wetting-drying cycles on the hydraulic conductivity of liners made of lime-stabilized sand-bentonite mixtures for sanitary landfills. *Environmental Earth Sciences*, *72*(1), 59–66. https://doi.org/10.1007/s12665-013-2936-4
2. Cao, Y.P., Sun, Q., Yang, X.Y., Dang, C., & Geng, J.S. (2022). Sandstone weathering under dry-wet cycling in NaCl solution. *Bulletin of Engineering Geology and the Environment*, *81*(11), Article 490. https://doi.org/10.1007/s10064-022-02992-6
3. Chen, C., Zhao, B.Y., Zhang, L.Y., & Huang, W. (2023). Mechanism of strength deterioration of red sandstone on reservoir bank slopes under the action of dry-wet cycles. *Scientifc Reports*, *13*, Article 20027. https://doi.org/10.1038/s41598-023-47397-x
4. Chen, X.X., He, P., & Qin, Z. (2019). Strength weakening and energy mechanism of rocks subjected to wet-dry cycles. *Geotechnical and Geological Engineering*, *37*(5), 3915–3923. https://doi.org/10.1007/s10706-019-00881-6
5. Fairhurst, C.E. & Hudson, J.A. (1999). Discussion: Draft ISRM suggested method for the complete stress-strain curve for intact rock in uniaxial compression. *International Journal of Rock Mechanics and Mining Sciences*, *36*(3), 279–289. https://doi.org/10.1016/S0148-9062(99)00006-6
6. Gao, D.Y., Sang, S.X., Liu, S.Q., Wu, J., Geng, J.S., Tao, W., & Sun, T.M. (2022). Experimental study on the deformation behaviour, energy evolution law and failure mechanism of tectonic coal subjected to cyclic loads. *International Journal of Mining Science and Technology*, *32*(6), 1301–1313. https://doi.org/10.1016/j.ijmst.2022.10.004
7. Hu, X., Sun, Q., Wang, S.F., Wei, S.N., Ding, X.Y., & Zhao, X.C. (2022). Study on deterioration characteristics of combustion metamorphic rocks under dry-wet cycling. *Bulletin of Engineering Geology and the Environment*, *81*(11), Article 467. https://doi.org/10.1007/s10064-022-02966-8
8. Huan, M., Jiang, S., Zhang, Y.C., Jiang, Y.J., Zhang, X.D., & Xu, C.S. (2024). A new stability analysis model for wet-dry sensitive rocks surrounding underground excavations based on disturbed state concept theory. *International Journal of Rock Mechanics and Mining Sciences*, *174*, Article 105653. https://doi.org/10.1016/j.ijrmms.2024.105653
9. Huang, Z., Zhang, W., Zhang, H., Zhang, J.B., & Zhao, J.H. (2022). Damage characteristics and new constitutive model of sandstone under wet-dry cycles. *Journal of Mountain Science*, *19*(7), 2111–2125. https://doi.org/10.1007/s11629-021-7239-8
10. Li, H., Zhao, B., Hou, Z., & Min, H. (2024). Experimental study on the mechanical properties of rock–concrete composite specimens under cyclic loading. *Buildings*, *14*(3), Article 854. https://doi.org/10.3390/buildings14030854
11. Li, Y.Q., Huang, D., & He, J. (2023). Energy evolution and damage constitutive model of anchored jointed rock masses under static and fatigue loads. *International Journal of Fatigue*, *167*(Part A), Article 107313. https://doi.org/10.1016/j.ijfatigue.2022.107313
12. Liu, S., Yang, G.S., & Dong, X.H. (2019). Experimental study on influence of wetting-drying cycles on mechanical characteristics and damage of red sandstone (in Chinese), *Coal Science and Technology*, *47*(4), 101–106.
13. Liu, X.X., Li, Y., & Wang, W.W. (2022). Study on mechanical properties and energy characteristics of carbonaceous shale with different fissure angles under dry-wet cycles. *Bulletin of Engineering Geology and the Environment*, *81*(8), Article 319. https://doi.org/10.1007/s10064-022-02823-8

14. Ma, D.H., Yao, H.Y., Xiong, J., Zhu, D.Y., & Lu, J.G. (2022). Experimental study on the deterioration mechanism of sandstone under the condition of wet-dry cycles. *KSCE Journal of Civil Engineering*, *26*(6), 2685–2694. https://doi.org/10.1007/s12205-022-1723-8

15. Ministry of Natural Resources, China. (2015). *Regulation for testing the physical and mechanical properties of rock – Part 19: Test for determining the deformability of rock in uniaxial compression* (DZ/T 0276.19-2015).

16. Wang, G.L., Zhang, T.Y., & Zhang, L. (2023). The law of strength damage and deterioration of jointed sandstone after dry-wet cycles. *Journal of Mountain Science*, *20*(4), 1170–1182. https://doi.org/10.1007/s11629-022-7605-1

17. Wang, Y., Feng, W.K., Hu, R.L., & Li, C.H. (2021). Fracture evolution and energy characteristics during marble failure under triaxial fatigue cyclic and confining pressure unloading (FC-CPU) conditions. *Rock Mechanics and Rock Engineering*, *54*(2), 799–818. https://doi.org/10.1007/s00603-020-02299-6

18. Zhao, B.Y., Li, Y.F., Huang, W., Yang, J.S., Sun, J.C., Li, W.C., Zhang, L.Y., & Zhang, L. (2021). Mechanical characteristics of red sandstone under cyclic wetting and drying. *Environmental Earth Sciences*, *80*(22), Article 738. https://doi.org/10.1007/s12665-021-10067-0

19. Zhao, B.Y., Wu, Y.J., Yang, J.S., Sun, J.C., Huang, W., Li, Z.Y., & Zhang, S.H. (2023). Mechanical properties of gas storage sandstone under uniaxial cyclic loading and unloading condition. *Periodica Polytechnica Civil Engineering*, *67*(2), 603–618. https://doi.org/10.3311/PPci.21620

20. Zhao, K., Zhang, L., Yang, D.X., Jin, J.F., Zheng, P., Wang, X., Ran, S.H., & Deng, D.M. (2024). Cyclic impact damage and water saturation effects on mechanical properties and Kaiser effect of red sandstone under uniaxial cyclic loading and unloading compression. *Rock Mechanics and Rock Engineering*, *57*(1), 181–195. https://doi.org/10.1007/s00603-023-03574-y

21. Zhao, Z.H., Yang, J., Zhou, D., & Chen, Y.F. (2017). Experimental investigation on the wetting-induced weakening of sandstone joints. *Engineering Geology*, *225*, 61–67. https://doi.org/10.1016/j.enggeo.2017.04.008

22. Zheng, J.C., Chen, W., Zheng, K.R., Gu, Y.P., Wang, F., Huang, Z., & Li, Y. (2023). Stability analysis of gravity anchor foundation of layered argillaceous sandstone under dry-wet cycles. *Journal of Mountain Science*, *20*(4), 1118–1130. https://doi.org/10.1007/s11629-022-7610-4

23. Zhou, Y., Zhao, D.J., Li, B., Wang, H.Y., Tang, Q.Q., & Zhang, Z.Z. (2021). Fatigue damage mechanism and deformation behaviour of granite under ultrahigh-frequency cyclic loading conditions. *Rock Mechanics and Rock Engineering*, *54*(9), 4723–4739. https://doi.org/10.1007/s00603-021-02524-w

24. Zhou, Y.Q., Sheng, Q., Fu, X.D., & Ding, H.F. (2023). The difference between the dynamic deformation properties of rock material under seismic load and cyclic loading: a case study on Kobe wave. *Mechanics of Time-Dependent Materials*, *27*(2), 401–426. https://doi.org/10.1007/s11043-022-09585-6

Manuscript received October 14, 2024; accepted for publication March 31, 2025; published online April 22, 2025.

Contents